Table 4
Friction factor data and proportional errors of smooth tube 2.

Mass flow rate	Re	Mass flux	Friction factor results			
			Blasius [5]	Petukhov [6]	Experiment	Correlation 2
kg/s	–	kg/m^{2}s	–	–	–	
0.0233	5446	464	0.0368	0.0376	0.0583	0.0549
0.0312	7274	620	0.0342	0.0345	0.0473	0.0481
0.0408	9532	812	0.0320	0.0319	0.0416	0.0425
0.0475	11,139	945	0.0308	0.0305	0.0380	0.0396
0.0575	13,296	1127	0.0294	0.0291	0.0360	0.0365
0.0675	15,636	1326	0.0283	0.0279	0.0333	0.0339
0.0742	17,467	1475	0.0275	0.0271	0.0325	0.0322
0.0833	19,640	1658	0.0267	0.0263	0.0319	0.0305
0.0917	21,646	1824	0.0261	0.0256	0.0304	0.0292
0.1008	23,831	2006	0.0254	0.0250	0.0292	0.0279
Proportional errors			%	%	%	%
			19.92	20.54	–	3.04

of correlation for power model is in the program 0.992 showing that the correlation model explains 99.292% of variability in the data.

Developed correlation according to Power model as a result of curve fitting process is given below:

Developed correlation of friction factor for 6/8 mm smooth tube 1 is obtained as:

$$f_{correlation1} = 0.269 \cdot Re^{-0.217}. \tag{4.1}$$

Pressure drop is obtained for the developed correlation of smooth tube 1 as:

$$\Delta P_{correlation2} = f_{correlation1} \cdot \frac{L}{D} \cdot \frac{\rho \cdot V_m{}^2}{2}. \tag{4.2}$$

Developed correlation of friction factor for 8/10 mm smooth tube 2 is determined as:

$$f_{correlation2} = 2.793 \cdot Re^{-0.456}. \tag{4.3}$$

Pressure drop is obtained for the developed correlation of smooth tube 2 as:

$$\Delta P_{correlation2} = f_{correlation2} \cdot \frac{L}{D} \cdot \frac{\rho \cdot V_m{}^2}{2}. \tag{4.4}$$

Proposed correlation 3 for the simulated smooth tube 3 is developed by using 6/8 mm and 8/10 mm tube data in order to predict smooth tube 3 having 7.48 mm inside diameter. Developed correlation according to Saturation Growth-Rate Model as a result of curve fitting process is given below:

Developed correlation of friction factor for smooth tube 3 is calculated as:

$$f_{correlation3} = \frac{0.026 \cdot Re}{-2915 + Re}. \tag{4.5}$$

Pressure drop is obtained for the developed correlation of smooth tube 3 as:

$$\Delta P_{correlation3} = f_{correlation3} \cdot \frac{L}{D} \cdot \frac{\rho \cdot V_m{}^2}{2}. \tag{4.6}$$

Developed correlation according to Power model as a result of curve fitting process is given below:

Result of curve fitting process produced correlations for microfin tube is given below:

$$f_{correlation4} = 0.605 \cdot Re^{-0.226} \tag{4.7}$$

$$\Delta P_{correlation4} = f_{correlation4} \cdot \frac{L}{D_e} \cdot \frac{\rho \cdot V_m{}^2}{2}. \tag{4.8}$$

Error for obtained results is calculated by means of equation below:

$$Error = \frac{1}{N}\sum_{i=1}^{N}\left|\left(\frac{Predicted\,value - Measured\,value}{Measured\,value}\right)\cdot 100.\right| \tag{4.9}$$

5. Results and discussion

In order to develop the empirical friction factor correlation and investigate the characteristics of pressure drop during single phase flow of pure water in horizontal smooth and microfin tubes with inner diameters of 6, 7.48 and 8 mm, the present study were performed at the Heat and Thermodynamics Division lab. in YTU. Calculated and experimental friction factors and their proportional errors of smooth tube 2 having 8 mm i.d. and microfin tube having 7.48 mm i.d. are shown in Tables 4 and 5, respectively. Comparison of pressure drop results for investigated smooth and microfin tubes using well-known equations and proposed ones in the literature and their alteration with Reynolds number and mass flux are shown from Figs. 2 to 4. Comparison of measured experimental pressure drop data for simulated smooth tube and microfin tube having equivalent inner diameter are

Table 5
Friction factor data and proportional errors of microfin tube.

Mass flow rate	Re	Mass flux	Friction factor results								
			Wang et al. [2]	Siddique and Alhazmy [10]	Jensen and Vlakancic [12]	Zdaniuk et al. [14]	Al Fahed et al. [15]	Webb et al. [19]	Haaland [28]	Experiment	Correlation 4
kg/s	–	kg/m^{2}s	–	–	–	–	–	–	–	–	–
0.0233	5725	526	0.050	0.076	0.085	0.032	0.078	0.023	0.062	0.086	0.085
0.0312	7657	695	0.050	0.070	0.079	0.029	0.071	0.021	0.060	0.080	0.079
0.0408	10,140	920	0.049	0.064	0.073	0.027	0.066	0.020	0.059	0.074	0.074
0.0475	11,850	1070	0.049	0.061	0.070	0.026	0.063	0.019	0.059	0.071	0.072
0.0575	14,353	1295	0.049	0.058	0.067	0.024	0.059	0.018	0.058	0.066	0.069
0.0675	16,842	1521	0.049	0.056	0.064	0.023	0.056	0.017	0.058	0.065	0.066
0.0742	18,582	1671	0.0495	0.0544	0.0633	0.0226	0.0552	0.0169	0.0585	0.0666	0.0653
0.0833	20,894	1877	0.0494	0.0527	0.0615	0.0218	0.0533	0.0163	0.0583	0.0638	0.0636
0.0917	23,027	2065	0.0493	0.0512	0.0600	0.0212	0.0518	0.0159	0.0581	0.0638	0.0622
0.1008	25,353	2271	0.0493	0.0498	0.0586	0.0206	0.0504	0.0155	0.0580	0.0604	0.0609
Proportional errors			%	%	%	%	%	%	%	%	%
			30.0	17.0	2,36	65.3	15.7	74.4	16.6	–	2,5

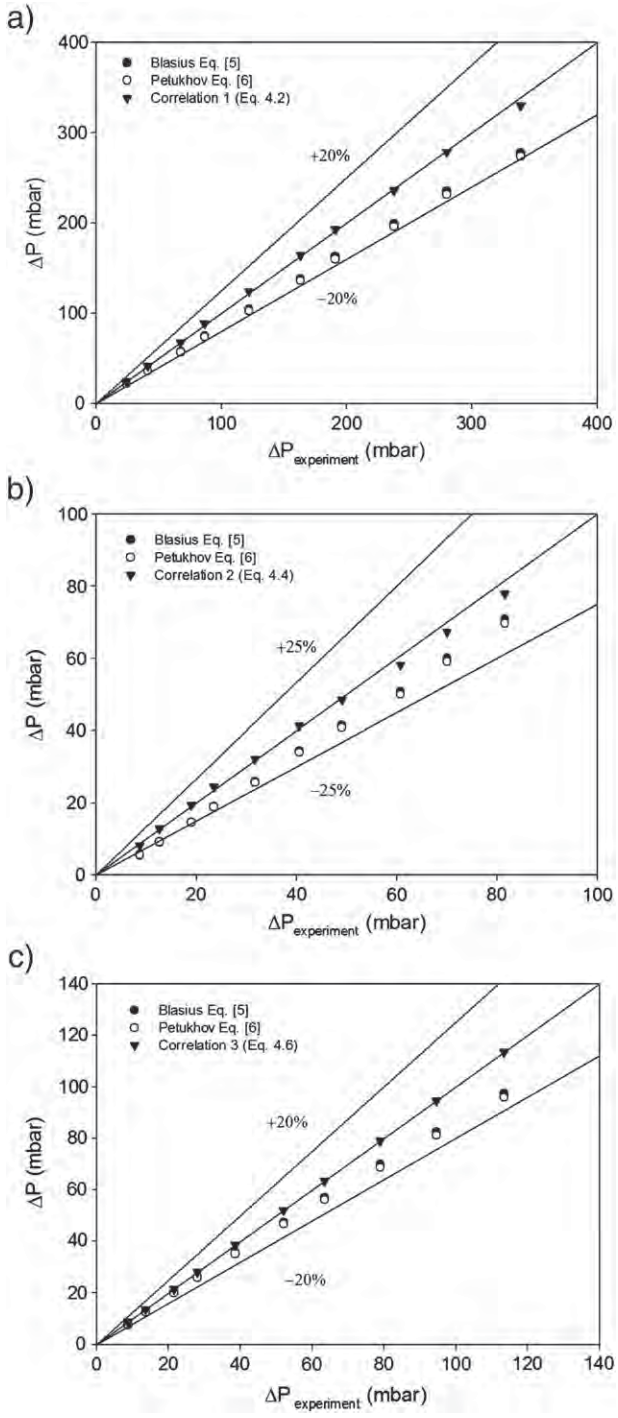

Fig. 2. Comparison of pressure drop results for the smooth tubes 1 (a), 2 (b) and 3 (c).

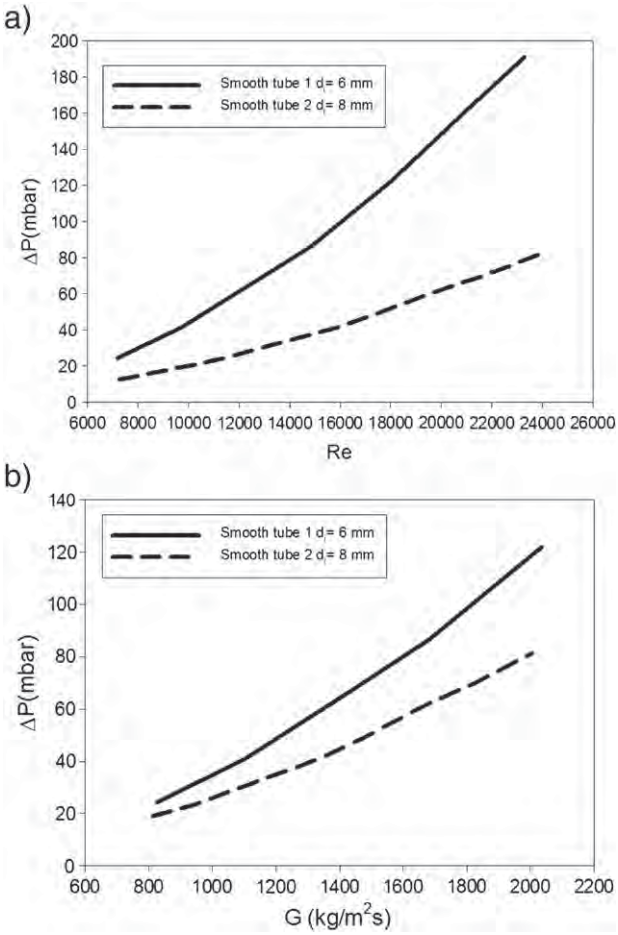

Fig. 3. Pressure drop comparison of smooth tubes according to Reynolds number (a) and mass flux (b).

illustrated in Table 6 and Fig. 5. The following paragraphs present the indirectly determined friction factor and measured pressure drops using relevant measured data. Discussion of the results will be given in turn as follows:

In Table 4, friction factor results of smooth tube 2 calculated according to Blasius equation [5], Petukhov equation [6], developed correlation of Eq. (4.3) and experimental friction factor and their proportional errors are shown. It should be noted that proportional errors of developed correlation 2 was calculated as 3.04% as shown in Table 4.

Friction factor data and proportional errors of microfin tube can be seen Table 5. It was observed that the friction factor decreased gradually as the Reynolds number increased. Decrease in the friction factor is related to sublayer thickness. When Reynolds number is increased, the thickness of sublayer decreases and it resulted in lower friction factor results.

Comparison of pressure drop results for the smooth tubes 1, 2 and 3 can be seen in Fig. 2(a), (b) and (c), respectively. It was observed that the experimental result were in good agreement with Blasius [5] and Petukhov [6] equations for all smooth tubes. It means that these equations can be used for prediction of the pressure drop of smooth tubes.

Fig. 3(a) and (b) illustrates pressure drop comparison of smooth tubes having different inside diameter according to Reynolds number and mass flux, respectively. As seen in Fig. 3, tube having lower inside diameter showed higher pressure drop when it is compared with higher one.

Fig. 4(a) and (b) shows variation of pressure drop with Reynolds number and mass flux for microfin tube, respectively. It was shown that the pressure drop increased gradually as the Reynolds number and mass flux increased. Fig. 4(c) compares experimental results with equations of other researchers given in Table 5. The experimental results were found in good agreement in the range of ±20% except Zdaniuk et al. [14] and Webb et al. [19] equations.

Fig. 5(a) and (b) represents pressure drop comparison of smooth tube 3 and microfin tubes according to Reynolds number and mass flux, respectively. Experimental pressure drop data for smooth and microfin tubes can be seen in Table 6. As it expected, the pressure drop for microfin tube was higher than the smooth tube. It means that the microfin tube produced more flow disturbance by the occurrence of the swirl flow and flow recirculation produced by the fins, which led to higher frictional pressure drop.

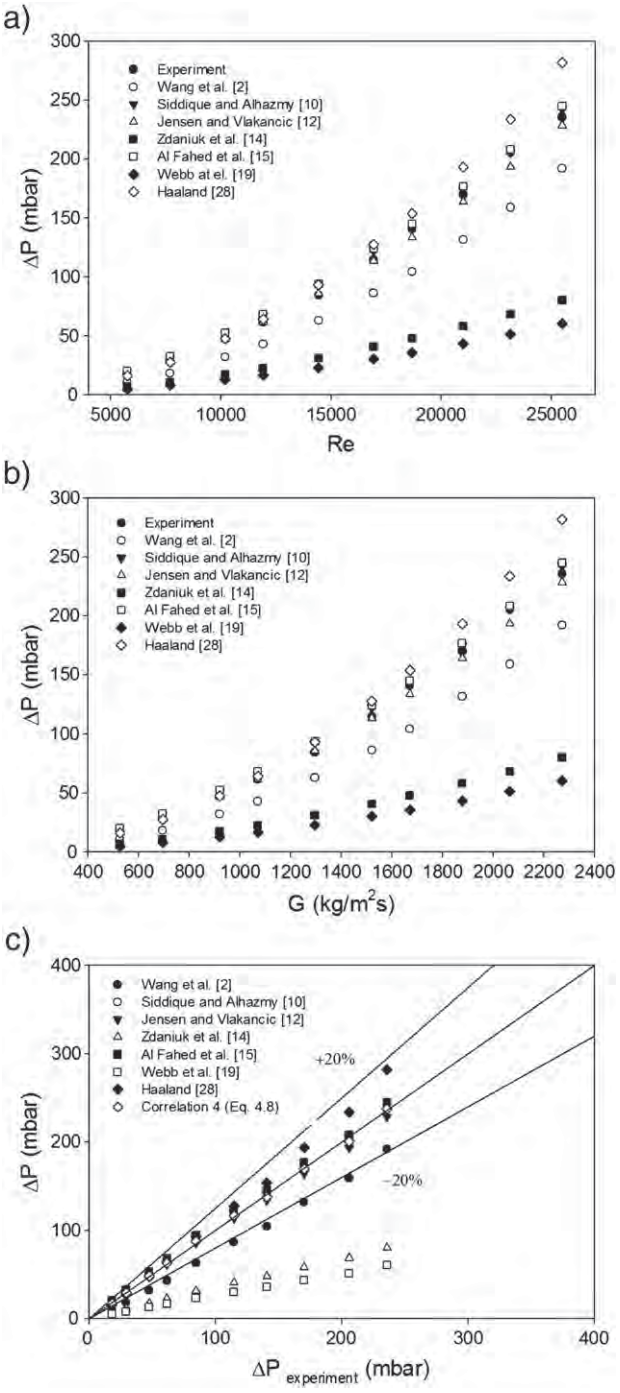

Fig. 4. Predicted and measured pressure drop results for microfin tube according to Reynolds number (a), mass flux (b) and comparison of them (c).

A large number of graphics could be generated from the output of the calculations, however, due to space limitation, only typical results are shown for limited data. It should be also noted that detailed information on the explanations above and some additional figures with different experimental parameters related to this study can be seen from the authors' previous publications [30–34].

6. Conclusion

Heat transfer enhancement has become a more important issue over the years. Microfin tubes play an important role in heat transfer enhancement applications. Many researchers have focused on two phase heat transfer characteristic of microfin tubes but single phase heat transfer characteristic of enhanced tubes are not well studied due to the new technological developments. In the present paper, pressure drop by means of microfin tube in single phase flow was discussed. Following results were obtained.

Table 6
Experimental pressure drop data for smooth and microfin tubes.

Smooth tube			Microfin tube			Pressure drop augmentation
Re	G	ΔP	Re	G	ΔP	
–	kg/m²s	mbar	–	kg/m²s	mbar	$P_{microfin}/P_{smooth}$
5809	528	8.70	5725	526	18.00	2.07
7759	705	13.60	7657	695	29.20	2.15
10,167	924	21.47	10,140	920	47.40	2.21
11,881	1075	28.02	11,850	1070	61.50	2.19
14,183	1283	38.54	14,353	1295	84.40	2.19
16,678	1509	52.01	16,842	1521	114.40	2.20
18,631	1679	63.42	18,582	1671	140.60	2.22
20,949	1886	78.97	20,894	1877	170.00	2.15
23,089	2075	94.58	23,027	2065	205.70	2.17
25,420	2282	113.41	25,353	2271	235.70	2.08

- It was found that the friction factor decreased gradually as the Reynolds number increased for both smooth and microfin tubes. With increase in Reynolds number, the thickness of sublayer decreases and hence in tube turbulent flow becomes more uniform.
- It was found that the pressure drop increased gradually as the Reynolds number increased for both smooth and microfin tubes.
- The pressure drop in smooth tube having lower inside diameter was higher than in the smooth tube having higher inside diameter.

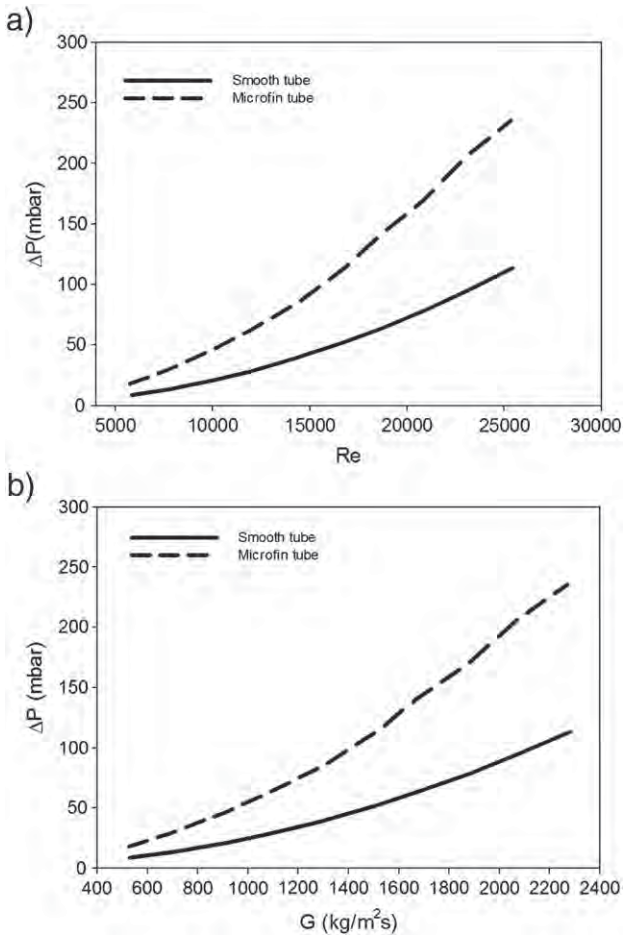

Fig. 5. Pressure drop comparison of smooth tube 3 and microfin tubes according to Reynolds number (a) and mass flux (b).

- The friction factor and pressure drop values for the microfin tube were higher than those for the smooth tube. This implies that the microfin tube produced more flow disturbance by the occurrence of the swirl flow and flow recirculation produced by the fins, which led to higher frictional pressure drop.
- Experimental results for smooth tubes compared with equations given in the literature. It is shown that there was good agreement for smooth tube results.
- Experimental results for microfin tube compared with equations given in the literature. It is shown that there was conflict about predict of microfin tube pressure drop characteristic prediction. By the means of experimental data, new correlation was developed in order to predict the friction factor for investigated microfin tube.

Acknowledgments

The present study was financially supported by Yildiz Technical University. The second author wishes to thank KMUTT for providing him with a Post-doctoral fellowship, while the third author wish to acknowledge the support provided by the Thailand Research Fund. The authors also wish to thank Wieland-Wilke AG (Ulm, Germany) for valuable donation of the micro-fin tube used in the present study.

References

[1] K. Fuji, N. Itoh, T. Innami, H. Kimura, N. Nakayama and T. Yanugidi, Heat transfer pipe, US Patent 4044797, assigned to Hitachi Ltd. 1977.
[2] C.C. Wang, C.B. Chiou, D.C. Lu, Single-phase heat transfer and flow friction correlations for micro-fin tubes, International Journal of Heat and Fluid Flow 17 (1996) 5–8.
[3] R.K. Shah, Assessment of modified Wilson plot techniques for obtaining heat exchanger design data, Proc. 9th Int. Heat Transfer Conf., 5, 1990, pp. 51–56.
[4] J.B. Copetti, M.H. Macagnan, D. De Souza, R.D. Oliveski, Experiments with micro-fin tube in single phase, International Journal of Refrigeration 27 (2004) 876–883.
[5] P.R.H. Blasius, Das AehnlichkeitsgesetzbeiReibungsvorgangen in Flüssigkeiten, Forschungsheft 131 (1913) 1–41.
[6] B.S. Petukhov, "Heat Transfer and Friction in Turbulent Referred to in Handbook of Single-Phase Convective Pipe Flow with Variable Physical Properties", In Heat Transferred. T. F. Irvine and J. P. New York: Wiley Interscience, 1987. Hartnett, 6. New York: Academic Press 1970.
[7] F.W. Dittus, L.M.K. Boelter, "Heat transfer in automobile radiators of the tubular type", University of California, Berkeley, Publications in Engineering 2 (1930) 443–461.
[8] V. Gnielinski, New equations for heat and mass transfer in turbulent pipe and channel flow, International Chemical Engineering 16 (1976) 359–368.
[9] L. Xiao-Wei, M. Ji-An, L. Zhi-Xin, Experimental study of single phase pressure drop and heat transfer in a micro-fin tube, Experimeantal Thermal and Fluid Science 32 (2007) 641–648.
[10] M. Siddique, M. Alhazmy, Experimental study of turbulent single-phase flow and heat transfer inside a micro-finned tube, International Journal of Refrigeration 31 (2008) 234–241.
[11] T.C. Carnavos, Heat transfer performance of internally finned tubes in turbulent flow', Heat Transfer Engineering 1 (1980) 32–37.
[12] M.K. Jensen, A. Vlakancic, Experimental investigation of turbulent heat transfer and fluid flow in internally finned tubes, International Journal of Heat and Mass Transfer 42 (1999) 1343–1351.
[13] S. Kakac, The effect of temperature dependent fluid properties on convective heat transfer, Handbook of Single-Phase Convective Heat Transfer, New York, John Wiley, 1987.
[14] G.J. Zdaniuk, L.M. Chamra, P.J. Mago, Experimental determination of heat transfer and friction in helically-finned tubes, Experimental Thermal and Fluid Science 32 (2008) 761–775.
[15] S.F. Al-Fahed, Z.H. Ayub, A.M. Al-Marsfie, B.M. Soliman, Heat transfer and pressure drop in a tube with internal microfins under turbulent water flow conditions, Experimental Thermal and Fluid Science 7 (1993) 249–253.
[16] E.E. Wilson, A basis for rational design of heat transfer apparatus, Transactions of ASME 37 (1915) 47–70.
[17] D.H. Han, K. Lee, Single phase heat transfer and flow characteristics of micro-fin tubes, Applied Thermal Engineering 25 (2005) 1657–1669.
[18] H.S. Wang, J.W. Rose, Prediction of effective friction factors for single-phase flow in horizontal microfin tubes, International Journal of Refrigeration 27 (2004) 904–913.
[19] R.L. Webb, R. Narayanamurthy, P. Thors, Heat transfer and friction characteristics of internal helical-rib roughness, Transaction of the ASME Journal of Heat Transfer 12 (2000) 301–318.
[20] T.S. Ravigururajan, A.E. Bergles, General correlations for pressure drop and heat transfer for single-phase turbulent flow in internally ribbed tubes, Augmentation of Heat Transfer in Energy Systems, ASME-HTD 52 (1985) 9–20.
[21] A. Cavallini, D. Del Col, L. Doretti, G.A. Longo, L. Rossetto, Pressure drop during condensation and vaporisation of refrigerants inside enhanced tubes, Heat Technology 15 (1) (1997) 3–10.
[22] P. Naphon, P. Sriromruln, Single-phase heat transfer and pressure drop in the micro-fin tubes with coiled wire insert, International Communications in Heat and Mass Transfer 33 (2006) 176–183.
[23] L.B. Brognaux, R.L. Webb, L.M. Chamra, Single phase heat transfer in micro-fin tubes, International Journal of Heat and Mass Transfer 40 (18) (1997) 4345–4357.
[24] Wieland Group Company, http://www.wieland.de/internet/en/produkte/Produits.jsp,01.10.2012.
[25] Y.A. Çengel, Heat Transfer: A Practical Approach, 3rd ed. McGraw Hill, 2006.
[26] L.F. Moody, Friction factors for pipe flows, Transactions of the ASME 66 (1944) 671–684.
[27] C.F. Colebrook, Turbulent flow in pipes, with particular reference to the transition region between smooth and rough pipe laws, Journal of the Institution of Civil Engineers 11 (1939) 133–156.
[28] S.E. Haaland, Simple and explicit formulas for the friction factor in turbulent pipe flow, Journal of Fluids Engineering 89–90 (1983).
[29] Curve Expert 1.3, http://www.curveexpert.net/,21.11.2012.
[30] N. Kayaci, M. Balcilar, M. Tabatabaei, A. Celen, O. Yıldız, A.S. Dalkilic, S. Wongwises, Determination of the single-phase forced convection heat transfer characteristics of TiO_2 nanofluids flowing in smooth and micro-fin tubes by means of CFD and ANN analyses, Current Nanoscience 9 (2013) 61–80.
[31] Ö. Ağra, H. Demir, Ş.Ö. Atayılmaz, F. Kantaş, A.S. Dalkılıç, Numerical investigation of heat transfer and pressure drop in enhanced tubes, International Communications in Heat and Mass Transfer 38 (2011) 1384–1391.
[32] H. Demir, A.S. Dalkilic, N.A. Kurekci, W. Duangthongsuk, S. Wongwises, Numerical investigation on the single phase forced convection heat transfer characteristics of TiO_2 nanofluids in a double-tube counter flow heat exchanger, International Communications in Heat and Mass Transfer 38 (2011) 218–228.
[33] K. Aroonrat, C. Jumpholkul, R. Leelaprachakul, A.S. Dalkilic, O. Mahian, S. Wongwises, Heat transfer and single phase flow in internally grooved tubes, International Communications in Heat and Mass Transfer 42 (2013) 62–68.
[34] N. Kayaci, A. Celen, M. Tabatabei, O. Yıldız, A.S. Dalkılıç, S. Wongwises, Numerical investigation of heat transfer enhancement using water based nanofluids flowing in enhanced tubes, ASME 2012 International Mechanical Engineering Congress & Exposition, November 9–15 2012, ASME, USA.

Efficiencies for Partially Wetted Spine Fins: Uniform Cross Section, Conical, Concave Parabolic, and Convex Parabolic Spines

Worachest Pirompugd
Department of Mechanical Engineering,
Faculty of Engineering,
Burapha University, Saensook,
Muang, Chonburi 20131, Thailand

Somchai Wongwises[1]
Fluid Mechanics, Thermal Engineering and
Multiphase Flow Research Lab. (FUTURE),
Department of Mechanical Engineering,
Faculty of Engineering,
King Mongkut's University of
Technology Thonburi,
Bangmod, Bangkok 10140, Thailand
e-mail: somchai.won@kmutt.ac.th

In this study, efficiencies for partially wetted fins for the uniform cross section spine, conical spine, concave parabolic spine, and convex parabolic spine are presented using an analytical method. Depending on the set of boundary conditions, there are two methods for deriving the efficiencies of partially wet fins for each spine. The eight equations for fin efficiencies were investigated. Fin efficiency is a function of the length of the dry portion. Thus, the equations for calculating the length of the dry portion are also presented. The findings indicate that a larger cross-sectional fin results in a higher conduction heat transfer rate. Contrarily, the fin efficiency is lower. This is different from the longitudinal fin, for which the trend lines of heat transfer rate and fin efficiency are the same. This converse relationship is due to the effect of the ratio of the cross-sectional area to the surface area. Moreover, partially wet fin efficiencies decrease with increased relative humidity. For convenience, the approximate equation for efficiencies for partially wet fins, which is derived from the equations for fully wet and fully dry fin efficiencies, is also presented. [DOI: 10.1115/1.4024017]

Keywords: concave parabolic spine, conical spine, uniform cross section spine, convex parabolic spine, partially wet fin efficiency

1 Introduction

A passive technique for heat transfer enhancement is to extend surfaces. By increasing surface and turbulence, fins can enhance heat transfer rate. For heat transfer evaluation, fin efficiency is necessarily known. Schmidt [1] and Kern and Kraus [2] derived dry fin efficiencies for longitudinal fins, spines, and circular fins. Subsequently, Arslanturk [3], Heggs and Somasundram [4], Joneidi et al. [5], Kulkarni and Joglekar [6], and Sharqawy et al. [7] presented methods for evaluating heat transfer rate and dry fin efficiency, and studied the influence of fin thermal conductivity on fin efficiency. Cortes et al. [8] presented a numerical method for evaluating dry fin efficiencies for fins of composite materials of variable thickness.

However, the fins used in many applications are in fully wet or partially wet surface conditions. Exemplarily, in evaporators, which typically use aluminum fins with the surface temperature generally being below the dew point temperature. As a result, simultaneous heat and mass transfer occurs along the fin surfaces. Moreover, if the dew point temperature is higher than the outside tube temperature but it is lower than the fin tip temperature, the condition the partially wet surface is seen. In 1970, Threlkeld [9] presented a method to obtain fin efficiency in fully wet conditions based on the enthalpy potential. Thus, fully wet fin efficiencies can be obtained using the Threlkeld method. Moreover, many researchers have studied extended heat exchangers in fully wet surface conditions and applied wet fin efficiency in the reduction method. In 2000, Liang et al. [10] investigated the fully wet and partially wet fin efficiencies of a plate fin-and-tube heat exchanger. However, Liang et al. [10] did not present the exact partially wet fin efficiency. They only note that the partially wet fin efficiency was obtained by multiplying the fully wet fin efficiency by some variable. In 2007, using an analytical method, Pirompugd et al. [11] presented circular fin efficiency in partially wet surface conditions. In 2012, using an analytical method, Pirompugd and Wongwises [12] presented partially wet fin efficiencies for longitudinal fins of rectangular, triangular, concave parabolic, and convex parabolic profiles. Moreover, using their results, they presented the approximation method for evaluating partially wet fin efficiencies from dry and wet fin efficiencies. Nevertheless, the extended surfaces in some applications are in partially wet surface conditions and may not be of longitudinal geometry. However, there is little literature concerning fin efficiency related to partially wet surface conditions. Thus, the objective of this present study is to derive partially wet fin efficiencies for fins of uniform cross section, conical, concave parabolic, and convex parabolic spines.

2 Mathematical Modeling

2.1 Dry and Wet Fin Efficiency. Differential equations for heat transfer and their solutions for the four types of spines in dry conditions were proposed by Kern and Kraus [2]. Then, the fin efficiency that is the ratio of the actual heat transfer rate of fin to the ideal heat transfer rate by assuming base temperature to entire fin ($\eta = (q_{\text{actual}}/q_{\text{ideal}})$) can be shown as

$$\text{Uniform cross section spine} : \eta_{\text{const,dry}} = \frac{\tanh mb}{mb} \tag{1}$$

$$\text{Conical spine} : \eta_{\text{cone,dry}} = \frac{\sqrt{2}I_2(2\sqrt{2}mb)}{mbI_1(2\sqrt{2}mb)} \tag{2}$$

[1]Corresponding author.

Contributed by the Heat Transfer Division of ASME for publication in the JOURNAL OF HEAT TRANSFER. Manuscript received September 21, 2012; final manuscript received March 11, 2013; published online July 18, 2013. Assoc. Editor: Giulio Lorenzini.

$$\text{Concave spine}: \eta_{\text{ccave,dry}} = \frac{2}{1+\sqrt{1+\frac{8}{9}(mb)^2}} \tag{3}$$

$$\text{Convex spine}: \eta_{\text{cvex,dry}} = \frac{3I_1\left(\frac{4}{3}\sqrt{2}mb\right)}{2\sqrt{2}mbI_0\left(\frac{4}{3}\sqrt{2}mb\right)} \tag{4}$$

where $m = \sqrt{(h_c P/k_f A)}$ for uniform cross section spines, P is the fin perimeter, and $m = \sqrt{(2h_c/k_f\delta_0)}$ for conical, concave parabolic, and convex parabolic spines. The subscript of "const", "cone", "ccave", and "cvex" means the uniform cross section spine, conical spine, concave parabolic spine, and convex parabolic spine. Moreover, the subscript of "part", "dry", and "wet" mean partially wet, fully dry, and fully wet conditions.

Moreover, Eqs. (1)–(4) are generally used for fins in dry conditions. For fully wet surface conditions, Threlkeld [9] presented a wet fin efficiency that accounts for the sensible and latent heat for the longitudinal fin of a rectangular profile. With the Threlkeld method, for uniform cross section, conical, concave parabolic, and convex parabolic pines, the enthalpy excess profiles and wet fin efficiencies can be developed as follows:

$$\text{Uniform cross section spine}: \gamma_{\text{const,wet}} = \frac{\gamma_0 \cosh m_T x}{\cosh m_T b} \tag{5}$$

$$\eta_{\text{const,wet}} = \frac{\tanh m_T b}{m_T b} \tag{6}$$

$$\text{Conical spine}: \gamma_{\text{cone,wet}} = \gamma_0\left(\frac{b}{x}\right)^{0.5}\frac{I_1(2\sqrt{2}m_T\sqrt{bx})}{I_1(2\sqrt{2}m_T b)} \tag{7}$$

$$\eta_{\text{cone,wet}} = \frac{\sqrt{2}I_2(2\sqrt{2}m_T b)}{m_T b I_1(2\sqrt{2}m_T b)} \tag{8}$$

$$\text{Concave spine}: \gamma_{\text{ccave,wet}} = \gamma_0\left(\frac{x}{b}\right)^{-1.5+0.5(9+8m_T^2 b^2)^{0.5}} \tag{9}$$

$$\eta_{\text{ccave,wet}} = \frac{2}{1+\sqrt{1+\frac{8}{9}(m_T b)^2}} \tag{10}$$

$$\text{Convex spine}: \gamma_{\text{cvex,wet}} = \frac{\gamma_0 I_0\left(\frac{4}{3}\sqrt{2}m_T b^{0.25}x^{0.75}\right)}{I_0\left(\frac{4}{3}\sqrt{2}m_T b\right)} \tag{11}$$

$$\eta_{\text{cvex,wet}} = \frac{3I_1\left(\frac{4}{3}\sqrt{2}m_T b\right)}{2\sqrt{2}m_T bI_0\left(\frac{4}{3}\sqrt{2}m_T b\right)} \tag{12}$$

where $m_T = \sqrt{(h_o P/k_f A)}$ for uniform cross section spines and $m_T = \sqrt{(2h_o/k_f\delta_0)}$ for conical, concave parabolic, and convex parabolic spines and

$$h_o = \frac{1}{\frac{C_{p,a}}{b'_{w,f}h_c} + \frac{y_w}{k_w}} \tag{13}$$

The definition and derivation of h_o can be found in Threlkeld [9].

2.2 Partially Wet Fin Efficiency. As mentioned above, if the dew point temperature is higher than the fin base temperature (T_0) but lower than the fin tip temperature (T_{tip}), the water vapor in moist air condenses onto the fin surface only near the fin base region. There are two regions in a spine: (1) the wet region between the fin base and the saturation point and (2) the dry region between the saturation point and the fin tip, as shown in Figs. 1(*a*), 1(*b*), 1(*c*), and 1(*d*). The fin is in partially wet surface conditions.

For the dry fin portion ($0 \le x < x_{\text{dry}}$), neglecting heat transfer through the fin tip, the differential equation in terms of temperature excess $\theta = T - T_a$ can be developed as follows:

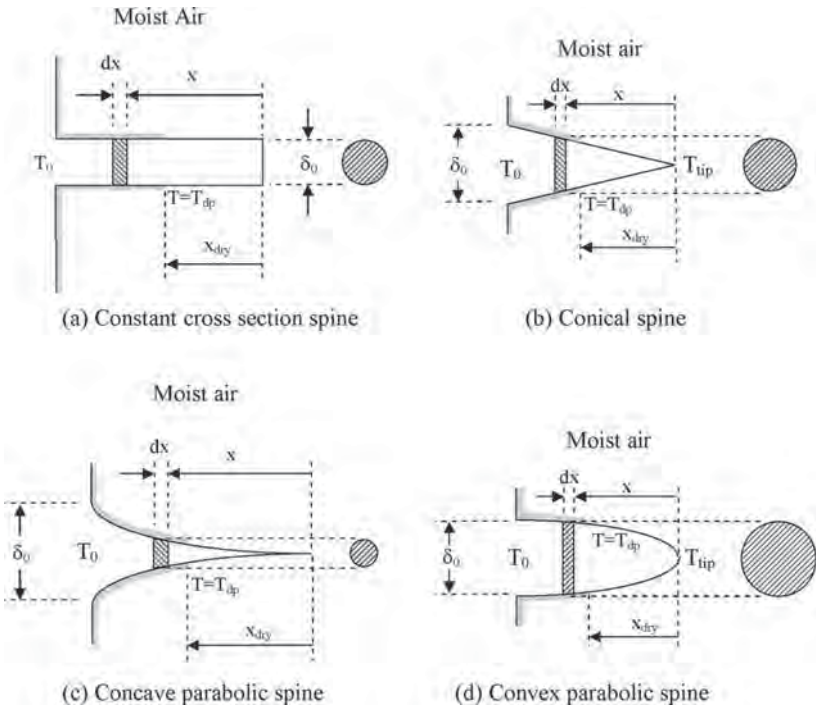

Fig. 1 Four spines in partially wet surface conditions

$$\text{Uniform cross section spine}: \frac{d^2\theta}{dx^2} - m\theta = 0 \tag{14}$$

$$\text{Conical spine}: \frac{d^2\theta}{dx^2} + \frac{2}{x}\frac{d\theta}{dx} - 2m^2\frac{b}{x}\theta = 0 \tag{15}$$

$$\text{Concave spine}: \frac{d^2\theta}{dv^2} + 3\frac{d\theta}{dv} - 2m^2b^2\theta = 0 \tag{16}$$

where $v = \ln x$

$$\text{Convex spine}: \frac{d^2\theta}{dx^2} + \frac{1}{x}\frac{d\theta}{dx} - 2m^2\sqrt{\frac{b}{x}}\theta = 0 \tag{17}$$

For the derivation of general solutions, Eqs. (14)–(17) must be subjected to the following two boundary conditions:

$$\left.\frac{d\theta}{dx}\right|_{x=0} = 0 \tag{18}$$

$$\theta|_{x=x_{\text{dry}}} = \theta_{dp} \tag{19}$$

where $\theta_{dp} = T_{dp} - T_a$

The first boundary condition (Eq. (18)) indicates that the heat transfer rate through the fin tip is zero. This is exactly true for the tiny fin that the fin thickness compared with length is very small. ($\delta_0 \ll b$). The second boundary condition (Eq. (19)) indicates that, at the saturation point ($x = x_{\text{dry}}$), the fin surface temperature is equal to the dew point temperature.

The solutions for Eqs. (14)–(17), with boundary conditions, i.e., Eqs. (18) and (19) are

$$\text{Uniform cross section spine}: \theta_{\text{const,part}} = \frac{\theta_{dp}\cosh mx}{\cosh mx_{\text{dry}}} \tag{20}$$

$$\text{Conical spine}: \theta_{\text{cone,part}} = \theta_{dp}\left(\frac{x}{x_{\text{dry}}}\right)^{-0.5}\frac{I_1(2\sqrt{2}m\sqrt{bx})}{I_1(2\sqrt{2}m\sqrt{bx_{\text{dry}}})} \tag{21}$$

$$\text{Concave spine}: \theta_{\text{ccave,part}} = \theta_{dp}\left(\frac{x}{x_{\text{dry}}}\right)^{-1.5+0.5(9+8m^2b^2)^{0.5}} \tag{22}$$

$$\text{Convex spine}: \theta_{\text{cvex,part}} = \theta_{dp}\frac{I_0\left(\frac{4\sqrt{2}}{3}mb^{0.25}x^{0.75}\right)}{I_0\left(\frac{4\sqrt{2}}{3}mb^{0.25}x_{\text{dry}}^{0.75}\right)} \tag{23}$$

For the wet portion ($x_{\text{dry}} \le x \le b$), the differential heat equations in terms of enthalpy excess ($\gamma = i - i_a$) can be written as follows:

$$\text{Uniform cross section spine}: \frac{d^2\gamma}{dx^2} - m_T\gamma = 0 \tag{24}$$

$$\text{Conical spine}: \frac{d^2\gamma}{dx^2} + \frac{2}{x}\frac{d\gamma}{dx} - 2m_T^2\frac{b}{x}\gamma = 0 \tag{25}$$

$$\text{Concave spine}: \frac{d^2\gamma}{dv^2} + 3\frac{d\gamma}{dv} - 2m_T^2b^2\gamma = 0 \tag{26}$$

$$\text{Convex spine}: \frac{d^2\gamma}{dx^2} + \frac{1}{x}\frac{d\gamma}{dx} - 2m_T^2\sqrt{\frac{b}{x}}\gamma = 0 \tag{27}$$

subject to three boundary conditions:

$$\left.\frac{d\gamma}{dx}\right|_{x=x_{\text{dry}}} = b'_{w,dp}\left.\frac{d\theta}{dx}\right|_{x=x_{\text{dry}}} \tag{28}$$

$$\gamma|_{x=x_{\text{dry}}} = \gamma_{dp} \tag{29}$$

$$\gamma|_{x=b} = \gamma_0 \tag{30}$$

where $\gamma_{dp} = i_{dp} - i_a$ and $\gamma_0 = i_0 - i_a$.

The first boundary condition in Eq. (28) is given by considering the conduction heat transfer from the dry portion to the wet portion. The secondary condition in Eq. (29) is similar to that of Eq. (19). The enthalpy excess of saturated air at the saturation point equals that at the dew point. The last boundary condition in Eq. (30) describes the enthalpy excess at the fin base.

The general solutions of Eqs. (24)–(27) can be shown as follows:

$$\text{Uniform cross section spine}: \gamma_{\text{const,part}} = C_1e^{m_Tx} + C_2e^{-m_Tx} \tag{31}$$

$$\text{Conical spine}: \gamma_{\text{tcone,part}} = x^{-0.5}\left[C_1I_1(2m_T\sqrt{2bx}) + C_2K_1(2m_T\sqrt{2bx})\right] \tag{32}$$

$$\text{Concave spine}: \gamma_{\text{ccave,part}} = C_1x^{-1.5+0.5(9+8m_T^2b^2)^{0.5}} + C_2x^{-1.5-0.5(9+8m_T^2b^2)^{0.5}} \tag{33}$$

$$\text{Convex spine}: \gamma_{\text{cvex,part}} = C_1I_0\left(\frac{4\sqrt{2}}{3}m_Tb^{0.25}x^{0.75}\right) + C_2K_0\left(\frac{4\sqrt{2}}{3}m_Tb^{0.25}x^{0.75}\right) \tag{34}$$

The constants C_1 and C_2 in Eqs. (31)–(34) can be solved by two boundary conditions. There are two methods for finding the solutions. The first method can be performed using Eqs. (29) and (30) and the second method can be done using Eqs. (28) and (30). The fin efficiency can then be obtained. However, fin efficiency is still a function of x_{dry} and it is difficult to substitute the x_{dry} obtained from the remaining boundary condition in the fin efficiency equation. Thus, fin efficiency will be presented in terms of x_{dry}, and x_{dry} can be obtained from the remaining boundary condition.

The first method, with the first set of boundary conditions represented by Eqs. (29) and (30), and Eqs. (31)–(34), can be solved as follows:

Uniform cross section spine:

$$\gamma_{\text{const1,part}} = \frac{\gamma_0e^{m_Tb} - \gamma_{dp}e^{m_Tx_{\text{dry}}}}{e^{2m_Tb} - e^{2m_Tx_{\text{dry}}}}e^{m_Tx} + \frac{\gamma_{dp}e^{(m_Tx_{\text{dry}}+2m_Tb)} - \gamma_0e^{(2m_Tx_{\text{dry}}+m_Tb)}}{e^{2m_Tb} - e^{2m_Tx_{\text{dry}}}}e^{-m_Tx} \tag{35}$$

Conical spine:

$$\gamma_{\text{cone1,part}} = \frac{b^{0.5}\gamma_0K_1(2\sqrt{2}m_T\sqrt{bx_{\text{dry}}}) - x_{\text{dry}}^{0.5}\gamma_{dp}K_1(2\sqrt{2}m_Tb)}{I_1(2\sqrt{2}m_Tb)K_1(2\sqrt{2}m_T\sqrt{bx_{\text{dry}}}) - I_1(2\sqrt{2}m_T\sqrt{bx_{\text{dry}}})K_1(2\sqrt{2}m_Tb)}x^{-0.5}I_1(2\sqrt{2}m_T\sqrt{bx}) + \frac{x_{\text{dry}}^{0.5}\gamma_{dp}I_1(2\sqrt{2}m_Tb) - b^{0.5}\gamma_0I_1(2\sqrt{2}m_T\sqrt{bx_{\text{dry}}})}{I_1(2\sqrt{2}m_Tb)K_1(2\sqrt{2}m_T\sqrt{bx_{\text{dry}}}) - I_1(2\sqrt{2}m_T\sqrt{bx_{\text{dry}}})K_1(2\sqrt{2}m_Tb)}x^{-0.5}K_1(2\sqrt{2}m_T\sqrt{bx}) \tag{36}$$

Concave parabolic spine:

$$\gamma_{\text{ccave1,part}} = \frac{\gamma_0 x_{\text{dry}}^{-1.5-0.5(9+8m_T^2b^2)^{0.5}} - \gamma_{dp} b^{-1.5-0.5(9+8m_T^2b^2)^{0.5}}}{x_{\text{dry}}^{-1.5-0.5(9+8m_T^2b^2)^{0.5}} b^{-1.5+0.5(9+8m_T^2b^2)^{0.5}} - x_{\text{dry}}^{-1.5+0.5(9+8m_T^2b^2)^{0.5}} b^{-1.5-0.5(9+8m_T^2b^2)^{0.5}}} x^{-1.5+0.5(9+8m_T^2b^2)^{0.5}}$$
$$+ \frac{\gamma_{dp} b^{-1.5+0.5(9+8m_T^2b^2)^{0.5}} - \gamma_0 x_{\text{dry}}^{-1.5+0.5(9+8m_T^2b^2)^{0.5}}}{x_{\text{dry}}^{-1.5-0.5(9+8m_T^2b^2)^{0.5}} b^{-1.5+0.5(9+8m_T^2b^2)^{0.5}} - x_{\text{dry}}^{-1.5+0.5(9+8m_T^2b^2)^{0.5}} b^{-1.5-0.5(9+8m_T^2b^2)^{0.5}}} x^{-1.5-0.5(9+8m_T^2b^2)^{0.5}} \tag{37}$$

Convex parabolic spine:

$$\gamma_{\text{cvex1,part}} = \frac{\gamma_0 K_0\left(\frac{4\sqrt{2}}{3} m_T b^{0.25} x_{\text{dry}}^{0.75}\right) - \gamma_{dp} K_0\left(\frac{4\sqrt{2}}{3} m_T b\right)}{I_0\left(\frac{4\sqrt{2}}{3} m_T b\right) K_0\left(\frac{4\sqrt{2}}{3} m_T b^{0.25} x_{\text{dry}}^{0.75}\right) - I_0\left(\frac{4\sqrt{2}}{3} m_T b^{0.25} x_{\text{dry}}^{0.75}\right) K_0\left(\frac{4\sqrt{2}}{3} m_T b\right)} I_0\left(\frac{4\sqrt{2}}{3} m_T b^{0.25} x^{0.75}\right)$$
$$+ \frac{\gamma_{dp} I_0\left(\frac{4\sqrt{2}}{3} m_T b\right) - \gamma_0 I_0\left(\frac{4\sqrt{2}}{3} m_T b^{0.25} x_{\text{dry}}^{0.75}\right)}{I_0\left(\frac{4\sqrt{2}}{3} m_T b\right) K_0\left(\frac{4\sqrt{2}}{3} m_T b^{0.25} x_{\text{dry}}^{0.75}\right) - I_0\left(\frac{4\sqrt{2}}{3} m_T b^{0.25} x_{\text{dry}}^{0.75}\right) K_0\left(\frac{4\sqrt{2}}{3} m_T b\right)} K_0\left(\frac{4\sqrt{2}}{3} m_T b^{0.25} x^{0.75}\right) \tag{38}$$

It must be noted that the subscript of 1 mean the 1st method, and subscript of 2 mean the 2nd method.

Then the fin efficiency can be evaluated by dividing the conduction heat transfer rate through the fin base by the convection heat transfer rate, with the assumption that all fin surface temperatures and fin base temperatures are equal. Then,

$$\eta_{\text{part}} = \frac{-\frac{k_f}{b'_{w,0}} A \frac{d\gamma}{dx}\Big|_{x=b}}{-\frac{h_c}{C_{p,a}} A' \gamma_0} \tag{39}$$

By substituting Eqs. (35)–(38) into Eq. (39), the fin efficiency can be rewritten as follows:

Uniform cross section spine:

$$\eta_{\text{const1,part}} = \frac{\gamma_0 (e^{2m_T x_{\text{dry}}} + e^{2m_T b}) - 2\gamma_{dp} e^{m_T (x_{\text{dry}} + b)}}{m_T b \gamma_0 (e^{2m_T b} - e^{2m_T x_{\text{dry}}})} \tag{40}$$

Conical spine:

$$\eta_{\text{cone1,part}} = \frac{\sqrt{2} b \gamma_0 [K_1(2\sqrt{2} m_T \sqrt{b x_{\text{dry}}}) I_2(2\sqrt{2} m_T b) + I_1(2\sqrt{2} m_T \sqrt{b x_{\text{dry}}}) K_2(2\sqrt{2} m_T b)]}{\mathrm{m}_T b^2 \gamma_0 [I_1(2\sqrt{2} m_T b) K_1(2\sqrt{2} m_T \sqrt{b x_{\text{dry}}}) - I_1(2\sqrt{2} m_T \sqrt{b x_{\text{dry}}}) K_1(2\sqrt{2} m_T b)]}$$
$$- \frac{\sqrt{2} \mathrm{b}^{0.5} x_{\text{dry}}^{0.5} \gamma_{dp} [I_1(2\sqrt{2} m_T b) K_2(2\sqrt{2} m_T b) + K_1(2\sqrt{2} m_T b) I_2(2\sqrt{2} m_T b)]}{\mathrm{m}_T b^2 \gamma_0 [I_1(2\sqrt{2} m_T b) K_1(2\sqrt{2} m_T \sqrt{b x_{\text{dry}}}) - I_1(2\sqrt{2} m_T \sqrt{b x_{\text{dry}}}) K_1(2\sqrt{2} m_T b)]} \tag{41}$$

Concave parabolic spine:

$$\eta_{\text{ccave1,part}} = \frac{1.5\gamma_0 [(-1.5 + 0.5(9 + 8m_T^2 b^2)^{0.5}) x_{\text{dry}}^{-1.5-0.5(9+8m_T^2b^2)^{0.5}} b^{-2.5+0.5(9+8m_T^2b^2)^{0.5}}}{m_T^2 b \gamma_0 \left[x_{\text{dry}}^{-1.5-0.5(9+8m_T^2b^2)^{0.5}} b^{-1.5+0.5(9+8m_T^2b^2)^{0.5}} - x_{\text{dry}}^{-1.5+0.5(9+8m_T^2b^2)^{0.5}} b^{-1.5-0.5(9+8m_T^2b^2)^{0.5}}\right]}$$
$$\times \frac{-(-1.5 - 0.5(9 + 8m_T^2 b^2)^{0.5}) x_{\text{dry}}^{-1.5+0.5(9+8m_T^2b^2)^{0.5}} b^{-2.5-0.5(9+8m_T^2b^2)^{0.5}}] - 1.5\gamma_{dp}(9 + 8m_T^2 b^2)^{0.5} b^{-4}}{m_T^2 b \gamma_0 \left[x_{\text{dry}}^{-1.5-0.5(9+8m_T^2b^2)^{0.5}} b^{-1.5+0.5(9+8m_T^2b^2)^{0.5}} - x_{\text{dry}}^{-1.5+0.5(9+8m_T^2b^2)^{0.5}} b^{-1.5-0.5(9+8m_T^2b^2)^{0.5}}\right]} \tag{42}$$

Convex parabolic spine:

$$\eta_{\text{cvex1,part}} = \frac{0.75\sqrt{2}\gamma_0 \left[K_0\left(\frac{4}{3}\sqrt{2} m_T x_{\text{dry}}^{0.75} b^{0.25}\right) I_1\left(\frac{4}{3}\sqrt{2} m_T b\right) + I_0\left(\frac{4}{3}\sqrt{2} m_T x_{\text{dry}}^{0.75} b^{0.25}\right) K_1\left(\frac{4}{3}\sqrt{2} m_T b\right)\right]}{m_T b \gamma_0 \left[I_0\left(\frac{4}{3}\sqrt{2} m_T b\right) K_0\left(\frac{4}{3}\sqrt{2} m_T x_{\text{dry}}^{0.75} b^{0.25}\right) - I_0\left(\frac{4}{3}\sqrt{2} m_T x_{\text{dry}}^{0.75} b^{0.25}\right) K_0\left(\frac{4}{3}\sqrt{2} m_T b\right)\right]}$$
$$- \frac{0.75\sqrt{2}\gamma_{dp} \left[I_0\left(\frac{4}{3}\sqrt{2} m_T b\right) K_1\left(\frac{4}{3}\sqrt{2} m_T b\right) + K_0\left(\frac{4}{3}\sqrt{2} m_T b\right) I_1\left(\frac{4}{3}\sqrt{2} m_T b\right)\right]}{m_T b \gamma_0 \left[I_0\left(\frac{4}{3}\sqrt{2} m_T b\right) K_0\left(\frac{4}{3}\sqrt{2} m_T x_{\text{dry}}^{0.75} b^{0.25}\right) - I_0\left(\frac{4}{3}\sqrt{2} m_T x_{\text{dry}}^{0.75} b^{0.25}\right) K_0\left(\frac{4}{3}\sqrt{2} m_T b\right)\right]} \tag{43}$$

x_{dry} can be derived from the first boundary condition of Eq. (28). By substituting Eqs. (20)–(23) and (35)–(38) into Eq. (28), the relations can be shown in Eqs. (44)–(47) as follows:

Uniform cross section spine:

$$\frac{2m_T\gamma_0 e^{m_T(x_{\mathrm{dry}}+b)} - m_T\gamma_{dp}(e^{2m_T x_{\mathrm{dry}}} + e^{2m_T b})}{e^{2m_T b} - e^{2m_T x_{\mathrm{dry}}}} = mb'_{w,dp}\theta_{dp}\tanh(mx_{\mathrm{dry}}) \tag{44}$$

Conical spine:

$$\begin{aligned}&\frac{b^{0.5}\gamma_0\left[K_1(2\sqrt{2}m_T\sqrt{bx_{\mathrm{dry}}})I_2(2\sqrt{2}m_T\sqrt{bx_{\mathrm{dry}}}) + I_1(2\sqrt{2}m_T\sqrt{bx_{\mathrm{dry}}})K_2(2\sqrt{2}m_T\sqrt{bx_{\mathrm{dry}}})\right]}{I_1(2\sqrt{2}m_T b)K_1(2\sqrt{2}m_T\sqrt{bx_{\mathrm{dry}}}) - I_1(2\sqrt{2}m_T\sqrt{bx_{\mathrm{dry}}})K_1(2\sqrt{2}m_T b)}\\ &-\frac{x_{\mathrm{dry}}^{0.5}\gamma_{dp}\left[I_1(2\sqrt{2}m_T b)K_2(2\sqrt{2}m_T\sqrt{bx_{\mathrm{dry}}}) + K_1(2\sqrt{2}m_T b)I_2(2\sqrt{2}m_T\sqrt{bx_{\mathrm{dry}}})\right]}{I_1(2\sqrt{2}m_T b)K_1(2\sqrt{2}m_T\sqrt{bx_{\mathrm{dry}}}) - I_1(2\sqrt{2}m_T\sqrt{bx_{\mathrm{dry}}})K_1(2\sqrt{2}m_T b)} = \frac{x_{\mathrm{dry}}b'_{w,dp}\theta_{dp}}{\sqrt{2}m_T\sqrt{b}}\cdot\frac{I_2(2\sqrt{2}m\sqrt{bx_{\mathrm{dry}}})}{I_1(2\sqrt{2}m\sqrt{bx_{\mathrm{dry}}})}\end{aligned} \tag{45}$$

Concave parabolic profile:

$$\begin{aligned}&\frac{\gamma_{dp}[(-1.5-0.5(9+8m_T^2b^2)^{0.5})b^{-1.5+0.5(9+8m_T^2b^2)^{0.5}}x_{\mathrm{dry}}^{-2.5-0.5(9+8m_T^2b^2)^{0.5}}}{x_{\mathrm{dry}}^{-1.5-0.5(9+8m_T^2b^2)^{0.5}}b^{-1.5+0.5(9+8m_T^2b^2)^{0.5}} - x_{\mathrm{dry}}^{-1.5+0.5(9+8m_T^2b^2)^{0.5}}b^{-1.5-0.5(9+8m_T^2b^2)^{0.5}}}\\ &-\frac{(-1.5+0.5(9+8m_T^2b^2)^{0.5})b^{-1.5-0.5(9+8m_T^2b^2)^{0.5}}x_{\mathrm{dry}}^{-2.5+0.5(9+8m_T^2b^2)^{0.5}}] + \gamma_0(9+8m_T^2b^2)^{0.5}x_{\mathrm{dry}}^{-4}}{x_{\mathrm{dry}}^{-1.5-0.5(9+8m_T^2b^2)^{0.5}}b^{-1.5+0.5(9+8m_T^2b^2)^{0.5}} - x_{\mathrm{dry}}^{-1.5+0.5(9+8m_T^2b^2)^{0.5}}b^{-1.5-0.5(9+8m_T^2b^2)^{0.5}}} = b'_{w,dp}\theta_{dp}\frac{-1.5+0.5(9+8m^2b^2)^{0.5}}{x_{\mathrm{dry}}}\end{aligned} \tag{46}$$

Convex parabolic profile:

$$\begin{aligned}&\frac{m_T\gamma_0\left[K_0\left(\frac{4}{3}\sqrt{2}m_T x_{\mathrm{dry}}^{0.75}b^{0.25}\right)I_1\left(\frac{4}{3}\sqrt{2}m_T x_{\mathrm{dry}}^{0.75}b^{0.25}\right) + I_0\left(\frac{4}{3}\sqrt{2}m_T x_{\mathrm{dry}}^{0.75}b^{0.25}\right)K_1\left(\frac{4}{3}\sqrt{2}m_T x_{\mathrm{dry}}^{0.75}b^{0.25}\right)\right]}{I_0\left(\frac{4}{3}\sqrt{2}m_T b\right)K_0\left(\frac{4}{3}\sqrt{2}m_T x_{\mathrm{dry}}^{0.75}b^{0.25}\right) - I_0\left(\frac{4}{3}\sqrt{2}m_T x_{\mathrm{dry}}^{0.75}b^{0.25}\right)K_0\left(\frac{4}{3}\sqrt{2}m_T b\right)}\\ &-\frac{m_T\gamma_{dp}\left[I_0\left(\frac{4}{3}\sqrt{2}m_T b\right)K_1\left(\frac{4}{3}\sqrt{2}m_T x_{\mathrm{dry}}^{0.75}b^{0.25}\right) + K_0\left(\frac{4}{3}\sqrt{2}m_T b\right)I_1\left(\frac{4}{3}\sqrt{2}m_T x_{\mathrm{dry}}^{0.75}b^{0.25}\right)\right]}{I_0\left(\frac{4}{3}\sqrt{2}m_T b\right)K_0\left(\frac{4}{3}\sqrt{2}m_T x_{\mathrm{dry}}^{0.75}b^{0.25}\right) - I_0\left(\frac{4}{3}\sqrt{2}m_T x_{\mathrm{dry}}^{0.75}b^{0.25}\right)K_0\left(\frac{4}{3}\sqrt{2}m_T b\right)} = mb'_{w,dp}\theta_{dp}\frac{I_1\left(\frac{4}{3}\sqrt{2}mx_{\mathrm{dry}}^{0.75}b^{0.25}\right)}{I_0\left(\frac{4}{3}\sqrt{2}mx_{\mathrm{dry}}^{0.75}b^{0.25}\right)}\end{aligned} \tag{47}$$

However, the iterative calculation is needed to solve x_{dry}

The second method, with the other set of boundary conditions represented by Eqs. (28) and (30), and Eqs. (31)–(34), can be solved as follows:

Uniform cross section spine:

$$\gamma_{\mathrm{const2,part}} = \frac{m_T\gamma_0 e^{-m_T(2x_{\mathrm{dry}}+b)} + mb'_{w,dp}\theta_{dp}e^{-m_T(x_{\mathrm{dry}}+2b)}\tanh(mx_{\mathrm{dry}})}{m_T(e^{-2m_T x_{\mathrm{dry}}} + e^{-2m_T b})}e^{m_T x} + \frac{m_T\gamma_0 e^{-m_T b} - mb'_{w,dp}\theta_{dp}e^{-m_T x_{\mathrm{dry}}}\tanh(mx_{\mathrm{dry}})}{m_T(e^{-2m_T x_{\mathrm{dry}}} + e^{-2m_T b})}e^{-m_T x} \tag{48}$$

Conical spine:

$$\begin{aligned}\gamma_{\mathrm{cone2,part}} =& \frac{\sqrt{2}m_T b\gamma_0 I_1(2\sqrt{2}m\sqrt{bx_{\mathrm{dry}}})K_2(2\sqrt{2}m_T\sqrt{bx_{\mathrm{dry}}}) + \sqrt{2}mb^{0.5}x_{\mathrm{dry}}^{0.5}b'_{w,dp}\theta_{dp}K_1(2\sqrt{2}m_T b)I_2(2\sqrt{2}m\sqrt{bx_{\mathrm{dry}}})}{\sqrt{2}m_T b^{0.5}x^{0.5}I_1(2\sqrt{2}m\sqrt{bx_{\mathrm{dry}}})\left[I_1(2\sqrt{2}m_T b)K_2(2\sqrt{2}m_T\sqrt{bx_{\mathrm{dry}}}) + K_1(2\sqrt{2}m_T b)I_2(2\sqrt{2}m_T\sqrt{bx_{\mathrm{dry}}})\right]}I_1(2\sqrt{2}m_T\sqrt{bx})\\ &+\frac{\sqrt{2}m_T b\gamma_0 I_1(2\sqrt{2}m\sqrt{bx_{\mathrm{dry}}})I_2(2\sqrt{2}m_T\sqrt{bx_{\mathrm{dry}}}) - \sqrt{2}mb^{0.5}x_{\mathrm{dry}}^{0.5}b'_{w,dp}\theta_{dp}I_1(2\sqrt{2}m_T b)I_2(2\sqrt{2}m\sqrt{bx_{\mathrm{dry}}})}{\sqrt{2}m_T b^{0.5}x^{0.5}I_1(2\sqrt{2}m\sqrt{bx_{\mathrm{dry}}})\left[I_1(2\sqrt{2}m_T b)K_2(2\sqrt{2}m_T\sqrt{bx_{\mathrm{dry}}}) + K_1(2\sqrt{2}m_T b)I_2(2\sqrt{2}m_T\sqrt{bx_{\mathrm{dry}}})\right]}K_1(2\sqrt{2}m_T\sqrt{bx})\end{aligned} \tag{49}$$

Concave parabolic spine:

$$\gamma_{\mathrm{ccave2,part}} = C_{1,\mathrm{ccave2}}x^{-1.5+0.5(9+8m_T^2b^2)^{0.5}} + \frac{C_{2,\mathrm{ccave2}}}{x^{1.5+0.5(9+8m_T^2b^2)^{0.5}}} \tag{50}$$

where

$$C_{1,\mathrm{ccave2}}=\frac{(-1.5-0.5\sqrt{9+8m_T^2b^2})\gamma_0 x_{\mathrm{dry}}^{-\sqrt{9+8m_T^2b^2}}b^{1.5-0.5\sqrt{9+8m_T^2b^2}}+(1.5-0.5\sqrt{9+8m^2b^2})b'_{w,dp}\theta_{dp}x_{\mathrm{dry}}^{1.5-0.5\sqrt{9+8m_T^2b^2}}b^{-\sqrt{9+8m_T^2b^2}}}{(-1.5-0.5\sqrt{9+8m_T^2b^2})x_{\mathrm{dry}}^{-\sqrt{9+8m_T^2b^2}}+(1.5-0.5\sqrt{9+8m_T^2b^2})b^{-\sqrt{9+8m_T^2b^2}}} \tag{51}$$

$$C_{2,\mathrm{ccave2}}=\frac{(1.5-0.5\sqrt{9+8m_T^2b^2})\gamma_0 b^{1.5-0.5\sqrt{9+8m_T^2b^2}}-(1.5-0.5\sqrt{9+8m^2b^2})b'_{w,dp}\theta_{dp}x_{\mathrm{dry}}^{1.5-0.5\sqrt{9+8m_T^2b^2}}}{(-1.5-0.5\sqrt{9+8m_T^2b^2})x_{\mathrm{dry}}^{-\sqrt{9+8m_T^2b^2}}+(1.5-0.5\sqrt{9+8m_T^2b^2})b^{-\sqrt{9+8m_T^2b^2}}} \tag{52}$$

Convex parabolic:

$$\gamma_{\mathrm{cvex2,part}}=\frac{\gamma_0 I_0\left(\frac{4}{3}\sqrt{2}mb^{0.25}x_{\mathrm{dry}}^{0.75}\right)K_1\left(\frac{4}{3}\sqrt{2}m_Tb^{0.25}x_{\mathrm{dry}}^{0.75}\right)+\frac{m}{m_T}b'_{w,dp}\theta_{dp}K_0\left(\frac{4}{3}\sqrt{2}m_Tb\right)I_1\left(\frac{4}{3}\sqrt{2}mb^{0.25}x_{\mathrm{dry}}^{0.75}\right)}{I_0\left(\frac{4}{3}\sqrt{2}mb^{0.25}x_{\mathrm{dry}}^{0.75}\right)\left[I_0\left(\frac{4}{3}\sqrt{2}m_Tb\right)K_1\left(\frac{4}{3}\sqrt{2}m_Tb^{0.25}x_{\mathrm{dry}}^{0.75}\right)+K_0\left(\frac{4}{3}\sqrt{2}m_Tb\right)I_1\left(\frac{4}{3}\sqrt{2}m_Tb^{0.25}x_{\mathrm{dry}}^{0.75}\right)\right]}I_0\left(\frac{4}{3}\sqrt{2}m_Tb^{0.25}x^{0.75}\right)$$
$$+\frac{\gamma_0 I_0\left(\frac{4}{3}\sqrt{2}mb^{0.25}x_{\mathrm{dry}}^{0.75}\right)I_1\left(\frac{4}{3}\sqrt{2}m_Tb^{0.25}x_{\mathrm{dry}}^{0.75}\right)-\frac{m}{m_T}b'_{w,dp}\theta_{dp}I_0\left(\frac{4}{3}\sqrt{2}m_Tb\right)I_1\left(\frac{4}{3}\sqrt{2}mb^{0.25}x_{\mathrm{dry}}^{0.75}\right)}{I_0\left(\frac{4}{3}\sqrt{2}mb^{0.25}x_{\mathrm{dry}}^{0.75}\right)\left[I_0\left(\frac{4}{3}\sqrt{2}m_Tb\right)K_1\left(\frac{4}{3}\sqrt{2}m_Tb^{0.25}x_{\mathrm{dry}}^{0.75}\right)+K_0\left(\frac{4}{3}\sqrt{2}m_Tb\right)I_1\left(\frac{4}{3}\sqrt{2}m_Tb^{0.25}x_{\mathrm{dry}}^{0.75}\right)\right]}K_0\left(\frac{4}{3}\sqrt{2}m_Tb^{0.25}x^{0.75}\right) \tag{53}$$

Then, the fin efficiency can be evaluated as in Eq. (39) as follows:

Uniform cross sections pine:

$$\eta_{\mathrm{const2,part}}=\frac{m_T\gamma_0(e^{-2m_Tx_{\mathrm{dry}}}-e^{-2m_Tb})+2mb'_{w,dp}\theta_{dp}\tanh(mx_{\mathrm{dry}})e^{-m_T(x_{\mathrm{dry}}+b)}}{m_T^2b\gamma_0(e^{-2m_Tx_{\mathrm{dry}}}+e^{-2m_Tb})} \tag{54}$$

Conical spine:

$$\eta_{\mathrm{cone2,part}}=\frac{\sqrt{2}m_Tb\gamma_0 I_1(2\sqrt{2bx_{\mathrm{dry}}}m)\left[I_2(2\sqrt{2}m_Tb)K_2(2\sqrt{2bx_{\mathrm{dry}}}m_T)-I_2(2\sqrt{2bx_{\mathrm{dry}}}m_T)K_2(2\sqrt{2}m_Tb)\right]}{m_T^2b^2\gamma_0 I_1(2\sqrt{2}m\sqrt{bx_{\mathrm{dry}}})\left[I_1(2\sqrt{2}m_Tb)K_2(2\sqrt{2}m_T\sqrt{bx_{\mathrm{dry}}})+K_1(2\sqrt{2}m_Tb)I_2(2\sqrt{2}m_T\sqrt{bx_{\mathrm{dry}}})\right]}$$
$$+\frac{\sqrt{2}mb^{0.5}x_{\mathrm{dry}}^{0.5}b'_{w,dp}\theta_{dp}I_2(2\sqrt{2bx_{\mathrm{dry}}}m_T)\left[I_1(2\sqrt{2}m_Tb)K_2(2\sqrt{2}m_Tb)+K_1(2\sqrt{2}m_Tb)I_2(2\sqrt{2}m_Tb)\right]}{m_T^2b^2\gamma_0 I_1(2\sqrt{2}m\sqrt{bx_{\mathrm{dry}}})\left[I_1(2\sqrt{2}m_Tb)K_2(2\sqrt{2}m_T\sqrt{bx_{\mathrm{dry}}})+K_1(2\sqrt{2}m_Tb)I_2(2\sqrt{2}m_T\sqrt{bx_{\mathrm{dry}}})\right]} \tag{55}$$

Concave parabolic spine:

$$\eta_{\mathrm{ccave2,part}}=\frac{\sqrt{9+8m_T^2b^2}(4.5-1.5\sqrt{9+8m^2b^2})b'_{w,dp}\theta_{dp}x_{\mathrm{dry}}^{1.5-0.5\sqrt{9+8m_T^2b^2}}b^{-2.5-0.5\sqrt{9+8m_T^2b^2}}+6m_T^2b^2\gamma_0\left(b^{-1-\sqrt{9+8m_T^2b^2}}-x_{\mathrm{dry}}^{-\sqrt{9+8m_T^2b^2}}\right)}{2m_T^2b\gamma_0\left[\left(-1.5-0.5\sqrt{9+8m_T^2b^2}\right)x_{\mathrm{dry}}^{-\sqrt{9+8m_T^2b^2}}+\left(1.5-0.5\sqrt{9+8m_T^2b^2}\right)b^{-\sqrt{9+8m_T^2b^2}}\right]} \tag{56}$$

Convex profile:

$$\eta_{\mathrm{cvex2,part}}=\frac{3\sqrt{2}\gamma_0 I_0\left(\frac{4}{3}\sqrt{2}mx_{\mathrm{dry}}^{0.75}b^{0.25}\right)\left[I_1\left(\frac{4}{3}\sqrt{2}m_Tb\right)K_1\left(\frac{4}{3}\sqrt{2}m_Tx_{\mathrm{dry}}^{0.75}b^{0.25}\right)-I_1\left(\frac{4}{3}\sqrt{2}m_Tx_{\mathrm{dry}}^{0.75}b^{0.25}\right)K_1\left(\frac{4}{3}\sqrt{2}m_Tb\right)\right]}{4m_Tb\gamma_0 I_0\left(\frac{4}{3}\sqrt{2}mb^{0.25}x_{\mathrm{dry}}^{0.75}\right)\left[I_0\left(\frac{4}{3}\sqrt{2}m_Tb\right)K_1\left(\frac{4}{3}\sqrt{2}m_Tb^{0.25}x_{\mathrm{dry}}^{0.75}\right)+K_0\left(\frac{4}{3}\sqrt{2}m_Tb\right)I_1\left(\frac{4}{3}\sqrt{2}m_Tb^{0.25}x_{\mathrm{dry}}^{0.75}\right)\right]}$$
$$+\frac{3\sqrt{2}b'_{w,dp}\theta_{dp}\frac{m}{m_T}\left[I_0\left(\frac{4}{3}\sqrt{2}m_Tb\right)K_1\left(\frac{4}{3}\sqrt{2}m_Tb\right)I_1\left(\frac{4}{3}\sqrt{2}mx_{\mathrm{dry}}^{0.75}b^{0.25}\right)+I_1\left(\frac{4}{3}\sqrt{2}m_Tb\right)K_0\left(\frac{4}{3}\sqrt{2}m_Tb\right)I_1\left(\frac{4}{3}\sqrt{2}mx_{\mathrm{dry}}^{0.75}b^{0.25}\right)\right]}{4m_Tb\gamma_0 I_0\left(\frac{4}{3}\sqrt{2}mb^{0.25}x_{\mathrm{dry}}^{0.75}\right)\left[I_0\left(\frac{4}{3}\sqrt{2}m_Tb\right)K_1\left(\frac{4}{3}\sqrt{2}m_Tb^{0.25}x_{\mathrm{dry}}^{0.75}\right)+K_0\left(\frac{4}{3}\sqrt{2}m_Tb\right)I_1\left(\frac{4}{3}\sqrt{2}m_Tb^{0.25}x_{\mathrm{dry}}^{0.75}\right)\right]} \tag{57}$$

To evaluate x_{dry}, the second boundary condition in Eq. (29) is continued. Then, $\gamma|_{x=x_{\mathrm{dry}}}$ can be calculated from Eqs. (48)–(50) and (53), and γ_{dp} is known. Using the iteration procedure, x_{dry} can then be calculated.

3 Results and Discussion

Like the results of Kern and Kraus [2] in fully dry conditions, the four very faint lines of η plotted against m_Tb are shown in Fig. 2.

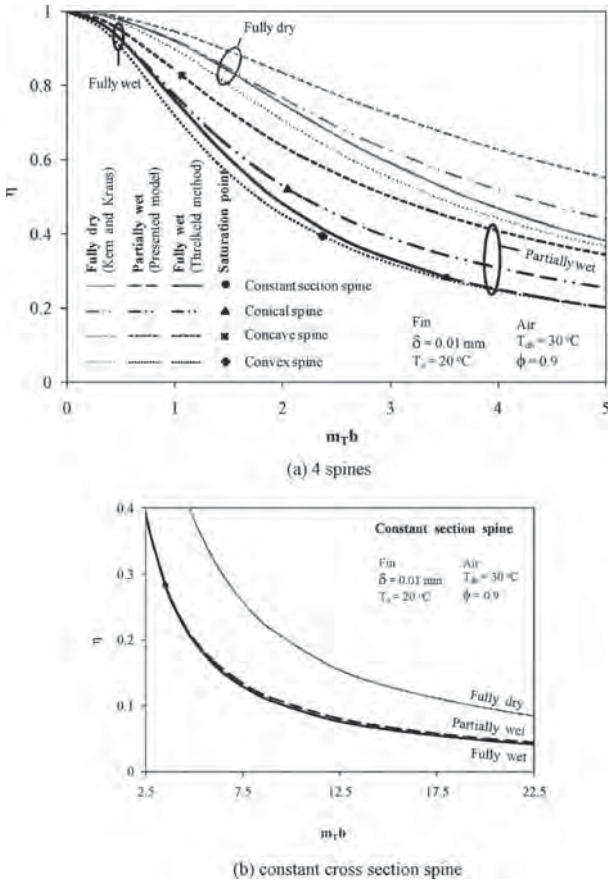

Fig. 2 Fin efficiency plotted against $m_T b$

It can be observed that the fin efficiencies decrease with increases of mb. At the same mb, the fin efficiency can be sorted from highest value to lowest value in the following order: concave parabolic spine, conical spine, uniform cross section spine, and convex parabolic spine. For fully wet conditions, as shown in Eqs. (6), (8), (10), and (12), the fin efficiencies are dependent only on $m_T b$. Figure 2 shows that the trends of the results are similar to those for dry conditions, but all values are lower. For partially wet surface conditions, as shown in Fig. 2, the fin efficiencies determined by Eqs. (40)–(43) and those determined by Eqs. (54)–(57) are not different. The fin efficiencies are not dependent only on $m_T b$, but they are more complicated than those in dry and wet conditions. Figure 2 shows the partially wet fin efficiencies plotted against $m_T b$ at 90% RH. Accordingly, at low $m_T b$, it can be found that the four gray lines representing the partially wet fin efficiencies have vanished. This is because the fins are in fully wet surface conditions. Moreover, one can see that the partially wet fin efficiencies are between the dry and wet fin efficiencies. The partially wet fin efficiencies are proximate to the fully wet fin efficiency at high RH, and are approximate to equal the fully dry fin efficiency at low RH. The partially wet fin efficiency still decreases with the increases of $m_T b$, and the order of the sorted results is the same as the order in dry and wet conditions. It must be noted that the m_T for the uniform cross section spine is $\sqrt{(h_o P/k_f A)}$ but m_T for the other spines is $\sqrt{(2h_o/k_f \delta_0)}$.

Figure 3 shows the temperature distribution along the distance from the fin base. According to the trend line, the slope at the fin base and the position of the saturation point can be evaluated for heat transfer performance. In the same conditions, the steep line at the fin base promotes good heat transfer. This can be described by the conductive heat transfer rate at the fin base as shown in Eq. (39). Moreover, more condensation, which promotes the heat transfer rate, takes place when the saturation point nears the fin tip. However, one can see that the trend lines in the dry portion are opposite those in the wet portion. Essentially, with the exception of the uniform cross section spine, it can be found that the sorting order of slope in Fig. 3 is opposite the sorting order of fin efficiency in Fig. 2. This can be described with the actual and ideal heat transfer rates as plotted in Fig. 4. From Fig. 4, with the exception of the uniform cross section spine, the order of actual and ideal heat transfer rates calculated from the part of the fraction over and below the line of Eq. (39) is convex parabolic spine, conical spine, and concave parabolic spine. The actual heat transfer rate can be described by the ordering in surface area because more surface area produces a higher heat transfer rate. However, for considering fin efficiency, the actual heat transfer rate must be

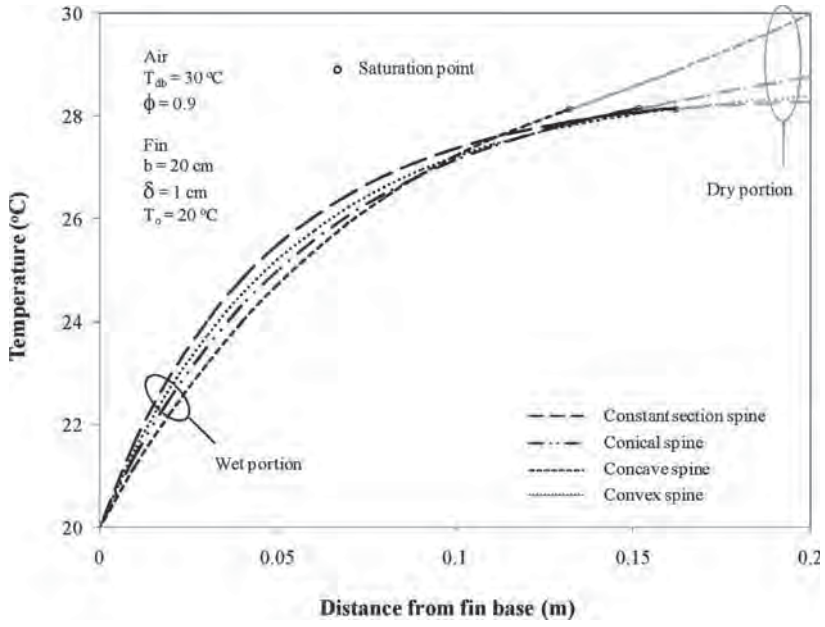

Fig. 3 Temperature distribution for four spines

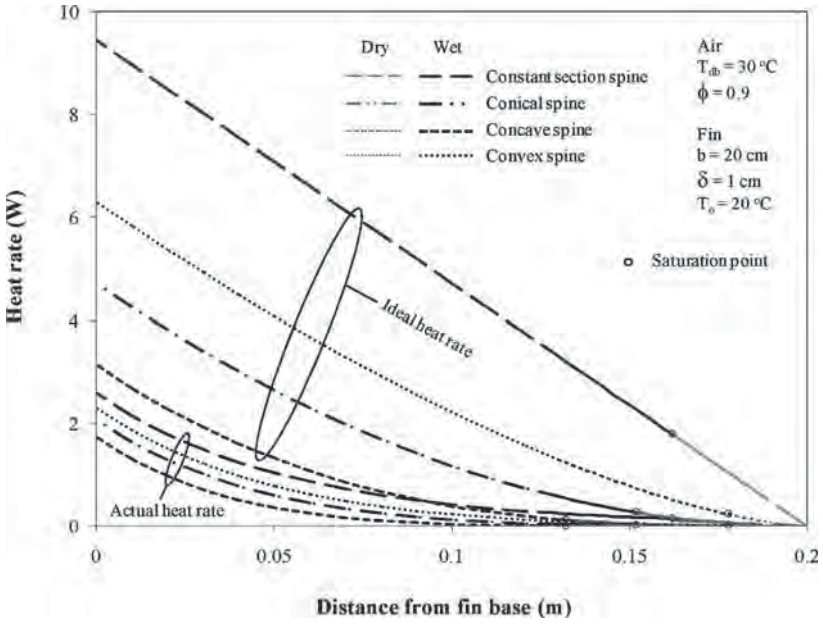

Fig. 4 Heat transfer through four spines

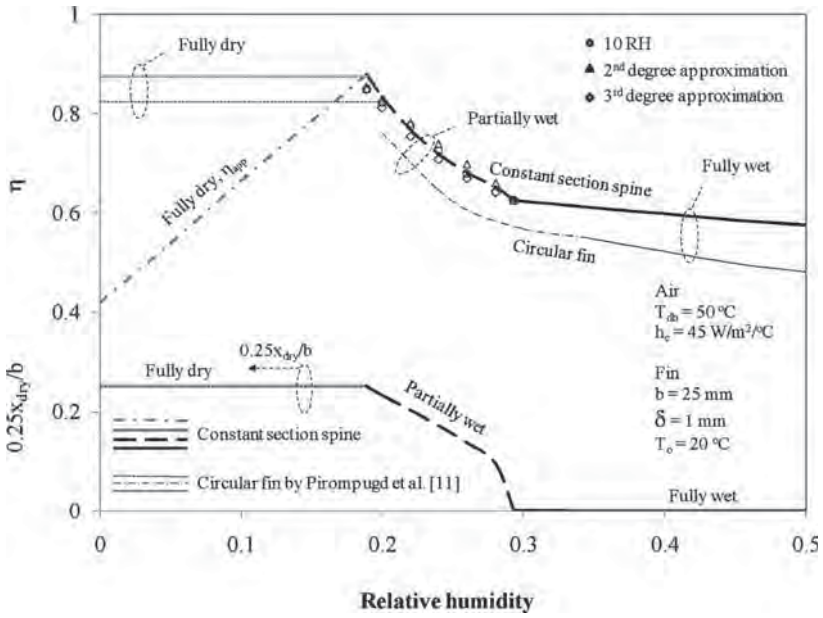

Fig. 5 Constant section spine efficiency plotted against relative humidity

compared with the ideal heat transfer rate. Figure 4 demonstrates that, with the exception of the uniform cross section spine, both the actual and ideal heat transfer rates of the convex parabolic spine are highest. Moreover, it can be observed that the increase in actual heat transfer rate is lower than the increase in ideal heat transfer rate. Thus, the fin efficiency of convex parabolic spine is lowest. This is the effect of the ratio of cross section area to surface area. This effect is not distinct in longitudinal fins.

Figures 5–8 show η and $0.25(x_{dry}/b)$ plotted against the relative humidity. The lines for partially wet and fully wet conditions are continuous, but there is a break between the lines of fully dry and partially wet conditions. The η_{app} for fully dry conditions calculated by dividing the actual heat transfer rate by the ideal heat transfer rate in fully wet conditions $(\eta = (q_{actual,dry}/q_{ideal,wet}))$ is presented in Figs. 5–8. For partially wet and fully wet conditions, the fin efficiencies decrease with increased relative humidity because the increase in the ideal or maximum heat transfer rate is higher than the increase in the actual heat transfer rate. These results are consistent with the results for a circular fin in partially wet and fully wet conditions as determined by Pirompugd et al. [11]. In 1999, Rosario and Rahman [13] presented an equation to determine the partially wet fin efficiency for a circular fin. That equation is a 2nd degree polynomial and is a function of dry portion length per total length of fin. Pirompugd and Wongwises [12] showed that, for longitudinal fins, the 1st or 2nd degree polynomial approximations cannot precisely predict partially wet fin efficiency. They derived the approximation by using ten times the relative humidity. Accordingly, the approximation for the spine in partially wet conditions is presented as follows:

$$\eta_{part} = \left(\frac{x_{dry}}{b}\right)^{10\times RH}\eta_{dry} + \left[1 - \left(\frac{x_{dry}}{b}\right)^{10\times RH}\right]\eta_{wet} \qquad (58)$$

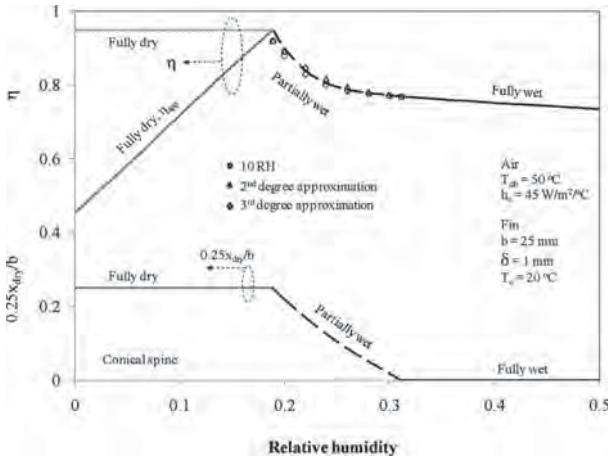

Fig. 6 Conical spine efficiency plotted against relative humidity

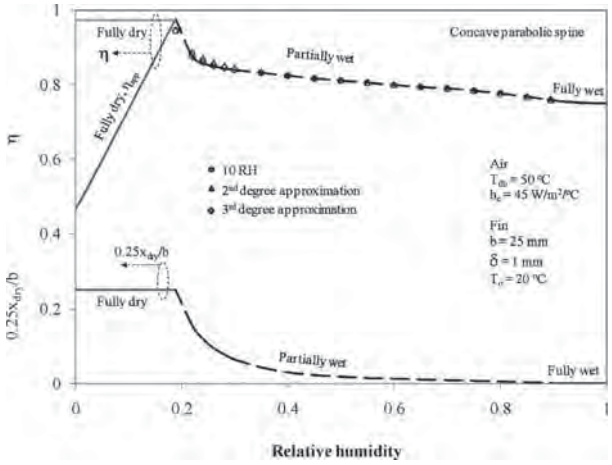

Fig. 7 Concave parabolic spine efficiency plotted against relative humidity

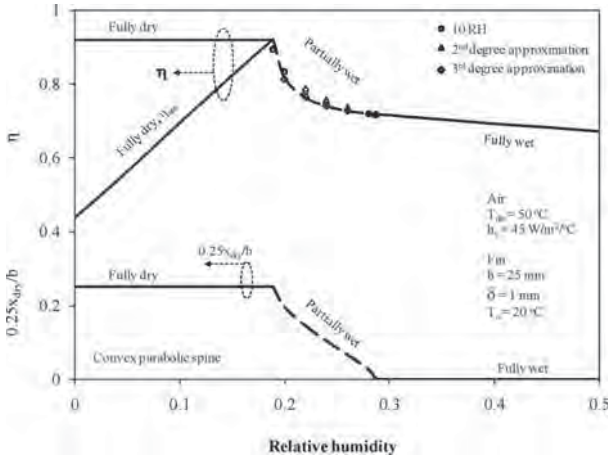

Fig. 8 Convex parabolic spine efficiency plotted against relative humidity

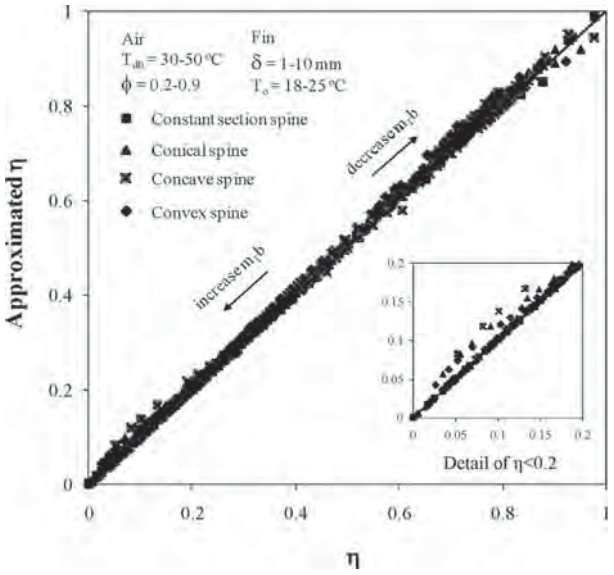

Fig. 9 Comparison of approximate η and η at many $M_T b$

As seen in Figs. 5–8, the results from Eq. (58) are consistent with the theoretical data. Moreover, Fig. 9 shows a comparison with the other conditions. According to the figure, at $\eta \geq 0.2$, almost all the measured data fall within $\pm$ 10%. However, error over $\pm$50% may occur when $\eta \leq 0.2$. Therefore, Eq. (58) can be applied only to extended surfaces of $\eta \geq 0.2$. The methods for evaluating x_{dry} have been described in the first method and second method for partially wet surface conditions. However, Eq. (58) is not necessary because this study has proposed a theoretical partially wet fin efficiency.

4 Conclusions

(1) The partially wet fin efficiencies for spines of uniform cross section area, conical, concave parabolic, and convex parabolic profiles are presented. Equations for evaluating the length of the dry portion are also proposed.
(2) The order of fin efficiency can be sorted, from highest to lowest, as follows: (1) concave parabolic spine, (2) conical spine, (3) uniform cross section spine, and (4) convex parabolic spine.
(3) The order of fin heat transfer rate can be sorted, from highest to lowest, as follows: (1) uniform cross section spine, (2) convex parabolic spine, (3) conical spine, (4) concave parabolic spine.
(4) With an increase in relative humidity, partially wet fin efficiencies decrease rapidly, but the decrease of fully wet fin efficiencies is slower. Contrarily, the dry fin efficiencies are independent of the relative humidity.
(5) Conveniently, the equation for predicting partially wet fin efficiency from fully wet and fully dry fin efficiencies is also presented. The methods for obtaining the length of the dry portion are also described.

Acknowledgment

The authors are indebted to the Thailand Research Fund, the Office of the Higher Education Commission, Burapha University and the National Research University Project for supporting this study.

Nomenclature

A = cross section area of fin, m^2
A' = fin surface area, m^2

b = distance from fin tip to fin base, m
$b'_{w,dp}$ = slope of the saturated air enthalpy curved at the dew point temperature, J kg^{-1} K^{-1}
$b'_{w,f}$ = slope of the saturated air enthalpy curved at the mean fin surface temperature, J kg^{-1} K^{-1}
$b'_{w,o}$ = slope of the saturated air enthalpy curved at the fin base temperature, J kg^{-1} K^{-1}
$C_{p,a}$ = air specific heat capacity, J kg^{-1} °C^{-1}
h_c = convection heat transfer coefficient, kg m^{-2} s^{-1}
i = saturated air enthalpy at fin surface, J kg^{-1}
i_a = air enthalpy at free stream, J kg^{-1}
I_0 = modified Bessel function solution of the first kind, order 0
I_1 = modified Bessel function solution of the first kind, order 1
I_2 = modified Bessel function solution of the first kind, order 2
k_f = thermal conductivity of the fin, W m^{-1} K^{-1}
k_w = thermal conductivity of the water film, W m^{-1} K^{-1}
K_0 = modified Bessel function solution of the second kind, order 0
K_1 = modified Bessel function solution of the second kind, order 1
K_2 = modified Bessel function solution of the second kind, order 2
m = $\sqrt{(h_c P/k_f A)}$ for uniform cross section spines, and $m = \sqrt{(2h_c/k_f\delta_0)}$ for conical, concave parabolic, and convex parabolic spines.
m_T = $\sqrt{(h_o P/k_f A)}$ for uniform cross section spines, and $m = \sqrt{(2h_o/k_f\delta_0)}$ for conical, concave parabolic, and convex parabolic spines.
P = the fin perimeter, m
RH = relative humidity
T = air temperature, °C
x = distance from fin tip, m
x_{dry} = distance from fin tip to saturation point, m
y_w = thickness of the water film, m
δ_0 = thickness of fin base, m
γ = air enthalpy difference between fin surface and air, J kg^{-1}
η = fin efficiency
θ = air temperature difference, °C

Appendix

The section shows the 1st method for derivation of efficiency of partially wet conical fin. From Fig. 10, the fin is in the partially wet condition. The fin base is cold and the surface temperature is generally lower than the dew point temperature. Then, the condensation of water vapor in the moist air takes place. There is simultaneous heat and mass transfer from moist air to the fin surface and both sensible and latent heat transfer takes place. The surface temperature increases with a decrease of x until it is equal to the dew point temperature. After this point, the surface temperature is higher than the dew point temperature. Then, there is only sensible heat transfer takes place in this region.

For the dry portion:

By Kern and Kraus [2], the differential equation for the dry portion can be written as

$$x^2\frac{d^2\theta}{dx^2} + 2x\frac{d\theta}{dx} - M^2x\theta = 0 \tag{A1}$$

with the boundary condition of

$$\text{at } x = 0, \frac{d\theta}{dx} = 0 \tag{A2}$$

$$\text{at } x = x_{\text{dry}}, \theta = \theta_{dp} \tag{A3}$$

where $M = \sqrt{2m^2b}$.

By Frobenius method, the solution of differential equation can be found in many mathematical handbook and can be shown as

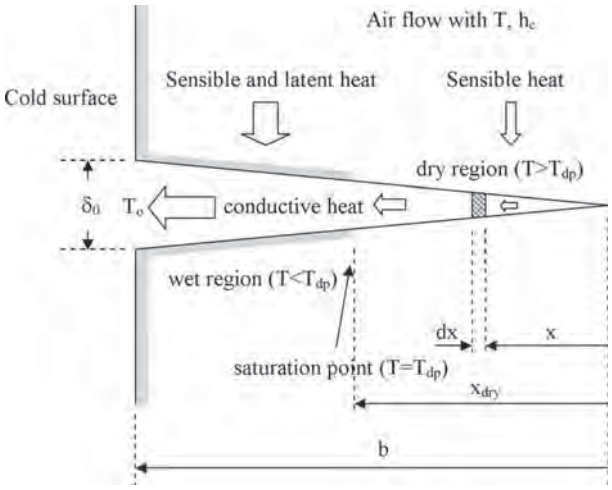

Fig. 10 Heat transfer along the conical spine

$$\theta = x^{-0.5}[C_1I_1(2M\sqrt{x}) + C_2K_1(2M\sqrt{x})] \tag{A4}$$

By the first boundary condition of Eq. (A2), $C_2 = 0$ and by the other boundary condition of Eq. (A3), the constant of C_1 can be obtained as

$$\theta_{dp} = x_{\text{dry}}^{-0.5}C_1I_1(2M\sqrt{x_{\text{dry}}}) \tag{A5}$$

$$C_1 = \frac{\theta_{dp}}{x_{\text{dry}}^{-0.5}I_1(2M\sqrt{x_{\text{dry}}})} \tag{A6}$$

$$\theta = \theta_{dp}\left(\frac{x}{x_{\text{dry}}}\right)^{-0.5}\frac{I_1(2M\sqrt{x})}{I_1(2M\sqrt{x_{\text{dry}}})} \tag{A7}$$

For the wet portion:

By method of Threlkeld [9], the differential equation for the wet portion can be written as

$$x^2\frac{d^2\gamma}{dx^2} + 2x\frac{d\gamma}{dx} - M_T^2x\gamma = 0 \tag{A8}$$

with the boundary condition of

$$\text{at } x = x_{\text{dry}}, \gamma = \gamma_{dp} \tag{A9}$$

$$\text{at } x = b, \gamma = \gamma_0 \tag{A10}$$

where $M_T = \sqrt{2m_T^2b}$.

By Frobenius method, the solution of differential equation can be found in many mathematical handbook and can be shown as

$$\gamma = x^{-0.5}[C_1I_1(2M_T\sqrt{x}) + C_2K_1(2M_T\sqrt{x})] \tag{A11}$$

By substituting Eqs. (A9) and (A10) into Eq. (A11),

$$\gamma_{dp} = x_{\text{dry}}^{-0.5}[C_1I_1(2M_T\sqrt{x_{\text{dry}}}) + C_2K_1(2M_T\sqrt{x_{\text{dry}}})] \tag{A12}$$

$$\gamma_0 = b^{0.5}[C_1I_1(2M_T\sqrt{b}) + C_2K_1(2M_T\sqrt{b})] \tag{A13}$$

Then, C_1 and C_2 can be obtained as

$$C_1 = \frac{b^{0.5}\gamma_0K_1(2M_T\sqrt{x_{\text{dry}}}) - x_{\text{dry}}^{0.5}\gamma_{dp}K_1(2M_T\sqrt{b})}{I_1(2M_T\sqrt{b})K_1(2M_T\sqrt{x_{\text{dry}}}) - I_1(2M_T\sqrt{x_{\text{dry}}})K_1(2M_T\sqrt{b})} \tag{A14}$$

$$C_2 = \frac{x_{\text{dry}}^{0.5}\gamma_{dp}I_1(2M_T\sqrt{b}) - b^{0.5}\gamma_0I_1(2M_T\sqrt{x_{\text{dry}}})}{I_1(2M_T\sqrt{b})K_1(2M_T\sqrt{x_{\text{dry}}}) - I_1(2M_T\sqrt{x_{\text{dry}}})K_1(2M_T\sqrt{b})} \tag{A15}$$

Then, Eq. (A11) can be rewritten as shown in Eq. (36) or

$$\gamma = \frac{b^{0.5}\gamma_0 K_1(2\sqrt{2}m_T\sqrt{bx_{\text{dry}}}) - x_{\text{dry}}^{0.5}\gamma_{dp}K_1(2\sqrt{2}m_T b)}{I_1(2\sqrt{2}m_T b)K_1(2\sqrt{2}m_T\sqrt{bx_{\text{dry}}}) - I_1(2\sqrt{2}m_T\sqrt{bx_{\text{dry}}})K_1(2\sqrt{2}m_T b)} x^{-0.5} I_1(2\sqrt{2}m_T\sqrt{bx}) + \frac{x_{\text{dry}}^{0.5}\gamma_{dp}I_1(2\sqrt{2}m_T b) - b^{0.5}\gamma_0 I_1(2\sqrt{2}m_T\sqrt{bx_{\text{dry}}})}{I_1(2\sqrt{2}m_T b)K_1(2\sqrt{2}m_T\sqrt{bx_{\text{dry}}}) - I_1(2\sqrt{2}m_T\sqrt{bx_{\text{dry}}})K_1(2\sqrt{2}m_T b)} x^{-0.5} K_1(2\sqrt{2}m_T\sqrt{bx}) \tag{A16}$$

For the heat transfer rate and fin efficiency:

When C_1 and C_2 are obtained, the heat transfer rate can be evaluate by the conductive heat transfer through the fin base and can be shown as

$$q_0 = \frac{k\pi\delta_0^2}{4b'_{w,o}}\left.\frac{d\gamma}{dx}\right|_{x=b} \tag{A17}$$

For differentiating $d\gamma/dx$, the by-pass technique is applied as

$$q_0 = \frac{k\pi\delta_0^2}{4b'_{w,o}}\left.\frac{d\gamma}{du}\frac{du}{dx}\right|_{x=b} \tag{A18}$$

where $u = 2M_T\sqrt{x}$

Then,

$$q_0 = \frac{k\pi\delta_0^2}{4b'_{w,o}}\frac{M_T}{b}[C_1 I_2(2M_T\sqrt{b}) - C_2 K_2(2M_T\sqrt{b})] \tag{A19}$$

The ideal heat transfer rate with assumption of entire fin surface temperature equal to fin base temperature can be written as

$$q_{\text{ideal}} = \frac{h_o}{C_{p,a}}\frac{\pi}{2}\delta_0 b\gamma_0 \tag{A20}$$

Then, the fin efficiency can be shown as Eq. (41) or

$$\eta = \frac{q_{\text{actual}}(\text{or } q_0)}{q_{\text{ideal}}} \tag{A21}$$

$$\eta = \frac{k\pi\delta_0^2}{4b'_{w,o}}\frac{M_T}{b}\frac{2C_{p,a}}{h_o\pi\delta_0 b\gamma_0}[C_1 I_2(2M_T\sqrt{b}) - C_2 K_2(2M_T\sqrt{b})] \tag{A22}$$

$$\eta = \frac{\sqrt{2}b\gamma_0[K_1(2\sqrt{2}m_T\sqrt{bx_{\text{dry}}})I_2(2\sqrt{2}m_T b) + I_1(2\sqrt{2}m_T\sqrt{bx_{\text{dry}}})K_2(2\sqrt{2}m_T b)]}{m_T b^2\gamma_0[I_1(2\sqrt{2}m_T b)K_1(2\sqrt{2}m_T\sqrt{bx_{\text{dry}}}) - I_1(2\sqrt{2}m_T\sqrt{bx_{\text{dry}}})K_1(2\sqrt{2}m_T b)]} - \frac{\sqrt{2}b^{0.5}x_{\text{dry}}^{0.5}\gamma_{dp}[I_1(2\sqrt{2}m_T b)K_2(2\sqrt{2}m_T b) + K_1(2\sqrt{2}m_T b)I_2(2\sqrt{2}m_T b)]}{m_T b^2\gamma_0[I_1(2\sqrt{2}m_T b)K_1(2\sqrt{2}m_T\sqrt{bx_{\text{dry}}}) - I_1(2\sqrt{2}m_T\sqrt{bx_{\text{dry}}})K_1(2\sqrt{2}m_T b)]} \tag{A23}$$

References

[1] Schmidt, T. E., 1949, "Heat Transfer Calculations for Extended Surfaces," Refrig. Eng., **57**, pp. 351–357.

[2] Kern, D. Q., and Kraus, A. D., 1972, *Extended Surface Heat Transfer*, McGraw-Hill, New-York.

[3] Arslanturk, C., 2005, "A Decomposition Method for Fin Efficiency of Convective Straight Fins With Temperature-Dependent Thermal Conductivity," Int. J. Heat Mass Transfer, **32**, pp. 831–841.

[4] Heggs, P. J., and Somasundram, I.M., 2007, "Fin Performance Ratios Greater Than Unity: Not Just a Theoretical Aspiration," Appl. Therm. Eng., **27**, pp. 951–961.

[5] Joneidi, A. A., Ganji, D. D., and Babaelahi, M., 2009, "Differential Transformation Method to Determine Fin Efficiency of Convective Straight Fins With Temperature Dependent Thermal Conductivity," Int. Commun. Heat Mass Transfer, **36**, pp. 757–762.

[6] Kulkarni, D. B., and Joglekar, M. M., 2009, "Residue Minimization Technique to Analyze the Efficiency of Convective Straight Fins Having Temperature-Dependent Thermal Conductivity," Appl. Math. Comput., **215**, pp. 2184–2191.

[7] Sharqawy, M. H., Moinuddin, A., and Zubair, S. M., 2012, "Heat and Mass Transfer From Annular Fins of Different Cross-Sectional Area. Part I. Temperature Distribution and Fin Efficiency," Int. J. Refrig., **35**, pp. 365–376.

[8] Cortes, C., Diez, L. I., and Campo, A., 2008, "Efficiency of Composite Fins of Variable Thickness," Int. J. Heat Mass Transfer **51**, pp. 2153–2166.

[9] Threlkeld, J. L., 1970, *Thermal Environmental Engineering*, Prentice-Hall, Englewood Cliffs, NJ.

[10] Liang, S. Y., Wong, T. N., and Nathan, G. K., 2000, "Comparison of One-Dimensional and Two-Dimensional Models for Wet-Surface Fin Efficiency of a Plate-Fin-Tube Heat Exchanger," Appl. Therm. Eng., **20**, pp. 941–962.

[11] Pirompugd, W., Wang, C. C., and Wongwises, S., 2007, "Finite Circular Fin Method for Heat and Mass Transfer Characteristics for Plain Fin-and-Tube Heat Exchangers Under Fully and Partially Wet Surface Conditions," Int. J. Heat Mass Transfer, **50**(3–4), pp. 552–565.

[12] Pirompugd, W., and Wongwises, S., 2013, "Partially Wet Fin Efficiency for Longitudinal Fin of Rectangular, Triangular, Concave, and Convex Profiles," Journal of Franklin Institute, http://dx.doi.org/10.1016/j.jfranklin.2013.02.019

[13] Rosario, L., and Rahman, M. M., 1999, "Analysis of Heat Transfer in a Partially Wet Radial Fin Assembly During Dehumidification," Int. J. Heat Fluid Flow, **20**, pp. 642–648.

Springer

KSME

Journal of Mechanical Science and Technology 27 (7) (2013) 2043~2052
www.springerlink.com/content/1738-494x
DOI 10.1007/s12206-013-0519-7

Parametric study and optimization of a food can corrugation design using a response surface method †

Pattaramon Jongpradist*, Rattharong Rojbunsongsri, Thoatsanope Kamnerdtong and Somchai Wongwises

Department of Mechanical Engineering, Faculty of Engineering, King Mongkut's University of Technology Thonburi, Bangkok, 10140, Thailand

(Manuscript Received March 2, 2012; Revised December 4, 2012; Accepted January 24, 2013)

Abstract

This paper presents the parametric design and functional optimization of a thin-walled food container with a corrugated surface. The configuration of the can corrugation should be designed to minimize the use of raw material subject to the constraints of the targeted structural performance. In the present study, the failure behaviors and the buckling strengths of a commercial food can under paneling pressure and axial loading are investigated with a series of experiments and finite element analyses. Full factorial design is implemented to study the effects of the geometric parameters of the corrugation (e.g., depth, radius, spacing and number of beadings) on its strength. Parameter optimization using a rotatable central composite design is employed to identify an optimal corrugation design by approximating the response surfaces of the can strength in terms of the significant design variables. The obtained surfaces are derived through the analysis of variance, and the suitability of the response is justified. A light- weight can body is then achieved by reduction of the can body thickness according to the required strength characteristics. Finite element analysis of the optimal model is also performed to confirm the predicted results. By using the proposed procedure, the can-body weight can be reduced by up to 12% compared with the original design.

Keywords: Buckling analysis; Corrugation design; Finite element analysis; Response surface method; Structural optimization

1. Introduction

The annual production of metal food and beverage containers in the United States has recently reached 100 billion cans per year [1]. Because of this large production volume, the can industry is actively pursuing new technologies to reduce costs. An appropriate container design is expected to minimize the can thickness and avoid compromising the structural performance requirements under the applicable manufacturing and transportation loads.

The three main loading conditions applied to the cans during the manufacturing processes are as follows: the vacuum pressure in the packaging procedure, the internal pressure during sterilization, and the compressive axial load during transportation and stacking. The can body of a cylindrical-shell shape possesses a high axial loading resistance but only a moderate resistance against paneling and internal pressure. To increase the can strength under a high out-of-plane pressure, most can structures are designed with a corrugated surface. However, the corrugation decreases the axial load resistance. Failure of the can structures from paneling pressure and axial load occur mostly due to shell instability. Calculations of the loading capability and the post-buckling behaviors of the shell are complicated due to the existence of several bifurcation points [2-4]. The analytical and the experimental results often vary significantly (e.g., Refs. [5, 6]) because the deformation behaviors depend on the imperfections of the geometry and the material properties [7].

Research on the container design using various tools has focused on analyses of the containers in use for different loading conditions. Sodiek and Sauer [8] studied the mechanical behaviors of food cans during the sterilization process and proposed a method for prediction of the loading capacity. Siad [9] suggested analytical formulae to predict the buckling of thin-walled orthotropic cylindrical shells under a uniform external pressure. The results were shown to be in agreement with experiments performed by Ref. [10]. Finite element analysis (FEA) has been employed to study the behaviors of food containers subject to different types of loading [11-13]. Certain optimization techniques for the lightest container design have also been widely proposed [14-16]. Yamazaki et al. [17] and Han et al. [18] studied the shape of the end of the can to minimize the weight of a beverage bottle. Ugail [19] demonstrated method for design of a light-weight food container shape with a required volume. Han et al. [20] applied a multi-objective optimization approach to obtain the proper rib design for a screw top bottle with a temperate touch surface for vending of

*Corresponding author. Tel.: +66 24709123, Fax.: +66 24709111
E-mail address: pattaramon.tan@kmutt.ac.th
† Recommended by Associate Editor Gang-Won Jang

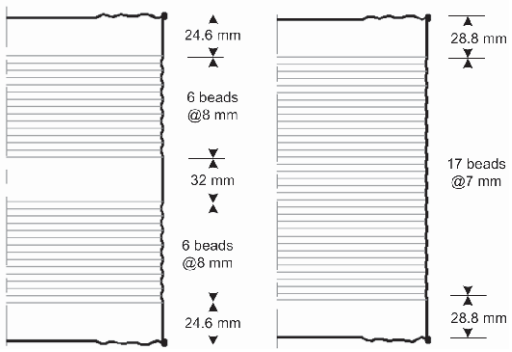

(a) mosel A (b) model B

Fig. 1. Beading configurations of the cans studied in the current work.

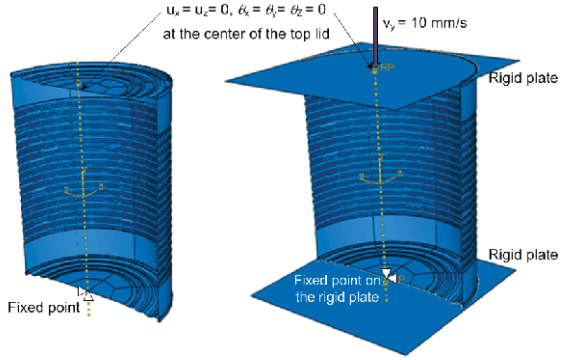

(a) (b)

Fig. 2. Boundary conditions for finite element analyses of the can under: (a) internal and vacuum pressures; (b) axial compressive load.

hot items. However, no application of an optimization technique for the study and design of the can-body corrugation have yet been performed, particularly, with consideration of the can structural performance, including the effects of a nonlinear structural response.

In the current work, finite element analysis using Abaqus software [21] is carried out to study the failure behavior and the strength of corrugated food containers under paneling pressure and axial load. Experiments performed on physical models are used to compare and validate the results from the FE models. The significant corrugation geometric parameters that affect the can structural performance are specified via a full factorial design based on the FEA results. The design parameters include the thickness of the can body, the beading depth, the spacing, the radius and the number of beadings.

The response surface methodology (RSM) [22], a statistical technique that uses quantitative data obtained from appropriately designed experiments to determine the regression model and operating conditions, is then applied to determine the optimal corrugation design. With the purpose of minimizing the can thickness, a numerical example is used to design the optimized corrugation for the given loading requirements.

2. Structural performance of a food container

In the cannery industry, the can sizes are categorized to avoid confusion from conflicting local names of cans. The can used in the current research is designated as 603 × 700, which would measure approximately 6-3/16 inches (157.2 mm) in the outside diameter of the double seam and 7 inches (177.8 mm) in the overall height. Both the lids and the body are produced from single-reduced continuous-annealed tinplate. The material properties of the tinplate are tested using five samples, and the average values are as follows: the elastic modulus of the tinplate is 219.86 GPa, the yield stress is 476.74 MPa, and the Poisson's ratio is 0.3. Two different models of beading configuration are considered, as illustrated in Fig. 1. Model A (or the 'half' beading configuration) consists of two sets of six beadings with a 32-mm spacing between. The thickness of the can body and the can lids is 0.28 mm. Model B (the so-called 'full' beading configuration) has a full corrugated surface of 17 beadings over the can body. The can-body and can-lid thicknesses are 0.25 mm and 0.28 mm, respectively. Both models display the same corrugation pattern at the can lids. The can structural performances are considered under three types of loadings, i.e., internal pressure, vacuum pressure, and compressive axial load. Three samples are tested for each model in the experiments for all load cases. The boundary conditions for analyses of the can under different loadings are shown in Fig. 2.

2.1 Internal pressure

The can deformation under internal pressure is studied by applying continuously increasing air pressure to the inside of the can. After a certain amount of pressure is applied, the can lids begin to bulge before a noticeable deformation of the can body occurs. The internal pressure requirement is such that the paneling growth (the maximum bulging of the can lid) does not exceed the reference level at the top of the seam. The average allowable amount of paneling growth (measured by using a dial gauge from three samples) is 4.496 mm, and the average internal pressure obtained from the test is 20.6 kPa.

To simulate the can lid deformation from internal pressure, a three-dimensional (geometrically and materially) nonlinear FEA is performed. The can body of a thin-walled cylindrical shell shape and the corrugated plate lids are modeled using 8-node reduced-integration quadrilateral shell (S8R) elements. The double seams along the rims of the can lids are stiffer than the other parts and are thus modeled by 20-node quadratic brick (C3D20) elements. The quadratic elements are preferred because of the curved boundaries of the can structure. An example of the finite element model including the type and the element size for each part is displayed in Fig. 3. The can material properties are assumed as elastic-perfectly plastic. The results from the FEA show that when the paneling growth is controlled to the measured value, the static internal pressure is 20.61 kPa. The radial displacement of the can-body shell remains minimal, which is in agreement with the experimental result.

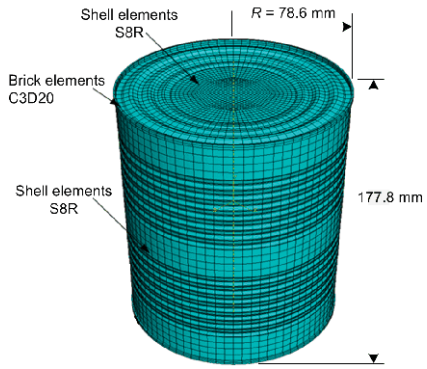

Fig. 3. Meshing and element types of the finite element model.

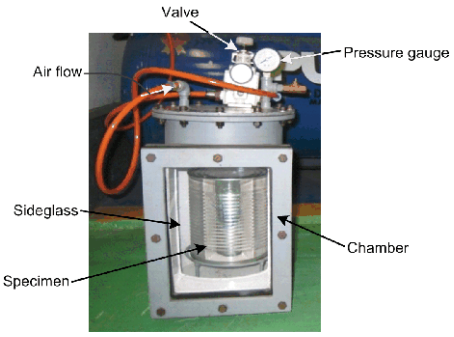

Fig. 4. Pressurized chamber for internal and vacuum load experiments.

Table 1. Comparisons of the plastic deformation of the can lid from FEA and experiments.

Method of analysis	Average deformation (mm)				
	O	*A*	*B*	*C*	*D*
Experiment	1.958	2.130	2.078	1.887	1.238
FEA	2.186	2.044	1.996	1.797	1.277
Difference (%)	+11.6	-4.0	-4.0	-4.8	+3.2

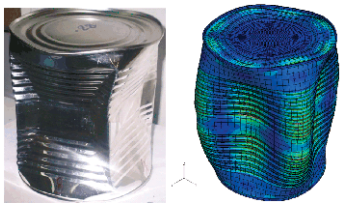

(a) model A

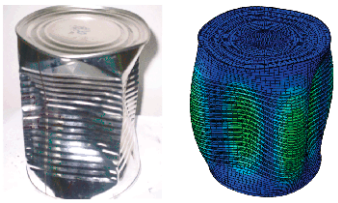

(b) model B

Fig. 5. Comparisons of buckling mode shape due to vacuum pressure in experiments and FEA.

2.2 Vacuum pressure

The deformation behavior and the can structural resistance under vacuum pressure are studied by placing the specimens in a closed chamber as shown in Fig. 4, where increasing external air pressure is applied. Similar to the previous case, when the pressure in the chamber is increased, the container lids first start to cave in while no visible deformation is observed in the can body.

Static and buckling tests are performed to study the can behaviors under vacuum pressure. First, an external pressure of 80 kPa is applied to the can, and the plastic deformations of the can are measured after the pressure is released. The measuring points are located along the radial direction of the can lid at the peaks of each lid corrugation, namely, at locations *A* to *D* and at the center *O*. The experimental deformation for each peak is obtained from an average of four measuring points located 90 degrees apart on the circumference.

The finite element simulation for this case is executed via a two-step analysis: in step one, a static pressure of 80 kPa is applied to the can, and in step two, the pressure is released. The plastic deformations of the can lids at locations *A* to *D* are recorded and compared in Table 1. The results from the experiments and the FEA are shown to be similar at all locations with less than 5% difference. A slightly larger yet acceptable difference is detected at the center of the can lid.

The next experiment examined the can structural strength and failure behavior under vacuum pressure. When the pressure in the chamber is increased although the high plastic deformation initially occurs at the can lids in both models, the eventual failure is due to the instability of the can body. The modes of failure for models A and B consist of four apexes located around the can body as shown in Figs. 5(a) and 5(b), respectively. The buckling strengths, read as the maximum value before the pressure inside the chamber drops, are 142 kPa and 126 kPa, respectively.

In the FEA simulations, this load case is simulated in a large-deformation static buckling analysis under a uniform vacuum pressure inside the can. The modes of failure obtained from the FEA for both models are analogous with those from the experiments (Fig. 5). The buckling paneling pressures of model A and B from the analysis are both comparable with their experimental results at 143 kPa and 129 kPa, respectively.

2.3 Compressive axial load

To evaluate the compressive axial resistance of the can structure, the specimens were tested under compression using a universal testing machine. As shown in Fig. 6, a linear-guide device is used to ensure movement in the vertical direction and a uniform load around the can axis. The crosshead speed is set to 10 mm/s. Failure from the compressive load occurs as buckling of the can, and the load drops rapidly. For both models, the can bodies buckle such that seven waves are formed around the can-body circumferences. In model A, the circum-

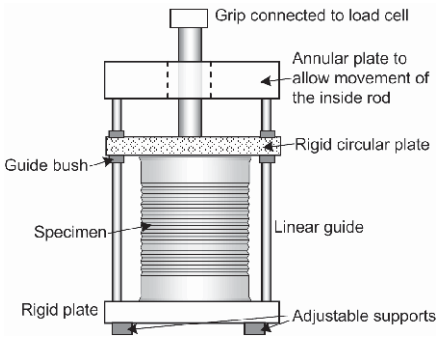

Fig. 6. Testing devices for axial load capacity.

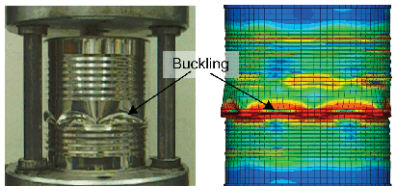

(a) model A

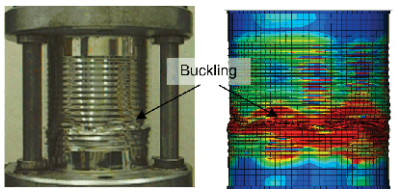

(b) model B

Fig. 7. Buckling of the can structure under axial compression.

ferential waves occur between the two sets of beadings (Fig. 7(a)) at an average compression of 10450 N with a maximum displacement of 1.89 mm. For model B, the buckling waves arise at locations around the first to the third corrugation from either side of the can ends. The average compressive load is 9884 N and the maximum displacement is 1.32 mm (Fig. 7(b)).

In the simulations, the can models are modified by the attachment of rigid plates to the top and the bottom of the can. The buckling mode shapes are first determined by static buckling analysis to measure the eigenfrequencies, followed by Riks analysis to study the buckling strength and the post-buckling behaviors.

The load-displacement response of a thin-walled structure under axial load usually produces a negative stiffness. To remain in equilibrium, the strain energy must be released. The Riks method is able to find the static equilibrium during the unstable phases of the model response.

To use the Riks procedure for solving a post-buckling problem, it is necessary to introduce an initial imperfection into the perfect geometry of the model. The definition of the geometric imperfection is created by a superposition of buckling eigenmodes obtained from a previous buckling analysis. The normalized displacement of the eigenmode shape and the imperfection scaling factor are multiplied and result in the imperfection amplitude. The imperfection amplitude alters the perfect structure to that of geometry with a deformation before the load is applied on the model.

Table 2. Normalized axial buckling resistances for various eigenmodes and imperfection sizes.

Eigenmode	Buckling load (N) for imperfection scaling factor			
	0.01t	**0.1t**	**0.2t**	**0.5t**
1	0.999	0.988	0.987	0.984
5	0.999	0.997	0.994	0.988
17	0.999	0.996	0.993	0.962

The imperfections used in the model were chosen in terms of percent of the shell thickness, *t*. An appropriate perturbation pattern in the initial condition corresponding to the eigenmodes obtained from the static buckling analysis is applied to trigger the buckling process. The top plate is assigned to move downward at the speed of the crosshead. The buckling resistance under the axial load is read from the maximum reaction force at the reference point on the top plate before the force drops. The stiffness of the structure and the maximum load are observed to decrease with increasing imperfection values. The respective buckling resistances of the perfect shell for model A and B are 11,584 N and 10,588 N. The buckling mode shapes from the FEA resemble those from the experiments. Table 2 shows an example of the normalized buckling resistance (as a ratio to the perfect shell buckling load) of model B for different eigenmodes and imperfection scaling factors. The sensitivity of the structure to the eigenmodes and imperfections appears to be marginal. The reduction of the buckling load in the models with imperfections of up to 50% of the shell thickness is less than 4%. Therefore, this study employs the first eigenmode shape with an imperfection scaling factor of 0.1 *t* to the axial buckling load analyses for all calculated models in the optimization design. Local imperfections are not introduced into the mode.

3. Effects of beading configuration and design parameters

As illustrated in the previous section, two beading configurations and five geometric parameters are investigated in the current work, as shown in Fig. 8. The parameters of interest include the thickness of the can body (*t*), the beading depth (*d*), the beading spacing (*s*), the beading radius (*r*) and the number of beadings (*n*).

3.1 Beading configuration

Model A and model B with the same material thickness of 0.28 mm, are examined to study the effects of the beading configuration. Because the thicknesses of the container are approximately uniform, the material volumes for models A and B can be computed by the multiplication of the can sur-

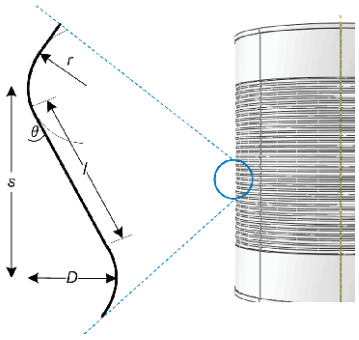

Fig. 8. Corrugation parameters.

face area and the can thickness.

The amount of tin-plate in the can body V (in mm^3) can be expressed in terms of the number of beadings n, the angle θ (in radians) and the length l (in mm) of the line shown in Fig. 8, as

$$V = \pi Dt[2n(2r\theta + l) + (H - 2ns)] \quad (1)$$

where D and H are the diameter and the height of the can body, respectively. The values of θ and l can be determined from their relationships to the beading spacing, s, and the beading depth, d:

$$s = l\cos\theta + 2r\sin\theta \quad (2)$$

$$d = l\sin\theta + 2r(1-\cos\theta)\,. \quad (3)$$

Eqs. (2) and (3) can be solved simultaneously to obtain θ as a function of other geometric parameters as

$$\theta = \sin^{-1}\left(\frac{4rs \pm \sqrt{16r^2s^2 - 4d(4r-d)((2r-d)^2 + s^2)}}{2((2r-d)^2 + s^2)}\right). \quad (4)$$

The length l can be calculated by substituting θ from Eq. (4) into either Eq. (2) or Eq. (3). Note that the two values of θ yield one positive and one negative value of l with the same magnitude. Thus, only the positive value of l is realistic.

The can model used in the current study has diameter D of 157.16 mm and height H of 177.8 mm. For the beading configuration of model A, there are two sets of six beadings (n = 12) with a spacing of 8 mm (s = 4 mm). The beading radius r is 2.8 mm, and the depth d is 0.7 mm. Substitution of all variables into Eq. (4) gives the angle θ of 0.201 radians. The length l is found from Eq. (2) or Eq. (3) as 2.94 mm. Therefore, the model A material volume, V_A, is calculated from Eq. (1) as 24,798 mm^3.

Model B has 17 beadings (n = 17) of radius r = 2.8 mm, depth d = 0.7 mm and spacing = 7 mm (s = 3.5 mm). Thus, we achieve a θ and l of 0.244 radians and 2.21 mm, respectively. Therefore, the model B material volume of the can body, V_B, is 24,939 mm^3. Thus, the material volumes for the two models are almost identical.

Table 3. Comparisons of structural performances for the two models.

Model	Material volume (mm^3)	Paneling strength (kPa)	Axial strength (N)
A	24,798	142	11584
B	24,939	158	11513
Difference (%)	+0.57%	+10.1%	-0.62%

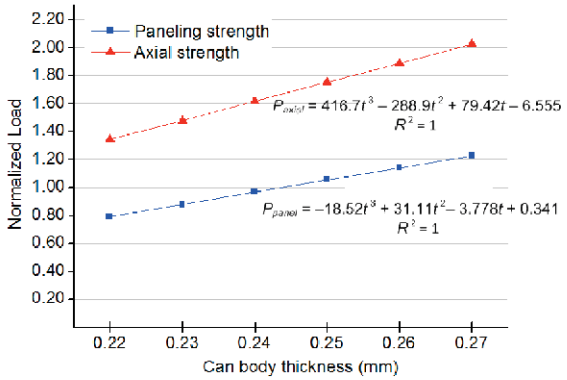

Fig. 9. Effects of changes the can-body thickness on the container strength.

The performances of models A and B with the same can body thickness of 0.28 mm under vacuum pressure and axial load as determined by FEA are shown in Table 3. Model B's pressure capacity is higher than that of model A by 10.1% while its axial strength is smaller by 0.62%. Because the beadings are designed to stiffen the unsupported wall section and to increase the paneling pressure, their influence on the axial load is smaller. The use of either design depends on the manufacturer's requirements and the intended usages. In the current study, the full beading configuration in model B is chosen as the prototype for optimization.

3.2 Design parameters

The design variables that affect the can strengths are the can-body thickness, the corrugation depth, the spacing, the radius and the number of beadings. Because the surface areas for the different corrugation designs quite similar, the key parameter that directly affects the amount of raw material used is the can thickness. Fig. 9 shows the FEA results for the paneling and axial strengths of the chosen model (Model B) for various can-body thicknesses. The ordinate is the normalized loading for the axial and paneling pressure resistances calculated by the ratio of the buckling strengths and the required loads. It can be observed that a decrease in the material thickness results in lower structural performance. The effects of the can thickness on both strengths are proportional to the magnitude of the bending stiffness and cubic relations are observed between the thickness and buckling strengths. Moreover, it was found that although can body thickness is one of the sig-

nificant parameters, its interactions with the other parameters are negligible. Therefore, the can-body thickness is excluded from the design of the optimization process. The corrugation shape needed to maximize the can performance should be first determined, and the can-body thickness is then adjusted according to the required safety factor.

The significance of the other design parameters (corrugation depth, spacing, radius and number of beadings) to the can structural strengths under paneling (vacuum) pressure and axial load are investigated using a two-level full factorial design. Two values (high and low) are used for each parameter. Note that the internal pressure condition does not affect the can body strength since failure under this condition is observed at the can lids. The normal probability plot shows that the most significant main effects on the paneling pressure are the spacing, the radius and the depth of corrugation. The spacing is found in the negative field while the radius and depth are found in the positive field. In addition, a subset of the factor interactions are found to be significant, which implies that the linear surface of the factors and the response is not suitable, and higher-order terms are required to achieve an adequate fit.

The corrugation spacing is a significant effect only for the paneling strength, in which a smaller spacing is more desirable. However, when the spacing is too small, the corrugation forming process is problematic or impossible in certain cases, especially when the corrugation radius is large. The corrugation formability can also be assessed mathematically using Eq. (4). When the designed corrugation shape can be formed efficiently, the value of the term inside the square roots in Eq. (4) will be large. When the obtained corrugation parameters are geometrically impossible, this term becomes negative.

Moreover, it can be observed that the main and interaction effects of the number of corrugations on both strengths are insignificant. Because the simultaneous optimization of many factors can cause a reduction in the changeable ranges of the design variables due to interactions between the parameters, the insignificant effects should be excluded from the response surface optimization. To avoid unrealistic geometrical connectivity problems, only the depth, radius and spacing are applied to the weight minimization problem under the structural performance constraints. The model with 17 beadings is therefore used in the optimization.

4. Optimal design of corrugation parameters

4.1 Formulation of weight minimization problem for the can body

The objective of the optimization is to minimize the can weight while ensuring that the container's strengths still meet the manufacturer's requirements. The axial strength A and the paneling pressure requirement P are restricted to be larger than the allowable minimum values A_{min} and P_{min}, respectively. The geometrical dimensions of the corrugation are selected as the design variables. For a given can size, the weight minimization of the can body is then posed as:

$$\text{Find design variables: } X = \{x_i\},\ i = 1, \ldots, n \tag{5}$$

where n is the number of design variables.

$$\text{Minimize} \quad f = V(X) \tag{6}$$

$$\text{subject to} \quad g_1 = 1\text{-}A(X)/A_{min} \le 0, \tag{7}$$

$$g_2 = 1\text{-}P(X)/P_{min} \le 0, \tag{8}$$

$$x_i^L \le x_i \le x_i^U \tag{9}$$

where x_i^L and x_i^U are the lower and upper bounds of the ith design variable, respectively.

The optimization via response surface methodology is performed based on the results from the finite element analyses. First, the path of steepest ascent is determined to evaluate a set of adjustments to the process variables that will move the process toward the optimum. Next, the response surface modeling procedure is applied to generate the approximated functions of the axial strength $A(X)$ and paneling pressure $P(X)$ in terms of the design variables.

A low-order polynomial in a selected relatively small region of the independent variable space is often appropriate. When the size of the region in which the response surface must be accurate enough to describe and approximate the real function is increased, a higher order polynomial or other response surface functions must be applied [23]. Often, the curvature in the true response surface is severe enough that a second-order model will likely be required. Central composite design (CCD) is the complete design which allows for efficient estimation of the terms in the second-order response surface model

$$y = \beta_0 + \Sigma_{i=1}^{n}\beta_i x_i + \Sigma_{i=1}^{n}\beta_{ii} x_i^2 + \Sigma\Sigma_{i<j=2}^{n}\beta_{ij} x_i x_j \tag{10}$$

where β_0, β_i, β_{ii} and β_{ij} are the constant, linear, quadratic and cross product coefficient, respectively. The variables x_i and x_j are the coded variables. The second-order model is widely used because it is flexible and works well in solving practical problems. In addition, in this type of model, the main effects and the interactions among the variables may be estimated by performing a minimum number of experiments and the parameters can be easily estimated using the least squares method [24]. For a two-level study, the total number of experiments to be performed is generally given as a sum of the $2n$ factorial runs, $2n$ axial runs, and n_c center runs, where n is the number of independent variables.

The adequacy of the selected model and the statistical significance of the regression coefficients are tested using analysis of variance (ANOVA). The measured and the model-predicted values of the response variables are used to compute the correlation coefficient R^2 and the relative standard error of prediction RSEP. The correlation between the measured and the predicted values indicates the goodness of fit of the model, whereas, the RSEP values are used to evaluate the predictive

Table 4. Effects of corrugation spacing, radius, and depth on the paneling and axial strengths.

Run	Independent variables						Dependent variables			
	Coded variables			Natural variables			Paneling strength (kPa)	Axial strength (N)	SF for paneling strength	SF for axial strength
	x_1	x_2	x_3	Spacing (mm)	Radius (mm)	Depth (mm)				
1	-1	-1	-1	6.15	2.5	0.51	104.1	12,361	1.301	1.482
2	1	-1	-1	7	2.5	0.51	100.7	12,352	1.259	1.481
3	-1	1	-1	6.15	3.47	0.51	109.5	12,299	1.369	1.475
4	1	1	-1	7	3.47	0.51	104.4	12,264	1.305	1.470
5	-1	-1	1	6.15	2.5	0.63	123.1	10,581	1.539	1.269
6	1	-1	1	7	2.5	0.63	118.9	10,661	1.486	1.279
7	-1	1	1	6.15	3.47	0.63	126.8	10,496	1.585	1.259
8	1	1	1	7	3.47	0.63	120.7	10,479	1.509	1.257
9	-1.682	0	0	5.86	2.985	0.57	121.9	11,333	1.524	1.359
10	1.682	0	0	7.29	2.985	0.57	116.2	11,409	1.453	1.368
11	0	-1.682	0	6.575	2.169	0.57	116.7	11,486	1.459	1.377
12	0	1.682	0	6.575	3.8	0.57	119.3	11,345	1.491	1.361
13	0	0	-1.682	6.575	2.985	0.47	95.2	13,015	1.19	1.561
14	0	0	1.682	6.575	2.985	0.67	127.2	10,050	1.59	1.205
15	0	0	0	6.575	2.985	0.57	118.8	11,416	1.485	1.369
16	0	0	0	6.575	2.985	0.57	118.8	11,416	1.485	1.369
17	0	0	0	6.575	2.985	0.57	118.8	11,416	1.485	1.369
18	0	0	0	6.575	2.985	0.57	118.8	11,416	1.485	1.369
19	0	0	0	6.575	2.985	0.57	118.8	11,416	1.485	1.369
20	0	0	0	6.575	2.985	0.57	118.8	11,416	1.485	1.369

ability of the selected model. The RSEP is computed as:

$$RSEP = \sqrt{\frac{\sum_{i=1}^{N}(y_{pred,i} - y_{meas,i})^2}{\sum_{i=1}^{N}(y_{meas,i})^2}} \times 100 \quad (11)$$

where $y_{pred,i}$ and $y_{meas,i}$ are the ith predicted and measured values, respectively.

4.2 Numerical example of optimal design

A design example for a food container of dimensions 603 × 700 with full beading corrugation is explained and discussed in this section. The paneling pressure and the axial load requirements are set as 80 kPa and 11,500 N, respectively.

To study the combined effect of the three significant variables of corrugation depth, radius and spacing, CCD is employed with an axial distance α of 1.682, which allows the design to possess the property of rotatability. After the method of steepest ascent, it was found that although the minimum spacing is preferable for the paneling strength, spacing lower than 6.15 mm may cause difficulties in the formation of the corrugation. Therefore, spacing between 6.15 and 7.00 mm are recommended. The appropriate minimum and maximum depths are obtained as 0.51 and 0.63 mm, while a radius between 2.50 and 3.47 mm is recommended.

The variables in the defined range of each parameter are coded to fall at ±1 for the factorial points, 0 for the center points and ±1.682 for the axial points. The complete designs consist of 20 combinations (including six replicates of the center point). All designs are carried out using finite element models as discussed in the earlier section. Because FEA gives the same responses for all replicates, only 15 necessary runs are performed. The combinations of the three independent variables together with the responses are shown in Table 4. The safety factor (SF) is computed by the ratio of the can strength and its required load.

Analyses of variance results of the two response variables for the prediction of paneling and axial strengths are shown in Tables 5 and 6. The suitability of the regression is justified by the fact that the Fisher's F-test statistic of the model is much higher than the critical F value ($F_{0.05,4,15} = 3.056$) for the considered probability ($P = 0.05$) and degrees of freedom, and the p-value approaches zero in both cases.

Based on the analysis of variance, the response surfaces of the paneling and axial strengths are approximated using a quadratic model. The model equations for the paneling strength (Y_{paneling}) and that of the axial strength (Y_{axial}) are obtained as:

Table 5. Analysis of variance of the response surface model for the prediction of paneling strength.

Source	DF	Seq. SS	Adj. SS	Adj. MS	F-test	p-value
Regression	9	1376.25	1376.25	152.916	61.53	0.000
Linear	3	1222.48	1222.48	407.493	163.9	0.000
Square	3	150.12	150.12	50.040	20.14	0.000
Interaction	3	3.64	3.64	1.215	0.49	0.698
Total	19	1401.1				

Table 6. Analysis of variance of the response surface model for the prediction of axial strength.

Source	DF	Seq. SS	Adj. SS	Adj. MS	F-test	p-value
Regression	9	10692060	10692060	1188007	4987.0	0.000
Linear	3	10657205	10657205	3552402	14823	0.000
Square	3	29822	29822	9941	41.48	0.000
Interaction	3	5033	5033	1678	7.00	0.008
Total	19	10694457				

$$Y_{paneling} = 118.877 - 2.079x_1 + 1.389x_2 + 9.125x_3 - 0.417x_1^2 - 0.788x_2^2 - 3.192x_3^2 - 0.45x_1x_2 - 0.225x_1x_3 - 0.45x_2x_3 \quad (12)$$

and

$$Y_{axial} = 11416.1 + 10.8x_1 - 47.9x_2 - 882x_3 - 16.9x_1^2 - 1.1x_2^2 + 40.2x_3^2 - 15.4x_1x_2 + 13.4x_1x_3 - 14.6x_2x_3 \quad (13)$$

where x_1, x_2 and x_3 are the coded variables for corrugation spacing, radius and depth, respectively. The regression coefficients are shown in Table 6.

The R^2 values for these response variables are greater than 0.98 indicating that the developed response surface models explain the response well. A particularly high value of the adjusted correlation coefficient R_{adj} also shows the high significance of the model. Additionally, considerably low RSEPs (0.91 and 0.10) underscore the adequacy of the fitted quadratic model.

The response surface plots of the paneling strength are illustrated in Fig. 10. For the specified ranges of the corrugation parameters, the maximum paneling strength is achieved when the corrugation spacing is less than 6 mm, the radius is between 3.20 and 3.50 mm and the corrugation depth ranges from 0.62 to 0.65 mm. Fig. 11 shows the surface plots for axial strength. From the steep surface plot along the depth axis, it is obvious that the effect driven by the corrugation depth is much more significant than that of the radius and the spacing. Moreover, the low-curvature surface located between the corrugation depth and the radius implies that the interaction of these two variables is not substantial. It can be observed from the plots that the maximum axial strength is obtained when the depth is lower than 0.50 mm.

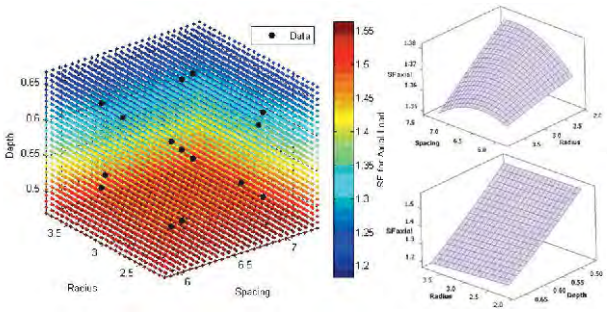

Fig. 10. Response surface plot of the safety factor for paneling pressure calculated from Eq. (12).

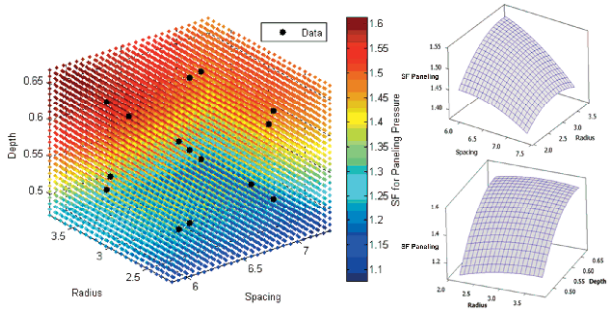

Fig. 11. Response surface plot of the safety factor for axial load calculated from Eq. (13).

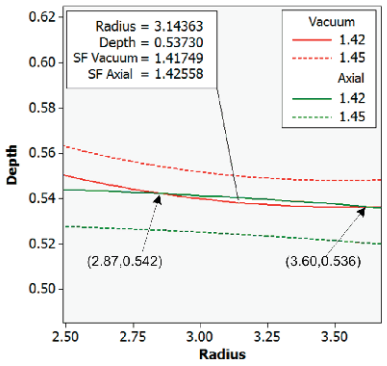

Fig. 12. Optimal region found by overlaying the paneling and axial safety factors for a spacing of 6.5 mm.

The optimal condition is determined using the desirability functions. In this study, the objective is to maximize the responses while emphasis is placed on remaining close to the target value. Thus, the weight of the desirability function is chosen to be greater than unity. The lower and upper bounds for the SFs are specified as 1.3 and 1.5, respectively, and the importance for both responses is set to 1. By using the optimizer, the highest desirability is attained at a value of 0.692 when the corrugation spacing, depth and radius are 5.86 mm, 0.54 mm and 3.65 mm, respectively. For this case, the SF for the paneling strength is 1.46 and that of the axial strength is 1.42.

Another approach for determining the optimal condition is to superimpose the contour plots of the two responses, as shown in Fig. 12. The final product is considered as optimal

Table 7. Safety factors and weight of the optimal design.

Can thickness (mm)	SF Paneling		SF Axial		Weight (g)
	Predicted	FE	Predicted	FE	
0.25	1.417	1.416	1.425	1.425	174.17
0.24	1.336	1.329	1.296	1.316	167.20
0.23	1.258	1.245	1.170	1.202	160.24
0.22	1.184	1.145	1.043	1.103	153.27

when the safety factors for both the paneling and axial strengths are highest. Therefore, the criteria for the optimization are targeted as higher than 1.3. By overlaying the responses, the optimal combined condition is found at a corrugation spacing of 6.5 mm, a depth between 0.536 and 0.542 mm and a radius between 2.87 and 3.60 mm. For this case, the SFs for both the paneling and axial strengths are approximately 1.42. Thus, the optimal configuration from the overlay plots is similar to that obtained from the optimizer. However, this method is not advised if several parameters are considered and the optimizer may be more convenient.

At the current stage, the optimal design gives the structure a higher safety factor but the can weight remains relatively unchanged (decreased by only 0.46%). The designed corrugation shape can be used with a reduced can-body thickness for the required safety factor such that the container weight is minimized. Because the can strengths are dependent on the can thickness, the slopes of the normalized loads from Fig. 9 are then used to estimate the safety factors and possible thickness reductions as listed in Table 7. The minimum can body thickness is found to be 0.22 mm, and the can body weight calculated from Eq. (1) is reduced by 12.4% compared with the original design. The predicted safety factors of the optimal model are also confirmed as comparable with the results from the FEA of the final model. The differences in the predicted and the FE strengths are less than 5.5% although the discrepancies are slightly larger for the axial load.

5. Conclusion

In this paper, parameter optimization using the response surface method has been applied to identify an optimal corrugation design for a food container that minimizes the container weight subject to predefined constraints on the paneling and axial strengths. Finite element analysis is applied to simulate the failure behaviors and calculate the can structural performances under loading in the manufacturing process. Full factorial design is used to define the key factors that affect the can strength. A central composite design is employed to approximate the response surfaces of the paneling and axial strengths in terms of the three significant design variables: corrugation depth, radius and spacing. A numerical optimal design example leads to the can-body weight minimization that reduces the container weight by up to 12.4%. A better understanding of the optimization of the corrugation design is achieved. It is clear from these results that using a RSM based on the design-of-experiments technique is able to reduce the computational costs of constructing approximate response surfaces and save time in designing the shape of the can corrugation to meet different levels of strength requirements.

Acknowledgment

The financial support from Thailand research fund (TRF) under grant MRG5380005 is gratefully acknowledged.

Nomenclature

d : Corrugation depth
D : Diameter of the can body
l, s : Corrugation parameters
r : Corrugation radius
n : Number of beadings
t : Thickness of the can body
V : Material volume
x_i : Coded variables
Y_{axial} : Axial strength
$Y_{paneling}$: Paneling strength
β_i : Response surface coefficients
θ : Corrugation angle

References

[1] J. Wang, Design optimization of rigid metal containers, *Finite Elem. Anal. Des*., 37 (2001) 273-286.
[2] F. Fujii, H. Noguchi and E. Ramm, Static path jumping to attain postbuckling equilibria of a compressed circular cylinder, *Computational Mech.*, 26 (2000) 259-266.
[3] A. N. Aljawi, Numerical simulation of axial crushing of circular tubes, *J. of King AbdulAziz University: Eng. Sci*., 14 (2002) 3-17.
[4] A. G. Arani, S. Golabi, A. Loghman and H. Daneshi, Investigating elastic stability of cylindrical shell with an elastic core under axial compression by energy method, *Journal of Mechanical Science and Technology*, 21 (2007) 983-996.
[5] N. Yamaki, *Elastic stability of circular cylindrical shells*, Amsterdam-New York-Oxford, North Holland (1984).
[6] D. Bushnell, *Computerized buckling analysis of shells*, Kluwer Academic Publishers, Dordrecht (1989).
[7] V. Papadopoutos and P. Iglesis, The effect of non-uniformity of axial loading on the buckling behavior of shells with random imperfections, *Int. J. of Solids and Struc*., 44 (2007) 6299-6317.
[8] M. Sodiek and R. Sauer, Mechanical behaviour of food cans under radial and axial load, *Third International Tin Plate Conference* (1984).
[9] L. Siad, Buckling of thin-walled orthotropic cylindrical shells under uniform external pressure: Application to corrugated tin cans, *Thin-Walled Structures*, 35 (1999) 101-115.
[10] C. T. F. Ross and M. Humphries, The buckling of corrugated circular cylinders under uniform external pressure,

Thin-Walled Structures, 17 (1993) 259-271.
[11] J. D. Reid, R. W. Bielenberg and B. A. Coon, Indenting, buckling and piercing of aluminum beverage cans, *Finite Elem. Anal. Des*., 37 (2001) 131-144.
[12] P. Teppunkulngam, P. Tantichattanont and T. Kamnertong, Study of loading capacity of corrugated food cans using finite element method, *Proc. of Mechanical Engineering Network Thailand 22nd Conference* 2008, October 15-17, 2008, Rungsit, Thailand.
[13] R. Rotbunsongsri, P. Jongpradist and T. Kamnerdtong, Parametric study of food can corrugation geometry by using finite element method, *Proc. of the Second TSME International Conference on Mechanical Engineering*, October 19-21, 2011, Krabi, Thailand.
[14] D. H. Chen and S. Ozaki, Numerical study of axially crushed cylindrical tubes with corrugated surface, *Thin-Walled Structures*, 47 (2009) 1387-1396.
[15] K. K. Choong and E. Ramm, Simulation of buckling process of shells by using finite element method, *Thin-Walled Structures*, 31 (1998) 39-72.
[16] C. T. F. Ross, A redesign of the corrugated tin can, *Thin-Walled Structures*, 26 (1996) 179-193.
[17] K. Yamazaki, R. Itoh, M. Watanabe, J. Han and S. Nishiyama, Applications of structural optimization techniques in light weighting of aluminum beverage can ends, *J. of Food Engineering*, 81 (2007) 341-346.
[18] J. Han, R. Itoh, S. Nishiyama and K. Yamazaki, Application of structure optimization technique to aluminum beverage bottle design, *Struct. Multidis Optim.*, 29 (2005) 304-311.
[19] H. Ugail, Parametric design and optimization of thin-walled structures for food packaging, *Optimization and Engineering*, 4 (2003) 291-307.
[20] J. Han, K. Yamazaki, R. Itoh and S. Nishiyama, Multiobjective optimization of a two-piece aluminum beverage bottle considering tactile sensation of heat and embossing formability, *Struct. Multidis. Optim.*, 32 (2006) 141-151.
[21] Simulia, *Abaqus Analysis User's Manual* (2011).
[22] R. H. Myers, D. C. Montgomery and C. M. Anderson-Cook, *Response surface methodology*, John Wiley & Sons, Inc., New Jersey (2009).
[23] G. Steenackers, F. Presezniak and P. Guillaume, Development of an adaptive response surface method for optimization of computation-intensive models, *Computers and Industrial Engineering*, 57 (2009) 847-855.
[24] N. Muhammad, Y. H. P. Manurung, M. Hafidzi, S. K. Abas, G. Tham and E. Haruman, Optimization and modeling of spot welding parameters with simultaneous multiple response consideration using multi-objective Taguchi method and RSM, *Journal of Mechanical Science and Technology*, 26 (8) (2012) 2365-2370.

Pattaramon Jongpradist is currently an Assistant Professor at Department of Mechanical Engineering, Faculty of Engineering, King Mongkut's university of Technology Thonburi. She received her B.Eng. degree from Chulalongkorn University, Thailand, her M.Eng. from Asian Institute of Technology, Thailand, and her Ph.D. in Mechanical Engineering from Memorial University, Canada, in 2006. Her current interest includes computational mechanics, such as techniques in finite element analysis and meshless methods, and behaviors of plate and shell structures.

Rattharong Rotbunsongsri is a graduate student in the Department of Mechanical Engineering at King Mongkut's university of Technology Thonburi. He also received his B.Eng. in Mechanical Engineering from King Mongkut's university of Technology Thonburi in 2009.

Thoatsanope Kamnerdtong is an Assistant Professor in the Department of Mechanical Engineering at King Mongkut's University of Technology Thonburi. His M.S. and Ph.D. degrees in Mechanical Engineering from Vanderbilt University, Nashville, Tennessee, USA. His research interests are in finite element analysis, failure analysis, micro-position and ultra-precision mechanisms, computer aided design and engineering (CAD/CAE), design and application in automotive and hard disk drive industries.

Somchai Wongwises is currently a Professor of Mechanical Engineering, Faculty of Engineering at King Mongkut's University of Technology Thonburi, Bangmod, Thailand. He received his Doktor Ingenieur (Dr.-Ing.) in Mechanical Engineering from the University of Hannover, Germany, in 1994. His research interests include Gas-Liquid Two-Phase Flow, Heat Transfer Enhancement, and Thermal System Design. Professor Wongwises is the head of the Fluid Mechanics, Thermal Engineering and Multiphase Flow Research Laboratory (Future).

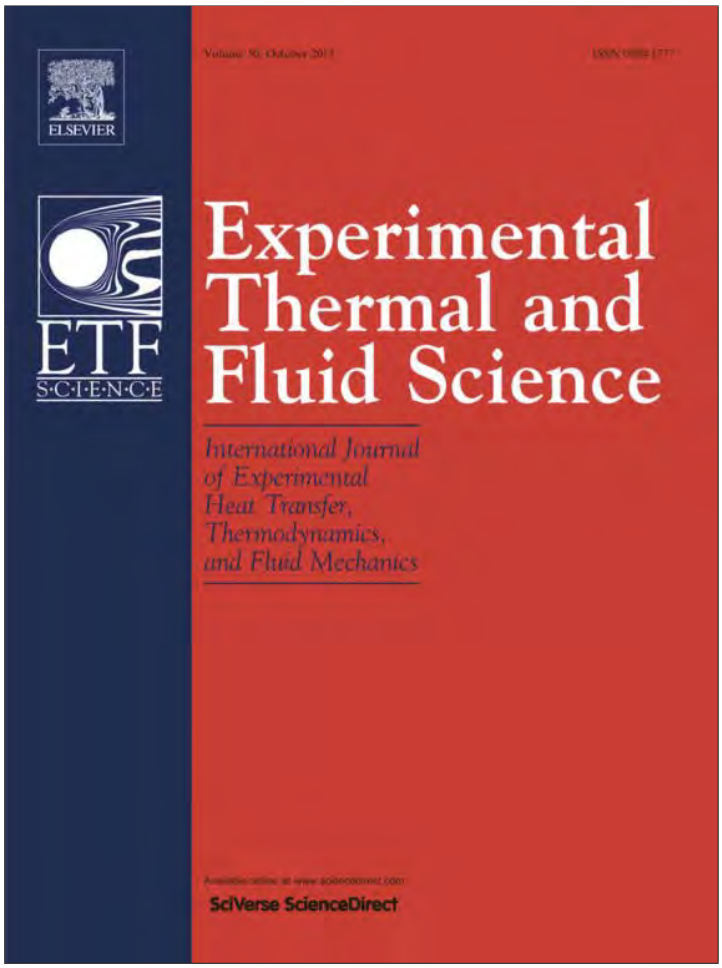

Experimental Thermal and Fluid Science 50 (2013) 222–228

Contents lists available at SciVerse ScienceDirect

Experimental Thermal and Fluid Science

journal homepage: www.elsevier.com/locate/etfs

Comparison of the heat transfer performance and friction characteristics between fixed and rotating turbine-type swirl generators fitted in a small circular tube

Weerapun Duangthongsuk [a,b], Somchai Wongwises [b,c,*]

[a] Department of Mechanical Engineering, South-East Asia University, Bangkok, Thailand
[b] Fluid Mechanics, Thermal Engineering and Multiphase Flow Research Lab. (FUTURE), Department of Mechanical Engineering, Faculty of Engineering, King Mongkut's University of Technology Thonburi, Bangmod, Bangkok 10140, Thailand
[c] The Academy of Science, The Royal Institute of Thailand, Sanam Suea Pa, Dusit, Bangkok 10300, Thailand

ARTICLE INFO

Article history:
Received 30 December 2012
Received in revised form 10 April 2013
Accepted 10 April 2013
Available online 30 April 2013

Keywords:
Nusselt number
Pressure drop
Swirl generator inserts
Passive technique

ABSTRACT

This paper is a continuation of the authors' previous work [W. Duangthongsuk, S. Wongwises, An experimental investigation of the heat transfer and pressure drop characteristics of a circular tube fitted with rotating turbine-type swirl generators, Exp. Therm. Fluid Sci. 45, (2013), 8–15.]. Swirl generators inserted into a conventional smooth tube is an innovative way to increase the thermal performance of the heat exchangers. The effect of the free rotation of a swirl device on the thermal performances and friction behaviors are investigated experimentally. Five turbine-type swirl generators with and without free rotation are inserted and installed equally distant along the test section. In the present study, DI water is used as a testing fluid and flows under a turbulent flow regime. A common stainless steel tube with an OD of 10 mm, ID of 9.2 mm, and length of 2.3 m is used as the test tube. A DC power supply is used to supply the heat load to the test section in order to meet the constant heat flux boundary condition. The data for a common smooth tube are compared with the data for fixed (FTSG) and freely rotating turbine type swirl generator (RTSG). The measured data illustrate that the heat transfer performance of the tube with RTSG inserts is 6.3% and 56% higher than that of the FTSG insert and the conventional smooth tube, respectively. Moreover, the heat transfer coefficient significantly increases when the fluid flows pass the RTSG and FTSG inserts. However, inserting the RTSG and FTSG into the common smooth tube results in an increase of the pressure drop. The tube with RTSG inserts gives the lowest pressure drop.

1. Introduction

In order to increase the thermal performance of the heat exchanger, two conventional heat transfer enhancement techniques are used. The first is the active technique and the other is the passive technique. For the active technique, external force such as jet impingement, stirring of the fluid, fluid and surface vibration, and electric field are required. Equally, the passive technique requires special surface geometries such as extended surface, displaced inserts, swirl flow inserts, and surface roughening. Focusing on the passive technique, swirl generator devices can be fitted both inside and outside of the tubes to create swirl flow, which leads to a decrease in the thermal boundary layer thickness for enhancing the thermal performance. At the same time, the tube being fitted with some devices can cause an increase in the pressure drop. The ratio of the heat transfer performance to the pressure drop should be maximized in order to improve the heat exchanger performance. As previously mentioned, many researchers have studied and have tried to develop the new type of swirl flow devices for increasing the thermal performance and reducing the pressure drop inside the common plain tube to be as low as possible. Several articles describing these attempts are depicted in the previous work of the authors [1]. However, the recent articles are in addition to those described [2–8].

From the above mentioned studies, many researchers illustrated that the use of swirl flow devices implanted in the common smooth tube gave higher thermal performances than the plain tube. However, this enhancement was supplemented by an increase in the penalty drop of pressure. Except the research wok of Zhang et al. [6], most of their works mentioned the swirl flow devices which are the fixed type swirl inserts. The effect of free rotation on the heat transfer performance and pressure drop characteristics which has never been seen before in the open literature is presented. The fixed and freely rotating turbine-type swirl

* Corresponding author at: Fluid Mechanics, Thermal Engineering and Multiphase Flow Research Lab. (FUTURE), Department of Mechanical Engineering, Faculty of Engineering, King Mongkut's University of Technology Thonburi, Bangmod, Bangkok 10140, Thailand.
E-mail address: somchai.won@kmutt.ac.th (S. Wongwises).

0894-1777/$ - see front matter © 2013 Elsevier Inc. All rights reserved.
http://dx.doi.org/10.1016/j.expthermflusci.2013.04.007

Nomenclature

A	area ($m^{2)}$
C_p	specific heat (J/kg K)
D	diameter (m)
f	friction factor
h	heat transfer coefficient (W/m^2 K)
I	electric current (A)
k	thermal conductivity (W/m K)
L	length of the test tube (m)
$\dot{m}$	mass flow rate (kg/s)
Nu	Nusselt number
Pr	Prandtl number
ΔP	pressure drop (Pa)
Q	heat transfer rate, W
Re	Reynolds number
T	temperature (°C)
u	velocity (m/s)
V	electric voltage (V)

Greek symbols

ε	roughness (m)
ρ	density (kg/m^3)
μ	viscosity (kg/ms)

Subscript

ave	average
elec	electric
f	fluid
in	inlet
m	average
out	outlet
s	surface
w	tube wall
x	local distance

generators (FTSG and RTSG) used in the present study are new designs. Both FTSG and RTSG are fitted inside the test section separately and tested in order to compare them with the data of a common plain tube.

2. Experimental apparatus and procedures

The experimental setup used in the present study is shown schematically in Fig. 1. It mainly consisted of two test sections: the first was conducted to test the conventional smooth tube, and the other was conducted to investigate the tube fitted with FTSG and RTSG. Moreover, the test loop consisted of a pump with a speed controller, two cooling tanks, and a rotameter. In this research, De-ionized (DI) water was used as the testing fluid, and it flowed through the test tubes under turbulent flow regimes and uniform wall heat flux boundary conditions. Straight stainless steel tubes with an inner diameter of 9.2 mm, 0.4 mm thickness, and 2,300 mm in length were used as the test sections. For the test section with both types of swirl generator inserts (FTSG and RTSG), RTSG was first installed and tested. Then, FTSG were mounted instead of FTSG for comparison. Both FTSG and RTSG used in the present study having 5 pieces and were located at x/L of 0.0, 0.2, 0.4, 0.6, and 0.8, respectively. FTSG and RTSG used in this research were made from aluminum material with twist angles of 60°, blade thickness of 0.5 mm, 2 cm in length, and 6.6 mm in outer diameter, and each FTSG or RTSG had four blades. Each FTSG and RTSG was installed inside the transparency tube to observe the flow fluid behavior after the flow passed the swirl devices. When the fluid was forced through the FTSG, swirl flow was created. Similarly, after fluid flowed through RTSG, continuously free rotation was obtained and swirl flow was produced simultaneously. Fig. 2 shows the detail of the FTSG and RTSG inserts used in the present work.

For measuring the available data, a differential pressure transmitter and the T-type thermocouples were installed at both ends of the section to measure the pressure drop and the bulk temperature of the working fluid, respectively. Likewise, in order to measure the wall temperature along the test section, 10 T-type thermocouples were placed at different longitudinal positions on the outer surface. For the thermocouple fixations at the outer wall of the test section, the thermal insulation tape was used to bind the thermocouple end around the tube. The positions of the wall temperature measurements and the FTSG and RTSG locations are described in Fig. 3. In order to meet the wall heat flux boundary condition, a DC power supply was used to adjust the heat load to the test section. Cooling tank No. 1, with a 4000 W electric heater, a 3.52 kW cooling capacity, and an RTD with a temperature controller, was used to keep the water temperature constant at a desired value. Also, cooling tank No. 2, with an 5.28 kW cooling capacity, and an RTD with a temperature controller, was used to cool the working fluid temperature leaving from the test section to the setting temperature. A rotameter was used to measure the flow rate of the working fluid. An inverter was used to control the water flow rate. In order to prevent the heat loss along the test section, the elastomer type insulator with thermal conductivity of 0.04 W/mK, 20 mm of thickness was used to shield the outer surface of the tube. The test section configurations and operating conditions are summarized in Table 1.

For instrument calibration, all of the thermocouples were well-calibrated in a controlled temperature bath, using standard precision mercury glass thermometers. The uncertainty of the temperature measurements as recorded by the data acquisition system was ±0.1 °C. An air-operated dead weight tester was used to calibrate the differential pressure transmitter. The uncertainty of the pressure measurement was ±0.030 kPa. The rotameter was specially calibrated by the manufacturer, and its accuracy was ±7% of full scale. Finally, in order to estimate the uncertainty of the measured data, the root mean sum square method was applied. The uncertainty of the measured heat transfer was approximately 5%.

The experiments were tested with different water flow rates. A Reynolds number ranged from 4500 to 9500 was conducted. The wall heat flux was kept constant at 15 kW/m^2 by adjusting the voltage regulator. The inlet water temperature was kept at 15 °C. During each experiment, the system was certified to approach a steady state before any data were recorded. After a steady state was reached, the wall temperatures and the inlet and outlet temperatures of the water and the pressure drop across the test section and the flow rates of water were recorded.

3. Data reduction

To determine the heat transfer performance and flow characteristics of the common plain tube with FTSG and RTSG inserts, the experimental system calibration is necessarily done. Thus, a conventional round tube is verified. The measured data of the heat transfer coefficient and friction are compared with the calculated

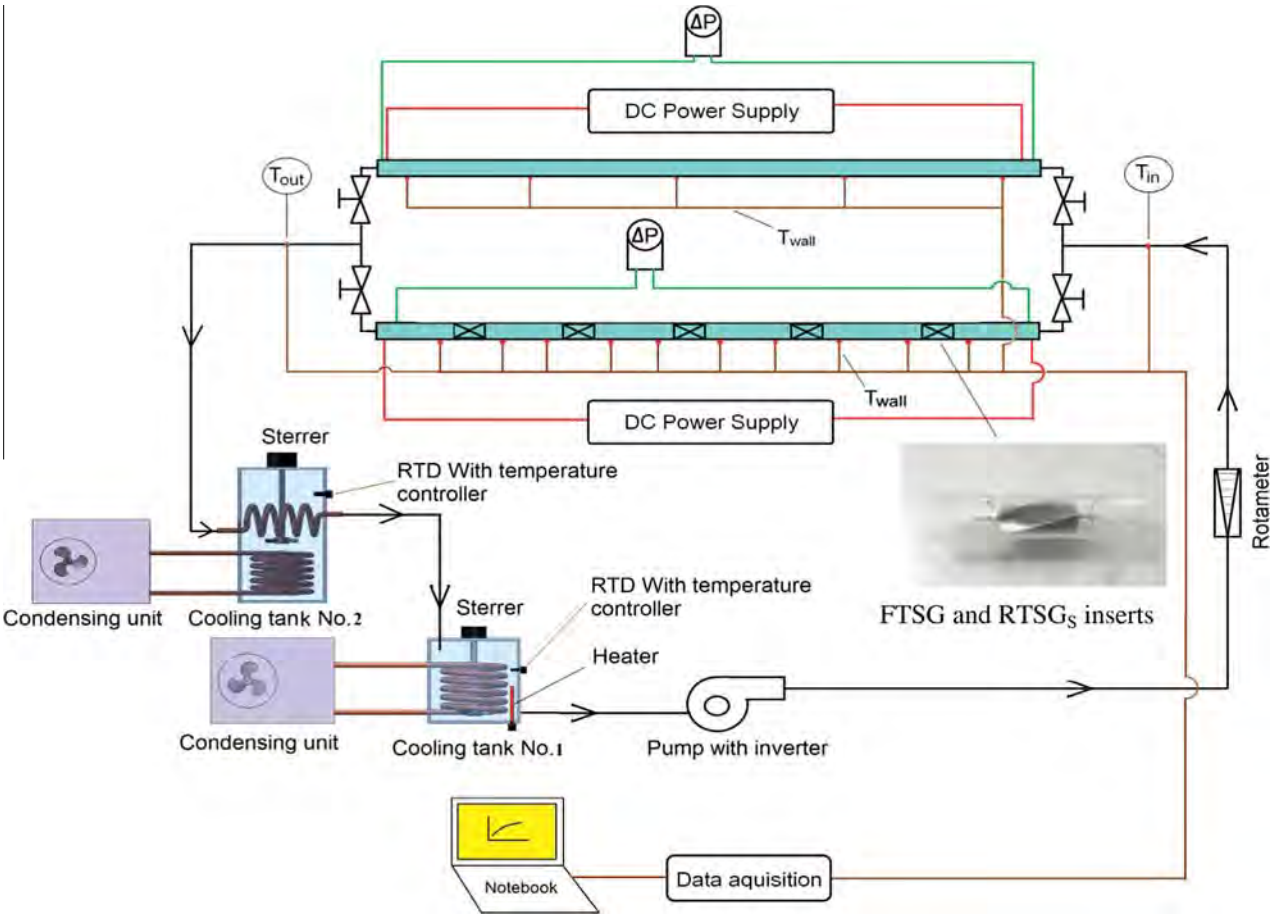

Fig. 1. Schematic diagram of the experimental apparatus [Duangthongsuk and Wongwises [1], with permission from Elsevier].

values obtained from Gnielinski's equation and Colebrook's equation, respectively.

The Gnielinski equation [9]:

$$Nu = \frac{(f/8)(\mathrm{Re} - 1000)\mathrm{Pr}}{1 + 12.7(f/8)^{0.5}(\mathrm{Pr}^{2/3} - 1)}, \tag{1}$$

where Nu is the Nusselt number, Re is the Reynolds number, Pr is the Prandtl number, and f is the friction factor.

The Colebrook equation [10]:

$$\frac{1}{\sqrt{f}} = -2.0\log\left(\frac{\varepsilon/D}{3.7} + \frac{2.51}{\mathrm{Re}\sqrt{f}}\right), \tag{2}$$

The pressure drop of working fluid can be calculated from:

$$\Delta P = f\frac{L}{D}\frac{u_m^2}{2}\rho, \tag{3}$$

where ΔP is the measured pressure drop, L is the length of the tube, D is the inner diameter of the tube, u_m is the average velocity of fluid, and ρ is the density of fluid.

Then, the heat transfer performance of plain tube with FTSG and RTSG inserts can be calculated from the following equation.

The heat load to the test section can be calculated from:

$$Q_{elec} = VI, \tag{4}$$

where V is the electric voltage, and I is the electric current.

The heat transferring into the fluid is computed from:

$$Q_f = \dot{m}Cp(T_{out} - T_{in}), \tag{5}$$

where $\dot{m}$ is the mass flow rate, Cp is the specific heat, and T_{in} and T_{out} are the temperatures of the fluid at the inlet and exit of the test section.

The average heat transfer rate is determined from:

$$Q_{ave} = \frac{Q_{elec} + Q_f}{2}, \tag{6}$$

where Q_{ave} is the average heat transfer rate. In the present study, the energy balance between heat supplied and working fluid are roughly less than 2.0%.

The local Nusselt number is calculated as follows:

$$h_x = \frac{q}{(T_w - T_f)_x}, \tag{7}$$

$$Nu_x = \frac{h_x D}{k}, \tag{8}$$

where h_x is the local heat transfer coefficient, Nu_x is the local Nusselt number, q is the wall heat flux, T_w is the wall temperature of the tube, T_f is the bulk temperature of the fluid at each section, and k is the thermal conductivity of the fluid.

The bulk fluid temperature at any position can be computed from:

$$T_{f,2} = T_{f,1} + \frac{q\pi Dx}{\dot{m}C_P}, \tag{9}$$

where q is the wall heat flux, T_f is the bulk temperature of the fluid at each section, and x is the length of the each section of test tube.

Finally, the average Nusselt number (h_{ave}) is also presented and can be calculated from.

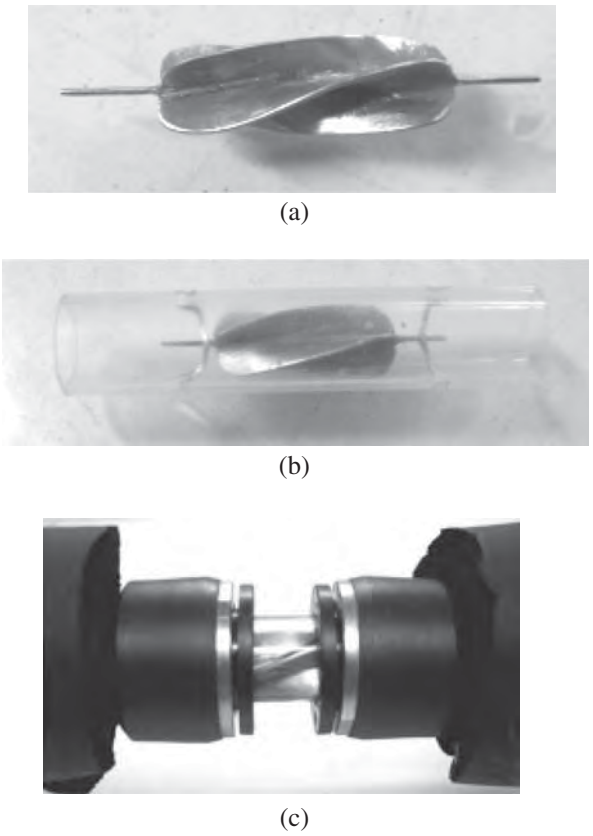

Fig. 2. Configuration of the swirl generator inserts used in the present study: (a) bare FTSG and RTSG, (b) fitted in an acrylic tube and (c) after fitting in the experimental system [Duangthongsuk and Wongwises [1], with permission from Elsevier].

$$Nu_{ave} = \frac{1}{L}\int_{x_1}^{x_2} Nu_x dx, \tag{10}$$

The Reynolds number is defined as follows:

$$\mathrm{Re} = \frac{\rho u_m D}{\mu}, \tag{11}$$

where L is the tube length, ρ is the density, and μ is the fluid viscosity.

Finally, the Prandtl number can be calculated from:

$$\mathrm{Pr} = \frac{\mu Cp}{k}. \tag{12}$$

In order to evaluate the flow characteristic of the common plain tube implanted with FTSG and RTSG, the data from the measured pressure drops of the common plain tubes are compared.

Table 1
Test section configurations and testing conditions.

Parameter	Quantity
1. Tube length (mm)	2300
2. Tube inside diameter (mm)	9.2
3. Tube thickness (mm)	0.4
4. Inlet fluid temperature (°C)	15
5. Wall heat flux (kW/m^2)	15
6. Reynolds number	4500–9500
7. Volume flow rate (LPM)	2–4

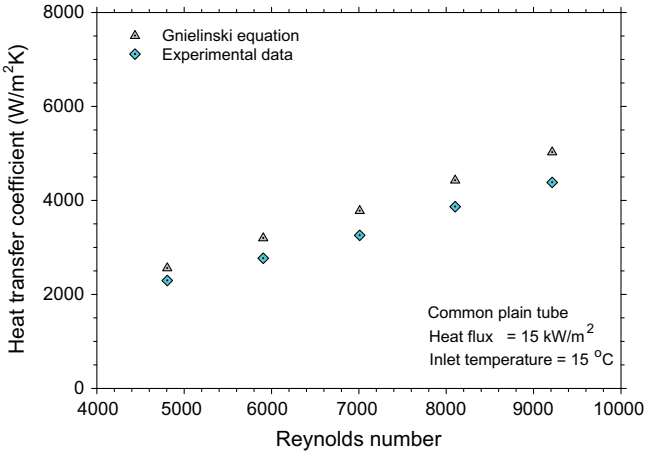

Fig. 4. Comparison between the Gnielinski equation and experimental data for heat transfer coefficient of common plain tube.

4. Results and discussion

In the present study, the experimental data can be categorized into two aspects: the first is the data for convective heat transfer performance, and the other is the pressure drop data. The results are described as follows:

4.1. Heat transfer performance

The heat transfer performance of the common plain tube is first measured for validating the experimental system. As a sequence, the measured data are compared with the predicted values from the Gnielinski equation [9]. As shown in Fig. 4, the results show good agreement between the measured values for the common plain tube and the calculated values.

The wall temperature variation along the test section for the conventional smooth tube and the FTSG and RTSG inserts is shown in Fig. 5a–c, respectively. For the conventional smooth tube, the measured data illustrate that the wall temperature increases with

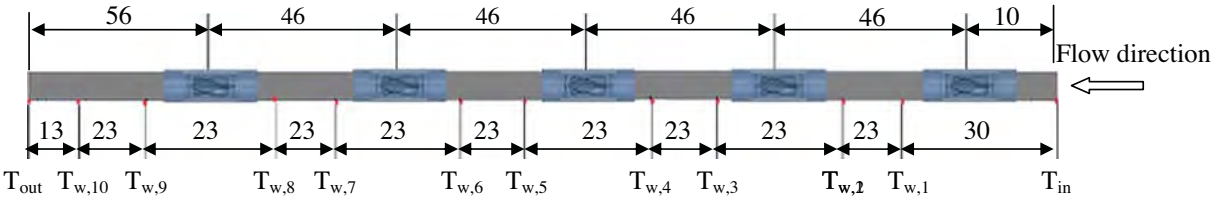

Fig. 3. The wall temperature measurement locations and the position of FTSG and RTFG inserts (unit: cm) [Duangthongsuk and Wongwises [1], with permission from Elsevier].

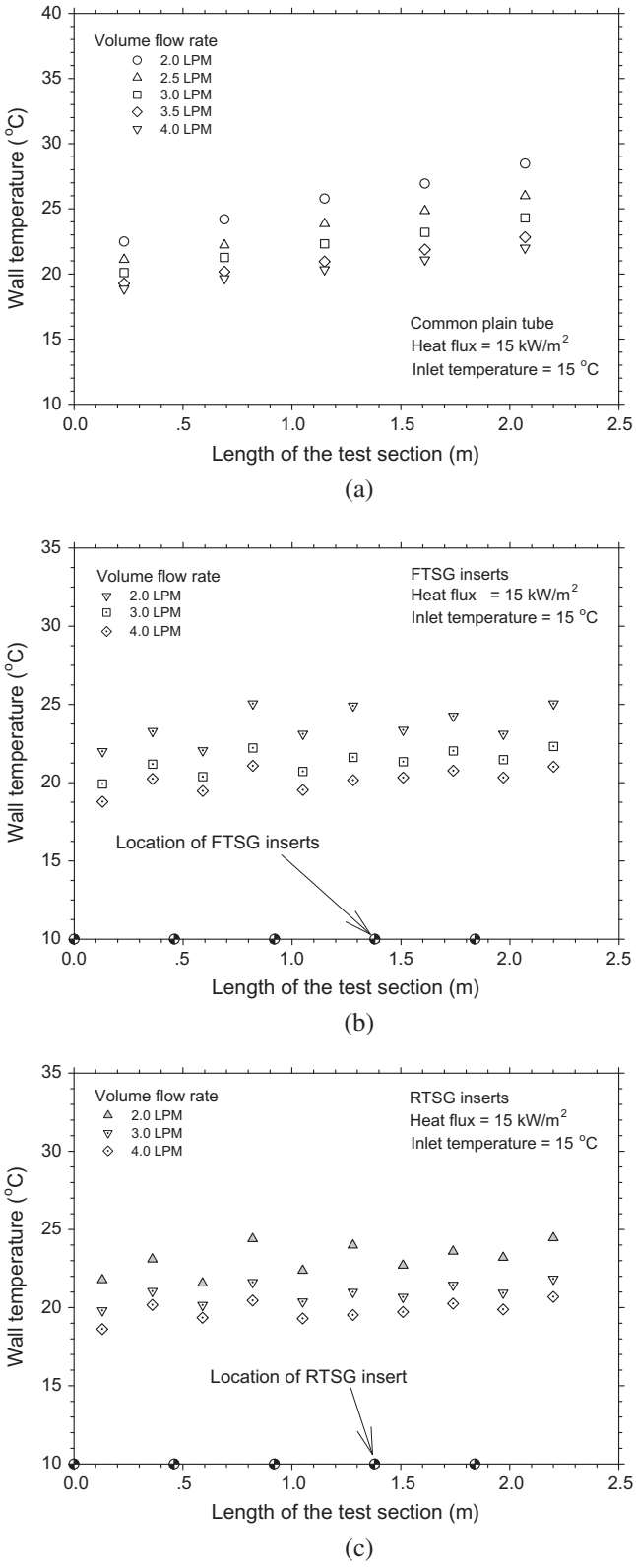

Fig. 5. The wall temperatures as function of tube length and volume flow rate: (a) for the common plain tube, (b) for FTSG inserts and (c) for RTSG inserts.

the tube length. This is due to the heat load continuously supplied to the test section. Thus an increase of the wall temperature is achieved. However, for the common tube fitted with the FTSG, unusual behavior is observed. As shown in Fig. 5b, it is clearly seen that the tube wall temperature is dropped behind the position of the FTSG. As shown in Fig. 5c, a similar tendency is obtained from the data of the RTSG inserts. A higher heat transfer rate is obtained due to swirling flow after each FTSG and RTSG, which leads to a reduction in the wall temperature.

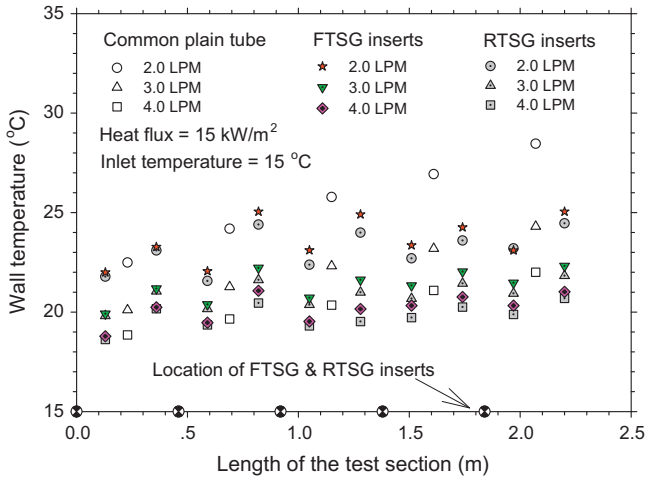

Fig. 6. Comparison between the wall temperatures obtained from the common plain tube and the tube with FTSG and RTSG inserts.

Comparison of the local wall temperature between plain tube, FTSG, and RTSG inserts is shown in Fig. 6. The measured data demonstrate that the wall temperature of the tube fitted with RTSG is slightly lower than that of the FTSG inserts. This may be because the swirling flows caused from continuous free rotation of the RTSG is more intensive than the FTSG inserts, which leads to high heat dissipation. Compared with the common plain tube, smaller tube wall temperature can be seen, especially at high x/L ratio. This behavior implies that the tubes implanted with swirl flow devices provide higher heat transfer performances than the common plain tube and the use of RTSG inserts provides a higher heat transfer performance than the FTSG inserts.

Variations of the local Nusselt number as a function of the flow rates and tube length for the common plain tube, FTSG, and the RTSG inserts are shown in Fig. 7a–c, respectively. For the common plain tube, the experimental data show that the local Nusselt number varies with the volume flow rate and remains constant along the test section. However, for both cases of the FTSG and RTSG inserts, abnormal behavior is observed. The local Nusselt number of the FTSG and RTSG inserts increases with increasing tube length. Moreover, focusing on the point after the FTSG and RTSG, a dramatically higher local Nusselt number is obtained. This result is due to the swirling flow after the FTSG and RTSG inserts, promoting greater heat transfer performance.

Comparison of the local Nusselt number between FTSG and RTSG inserts is shown in Fig. 8. The results show that the tube with RTSG inserts provides a slightly higher Nusselt number than that for the FTSG inserts. This behavior may be caused from the effect of the free rotation of the RTSG inserts can create a high disturbance of the fluid flow, which leads to an increase in the Nusselt number. This means that the use of RTSG inserts provides a higher heat transfer performance than the FTSG inserts.

Similarly, a comparison between the average Nusselt number obtained from the tube fitted with FTSG and that obtained from the RTSG inserts is shown in Fig. 9. The measured results show that the average Nusselt number of the RTSG inserts is approximately an average of 6.3% and 56% higher than that of the FTSG insert and the plain tube, respectively, and varied with Reynolds number. This result is due to more intensive swirling flow after the RTSG than the FTSG, which leads to enhancing the heat transfer performance.

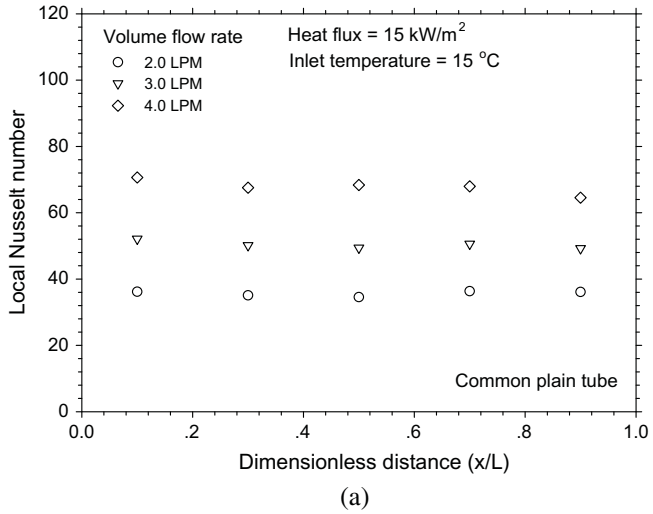

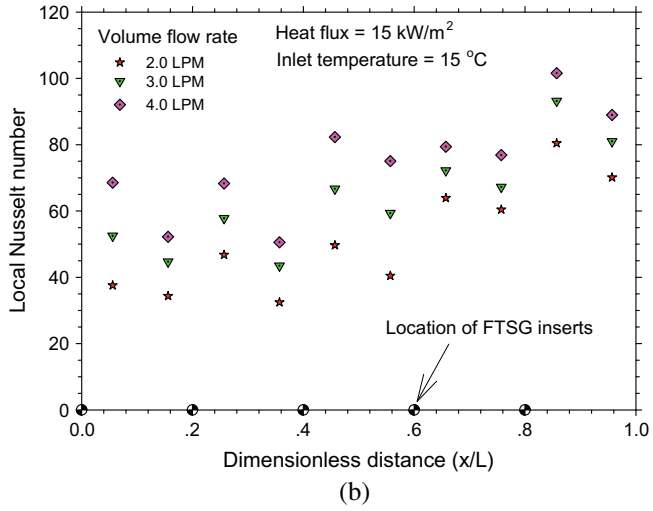

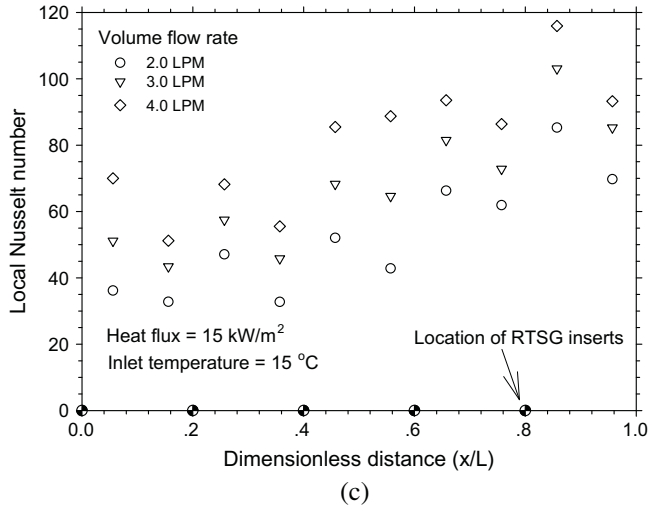

Fig. 7. Local Nusselt number as function of volume flow rate and dimensionless distance: (a) for the common plain tube, (b) for FTSG inserts and (c) for RTSG inserts.

4.2. Pressure drop

Similar to the heat transfer performance, the reliability and accuracy of the pressure drop data should first be verified. The data

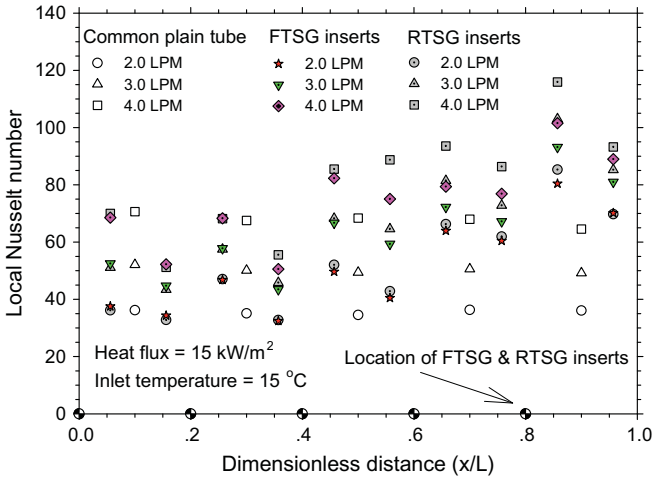

Fig. 8. Comparison between local Nusselt number obtained from the common plain tube and those obtained from FTSG and RTSG inserts.

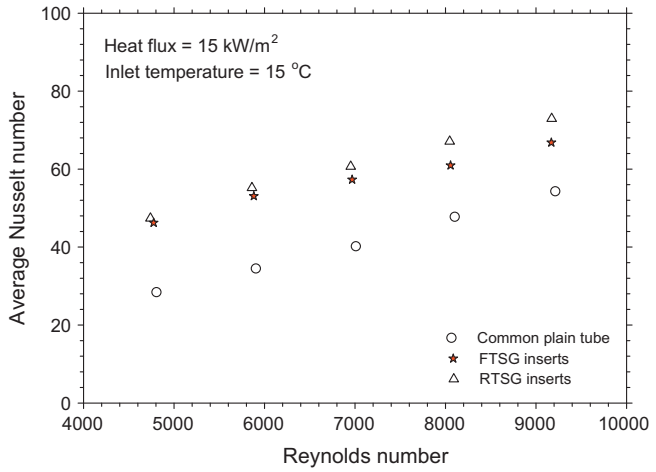

Fig. 9. Comparison of the average Nusselt number between the common plain tube, FTSG and RTSG inserts.

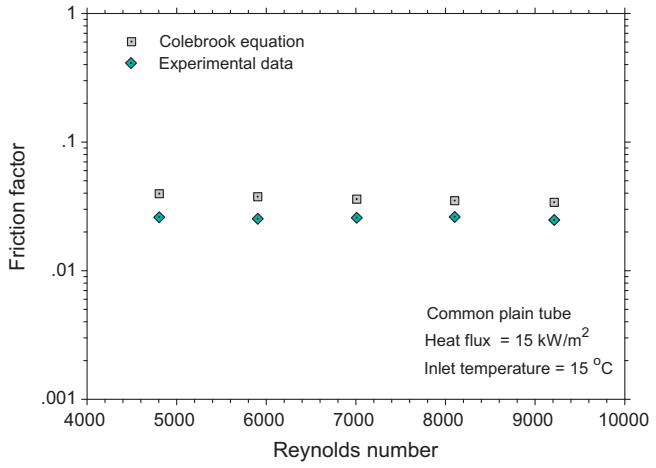

Fig. 10. Comparison between the Colebrook equation and the measured data for friction factor of common plain tube.

of the measured friction factors are compared with those obtained from the Colebrook equation [10]. As shown in Fig. 10, the exper-

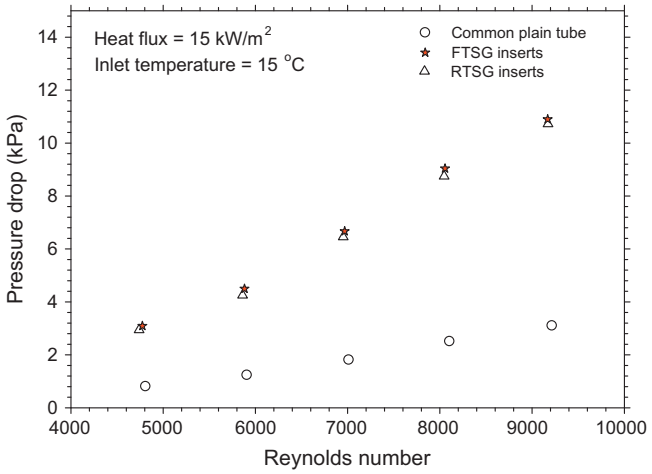

Fig. 11. Comparison of the pressure drop obtained from the common plain tube, FTSG and RTSG inserts.

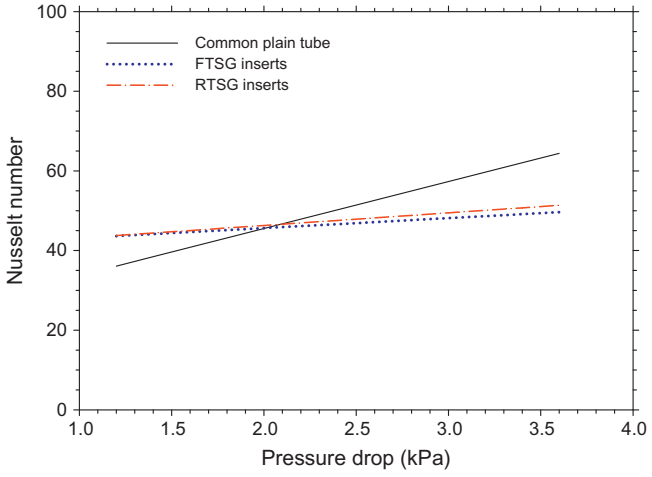

Fig. 12. Relationship between Nusselt number and pressure drop for all tubes.

imental friction factor agrees well with those of calculated values for the common plain tube.

In general, the addition of some swirl flow devices into the main flow will provide a higher penalty drop in the pressure. The value of a pressure drop should be minimized as well as possible. As shown in Fig. 11, the measured data indicate that the pressure drop of the tube with RTSG inserts is smaller than that of the tube with FTSG inserts by a few percent. It is caused from the effect of free rotation of the RTSG, which can not resist the flow as a case of FTSG inserts.

Fig. 12 shows the variation of the Nusselt number with pressure drop in the plain tube, FTSG and RTSG inserts. At pressure drop less than 2.0 kPa (lower flow rate), it can be seen that the average Nusselt number of RTSG and FTSG inserts are significantly higher than that of the common plain tube at the same pressure drop (or the same pumping power). However, opposite behaviors is obtained for the pressure drop greater than 2.0 kPa (higher flow rate). As shown above, the use of swirl flow device inserts can create higher heat transfer performance and pressure drop than the common plain tube simultaneously. This means that the tubes with swirl generator inserts consume much more pumping power than the plain tube and also give lower heat transfer performance, especially at high pressure drop (higher flow rate). Thus, an attempt to minimize the pressure drop in the case of swirl device inserts is the challenge task in order to meet the highest performance of the heat transfer apparatus.

5. Conclusions

This paper presents an experimental investigation on the heat transfer and pressure drop behaviors of a common circular tube with fixed (FTSG) and freely rotating turbine-type swirl generator (RTSG) inserts. Both types of the swirl devices are new designs. The measured data for the common circular tube are used for comparison. Major findings have been given as follows:

- The tube fitted with RTSG gives a larger heat transfer performance than that of the FTSG inserts. For both cases, unusual local heat transfer behaviors are observed.
- The tube with RTSG inserts promotes higher heat transfer performance than the FTSG and common plain tube by about 6.3% and 56%, respectively.
- The tube fitted with RTSG gives a smaller pressure drop than the FTSG and the common plain tube by approximately a few percent.
- Use of the RTSG insert instead of FTSG insert gives a higher heat transfer performance and lower pressure drop.

Acknowledgments

The authors would like to express their appreciation to the Thailand Research Fund, the Office of the Higher Education Commission and the National Research University Project for providing financial support.

References

[1] W. Duangthongsuk, S. Wongwises, An experimental investigation of the heat transfer and pressure drop characteristics of a circular tube fitted with rotating turbine-type swirl generators, Experimental Thermal and Fluid Science 45 (2013) 8–15.
[2] G. Pathipakka, P. Sivashanmugam, Heat transfer behaviour of nanofluids in a uniformly heated circular tube fitted with helical inserts in laminar flow, Supperlattices and Microstructures 47 (2010) 349–360.
[3] M. Chandrasekar, S. Suresh, A. Chandra Bose, Experimental studies on heat transfer and friction factor characteristics of Al_2O_3/water nanofluid in a circular pipe under laminar flow with wire coil inserts, Experimental Thermal and Fluid Science 34 (2010) 122–130.
[4] S. Suresh, P. Selvakumar, M. Chandra Bose, V.S. Raman, Experimental studies on heat transfer and friction factor characteristics of Al_2O_3/water nanofluid under turbulent flow with spiraled rod inserts, Chemical Engineering and Processing: Process Intensification 53 (2012) 24–30.
[5] M. Saeedinia, M.A. Akhavan-Behabadi, M. Nasr, Experimental study on heat transfer and pressure drop of nanofluid flow in a horizontal coiled wire inserted tube under constant heat flux, Experimental Thermal and Fluid Science 36 (2012) 158–168.
[6] Z. Zhang, Y. Ding, C. Guan, H. Yan, W. Yang, Heat transfer enhancement in double-pipe heat exchanger by means of rotor-assembled strands, Chemical Engineering and Processing: Process Intensification 60 (2012) 26–33.
[7] H. Bas, V. Ozceyhan, Heat transfer enhancement in a tube with twisted tape inserts placed separately from the tube wall, Experimental Thermal and Fluid Science 41 (2012) 51–58.
[8] S. Bhattacharyya, S.K. Saha, Thermohydraulics of laminar flow through a circular tube having integral helical rib roughness and fitted with centre-cleared twisted-tape, Experimental Thermal and Fluid Science 42 (2012) 154–162.
[9] V. Gnielinski, New equations for heat and mass transfer in turbulent pipe and channel flow, International Journal of Chemical Engineering 16 (1976) 359–368.
[10] C.F. Colebrook, Turbulent flow in pipes with particular reference to the transition between the smooth and rough pipe laws, Journal- Institution of Civil Engineers 11 (1939) 133.

International Communications in Heat and Mass Transfer 47 (2013) 98–104

Contents lists available at ScienceDirect

International Communications in Heat and Mass Transfer

journal homepage: www.elsevier.com/locate/ichmt

Performance characteristics of a microchannel heat sink using TiO_2/water nanofluid and different thermophysical models ☆

Piyanut Nitiapiruk [a], Omid Mahian [b,*], Ahmet Selim Dalkilic [c], Somchai Wongwises [a,d,**]

[a] Fluid Mechanics, Thermal Engineering and Multiphase Flow Research Lab. (FUTURE), Department of Mechanical Engineering, Faculty of Engineering, King Mongkut's University of Technology Thonburi, Bangmod, Bangkok 10140, Thailand
[b] Young Researchers Club and Elites, Mashhad Branch, Islamic Azad University, Mashhad, Iran
[c] Heat and Thermodynamics Division, Department of Mechanical Engineering, Yildiz Technical University, Yildiz, Besiktas, Istanbul 34349, Turkey
[d] The Academy of Science, The Royal Institute of Thailand, Sanam Suea Pa, Dusit, Bangkok 10300, Thailand

ARTICLE INFO

Available online 13 July 2013

Keywords:
Microchannel
Nanofluids
Thermophysical properties
Performance characteristics

ABSTRACT

In this paper, the performance of a microchannel heat sink using TiO_2/water nanofluid is experimentally investigated. The dimensions of the microchannel are 500 μm width, 800 μm height, and 40 mm length, where the number of flowing channels is 40.The effects of uncertainties in thermophysical properties on the Nusselt number and friction factor are investigated by using three different sets of thermophysical models, which are based on experimental and theoretical relations. It is concluded that the use of the model which is based on experimental data is very important to estimate the friction factor, while the use of different models to calculate of thermal conductivity has no considerable effect on the prediction of Nusselt number.

1. Introduction

The use of nanofluids in various fields of thermal engineering has been developed. The nanofluids are used to enhance the efficiency and performance of thermal systems. For instance, the nanofluids could be utilized in cooling of electronics, combustion, fuel cell, medicine, heat exchangers [1,2] and renewable energy systems [3] while some review papers have been reported on the enhancement of heat transfer using nanofluids [4–6].

It is over than two decades that microchannel heat sinks have attracted special attention because of their ability to generate high heat transfer rate, small size, and small coolant requirements [7]. Many studies both experimentally and theoretically have been done on the performance of microchannels using common fluids. However, relatively there are few reports on the performance of microchannels where the working fluid is a nanofluid. Also, the number of experimental studies is less than the theoretical ones because of difficulties to perform experiments with microchannels and nanofluids. Here, the former experimental works on the flow of nanofluids in microchannels are reviewed briefly. Chein and Chuang [8] tested a microchannel heat sink using CuO/water nanofluid with volume fractions of 0.2% to 0.4%. They concluded that using nanofluids in high volume flow rates is not beneficial, but at low flow rates, the use of nanofluids is more helpful than water to absorb the heat from microchannel. Jung et al. [9] measured the convective heat transfer coefficient and friction factor of Al_2O_3/water nanofluid through a rectangular microchannel. They found that the convective heat transfer coefficient of the nanofluid with volume fraction of 1.8% is higher than water by 32% while the authors revealed that using the nanofluid has no considerable effect on the magnitude of friction factor. Ho et al. [10] tested the effects of Al_2O_3/water nanofluid on the heat transfer rate and friction factor in a microchannel heat sink with 25 flowing channels. For each channel, the length, width, and height are 50 mm, 283 μm and 800 μm, respectively. They indicated that the use of nanofluid is more beneficial than water. Also, it is found that the use of nanofluids results in a slight increase of friction factor. Wang et al. [11] investigated the performance of a microchannel heat sink using ZnO/water. They concluded that at a low Reynolds number (i.e. 3.8), the heat transfer coefficient of the nanofluid is higher than water by 13%. Vafaei and Wen [12] studied the subcooled flow boiling of Al_2O_3/water nanofluid in a microchannel. They found that the critical heat flux increases up to 51%, by using only 0.1% volume fraction of nanoparticles. Xu et al. [13] compared the effects of two different working fluids including water and Al_2O_3/water nanofluid (mass fraction = 0.2%) on the boiling thermal performance of a rectangular microchannel. They concluded that using the nanofluid enhances heat transfer rate and avoids boiling instability. Byrne et al. [14] used CuO/water nanofluids with and without surfactantin a parallel microchannel flow configuration.

☆ Communicated by W.J. Minkowycz.

* Corresponding author.
** Correspondence to: S. Wongwises, Fluid Mechanics, Thermal Engineering and Multiphase Flow Research Lab. (FUTURE), Department of Mechanical Engineering, Faculty of Engineering, King Mongkut's University of Technology Thonburi, Bangmod, Bangkok 10140, Thailand.
E-mail addresses: omid.mahian@gmail.com (O. Mahian), somchai.won@kmutt.ac.th (S. Wongwises).

0735-1933/$ – see front matter © 2013 Elsevier Ltd. All rights reserved.
http://dx.doi.org/10.1016/j.icheatmasstransfer.2013.07.001

Nomenclature

A	area, m^2
d_f	diameter of molecule of base fluid (m)
d_p	diameter of nanoparticle (m)
D_h	hydraulic diameter (m)
f	friction factor
h	heat transfer coefficient (W/m^2 K)
I	electric current (A)
k	thermal conductivity (W/mK)
L	length (m)
M	molecular weight of water (g/mol)
$\dot{m}$	mass flow rate (kg/s)
N	number of microchannel
Nu	Nusselt number
ΔP	pressure drop (Pa)
q	heat flux (W/m^2)
Q	heat transfer rate (W)
Re	Reynolds number
T	temperature (K)
u_m	mean velocity (m/s)
V	electric voltage (V)
W	width, m

Greek symbols

φ	volume fraction
μ	dynamic viscosity (kg/m s)
ρ	density (kg/m^3)

Subscript

ave	average
ch	channel
f	base fluid
in	inlet
out	outlet
w	wall

They observed that the heat transfer rate increases by 17% for low concentration of nanofluid that is 0.01%. Kalteh et al. [15] estimated the heat transfer rate for a wide rectangular microchannel heat sink (94.3 mm, 28.1 mm and 580 μm; length, width and height, respectively) where the working fluid is Al_2O_3/water nanofluid. They found that the Nusselt number increases with an increase in the Reynolds number and volume fraction of nanoparticles. They also concluded that a decrease in particle's size enhances the heat transfer rate. Duangthongsuk et al. [16] examined the heat transfer and pressure drop due to flow of Al_2O_3/water nanofluid (concentrations up to 3 wt.%) in a microchannel heat sink. They perceived that heat transfer increases by 15% where as using the nanofluid has no significant effect on pressure drop compared to water. Ning and Luo [17] experimented three microchannels with different hydraulic diameters using Al_2O_3/water nanofluid. They observed that with increasing the particle loading the Nusselt number increases while pressure drop decreases a little. In another work, the flow boiling heat transfer in a single microchannel with a size of 7500 × 100 × 250 μm is investigated using water and Al_2O_3/water nanofluid with weight concentration of 0.2% [18]. Recently, Anoop et al. [19] investigated the forced convection heat transfer of silica/water nanofluids in a microchannel with the size of 8 mm × 12 mm × 100 μm (width × length × height) where the wall temperature is kept as constant. Regarding the effects of uncertainties in thermophysical properties on the flow and heat transfer characteristics of nanofluids, Duangthongsuk and Wongwises [20] in study of turbulent flow of TiO_2 nanofluid in a heat exchanger concluded that the different models have no significant effect on the results. In another work, Mahian et al. [21] studied the effects of uncertainties in thermophysical models on prediction of entropy generation due to nanofluid flow between two rotating cylinders. They considered six different models and showed that the use of different models may give opposite results, so that one model predicts that using nanofluids increases the entropy generation, while another model predicts the decrease of entropy generation.

In this study, the heat transfer and pressure drop ofTiO_2/Water nanofluid flowing in a microchannel heat sink are experimentally investigated. The effects of uncertainties in thermophysical properties(Thermal conductivity and viscosity) on the prediction of Nusselt number and friction factor in a microchannel are investigated. Three sets of models are used to predict the viscosity and thermal conductivity. The size of the microchannel, the amounts of heat flux applied to the microchannel are completely in accordance with real situations observed in the personal computers.

2. Nanofluids preparation

In the present study, TiO_2/water nanofluid solution with a concentration of40 wt.% is provided from Degussa Company, Germany. The original solution is diluted before the beginning of experiments through adding water to prepare nanofluids with volume fractions of 0.5%, 1%, and 2%. In the preparation of nanofluids, the most important issue is the prevention of sedimentation of nanoparticles. An ultrasonic vibrator is used for 4 hours to sonicate the mixture to avoid the sedimentation.No sedimentation of nanoparticles has been observedduring the experiments

3. Experimental apparatus and procedure

The schematic of the experimental set up is shown in Fig. 1. The system consists of a temperature-controlled inlet tank, a temperature-controlled outlet tank, and a test section. The temperature of nanofluid is adjusted before entering the test section with cooling coils and a heater. Then, the nanofluid is pumped to the test section. The temperature of nanofluid is measured at four points in the inlet of the test section and at four points in the outlet of it, using T-type thermocouples with an accuracy of 0.1 °C. To measure the wall temperature of the microchannel, six T-type thermocouples are used, and to measure the pressure drop within the microchannel a differential pressure transmitter with accuracy of 0.01 kPa is used. The pressures are measured at three positions in the inlet and three positions in the outlet of the microchannel. The microchannel is heated using a power supply with the power of 90 W, where the output current is between 0 and 3 A and the output voltage is between 0 and 30 V. Three different values of heat flux including 50.6, 60.7, and 69.1 W are applied to the microchannel at each test. After heating, the nanofluid enters the temperature-controlled outlet tank to circulate. The range of flow rate is between 344 and 2363 cm^3/min with Reynolds numbers of250–1700. The time required to reach steady state conditions for each test is about 20–60 min. Fig. 2 illustrates two perspectives of the test section. The positions of the eight thermocouples in the inlet and outlet of the microchannel, data logger, pressure transmitter, and power supply are shown in Fig. 2(a). Fig. 2(b) displays the flow pattern of the nanofluid where the nanofluid passes through the microchannels. The width and height of microchannel are 500 μm, and 800 μm respectively. The 500 μm thick fins run throughout the total length of 40 mm, with a total width of40.5 mm and thickness of4 mm.

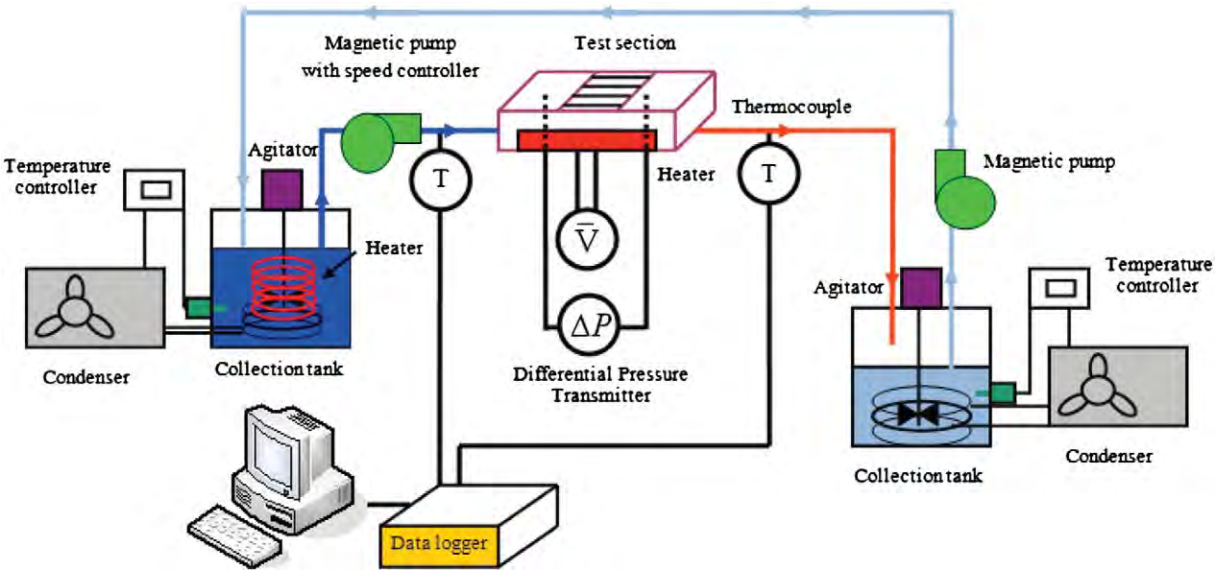

Fig. 1. Schematic diagram of experimental apparatus.

4. Data reduction

First, the relations that are used to calculate the thermophysical properties of nanofluid are presented. The density of nanofluids is calculated by using the following relation [22]:

$$\rho_{nf} = \phi \cdot \rho_p + (1-\phi) \cdot \rho_w \quad (1)$$

where ρ_{nf},ρ_p, and ρ_w are densities of the nanofluid, nanoparticle, and water, respectively.To study the effects of uncertainties in thermophysical properties (thermal conductivity and viscosity)on the performance characteristics of the microchannel three sets of models are used in as follows:

Model # 1 This model is the combination of the most used theoretical equations. The viscosity in model #1 is calculated by the

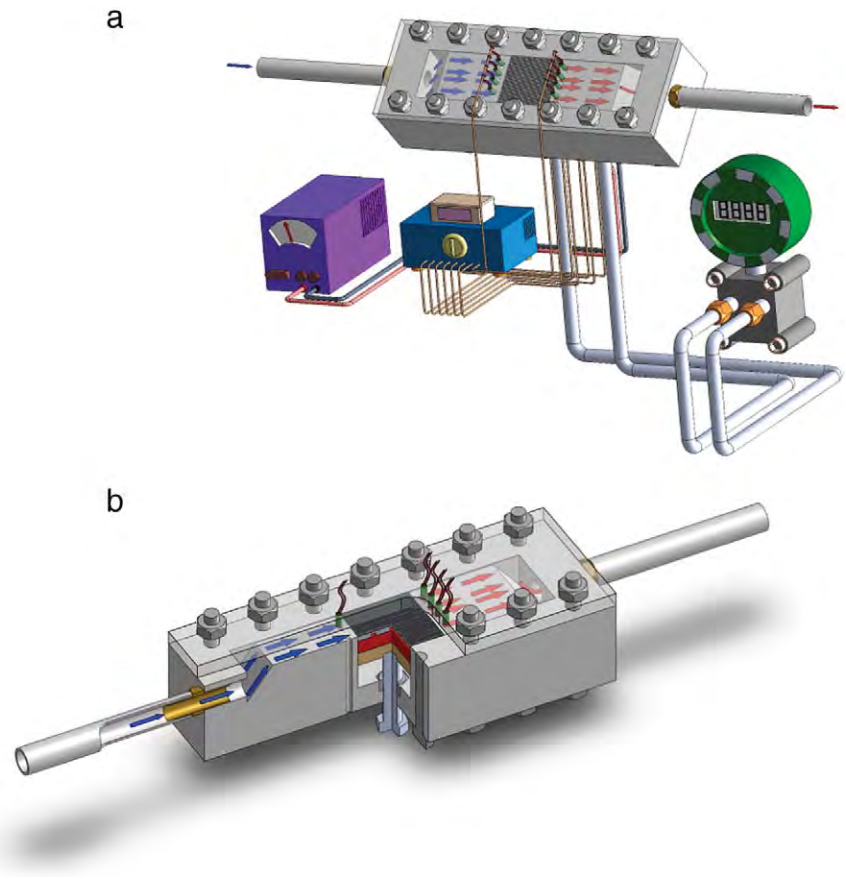

Fig. 2. Prospectives of the microchannel: (a) overview of the microchannel and measurement devices and (b) cross-sectional view of microchannel test section.

Brinkman relation [22]:

$$\frac{\mu_{nf}}{\mu_f} = \frac{1}{(1-\phi)^{2.5}} \tag{2}$$

For the thermal conductivity of model#1, the Maxwell equation [22] is utilized:

$$\frac{k_{nf}}{k_f} = \frac{k_p + 2k_f + 2\phi\left(k_p - k_f\right)}{k_p + 2k_f - \phi\left(k_p - k_f\right)} \tag{3}$$

Model # 2 In this model that is the combination of the newer relations, the viscosity is calculated as [23]:

$$\frac{\mu_{nf}}{\mu_f} = \frac{1}{1-34.87\left(d_p/d_f\right)^{-0.3}\phi^{1.03}} \tag{4}$$

where d_p is nanoparticle size, and d_f is the molecule diameter of base fluid which can be calculated by:

$$d_f = \left[\frac{6M}{N\pi\rho_{f,0}}\right]^{1/3} \tag{5}$$

where M is the molecular weight of base fluid, N is the Avogadro number, and $\rho_{f,0}$ is the density of base fluid calculated at the temperature of 293 K.To obtain the thermal conductivity, the Yu and Choi relation is used [24]:

$$\frac{k_{nf}}{k_f} = \frac{k_p + 2k_f + 2\left(k_p - k_f\right)(1+\beta)^3\phi}{k_p + 2k_f - \left(k_p - k_f\right)(1+\beta)^3\phi} \tag{6}$$

where $\beta = 0.1$.

Model # 3 This model is based on experimental data. Duangthongsuk and Wongwises [25] based on their experimental data on TiO_2/water nanofluid, presented following models to calculate the viscosity and thermal conductivity as: Viscosity:

$$\frac{\mu_{nf}}{\mu_f} = \left(a + b\phi + c\phi^2\right) \tag{7}$$

Thermal conductivity:

$$\frac{k_{nf}}{k_f} = d + e\phi \tag{8}$$

where a, b, c, d and e are functions of temperature.

Using the above models the Nusselt number and friction factor are calculated and the results are compared.

The amount of heat transfer to the nanofluid in the microchannel is determined as:

$$Q_{nf} = VI \tag{9}$$

where Q_{nf} is heat transferred to nanofluid, V is electrical voltage, and I is electrical current.The average convective heat transfer coefficient for the nanofluid is obtained as:

$$\overline{h}_{nf} = \frac{Q_{nf}}{A \cdot \left(T_{wall} - T_{nf}\right)} \tag{10}$$

where $\overline{h}_{nf}$ is the average convective heat transfer coefficient of the nanofluid, T_{wall} is the wall temperature of microchannel, T_{nf} is the temperature of nanofluid, and A is the surface area of the channels.Nusselt number is obtained based on the following relation:

$$\overline{N}u_{nf} = \frac{\overline{h}_{nf} \cdot D_h}{k_{nf}} \tag{11}$$

where $\overline{N}u_{nf}$ is the Nusselt number of nanofluids and D_h is the hydraulic diameter of the channel.To calculate the friction factor in the channel, following relation is used:

$$f_{nf} = \frac{2D_h\Delta P}{L\rho_{nf}u_m^2} \tag{12}$$

where ΔP is he pressure drop and it is obtained based on the experiments. Also, L is the length of the microchannel and u_m is the average velocity of the nanofluid in the microchannel. It should be noted that the friction factor will be depended to viscosity where the right hand side of Eq. (12), is defined based on the Reynolds number.

It is helpful to define the augmentation Nusselt number, which is the ratio between the Nusselt number of nanofluid to the Nusselt number of base fluid, as follows:

$$Nu_a = \frac{\overline{N}u_{nf}}{\overline{N}u_f} \tag{13}$$

This relation helps to find that using a nanofluid at a specified volume fraction how much is beneficial compared to the base fluid. A greater augmentation Nusselt number implies that using the nanofluid is more beneficial than the base fluid from the heat transfer point of view.

It should be noted that the uncertainty in Nusselt number and heat transfer coefficient does not exceed 4%.

5. Results and discussions

In this section, first, the results related to heat transfer coefficient are presented. Next, the effects of uncertainties in viscosity and thermal conductivity on the Nusselt number are discussed. Fig. 3 shows the variations of heat transfer coefficient with the Reynolds number for different volume fractions at heat fluxof69.1 W.

It is observed that the convective heat transfer coefficient increases with increasing the volume fraction of nanoparticles. This happens because of some factors such as Brownian motion of nanoparticles, higher thermal conductivity of nanoparticles. However, it is unknown that how much the heat transfer coefficient increases with increasing the volume fraction. For instance, it is seen from Fig. 3 that at low Reynolds

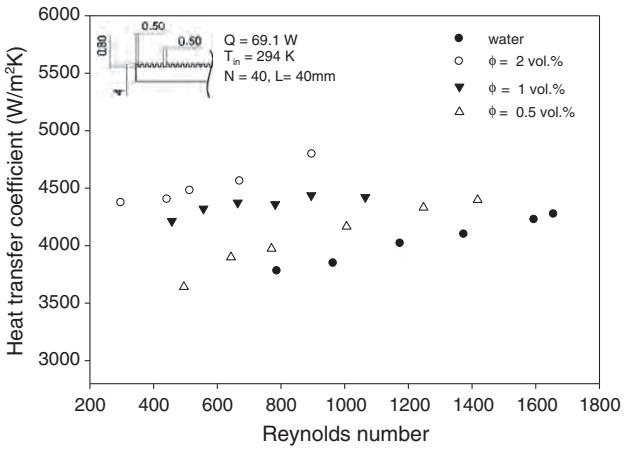

Fig. 3. Heat transfer coefficient at different volume fractions for Q = 69.1 W.

numbers (Re ≈ 400), with increasing the volume fraction from 0.5% to 1% the heat transfer coefficient increases more than 500 W/m^{2}K, while the amount of increase in the heat transfer coefficient is not more than 200 W/m^{2}K where the volume fraction increases from 1.5% to 2%. It is also perceived that with increasing the Reynolds number the heat transfer coefficient increases especially at the volume fraction of 0.5%. The gradient of heat transfer coefficient at concentration of 0.5% is greater than other concentrations because the unfavorable effects of viscous forces for $\phi = 0.5\%$ are lowest compared to other concentrations.

Figs. 4–6 show the variations of the Nusselt number with the volume fraction for the three sets of models, two amounts of Reynolds number including 400 and 1200 and three values of heat flux. From the figures it is found that the difference between the Nusselt numbers predicted by the three models is approximately 2%, and occurs at the concentration of 2%. In other concentrations (i.e. 0.5% and 1%), the difference is lower. Therefore, it is concluded that even using the Maxwell model which is a temperature-independent model may be reasonable for calculating the Nusselt number in the microchannels. From Figs. 4–6, it is also observed that the Nusselt number increases between 13% and 20% with increasing the volume fraction from 0 to 2%.

Table 1 provides the augmentation Nusselt numbers at different volume fractions for model 3 and for the three heat fluxes applied to the microchannel. It can be seen that the augmentation Nusselt number has the maximum amount at the maximum volume fraction

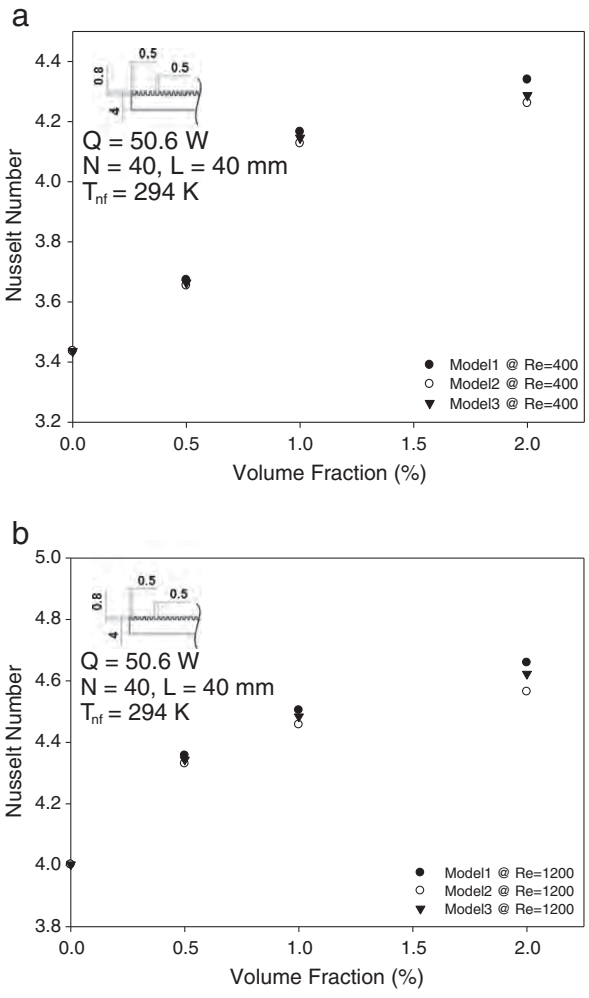

Fig. 4. Effects of uncertainties on the Nusselt number for Q = 50.6 W for (a) Re = 400 and (b) Re = 1200.

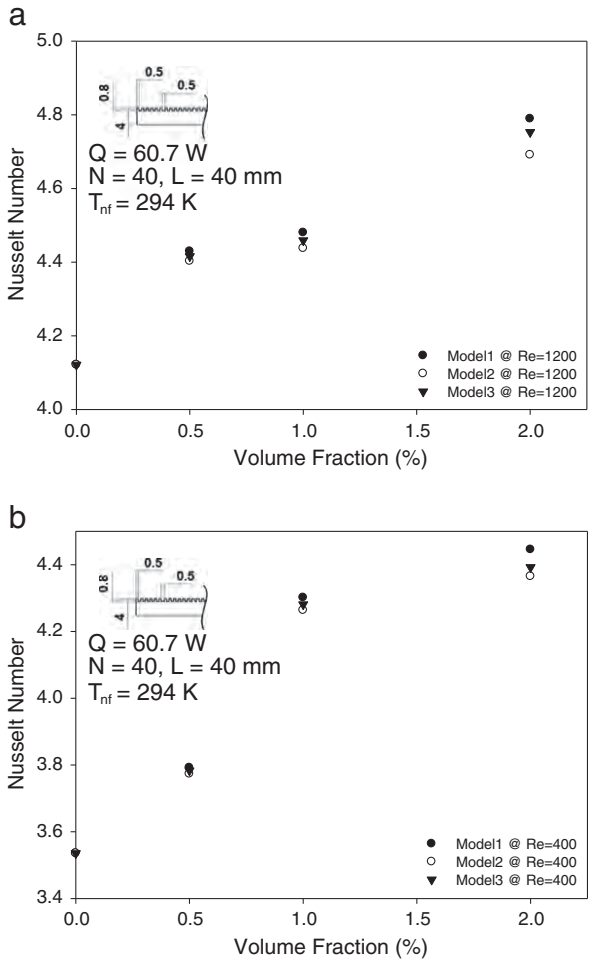

Fig. 5. Effects of uncertainties on the Nusselt number for Q = 60.7 W for (a) Re = 400 and (b) Re = 1200.

(2%) and minimum values of the Reynolds number (Re = 400) and heat flux (Q = 50.6 W). In other words, for Re = 400, and Q = 50.6 W, adding nanoparticles by 2% gives the best results from the heat transfer point of view compared other values of heat flux and the Reynolds number. On the other hand, the augmentation Nusselt number is minimized at Re = 400, Q = 69.1 W for concentration of 0.5.

Fig. 7 shows the effects of different models on the friction factor for Re = 400 and Re = 1200, and various volume fractions of nanoparticles. It can be observed that the difference between the results predicted by the models increases with increasing the volume fraction as expected. As shown in Fig. 7(a), for Re = 400, based on model #2 the friction factor increases with increasing the volume fraction while the models 1 and 3 predict that with increasing the volume fraction from 1.5% to 2%, the friction factor decreases. It is concluded that model # 2 fails to predict the trend of variations of friction factor. The increase of concentration from 1.5 to 2%, leads to a decrease in friction factor because of increasing the nanofluid density. In this case, the density of nanofluid increases with a higher rate compared to the pressure drop increase, and hence the friction factor decreases (see Eq. (12)). It can be seen also that model #3 gives the smallest amount of friction factor. At $\phi = 2\%$, the difference between the friction factors predicted by models 1 and 3 is about 14%, while the difference between the friction factors predicted by models 1 and 2 is about 21%. This shows that using model#3 which is based on experimental data is necessary to have an accurate estimation of friction factor. For Re = 1200 (Fig. 7(b)), it is found that all models predict the same trend for the friction factor where the volume

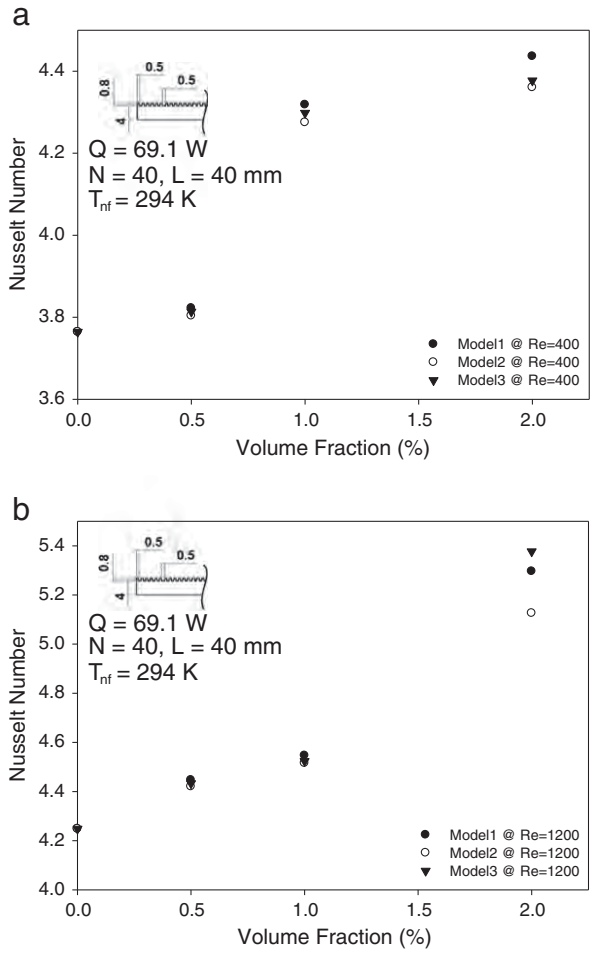

Fig. 6. Effects of uncertainties on the Nusselt number for Q = 69.1 W for (a) Re = 400 and (b) Re = 1200.

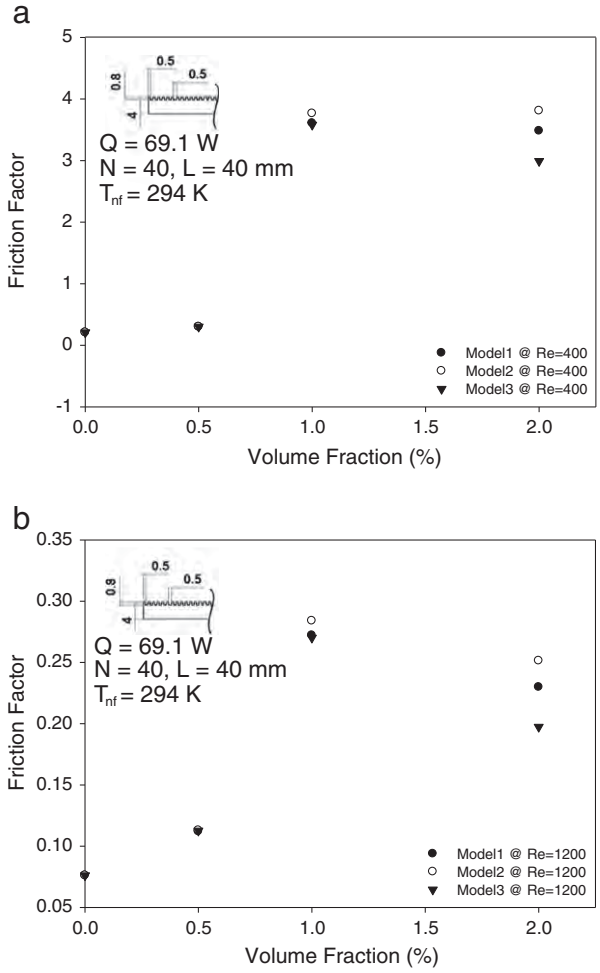

Fig. 7. Effects of uncertainties on the friction factor for Q = 69.1 W and (a) Re = 400, (b) Re = 1200.

fraction increases from 1.5% to 2%. However, the differences among the models are large, similar to the case of Re = 400.

6. Conclusion

An experimental study is performed on the flow and heat transfer of TiO_2/water nanofluid (with volume fractions between 0.5% and 2%) in a microchannel with a focus on the effects of uncertainties in thermal conductivity and viscosity models on the prediction of Nusselt number and friction factor. The size of microchannel and heat fluxes applied to the microchannels, are selected based on practical applications. To do this, three sets of models are used to calculate the thermal conductivity and viscosity of nanofluids. The results show that even the use of a very old model such as Maxwell model to calculate the thermal conductivity gives very good estimation of the Nusselt number. It is found that the difference among the Nusselt numbers predicted by the various models is about 2% (at ϕ = 2%), which is not considerable. However, for the friction factor, it is observed that the differences between the friction factors predicted by the three models at ϕ = 2% are great, so that using the viscosity obtained based on the experimental data is necessary to estimate the friction factor. From the values obtained for the augmentation Nusselt number, it is concluded that the use of nanofluid with volume fraction of 2% in the minimum amounts of heat flux and Reynolds number is more advantageous compared other situations.

Table 1
Augmentation Nusselt number at different heat fluxes and volume fractions.

	Nu_a at Q = 50.6 W		Nu_a at Q = 60.7 W		Nu_a at Q = 69.1 W	
Volume fraction (%)	Re = 400	Re = 1200	Re = 400	Re = 1200	Re = 400	Re = 1200
0	1	1	1	1	1	1
0.5	1.066332	1.085192	1.070055	1.071436	1.013103	1.043571
1	1.206521	1.120315	1.210766	1.081913	1.165728	1.086858
2	1.24769	1.154983	1.242311	1.15319	1.163649	1.170568

Acknowledgements

The present study was supported financially by the Thailand Research Fund and the National Research University Project, whose guidance and assistance are gratefully acknowledged. The second and third authors would like to thank Professor Somchai Wongwises for providing them for support during their research in the Department of Mechanical Engineering, King Mongkut's University of Technology Thonburi.

References

[1] R. Saidur, K.Y. Leong, H.A. Mohammad, A review on applications and challenges of nanofluids, Renewable and Sustainable Energy Reviews 15 (3) (2011) 1646–1668.
[2] W. Duangthongsuk, S. Wongwises, An experimental study on the heat transfer performance and pressure drop of TiO2-water nanofluids flowing under a turbulent flow regime, International Journal of Heat and Mass Transfer 53 (1–3) (2010) 334–344.
[3] O. Mahian, A. Kianifar, S.A. Kalogirou, I. Pop, S. Wongwises, A review of the applications of nanofluids in solar energy, International Journal of Heat and Mass Transfer 57 (2) (2013) 582–594.

[4] W. Daungthongsuk, S. Wongwises, A critical review of convective heat transfer of nanofluids, Renewable and Sustainable Energy Reviews 11 (5) (2007) 797–817.
[5] V. Trisaksri, S. Wongwises, Critical review of heat transfer characteristics of nanofluids, Renewable and Sustainable Energy Reviews 11 (3) (2007) 512–523.
[6] L. Godson, B. Raja, D. Mohan Lal, S. Wongwises, Enhancement of heat transfer using nanofluids—an overview, Renewable and Sustainable Energy Reviews 14 (2) (2010) 629–641.
[7] R. Chein, G. Huang, Analysis of microchannel heat sink performance using nanofluid, Applied Thermal Engineering 25 (17–18) (2005) 3104–3114.
[8] R. Chein, J. Chuang, Experimental microchannel heat sink performance studies using nanofluids, International Journal of Thermal Sciences 46 (1) (2007) 57–66.
[9] J.Y. Jung, H.-S. Oh, H.-Y. Kwak, Forced convective heat transfer of nanofluids in microchannels, International Journal of Heat and Mass Transfer 52 (1–2) (2009) 466–472.
[10] C.J. Ho, L.C. Wei, Z.W. Li, An experimental investigation of forced convective cooling performance of a microchannel heat sink with Al2O3/water nanofluid, Applied Thermal Engineering 30 (2–3) (2010) 96–103.
[11] Y. Wang, S.J. Chung, J.P. Leonard, S.K. Cho, T. Phuoc, Y. Soong, M.K. Chyu, Cooling performance of nanofluids in a microchannel heat sink, Proceedings of the ASME Micro/Nanoscale Heat and Mass Transfer International Conference 2009, MNHMT2009, 1, 2009, pp. 617–623.
[12] S. Vafaei, D. Wen, Critical heat flux (CHF) of subcooled flow boiling of alumina nanofluids in a horizontal microchannel, Journal of Heat Transfer 132 (10) (2010) 1–7.
[13] L. Xu, Y.-X. Li, J.-L. Xu, G.-H. Liu, Flow boiling heat transfer performance of nanofluids in a microchannel, Journal of Chemical Engineering of Chinese Universities 25 (4) (2011) 559–564.
[14] M.D. Byrne, R.A. Hart, A.K. Da Silva, Experimental thermal-hydraulic evaluation of CuO nanofluids in microchannels at various concentrations with and without suspension enhancers, International Journal of Heat and Mass Transfer 55 (9–10) (2012) 2684–2691.
[15] M. Kalteh, A. Abbassi, M. Saffar-Avval, A. Frijns, A. Darhuber, J. Harting, Experimental and numerical investigation of nanofluid forced convection inside a wide microchannel heat sink, Applied Thermal Engineering 36 (1) (2012) 260–268.
[16] W. Duangthongsuk, A.S. Dalkilic, S. Wongwises, Convective heat transfer of Al_2O_3-water nanofluids in a microchannel heat sink, Current Nanoscience 8 (3) (2012) 317–322.
[17] C.-J. Ning, X.-P. Luo, Heat transfer and pressure drop of Al 2O3 nanofluids in microchannels, Journal of Central South University (Science and Technology) 43 (8) (2012) 3000–3006.
[18] L. Xu, J. Xu, Nanofluid stabilizes and enhances convective boiling heat transfer in a single microchannel, International Journal of Heat and Mass Transfer 55 (21–22) (2012) 5673–5686.
[19] K. Anoop, R. Sadr, J. Yu, S. Kang, S. Jeon, D. Banerjee, Experimental study of forced convective heat transfer of nanofluids in a microchannel, International Communications in Heat and Mass Transfer 39 (9) (2012) 1325–1330.
[20] W. Duangthongsuk, S. Wongwises, Effect of thermophysical properties models on the predicting of the convective heat transfer coefficient for low concentration nanofluid, International Communications in Heat and Mass Transfer 35 (2008) 1320–1326.
[21] O. Mahian, S. Mahmud, S. Zeinali Heris, Effect of uncertainties in physical properties on entropy generation between two rotating cylinders with nanofluids, Journal of Heat Transfer 134 (10) (2012) 101704.
[22] K. Khanafer, K. Vafai, A critical synthesis of thermophysical characteristics of nanofluids, International Journal of Heat and Mass Transfer 54 (2011) 4410–4428.
[23] M. Corcione, Heat transfer features of buoyancy-driven nanofluids inside rectangular enclosures differentially heated at the sidewalls, International Journal of Thermal Sciences 49 (2010) 1536–1546.
[24] W. Yu, S.U.S. Choi, The role of interfacial layers in the enhanced thermal conductivity of nanofluids: a renovated Maxwell model, Journal of Nanoparticle Research 5 (2003) 167–171.
[25] W. Duangthongsuk, S. Wongwises, Measurement of temperature-dependent thermal conductivity and viscosity of TiO_2 water nanofluids, Experimental Thermal and Fluid Science 33 (2009) 706–714.

Lazarus Godson Asirvatham[1]
e-mail: godson@karunya.edu;
godasir@yahoo.co.in

Rajesh Nimmagadda
e-mail: rajesh.mech335@gmail.com

Department of Mechanical Engineering,
Karunya University,
Coimbatore 641 114, Tamil Nadu, India

Somchai Wongwises
Fluid Mechanics,
Thermal Engineering and Multiphase Flow
Research Lab (FUTURE),
Department of Mechanical Engineering,
Faculty of Engineering,
King Mongkut's University of Technology,
Thonburi, 126 Bangmod,
Tongkru, Bangkok 10140, Thailand;
The Academy of Science,
The Royal Institute of Thailand,
Sanam Suea Pa, Dusit,
Bangkok 10300, Thailand
e-mail: somchai.won@kmutt.ac.th

Operational Limitations of Heat Pipes With Silver-Water Nanofluids

The paper presents the enhancement in the operational limits (boiling, entrainment, sonic, viscous and capillary limits) of heat pipes using silver nanoparticles dispersed in de-ionized (DI) water. The tested nanoparticles concentration ranged from 0.003 vol. % to 0.009 vol. % with particle diameter of <100 nm. The nanofluid as working fluid enhances the effective thermal conductivity of heat pipe by 40%, 58%, and 70%, respectively, for volume concentrations of 0.003%, 0.006%, and 0.009%. For an input heat load of 60 W, the adiabatic vapor temperatures of nanofluid based heat pipes are reduced by 9 °C, 18 °C, and 20 °C, when compared with DI water. This reduction in the operating temperature enhances the thermophysical properties of working fluid and gives a change in the various operational limits of heat pipes. The use of silver nanoparticles with 0.009 vol. % concentration increases the capillary limit value of heat pipe by 54% when compared with DI water. This in turn improves the performance and operating range of the heat pipe. [DOI: 10.1115/1.4024616]

Keywords: silver, heat pipe, boiling limit, entrainment limit, capillary limit, sonic limit, viscous limit, nanofluid

1 Introduction

Heat pipes are widely used in thermal management of microelectronic devices. The heat transport capability of heat pipe is limited by the working fluid transport properties. The excessive heat transport capacity of the working fluid can be obtained by suspending nanoparticles in base fluids. Choi and Eastman [1] first applied these nanofluids in thermal engineering for efficient heat transfer due to its enhanced thermal conductivity. Many researchers like Shafai et al. [2] and Liu et al. [3] studied the effects of nanofluids on the performance of cylindrical heat pipes and cylindrical microgrooved heat pipes and found that nanofluids as working fluids enhance the performance of heat pipes. Nemec et al. [4] proposed a mathematical model to verify the heat transfer limitations of heat pipe. The modeling was done for ethanol heat pipe operating in the temperature varying from −30 °C to 140 °C with sintered wick and grooved capillary structure. The effect of these limitations on the cooling performance of heat pipes was evaluated. Finally, the study concluded that the increased permeability and increased pore dimensions decreases the capillary pressure. Since, the capillary limit is the primary heat transport limitation of the heat pipe. It was also observed that the capillary limit had the highest influence regarding circulation of the working fluid.

Nemec and Huzvar [5] presented a mathematical analysis of total heat power of the sodium heat pipe on the basis of heat transport limitation equations. The heat pipe was made up of steel with sodium as working fluid and operating temperature ranging from 500 K to 1000 K. It was found that the viscous and sonic limits reach very high values and are not important for influencing the total performance of the heat pipe. The results reported that the capillary limit was the maximum heat transport limitation and subsequently the other limits, such as the entrainment and boiling limits, also influence the heat pipe performance. Naik et al. [6] designed, fabricated, and tested the heat pipe with axially grooved wick for horizontal and gravity assisted conditions. The design was based on five primary heat transport limits which include viscous, sonic, capillary, entrainment, and boiling limits. Three different working fluids, such as methanol, acetone, and distilled water were used and the maximum heat transfer coefficient was found to be 3550 W/m^2 °C, 1700 W/m^2 °C, and 2400 W/m^2 °C, respectively, in horizontal and vertical orientation. Faghri [7] and Peterson [8] explained the modelling of heat pipes based on the various operational limits and suggested that these operational limits mainly depend on the operating temperature and thermophysical properties of working fluids. Thuchayapong et al. [9] presented a numerical approach with finite element method (FEM) to study the effect of capillary pressure on the performance of heat pipe. The two-dimensional heat transfer and fluid flow in a heat pipe at steady-state condition was numerically simulated using FEM. The numerical results indicated that the capillary pressure gradient inside the copper mesh wick at the end of the evaporator section was found to be very high. The finding of the numerical analysis suggested that the capillary pressure was one of the key parameters in the design and efficiency of the heat pipe. Riehl and Santos [10] investigated the operational behaviour of loop heat pipes and pulsating heat pipes (PHPs) with copper-water nanofluids with nanoparticles sizes (diameter) below 40 nm. Results have demonstrated that the liquid's thermal conductivity is enhanced by 20% for a nanoparticles concentration of 5% by mass. Further it is noted that the improvements on the overall device's operation have been observed when using the nanofluid with lower temperatures, as well as a direct influence on the thermal conductance throughout the PHP.

Chiang et al. [11] developed a magnetic-nanofluid (MNF) heat pipe (MNFHP) with magnetically enhanced thermal properties. The results showed that an optimal thermal conductivity exists in the applied field of 200 Oe. Furthermore, the minor thermal performance of MNF at the condenser limited the thermal conductivity of the entire MNFHP, which was 1.6 times greater than that

[1]Corresponding author.

Contributed by the Heat Transfer Division of ASME for publication in the Journal of Heat Transfer. Manuscript received May 28, 2012; final manuscript received March 9, 2013; published online September 23, 2013. Assoc. Editor: Sujoy Kumar Saha.

filled with water for the input power of 60 W. Liu and Li [12] reviewed the research done on heat pipes using nanofluids as working fluids in recent years. The effect of characteristics and mass concentrations of nanoparticles on the thermal performance, the mechanism of enhancement, or degradation of heat transfer and the relative reduction of the total heat resistance for various heat pipes with nanofluids are summarized in comparison with the existing ones and also presented a perspective on possible future research applications. Putra et al. [13] investigated the thermal performance and the effect of coatings on the structure of screen mesh wick heat pipes with Al_2O_3–water, Al_2O_3–ethylene glycol, TiO_2–water, TiO_2–ethylene glycol, and ZnO–ethylene glycol nanofluids with the concentration of the nanoparticles varied from 1% to 5% of the volume of the base fluid. It is observed that the screen mesh wick heat pipe with Al_2O_3–water nanofluid with 5% volume concentration yielded the best performance. Further it is noted that the use of nanofluids resulted in the formation of a thin coating on the screen mesh surface from the element of the nanoparticles which enhanced the thermal performance in the heat pipes. Hajian et al. [14] experimentally studied the thermal performance of silver-DI water nanofluids with concentrations of 50, 200, and 600 ppm in a medium-sized cylindrical meshed heat pipe, under both transient and steady-state conditions. The results showed that the thermal resistance and response time of the heat pipe decreased up to 30% and 20%, respectively, compared with DI water.

Alizad et al. [15] analyzed the thermal performance, transient behavior, and operational start-up characteristics of flat-shaped heat pipes using CuO, Al_2O_3, and TiO_2 nanofluids. The results showed an enhancement in the heat pipe performance while achieving a reduction in the thermal resistance for both flat-plate and disk-shaped heat pipes throughout the transient process.

Tsai et al. [16] investigated the thermal performance of disk-shaped miniature heat pipe (DMHP) with gold and carbon nanoparticles suspended in DI water as nanofluids. The measured results showed that the significant reduction in thermal resistance of DMHP for nanofluid when compared with that of DI water. Putra et al. [17] investigated the application of nanofluids to a heat pipe liquid-block and the thermoelectric cooling of electronic equipment. The results showed higher thermal performance in the heat pipe liquid-block and thermoelectric cooled system with nanofluids as a working fluid. Jamshidi et al. [18] experimentally investigated the thermal characteristics of closed loop pulsating heat pipe with nanofluids for (30%, 40%, 50%, 70%, 80%) volumetric filling ratio with an input heat power of (5–70 W). The results showed that the best thermal performance for water and ethanol as working fluids when the corresponding filling ratios are 40% and 50%, respectively.

Ji et al. [19] experimentally studied the effect of four different sizes of Al_2O_3 particles with average diameters of 50 nm, 80 nm, 2.2 μm, and 20 μm on the heat transfer performance of an oscillating heat pipe (OHP). Experimental results showed that the Al_2O_3 particles added in the OHP significantly enhances the heat transfer performance and it depends on the particle size. It has been found that the OHP charged with water and 80 nm Al_2O_3 particles, gave the best heat transfer performance among four particles investigated. Li et al. [20] experimentally investigated the two-phase flows in an OHP charged with DI water and a nanofluid. It is observed that the nanofluid OHP had a much lower thermal resistance than the DI water OHP with the most effective heat transfer in the nanofluid OHP occurring in the slug flow regime. Huminic et al. [21] presented an experimental investigation on the thermal performance of thermosyphon heat pipe using iron oxide nanoparticles suspended in DI water as a working fluid with 0%, 2%, and 5.3% concentration of nanoparticles. Results showed that the addition of 5.3% (by volume) of iron oxide nanoparticles in water presented improved thermal performance compared with the operation with DI water.

Liu and Zhu [22] analyzed the application of aqueous nanofluids in a horizontal mesh heat pipe adopting the fuzzy theory to control the frequency of compressor of water chilling unit, secondary pump, and ventilator of air conditioner box, so as to realize the thermal comfort of room and fixed outlet temperature. The experimental results reported that when the outlet temperature of chilling water is set as 12 °C, the thermal comfort of room is maintained at 0.5 and the energy is saved effectively. Wang et al. [23] performed an experimental study and investigated the operational characteristics of a cylindrical miniature grooved heat pipe using aqueous CuO nanofluid as the working fluid. The experiment results showed that the heat pipe with nanofluid apparently improved the thermal performance under steady operation. The total heat resistance and the maximum heat removal capacity of the heat pipe using nanofluids reduced by 50% and increased by 40% compared with that of the heat pipe using water, respectively. Li et al. [24] investigated the influence of the water-based CuO nanofluid with an average diameter of 50 nm on both steady and transient operation characteristics of a small capillary pumped loop (CPL) with mesh wicked construction. The experiment results of the transient operation indicated that both the start-up time and evaporator wall temperature were reduced and the operation characteristics of the CPL were improved after substituting the nanofluid for water as the working fluid. Liu et al. [25] experimentally studied the thermal performance of an inclined miniature grooved heat pipe using water-based CuO nanofluid as the working fluid. The inclination angle and the operating pressure on the heat transfer of the heat pipe using the nanofluid with the mass concentration of CuO nanoparticles of 1.0 wt. % were investigated. Experimental results showed that an inclination angle of 45 deg indicated the best heat transfer performance of heat pipes using both water and the nanofluid.

Shafahi et al. [26] analyzed the thermal performance of flat-shaped heat pipes using nanofluids. The presence of nanoparticles within the working fluid resulted in a decrease in the thermal resistance and an increase in the maximum heat load capacity of the flat-shaped heat pipe. Qu et al. [27] investigated the thermal performance of an oscillating heat pipe charged with water and spherical Al_2O_3 particles of 56 nm in diameter. Experimental results showed that the alumina nanofluids significantly improved the thermal performance of the oscillating heat pipe (OHP), with an optimal mass fraction of 0.9 wt. % for maximum heat transfer enhancement. The thermal resistance was decreased by 0.14 °C/W when compared with pure water. Kang et al. [28] experimentally studied the thermal performance of silver nanoparticles having the size of 10 nm and 35 nm in diameter suspended in pure water in sintered circular heat pipe with concentrations ranged from 1, 10, and 100 mg/l. The results indicated that at a same charge volume, the nanofluids filled heat pipe temperature distribution demonstrated that the temperature difference decreased 0.56–0.65 °C compared with DI water at an input power of 30–50 W. Yang et al. [29] carried out an experiment to study the heat transfer performance of a horizontal microgrooved heat pipe using CuO nanofluid as the working fluid. The Mass concentration of CuO nanoparticles varied from 0.5 wt. % to 2.0 wt. % with an average diameter 50 nm. Experimental results showed that the CuO nanofluid improved the thermal performance of the heat pipe.

Liu et al. [30] experimentally studied the nucleate boiling heat transfer of water-CuO nanoparticles suspension (nanofluids) at different operating pressures and different nanoparticle mass concentrations in a miniature flat heat pipe (MFHP) with microgrooved heat transfer surface of its evaporator. The experimental results indicated that the operating pressure has great influence on the nucleate boiling characteristics in the MFHP evaporator. The heat transfer coefficient and the critical heat flux (CHF) of nanofluids increased by about 25% and 50%, respectively, at atmospheric pressure, whereas about 100% and 150%, respectively, at the pressure of 7.4 kPa. Ma et al. [31] studied the effect of nanofluid on the heat transport capability in an OHP by combining nanofluids with thermally excited oscillating motion in an oscillating heat pipe. The results showed an increase in the heat transport capability of the OHP when charged with nanofluid. Tsai et al.

[32] studied the effect of structural character of gold nanoparticles in nanofluid on heat pipe thermal performance. Results showed a reduction on thermal resistance of heat pipe with nanofluid as compared with DI water at the same charge volume. The measured results also indicated that the thermal resistance of a vertical meshed heat pipe varied with the size of gold nanoparticles.

From the above mentioned literature, it is observed that all the researchers have stated that the heat transport limitations, such as viscous, sonic, capillary, entrainment, and boiling limits are the key design parameters on the heat pipe performance. Peterson [8] has reported that the operational limits of the heat pipe mainly depend on the thermophysical properties of working fluids and significantly varies with the change in the operating temperature. Surprisingly, the amount of literature available with regard to the heat pipe limitations is quite small. Moreover, no published work has been reported in the open literature that deals with the various operational limitations of the heat pipe using the low volume concentration of pure metal nanoparticles. Hence in the present work, the silver nanoparticles with 0.003%, 0.006%, and 0.009% volume concentrations are dispersed in DI water and used as the working fluid in the heat pipe. The heat pipe is tested for a maximum heat load of up to 100 W. The effect of heat load and volume concentration on the various limitations of the heat pipe are experimentally investigated and presented.

2 Experimentation

2.1 Nanofluid Preparation. Silver-water nanofluid is prepared using a two step method. The silver nanoparticles (manufactured by Sigma Aldrich; the product number is 576,832, Silver nanopowder, <100 nm, 99.5% metals) is mixed with de-ionized water without any additive. The nanofluid is then sonicated using the ultrasonic processor, UP400S (Hielscher) ultra sound technology, with rated voltage, Nennspannung 200–240 and rated current, Nennstrom 4 A and rated frequency, Nennfrequenz 50/60 Hz) for about 45 min for stable suspension of the nanoparticles. After preparation of nanofluids, a stability test was conducted by taking some small sample of nanofluid for the maximum concentration (0.009 vol. %) and physically observed if there is any settling occurs. The photo was taken after 24 and 48 h as shown in Fig. 1. It is clearly seen from Fig. 1 that the settling does not occur in 48 h. Hence, the prepared nanofluid is considered to be stable throughout the experiment. Furthermore, the scanning electron microscopic (SEM) analysis is done on silver nanoparticles to characterize the average particle diameter. Figure 2(*a*) shows the SEM image of 0.009% volume concentration of silver nanoparticles. It is clearly seen from the image that the size of the nanoparticles is found to be less than 100 nm. It is also found that in some places, the size exceeds 100 nm due to the agglomeration of the nanoparticles. Figure 2(*b*) shows the histogram of the size distribution in percentage against the particle size of the silver nanoparticles. The SEM micrographs confirmed the spherical shape of the silver nanoparticles and revealed a single modal particle size distribution with average diameters of 160 nm estimated by measuring the diameter of randomly selected particles in enlarged SEM image.

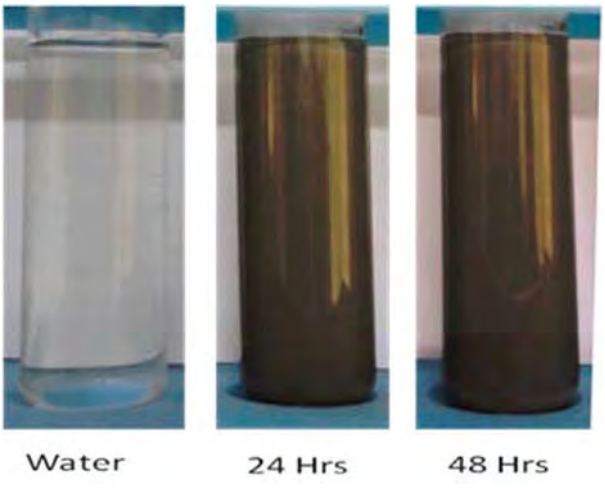

Fig. 1 Stability test for 0.009 vol. % silver/water nanofluid

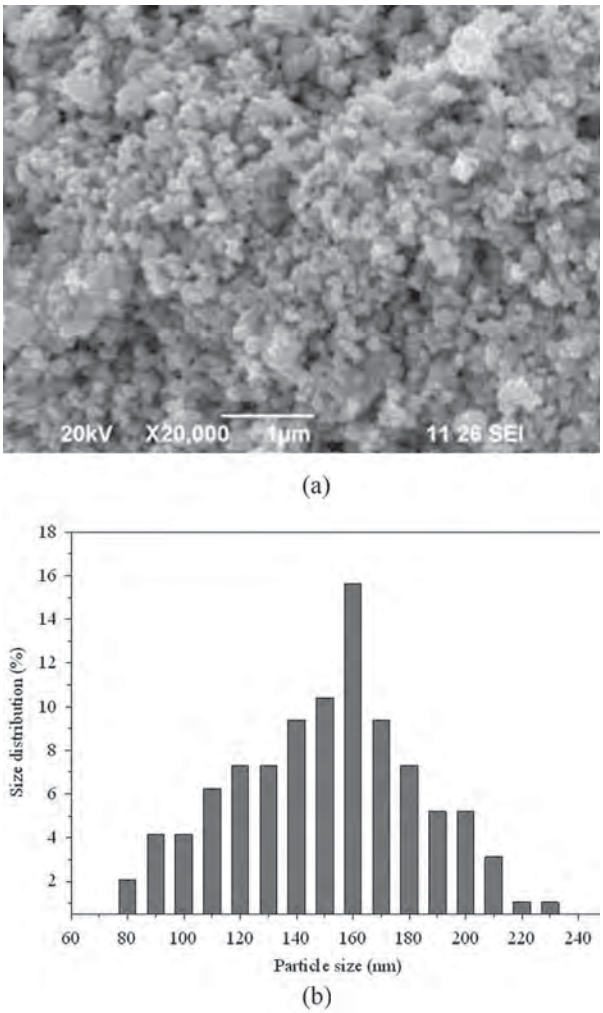

Fig. 2 (*a*) SEM image of 0.009% volume concentration of silver nanoparticles and (*b*) particle distribution percentage against size of silver nanoparticles

2.2 Experimental Setup and Procedure. The schematic layout of test facility to measure the effect of nanoparticles concentration on the operational limitations of heat pipe is shown in Fig. 3.The heat pipe is made up of copper material with a length of 180 mm and outer diameter of 10 mm, respectively. The inner diameter of the heat pipe is 9 mm and lengths of evaporator section, adiabatic section, and condenser section of the heat pipes are, 50 mm, 50 mm and 80 mm, respectively, with wall thickness of 0.5 mm. The screen mesh wick wrapped inside the heat pipe is made up of copper with a wire diameter of 0.105 mm and mesh number 100/in. The condenser section of the heat pipe is made up of acrylic material with Teflon end closures. The test set up is equipped with a pump and flow meter (with an uncertainty of $0.17 \pm 10 \times 10^{-6}$ m^3/s) to circulate cooling water at a constant flow rate of 4.33×10^{-6} m^3/s through the condenser section. The

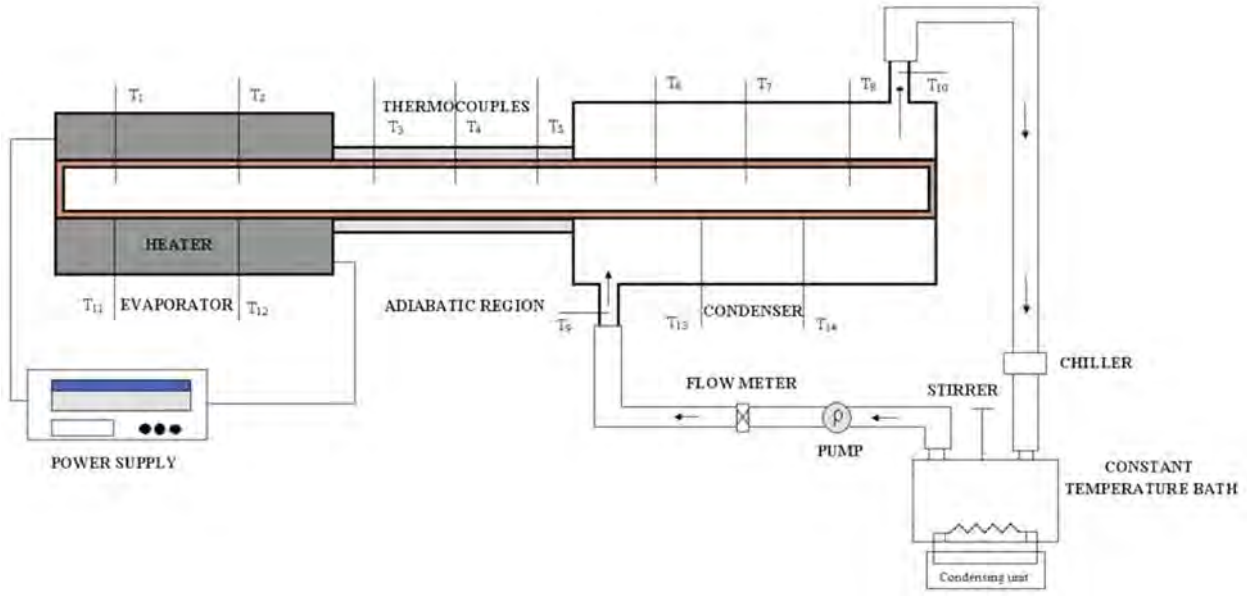

Fig. 3 Schematic diagram of the experimental setup

inlet temperature of the circulating water is maintained at 24 °C for all the test conditions by using a constant temperature chilled water bath. Two T-type thermocouples are fixed between the inlet and outlet of the condenser to measure the inlet and outlet temperatures of the circulating cooling water. Eight T-type thermocouples (uncertainty ±0.5 °C), are inserted in to the heat pipe (two in evaporator, three in adiabatic and three in condenser section, respectively) to measure the inside vapor temperatures. The surface temperatures in the evaporator and condenser are also measured by fixing four T-type thermocouples two on each section. The thermocouples are calibrated separately under the experimental heat loads before the experiments are being conducted. A data logger (Model-(DA 100-13-1 F), Yokogawa-N 200) is used to measure the fluctuation in the measured temperatures of the thermocouples for a sample of 40 readings for each applied heat load. It is observed from this uncertainty study that the temperature reading measured by each of the thermocouple is ±0.5 °C. However, the operational limitations calculated in the present study depend up on the mean adiabatic vapor temperature (operating temperature) of the heat pipe. The thermocouples used in the adiabatic section are calibrated twice and no maximum deviation in the measured temperature is observed more than ±0.5 °C. The input heat load is applied by using a digital wattmeter with an uncertainty of ±0.5 W (Make MECO). An electric heater made up of nichrome wire is wounded on the evaporator section. The heater coil is energized by using a 220 V ac supply. Glass wool is used to insulate the evaporator and adiabatic sections to minimize the heat loss to the surroundings. The experiments are conducted on four identical heat pipes fabricated as per the above mentioned dimensions. One of the four heat pipes is filled with DI water and the remaining three are filled with 0.003%, 0.006%, and 0.009% volume concentrations of silver nanoparticles. The amount of working fluid charged in all the four heat pipes remains constant. The testing conditions, such as condenser coolant circulation rate and inlet temperature, are identical to obtain the performance accuracy. The initial heat load of 20 W is applied on the heat pipe by switching on the power supply and energizing the heater. The input heat load is gradually increased from 20 W to 100 W in five steps. During the experimental test, the vapor and surface temperature readings of the heat pipe are measured using a data logger (Model-(DA 100-13-1 F), Yokogawa-N 200). The entire data acquisition system is monitored and controlled by using a personal computer.

2.3 Thermophysical Properties of Nanofluid. The thermophysical properties of silver-water nanofluid are calculated based on the following equations.

The density is calculated from Pak and Cho [33] using the following equation:

$$\rho_{nf} = \varphi\rho_p + (1-\varphi)\rho_b \tag{1}$$

The specific heat is calculated from Xuan and Roetzel [34] as follows:

$$(\rho C_p)_{nf} = \varphi(\rho C_p)_p + (1-\varphi)(\rho C_p)_b \tag{2}$$

where $(\rho C_p)_{nf}$ is the heat capacity of the nanofluid, $(\rho C_p)_p$ is the heat capacity of the nanoparticles, and $(\rho C_p)_b$ is the heat capacity of the base fluid. The other properties, such as viscosity and thermal conductivity, are measured using the following equations proposed by the present authors. The detailed measurement techniques and procedure are given elsewhere [35] in a published literature by the present authors for reference.

$$\frac{\mu_{nf}}{\mu_b} = (1.005 + 0.497\varphi - 0.1149\varphi^2) \tag{3}$$

$$\frac{k_{nf}}{k_b} = (0.9692\varphi + 0.9508) \tag{4}$$

2.4 Data Reduction. The maximum heat transport capability of heat pipe is governed by various operational limits. The present study deals with the five primary heat transport limitations, including boiling, entrainment, capillary, sonic, and viscous limits. All the equations for calculating the operating limits of heat pipes are taken from Peterson [8].

2.4.1 Capillary Limit. The pumping ability of the capillary structure to provide the circulation of the working fluid is limited for a given working fluid and wick structure. This limit is termed as capillary or hydrodynamic limit. The wick structure will develop a pressure head and this will cause stable circulation of working fluid in the heat pipe. For an effective operation of the heat pipe, the net capillary pressure difference or capillary head should be greater than or equal to all the pressure losses occurring throughout the liquid and vapor flow paths of the heat pipe.

$$\Delta P_{cm} \geq \Delta P_l + \Delta P_v + \Delta P_{ph,e} + \Delta P_{ph,c} + \Delta P_g \quad (5)$$

where ΔP_l is the sum of inertial and viscous pressure drops occurring in liquid phase, ΔP_v is the sum of inertial and viscous pressure drops occurring in vapor phase, $\Delta P_{ph,e}$ is the pressure gradient across phase transition in evaporator, $\Delta P_{ph,c}$ is the pressure gradient across phase transition in condenser, and ΔP_g is the pressure drop in the liquid due to the effect of the gravitational force in the direction of the heat pipe axis.

$$\Delta P_{cm} \text{ maximum capillary pressure} = \frac{2\sigma\cos\theta}{r_c}$$

$$\Delta P_l = [\mu_l/(KA_w\lambda\rho_l)]L_{eff}Q \quad (6)$$

$$\Delta P_v = \left[(C(f_v\mathrm{Re}_v)\mu_v)/\left(2(r_{h,v})^2A_v\rho_v\lambda\right)\right] \quad (7)$$

$$\Delta P_g = \rho_l g d_v \cos\varphi \quad (8)$$

If the above expression is satisfied, then the capillary structure is capable of returning an adequate amount of working fluid to the evaporator in order to prevent the dry-out.

2.4.2 Capillary Pressure. The main phenomenon that governs the operation of the heat pipe is capillary pressure difference developed across liquid–vapor interfaces in evaporator and condenser regions. The pumping ability depends on the capillary pressure. Vaporization in the evaporator region and condensation in the condenser region causes a difference in the local capillary radius. Vaporization causes the meniscus to recede in to the wicking structure, reducing the radius of curvature in the evaporator portion. Similarly, condensation causes a greater radius of curvature in condenser region at liquid interface. This resulting difference in the two radii will provide the capillary pumping pressure necessary for operation of heat pipe. The capillary pressure is calculated based on the following equation:

$$\Delta P_{cm} = \text{maximum capillary pressure} = \frac{2\sigma\cos\theta}{r_c} \quad (9)$$

for perfectly wetting system, contact angle between fluid and wick $\theta = 0$ deg.

2.4.3 Boiling Limit. The boiling limit also called as heat flux limit is comprised two separate phenomena: (1) bubble formation and (2) growth or collapse of bubble.

The bubble formation is governed by the size and number of nucleation sites on the solid surface and the difference between heat pipe wall temperature and working fluid temperature. The growth or collapse of bubbles formed on plane flat surface depends on liquid temperature and corresponding pressure difference across the liquid–vapor interface caused by the vapor pressure and surface tension of the liquid. The boiling limit depends on radial heat flux or circumferential heat flux applied to the evaporator. If the heat pipe wall temperature becomes excessively high, nucleate boiling phenomena of the working fluid will take place in the wick. This causes the vapor bubbles to block the return of the working fluid back to evaporator and results in evaporator dry-out. The heat pipe should be operated within this limit to avoid nucleate boiling phenomena. The boiling limit is calculated based on the following equation:

$$\text{Boiling limit, } Q_{bo} = Q_{bo} = 2\pi\frac{L_{eff}k_{eff}T_v}{h_{fg}\rho_v \ln\left(\frac{r_i}{r_v}\right)}\left[\frac{2\sigma}{r_n} - \Delta P_{cm}\right] \quad (10)$$

where L_{eff} is the effective length of heat pipe that is equal to 0.5 $L_e + L_a + 0.5\,L_c$

k_{eff} is the effective thermal conductivity of the liquid–wick combination

$$k_{eff} = \frac{(k_l(k_l + k_w - (1-\in)(k_l - k_w)))}{k_l + k_w + (1-\in)(k_l - k_w)}$$

$\longrightarrow$For wrapped screen wick

k_l is the liquid thermal conductivity and k_w is the wick thermal conductivity, $\in$ is the wick porosity that is equal to $1-1.05\pi\mathrm{N}d_w/4$, d_w is the wire diameter of the wick, and N is the screen mesh number, 1.05 is the wick crimping factor, ΔP_{cm} is the mMaximum capillary pressure $= 2\sigma\cos\theta/r_c$ where r_c is the effective capillary radius that is equal to $1/2N$ for wire screen wick, $\cos\theta$ is the wetting angle, and r_n is the nucleation site radius.

2.4.4 Entrainment Limit. This limit depends on vapor velocities, when the vapor velocity in the heat pipe is sufficiently high, the shear forces between liquid–vapor interfaces may become greater than the liquid surface tension forces in the wick. This may cause the liquid droplets being picked up or entrained in the vapor flow and will be carried back to condenser. This entrainment of liquid droplets will limit the axial heat transport capability of heat pipe. The entrainment limit is calculated based on the following equation:

$$\text{Entrainment limit } Q_{en} = A_v h_{fg}\left[\frac{\sigma\rho_v}{2r_{hw}}\right]^{1/2} \quad (11)$$

where A_v is the cross-sectional area of the vapor core $= \pi d_v^2/4$ and r_{hw} is the wick surface pore hydraulic radius $= 1/2N - d_w/2$.

2.4.5 Sonic Limit. In a converging–diverging nozzle, the mass flow rate is constant but the vapor velocity varies due to varying cross-sectional area. Whereas in the case of heat pipes, the area is constant and the vapor velocity varies because of evaporation and condensation along the heat pipe. Decreased condenser temperature results in a decrement in the evaporator temperature; however, the vapor velocity may reach sonic or supersonic values at a particular condenser temperature. Any further reduction in the condenser temperature will not reduce evaporator temperature. This mainly arises during start-up or steady-state operation. The sonic limit is calculated based on the following equation:

$$Q_s = A_v\rho_v h_{fg}[(\gamma_v R_v T_v)/(2(\gamma_v + 1))]^{1/2} \quad (12)$$

where γ_v = specific heat ratio of vapor, $R_v = \overline{R}/\mathrm{M} = 8.314 \times 10^3/18 = 462$ J/Kg k, M is molecular weight of vapor = 18 moles, and $\overline{R}$ is the universal gas constant.

2.4.6 Viscous Limit. The vapor pressure difference between evaporator and condenser will be low at low operating temperatures. This will cause the viscous forces to dominate the pressure gradient. When this happens, the pressure gradients will not be sufficient to generate vapor flow and the vapor will be stagnating. This no-flow or low-flow condition refers to viscous limitation. The viscous limit is calculated based on the following equation:

$$Q_{vi} = d_v^2 h_{fg} A_v\left(\frac{P_v\rho_v}{4(f_v\mathrm{Re}_v)L_e\mu_v}\right) \quad (13)$$

where Re_v = local axial Reynolds number in the vapor.

2.4.7 Uncertainty Analysis of the Measured Parameters.

2.4.7.1 Uncertainty in evaporator and adiabatic section. The uncertainty in the calculated operational limitations depends on the corresponding measured temperature at which they are calculated. This in turn will depend on the accuracy of the thermocouples and the uncertainty in the wattmeter ($\pm 0.5\%$) used to supply the corresponding heat load. It is found from thermocouple calibration that the eight T-type thermocouples used in the present

study has an uncertainty of ±0.5 °C. The uncertainty in heat load is calculated using Eq. (14). It is calculated based on the uncertainties in the applied voltage ∂V and the applied current ∂I to the heater coil. It also includes the uncertainties in the measured length ∂L_E and diameter ∂d_E of the evaporator region over which heater coil is wrapped. The least count of the vernier calipers used to measure this length and diameter is taken as the uncertainty value.

$$\frac{\partial Q}{Q} = \left[\left(\frac{\partial V}{V}\right)^2 + \left(\frac{\partial I}{I}\right)^2 + \left(\frac{\partial L_E}{L_E}\right)^2 + \left(\frac{\partial d_E}{d_E}\right)^2\right]^{1/2}$$

$$\frac{\partial Q}{60} = \left[\left(\frac{0.5}{20}\right)^2 + \left(\frac{0.1}{3}\right)^2 + \left(\frac{0.02}{50}\right)^2 + \left(\frac{0.02}{10}\right)^2\right]^{1/2} \quad (14)$$

$$\partial Q = 2.53 \text{ W}$$

$$\frac{\partial Q}{Q} = \left(\frac{2.53}{60} \times 100\right) = 4.2\%$$

2.4.7.2 Uncertainty in condenser section. The uncertainty in the condenser section based on energy balance principle between the heat absorbed in the evaporator and heat rejected in the condenser. The uncertainty in the coolant flow rate maintained in the condenser is $\pm 0.17 \times 10^{-6}$ m^3/s. The uncertainty in the heat rejected from the condenser is calculated using Eq. (15):

$$\omega = \left[\left(\frac{\partial Q}{\partial m}\omega_m\right)^2 + \left(\frac{\partial Q}{\partial C_p}\omega_{C_p}\right)^2 + \left(\frac{\partial Q}{\partial \Delta T}\omega_{\Delta T}\right)^2\right]^{1/2} \quad (15)$$

The maximum uncertainty in the heat absorbed in the evaporator and heat rejected in the condenser is found to be 3.16%. The average values of uncertainties in the heat load applied in evaporator, adiabatic, and condenser sections based on the applied voltage, current, temperature, and mass flow rate are 3.68%. Therefore, it is found that an uncertainty data of the calculated limitations in the evaporator, adiabatic, and condenser sections are around 4%.

3 Results and Discussion

The experiments are conducted with test section kept in horizontal orientation as shown in Fig. 3. Table 1 shows the mean adiabatic vapor temperatures for which all the limit values are calculated and plotted. The experimental results are compared between water and nanofluid for all the concentrations and the enhancement in various operational limits with respect to water and nanofluid are discussed and presented.

The capillary limit as a function of adiabatic vapor temperature is shown in Fig. 4. It is noted that as the nanoparticle's volume concentration and adiabatic vapor temperature increases, the capillary limit also increases and the maximum increment is found to be 54.20% for 0.009 vol. % concentration when compared with DI water. The surface tension of the working fluid and effective capillary radius of the wick influences the maximum capillary pressure head and acts as the pumping force for the operation of the heat pipe. High surface tension values of working fluid are observed as shown in Table 2 at high nanoparticle concentrations. This increment is directly proportional to the increase in the capillary pressure. Moreover, the increase in the liquid density, latent heat of vaporization, and the surface tension of the working fluid are accountable for the increase in the capillary limit.

Table 1 Operating temperatures of heat pipe test section

Q (W)	Adiabatic vapor temperature (°C) Water	0.003 Vol. %	0.006 Vol. %	0.009 Vol. %	Mean adiabatic vapor temperature (°C)
20	68	53	50	50	55.25
40	76	67	60	57	65
60	87	78	69	67	75.25
80	94	91	79	76	85
100	103	99	91	87	95

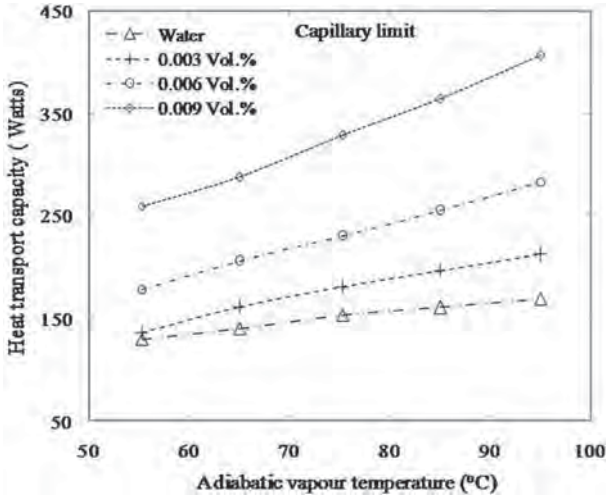

Fig. 4 Capillary limit with respect to adiabatic vapor temperature

The boiling limit as a function of adiabatic vapor temperature is shown in Fig. 5. It is observed that the boiling limit increases with the increase in the volume concentration of the nanoparticles and decreases with the increase in the adiabatic vapor temperature. An enhancement of 87.34% in boiling limit is observed for 0.009 vol. % concentration based heat pipe when compared with DI water. Similarly, for 0.003 vol. % and 0.006 vol. %, a significant enhancement of 53.48% and 77.66% is observed when compared with DI water. The increment in the nanoparticle volume concentration increases the effective thermal conductivity of working fluid, this leads to an enhancement in the effective thermal conductivity of liquid–wick combination (K_{eff}) Also, the surface tension of the nanofluid increases with respect to volume concentration. The other properties, such as vapor density and latent heat of vaporization also influence the boiling limit. The increment in heat load causes an increment in the adiabatic vapor temperature and raises the vapor density. This combined enhancement effect leads to an increment in the boiling limit when using nanofluids and the same decreases with respect to increase in adiabatic vapor temperature. The physical phenomena that lies behind the boiling limit enhancement is that during heat pipe operation the nanoparticles gets deposited on the wall and forms a layer on the heating surface in the evaporator. This layer improves the boiling performance of the working fluid by creating more number of localized spots for bubble formation leading to effective heat transfer by reducing the wall temperature.

The entrainment limit as a function of adiabatic vapor temperature is shown in Fig. 6. It is clearly seen that the entrainment limit increases with the increase in the adiabatic vapor temperature and volume concentration of the nanoparticles. An enhancement of 10.73% in the entrainment limit is observed for 0.009 vol. % concentration of the nanoparticles. The properties that significantly affect the entrainment limit are surface tension of the working fluid, vapor density, and latent heat of vaporization. It is observed that the surface tension values significantly increases by 11.35%, 28.48%, and 52.74% with respect to volume concentration as shown in Table 2 when compared with DI water. This change in the thermophysical properties as a function of operating temperature and concentration enhances the entrainment limit value. The underlying phenomena in the enhancement of entrainment limit is

Table 2 Thermophysical properties of working fluids

	T_v (°C)	P_v (Kg · m^3)	h_{fg} (J/Kg)	σ (N/m)	P_v (Pa)	μ_v (Pa s)	μ_1 (Pa s)	ρ_1 (Kg m^3)
	68	0.18288	2,338,000	0.064838	28599	0.000011195	0.0004152	978.86
	76	0.25184	2,318,100	0.063402	40239	0.000011456	0.0003728	974.22
DI water	87	0.38064	2,290,200	0.061378	62556	0.000011828	0.0003255	967.29
	94	0.48777	2,272,100	0.06006	81541	0.000012065	0.0003006	962.57
	103	0.66056	2,248,500	0.058332	112770	0.000012372	0.0002731	956.18
	53	0.095494	2,374,700	0.081138	14312	0.000010711	0.0005238	1015.12
	67	0.17549	2,340,500	0.079013	27368	0.000011162	0.0004238	1007.95
0.003 Vol. %	78	0.27209	2,313,000	0.077038	43703	0.000011526	0.0003657	1001.53
	91	0.43918	2,279,900	0.074628	72890	0.000011963	0.0003201	993.15
	99	0.57847	2,259,000	0.073104	97852	0.000012235	0.0002866	987.59
	50	0.083147	2,381,900	0.107944	12352	0.000010616	0.0005512	1045.012
	60	0.13043	2,357,700	0.106238	19946	0.000010935	0.0004701	1040.2
0.006 Vol. %	69	0.19052	2,335,500	0.104659	29876	0.000011228	0.0004128	1035.37
	79	0.28271	2,310,500	0.102856	45527	0.000011559	0.0003617	1029.4957
	91	0.43918	2,279,900	0.100628	72890	0.000011963	0.0003133	1021.7723
	50	0.083147	2,381,900	0.150944	12352	0.000010616	0.000552	1073.52
	57	0.11433	2,365,000	0.149755	17336	0.000010838	0.000493	1070.23
0.009 Vol. %	67	0.17549	2,340,500	0.148013	27368	0.000011162	0.0004251	1065.02
	76	0.25184	2,318,100	0.146402	40239	0.000011459	0.0003764	1059.86
	87	0.38064	2,290,200	0.144378	62556	0.000011828	0.0003286	1052.99

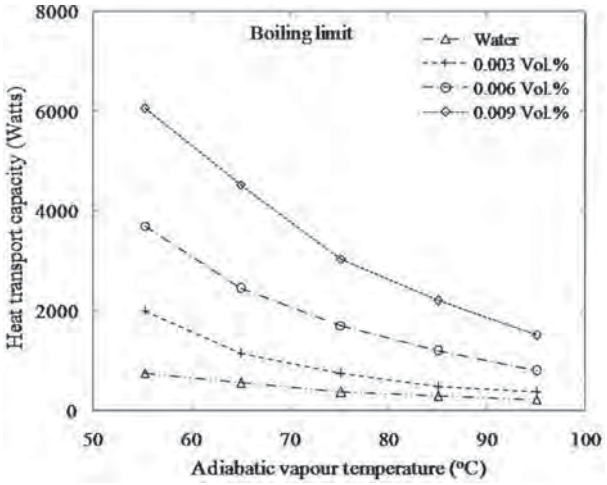

Fig. 5 Boiling limit with respect to adiabatic vapor temperature

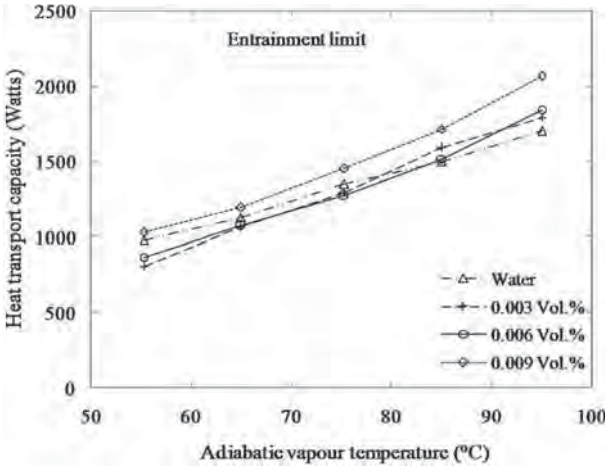

Fig. 6 Entrainment limit with respect to adiabatic vapor temperature

that, as the surface tension of the working fluid increases with respect to concentration the adhesive property between the working fluid and wick also increases and obviously resulting in high velocity vapors at high operating temperatures which cannot entrain or tear the liquid from the wick surface and carry back to the condenser.

The sonic limit with respect to the adiabatic vapor temperature is shown in Fig. 7. The rate of cooling maintained in the condenser is constant for all the heat pipes under various heat loads. Hence, the condenser pressure remains constant. It is observed that the sonic limit is directly proportional to the adiabatic vapor temperature and inversely proportional to the nanoparticle volume concentration in the base fluid. A reduction in sonic limit value by 20.6%, 42.88%, and 49% is observed for 0.003%, 0.006%, and 0.009% volume concentrations of nanofluids when compared with DI water. An increase in the heat load of heat pipe causes a raise in the vapor pressure, vapor density, and adiabatic vapor temperature. As mentioned before, the properties, such as vapor density, adiabatic vapor temperature, and latent heat of vaporization significantly influences the sonic limit. The operating temperatures of heat pipes with nanofluid are less when compared with DI water. This reduction in adiabatic vapor temperature reduces the vapor density by 9%, 19%, and 26%, respectively, for 0.003%,

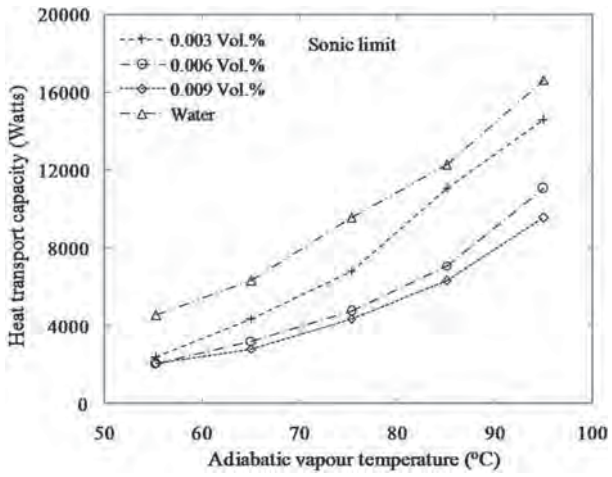

Fig. 7 Sonic limit with respect to adiabatic vapor temperature

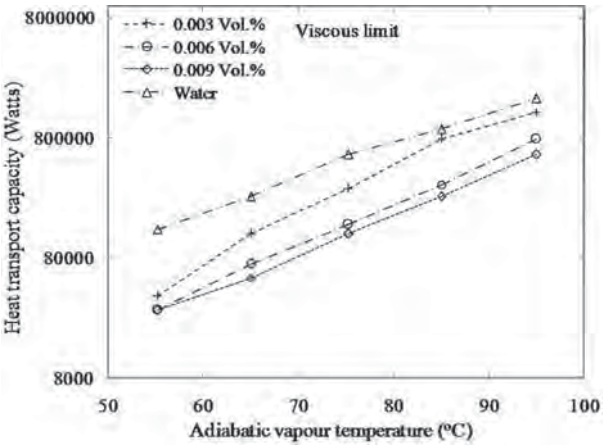

Fig. 8 The logarithmic plot of viscous limits with respect to adiabatic vapor temperature

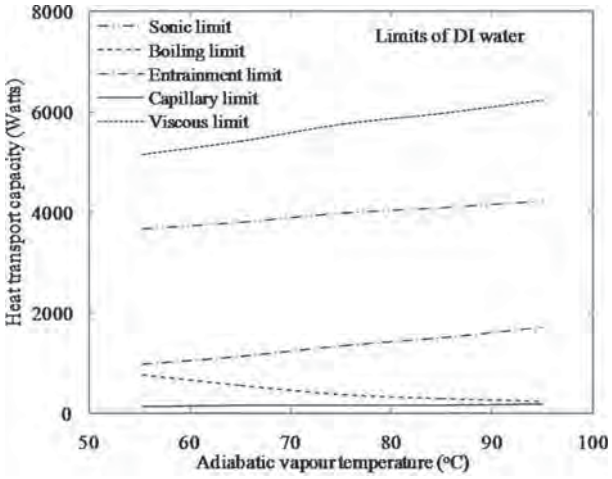

Fig. 10 Operating limits of DI water-based heat pipe against adiabatic vapor temperature

0.006%, and 0.009% volume concentrations when compared with DI water which lead to the reduction in the sonic limit. The influence of latent heat of vaporization on sonic limit is less when compared with vapor density and operating temperature.

The logarithmic plot of viscous limit as a function of adiabatic vapor temperature is shown in Fig. 8. It is observed that the viscous limit gradually increases with respect to adiabatic vapor temperature and reduces as concentration level of nanoparticles in base fluid increases. The key properties that influence the viscous limit are vapor pressure, vapor density, latent heat of vaporization, and dynamic viscosity of vapor. As mentioned earlier, the use of nanofluids reduces the adiabatic vapor temperature of heat pipe which in turn drastically reduces the vapor pressure and vapor density and conversely increases the latent heat of vaporization of working fluid. However, this increase in latent heat is very small when compared with the influence of vapor pressure and vapor density on viscous limit. Hence, viscous limit decreases with the use of nanofluids when compared with DI water. It is noted that the viscous limit decreases by 29.65%, 63%, and 71.05%, respectively, for 0.003%, 0.006%, and 0.009% volume concentration of nanoparticles in base fluid when compared with DI water. The present values of viscous limit are very high when compared with other operational limits for constant adiabatic vapor temperature. A similar trend and high values in the viscous limits have also been observed by other researchers [4,5] which state that the viscous limit will not influence the performance of heat pipes.

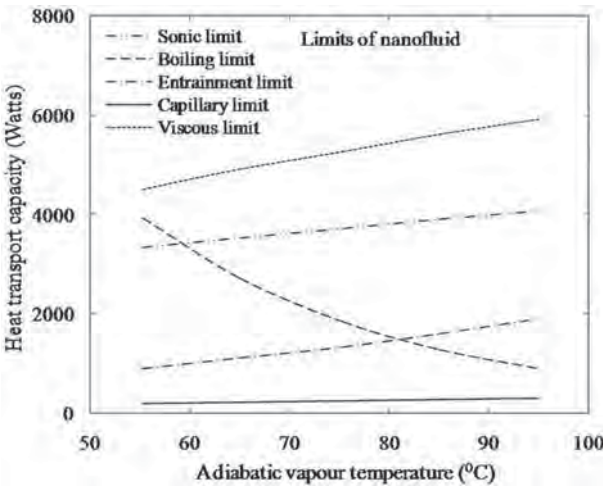

Fig. 9 Operating limits of nanofluid based heat pipes against adiabatic vapor temperature

The various operational limits as a function of mean adiabatic vapor temperature for nanofluid (by taking the average values of all the concentrations of silver nanoparticles) and for DI water are plotted and shown in Figs. 9 and 10. The plot represents the logarithmic values of sonic and viscous limits along with other operating limits with respect to the experimentally recorded mean adiabatic vapor temperatures. It is observed that the viscous and sonic limit values obtained are found to be very high when compared with that of the other limits. To incorporate all the operating limits in a single plot, the very high values of viscous and sonic limits are taken as the logarithmic values multiplied with 1000 as common multiplier. Bejan and Kraus [36] and Ahmad and Rajab [37] reported that the heat input to the heat pipe can be limited to a certain value beyond which heat pipe fails to operate or works with very low performance. It is suggested that the capillary, boiling, and entrainment limits are the failure limitations of heat pipes which are characterized by insufficient liquid flow to the evaporator for a given heat input and resulting in dry-out of the evaporator wick structure. The other two limits, such as sonic and viscous limits are termed as the nonfailure limits of heat pipe. It is observed from the present study that the failure limits (boiling, entrainment and capillary limits) of heat pipe are found to be higher and the nonfailure limits (sonic and viscous limits) are lower for nanofluids when compared with that of DI water. It is also seen that the capillary limit is an essential parameter that primarily influences the heat pipes performance. It is also reported that the higher values of nonfailure limits do not affect the heat pipe performance and the same trend is also observed by researchers [4,5]. The main phenomenon that deals with the enhancement in heat pipe performance with the use of nanofluids is the increase in the number of localized spots by the deposited nanoparticles layer in the evaporator surface. This localized spots effectively increase the boiling of the working fluid by increasing the bubble formation and growth. It is also observed that the boiling limit values of nanofluid gradually decreases with increment in adiabatic vapor temperature, since gradual increase in heat loads causes the boiling phenomena to come closer to nucleate boiling. Addition of nanoparticles to the base fluid also increases the adhesiveness of working fluid toward wick structure due to increased surface tension. This prevents the liquid droplets to be carried back to condenser by the high velocity vapors and hence an increment in the entrainment limit is recorded. This high surface tension values and adhesiveness also increases the capillary pressure head and results in an increment in the capillary limit. It is observed that the average capillary limit value of all the

concentrations increases by 38.63% when compared with DI water and this increases the operating range of heat pipes employed with nanofluids.

4 Conclusion

The present study shows the variation in the operational limitations of heat pipes using silver-water nanofluid. It is observed that the use of silver nanoparticles with volume concentrations of 0.003%, 0.006%, and 0.009% gives the reduction in the adiabatic vapor temperature for a given input heat load of 60 W. This reduction in operating temperatures enhances the failure limitations (capillary, boiling, and entrainment limits) of heat pipes by 54%, 87.34%, and 10.73% when compared with DI water. The enhancement in terms of failure limits of heat pipes with the use of nanofluids improves the heat pipes performance and operating range by providing sufficient amount of working fluid to the evaporator region and preventing the evaporator dry-out even beyond the optimum heat transport capability observed in the case of DI water-based heat pipe. It is also observed that the capillary limit is the lowest value among the failure and nonfailure limitations of heat pipe. The heat pipe fails to operate beyond this limit due to the incapability of the wick structure in providing sufficient amount of working fluid to the evaporator. The use of silver nanoparticles with 0.009 vol. % concentration increases the capillary limit value of heat pipe by 54% when compared with DI water.

Acknowledgment

The authors would like to thank Mr. Seelan, Mr. P. Augustine, and Mr. Jeyakumar of Karunya University for helping in the fabrication of the experimental test facility. The third author thanks the Thailand Research Fund for the support.

Nomenclature

A = cross-sectional area (m^2)
C = constant depending on Mach number (value taken as 1)
c_p = specific heat capacity (J kg K)
d = diameter (m)
f = drag coefficient
g = acceleration due to gravity (m/s^2)
h = latent heat (J/kg)
k = thermal conductivity (W/m K)
K = wick permeability (m^2)
L = length (m)
M = molecular weight of vapor (moles)
N = wick screen mesh number (m^{-1})
P = pressure (Pa)
Q = heat load (W)
r = radius (m)
Re = Reynolds number
R = specific gas constant (J/kg K)
$\overline{R}$ = universal gas constant (J/kg mol K)
S = wick crimping factor
T = temperature (K)

Greek Symbols

Δ = difference
γ = specific heat ratio of vapors
σ = surface tension (N/m)
$\in$ = wick porosity
φ = volume fraction
μ = dynamic viscosity (kg/m s)
ρ = density (kg/m^3)
θ = inclination angle (deg)
λ = latent heat of vaporization (J/kg K)
ω = uncertainty

Subscripts

a = adiabatic
b = basefluid
bo = boiling
c = condenser, capillary
cm = maximum capillary
e = evaporator
en = entrainment
eff = effective
fg = vaporization
g = gravity
hw = wick surface pore hydraulic
i = inner
l = liquid
n = nucleation
nf = nanofluid
p = particle
ph = phase transition
so = sonic
v = vapor
vi = viscous
w = wick, wire

References

[1] Choi, S. U. S., and Eastman, J. A., 1995, "Enhancing Thermal Conductivity of Fluids With Nanoparticles," Proceedings of the ASME International Mechanical Engineering Congress and Exhibition, San Francisco, CA, pp. 99–105.
[2] Shafai, M., Bianco, V., Vafai, K., and Manca, O., 2010, "An Investigation of the Thermal Performance of Cylindrical Heat Pipes Using Nanofluids," Int. J. Heat Mass Transfer, **53**, pp. 376–383.
[3] Liu, Z. H., Li, Y., and Bao, R., 2011, "Compositive Effect of Nanoparticle Parameter on Thermal Performance of Cylindrical Micro-Grooved Heat Pipe Using Nanofluids," Int. J. Therm. Sci., **50**, pp. 558–568.
[4] Nemec, P., Caja, A., and Malcho, M., 2011, "Mathematical Model for Heat Transfer Limitations of Heat Pipe," Math. Comput. Modell., 57, pp. 126–136.
[5] Nemec, P., and Huzvar, J., 2007, "Mathematical Calculation of Total Heat Power of the Sodium Heat Pipe," Institute of Inorganic Chemistry, Slovak Academy of Science, Article for Solution to Project APVV-0517-07.
[6] Naik, R., Varadarajan, V., and Pundarika, G., 2011, "Design, Fabrication and Performance Evaluation of Axially Grooved Wick Assisted Heat Pipe," Int. J. Emerg. Trends Eng. Dev., **2**(1), pp. 25–39.
[7] Faghri, A., 1995, *Heat Pipe Science and Technology*, Taylor and Francis Publication, Washington, DC.
[8] Peterson, G. P., 1994, *An Introduction to Heat Pipes, Modeling, Testing and Applications*, Wiley-Interscience Publication, John Wiley and Sons, New York.
[9] Thuchayapong, N., Nakanob, A., Sakulchangsatjataia, P., and Terdtoona, P., 2012, "Effect of Capillary Pressure on Performance of a Heat Pipe: Numerical Approach With FEM," Appl. Therm. Eng., 32, pp. 93–99.
[10] Riehl, R. R., and Santos, N. D., 2012, "Water-Copper Nanofluid Application in an Open Loop Pulsating Heat Pipe," Appl. Therm. Eng., **42**, pp. 6–10.
[11] Chiang, Y. C., Chieh, J.-J., and Ho, C. C., 2012, "The Magnetic-Nanofluid Heat Pipe With Superior Thermal Properties Through Magnetic Enhancement," Nanoscale Res. Lett., **7**, pp. 322–328.
[12] Liu, Z. H., and Li, Y. Y., 2012, "A New Frontier of Nanofluid Research—Application of Nanofluids in Heat Pipes," Int. J. Heat Mass Transfer, **55**, pp. 6786–6797.
[13] Putra, N., Septiadi, W. N., Rahman, H., and Irwansyah, R., 2012, "Thermal Performance of Screen Mesh Wick Heat Pipes With Nanofluids," Exp. Therm. Fluid Sci., **40**, pp. 10–17.
[14] Hajian, R., Layeghi, M., and Abbaspour Sani, K., 2012, "Experimental Study of Nanofluid Effects on the Thermal Performance With Response Time of Heat Pipe," Energy Convers. Manage., **56**, pp. 63–68.
[15] Alizad, K., Vafai, K., and Shafahi, M., 2012, "Thermal Performance and Operational Attributes of the Startup Characteristics of Flat-Shaped Heat Pipes Using Nanofluids," Int. J. Heat Mass Transfer, **55**(1–3), pp. 140–155.
[16] Tsai, T. H., Chien, H. T., and Chen, P. H., 2011, "Improvement on Thermal Performance of a Disk-Shaped Miniature Heat Pipe With Nanofluid," Nanoscale Res. Lett., **6**, pp. 590–596.
[17] Putra, N., Yanuar, Iskandar, F. N., 2011, "Application of Nanofluids to a Heat Pipe Liquid-Block and the Thermoelectric Cooling of Electronic Equipment," Exp. Therm. Fluid Sci., **35**(7), pp. 1274–1281.
[18] Jamshidi, H., Arabnejad, S., Shafii, M. B., Saboohi, Y., 2011, "Thermal Characteristics of Closed Loop Pulsating Heat Pipe With Nanofluids," J. Enhanced Heat Transfer, **18**(3), pp. 221–237.
[19] Ji, Y., Ma, H., Su, F., and Wang, G., 2011, "Particle Size Effect on Heat Transfer Performance in an Oscillating Heat Pipe," Exp. Therm. Fluid Sci., **35**(4), pp. 724–727.
[20] Li, Q. M., Zou, J., Yang, Z., Duan, Y.-Y., and Wang, B.-X., 2011, "Visualization of Two-Phase Flows in Nanofluid Oscillating Heat Pipes," ASME J. Heat Transfer, **133**(5), p. 052901.

[21] Huminic, G., Huminic, A., Morjan, I., and Dumitrache, F., 2011, "Experimental Study of the Thermal Performance of Thermosyphon Heat Pipe Using Iron Oxide Nanoparticles," Int. J. Heat Mass Transfer, **54**(1–3), pp. 656–661.
[22] Liu, Z., and Zhu, Q., 2011, "Application of Aqueous Nanofluids in a Horizontal Mesh Heat Pipe," Energy Convers. Manage., **52**(1), pp. 292–300.
[23] Wang, G. S., Song, B., and Liu, Z. H., 2012, "Operation Characteristics of Cylindrical Miniature Grooved Heat Pipe Using Aqueous CuO Nanofluids," Exp. Therm. Fluid Sci., **34**(8), pp. 1415–1421.
[24] Li, Y., Lv, L., and Liu, Z., 2010, "Influence of Nanofluids on the Operation Characteristics of Small Capillary Pumped Loop," Energy Convers. Manage., **51**(11), pp. 2312–2320.
[25] Liu, Z. H., Li, Y. Y., and Bao, R., 2010, "Thermal Performance of Inclined Grooved Heat Pipes Using Nanofluids," Int. J. Therm. Sci., **49**(9), pp. 1680–1687.
[26] Shafahi, M., Bianco, V., Vafai, K., and Manca, O., 2010, "Thermal Performance of Flat-Shaped Heat Pipes Using Nanofluids," Int. J. Heat Mass Transfer, **53**(7–8), pp. 1438–1445.
[27] Qu, J., Wu, H. Y., and Cheng, P., 2010, "Thermal Performance of an Oscillating Heat Pipe With Al_2O_3-Water Nanofluids," Int. Commun. Heat Mass Transfer, **37**(2), pp. 111–115.
[28] Kang, S. W., Wei, W. C., Tsai, S. H., and Huang, C. C., 2009, "Experimental Investigation of Nanofluids on Sintered Heat Pipe Thermal Performance," Appl. Therm. Eng., **29**(5–6), pp. 973–979.
[29] Yang, X. F., Liu, Z. H., and Zhao, J., 2008, "Heat Transfer Performance of a Horizontal Micro-Grooved Heat Pipe Using CuO Nanofluid," J. Micromech. Microeng. **18**(3), p. 035038.
[30] Liu, Z. H., Xiong, J. G., and Bao, R., 2007, "Boiling Heat Transfer Characteristics of Nanofluids in a Flat Heat Pipe Evaporator With Micro-Grooved Heating Surface," Int. J. Multiphase Flow, **33**(12), pp. 1284–1295.
[31] Ma, H. B., Wilson, C., Borgmeyer, B., Park, K., Yu, Q., Choi, S. U. S., and Tirumala, M., 2006, "Effect of Nanofluid on the Heat Transport Capability in an Oscillating Heat Pipe," Appl. Phys. Lett., **88**(14), p. 143116.
[32] Tsai, C. Y., Chien, H. T., Ding, P. P., Chan, B., Luh, T. Y., and Chen, P. H., 2004, "Effect of Structural Character of Gold Nanoparticles in Nanofluid on Heat Pipe Thermal Performance," Mater. Lett., **58**(9), pp. 1461–1465.
[33] Pak, B. C., and Cho, I. Y., 1998, "Hydrodynamic and Heat Transfer Study of Dispersed Fluids With Sub-Micron Metallic Oxide Particles," Exp. Heat Transfer, **11**, pp. 151–170.
[34] Xuan, Y., and Roetzel, W., 2000, "Conceptions for Heat Transfer Correlation of Nanofluids," Int. J. Heat Mass Transfer, **43**, pp. 3701–3707.
[35] Godson, L., Raja, B., Lal, M. D., Wongwises, S., 2010, "Experimental Investigation of Thermal Conductivity and Viscosity of Silver-Deionized Water Nanofluid," Exp. Heat Transfer, **23**(4), pp. 317–332.
[36] Bejan, A., and Kraus, A. D., 2003, *Heat Transfer Handbook*, John Wiley & Sons, Inc., Hoboken, NJ.
[37] Ahmad, H., and Rajab, H., 2010, "An Experimental Study of Parameters Affecting a Heat Pipe Performance," Al-Rafidain Eng. J., **18**(3), pp. 97–116.

JOURNAL OF THERMOPHYSICS AND HEAT TRANSFER
Vol. 27, No. 4, October–December 2013

Nanofluids Flow Between Two Rotating Cylinders: Effects of Thermophoresis and Brownian Motion

Meisam Habibi Matin*
Kermanshah University of Technology, 67178-63766 Kermanshah, Iran
Omid Mahian†
Islamic Azad University, 91735 Mashhad, Iran
and
Somchai Wongwises‡
King Mongkut's University of Technology Thonburi, Bangkok 10140, Thailand

DOI: 10.2514/1.T4122

In this paper, the effects of thermophoresis and Brownian motion on the heat transfer of nanofluids between two rotating cylinders are investigated. The flow between the cylinders is considered laminar and steady, whereas the walls of the cylinders are kept at different constant temperatures. The governing equations, including momentum, energy, and volume fraction in cylindrical coordinates, are simplified and solved. An exact solution for the velocity distribution is presented and the homotopy perturbation method is employed to obtain the temperature field. The results obtained from the homotopy perturbation method are validated with the results of a numerical solution. The effects of various quantities of the Eckert and Prandtl numbers, the rotational velocity ratio of the cylinders, Brownian motion, and thermophoresis parameters on the temperature field, and Nusselt number in the annulus are examined.

I. Introduction

FLUID flow and heat transfer between two concentric rotating cylinders is a classical problem in fluids engineering. It has significant applications such as electrical motors and generators, mixing equipment, journal bearings, and swirl nozzles [1,2].

Water, ethylene glycol, and oil as the traditional fluids in thermal engineering systems have low thermal conductivity and hence, the heat transfer enhancement is limited. An innovative technique to enhance the heat transfer is the use of a nanofluid, which is a mixture of common liquids and very fine particles (1–100 nm), introduced by Choi [3].

Currently, nanofluids are applied in various thermal systems to enhance the heat transfer rate and thermal efficiency. Nanofluids can be used in different fields of thermal engineering such as solar energy [4], heat exchangers, nuclear reactors, and cooling of electronic devices [5]. In addition, the readers can refer to the most recent theoretical and experimental works that have been done on nanofluids in different geometries and conditions [6–22].

Different factors, such as the thermal conductivity increase, particle migration, dispersion and chaotic movement of nanoparticles, Brownian motion, and thermophoresis, could be effective in the enhancement of the heat transfer rate where the nanofluid is used as a working fluid. The most obvious factor is the increase of thermal conductivity of base fluid due to adding nanoparticles that have higher thermal conductivity in comparison with the base fluid. Two other main factors are Brownian motion and thermophoresis effects.

Here, a brief review of the former works related to the nanofluid flow in a cylindrical annulus in both natural and forced convection cases is performed. Abu-Nada et al. [23] investigated the natural convection due to four different nanoparticles including Cu, Ag, Al_2O_3 and TiO_2 suspended in pure water in a horizontal annulus. They presented the results for different values of Rayleigh number, gap magnitude, and volume fraction. Abu-Nada [24] studied the effects of uncertainties in thermophysics models on the predicting of heat transfer rate due to free convection of Al_2O_3/water nanofluid in an annulus. He used four sets of models to calculate the thermal conductivity and viscosity. These models include temperature-dependent and temperature-independent relations. His results show that opposite predictions of average Nusselt number trend may be obtained by using different models. Later on, Abu-Nada [25] developed his former work [24] for CuO/water nanofluid. Abouali and Falahatpisheh [26] presented a numerical study of natural convection of Al_2O_3/water nanofluid between two vertical cylinders where the bottom and top ends are insulated. Izadi et al. [27] investigated the forced convection of Al_2O_3/water nanofluid between two cylindrical tubes where the flow is developing. Shahi et al. [28] numerically studied the natural convection of Cu/water nanofluid in an annulus at different angles with respect to the horizontal surface where the ends of the annulus are adiabatic. Moghari et al. [29] examined the mixed convection of Al_2O_3/water nanofluid in a horizontal iso-flux annulus by considering the effects of Brownian motion of nanoparticles. Cianfrini et al. [30] theoretically investigated the natural convection heat transfer due to a nanofluid between two long horizontal cylinders where the wall of the annulus is subject to a constant wall temperature. They found that there is an optimal volume fraction of nanoparticles for which the heat transfer rate is maximized. Soleimani et al. [31] numerically solved the natural convection in a semi-annulus enclosure where the working fluid is Cu/water nanofluid. They obtained the optimal angle of the arc in which the heat transfer reaches maximum. Sheikhzadeh et al. [32] performed a numerical study of natural convection of Cu/water nanofluid between two concentric cylinders where four fins are mounted on the wall of the inner cylinder. Later on, Sheikhzadeh et al. [33] investigated the effects of different parameters including the number of fins installed on the inner cylinder, fin length, and the volume fraction of nanoparticles. Nasrin et al. [34] investigated the effects of viscosity variation of Al_2O_3/water nanofluid on natural convection in an annulus. They assumed that the nanofluid confined in the annulus produces heat internally. In another work, Parvin et al. [35] focused on natural convection of Al_2O_3/water nanofluid in the annulus where two models are used to calculate the thermal conductivity. They assumed that the inner cylinder is under constant heat flux while the outer one is kept at constant temperature. Ashorynejad et al. [36] used the Lattice Boltzmann method to study

Received 31 January 2013; revision received 7 April 2013; accepted for publication 25 April 2013; published online 24 June 2013.

*Department of Mechanical Engineering; m.habibi@aut.ac.ir (Corresponding Author).
†Ph.D. Student, Young Researchers Club and Elites.
‡Faculty of Engineering, Department of Mechanical Engineering, Bangmod; currently Professor, Fluid Mechanics, Thermal Engineering and Multiphase Flow Research Laboratory (FUTURE).

the effects of magnetic field on natural convection of Ag/water nanofluid between two horizontal cylinders. The previously mentioned works were concerning the first law of thermodynamics analysis. Some works performed by Mahian et al. [37–39] on the entropy generation between two rotating cylinders used nanofluids in different conditions.

A review of the literature shows that there is no reported research on Brownian motion and thermophoresis effects of a nanofluid on heat transfer between two rotating cylinders. Buongiorno [40] proposed a mathematical nanofluid model by taking into account the Brownian motion and thermophoresis effects on flow and heat transfer fields. In this model, an additional equation for nanoparticle volume fraction is introduced so that the volume fraction distribution could be obtained.

This paper aims to present analytical and numerical studies of the Brownian motion and thermophoresis effects of a nanofluid on heat transfer between two isothermal cylinders. The mathematical model proposed by Buongiorno [40] is used to take into consideration the Brownian motion and thermophoresis effects. An exact solution for the velocity distribution is presented. Energy and volume fraction equations are naturally coupled. These equations are decoupled after some manipulations and it leads to convert the energy equation to an ordinary differential equation. The homotopy perturbation method (HPM) is used to solve the energy equation and consequently the temperature field is obtained. The results obtained from the HPM are validated with the results of a numerical solution.

II. Problem Formulation

Consider the steady, laminar, and fully developed flow and heat transfer of a nanofluid between two rotating cylinders. The schematic of the problem is shown in Fig. 1. The inner and outer cylinders have radii of r_i and r_o, respectively, whereas the inner and outer walls of the annulus are kept at temperatures of T_i and T_o. The inner and outer cylinders can rotate with constant angular velocities ω_i and ω_o, respectively. Assuming a two-dimensional problem that corresponds to no relative axial motion between the cylinders and ignoring the radial velocity component compared to the tangential u_θ, the momentum equation reads

$$\frac{\partial^2 u_\theta}{\partial r^2}+\frac{1}{r}\frac{\partial u_\theta}{\partial r}-\frac{1}{r^2}u_\theta=0 \tag{1}$$

Also, by neglecting the convection term and taking into account the viscous dissipation term, the energy equation becomes

$$\begin{aligned}&\frac{\alpha}{r}\frac{\partial}{\partial r}\left(r\frac{\partial T}{\partial r}\right)+\frac{(\rho C_P)_S}{(\rho C_P)_f}\\&\quad\times\left[D_B\left(\frac{\partial\phi}{\partial r}+\frac{\phi}{r}\right)\left(\frac{\partial T}{\partial r}+\frac{T}{r}\right)+\frac{D_T}{T_C}\left(\frac{\partial T}{\partial r}+\frac{T}{r}\right)^2\right]\\&\quad+\mu\left(\frac{\partial u_\theta}{\partial r}-\frac{u_\theta}{r}\right)^2=0\end{aligned} \tag{2}$$

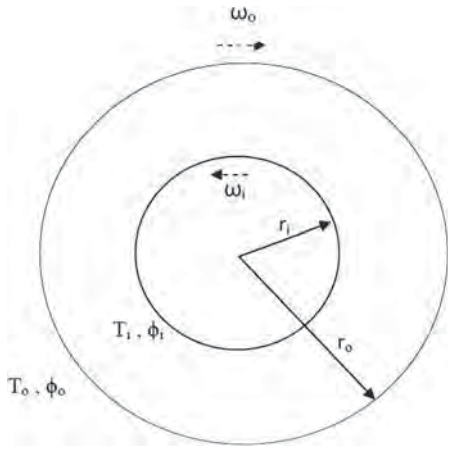

Fig. 1 Schematic of the problem and boundary conditions.

The equation of nanoparticle volume fraction can be written as

$$D_B\left(\frac{\partial\phi}{\partial r}+\frac{\phi}{r}\right)+\frac{D_T}{T_C}\left(\frac{\partial T}{\partial r}+\frac{T}{r}\right)=\xi \tag{3}$$

In the preceding relations, T and ϕ are the temperature and nanoparticles volume fraction. μ, α, and k are the dynamic viscosity, thermal diffusion coefficient, and the thermal conductivity of the base fluid, respectively. Here, D_B and D_T are Brownian diffusion coefficient and thermophoresis diffusion coefficient, respectively. Here, ρ and C_p are the density and heat capacity where the subscripts of S and f represents the solid and fluid. In the volume fraction equation, ξ is a constant. The following boundary conditions are used for the inner and outer cylinders

$$\begin{aligned}&r=r_i\rightarrow u_\theta=r_i\omega_i, \qquad T=T_i=T_h, \qquad \phi=\phi_i\\&r=r_O\rightarrow u_\theta=r_O\omega_O, \qquad T=T_O=T_C, \qquad \phi=\phi_O\end{aligned} \tag{4}$$

The following dimensionless parameters are defined

$$\begin{aligned}&\lambda=\frac{\omega_i}{\omega_o}, \quad \Pi=\frac{r_i}{r_o}, \quad Pr=\frac{\nu_f}{\alpha_f}, \quad Ec=\frac{r_o^2\omega_o^2}{C_P\Delta T}, \quad R=\frac{r}{r_o},\\&U=\frac{u_\theta}{r_o\omega_o}, \quad \theta=\frac{T-T_C}{T_h-T_C}, \Phi=\frac{\phi-\phi_o}{\phi_i-\phi_o}, \quad \theta_r=\frac{T_o}{\Delta T},\\&\phi_r=\frac{\phi_o}{\Delta\phi}, \quad Nb=\frac{(\rho C_P)_S}{(\rho C_P)_f}\frac{D_B\Delta\phi}{\nu_f}, \quad Nt=\frac{(\rho C_P)_S}{(\rho C_P)_f}\frac{D_T\Delta T}{\nu_f T_C}\end{aligned} \tag{5}$$

In the preceding relations Pr, Nb, Nt, and Ec are the Prandtl number, the Brownian motion parameter, the thermophoresis parameter, and the Eckert number, respectively. Also, U, Φ, θ, θ_r, and ϕ_r are dimensionless velocity, dimensionless volume fraction, dimensionless temperature, temperature ratio, and volume fraction ratio, respectively. Using the dimensionless parameters defined in Eq. (5), the dimensionless forms of governing equations can be written as

$$\frac{\partial^2 U}{\partial R^2}+\frac{1}{R}\frac{\partial U}{\partial R}-\frac{U}{R^2}=0 \tag{6}$$

$$\begin{aligned}&\frac{1}{R}\frac{\partial}{\partial R}\left(R\frac{\partial\theta}{\partial R}\right)+NbPr\left(\frac{\partial\Phi}{\partial R}+\frac{\Phi+\Phi_r}{R}\right)\left(\frac{\partial\theta}{\partial R}+\frac{\theta+\theta_r}{R}\right)\\&\quad+NtPr\left(\frac{\partial\theta}{\partial R}+\frac{\theta+\theta_r}{R}\right)^2+EcPr\left(\frac{\partial U}{\partial R}-\frac{U}{R}\right)^2=0\end{aligned} \tag{7}$$

$$Nb\left(\frac{\partial\Phi}{\partial R}+\frac{\Phi+\Phi_r}{R}\right)+Nt\left(\frac{\partial\theta}{\partial R}+\frac{\theta+\theta_r}{R}\right)=\beta_1 \tag{8}$$

Subject to the following dimensionless boundary conditions

$$\begin{aligned}&R=\Pi\rightarrow U=\Pi\lambda, \qquad \theta=1, \qquad \Phi=1\\&R=1\rightarrow U=1, \qquad \theta=0, \qquad \Phi=0\end{aligned} \tag{9}$$

III. Solution to the Problem

A. Velocity Distribution

The exact solution of the momentum equation, Eq. (6), is obtained as

$$U=C_1R+\frac{C_2}{R} \tag{10}$$

where

$$C_1=\frac{1-\Pi^2\lambda}{1-\Pi^2}, \qquad C_2=\frac{\Pi^2(\lambda-1)}{1-\Pi^2} \tag{11}$$

By using the solution of the velocity, the skin friction coefficient on the inner cylinder can be expressed as

$$f_i = \frac{1}{Re}\frac{\partial U}{\partial R}\bigg|_{R=\Pi}$$

in which

$$Re = \frac{\rho_f r_0^2 \omega_0}{\mu_f}$$

is the rotational Reynolds number.

The energy and volume fraction equations, Eqs. (7) and (8), are nonlinearly coupled. Integrating from the volume fraction equation, Eq. (8), and substituting the boundary conditions for dimensionless temperature and volume fraction gives

$$Nb(\Phi + \Phi_r) + Nt(\theta + \theta_r) = \frac{\beta_1}{2}R + \frac{\beta_2}{R} \tag{12}$$

where

$$\beta_1 = 2\frac{Nb + Nt + Nb\Phi_r + Nt\theta_r - \frac{1}{\Pi}(Nb\Phi_r + Nt\theta_r)}{\Pi - \frac{1}{\Pi}}$$
$$\beta_2 = Nb\Phi_r + Nt\theta_r - \frac{\beta_1}{2} \tag{13}$$

The approximation for the dimensionless temperature θ in terms of the power series parameter p is written as

$$\theta = \theta_0 + p\theta_1 + p^2\theta_2 + p^3\theta_3 + \ldots = \sum_{i=0}^{n} p^i\theta_i \tag{15}$$

Substituting Eq. (15) into Eq. (14a) and after manipulations, a set of recursive ordinary differential equations, along with their boundary conditions, are obtained and solved. To save space, only three terms of the homotopy series are presented. The calculations are made by the MAPLE software for the dimensionless temperature (for $\Pi = 0.5$)

$$\theta_0 = -2R + 2 \tag{16}$$

$$\theta_1 = 2bR^2 + (2\ln R - 2b\ln R - 3b - e\ln R - d - 2\ln 2 + 2b\ln 2 + e\ln 2)R - e\ln 2 + \frac{7}{6}d + 2\ln 2 - 2b\ln 2 + b - \frac{1}{6}\frac{d}{R^2} \tag{17}$$

$$\theta_2 = -R^3b^2 + (eb\ln R + b^2 - eb\ln 2 + bd - 2b^2\ln 2 + 2b\ln 2 - 2b\ln R - be + 2b^2\ln R)R^2 + \begin{pmatrix} -\frac{\mathrm{d}}{3} - 5b\ln 2 + 5(\ln 2)^2 b + \frac{3}{2}(\ln 2)^2 e + 3b^2\ln 2 - \mathrm{d}\ln 2 + \frac{3}{2}be - \frac{5}{3}bd + \frac{1}{4}b^2 + \frac{7}{6}bd\ln 2 \\ -(\ln 2)^2 eb - 2(\ln 2)^2 b^2 - 3(\ln 2)^2 + eb\ln 2\ln R + eb\ln 2 - (\ln R)^2 - e\ln 2\ln R + 2b^2\ln 2\ln R \\ -4b\ln 2\ln R - \frac{7}{6}bd\ln R - b^2\ln R + 3b\ln R + \mathrm{d}\ln R + b(\ln R)^2 + \frac{1}{2}e(\ln R)^2 + 2\ln 2\ln R \end{pmatrix} R - b^2\ln 2 + 2b^2(\ln 2)^2 + \frac{7}{18}\mathrm{d} - \frac{1}{4}b^2 - \frac{1}{2}be + \frac{3}{4}bd + d\ln 2 - 5b(\ln 2)^2 + 3b\ln 2 + 3(\ln 2)^2 + eb(\ln 2)^2 - \frac{3}{2}e(\ln 2)^2 - \frac{7}{6}bd\ln 2 - \frac{1}{12}\frac{bd}{R} - \frac{1}{18}\frac{d}{R^2} \tag{18}$$

Eliminating the dimensionless volume fraction parameter Φ from the energy equation by using Eq. (12), one reaches the following ordinary differential equation

$$\frac{\partial^2\theta}{\partial R^2} + \left(\frac{1}{R} + \beta_1 Pr\right)\frac{\partial\theta}{\partial R} + \frac{\beta_1 Pr}{R}(\theta + \theta_r) + \frac{4EcPr\Lambda^2}{R^4} = 0 \tag{14}$$

The preceding equation should be solved to obtain the temperature field and consequently the Nusselt number. Here, Eq. (14) is solved both analytically and numerically, and the results of both solutions are compared. A semi-analytical solution is carried out to obtain a parametric correlation for temperature distribution. In the present study, HPM is used as a semi-analytic method.

B. Thermal Field

1. *Homotopy Perturbation Solution*

We are now ready to apply the HPM to solve the ordinary differential equation (14) with its boundary conditions, as defined in Eq. (9). First, we construct a homotopy for Eq. (14) as follows

$$(1-p)\left(\frac{\mathrm{d}^2\theta}{\mathrm{d}R^2} - \frac{\mathrm{d}^2\theta_0}{\mathrm{d}R^2}\right) + p\left[\frac{\mathrm{d}^2\theta}{\mathrm{d}R^2} + \left(\frac{1}{R} + \beta_1 Pr\right)\frac{\mathrm{d}\theta}{\mathrm{d}R} + \frac{\beta_1 Pr}{R}(\theta + \theta_r) + \frac{4EcPr\Lambda^2}{R^4}\right] = 0 \tag{14a}$$

In the preceding relations parameters b, e, d, and Λ are

$$b = -\frac{4}{3}Pr(Nb + Nt - Nb\Phi_r - Nt\Theta_r)$$
$$e = b\theta_r$$
$$d = 4EcPr\Lambda^2$$
$$\Lambda = \frac{\lambda}{3} - \frac{1}{3} \tag{19}$$

For more details on the homotopy perturbation method, the readers can refer to [41–44].

2. *Numerical Solution*

Equation (14) is solved using the finite difference method, and the obtained results are compared with the results of HPM. It should be mentioned that the HPM solution is valid in a limited range of the key parameters of the problem, but this method is presented here to give a parametric relation that can be useful. The range of parameters for which the HPM provides acceptable results is as follows

$$Nb < 6, \qquad Nt < 2, \qquad \theta_r < 10, \qquad \Phi_r < 3,$$
$$Ec < 0.5, \qquad Pr < 10, \qquad -20 < \lambda < 20$$

A comparison between the results obtained from the HPM (up to four terms) and numerical solutions is presented in Table 1. It is seen that for the third and fourth terms of the series, the numerical and analytical results are in good agreement.

Table 1 Comparison between numerical and analytical results for $Nb = 3$, $Nt = 0.5$, $\theta_r = 4$, $\Phi_r = 0.5$, $Ec = 0.1$, $Pr = 2$, $\lambda = 7$, and $\Pi = 0.5$

R	Numerical	HPM (4 terms)	HPM (3 terms)	HPM (2 terms)	HPM (1 term)
0.5	1.0	1.0	1.0	1.0	1.0
0.6	1.083442	1.083638	1.085524	1.073379	0.8
0.7	0.916858	0.91692	0.920113	0.921441	0.6
0.8	0.644526	0.64441	0.646892	0.660229	0.4
0.9	0.329146	0.329011	0.329903	0.343878	0.2
1.0	0.0	0.0	0.0	0.0	0.0

The quantity of physical interest is the local Nusselt number Nu_L. From the fundamental heat transfer concepts, by writing energy balance on the inner cylinder, we can derive the relation for the Nusselt local number

$$k_f \left.\frac{\partial T}{\partial r}\right|_{r_i} = h_{nf}(T_h - T_C) \Rightarrow -k_f \frac{\Delta T}{r_o}\left.\frac{\partial \Theta}{\partial R}\right|_{R=\Pi} = h_{nf}\Delta T \Rightarrow Nu_i = \frac{h_{nf} r_o}{k_f} = \left.\frac{\partial \theta}{\partial R}\right|_{R=\Pi} \tag{20}$$

This definition also implies the mean Nusselt number because the temperature is independent of tangential coordinate.

C. Volume Fraction Distribution

It is clear from Eq. (12) that by obtaining the temperature, the nanoparticle volume fraction could be obtained as

$$\Phi = \frac{1}{Nb}\left[\frac{\beta_1}{2}R + \frac{\beta_2}{R} - Nt(\theta + \theta_r)\right] - \Phi_r \tag{21}$$

Also, the relation for the Sherwood number on the inner cylinder is presented below:

$$Sh_i = \left.\frac{\partial \Phi}{\partial R}\right|_{R=\Pi} \tag{22}$$

IV. Results and Discussion

Figure 2 displays the velocity distribution in the annulus as a function of radial distance for various values of velocity ratio where the radius ratio is 0.2. As seen, increasing the magnitude of λ, the velocity reaches a minimum point in the vicinity of the inner cylinder. This minimum point can be obtained by taking the velocity gradient equal to zero at the inner cylinders. Generally, the velocity ratio for which the minimum velocity occurs on the inner cylinder is obtained by

$$\lambda = \frac{2}{\Pi^2 + 1}\left(\text{obtained from} \left.\frac{\partial U}{\partial R}\right|_{R=\Pi} = 0\right)$$

Here, in radius ratio of 0.2, the minimum point can be found in the velocity profile for $\lambda \geq 1.92$. As the velocity ratio increases, this minimum point moves toward the outer cylinder. The velocity distribution is linear where the cylinders rotate with the same velocity but in opposite directions ($\lambda = -1$).

The effects of the Brownian motion parameter on the dimensionless temperature are presented in Fig. 3. As shown, with an increase in the Brownian motion parameter, the absolute dimensionless temperature decreases in the whole of the annulus, so that for high values of N_b (say 5 and 6) the temperature reaches a minimum point near the outer cylinder. With increasing the Brownian

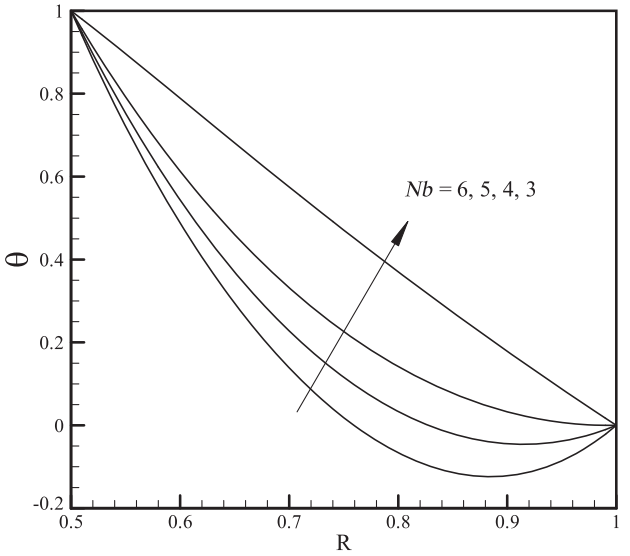

Fig. 3 Dimensionless temperature distribution for different values of Brownian motion parameter at $Nt = 0.5$, $\theta_r = 4$, $\Phi_r = 0.5$, $Ec = 0.01$, $Pr = 3$, and $\lambda = 7$.

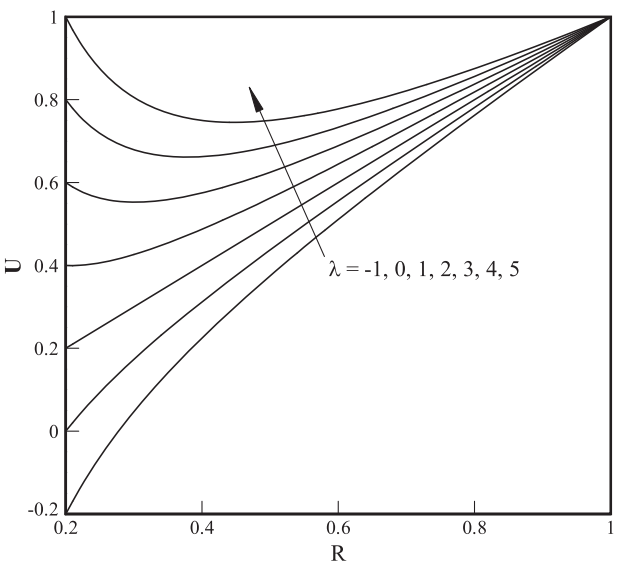

Fig. 2 Dimensionless velocity distribution for different values of velocity ratio.

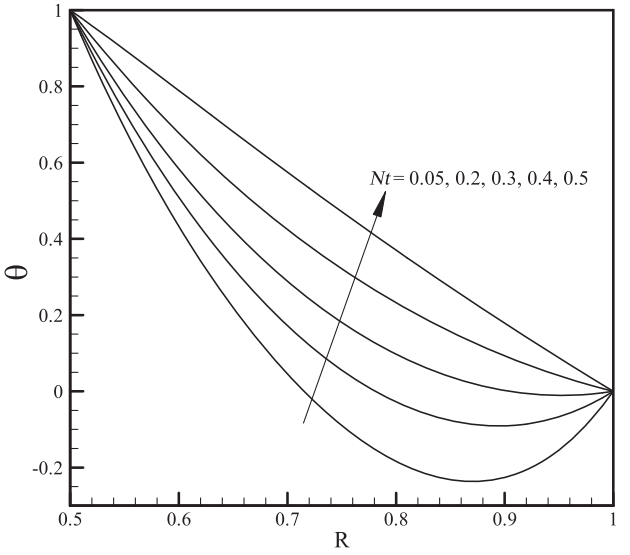

Fig. 4 Dimensionless temperature distribution for different values of thermophoresis parameter at $Nb = 3$, $\theta_r = 4$, $\Phi_r = 0.5$, $Ec = 0.01$, $Pr = 3$, and $\lambda = 7$.

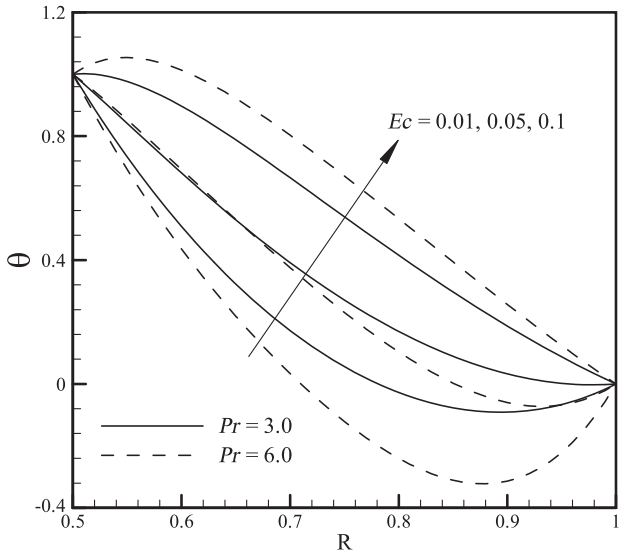

Fig. 5 Dimensionless temperature distribution for different values of Prandtl and Eckert numbers at $Nt = 0.2$, $Nb = 3$, $\theta_r = 4$, $\Phi_r = 0.5$, and $\lambda = 7$.

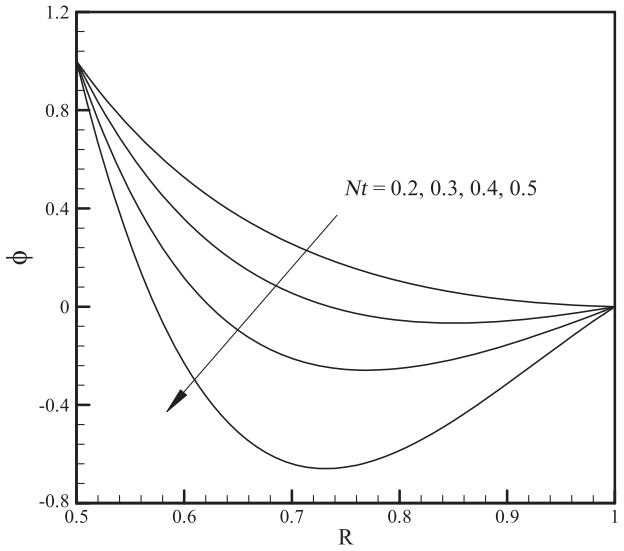

Fig. 7 Dimensionless nanoparticles volume fraction for different values of thermophoresis parameter at $Nb = 3$, $\theta_r = 4$, $\Phi_r = 0.5$, $Ec = 0.01$, $Pr = 3$, and $\lambda = 7$.

motion of nanoparticles, the thickness of thermal boundary layer increases, and hence, the temperature gradients in the annulus fall down. The variation of dimensionless temperature in the annulus is plotted in Fig. 4 for different thermophoresis parameters. It is found that an increase in the thermophoresis parameter leads to the increase in the dimensionless temperature. This shows the opposite effects of the thermophoresis parameter on the temperature field, compared to the Brownian motion parameter. The effects of both Prandtl and Eckert numbers on the dimensionless temperature are presented in Fig. 5. The Eckert number indicates the magnitude of viscous dissipation effects due to nanofluid flow in the annulus. As expected, with an increase in Eckert number the fluid temperature in the annulus increases because the kinetic energy due to fluid flow converts to heat, and consequently the temperature in the annulus increases. It is also observed that the fluid temperature increases with increasing Pr. From the physical point of view, as the Prandtl number increases, the thermal diffusivity in the annuli decreases so that the diffusion of heat generated by the viscous dissipation decreases. Consequently, because of the accumulation of heat between the cylinders, the fluid temperature increases. The effects of Brownian motion on the nanoparticles volume fraction are presented in Fig. 6. It is observed that as the Brownian motion increases, the dimensionless volume fraction increases. Returning to Eq. (12), it is reasonable that for fixed values of the other parameters at a certain position R, with a decrease in the dimensionless temperature resulted from increasing Nb (see Fig. 3), the dimensionless volume fraction increases.

Figure 7 shows the dimensionless nanoparticle volume fraction for different values of the thermophoresis parameter. As the thermophoresis increases, the nanoparticles volume fraction decreases. Returning to Eq. (12), it is reasonable that for fixed values of the other parameters at a certain position R, with an increase in the dimensionless temperature resulted from increasing Nt (see Fig. 4), the dimensionless volume fraction decreases.

Figures 8 and 9 present the dimensionless nanoparticles volume fraction for different values of Eckert number and velocity ratio, respectively. It is seen that when the Eckert number and the velocity ratio increase, the volume fraction profiles fall down in the annuli. This is due to this fact that as the Eckert number increases, the temperature inside the annulus rises because of the viscous effects and as a result, the concentration of the nanofluid (nanoparticles volume fraction) is reduced. In addition, a higher velocity ratio means a higher relative velocity between the layers of the nanofluid, which

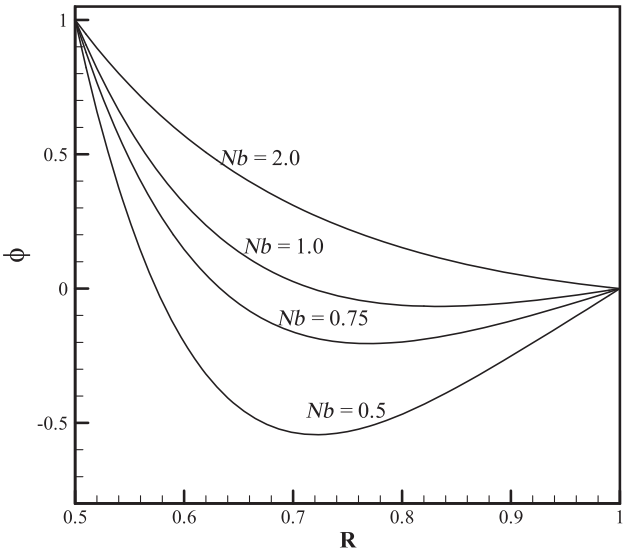

Fig. 6 Dimensionless nanoparticles volume fraction for different values of Brownian motion parameter at $Nt = 0.5$, $\theta_r = 4$, $\Phi_r = 0.5$, $Ec = 0.01$, $Pr = 3$, and $\lambda = 7$.

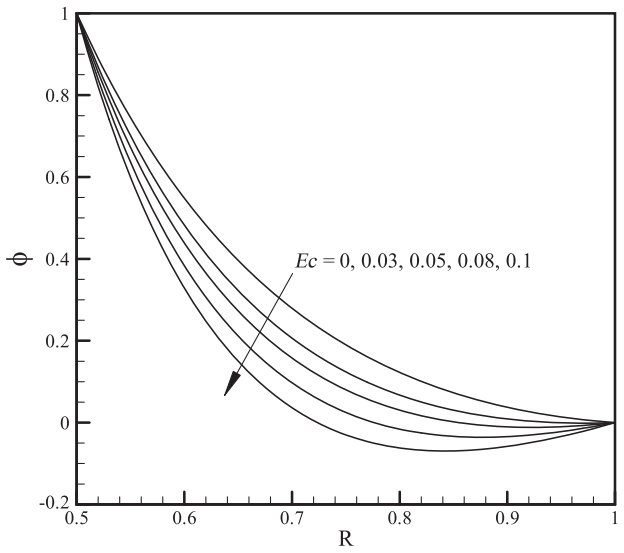

Fig. 8 Dimensionless nanoparticles volume fraction for different values of Eckert number at $Nt = 0.2$, $Nb = 0.5$, $\theta_r = 4$, $\Phi_r = 0.5$, $Pr = 3$, and $\lambda = 7$.

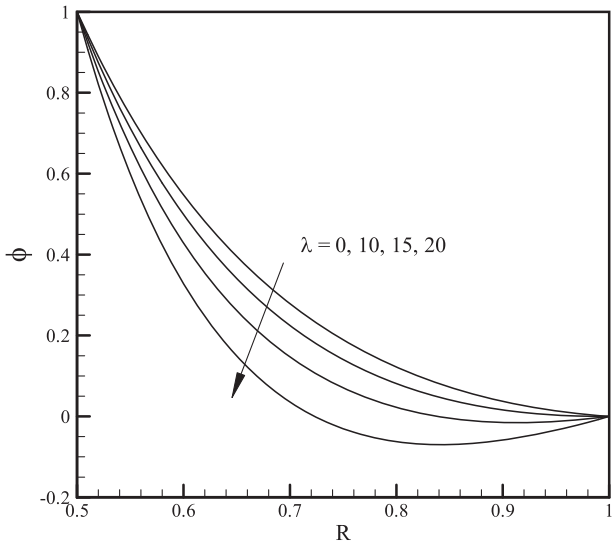

Fig. 9 Dimensionless nanoparticles volume fraction for different values of velocity ratio at $Nt = 0.2$, $Nb = 0.5$, $\theta_r = 4$, $\Phi_r = 0.5$, $Ec = 0.01$, and $Pr = 3$.

leads to higher viscous force between the cylinders and causes a higher temperature and as a result, the concentration of nanofluid decreases.

The variation of Nusselt number in the inner cylinder is plotted as a function of the Brownian motion parameter in Fig. 10 for different values of thermophoresis parameter. It is perceived that the Nusselt number decreases with an increase in the Brownian motion. On the other hand, Nusselt number increases with the increase of thermophoresis parameter. The changes in the Nusselt number are higher for smaller values of the parameter *Nb*. These results can be explained by the fact that as the Brownian motion decreases, or thermophoresis effect increases, the temperature gradients increase and finally lead to an increase in the heat transfer rate (as seen in Figs. 3 and 4).

The Nusselt number vs the velocity ratio at different values of the temperature ratio θ_r is plotted in Fig. 11. The lower temperature ratio results in the increase in Nusselt number. It is interesting to note that as the velocity ratio increases, first the Nusselt number decreases and reaches a minimum value, and then increases. The Nusselt number is minimum at $\lambda = 1.0$ regardless the temperature ratio. From the physical point of view, at $\lambda = 1.0$, there is no relative motion between

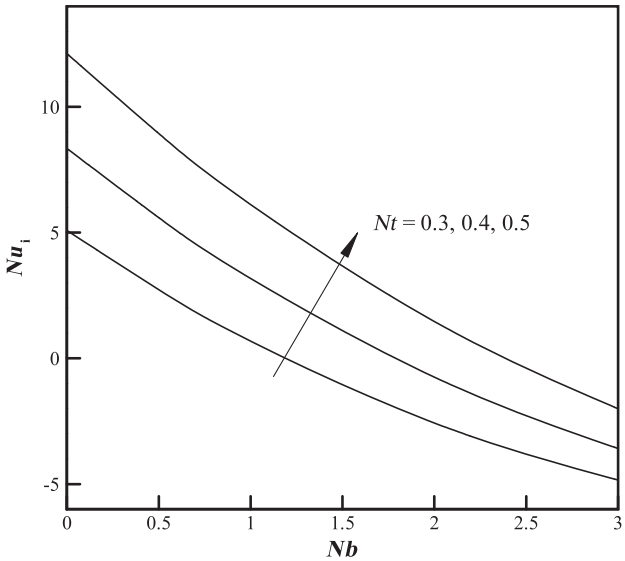

Fig. 10 Nusselt number (inner cylinder) vs Brownian motion parameter for different values of thermophoresis parameter at $\theta_r = 4$, $\Phi_r = 0.5$, $Ec = 0.01$, $Pr = 3$, and $\lambda = 7$.

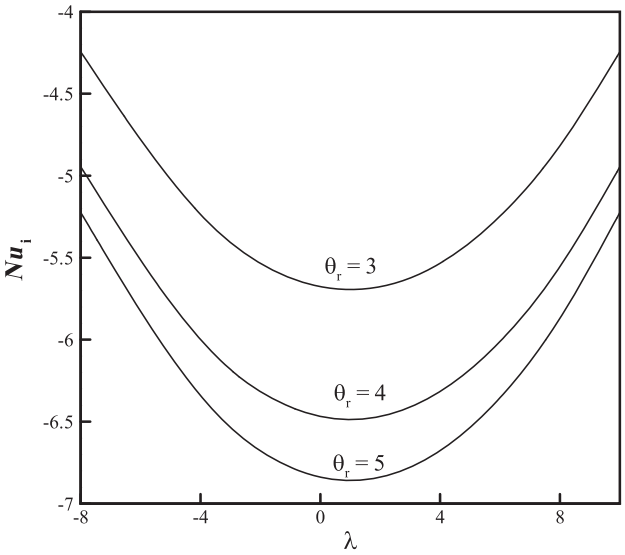

Fig. 11 Nusselt number (inner cylinder) vs velocity ratio for different values of Eckert temperature ratio at $Nt = 0.2$, $Nb = 3$, $\Phi_r = 0.5$, $Ec = 0.01$, and $Pr = 3$.

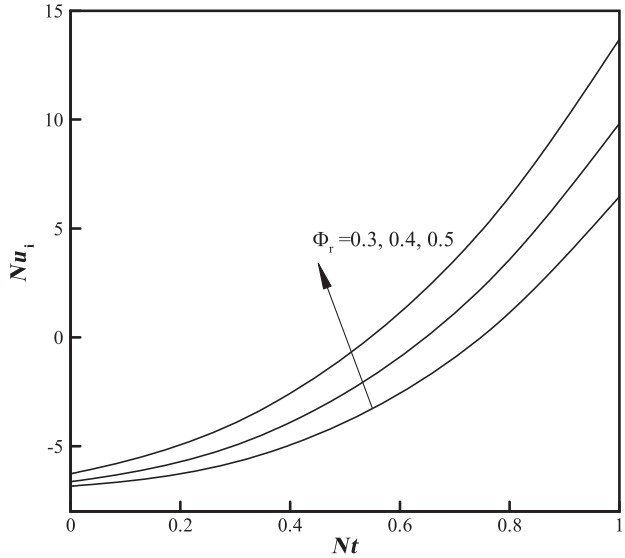

Fig. 12 Nusselt number (inner cylinder) vs thermophoresis parameter for different values of volume fraction ratio at $Nb = 3$, $\theta_r = 4$, $Ec = 0.01$, $\lambda = 10$, and $Pr = 3$.

the two cylinders so it is similar to the case in which the nanofluid is stationary in the system. In such a case, the fluid layers have no relative motion and hence the viscous dissipation due to shear stresses is minimized. Figure 12 illustrates the Nusselt number vs thermophoresis parameter in the presence of volume fraction ratio. As seen, the higher volume fraction ratios lead to a higher Nusselt number. It is found that the change in the Nusselt number increases for higher values of the thermophoresis parameter.

V. Conclusions

Analytical and numerical solutions to the flow and heat transfer of a nanofluid between two rotating cylinders are presented, considering the effects of Brownian motion and thermophoresis. The momentum, energy, and volume fraction equations are simplified and solved in the cylindrical coordinate system. The homotopy perturbation method (HPM) is employed to solve the energy equation, whereas the results obtained from the HPM are compared to the results of a numerical solution. The following results are found from the study:

1) Temperature decreases in the whole of the annulus with increasing the Brownian motion parameter, whereas the increase of thermophoresis parameter has an opposite effect.

2) With an increase in the Brownian motion parameter, the Nusselt number of the inner cylinder decreases, while the Nusselt number increases with increases of the thermophoresis parameter.

3) With an increase in the angular velocity of outer cylinder (considering a constant velocity for the inner cylinder), the volume fraction in the annulus fall down.

Acknowledgment

The second and third authors would like to thank the Thailand Research Fund and the National Research University Project for supporting this study.

References

[1] Mahian, O., Mahmud, S., and Pop, I., "Analysis of First and Second Laws of Thermodynamics Between Two Isothermal Cylinders with Relative Rotation in the Presence of MHD Flow," *International Journal of Heat and Mass Transfer*, Vol. 55, Nos. 17–18, 2012, pp. 4808–4816. doi:10.1016/j.ijheatmasstransfer.2012.04.048

[2] Fénot, M., Bertin, Y., Dorignac, E., and Lalizel, G., "A Review of Heat Transfer Between Concentric Rotating Cylinders with or Without Axial Flow," *International Journal of Thermal Sciences*, Vol. 50, No. 7, 2011, pp. 1138–1155. doi:10.1016/j.ijthermalsci.2011.02.013

[3] Choi, S. U. S., "Enhancing Thermal Conductivity of Fluids with Nanoparticles," *The Proceedings of the ASME International Mechanical Engineering Congress and Exposition*, ASME, San Francisco, CA, FED 231/MD 66, 1995, pp. 99–105.

[4] Mahian, O., Kianifar, A., Kalogirou, S. A., Pop, I., and Wongwises, S., "A Review of the Applications of Nanofluids in Solar Energy," *International Journal of Heat and Mass Transfer*, Vol. 57, No. 2, 2013, pp. 582–594. doi:10.1016/j.ijheatmasstransfer.2012.10.037

[5] Saidur, R., Leong, K. Y., and Mohammad, H. A., "A Review on Applications and Challenges of Nanofluids," *Renewable and Sustainable Energy Reviews*, Vol. 15, No. 3, 2011, pp. 1646–1668. doi:10.1016/j.rser.2010.11.035

[6] Makinde, O. D., and Aziz, A., "Boundary Layer Flow of a Nanofluid Past a Stretching Sheet with a Convective Boundary Condition," *International Journal of Thermal Sciences*, Vol. 50, No. 7, 2011, pp. 1326–1332. doi:10.1016/j.ijthermalsci.2011.02.019

[7] Motsumi, T. G., and Makinde, O. D., "Effects of Thermal Radiation and Viscous Dissipation on Boundary Layer Flow of Nanofluids over a Permeable Moving Flat Plate," *Physica Scripta*, Vol. 86, No. 4, 2012, Paper 045003. doi:10.1088/0031-8949/86/04/045003

[8] Makinde, O. D., "Analysis of Sakiadis Flow of Nanofluids with Viscous Dissipation and Newtonian Heating," *Applied Mathematics and Mechanics*, Vol. 33, No. 12, 2012, pp. 1545–1554. doi:10.1007/s10483-012-1642-8

[9] Olanrewaju, M., and Makinde, O. D., "On Boundary Layer Stagnation Point Flow of a Nanofluid over a Permeable Flat Surface with Newtonian Heating," *Chemical Engineering Communications*, Vol. 200, No. 6, 2013, pp. 836–852. doi:10.1080/00986445.2012.721825

[10] Ji, Y., Ma, H. B., and Chen, H., "Volume Fraction Effect on Heat Transfer Performance of an Oscillating Heat Pipe," *Journal of Thermophysics and Heat Transfer*, Vol. 27, No. 1, 2013, pp. 111–115. doi:10.2514/1.T3867

[11] Farzin, F., Heris, S. Z., and Rahimi, S., "Laminar Convective Heat Transfer and Pressure Drop of TiO2/Turbine Oil Nanofluid," *Journal of Thermophysics and Heat Transfer*, Vol. 27, No. 1, 2013, pp. 127–133. doi:10.2514/1.T3935

[12] Khan, W. A., Aziz, A., and Uddin, N., "Buongiorno Model for Nanofluid Blasius Flow with Surface Heat and Mass Fluxes," *Journal of Thermophysics and Heat Transfer*, Vol. 27, No. 1, 2013, pp. 134–141. doi:10.2514/1.T3916

[13] Abdel-Rahman, G. M., "Thermal Radiation and Unsteady Magneto-hydrodynamic Flow of Nanofluid in Stretching Porous Medium," *Journal of Thermophysics and Heat Transfer*, Vol. 27, No. 1, 2013, pp. 142–150. doi:10.2514/1.T3889

[14] Mahmoud, M. A. A., and Waheed, S. E., "Hydromagnetic Hiemenz Slip Flow of Convective Micropolar Fluid Towards a Stretching Plate," *Journal of Thermophysics and Heat Transfer*, Vol. 27, No. 1, 2013, pp. 151–160. doi:10.2514/1.T4016

[15] Azari, A., Kalbasi, M., and Rahimi, M., "Numerical Study on the Laminar Convective Heat Transfer of Alumina/Water Nanofluids," *Journal of Thermophysics and Heat Transfer*, Vol. 27, No. 1, 2013, pp. 170–173. doi:10.2514/1.T3834

[16] Jin, J. S., and Lee, J. S., "Effects of Aggregated Sphere Distribution and Percolation on Thermal Conduction of Nanofluids," *Journal of Thermophysics and Heat Transfer*, Vol. 27, No. 1, 2013, pp. 173–178. doi:10.2514/1.T3915

[17] Vermahmoudi, Y., Peyghambarzadeh, S. M., Naraki, M., and Hashemabadi, S. H., "Statistical Analysis of Nanofluid Heat Transfer in a Heat Exchange System," *Journal of Thermophysics and Heat Transfer*, Vol. 27, No. 2, 2013, pp. 320–325. doi:10.2514/1.T4062

[18] Noghrehabadi, A., Behseresht, A., Ghalambaz, M., and Behseresht, J., "Natural-Convection Flow of Nanofluids over Vertical Cone Embedded in Non-Darcy Porous Media," *Journal of Thermophysics and Heat Transfer*, Vol. 27, No. 2, 2013, pp. 334–341. doi:10.2514/1.T3965

[19] Uddin, M. J., Khan, W. A., and Ismail, A. I. Md., "Free Convective Flow of Non-Newtonian Nanofluids in Porous Media with Gyrotactic Microorganism," *Journal of Thermophysics and Heat Transfer*, Vol. 27, No. 2, 2013, pp. 326–333. doi:10.2514/1.T3983

[20] Asirvatham, L. G., Nimmagadda, R., and Wongwises, S., "Heat Transfer Performance of Screen Mesh Wick Heat Pipes Using Silver-Water Nanofluid," *International Journal of Heat and Mass Transfer*, Vol. 60, No. 1, 2013, pp. 201–209. doi:10.1016/j.ijheatmasstransfer.2012.11.037

[21] Godson, L., Raja, B., Mohan Lal, D., and Wongwises, S., "Convective Heat Transfer Characteristics of Silver-Water Nanofluid Under Laminar and Turbulent Flow Conditions," *Journal of Thermal Science and Engineering Applications*, Vol. 4, No. 3, 2012, Paper 031001. doi:10.1115/1.4006027

[22] Duangthongsuk, W., Dalkilic, A. S., and Wongwises, S., "Convective Heat Transfer of Al_2O_3–Water Nanofluids in a Microchannel Heat Sink," *Current Nanoscience*, Vol. 8, No. 3, 2012, pp. 317–322. doi:10.2174/157341312800620368

[23] Abu-Nada, E., Masoud, Z., and Hijazi, A., "Natural Convection Heat Transfer Enhancement in Horizontal Concentric Annuli Using Nanofluids," *International Communications in Heat and Mass Transfer*, Vol. 35, No. 5, 2008, pp. 657–665. doi:10.1016/j.icheatmasstransfer.2007.11.004

[24] Abu-Nada, E., "Effects of Variable Viscosity and Thermal Conductivity of Al_2O_3–Water Nanofluid on Heat Transfer Enhancement in Natural Convection," *International Journal of Heat and Fluid Flow*, Vol. 30, No. 4, 2009, pp. 679–690. doi:10.1016/j.ijheatfluidflow.2009.02.003

[25] Abu-Nada, E., "Effects of Variable Viscosity and Thermal Conductivity of Cuo-Water Nanofluid on Heat Transfer Enhancement in Natural Convection: Mathematical Model and Simulation," *Journal of Heat Transfer*, Vol. 132, No. 5, 2010, pp. 1–9. doi:10.1115/1.4000440

[26] Abouali, O., and Falahatpisheh, A., "Numerical Investigation of Natural Convection of Al_2O_3 Nanofluid in Vertical Annuli," *Heat and Mass Transfer*, Vol. 46, No. 1, 2009, pp. 15–23. doi:10.1007/s00231-009-0540-7

[27] Izadi, M., Behzadmehr, A., and Jalali-Vahida, D., "Numerical Study of Developing Laminar Forced Convection of a Nanofluid in an Annulus," *International Journal of Thermal Sciences*, Vol. 48, No. 11, 2009, pp. 2119–2129. doi:10.1016/j.ijthermalsci.2009.04.003

[28] Shahi, M., Mahmoudi, A. H., and Talebi, F., "A Numerical Investigation of Conjugated-Natural Convection Heat Transfer Enhancement of a Nanofluid in an Annular Tube Driven by Inner Heat Generating Solid Cylinder," *International Communications in Heat and Mass Transfer*, Vol. 38, No. 4, 2011, pp. 533–542. doi:10.1016/j.icheatmasstransfer.2010.12.022

[29] Moghari, R. M., Akbarinia, A., Shariat, M., Talebi, F., and Laur, R., "Two Phase Mixed Convection Al_2O_3–Water Nanofluid Flow in an Annulus," *International Journal of Multiphase Flow*, Vol. 37, No. 6, 2011, pp. 585–595. doi:10.1016/j.ijmultiphaseflow.2011.03.008

[30] Cianfrini, M., Corcione, M., and Quintino, A., "Natural Convection Heat Transfer of Nanofluids in Annular Spaces Between Horizontal

Concentric Cylinders," *Applied Thermal Engineering*, Vol. 31, Nos. 17–18, 2011, pp. 4055–4063. doi:10.1016/j.applthermaleng.2011.08.010

[31] Soleimani, S., Sheikholeslami, M., Ganji, D. D., and Gorji-Bandpay, M., "Natural Convection Heat Transfer in a Nanofluid Filled Semi-Annulus Enclosure," *International Communications in Heat and Mass Transfer*, Vol. 39, No. 4, 2012, pp. 565–574. doi:10.1016/j.icheatmasstransfer.2012.01.016

[32] Sheikhzadeh, G. A., Arbaban, M., and Arefmanesh, A. "Effects of Radial Fins on the Laminar Natural Convection of a Nanofluid in Concentric Annuli," *Computational Thermal Sciences*, Vol. 4, No. 2, 2012, pp. 151–158. doi:10.1615/ComputThermalScien.2012004025

[33] Sheikhzadeh, G. A., Arbaban, M., and Mehrabian, M. A., "Laminar Natural Convection of Cu-Water Nanofluid in Concentric Annuli with Radial Fins Attached to the Inner Cylinder," *Heat and Mass Transfer*, Vol. 49, No. 3, 2013, pp. 391–403. doi:10.1007/s00231-012-1084-9

[34] Nasrin, R., Alim, M., and Chamkha, A. J., "Effect of Viscosity Variation on Natural Convection Flow of Water-Alumina Nanofluid in an Annulus with Internal Heat Generation," *Heat Transfer — Asian Research*, Vol. 41, No. 6, 2012, pp. 536–552. doi:10.1002/htj.21016

[35] Parvin, S., Nasrin, R., Alim, M. A., Hossain, N. F., and Chamkha, A. J., "Thermal Conductivity Variation on Natural Convection Flow of Water-Alumina Nanofluid in an Annulus," *International Journal of Heat and Mass Transfer*, Vol. 55, Nos. 19–20, 2012, pp. 5268–5274. doi:10.1016/j.ijheatmasstransfer.2012.05.035

[36] Ashorynejad, H. R., Mohamad, A. A., and Sheikholeslami, M., "Magnetic Field Effects on Natural Convection Flow of a Nanofluid in a Horizontal Cylindrical Annulus Using Lattice Boltzmann Method," *International Journal of Thermal Sciences*, Vol. 64, No. 2, 2013, pp. 240–250. doi:10.1016/j.ijthermalsci.2012.08.006

[37] Mahian, O., Mahmud, S., and Heris, S. Z., "Analysis of Entropy Generation Between Co-Rotating Cylinders Using Nanofluids," *Energy*, Vol. 44, No. 1, 2012, pp. 438–446. doi:10.1016/j.energy.2012.06.009

[38] Mahian, O., Mahmud, S., and Heris, S. Z., "Effect of Uncertainties in Physical Properties on Entropy Generation Between Two Rotating Cylinders with Nanofluids," *ASME Journal of Heat Transfer*, Vol. 134, No. 10, 2012, Paper 101704. doi:10.1115/1.4006662

[39] Mahian, O., Mahmud, S., and Wongwises, S., "Entropy Generation Between Two Rotating Cylinders with Magnetohydrodynamic Flow Using Nanofluids," *Journal of Thermophysics and Heat Transfer*, Vol. 27, No. 1, 2013, pp. 161–169. doi:10.2514/1.T3908

[40] Buongiorno, J., "Convective Transport in Nanofluids," *ASME Journal of Heat Transfer*, Vol. 128, Nos. 1–2, 2006, pp. 240–250. doi:10.1115/1.2150834

[41] He, J. H., "Homotopy Perturbation Method for Solving Boundary Value Problems," *Physical Letters A*, Vol. 350, Nos. 1–2, 2006, pp. 87–88. doi:10.1016/j.physleta.2005.10.005

[42] Ariel, P., Hayat, T., and Asghar, S., "Homotopy Perturbation Method and Axisymmetric Flow over a Stretching Sheet," *International Journal of Nonlinear Sciences and Numerical Simulation*, Vol. 7, No. 4, 2006, pp. 399–406. doi:10.1515/IJNSNS.2006.7.4.399

[43] Nourazar, S. S., Matin, M. H., and Simiari, M., "The HPM Applied to MHD Nanofluid Flow over a Horizontal Stretching Plate," *Journal of Applied Mathematics*, 2011. doi:10.1155/2011/876437

[44] Rashidi, M. M., Keimanesh, M., and Rajvanshi, S. C., "Study of Pulsatile Flow in a Porous Annulus with the Homotopy Analysis Method," *International Journal of Numerical Methods for Heat and Fluid Flow*, Vol. 22, No. 8, 2012, pp. 971–989. doi:10.1108/09615531211271817

International Communications in Heat and Mass Transfer 48 (2013) 141–148

Contents lists available at ScienceDirect

International Communications in Heat and Mass Transfer

journal homepage: www.elsevier.com/locate/ichmt

A numerical correlation development study for the determination of Nusselt numbers during boiling and condensation of R134a inside smooth and corrugated tubes ☆

M. Balcilar [a], K. Aroonrat [b], A.S. Dalkilic [c,*], S. Wongwises [b]

[a] Computer Engineering Department, Yildiz Technical University, Davutpasa, Esenler, Istanbul 34220, Turkey
[b] Fluid Mechanics, Thermal Engineering and Multiphase Flow Research Lab. (FUTURE), Department of Mechanical Engineering, King Mongkut's University of Technology Thonburi, Bangmod, Bangkok 10140, Thailand
[c] Heat and Thermodynamics Division, Department of Mechanical Engineering, Yildiz Technical University, Yildiz, Besiktas, Istanbul 34349, Turkey

ARTICLE INFO

Available online 9 September 2013

Keywords:
Condensation
Boling
Nusselt number
Heat transfer coefficient
Modeling
Neural network

ABSTRACT

In this study, the closed form of artificial neural network method is used to have a reliable empirical correlation to estimate the measured Nusselt numbers of R134a flowing downward and horizontally inside smooth and corrugated copper tubes by means of some dimensionless numbers. R134a and water are used as working fluids flowing in the tube side and annular side of a double tube heat exchanger, respectively. The training sets have the experimental data of in-tube condensation and in-tube boiling tests including various mass fluxes and saturation temperatures of R134a. Inputs of the formula are the dimensionless numbers obtained from measured values of test section such as Froude number, Weber number, Bond number, Lockhart and Martinelli number, void fraction, the ratio of density to dynamic viscosity, liquid, vapor and equivalent Reynolds numbers, surface tension parameter and liquid Prandtl number, while the output of the formula is the experimental Nusselt numbers in the analysis. Nusselt numbers of R134a are modeled using closed form of multi-layer perceptron (MLP) method of artificial neural network (ANN). Analyses of the ANN method are accomplished by means of 1177 data points. The performance of the closed form of multi-layer perceptron (MLP) with three inputs and one hidden neuron architecture was found to be in good agreement, predicting the experimental Nusselt numbers with their deviations being within the range of ± 30% for all tested conditions. Empirical correlations are proposed for both condensation and boiling flows separately. A single empirical correlation is found to be capable of predicting the experimental Nusselt numbers of both condensation and boiling flows together. Dependency of output of the ANNs from input values is also investigated in the paper. Vapor Reynolds number, equivalent Reynolds number, Weber number and Froude number are found to be the most affective parameters as a result of the dependency analyses.

1. Introduction

Heat exchangers using in-tube condensation have great significance in the refrigeration, automotive and process industries. Effective heat exchangers have been rapidly developed due to the demand for more compact systems, higher energy efficiency, lower material costs and other economic incentives. The surface area of heat exchangers has a directly significant effect on their heat-transfer performance. Improvements to make heat transfer equipment more energy-efficient would need to focus on miniaturization on the one hand and an astronomical increase in heat flux on the other. Normally, heat-transfer enhancement techniques necessarily reduce the thermal resistance in a conventional heat exchanger by promoting a higher convection heat-transfer coefficient in order to minimize the size of the heat exchanger. Recent numerical studies of authors on these subjects regarding the two-phase flows in the literature are summarized in the following paragraphs.

Dalkilic and Wongwises [1,2], Laohalertdecha et al. [3], and Balcilar et al. [4] reviewed the studies on in-tube condensation using smooth and enhanced tubes intensively since two-phase flow in tubes is the most challenging phenomenon in the heat exchanger systems. All effective possible research subjects of in-tube condensation were classified generally according to the tube orientation (horizontal, vertical, and inclined tubes) and tube geometry (smooth and enhanced tubes). Detailed information on the in-tube condensation studies of heat transfer, pressure drop, flow pattern, void fraction, and refrigerants in the literature were given. Their papers not only mention the new enhancement techniques of heat transfer, but also include some information on the new refrigerants, theoretical, numerical and empirical models in the literature.

☆ Communicated by W.J. Minkowycz.

* Corresponding author.
E-mail address: dalkilic@yildiz.edu.tr (A.S. Dalkilic).

0735-1933/$ – see front matter © 2013 Elsevier Ltd. All rights reserved.
http://dx.doi.org/10.1016/j.icheatmasstransfer.2013.08.012

Nomenclature

Bo	Bond number
d	internal tube diameter, m
f	function
Fr	Froude number
G	mass flux, kg m^{-2} s^{-1}
j	superficial velocity
Pr	Prandtl number
R	ratio of density to dynamic viscosity
Re	Reynolds number
x	average vapor quality
We	Weber number
X_{tt}	Lockhart and Martinelli parameter

Greek Symbols

α	void fraction
ρ	density, kg m^{-3}
μ	dynamic viscosity, kg m^{-1} s^{-1}
σ	surface tension, N m^{-1}
Ψ	surface tension parameter

Subscripts

ANN	artificial neural network
eq	equivalent
exp	experiment
g	gas
h	hydraulic
l	liquid
TP	two-phase

Artificial intelligence methods such as genetic algorithms (GAs) and artificial neural networks (ANNs) modeling validated by the experimental work, have been gaining increased popularity in correlating two-phase flows in tubes. However, investigations into the prediction of in-tube condensation and evaporation's characteristics by means of artificial intelligence techniques are not sufficient in the literature. Authors of this paper have these publications on the determination of heat transfer characteristics of two-phase flows in-tubes numerically [5–10].

Improvements in condensation heat transfer in horizontal tubes have been the subject of significant concern in the design and operation of air conditioning and refrigeration systems. Performance of smooth tubes has been determined by many researchers with pure refrigerants as operating fluids. Generally, empirical methods have been offered to compute the condensation heat transfer coefficients in horizontal smooth-tubes. In the past, some researchers have studied several enhancement techniques, such as rough surfaces and twisted-tape inserts, while on the other hand, micro-fin and corrugated tubes have recently been used intensively because of their high condensation heat transfer performance and moderate pressure drop. Authors of this paper have these publications on the determination of two-phase heat transfer coefficient in smooth and enhanced tubes [11–22]. This paper is a continuation of the authors' previous works and includes all their previous works about condensation and boiling in tubes.

The leading aim of this study is to model the condensation and boiling in smooth and corrugated tubes in MATLAB with the methods of MLP and NLS, and then determine the most affected parameters and develop reliable correlations with several sets of basic heat transfer data [11,19–21] belonging to the condensation and boiling flow in smooth and corrugated tubes. The proposed correlations are believed to be useful in predicting the heat transfer characteristics of new smooth and corrugated tubes, without additional experiments, due to the use of reliable data from the authors' laboratory in King Mongkut's University of Technology Thonburi.

2. Experimental apparatus and method

Detailed descriptions of the experimental apparatuses and summary of test conditions in terms of flow type, refrigerant, mass flux, average pressure, inlet and outlet vapor qualities and number of data points belonging to the data for studying condensation and evaporation of R134a inside horizontal/vertical smooth and corrugated tubes can be found either in authors' previous publications and in Table 1 partly.

3. Calculation procedure for the analyses

3.1. Error analysis

The error analyses' calculation procedure for the average values of the experimental and calculated results of the two-phase pressure drops regarding with R square error, proportional error and mean square error (MSE) can be seen from authors' previous publications.

3.2. The generalized artificial neural networks (ANNs) model

The detailed information on the ANN analyses of the determination condensation heat transfer coefficient, pressure drop and correlation development can be seen from the authors' previous publications. It should be noted that the authors benefitted from either their own experimental database or their database of independent laboratories in these publications.

Table 1
Experimental parameters and operating conditions.

Data set / Specifications	Data set 1 [11]	Data set 2 [19]	Data set 3 [20]	Data set 4 [21]
Phase change type	Condensation	Condensation	Boiling	Boiling
Refrigerant type	R134a	R134a	R134a	R134a
Tube type	Smooth	Smooth and 5 different corrugated tubes	Smooth and 5 different corrugated tubes	Smooth and 5 different corrugated tubes
Tube orientation	Vertical	Horizontal	Vertical	Horizontal
Inner diameter (m)	0.0081	0.0081	0.0087	0.0081
Tube length (m)	0.5	2.5	0.85	2.5
Mass flux (kg m^{-2} s^{-1})	260, 300, 340, 400, 455, 515	200, 300, 400, 500, 600, 700	200, 300, 400	300, 400, 500
Saturation pressure (bar)	10, 12	10, 11.3, 12.7	4,5, 5.7	4,5, 5.7
x_{avg}	0.7–0.96	0.07–0.82	0.14–0.86	0.09–0.81
Number of data points	368	280	302	227

Table 2
Proposed correlations and their error rates.

Eq. number	Proposed correlation	Data set	MSE	RMSE	R^2	Data number
1	$Nu = \frac{b_1}{1+\exp\left[b_2\psi+b_3\frac{Re_{eq}}{10000}+b_4 Pr_l+b_5\right]}$ $b_1 = 2207.661, b_2 = 6.857,$ $b_3 = -0.171, b_4 = -0.37, b_5 = 3.213$	All data	6140	78.34	0.8	1177
2	$Nu = \frac{b_1}{1+\exp\left[b_2\psi+b_3\frac{Re_g}{10000}+b_4\frac{Re_g}{10000}+b_5\right]}+b_6$ $b_1 = -1385.293, b_2 = -17.339, b_3 = 0.641,$ $b_4 = 0.108, b_5 = -2.656, b_6 = 1614.92$	1–3	6063.5	77.9	0.84	670
3	$Nu = \frac{100000}{1+\exp\left[b_1\frac{Re_g}{10000}+b_2\frac{Re_g}{10000}+b_3\frac{Re_{eq}}{10000}+b_4\right]}$ $b_1 = -4.606, b_2 = -1.73, b_3 = 4.615,$ $b_4 = 5.827$	2–4	4374.6	66.14	0.71	507
4	$Nu = \frac{100000}{1+\exp\left[b_1 Bo+b_2\psi+b_3\frac{Re_{eq}}{10000}+b_4\right]}$ $b_1 = 0.014, b_2 = 3.958, b_3 = -0.118,$ $b_4 = 3.112$	1–2	7946.6	89.14	0.8	648
5	$Nu = \frac{22650}{1+\exp\left[b_1 Bo+b_2\frac{Re_g}{10000}+b_3\frac{Re_{eq}}{10000}+b_4\right]}+b_5$ $b_1 = -0.083, b_2 = -0.292, b_3 = -1.749,$ $b_4 = 7.774, b_5 = 228.98$	3–4	2322.2	48.19	0.77	529
6	$Nu = \frac{2286}{1+\exp\left[b_1 Bo+b_2\frac{Re_g}{10000}+b_3 Pr_l+b_4\right]}+263$ $b_1 = -6.23, b_2 = -7.91, b_3 = -138.177,$ $b_4 = 604.191$	1	11304	106.32	0.68	368
7	$Nu = \frac{-466}{1+\exp[b_1 Fr+b_2 X_{tt}+b_3]}+741$ $b_1 = 0.003, b_2 = -1.109, b_3 = -1.098$	2	4279	65.4	0.58	280
8	$Nu = \frac{b_1}{1+\exp\left[b_2 Bo+b_3\frac{Re_{eq}}{10000}+b_4\right]}$ $b_1 = 645.682, b_2 = -0.065, b_3 = -0.171,$ $b_4 = 1.667$	3	382	19.5	0.75	302
9	$Nu = \frac{b_1}{1+\exp\left[b_2 Bo+b_3\frac{Re_{eq}}{10000}+b_4 Pr_l\right]}$ $b_1 = 1790.746, b_2 = -0.056, b_3 = -0.212,$ $b_4 = 0.944$	4	2421	49.2	0.88	227

3.3. The closed form of MLP

The success of the modeling experimental data with MLP has been reported many times by the researchers. But the worst part of this method is the mathematical expression of the relationship between input and output grows by growing architecture of MLP. Because of the relationship between inputs and outputs is not showing as a simple equation, this method is called by the researchers as black box. The success of correlation decreases when the model architecture is quite small, but this time, the closed form of the model is too simplified, and it can be shown as a simple equation. For that reason, in this study, the closed form of MLP with 3-1-1 architecture is used. In this model the transfer function of hidden layer is considered to be tansig function. According to this consideration the output of hidden layer is written as Eq. (1).

$$O_h = \frac{1}{1+\exp\left[w_1^1 \cdot I_1 + w_2^1 I_2 + w_3^1 I_3 + b_1\right]} \quad (1)$$

Because of the transfer function of output layer is considered to be linear function, the output of the model, in other word, the closed form of model is written as Eq. (2).

$$O = \frac{w_1^2}{1+\exp\left[w_1^1 \cdot I_1 + w_2^1 I_2 + w_3^1 I_3 + b_1\right]} + b_2 \quad (2)$$

3.4. The non-linear least square (NLS) algorithm

The non-linear least square (NLS) method allows the user to determine the most optimal non-linear function coefficients in order to fit data collected from an experimental environment to a non-linear function (non-linear curve fitting). This method tries to minimize the mean square error, beginning from the first estimated values determined by the user. Since it advances step by step through optimizing this point, it finds the local minimum and not the global minimum by starting from this initial point. The method is tested by starting from different initial points, and thus the global minimum value of model is determined.

3.5. Correlation development for the two-phase pressure drop

There have been a number of studies on the in-tube condensation and evaporation pressure drops of smooth and enhanced tubes in the literature. Generally, empirical methods have been used to compute

Table 3
The most predictive input parameters according to the error rates.

Inputs											Input number	Data Set	Output
Fr	We	Bo	X_{tt}	α	ψ	Re_l	Re_g	Re_{eq}	R	Pr_l			R^2 – Nu (%)
0	0	0	0	0	0	0	1	0	0	0	1	All	0.891
0	0	1	0	0	0	0	1	0	0	0	2	All	0.896
0	0	0	0	0	1	0	0	1	0	1	3	All	0.897
0	0	0	0	0	0	0	1	0	0	0	1	1–3	0.914
0	0	0	0	0	0	0	1	0	1	0	2	1–3	0.916
0	0	0	0	0	1	1	1	0	0	0	3	1–3	0.917
1	0	0	0	0	0	0	0	0	0	0	1	2–4	0.765
1	0	0	0	0	0	0	0	0	10	0	2	2–4	0.806
0	0	0	0	0	0	1	1	1	0	0	3	2–4	0.843
0	0	0	0	0	0	0	1	0	0	0	1	1–2	0.883
0	0	0	0	0	1	0	0	1	0	0	2	1–2	0.89
0	0	1	0	0	1	0	0	1	0	0	3	1–2	0.894
0	0	0	0	0	0	0	0	1	0	0	1	3–4	0.855
0	0	1	0	0	0	0	0	1	0	0	2	3–4	0.879
0	0	1	0	0	0	0	1	1	0	0	3	3–4	0.881

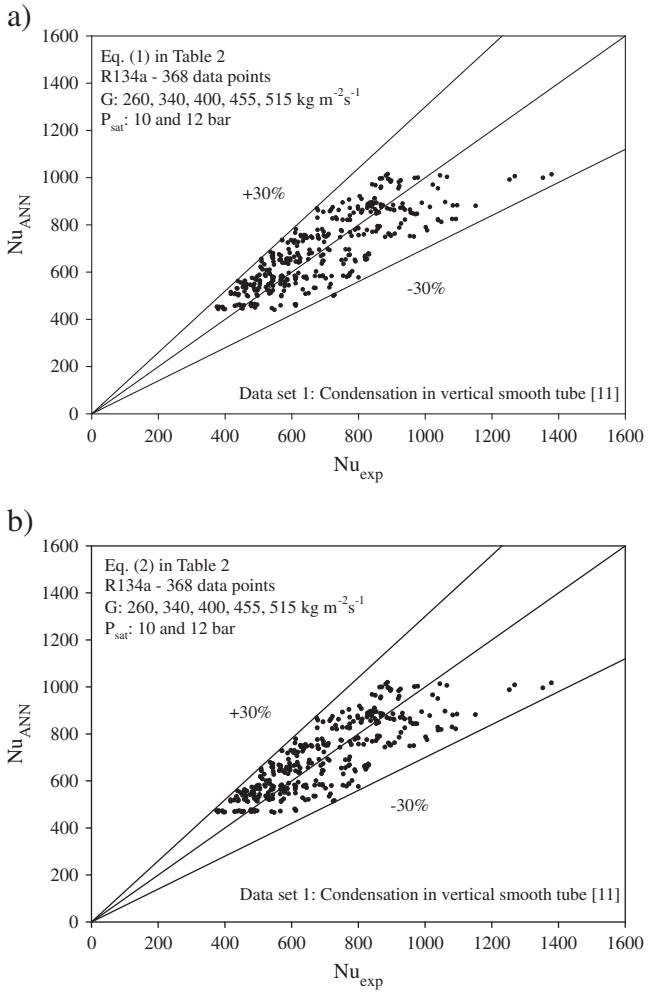

Fig. 1. Performance comparison of Eq. (1) (a) and Eq. (2) (b) for the data set 1.

the Nusselt numbers and convective heat transfer coefficients in tubes. As a result, Eq. (3) is formed to predict the Nusselt number of evaporation and condensation in terms of the above explanations as follows

$$Nu = \frac{b_1}{1 + \exp\left[b_2\psi + b_3\frac{Re_{eq}}{10000} + b_4 Pr_l + b_5\right]} \tag{3}$$

where the coefficients from b_1 to b_5 are the constants. It should be noted that detailed information on the developed correlations can be seen in Table 2.

The inputs of model have the following dimensionless numbers to determine their effects on the Nusselt number selected as the output of the analyses. Table 3 shows the significance of these input parameters below considering their error values of R^2.

The all liquid equivalent Re number is determined from:

$$Re_{eq} = \frac{G_{eq} d_h}{\mu_l} \tag{4}$$

and equivalent liquid mass flux and the ratio of density to dynamic viscosity are defined as:

$$G_{eq} = G\left((1-x) + x\left(\frac{\rho_l}{\rho_g}\right)^{0.5}\right) \tag{5}$$

$$R = \frac{\rho_l \mu_l}{\rho_g \mu_g} \tag{6}$$

and Bond number and the Froude number are defined respectively as:

$$Bo = g\left(\rho_l - \rho_g\right)\left(\frac{(d_h/2)^2}{\sigma}\right) \tag{7}$$

$$Fr = \frac{G^2}{g d_h {\rho_{TP}}^2} \tag{8}$$

where the two-phase density and the Lockhart and Martinelli parameter is determined from:

$$\rho_{TP} = \left(\frac{x}{\rho_g} + \frac{1-x}{\rho_l}\right)^{-1} \tag{9}$$

$$X_{tt} = \left(\frac{1-x}{x}\right)^{0.9}\left(\frac{\mu_g}{\mu_l}\right)^{0.1}\left(\frac{\rho_g}{\rho_l}\right)^{0.5} \tag{10}$$

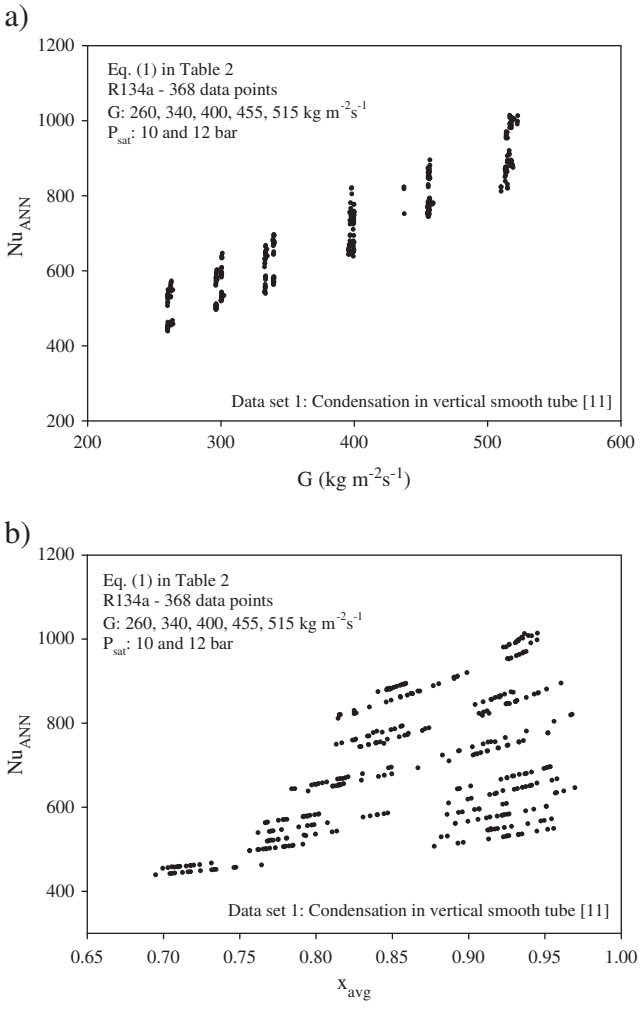

Fig. 2. Alteration of obtained Nusselt numbers with mass flux (a) and average vapor quality (b) for data set 1.

and the all liquid Reynolds number and all gas Reynolds number equations can be expressed as:

$$Re_l = \frac{Gd_h}{\mu_l} \tag{11}$$

$$Re_g = \frac{Gd_h}{\mu_g} \tag{12}$$

and the void fraction, α, can be determined from Butterworth's correlation as follows:

$$\alpha = \frac{1}{1 + 0.28\left(\frac{1-x}{x}\right)^{0.64}\left(\frac{\rho_g}{\rho_l}\right)^{0.36}\left(\frac{\mu_l}{\mu_g}\right)^{0.07}} \tag{13}$$

and Weber number, We, is used as:

$$We = \frac{G^2 d_h}{\sigma \rho_{TP}} \tag{14}$$

and surface tension parameter, ψ, and the liquid superficial velocity, j_l, are calculated respectively.

$$\psi = \frac{j_l \mu_l}{\sigma} \tag{15}$$

$$j_l = \frac{G(1-x)}{\rho_l(1-\alpha)} \tag{16}$$

4. Results and discussion

The following paragraphs numerically present the discussion of calculated Nusselt numbers of condensation and boiling flows of R134a using the database of authors' previous studies [11,19–21] in horizontal/vertical smooth and corrugated tubes. It should be noted that detailed explanations and some additional figures and tables containing different experimental parameters related to their studies on the heat transfer characteristics can be seen in the applied reference databases [11,19–21], which demonstrate the accuracy of the experiments. A discussion of the results follows.

There are one-type of closed form formula in the paper. It is developed for the calculation of the coefficients in correlations in Table 2 using the experimental databases in Table 1. The inputs of closed form are selected in the set of Froude number, Weber number, Bond number, Lockhart and Martinelli number, void fraction, the ratio of density to dynamic viscosity, liquid, vapor and equivalent Reynolds numbers, surface tension parameter and liquid Prandtl number, while the output of the closed form is the experimental Nusselt numbers in the analysis. Four-fold cross validation was used

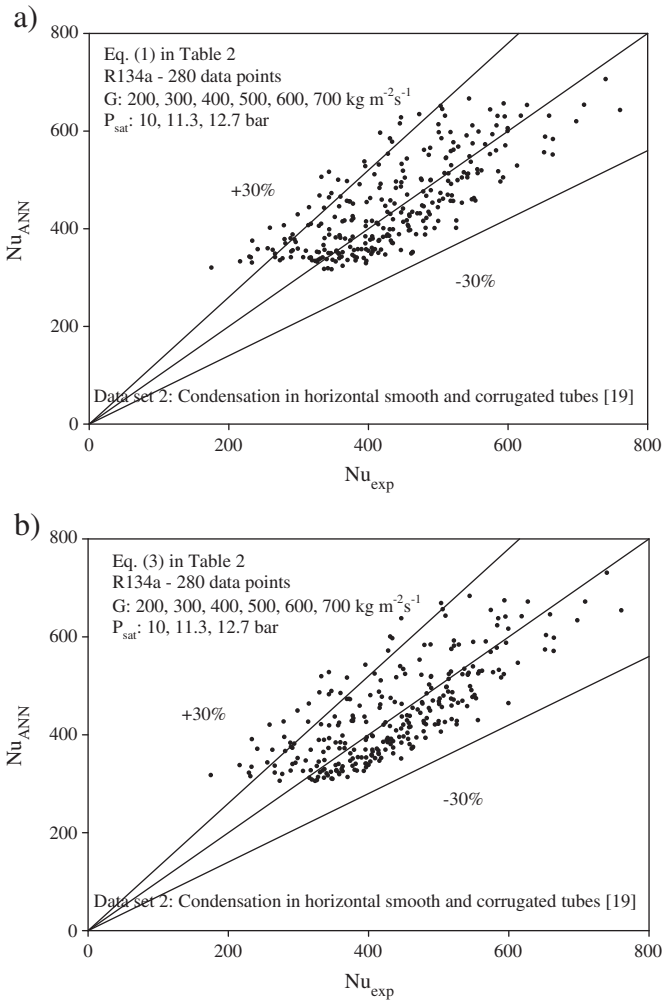

Fig. 3. Performance comparison of Eq. (1) (a) and Eq. (3) (b) for the data set 2.

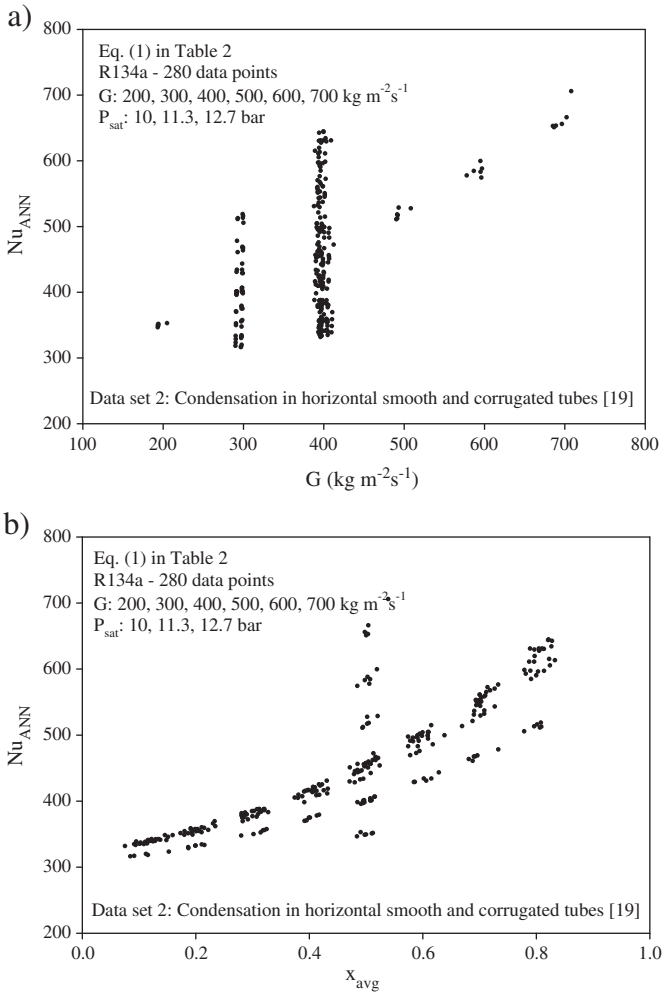

Fig. 4. Alteration of obtained Nusselt numbers with mass flux (a) and average vapor quality (b) for data set 2.

for regression analysis. It means that 1177 data points (all data of boiling and condensation in smooth and corrugated tubes) were divided by 4 sets randomly and one of the sets selected for the test process, and the rest of them (3 sets) were selected for the training process. These processes were continued until there were no untested data sets. Four different data sets of researchers [11,19–21] are defined in Table 1 and used for all analyses. It should be noted that although various architectures were tested for elimination, only the typical one was used in the paper due to limited space.

Table 1 shows the operating conditions of the database. 1177 data points were used in the analyses. 648 of them belong to in tube flow of condensation of vertical and horizontal orientations whereas 529 of them belong in tube flow of boiling of vertical and horizontal orientations. There were 5 different corrugated tubes and a smooth tube having 8 mm i.d. tested in the experiments. Mass fluxes and vapor qualities had a wide range for the accuracy of the developed correlations.

Table 2 includes 9 different developed correlations for each dataset or combination of them separately. Their R^2 values show their success and reliability. Eq. (1) in Table 2 has the most importance among others in the paper. It can predict all data including condensation/boiling in smooth/corrugated horizontal/vertical tubes at the same time with an acceptable accuracy as shown in all figures. The difference between the R^2 results is due to the hardness of generalization in the two-phase flow.

Table 3 illustrates the dependency of the output parameter from the input ones, in other words, these tables imply the most important affective dimensionless number on the prediction of the Nusselt number. It is possible from this table to determine the first 3 most affective parameters of databases separately. From this table, it is possible to reveal that vapor Reynolds number, equivalent Reynolds number and Weber number have the most influence on the Nusselt number considering all databases with their R^2 values over 0.8. Moreover, Froude number has also some importance apart from other input parameters. In this analysis, when the input parameter number is one in all databases, vapor Reynolds number seems to be dominant on the prediction of the Nusselt number with the R^2 value of 0.891. When there are 2 known input parameters, vapor Reynolds number and Bond number have the R^2 value of 0.896. When there are 3 known input parameters, vapor Reynolds number, Bond number and surface tension parameter have the R^2 value of 0.897. Datasets 1–3 refer to condensation and boiling datasets in vertical smooth and corrugated tubes, datasets 2–4 refer to condensation in horizontal tubes and boiling in vertical smooth and corrugated tubes, datasets 1–2 refer to condensation in horizontal and vertical smooth and corrugated tubes, datasets 3–4 refer to boiling in horizontal and vertical smooth and corrugated tubes as they can be realized from Table 1. These tables show that the accuracy of the estimated output value by means of input values increases along an increasing number of proper input parameters. In addition, they show the existence of less important input parameters on the prediction of the Nusselt number. It should be noted that it is possible to derive more results from these tables for each database specifically.

In this paper, an intensive concentration has been focused on the determination of the Nusselt numbers using all datasets by means of Eq. (1) in Table 2. The predictability (a) and performance comparison with other developed correlations (b) can be seen from Figs. 1, 3, 5 and 7. As it can be seen from these figures, majority of data points fall

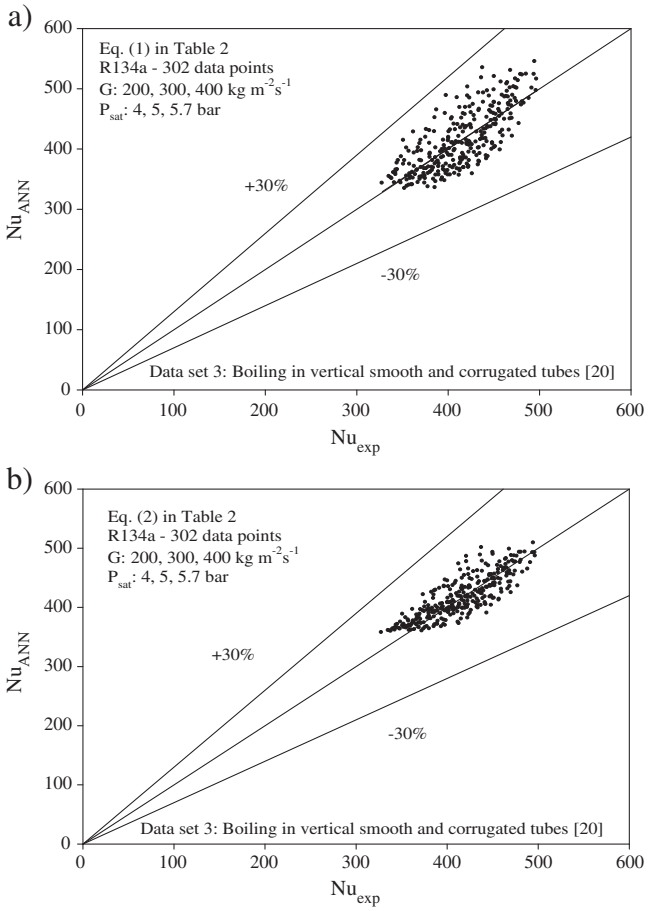

Fig. 5. Performance comparison of Eq. (1) (a) and Eq. (2) (b) for the data set 3.

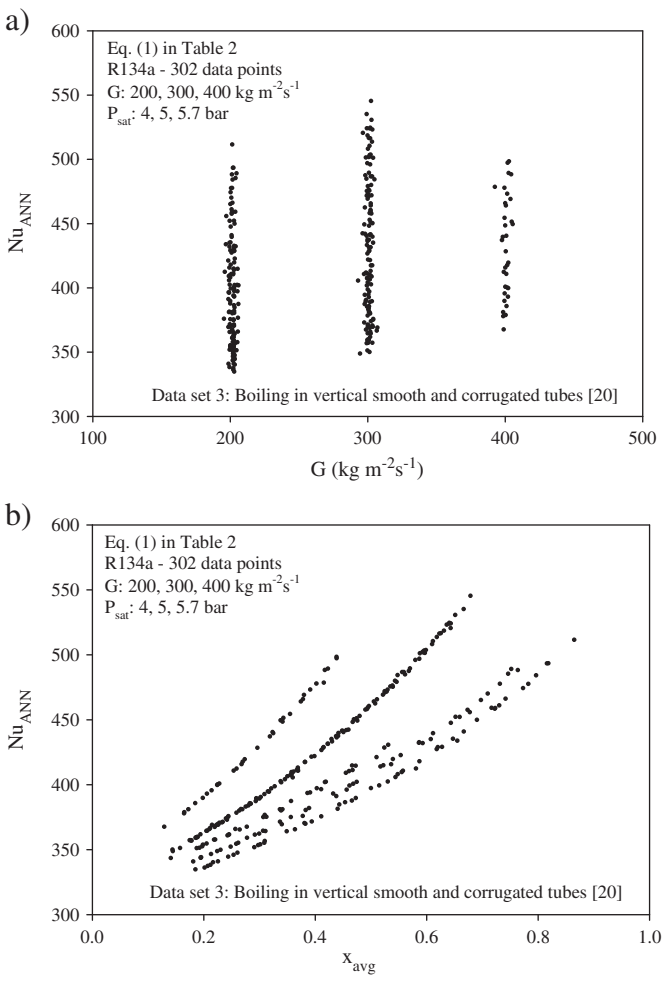

Fig. 6. Alteration of obtained Nusselt numbers with mass flux (a) and average vapor quality (b) for data set 3.

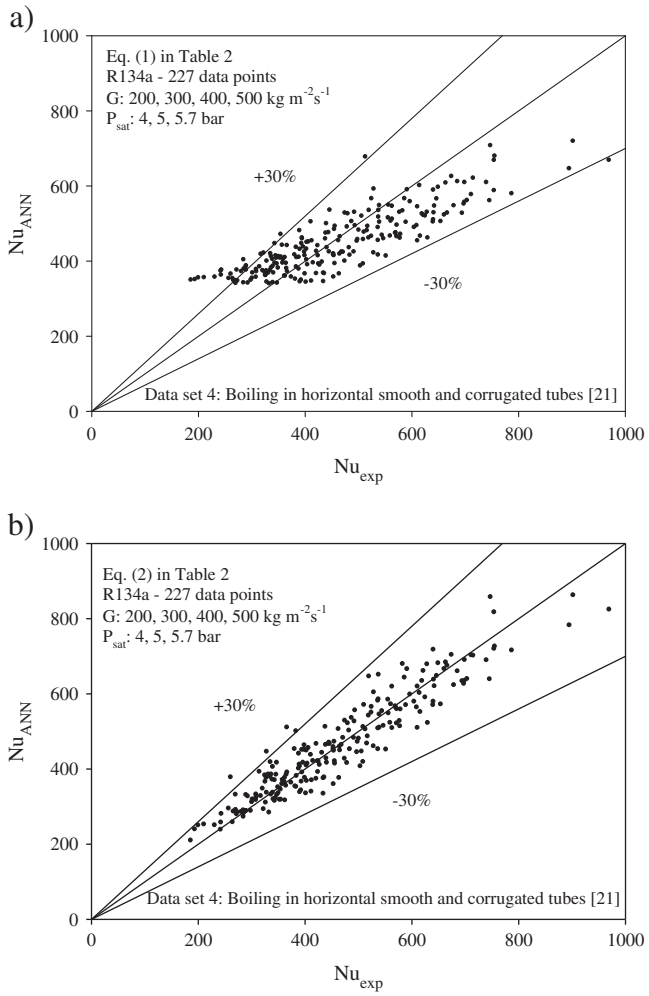

Fig. 7. Performance comparison of Eq. (1) (a) and Eq. (2) (b) for the data set 4.

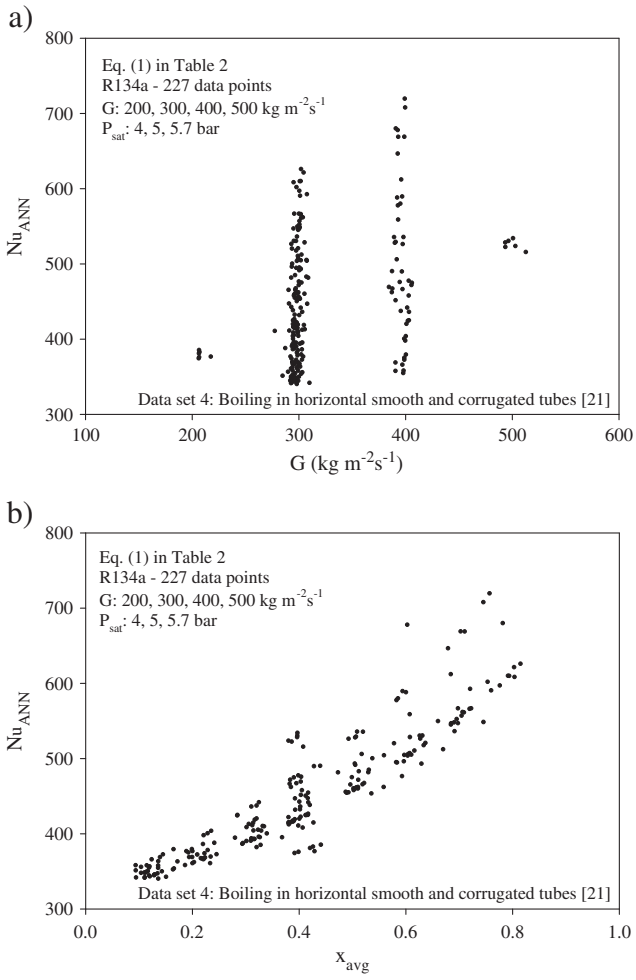

Fig. 8. Alteration of obtained Nusselt numbers with mass flux (a) and average vapor quality (b) for data set 4.

under the ±30% deviation bands for all proposed correlations. Figs. 2, 4, 6 and 8 show the proposed correlations' results meaningfulness considering the trends in the alterations of the obtained Nusselt numbers and mass fluxes (a) and average vapor qualities (b). As expectedly, Nusselt numbers increases with increasing mass fluxes and vapor qualities in all datasets.

5. Conclusion

Numerical analyses have been performed to determine the Nusselt numbers and to develop reliable correlations of condensation and boiling in smooth and corrugated tubes by means of computational numerical techniques. In order to derive reliable correlations, the authors' experimental databases in the literature [11, 19–21] are used in the analyses. This paper reports that although there are numerous studies on the determination of two-phase Nusselt numbers in tubes, application of artificial neural networks (ANN) together with non-linear least squares (NLS) to the in-tube boiling and condensation for the aim of correlation development does not exist in the literature. For that reason, the content of this study is expected to fill this gap in the literature.

Not only this paper proposes some correlations for boiling and condensation datasets but also it enables researchers to predict both condensation and boiling flows in smooth/corrugated horizontal/vertical tubes by means of a single correlation with a reasonable deviation.

Dependency of output of the ANNs closed form from input values is investigated in the paper. Vapor Reynolds number, equivalent Reynolds number, Weber number and Froude number are found to be the most affective parameters as a result of the dependency analyses.

Acknowledgments

The fourth author wishes to thank King Mongkut's University of Technology Thonburi (KMUTT) for providing him with a Post-doctoral fellowship. The fifth author is indebted to the Thailand Research Fund and the National Science and Technology Development Agency for their financial support.

References

[1] A.S. Dalkilic, S. Wongwises, Intensive literature review of condensation inside smooth and enhanced tubes, Int. J. Heat Mass Transfer 52 (2009) 3409–3426.
[2] A.S. Dalkilic, S. Wongwises, Book chapter, "Condensation heat transfer in smooth and enhanced geometries — A review of 2010 literature", in the book "Refrigeration Systems, Design Technologies and Developments", ISBN 978-1-62417-230-4, Nova Publishers, 2013.
[3] S. Laohalertdecha, A.S. Dalkilic, S. Wongwises, A review on the heat-transfer performance and pressure-drop characteristics of various enhanced tubes, Int. J. Air Cond. Refrig. 20 (2012) 1–20.
[4] M. Balcilar, A. Celen, N. Kayaci, A.S. Dalkilic, S. Wongwises, A critical review on the numerical methods of two-phase flows, ASME 2012 International Mechanical Engineering Congress & Exposition (2012) November 9–15, USA, 2012.
[5] M. Balcilar, A.S. Dalkilic, S. Wongwises, Artificial neural networks (ANNs) techniques for the determination of condensation heat transfer characteristics during downward annular flow of R134a inside a vertical smooth tube, Int. Commun. Heat Mass Transfer 38 (2011) 75–84.

[6] M. Balcilar, A.S. Dalkilic, B. Bolat, S. Wongwises, Investigation of empirical correlations on the determination of condensation heat transfer characteristics using computational numerical methods during downward annular flow of R134a inside a vertical smooth tube, J. Mech. Sci. Technol. 25 (10) (2011) 1–20.
[7] O. Agra, H. Demir, S. Ozgur Atayilmaz, F. Kantas, A.S. Dalkilic, Numerical investigation of heat transfer and pressure drop in enhanced tubes, Int. Commun. Heat Mass Transfer 38 (2011) 1384–1391.
[8] M. Balcilar, A.S. Dalkilic, K. Aroonrat, S. Wongwises, Neural network based analyses for the determination of evaporation heat transfer characteristics during downward flow of R134a inside a vertical smooth and corrugated tube, Arab. J. Sci. Eng. (2013), http://dx.doi.org/10.1007/s13369-013-0659-1(Accepted for Publication-Article in press).
[9] M. Balcilar, A.S. Dalkilic, O. Agra, S.O. Atayilmaz, S. Wongwises, A correlation development for predicting the pressure drop of various refrigerants during condensation and evaporation in horizontal smooth and micro-fin tubes, Int. Commun. Heat Mass Transfer 39 (2012) 937–944.
[10] A.S. Dalkilic, S. Laohalertdecha, S. Wongwises, Effect of void fraction models on the two-phase friction factor of R134a during condensation in vertical downward flow in a smooth tube, Int. Commun. Heat Mass Transfer 35 (2008) 921–927.
[11] A.S. Dalkilic, S. Laohalertdecha, S. Wongwises, New experimental approach on the determination of condensation heat transfer coefficient using frictional pressure drop and void fraction models in a vertical tube, Energy Convers. Manag. 51 (2010) 2535–2547.
[12] A.S. Dalkilic, S. Yildiz, S. Wongwises, Experimental investigation of convective heat transfer coefficient during downward laminar flow condensation of R134a in a vertical smooth tube, Int. J. Heat Mass Transfer 52 (2009) 142–150.
[13] A.S. Dalkilic, S. Laohalertdecha, S. Wongwises, Experimental investigation on heat transfer coefficient of R134a during condensation in vertical downward flow at high mass flux in a smooth tube, Int. Commun. Heat Mass Transfer 36 (2009) 1036–1043.
[14] A.S. Dalkilic, S. Wongwises, Experimental study on the condensation heat transfer coefficients in high mass flux region in annular flow regime of HFC-134a inside the vertical smooth tube, Heat Transfer Eng. 32 (2011) 33–44.
[15] A.S. Dalkilic, I. Teke, S. Wongwises, Experimental analysis for the determination of the convective heat transfer coefficient by measuring pressure drop directly during annular condensation flow of R134a in a vertical smooth tube, Int. J. Heat Mass Transfer 54 (2011) 1008–1014.
[16] S. Saisorn, J. Kaew-On, S. Wongwises, Flow pattern and heat transfer characteristics of R-134a refrigerant during flow boiling in a horizontal circular mini-channel, Int. J. Heat Mass Transfer 53 (2010) 4023–4038.
[17] A.S. Dalkılıç, İ. Teke, S. Wongwises, Heat transfer enhancement during downward laminar flow condensation of R134a in vertical smooth and micro-fin tubes, Isi Bilimi Ve Teknigi Dergisi/J. Therm. Sci. Technol. 32 (2012) 19–31.
[18] A.S. Dalkilic, B. Kundu, S. Wongwises, An experimental investigation of the Reynolds analogy and its modifications applied to annular condensation laminar flow of R134a in a vertical tube, Arab. J. Sci. Eng. 38 (2013) 1493–1507.
[19] S. Laohalertdecha, S. Wongwises, Condensation heat transfer and flow characteristics of R-134a flowing through corrugated tubes, Int. J. Heat Mass Transfer 54 (2011) 2673–2682.
[20] K. Aroonrat, S. Wongwises, Evaporation heat transfer and friction characteristics of R-134a flowing downward in a vertical corrugated tube, Exp. Therm. Fluid Sci. 35 (2011) 20–28.
[21] S. Laohalerdecha, A.S. Dalkilic, S. Wongwises, Correlations for evaporation heat transfer coefficient and two-phase friction factor for R134a flowing through corrugated tubes, Int. Commun. Heat Mass Transfer 38 (2011) 1406–1413.
[22] A.S. Dalkilic, S. Laohalertdecha, S. Wongwises, Experimental research on the similarity of annular flow models and correlations for the condensation of R134a at high mass flux inside vertical and horizontal tubes, International Mechanical Engineering Congress and Exposition, ASME (2009), November 13–19, USA, 2009.

DESIGN OF A VERTICAL ANNULUS WITH MHD FLOW USING ENTROPY GENERATION ANALYSIS

by

Omid MAHIAN [a], Hakan F. OZTOP [b*], Ioan POP [c], Shohel MAHMUD [d], and Somchai WONGWISES [e]

[a] Department of Mechanical Engineering, Ferdowsi University of Mashhad, Mashhad, Iran
[b] Department of Mechanical Engineering, Technology Faculty, Firat University, Elazig, Turkey
[c] Faculty of Mathematics, University of Cluj, Cluj, Romania
[d] School of Engineering, University of Guelph, Guelph, Ont., Canada
[e] Fluid Mechanics, Thermal Engineering and Multiphase Flow Research Lab. (FUTURE), Department of Mechanical Engineering, Faculty of Engineering, King Mongkut´s University of Technology Thonburi, Bangmod, Bangkok, Thailand

Original scientific paper
DOI: 10.2298/TSCI121017038M

Optimal design of a heat exchanger is one of the concerns of energy conversion engineers. In the present work, the mixed convection flow between two vertical concentric pipes with constant heat flux at the boundaries and MHD flow effects is considered. To determine the optimal design for such a heat exchanger, at first, the momentum and energy equations are simplified and solved analytically. Next, using entropy generation analysis and cost analysis, the operational costs due to entropy generation are estimated. It is concluded that with an increase in the Hartmann number, the energy costs increase. In addition, for two small deviations from the base radius ratio ($\Pi = 2$) including $\Pi = 19$ and $\Pi = 2.1$, the changes in the energy cost are calculated. It is found that for $\Pi = 1.9$ the energy cost increases by 17.5% while for $\Pi = 2.1$ the energy cost is reduced by 13.6%.

Key words: *vertical annulus, magnetic field, mixed convection, entropy generation, cost analysis.*

Introduction

Mixed convection inside a vertical annulus in the presence of magnetic field has many practical applications. Some applications are found in industrial heat exchangers, micro electronic devices, cooling of nuclear reactors, petroleum equipment, and so forth. The optimal design of such equipments is necessary before the manufacturing process to reduce the operating and energy costs. Bejan's entropy generation minimization (EGM) method is a recognized approach to optimize the performance of thermal-fluid devices. This method also can be used to determine the optimum heat exchanger dimensions [1].

Generally, the entropy generation problems are non-linear. Therefore, a helpful way to study of entropy generation through a process with complex equations is the simplification of the governing equations with reasonable assumptions to obtain analytical solutions. In this context, Yilbas [2] examined the entropy generation for a rotating outer cylinder and differentially heated isothermal boundary condition with neglecting the irreversibility induced by viscous dissipation. The author [2] assumed a linear velocity profile in his work. Mahmud and Fraser [3, 4]

* Corresponding author; e-mail: hfoztopl@gmail.com

solved analytically the dimensionless entropy generation equation for the flow and heat transfer between two rotating cylinders with isoflux and isothermal boundary conditions. Tasnim and Mahmud [5] considered the fully developed laminar and mixed convection flow in a vertical annulus with circular cross-section and obtained analytical expressions for entropy generation in the annulus. They obtained the optimum radius ratio, at which the entropy generation is minimized. Tasnim and Mahmud [6] considered a fluid with temperature-dependent viscosity and developed their previous work [5]. Mirzazadeh *et al.* [7] studied the entropy generation due to flow and heat conduction of a non-linear viscoelastic fluid between concentric rotating cylinders. Mahian *et al.* [8] investigated analytically the entropy generation between two rotating cylinders using nanofluids with different volume fractions and isoflux boundary conditions. In another work, Mahian *et al.* [9] presented an analytical solution of the second law analysis between two rotating cylinders using nanofluids. They studied the effects of uncertainties in the models presented for thermophysical properties of nanofluids on entropy generation.

The study of flow and heat transfer in a closed cavity or a channel in the presence of MHD flow is important because of engineering applications such as MHD micropumps, micro electronic devices, electronic packages, cooling of nuclear reactors, and MHD marine propulsion [10]. Here, several works in which the effects of MHD flow on entropy generation for various flows and geometries are investigated, briefly have been reviewed. Salas *et al.* [11] and Ibanez *et al.* [12] analysed the second law for MHD induction devices, such as electromagnetic pumps, and electrical generators. Mahmud *et al.* [13] examined the entropy generation due to mixed convection in a channel made of two parallel plates. Later on, Tasnim *et al*. [14] solved the same problem using porous media. Mahmud and Fraser [15] analytically investigated the entropy generation due to mixed convection-radiation interaction in a vertical porous channel in the presence of MHD flow. In another paper, Mahmud and Fraser [16] studied the problem of entropy generation in a porous cavity with laminar natural convection and MHD flow. Mahmud and Fraser [17] presented a general equation for entropy generation for a single-plate thermoacoustic system, which is subjected to a constant magnetic field. Ibanez and Cuevas [18] considered a stationary buoyant MHD flow of a liquid metal immersed in a MHD flow through a vertical rectangular duct. They obtained the optimum conductance ratio of the wall in which the entropy generation is minimized. The effects of slip and Joule dissipation on the entropy generation in a single rotating disk in the presence of MHD flow are investigated by Arikoglu *et al.* [19]. Aiboud and Saouli [20] applied the analysis of entropy generation for a viscoelastic MHD flow over a stretching surface. Recently, Mahian *et al.* [21] investigated the entropy generation between two isothermal rotating cylinders in the presence of magnetic field. They revealed that the entropy generation increases with an increase in MHD flow. Mahian *et al.* [22] studied the effects of nanofluids on entropy generation between two cylinders in the presence of MHD flow. They obtained the conditions in which using nanofluids results in a decrease in entropy generation.

In the present work, the energy costs of a vertical annulus heat exchanger with MHD flow and constant heat flux at the boundaries in different conditions are determined by using Bejan' EGM method.

Mathematical modelling

Analysis of the First law of thermodynamics

A steady, laminar and fully developed mixed convection flow of a Newtonian, incompressible fluid is considered where the fluid enters a vertical annulus with length of L and inlet

velocity U_0 and an inlet temperature T_0. In practical situations, a differential pressure transmitter can be installed to measure the pressure losses through the heat exchanger. A constant heat flux is imposed on the boundary of the inner pipe. The cooling fluid flows inside the annulus and cools the surface of the inner pipe and a portion of the heat is dissipated to the surrounding based on the energy balance. The heat exchanger is subjected to a transverse magnetic field with constant strength of B_0. The schematic of problem is indicated in fig. 1.

The governing equations for 2-D flow in the heat exchanger can be written in general as:

– continuity

$$\frac{\partial V_\mathrm{r}}{\partial r}+\frac{V_\mathrm{r}}{r}+\frac{\partial V_\mathrm{z}}{\partial z}=0 \tag{1}$$

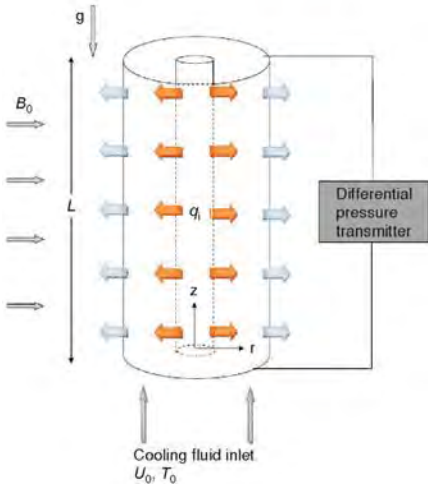

Figure 1. Schematic of heat exchanger considered in the study

– r-momentum

$$\rho\left(V_\mathrm{r}\frac{\partial V_\mathrm{r}}{\partial r}+V_z\frac{\partial V_\mathrm{r}}{\partial z}\right)=-\frac{\partial P}{\partial r}+\mu\left(\frac{\partial^2 V_\mathrm{r}}{\partial r^2}+\frac{1}{r}\frac{\partial V_\mathrm{r}}{\partial r}-\frac{V_\mathrm{r}}{r^2}+\frac{\partial^2 V_\mathrm{r}}{\partial z^2}\right) \tag{2}$$

– z-momentum

$$\rho\left(V_\mathrm{r}\frac{\partial V_\mathrm{z}}{\partial r}+V_z\frac{\partial V_\mathrm{z}}{\partial z}\right)=-\frac{\partial P}{\partial z}+\mu\left(\frac{\partial^2 V_\mathrm{z}}{\partial r^2}+\frac{1}{r}\frac{\partial V_\mathrm{z}}{\partial r}+\frac{\partial^2 V_\mathrm{z}}{\partial z^2}\right)-\rho\mathrm{g}-\sigma B_0^2 V_\mathrm{z} \tag{3}$$

– energy

$$\rho C_p\left(V_r\frac{\partial T}{\partial r}+V_z\frac{\partial T}{\partial z}\right)=k\left[\frac{1}{r}\frac{\partial}{\partial r}\left(r\frac{\partial T}{\partial r}\right)+\frac{\partial^2 T}{\partial z^2}\right]+\sigma B_0^2 V_z^2 \tag{4}$$

As mentioned before, the flow is assumed as hydrodynamically and thermally fully developed; hence, using the order of magnitude the radial velocity (V_r) can be neglected in comparison with the axial velocity (V_z). With this assumption, the continuity equation reduces to $\partial V_\mathrm{z}/\partial \mathrm{z} = 0$. Therefore, using the Boussinesq approximation in the buoyancy term, and neglecting the axial effects (see refs. [5, 6]), the simplified dimensionless equations can be expressed as:

$$\frac{\partial^2 U}{\partial R^2}+\frac{1}{R}\frac{\partial U}{\partial R}=-\frac{\mathrm{Gr}}{\mathrm{Re}}\theta+M^2U+\frac{\partial P^*}{\partial Z} \tag{5}$$

$$\frac{\partial^2 \theta}{\partial R^2}+\frac{1}{R}\frac{\partial \theta}{\partial R}=0 \tag{6}$$

where the dimensionless parameters are defined as:

$$R=\frac{r}{r_\mathrm{o}},\quad U=\frac{V_\mathrm{z}}{U_0},\quad \mathrm{Re}=\frac{U_0 r_\mathrm{o}}{\upsilon},\quad \lambda=\frac{r_\mathrm{i}}{r_\mathrm{o}},\quad P^*=\frac{P}{U_0\mu}r_\mathrm{o},\quad Z=\frac{z}{r_\mathrm{o}},\quad M=\sqrt{\frac{\sigma}{\mu}}B_0 r_0 \tag{7}$$

In the above relations M is the Hartmann number, and σ – the electrical conductivity of fluid. The subscripts of *i* and *o* indicate the characteristics of inner and outer pipes, respectively. The Grashof number and dimensionless temperature are defined as:

$$\mathrm{Gr} = \frac{g\beta q_\mathrm{i} r_o^4}{k\upsilon^2}, \quad \theta = \frac{T - T_0}{\frac{q_\mathrm{i} r_\mathrm{o}}{k}} \tag{8}$$

The velocity boundary conditions with no slip assumption are written as:

$$\begin{aligned} R = \lambda &\Rightarrow U = 0 \\ R = 1 &\Rightarrow U = 0 \end{aligned} \tag{9}$$

The thermal boundary conditions are given by:

$$\begin{aligned} R = \lambda &\Rightarrow \frac{\partial\theta}{\partial R} = -1 \\ R = 1 &\Rightarrow \frac{\partial\theta}{\partial R} = f(q_\mathrm{i}) \end{aligned} \tag{10}$$

Analysis of the Second law of thermodynamics

Entropy generation rate in the presence of MHD flow can be written as:

$$\dot{S}_{gen}^{m} = \frac{k}{T_0^2}[\nabla T]^2 + \frac{\mu}{T_0}\phi + \frac{1}{T_0}[(J - QV)(E + V \times B)] \tag{11}$$

where

$$J = \sigma(E + V \times B) \tag{12}$$

In the above equations, ϕ is viscous dissipation, J – the electric current, Q – the electric charge density, V – the velocity vector, E – the electric field, and B – the magnetic induction. Neglecting QV in comparison with J and disregarding E in comparison with $V \times B$, the relation (11) reduces to the:

$$\dot{S}_{gen}''' = \frac{k}{T_0^2}\left(\frac{\partial T}{\partial r}\right)^2 + \frac{\mu}{T_0}\left(\frac{\partial V_z}{\partial r}\right)^2 + \frac{\sigma B_0^2}{T_0}V_z^2 \tag{13}$$

The dimensionless entropy generation rate is determined as:

$$N_\mathrm{S} = \frac{\dot{S}_{gen}'''}{\frac{\mu U_0^2}{T_0 r_o^2}} = \frac{\Omega}{\mathrm{Br}}\left(\frac{\partial\theta}{\partial R}\right)^2 + \left(\frac{\partial U}{\partial R}\right)^2 + M^2U^2 = N_\mathrm{H} + N_\mathrm{F} + N_\mathrm{M} \tag{14}$$

where N_H, N_F, and N_M on the right hand of the equation are the irreversibilities due to heat transfer, fluid friction, and magnetic field, respectively. Also, the Brinkman number (Br) and the parameter Ω are defined as:

$$\mathrm{Br} = \frac{U_0^2\mu}{q_\mathrm{i} r_\mathrm{o}}, \quad \Omega = \frac{q_\mathrm{i} r_\mathrm{o}}{kT_0} \tag{15}$$

The irreversibility distribution can be obtained using the definition of Bejan number (Be) that is the ratio of entropy generation due to heat transfer to the overall entropy generation as [23]:

$$\mathrm{Be} = \frac{N_\mathrm{H}}{N_\mathrm{H} + N_\mathrm{F} + N_\mathrm{M}} \tag{16}$$

The average volumetric entropy generation number is given by:

$$N_{\mathrm{S,\,ave}} = \frac{1}{\forall}\int_{\forall} N_{\mathrm{S}}\mathrm{d}\forall \tag{17}$$

Solution of the problem

Velocity and temperature fields

The eqs. (5) and (6) are coupled *via* the buoyancy term in the momentum equation.

Therefore, first, the energy equation must be solved. The solution of the energy equation is:

$$\theta(R) = -\lambda \ln R + C \tag{18}$$

where C is the constant of integration. In this stage, the constant C cannot be obtained because of the isoflux boundary conditions. The velocity field is obtained using the temperature distribution and solving the related differential equation as:

$$U(R) = \Gamma_5 K_0(MR) + \Gamma_6 I_0(MR) - \frac{\left(\dfrac{\partial P^*}{\partial Z}\right) + \left(\dfrac{\mathrm{Gr}}{\mathrm{Re}}\right)\lambda \ln R}{M^2} + \frac{\left(\dfrac{\mathrm{Gr}}{\mathrm{Re}}\right)}{M^2} C \tag{19}$$

where the constants Γ_5 and Γ_6 are equal to:

$$\Gamma_5 = -\frac{\dfrac{\mathrm{Gr}}{\mathrm{Re}} C[I_0(M\lambda) - I_0(M)] - \dfrac{\partial P^*}{\partial Z}[I_0(M\lambda) - I_0(M)] + \dfrac{\mathrm{Gr}}{\mathrm{Re}}\lambda \ln \lambda I_0(M)}{M^2[K_0(M)I_0(M\lambda) - K_0(M\lambda)I_0(M)]}$$

$$\Gamma_6 = -\frac{\dfrac{\mathrm{Gr}}{\mathrm{Re}} C[K_0(M\lambda) - K_0(M)] - \dfrac{\partial P^*}{\partial Z}[K_0(M\lambda) - K_0(M)] + \dfrac{\mathrm{Gr}}{\mathrm{Re}}\lambda \ln K_0(M)}{M^2[K_0(M)I_0(M\lambda) - K_0(M\lambda)I_0(M)]} \tag{20}$$

The unknown constant C can be determined using the continuity equation that is:

$$\int_{r_i}^{r_o} \rho V_z(z) 2\pi r \mathrm{d}r = \rho U_0[\pi(r_0^2 - r_i^2)] \tag{21}$$

which in dimensionless form is:

$$2\int_{\lambda}^{1} U(R) R \mathrm{d}R = 1 - \lambda^2 \tag{22}$$

By substituting the velocity profile from eq. (19) into the above relation and solving the equation, the constant C is calculated. The expression obtained for C is long, therefore to save the space, the constant C is not presented here, but it is a function of involving parameters in the problem as:

$$C = h\left(M, \lambda, \frac{\mathrm{Gr}}{\mathrm{Re}}, \frac{\partial P^*}{\partial Z}\right) \tag{23}$$

Entropy generation

The local entropy generation is obtained using Eq. (14) and the velocity and temperature distributions as:

$$N_S = \frac{\Omega}{\mathrm{Br}}\left(\frac{-\lambda}{R}\right)^2 + \left(-\Gamma_5 MK_1(MR) + \Gamma_6 MI_1(MR) - \frac{\lambda\left(\frac{\mathrm{Gr}}{\mathrm{Re}}\right)^2}{M^2 R}\right) + \\ + M^2\left[\Gamma_5 K_0(MR) + \Gamma_6 I_0(MR) - \frac{\frac{\partial P^*}{\partial Z} + \frac{\mathrm{Gr}}{\mathrm{Re}}\lambda\ln(R)}{M^2} + \frac{\frac{\mathrm{Gr}}{\mathrm{Re}}}{M^2}C\right]^2 \tag{24}$$

The average volumetric entropy generation number is calculated based on eq. (17) as:

$$N_{\mathrm{S,\,ave}} = \frac{2}{1-\lambda^2}\int_{\lambda}^{1} N_{\mathrm{S}} R\,\mathrm{d}R \tag{25}$$

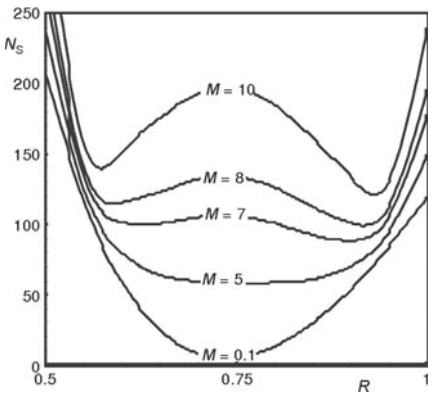

Figure 2. Effects of MHD flow on entropy generation number for Gr/Re = 10 and Ω/Br = 10

Results and discussion

Local entropy generation

The effects of Hartmann number on local entropy generation for Gr/Re =10, dP^*/dZ = 0.1 and Ω/Br = 10 are shown in fig. 2. It is seen that an increase in the Hartmann number leads to an increase in entropy generation number. The entropy generation number is greater near the walls (especially near the inner wall) due to higher gradients of temperature and velocity. The effects of parameter Gr/Re on the entropy generation and Bejan numbers for M = 1 and Ω/Br = 20 are displayed in fig. 3. It is observed that the entropy generation number has an un-

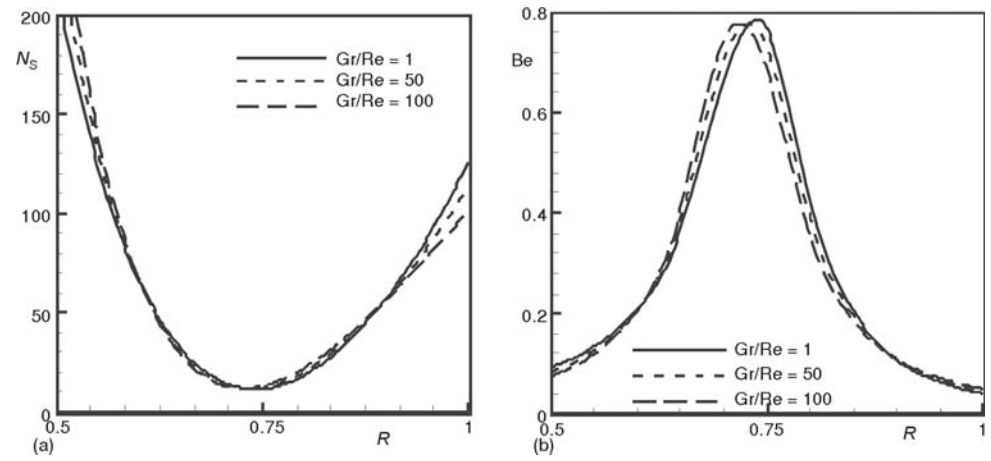

Figure 3. Effects of Gr/ Re on (a) entropy generation and (b) Bejan numbers for M =1 and Ω/Br = 20

predictable trend in the gap. The interactions among the viscous effects near the walls, the reduction of heat flux along the radial distance and buoyancy forces make this irregular behaviour. The effects of Gr/Re on the Bejan number are drawn in fig. 3(b). It is found that the Bejan number is approximately maximized in the middle of the annulus. At this point, the contribution of viscous effects to entropy generation is lowest. This maximum point moves towards the outer cylinder with a decrease in the force of natural convection and heat flux.

Design and cost analysis

In this section, by using the Bejan's EGM method and cost analysis the operational costs due to entropy generation in the heat exchanger at different conditions are determined. The operational cost due to entropy generation is reduced by optimal design and hence leads to the most saving in energy consumption cost.

Sahin *et al.* [24] calculated the total cost of irreversibility for the flow in a pipe in the absence of magnetic field as:

$$\dot{C} = C_{\mathrm{H}} T_0 (\dot{S}_{\mathrm{gen}})_{\mathrm{H}} + C_{\mathrm{F}} T_0 (\dot{S}_{\mathrm{gen}})_{\mathrm{F}} \tag{26}$$

In the above relation, $\dot{C}$ is the total cost of irreversibility (\$ per day), C_{H} – the unit cost of irreversibility due to heat transfer, C_{F} – the unit cost of irreversibility due to fluid friction, $\dot{S}_{\mathrm{gen}}$ – the entropy generation. In this work, eq. (26) is developed to the following relation in the presence of MHD flow:

$$\dot{C} = C_{\mathrm{H}} T_0 (\dot{S}_{\mathrm{gen}})_{\mathrm{H}} + C_{\mathrm{F}} T_0 (\dot{S}_{\mathrm{gen}})_{\mathrm{F}} + C_{\mathrm{M}} T_0 (\dot{S}_{\mathrm{gen}})_{\mathrm{M}} \tag{27}$$

Here, it is assumed that $C_{\mathrm{E}} = C_{\mathrm{H}} = C_{\mathrm{F}} = C_{\mathrm{M}} = 0.2$, where C_{E} is the unit cost of irreversibility in the system. Therefore, the above relation for the heat exchanger with length of 1 m can be rewritten as:

$$\dot{C} = C_{\mathrm{E}} T_0 \left(\frac{\mu U_0^2}{T_0 r_0^2} \right) \forall N_{\mathrm{S,\,ave}} = \pi C_{\mathrm{E}} \mu U_0^2 (1 - \lambda^2) N_{\mathrm{S,ave}} \tag{28}$$

The above relation in terms of mass flow rate and (inverse of λ) can be expressed as:

$$\dot{C} = \frac{C_{\mathrm{E}} \dot{m}^2 \upsilon \Pi^2}{\pi \rho r_o^4 (\Pi^2 - 1)} N_{\mathrm{S,\,ave}} \tag{29}$$

where ρ and υ are density viscosity and kinematic viscosity of the working fluid at the inlet temperature. If the base radius ratio is 2 ($\Pi = 2$), using the relation (30) one can calculate the amount of changes in energy cost, $\dot{C}_{\mathrm{r}}$, in comparison with another radius ratio:

$$\dot{C}_{\mathrm{r}} = \frac{\dot{C})_{\Pi=2} - \dot{C})_{\Pi}}{\dot{C})_{\Pi=2}} \cdot 100 \tag{30}$$

Now as a numerical example, the engine oil with mass flow rate of 0.85 kg/s is considered as the cooling fluid in the heat exchanger where the outer radius is 1. 5 cm.

The total cost due to irreversibility, $\dot{C}$ (\$/ day), is presented in fig. 4 for Gr/Re = 0.1 and Gr/Re = 50, three different Hartmann numbers and the radius ratio between 1.5 and 6, where it is assumed the system works 10 hours in a day. It is observed that the total cost of irreversibility for the system in one day is approximately 0.5-10 \$ depends on the radius ratio of the heat exchanger. The total cost of irreversibility increases with increases in the Hartmann number because the average volumetric entropy generation number increases with the increase of *M*. It is also seen that with an increase in the radius ratio, the total costs due to entropy generation de-

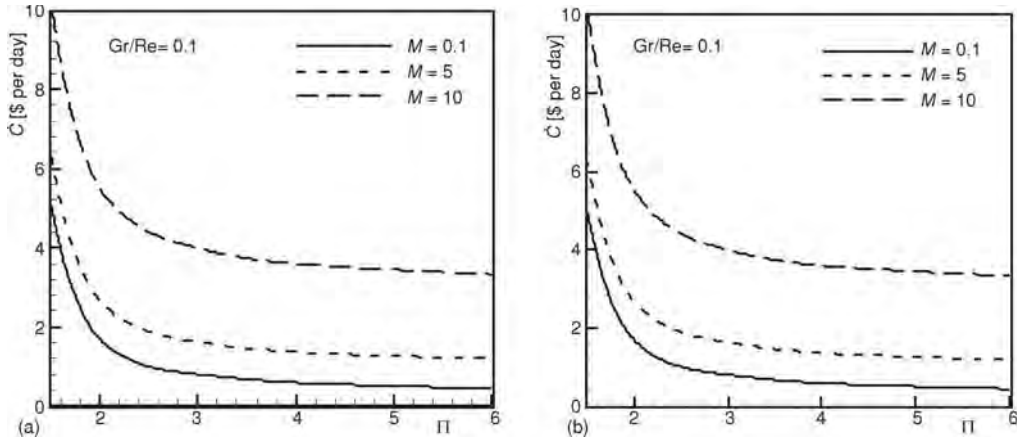

Figure 4. Effects of MHD flow and Gr/Re on total cost of irreversibility; (a) Gr/Re = 0.1, (b) Gr/Re = 50

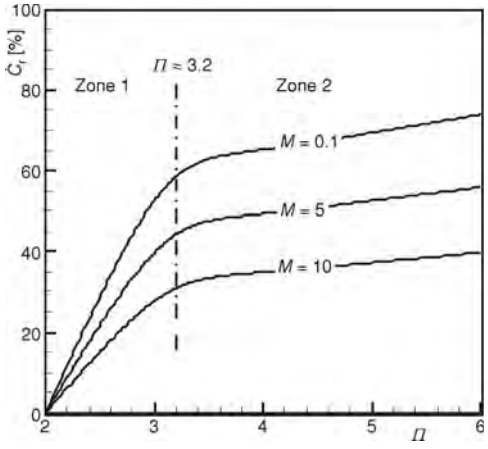

Figure 5. Effects of Hartmann number and Gr/Re on savings in operational costs

crease. This happens because the gradients of temperature and especially velocity with increasing the radius ratio are increased. From fig. 4, it is also observed that the parameter of Gr/Re has no visible effect on the total costs. Of course, with the increase of Gr/Re from 0.1 to 50, the total costs increase slightly.

Figure 5 shows the amount of changes in energy cost, $\dot{C}_r$, for different values of Hartmann number, $2 \le \Pi \le 6$ and Gr/Re = 50. The graph can be divided into two zones as indicated in the figure. In the first zone ($\Pi \le 3.2$), the amount of $\dot{C}_r$ increases rapidly, whereas for $\Pi > 3.2$ the rate of increases in $\dot{C}_r$ is reduced. As shown, $\dot{C}_r$ is higher in magnitude for smaller magnetic fields. It is also concluded that where the radius ratio increases from 2 to 6, the savings in energy cost are approximately 74%, 56%, and 40% for the Hartmann numbers of 0.1, 5, and 10, respectively.

Finally, the effects of a small deviation in the radius ratio are investigated. This deviation may be produced in the manufacturing process. If the base radius ratio is 2, the effects of a deviation of ±0.1 in the radius ratio on the amount of $\dot{C}_r$ are investigated. It is found, for $\Pi = 1.9$ and $M = 0.1$, the amount of $\dot{C}_r$ is –17.5%. The negative sign means that where the radius ratio decreases from 2 to 1.9, the total costs due to entropy generation increase by 17.5%. On the other hand, for $\Pi = 2.1$, it is found that the costs decrease between 6.3-13.6% depend on the Hartmann number. It should be noted that the costs required to produce the pipes in different sizes and the changes in costs due to heat transfer enhancements are not considered in this study.

Conclusions

An entropy generation analysis is performed for flow and heat transfer between two vertical cylinders subjected to constant heat flux and MHD flow. The equations of momentum

and energy in cylindrical co-ordinates are simplified and solved analytically. The results are presented for different values of Hartmann number and a flow parameter Gr/Re. The Bejan's EGM (entropy generation minimization) method and cost analysis are used to find the effects of different radius ratios on the total costs due to irreversibilities in the system where engine oil is considered as the working fluid. It is perceived that with an increase in the Hartmann number, the energy costs increase while the total cost does not change with increases in Gr/Re. In addition, for two small deviations from the base radius ratio ($\Pi = 2$) including $\Pi = 1.9$ and $\Pi = 2.1$, the changes in the energy cost are estimated. It is found that for $\Pi = 1.9$ the energy cost increases by 17.5% while for $\Pi = 2.1$the energy consumption cost reduces by 13.6%.

Acknowledgment

Omid Mahian, Hakan F. Oztop, Ioan Pop, Shohel Mahmud, and Somchai Wongwises would like to thank the Thailand Research Fund and the National Research University Project for the support.

Nomenclature

Be – Bejan number (= $N_H/N_H + N_F + N_M$), [–]
Br – Brinkman number (= $U_0^2\mu/q_i r_0$) , [–]
B_0 – constant magnetic flux density, [T]
C – constant of integration in energy equation, [–]
C_E – unit cost of irreversibility, [\$W^{-1}h^{-1}]
C_H – unit cost of irreversibility due to heat transfer, [\$W^{-1}h^{-1}]
C_F – unit cost of irreversibility due to fluid friction, [\$W^{-1}h^{-1}]
C_M – unit cost of irreversibility due to MHD flow, [\$W^{-1}h^{-1}]
$\dot{C}$ – total cost of irreversibility, [\$ per day]
$\dot{C}_r$ – amount of changes in energy cost, [%]
E – electric field , [Vm^{-1}]
g – constant of gravity, [m^{2}s^{-1}]
Gr – Grashof number, (= $g\beta q_i r_o^4/k\upsilon^2$), [–]
J – electric current , [A]
k – thermal conductivity, [Wm^{-1}K^{-1}]
M – Hartmann number, (= $(\sigma/\mu)^{1/2}B_0 r_0$), [–]
N_F – entropy generation number, fluid friction, [–]
N_H – entropy generation number, heat transfer, [–]
N_M – entropy generation number, MHD flow, [–]
N_S – entropy generation number, total, [–]
P – pressure [Pa]
P^* – dimensionless pressure (= $Pr_0/\mu U_0$), [–]
Q – electric charge density, [Asm^{-3}]
R – dimensionless radius (= r/r_0), [–]
r – radius,[m]
S_G – entropy generation rate, [Wm^{-3}K^{-1}]
T – temperature, [K]
T_0 – inlet temperature, [K]
U – dimensionless velocity, [ms^{-1}]
U_0 – velocity inlet, [ms^{-1}]
$\forall$ – volume, [m^3]

Greek symbols

β – thermal expansion coefficient,[K^{-1}]
Γn – constants, $n = 1, 2,\ldots$
θ – dimensionless temperature, [–]
λ – radius ratio (= r_i/r_o)
μ – dynamic viscosity, [kgm^{-1}s^{-1}]
υ – kinematic viscosity, [m^{2}s^{-1}]
Π – radius ratio, (= r_o/r_i)
ρ – density, [kgm^{-3}]
Ω – dimensionless temperature difference, [–]

Subscript

i – value at the inner cylinder
o – value at the outer cylinder

References

[1] Dagtekin, I., *et al*., An Analysis of Entropy Generation through a Circular Duct with Different Shaped Longitudinal Fins for Laminar Flow, *International Journal of Heat and Mass Transfer, 48* (2005), pp. 171-181
[2] Yilbas, B. S., Entropy Analysis of Concentric Annuli with Rotating outer Cylinder, *Int. J. Exergy, 1* (2001), pp. 60-66
[3] Mahmud, S., Fraser, R. A., Second Law Analysis of Heat Transfer and Fluid Flow Inside a Cylindrical Annular Space, *Int. J. Exergy, 2* (2002), pp. 322-329

[4] Mahmud, S., Fraser, R. A., Analysis of Entropy Generation Inside Concentric Cylindrical Annuli with Relative Rotation, *Int. J. Thermal Sciences, 42* (2003), pp. 513-521
[5] Tasnim, S. H., Mahmud, S., Mixed Convection and Entropy Generation in a Vertical Annular Space, *Int. J. Exergy, 2* (2002), pp. 373-379
[6] Tasnim, S. H., Mahmud, S., Entropy Generation in a Vertical Concentric Channel with Temperature Dependent Viscosity, *Int. Commun. Heat Mass Transfer, 29* (2002), pp. 907-918
[7] Mirzazadeh, M., *et al*., Entropy Analysis for Non-Linear Viscoelastic Fluid in Concentric Rotating Cylinders, *Int. J. Thermal Sciences, 47* (2008), pp. 1701-1711
[8] Mahian, O., *et al*., Analysis of Entropy Generation between Co-Rotating Cylinders Using Nanofluids, *Energy, 44* (2012), pp. 438-446
[9] Mahian , O., *et al.*, Effect of Uncertainties in Physical Properties on Entropy Generation between Two Rotating Cylinders with Nanofluids, *ASME J. Heat Transfer,134* (2012), 101704
[10] Jery, A. E., *et al*., Effect of an External Oriented Magnetic Field on Entropy Generation in Natural Convection, *Entropy, 12* (2010), pp. 1391-1417
[11] Salas, H., *et al*., Entropy Generation Analysis of Magnetohydrodynamic Induction Devices, *J. Phys D: Appl Phys., 32* (1999), pp. 2605-2608
[12] Ibanez, G., *et al*., Optimization Analysis of an Alternate Magnetohydrodynamic Generator, *Energy Conversion and Management, 43* (2002), pp. 1757-1771
[13] Mahmud, S., *et al*., Thermodynamic Analysis of Mixed Convection in a Channel with Transverse Hydromagnetic Effect, *Int. J. Thermal Sci., 42* (2003), pp. 731-740
[14] Tasnim, S. H., *et al*., Entropy Generation in a Porous Channel with Hydromagnetic Effect, *Energy, 2* (2002), pp. 300-308
[15] Mahmud, S., Fraser, R. A., Mixed Convection-Radiation Interaction in a Vertical Porous Channel: Entropy Generation, *Energy, 28* (2003), pp. 1557-1577
[16] Mahmud, S., Fraser, R. A., Magnetohydrodynamic Free Convection and Entropy Generation in a Square Porous Cavity, *Int. J. Heat Mass Transfer, 47* (2004), pp. 3245-3256
[17] Mahmud, S., Fraser, R. A., The Thermagoustic Irreversibility for a Single-Plate Thermoacoustic System, *Int. J. Heat Mass Transfer, 49* (2006), pp. 3448-3461
[18] Ibanez, G., Cuevas, S., Optimum Wall Conductance Ratio in Magnetoconvective Flow in a Long Vertical Rectangular Duct, *Int. J. Thermal Sci., 47* (2008), pp. 1012-1019
[19] Arikoglu, A., *et al*., Effect of Slip on Entropy Generation in a Single Rotating Disk in MHD Flow, *Appl Energy, 85* (2008), pp. 1225-1236
[20] AIboud, S., Saouli, S., Entropy Analysis for Viscoelastic Magnetohydrodynamic Flow over a Stretching Surface, *Int. J. Non-Linear Mech, 45* (2010), pp. 482-489
[21] Mahian, O., *et al*., Analysis of First and Second Laws of Thermodynamics between Two Isothermal Cylinders with Relative Rotation in the Presence of MHD Flow, *Int. J. Heat Mass Transfer, 55* (2012), pp. 4808-4816
[22] Mahian, O., *et al*., Entropy Generation between Two Rotating Cylinders in the Presence of MHD Flow Using Nanofluids, *Journal of Thermophysics and Heat Transfer, 27* (2013), pp. 161-169
[23] Paoletti, S., *et al*., Calculation of Exergetic Losses in Compact Heat Exchanger Passages, *ASME AES, 10* (1980), pp. 21-29
[24] Sahin, A. Z., *et al*., Effect of Fouling on Operational Cost in Pipe Flow Due to Entropy Generation, *Energy Conversion & Management, 41* (2000), pp. 1485-1496

Paper submitted: October 17, 2012
Paper revised: April 10, 2013
Paper accepted: April 10, 2013

Dispersion of ZnO Nanoparticles in a Mixture of Ethylene Glycol–Water, Exploration of Temperature-Dependent Density, and Sensitivity Analysis

Omid Mahian, Ali Kianifar & Somchai Wongwises

Journal of Cluster Science
Including Nanoclusters and Nanoparticles

ISSN 1040-7278
Volume 24
Number 4

J Clust Sci (2013) 24:1103-1114
DOI 10.1007/s10876-013-0601-4

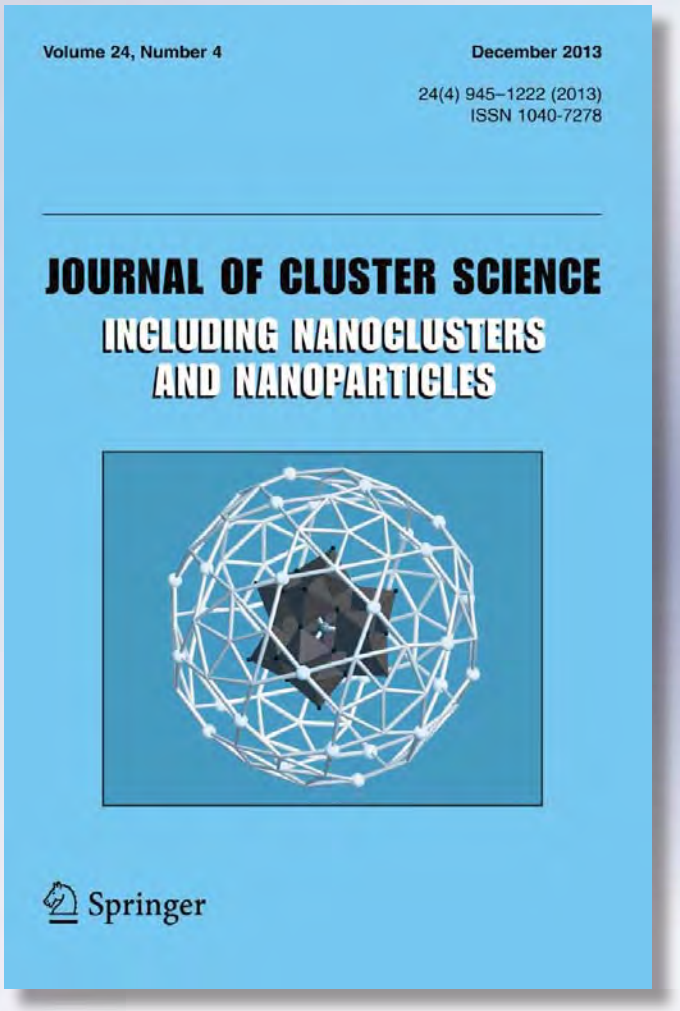

Springer

J Clust Sci (2013) 24:1103–1114
DOI 10.1007/s10876-013-0601-4

ORIGINAL PAPER

Dispersion of ZnO Nanoparticles in a Mixture of Ethylene Glycol–Water, Exploration of Temperature-Dependent Density, and Sensitivity Analysis

Omid Mahian · Ali Kianifar · Somchai Wongwises

Received: 18 April 2013 / Published online: 11 June 2013

Abstract Experimental studies are performed to evaluate the stability of zinc oxide (ZnO) nanoparticles suspended in a mixture of ethylene glycol and water with weight ratio of 40–60 as the base fluid. Different methods have been employed to disperse ZnO nanoparticles. It is found that using Gum Arabic leads to clustering and settle the nanoparticles. Also, the use of DI ammonium hydrogen citrate with weight ratio 1:1 (surfactant:nanoparticles) gives the acceptable stability. The density of nanofluids is measured and the results are compared with theoretical results. A helpful correlation for the measured densities of the stable nanofluids in a temperature range of 25–40 °C is presented which can used in practical applications. Finally based on the correlation a sensitivity analysis has been done. It is found that at higher temperatures the density is more sensitive to the increases in volume fraction.

Keywords Dispersion · Stability · ZnO nanoparticles · Surfactant · Density · Sensitivity analysis

Introduction

Nanometer-sized particles suspended in liquids such as water, glycol, ethylene glycol, and engine oil are called "Nanofluids" [1]. Nanofluids have attracted special attention in many fields of science and technology such as solar energy [2], medical

O. Mahian (✉) · A. Kianifar
Department of Mechanical Engineering, Ferdowsi University of Mashhad, Mashhad, Iran
e-mail: omid.mahian@gmail.com

S. Wongwises (✉)
Fluid Mechanics, Thermal Engineering and Multiphase Flow Research Laboratory (FUTURE), Department of Mechanical Engineering, Faculty of Engineering, King Mongkut's University of Technology Thonburi, Bangmod, Bangkok 10140, Thailand
e-mail: somchai.won@kmutt.ac.th

applications, chemical reactions [3], cooling of electronic devices, and thermal storage materials [4].

The first step in using nanofluids in various applications is the preparation of a stable nanofluid. The method of preparation of nanofluids has a significant effect on the properties of these suspensions [5]. Some of the techniques such as adding a suitable surfactant or sonication are used to increase the stability time of these suspensions. In this study, nanofluids containing ZnO nanoparticles have been investigated where the base fluid is a mixture of water and ethylene glycol. Here, the previous studies concerning the nanofluids containing ZnO nanoparticles are reviewed.

Vajjha et al. [6] measured the density of ZnO nanoparticles suspended in a mixture of EG/water (60:40) at a temperature range of 0–50 °C. They found that with an increase in the volume fraction, the difference between the measured data and the theoretical results increases. Yu et al. [7] prepared ZnO nanoparticles suspended in ethylene glycol without any surfactant. They measured the thermal conductivity and viscosity of the nanofluids for volume fractions up to 5 %. Neogy and Raychaudhuri [8] investigated the effects of temperature and volume fraction on the heat transport factor (that is the product of thermal conductivity and heat capacity) at different frequencies for ZnO suspensions.

Chung et al. [9] prepared ZnO/water nanofluids with different methods of sonication. They noted that ZnO nanoparticles could be dispersed in the water with a fragmentation process well.

Raykar and Singh [10] used Acetylacetone (acac) as a surfactant to obtain a stable suspension with volume fractions up to 0.5 % of water and ZnO nanoparticles. Next, they measured thermal conductivity and viscosity of the nanofluids.

Jalal et al. [11] after synthesizing of ZnO nanoparticles with the aid of microwave decomposition, dispersed the nanoparticles in glycerol using ammonium citrate as the surfactant. Then, the authors investigated the antibacterial properties of the nanofluids. In another work, Moosavi et al. [12] prepared suspensions of ZnO nanoparticles dispersed in two base fluids including glycerol and ethylene glycol using ammonium citrate as the surfactant. They measured thermal conductivity, viscosity and surface tension of the nanofluids for volume fractions by 3 %. In references of [11] and [12], the weight ratio of surfactant to nanoparticles is 1:1. Singh [13] synthesized ZnO nanoparticles and prepared nanofluids with volume fractions up to 0.5 % to study the thermal conductivity. Lee et al. [14] prepared ZnO/EG nanofluids by one step pulsed wire evaporation (PWE) approach without any surfactant. They measured the thermal conductivity of nanofluids with volume fraction up to 5.5 %.

Singh et al. [15] dispersed ZnO nanoparticles in polyvinyl alcohol and used sonication to have a stable nanofluid. Kole and Dey [16] prepared a solution of ZnO nanoparticles and ethylene glycol under 60 h sonication and without any surfactant. They measured the thermal conductivity of the nanofluids with volume fractions up to 3.75 %, while the nanofluids exhibit acceptable stability.

Later on, Kole and Dey [17] investigated the effects of sonication time (up to 100 h) on the effective thermal conductivity of ZnO/EG nanofluids. They showed

that there is an optimum sonication time in which the thermal conductivity is optimized. Lee et al. [18] prepared ZnO/EG nanofluids with volume fractions up to 5.5 % by the pulsed wire evaporation method. They concluded that all of the nanofluids show a Newtonian behaviour. Colangelo et al. [19] measured the thermal conductivity of ZnO nanoparticles suspended in Diathermic oil. They used no surfactant for stability of the nanofluids. The maximum particle loading for ZnO nanoparticles is 2 %. Zafarani-Moattar and Cegincara [20] measured the density and viscosity of ZnO nanoparticles suspended in poly ethylene glycol and water at a temperature range of 20–45 °C.

Cabaleiro et al. [21] measured the density, thermal conductivity, rheological behaviors of ZnO nanoparticles suspended in ethane-1,2-diol and a mixture of water and ethane-1,2-diol for a temperature range of 10–50 °C. Saleh et al. [22] measured the thermal conductivity of ZnO/EG nanofluids with volume fractions by 0.5 %. They did not use any surfactant to stable the nanofluids.

Suganthi et al. [23] measured thermal conductivity of ZnO–propylene glycol nanofluids for volume fractions less than 2 % and temperatures between 10–60 °C. The nanofluids are prepared by the aid of probe ultrasonication and without any surfactant.

Suganthi and Rajan [24] measured the viscosity of ZnO–water nanofluids at a volume fraction range of 0.25–2 %. They could prepare the nanofluids with a stable state using sonication (probe ultrasonication) without any additives. Recently in a comprehensive study, Witharana et al. [25] investigated the effects of different conditions on the stability of ZnO nanoparticles suspended in propylene glycol, ethylene glycol, and a mixture of PG and EG in water. Beside the above special studies, Ghadimi et al. [26] reviewed different methods for stability of different nanofluids.

The main aim of this study is to present some experiences obtained during the tests conducted to have stable ZnO suspensions where the base fluid is a mixture of EG and water (40:60 wt%). The mixture of EG and water has a higher boiling point compared to the water, which means that the mixture is more suitable for applications under high temperatures. On the other hand, the viscosity of the mixture is lower than the pure EG, hence, by using the mixture the pumping power required in industrial applications would be reduced. First, the methods which were not successful to prepare the stable nanofluids are presented. Afterwards, a successful method to obtain the stable nanofluids is suggested. Finally, the density of nanofluids at a temperature range of 25–40 °C is measured for volume fractions up to 4 %, and a helpful correlation is achieved for practical applications.

Nanofluid Preparation

ZnO nanoparticles with the average size of 20 nm were purchased from MKnano Company. The aim is to make a stable suspension with ZnO nanoparticles in the mixture of EG/water. Different approaches have tried to obtain a stable nanofluid. Two surfactants including Gum Arabic and DI ammonium hydrogen citrate were used in the study. Figure 1 shows a photograph of the nanoparticles, and the two

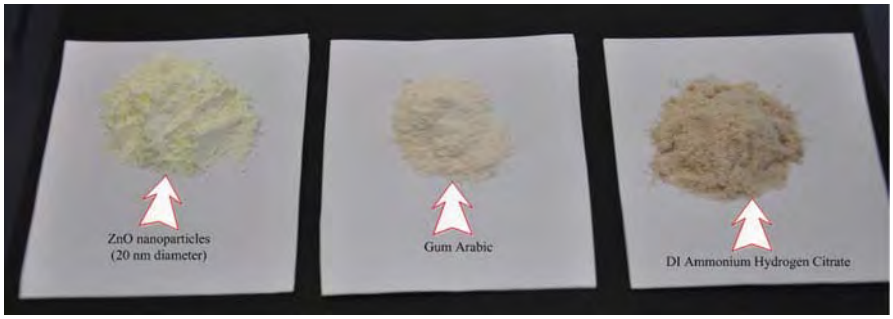

Fig. 1 Photo of the nanoparticles and two surfactants

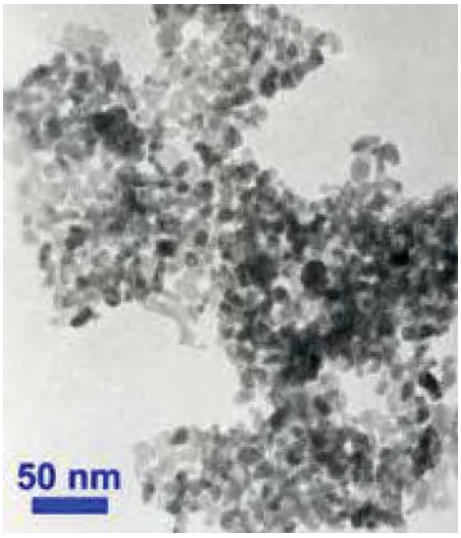

Fig. 2 TEM image of the nanoparticles

surfactants. Also, Fig. 2 shows the TEM image from the nanoparticles. It should be noted that the density of ZnO nanoparticles, DI Ammonium Hydrogen Citrate, and Gum Arabic are 5,610, 1,500, and 1,350 kg/m^3, respectively. The ultrasonic bath used in the experiments has a power of 600 W and frequency of 40 kHz.

First, the authors would like to mention the unsuccessful approaches to prepare stable ZnO–EG/water nanofluids so that other researchers avoid trying, then the successful method is presented. It should be noted that there is no a special way to have stable nanofluids. The companies that produce nanofluids do not give the details of dispersion of nanoparticles into base fluids to the costumers. Therefore, the researchers have to find the best surfactant by trial and error.

Experience No # 1: Nanofluid Preparation without Surfactant

First, it was attempted to get a stable suspension without using any surfactant. Because using any surfactant changes the properties of pure nanofluid. Also, for the

Fig. 3 Nanofluid without surfactant

beginning the low volume fraction of 0.5 % was tried. A weighing scale with an accuracy of 0.001 g is used to weigh the required amount of ZnO nanoparticles for concentration of 0.5 %. Also, to weigh the base fluid a weighing scale with an accuracy of 1 g is utilized. After weighing the base fluid (EG) and the nanoparticles, the nanoparticles were added to the base fluid in small doses at several steps, so that in each step the nanoparticles were well mixed with the base fluid well. The mixture of nanoparticles and the base fluid were stirred about 30 min. Next, the suspension was sonicated. After 2 h, the suspension was pulled out from the ultrasonic. The suspension was stirred for about 15–30 min and again was inserted inside the bath to sonicate for 2 h. In the first look, it was observed that the nanoparticles were settled in the glass container. Figure 3 shows a photograph of the suspension which is taken once the nanofluid was pulled out from the ultrasonic bath.

Experience No # 2: Adding DI Ammonium Hydrogen Citrate to the Base Fluid Before Nanoparticles

For this case, it was attempted to get a stable nanofluid with volume fraction of 1 % using the DI ammonium hydrogen citrate as the surfactant. The molecular formula of DI ammonium hydrogen citrate is $(NH_4)_2HC_6H_5O_7$. The mixture of EG/water (40:60) and the surfactant was stirred for about 30 min and then is inserted in the ultrasonic bath for about 1 h. Next, the nanoparticles were added bit by bit to the mixture and simultaneously were stirred for 15–30 min. The final suspension was inserted inside the ultrasonic bath for about 2 h. At first, it seems that the nanofluid is stable. However, the photographs that are taken after 1 and 6 days after preparing the nanofluids which show this approach has been failed (see Fig. 4). As seen, the

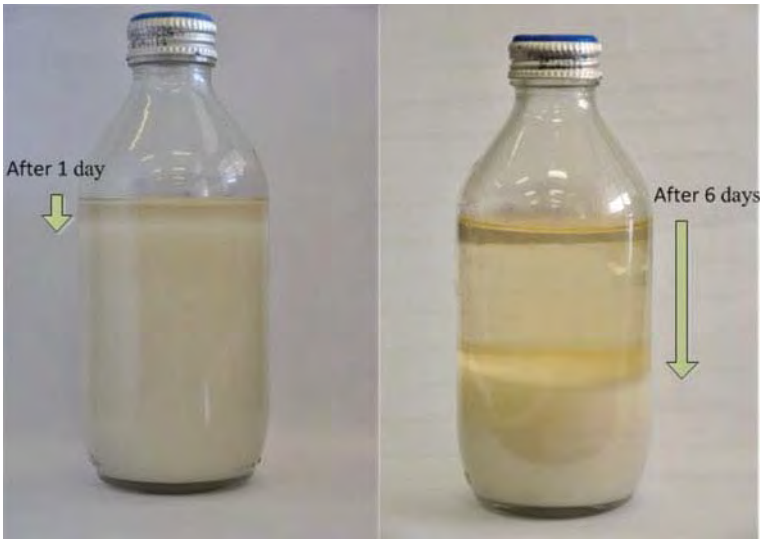

Fig. 4 Sedimentation of nanofluid due to adding DI Ammonium Hydrogen Citrate to the base fluid before nanoparticles

sedimentation rate of nanoparticles after 6 days is considerable. In this experiment, the weight ratio of surfactant to nanoparticles was 1:1. It should be noted that for lower volume fractions (i.e. 0.5 %), this method is repeated to be sure that the reason for the instability is not a high volume fraction, but the same results are obtained.

Experience No # 3: Adding Gum Arabic to the Base Fluid After Nanoparticles

In this experience, it was attempted to make a nanofluid with concentration of 0.5 % using Gum Arabic. First, the nanoparticles were added to the base fluid and the mixture was stirred for about 30 min and then was inserted into the ultrasonic bath for 1 h. After that, the Gum Arabic with weight ratio of 1:10 (Gum Arabic to nanoparticles) was added to the mixture of base fluid and nanoparticles. Next, the suspension was inserted for 4 h in the ultrasonic bath. After pulling out, it was observed that the Gum Arabic and nanoparticles are clustered at the bottom of the glass container. This shows that even with longer sonication, but not a suitable surfactant, the nanofluid is instable. Figure 5 displays this phenomenon.

Experience No # 4: Adding DI Ammonium Hydrogen Citrate to the Base Fluid After Nanoparticles

In this case, three weight ratios of surfactant to nanoparticles including 1:10, 1:2, and 1:1 were tested where the volume fraction of 0.5 % was considered. It should be noted that the thermal and chemical properties of nanofluids will be changed with the use of a surfactant, thus at first, low amounts of surfactant is tried (1:10). It was

Fig. 5 Clustering the Gum Arabic and nanoparticles in the bottom of the glass

observed that when the weight ratio of 1:10 is used, the sedimentation of nanoparticles in the glass container is visible so that the nanoparticles are adhered to the glass (see Fig. 6). With an increase in the surfactant (weight ratio of 1:2), the nanoparticles do not adhere to the bottom of the glass container, but separation occurs between the liquid and solid phase. With increasing the surfactant where the weight ratio is 1:1, a good stability and dispersion is observed in the nanofluid (see Fig. 7). The instability in low amounts of surfactant may due to the high density of nanoparticles which needs higher quantities of surfactant to avoid the sedimentation. The timing and sequence of sonication and mixing were the same in experiences 3 and 4.

From the above discussions, it is concluded that DI Ammonium Hydrogen Citrate should be used as the surfactant with a weight ratio of 1:1.

Density Measurement

Nanofluids with volume fractions of 0.25, 0.5, 1, 2, and 4 % were prepared and then their densities were measured with a 25 ml capillary type pycnometer. It should be stated that the stability time of nanofluids decreases with an increase in the volume fraction. To investigate the accuracy of the pycnometer, the density of the EG/water mixture was measured at different temperatures (25–40 °C). A small basin of hot water was used to increase and regulate the temperature of nanofluids. After filling the pycnometer with the nanofluid and adjusting the desired temperature, the mass of pycnometer is measured by the weighing scale with an accuracy of 0.001 g. The weight of pycnometer is 20.720 g while its accuracy in volume measurement is 2.887×10^{-7} m^3 (given by the company). To investigate the accuracy of the

Fig. 6 Nanofluid with DI Ammonium Hydrogen Citrate where weight ratio is 1:10

Fig. 7 Nanofluid with good stability

device, some comparisons are made between the data obtained in the present study and the data reported in the literature [27]. It is found that the maximum difference between the measured data and the data reported in the literature is 6 %. For example, at 30 °C the measured density is 1,115.4 kg/m^3, whereas for this condition in the literature the density is reported equal to 1,051.794 kg/m^3 which indicates a difference with a magnitude of 6 %. Table 1 shows the data obtained for density from the measurements for different nanofluids.

Table 1 Density in different temperatures and volume fractions

ϕ (%)	Density (kg/m^3)			
	T(C)			
	25	30	35	40
0	1122.41	1115.40	1112.85	1107.80
0.25	1142.20	1139.40	1138.24	1136.12
0.5	1155.48	1152.72	1149.72	1148.72
1	1183.08	1174.92	1170.8	1167.36
2	1235.76	1232.08	1228.92	1219.56
4	1328.72	1326.60	1323.76	1319.40

Figure 8 shows the variations of density at different volume fractions with temperature. It is seen that with increasing the particle loading of nanoparticles the density increases considerably, but the density decreases slightly with the temperature.

In the literature, the following relation is suggested to calculate the density of nanofluids [28]:

$$\rho_{nf} = \rho_f(1-\phi) + \rho_p\phi \tag{1}$$

where $\rho_{nf}$is the density of nanofluid, $\rho_f$is the fluid density, $\rho_p$is the particle density and ϕ is the volume fraction of nanoparticles. Figure 9 presents a comparison between the present data and the theoretical density. As it is seen, the theory relation underestimates the experimental data. The difference between the two data (experimental and theoretical) is about 7 % in all volume fractions. This happens because in the theory equation, the density of surfactant is not considered. The

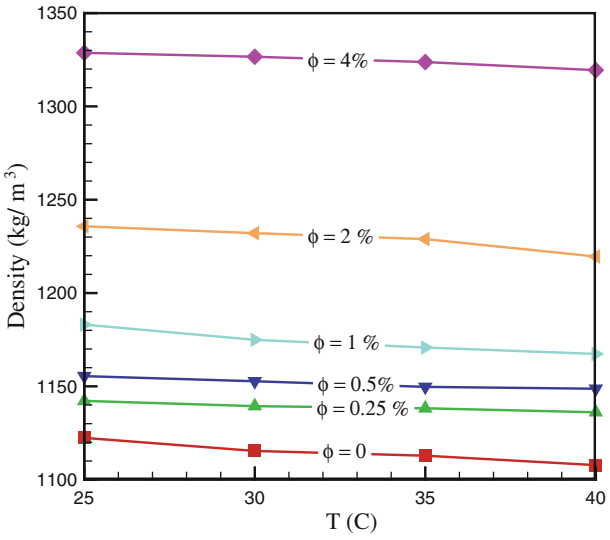

Fig. 8 Experimental results of density for ZnO/EG–water

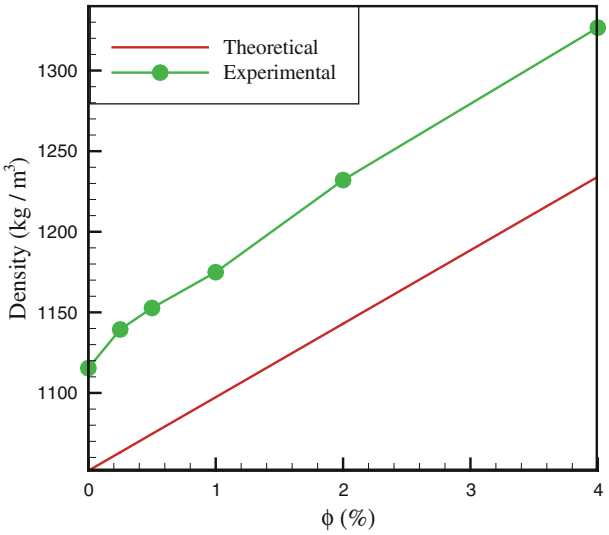

Fig. 9 Comparison between the measured data and theoretical equation

uncertainty analysis shows that the uncertainty does not exceed 2 %. In general, the following relation can be used to calculate the density of nanofluid in the presence of a surfactant:

$$\rho_{nf} = \left(\frac{m_f + m_s + m_p}{V_f + V_s + V_p}\right) = \left(\frac{\rho_f V_f + \rho_s V_s + \rho_p V_p}{V_f + V_s + V_p}\right) = \left(\frac{\rho_f V_f + \rho_s V_s}{V_f + V_s + V_p}\right) + \rho_p \phi \quad (2)$$

In the above relation, V is the volume, and the subscript "s" refers to the surfactant.

Correlation

In this section using the experimental data and regression analysis a correlation is obtained as follows:

$$\rho_{nf,c} = 1146.948 + 51.123\phi - 0.743\,T \quad (3)$$

where subscript "c" is the abbreviation of correlation word. The above correlation is valid for ZnO/EG–water nanofluid with volume fractions less than 4 %, and the temperature range of 25–40 °C. The value of R^2 for this correlation is 99.6 % which shows the high accuracy of it.

The differences do not exceed 0.8 % for all volume fractions and temperatures.

Sensitivity Analysis

In this section a sensitivity analysis is performed to show that how much the density is sensitive to the changes of volume fraction and temperature. For this purpose, first

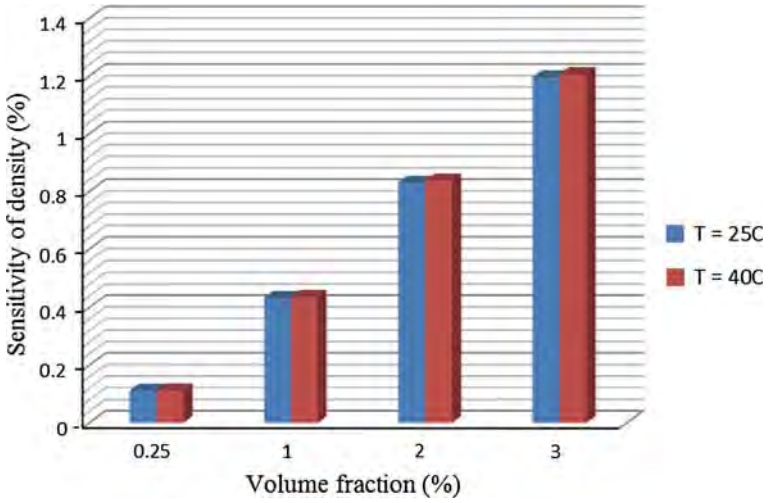

Fig. 10 Results of sensitivity analysis for density of ZnO nanofluids at different volume fractions as the base condition

a base condition should be defined. For example, the volume fraction of 1 % is assumed as the base condition. Now, it should be investigated that how much the density increases or decreases with specified changes in volume fraction. Here, the change of volume fraction is considered 10 %. Therefore, the sensitivity of density to volume fraction at different temperatures when the volume fraction changes 10 % (from 1 to 1.1 % where 1 % is base condition), can be calculated by dividing the difference between density after 10 % change and the density at the base condition to the density in the base condition.

Figure 10 shows the results of the sensitivity analysis at two temperatures of 25 and 40 °C where different volume fractions are selected as the base condition. As it is observed, the sensitivity of density of ZnO nanofluids to changes in temperature is very small. From the sensitivity analysis; it is found that at higher temperatures, density is more sensitive to the changes in volume fraction. As known, the changes of density are important in engineering systems. The sensitivity analysis reveals that under higher temperatures the engineers should be more careful to increase the volume fraction of a system because the sensitivity increases with increasing temperature. Also, it is seen that the sensitivity increases about 10 times when the volume fraction increases from 0.25 to 3. This shows the importance of adding nanoparticles in high volume fractions.

Conclusion

An experimental study was performed to prepare samples of ZnO–EG/water nanofluids with good stability. In this way, different approaches were tested. At first, it was attempted to reach a nanofluid with good stability without any surfactant, but

this effort was unsuccessful. After that, two surfactant including DI Ammonium Hydrogen Citrate and Gum Arabic were tried. Among different ways, it was found that when the DI Ammonium Hydrogen Citrate is added to the mixture of base fluid and nanoparticles, the nanofluids are stable. Also, it was experienced that the weight ratio of nanoparticle to surfactant should be equal. The density of nanofluids with volume fractions by 4 % and in a temperature range of 25–40 °C was measured and a helpful correlation was presented for practical applications. Finally, based on the correlation, a sensitivity analysis is performed. The sensitivity analysis showed that density is more sensitive to the addition of nanoparticles at higher temperatures.

Acknowledgments The first and third authors wish to thank the Thailand Research Fund, and the National Research University Project to support this study. The authors would like to thank from Mr. Raviwat Srisomba to take the photos, from Mr. Chaiwat Jumpholkul for his help and from Professor Elaheh K. Goharshadi from Ferdowsi university of Mashhad for her valuable guidance.

References

1. P. Estellé, S. Halelfadl, N. Doner, and T. Maré (2013). *Curr. Nanosci.* **9**, 225.
2. O. Mahian, A. Kianifar, S. A. Kalogirou, I. Pop, and S. Wongwises (2013). *Int. J. Heat Mass Transf.* **57**, 582.
3. R. Taylor, S. Coulombe, T. Otanicar, P. Phelan, A. Gunawan, W. Lv, G. Rosengarten, R. Prasher, and H. Tyagi (2013). *J. Appl. Phys.* **113**, 011301.
4. R. Saidur, K. Y. Leong, and H. A. Mohammad (2011). *Renew. Sustain. Energy Rev.* **15**, 1646.
5. B. Aladag, S. Halelfadl, N. Doner, T. Maré, S. Duret, and P. Estellé (2012). *Appl. Energy* **97**, 876.
6. R. S. Vajjha, D. K. Das, and B. M. Mahagaonkar (2009). *Petroleum Sci. Technol.* **27**, 612.
7. W. Yu, H. Xie, L. Chen, and Y. Li (2009). *Thermochim. Acta* **491**, 92.
8. R. K. Neogy and A. K. Raychaudhuri (2009). *Nanotechnology* **20**, 305706.
9. S. J. Chung, J. P. Leonard, I. Nettleship, J. K. Lee, Y. Soong, D. V. Martello, and M. K. Chyu (2009). *Powder Technol.* **194**, 75.
10. V. S. Raykar and A. K. Singh (2010). *Thermochim. Acta* **502**, 60.
11. R. Jalal, E. K. Goharshadi, M. Abareshi, M. Moosavi, A. Yousefi, and P. Nancarrow (2010). *Mater. Chem. Phys.* **121**, 198.
12. M. Moosavi, E. K. Goharshadi, and A. Youssefi (2010). *Int. J. Heat Fluid Flow* **31**, 599.
13. A. Singh (2010). *Adv. Powder Technol.* **21**, 609.
14. W. H. Lee, C. K. Rhee, J. Koo, J. Lee, S. P. Jang, S. U. Choi, K. W. Lee, H. Y. Bae, G. J. Lee, C. K. Kim, S. W. Hong, Y. Kwon, D. Kim, S. H. Kim, K. S. Hwang, H. Jin Kim, H. J. Ha, S. H. Lee, C. J. Choi, and J. H. Lee (2011). *Nanoscale Res. Lett.* **6**, 4.
15. D. K. Singh, D. K. Pandey, R. R. Yadav, and D. Pramana (2012). *J. Phys.* **78**, 759.
16. M. Kole and T. K. Dey (2012). *Appl. Therm. Eng.* **37**, 112.
17. M. Kole and T. K. Dey (2012). *Thermochim. Acta* **535**, 58.
18. G.-J. Lee, C. K. Kim, M. K. Lee, C. K. Rhee, S. Kim, and C. Kim (2012). *Thermochim. Acta* **542**, 24.
19. G. Colangelo, E. Favale, A. Risi, and D. Laforgia (2012). *Appl. Energy* **97**, 828.
20. M. T. Zafarani-Moattar and R. Majdan-Cegincara (2012). *J.Chem. Thermodyn.* **54**, 55.
21. D. Cabaleiro, M. J. Pastoriza-Gallego, M. M. Piñeiro, and L. Lugo (2013). *J. Chem. Thermodyn.* **58**, 405.
22. R. Saleh, N. Putra, S. P. Prakoso, and W. N. Septiadi (2013). *Int. J. Ther. Sci.* **63**, 125.
23. K. S. Suganthi, M. Parthasarathy, and K. S. Rajan (2013). *Chem. Phys. Lett.* **561**, 120.
24. K. S. Suganthi and K. S. Rajan (2012). *Int. J. Heat Mass Transf.* **55**, 7969.
25. S. Witharana, I. Palabiyik, Z. Musina, and Y. Ding (2013). *Powder Technol.* **239**, 72.
26. A. Ghadimi, R. Saidur, and H. S. C. Metselaar (2011). *Int. J. Heat Mass Transf.* **54**, 4051.
27. ASHRAE *ASHRAE handbook: fundamentals* (American Society of Heating, Refrigerating and Air-Conditioning Engineers Inc., Atlanta, 2005), p. 437.
28. K. Khanafer and K. Vafai (2011). *Int. J. Heat Mass Transf.* **54**, 4410.

International Communications in Heat and Mass Transfer 49 (2013) 78–85

Contents lists available at ScienceDirect

International Communications in Heat and Mass Transfer

journal homepage: www.elsevier.com/locate/ichmt

A generalized numerical correlation study for the determination of pressure drop during condensation and boiling of R134a inside smooth and corrugated tubes ☆

M. Balcilar [a], K. Aroonrat [b], A.S. Dalkilic [c,*], S. Wongwises [b]

[a] Computer Engineering Department, Yildiz Technical University, Davutpaşa, Istanbul 34349, Turkey
[b] Fluid Mechanics, Thermal Engineering and Multiphase Flow Research Lab. (FUTURE), Department of Mechanical Engineering, Faculty of Engineering, King Mongkut's University of Technology Thonburi, Bangmod, Bangkok 10140, Thailand
[c] Heat and Thermodynamics Division, Department of Mechanical Engineering, Faculty of Mechanical Engineering, Yildiz Technical University, Yildiz, Besiktas, Istanbul 34349, Turkey

ARTICLE INFO

Available online 7 September 2013

Keywords:
Condensation
Boling
Pressure drop
Modeling
Neural network
Corrugated tubes

ABSTRACT

The measured pressure drop of R134a, flowing downward and horizontally inside smooth and corrugated copper tubes, is estimated by the closed form of artificial neural network method to have a reliable empirical correlation using some dimensionless numbers. The working fluids are R134a and water flowing in the test tube and annular tube, respectively. This paper is a continuation of the authors' previous work and includes all their previous works about condensation and boiling in tubes. All data used in the present paper are obtained from the authors' previous studies. The training sets have the experimental data of convective condensation and boiling experiments including various mass fluxes and saturation temperatures of R134a. Froude number, Weber number, Bond number, Lockhart and Martinelli number, void fraction, the ratio of density to dynamic viscosity, liquid, vapor and equivalent Reynolds numbers, surface tension parameter and liquid Prandtl number are the inputs of the formula as the dimensionless numbers obtained from measured values of test section, while the output of the formula is the measured pressure drops in the analysis. A closed form of multi-layer perceptron (MLP) method of artificial neural network (ANN) is used to estimate the experimental pressure drop of R134a numerically. 1177 data points are used in the analyses of the ANN method to be able to have a single generalized empirical correlation for both condensation and boiling flows. The evaluation of the closed form of multi-layer perceptron (MLP) with two or three inputs and one hidden neuron architecture was successful predicting the measured pressure drops with their error bands being within the range of ±30% for all used data. The proposition of empirical correlations are performed for both condensation and boiling flows separately. A single empirical correlation is able to calculate the measured pressure drop of both condensation and boiling flows together. Moreover, the dependency of output of the proposed formula from input values is examined in the study. By means of the dependency analyses, liquid Prandtl number, Butterworth's void fraction and Lockhart and Martinelli parameter are found to be the most dominant parameters among other dimensionless numbers.

1. Introduction

Some reviews on in-tube condensation having smooth and enhanced tubes were performed by Dalkilic and Wongwises [1,2] and Laohalertdecha et al. [3] to show that a two-phase flow in tubes is the hardest phenomenon in the system of heat exchangers. Classifications regarding the tubes' orientation geometry on in-tube condensation were prepared. Detailed information was given on the convective condensation investigations of heat transfer, pressure drop, flow pattern, void fraction and refrigerants in the available sources. Their papers not only mention the latest improvements on heat transfer but also include some useful knowledge on the alternative refrigerants, theoretical, numerical and empirical models in the literature.

A two-phase flow has the important characteristic regarding the orientation and interaction of the liquid and vapor phases inside the tubes regarding with flow regime and flow pattern. The geometry of the tube affects interfacial area of the phases, and due to this, mass, momentum and energy exchange between phases have great significance in the design. The tube position, the geometry of the tube, flow rates, superficial velocities and physical properties such as density, viscosity and surface tension of the two phases cause various flow regimes. Mostly, flow patterns are detected by visual ways and these include bubble flow, slug flow, churn flow, wispy-annular flow and annular flow for both vertical and horizontal flow. Authors of this paper have publications on determination of flow regimes [4,5].

Lately, two of the most important criteria are the ozone-depleting potential (ODP) and global-warming potential (GWP) in the progress of alternative refrigerants excepting the refrigerant CFCs and

☆ Communicated by: W.J. Minkowycz.
* Corresponding author. Tel.: +90 2123832821; fax: +90 2123833024.
E-mail address: dalkilic@yildiz.edu.tr (A.S. Dalkilic).

0735-1933/$ – see front matter © 2013 Elsevier Ltd. All rights reserved.
http://dx.doi.org/10.1016/j.icheatmasstransfer.2013.08.010

Nomenclature

Bo	Bond number
d	internal tube diameter, m
f	function
Fr	Froude number
G	mass flux, kg m^{-2} s^{-1}
j	superficial velocity
Pr	Prandtl number
R	ratio of density to dynamic viscosity
Re	Reynolds number
x	average vapor quality
We	Weber number
X_{tt}	Lockhart and Martinelli parameter

Greek Symbols

α	void fraction
ρ	density, kg m^{-3}
μ	dynamic viscosity, kg m^{-1} s^{-1}
σ	surface tension, N m^{-1}
Ψ	surface tension parameter
ΔP	pressure drop, kPa

Subscripts

eq	equivalent
exp	experiment
g	gas
h	hydraulic
l	liquid
TP	two-phase

HCFCs, both of which have high ODP and GWP by reason of the their contribution to ozone layer depletion and global warming. Despite their harmful GWP, substitutions to CFCs and HCFCs, such as hydro fluorocarbon (HFC) refrigerants, with their zero ODP, have been selected for use in various devices commonly. HFC refrigerants also have more proper specifications such as non-flammability, stability and similar vapor pressure than CFCs and HCFCs. All new land-based systems have usually Ammonia (R717), frequently in arrangement with other refrigerants such as water-based blends of propylene glycol or ethylene glycol and CO_2 in systems of cascade. The high-temperature sides of the systems have this fluid which has toxicity, zero ODP and zero GWP. Authors of this paper have publications on obtaining of the most proper refrigerants and their blends in the cycles of refrigeration [6,7].

To have a reliable correlation during two-phase flows in tubes, genetic algorithms (GAs) and artificial neural networks (ANNs) modeling as artificial intelligence methods confirmed by the experimental work have been having augmented status. On the other hand, there are rare research on the determination of the characteristics of in-tube condensation and evaporation using artificial intelligence techniques in the literature. Authors of this paper have publications on determination of heat transfer characteristics of two-phase flows in-tubes numerically [8–11].

The industrial processes and various applications have the two-phase pressure drop as an important design consideration. A large number of studies on this subject exist owing to its significance. The convective two-phase total pressure drop has the frictional, acceleration and gravitational parts. The acceleration and gravitational components are calculated using void fraction, and calculation of either the two-phase friction factor or the two-phase frictional multiplier is necessary for computing the frictional part of pressure drop similarly. Authors of this paper have publications on determination of pressure drop, friction factor and void fraction of two-phase flows in tubes [12–19].

The efficient plan and processing of air conditioning and refrigeration systems depend on the improvements in condensation heat transfer in horizontal tubes. Many researchers have tested smooth tubes' performance with pure refrigerants as working fluids. Condensation heat transfer coefficients have been calculated by empirical methods in horizontal smooth tubes in general. Formerly, various augmentation techniques, such as rough surfaces and twisted-tape inserts, have been investigated by some researchers, alternatively, micro-fin and corrugated tubes have lately been tested intensively as a result of their high heat transfer capability and moderate pressure drop. Authors of this paper have publications on determination of two-phase heat transfer coefficient in smooth and enhanced tubes [20–29].

The major aim of this study is to develop a model on the condensation and boiling in smooth and corrugated tubes using MATLAB with the non-linear least squares (NLS) and then conclude the dominant parameters and correlate better predictive correlations using them with reliable experimental database [16,27–29] belonging to the condensation and boiling flow in smooth and corrugated tubes. This paper is the one in a series of the authors' previous work. Only the data obtained from the authors' previous studies on condensation and boiling in tubes are used in the present study. The developed empirical correlations are supposed to be beneficial for the investigation of the heat transfer fundamentals for new smooth and corrugated tubes, without doing extra experiments, thanks to the availability of reliable data from the authors' laboratory in King Mongkut's University of Technology Thonburi.

2. Experimental setup and data reduction

Comprehensive presentations of the experimental setups and operating conditions regarding flow type, refrigerant, mass flux, average pressure, inlet and outlet vapor qualities and data point numbers belonging to the data for the subjects of condensation and evaporation of R134a inside horizontal/vertical smooth/corrugated tubes exist either in authors' previous publications or partially in all figures.

3. Calculation method for the analyses

Calculation method for the error analyses of the mean values of measured and determined results of the two-phase pressure drops regarding R^2 error, proportional error and mean square error (MSE), heat transfer coefficient determination, pressure drop's ANN studies and correlation development for convective condensation exist in authors' previous publications.

The achievement of the modeling experimental data with multilayer perceptron (MLP) has been stated numerous times by the researchers. However, the downside of this method is the mathematical expression of the relationship between inputs and outputs growing by increasing architectural size of MLP. Because of the relationship between inputs and outputs cannot be described with a simple equation, researchers call this as black box. The success of correlation decreases when the model architecture is quite small, however since the closed form of the model also simplifies, it can be shown as simple equation. For that reason, in this study, the closed form of MLP with 3–1–1 architecture (it was used 2–1–1 architecture in some formulas) is used. In this model, the transfer function of hidden layer is considered to be tansig function.

Table 1
Proposed correlations and their error rates.

Eq. number	Proposed correlation	Data set	MSE	RMSE	R^2	Data number
1	$\Delta P=\left(\frac{G^2}{\rho_g}\right)\left(\frac{b_1}{1+\exp\left(b_2\mathrm{Re_l}+b_3\mathrm{Re_g}+b_4\mathrm{Re_{eq}}+b_5\right)}+b_6\right)$ $b_1=-0.006002$, $b_2=0.003294$, $b_3=0.001297$, $b_4=-0.003532$, $b_5=4.064121$, $b_6=0.007255$	All data	4.233	2.057	0.88	1177
2	$\Delta P=\left(\frac{G^2}{\rho_g}\right)\left(\frac{b_1}{1+\exp(b_2Fr+b_3We+b_4\psi+b_5)}+b_6\right)$ $b_1=0.004888$, $b_2=-0.04286$, $b_3=0.016243$, $b_4=-747.278$, $b_5=11.15224$, $b_6=0.001272$	1–3	3.168	1.78	0.74	670
3	$\Delta P=\left(\frac{G^2}{\rho_g}\right)\left(\frac{b_1}{1+\exp(b_2Fr+b_3\alpha+b_4\mathrm{Pr_l}+b_5)}+b_6\right)$ $b_1=0.030521$, $b_2=0.00052$, $b_3=-3.91275$, $b_4=-1.4453$, $b_5=9.324669$, $b_6=-0.00113$	2–4	0.976	0.988	0.97	507
4	$\Delta P=\left(\frac{G^2}{\rho_g}\right)\left(\frac{b_1}{1+\exp(b_2Bo+b_3\mathrm{Re_l}+b_4R+b_5)}+b_6\right)$ $b_1=0.005538$, $b_2=-1.82695$, $b_3=0.000206$, $b_4=-0.09426$ $b_5=77.58698$, $b_6=0.00119$	1–2	0.324	0.57	0.98	648
5	$\Delta P=\left(\frac{G^2}{\rho_g}\right)\left(\frac{b_1}{1+\exp(b_2X_{tt}+b_3R+b_4\mathrm{Pr_l}+b_5)}+b_6\right)$ $b_1=0.004354$, $b_2=5.896766$, $b_3=0.048752$, $b_4=-165.881$, $b_5=548.7939$, $b_6=0.003914$	3–4	7.449	2.729	0.83	529
6	$\Delta P=\left(\frac{G^2}{\rho_g}\right)\left(\frac{b_1}{1+\exp(b_2Fr+b_3\mathrm{Pr_l}+b_4)}+b_5\right)$ $b_1=0.014646$, $b_2=0.000578$, $b_3=-3.92449$, $b_4=9.013503$ $b_5=-0.01274$	1	0.0154	0.1243	0.99	368
7	$\Delta P=\left(\frac{G^2}{\rho_g}\right)\left(\frac{b_1}{1+\exp(b_2\mathrm{Re_l}+b_3\mathrm{Pr_l}+b_4)}+b_5\right)$ $b_1=0.003822$, $b_2=0.000176$, $b_3=-12.4623$, $b_4=38.50283$ $b_5=0.003437$	2	0.4622	0.6799	0.98	280
8	$\Delta P=\left(\frac{G^2}{\rho_g}\right)\left(\frac{b_1}{1+\exp(b_2Fr+b_3X_{tt}+b_4)}+b_5\right)$ $b_1=0.041218$, $b_2=0.00018$, $b_3=1.04458$, $b_4=0.458855$ $b_5=-0.00818$	3	6.908	2.628	0.65	302
9	$\Delta P=\left(\frac{G^2}{\rho_g}\right)\left(\frac{b_1}{1+\exp(b_2Fr+b_3\mathrm{Re_l}+b_4)}+b_5\right)$ $b_1=0.006999$, $b_2=0.00172$, $b_3=0.000174$, $b_4=-2.727289$ $b_5=0.003662$	4	1.1577	1.0759	0.97	227

According to this consideration, the output of hidden layer is written as Eq. (1).

$$O_h=\frac{1}{1+\exp\left[w_1^1.I_1+w_2^1I_2+w_3^1I_3+b_1\right]} \tag{1}$$

Because the transfer function of output layer is considered to be a linear function, the output of the model, in other words, the closed form of model, is written as follows:

$$O=\frac{w_1^2}{1+\exp\left[w_1^1.I_1+w_2^1I_2+w_3^1I_3+b_1\right]}+b_2 \tag{2}$$

Many investigations on the convective condensation and evaporation pressure drop of plain and augmented tubes exist in the available sources. Commonly, researchers have benefitted from empirical methods to determine the pressure drop and its components in tubes. Finally, Eq. (3) is correlated to estimate the pressure drop of evaporation and condensation regarding with the below explanation as follows.

$$\Delta P=\left(\frac{G^2}{\rho_g}\right)\left(\frac{b_1}{1+\exp\left(b_2\mathrm{Re_l}+b_3\mathrm{Re_g}+b_4\mathrm{Re_{eq}}+b_5\right)}+b_6\right) \tag{3}$$

Table 2
Best input parameters of data sets.

Input	Data set	Input number	OUTPUT
			$R^2-\Delta P$ (%)
$\mathrm{Pr_l}$	All	1	0.782
A	All	1	0.642
X_{tt}	All	1	0.615
$\mathrm{Pr_l}$	1–3	1	0.72
R	1–3	1	0.72
$\mathrm{Re_{eq}}$	1–3	1	0.633
We	2–4	1	0.908
R	2–4	1	0.908
$\mathrm{Pr_l}$	2–4	1	0.908
Bo	1–2	1	0.961
$\mathrm{Pr_l}$	1–2	1	0.703
X_{tt}	1–2	1	0.844
We	3–4	1	0.804
Fr	3–4	1	0.846
$R-\mathrm{Pr_l}$	3–4	1	0.803

where the coefficients from b_1 to b_6 are the constants. The detailed information on the developed correlations can be seen in Table 1.

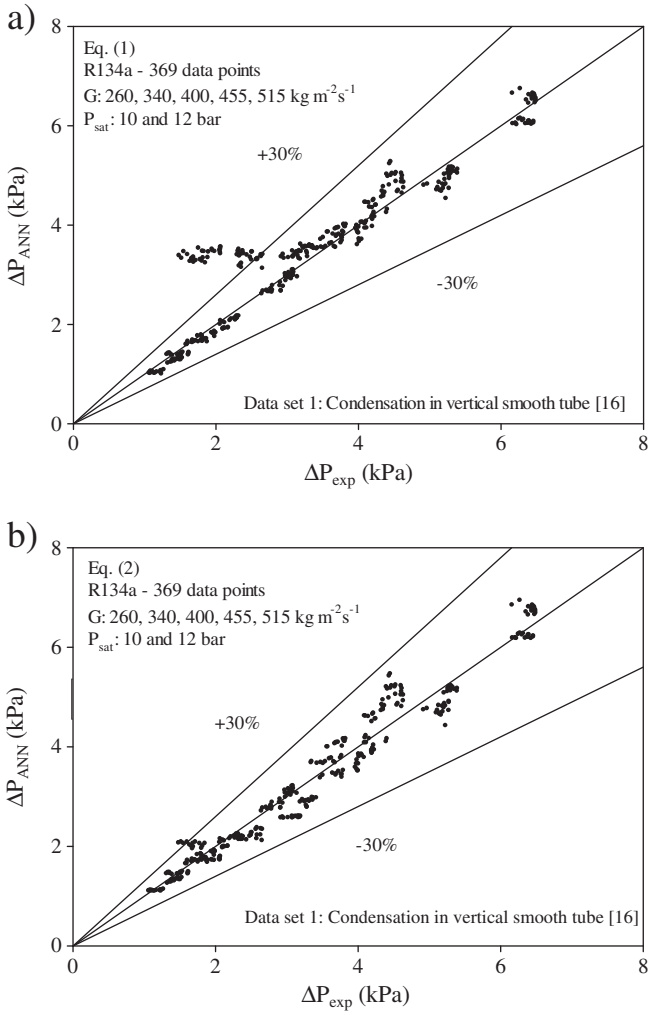

Fig. 1. Performance comparison of Eq. (1) (a) and Eq. (2) (b) for the data set 1.

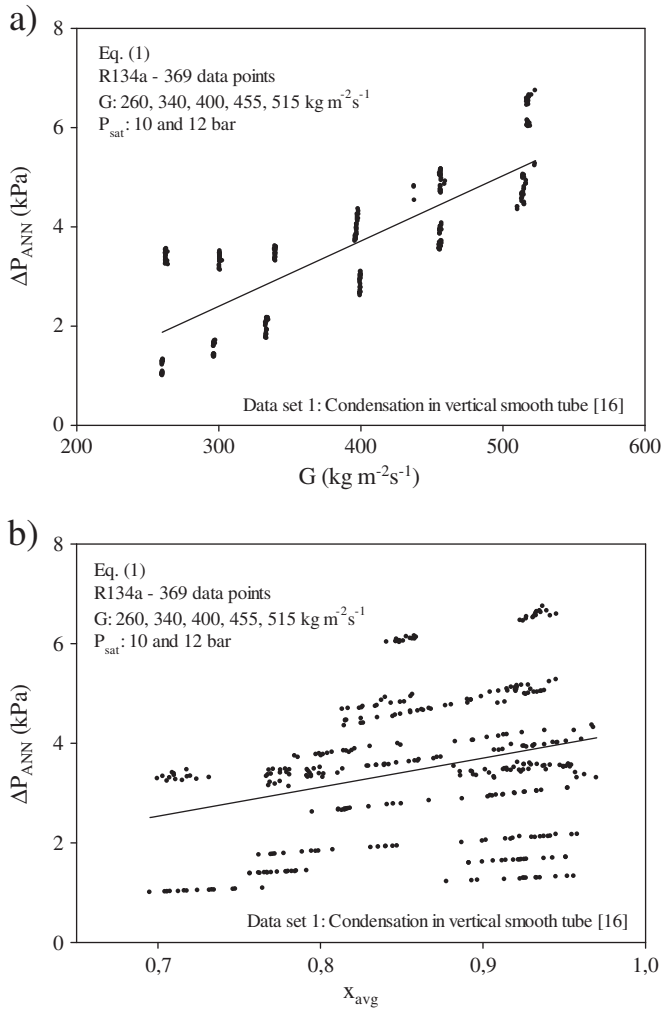

Fig. 2. Alteration of obtained pressure drops with mass flux (a) and average vapor quality (b) for data set 1.

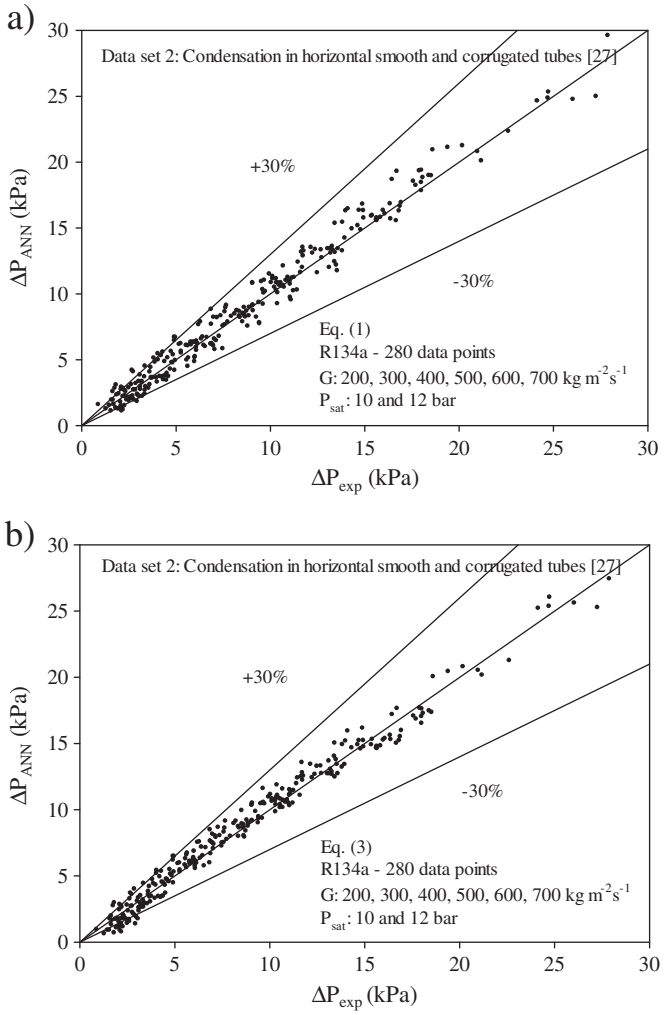

Fig. 3. Performance comparison of Eq. (1) (a) and Eq. (3) (b) for the data set 2.

The inputs of model have the following dimensionless numbers to determine their effects on the pressure drop selected as the output of the analyses. Table 2 shows the significance of these input parameters below, considering their error values of R^2.

All the liquid equivalent of Re number is calculated as

$$\mathrm{Re}_{eq} = \frac{G_{eq} d_E}{\mu_l} \tag{4}$$

and equivalent liquid mass flux is given as

$$G_{eq} = G\left((1-x) + x\left(\frac{\rho_l}{\rho_g}\right)^{0.5}\right) \tag{5}$$

and the ratio of density to dynamic viscosity is determined as

$$R = \frac{\rho_l \mu_l}{\rho_g \mu_g} \tag{6}$$

and Bond number is calculated as

$$\mathrm{Bo} = g\left(\rho_l - \rho_g\right)\left(\frac{(d_h/2)^2}{\sigma}\right) \tag{7}$$

and the Froude number is calculated as

$$Fr = \frac{G^2}{g d_h \rho_{TP}{}^2} \tag{8}$$

where the two-phase density is calculated from

$$\rho_{TP} = \left(\frac{x}{\rho_g} + \frac{1-x}{\rho_l}\right)^{-1} \tag{9}$$

and the Lockhart and Martinelli parameter is given as

$$X_{tt} = \left(\frac{1-x}{x}\right)^{0.9}\left(\frac{\mu_g}{\mu_l}\right)^{0.1}\left(\frac{\rho_g}{\rho_l}\right)^{0.5} \tag{10}$$

and the all liquid Reynolds number is defined as

$$\mathrm{Re}_l = \frac{G d_h}{\mu_l} \tag{11}$$

and all gas Reynolds number can be calculated as

$$\mathrm{Re}_g = \frac{G d_h}{\mu_g} \tag{12}$$

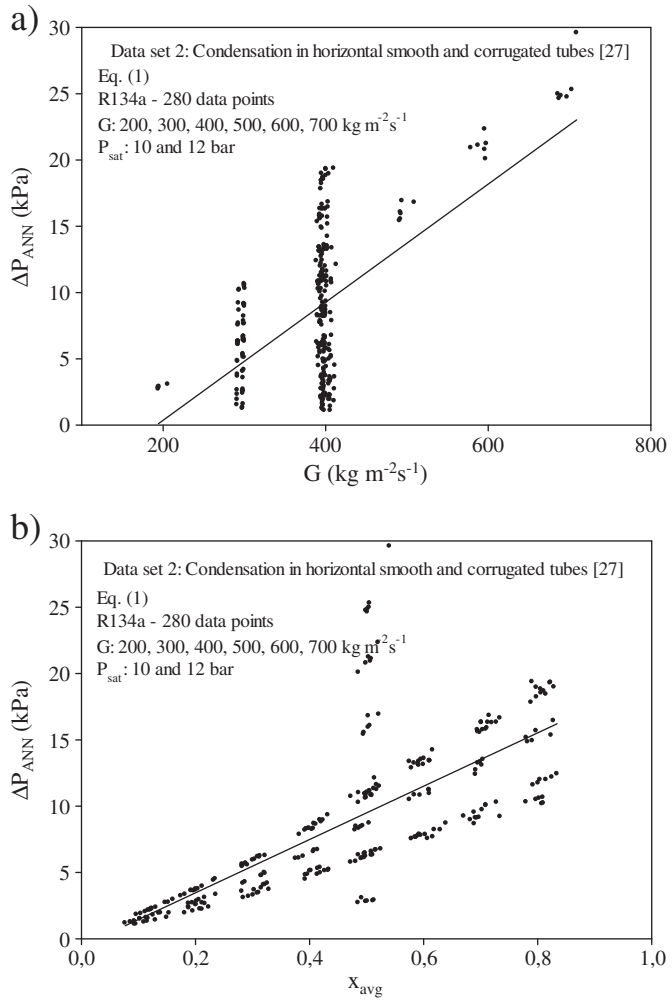

Fig. 4. Alteration of obtained pressure drops with mass flux (a) and average vapor quality (b) for data set 2.

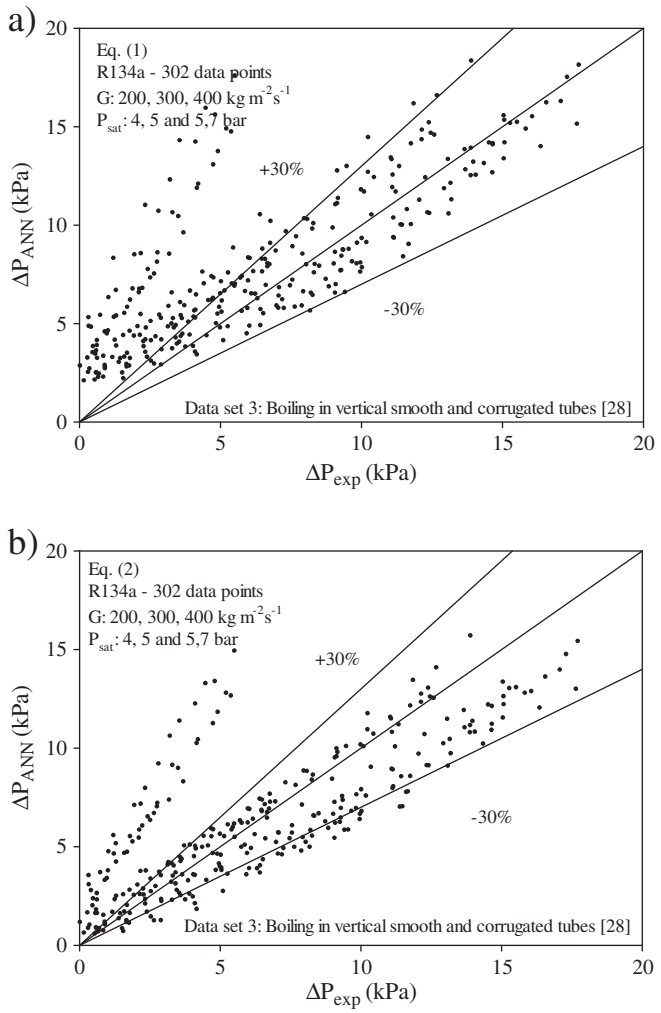

Fig. 5. Performance comparison of Eq. (1) (a) and Eq. (2) (b) for the data set 3.

and the void fraction, α, can be calculated from Butterworth's equation as follows:

$$\alpha = \frac{1}{1 + 0.28\left(\frac{1-x}{x}\right)^{0.64}\left(\frac{\rho_g}{\rho_l}\right)^{0.36}\left(\frac{\mu_l}{\mu_g}\right)^{0.07}} \tag{13}$$

and the Weber number, We, is defined as

$$We = \frac{G^2 d_h}{\sigma \rho_{TP}} \tag{14}$$

and surface tension parameter, ψ, is obtained as

$$\psi = \frac{j_l \mu_l}{\sigma} \tag{15}$$

where the liquid superficial velocity, j_l, is determined as

$$j_l = \frac{G(1-x)}{\rho_l(1-\alpha)} \tag{16}$$

4. Results and discussion

The next explanations illustrate the results and discussion of obtained total pressure drop of condensation and boiling flows of R134a using the database of authors previous studies [16,27–29] in horizontal/vertical smooth and corrugated tubes numerically. The comprehensive explanation and some extra figures and tables including dissimilar measured parameters in terms of their works on the heat transfer characteristics exist in the used references [16,27–29], which show the correctness of the measurements. A discussion of the conclusions can be found below.

In this research, two kind of closed form MLP was used. According to Table 1, the first 5 empirical correlations were modeled with 3–1–1 architecture, and the last 4 correlations were modeled with 2–1–1 architecture. The calculations of the coefficients in correlations in Table 1 are found by means of this developed formula using the experimental databases in [16,27–29]. Froude number, Weber number, Bond number, Lockhart and Martinelli number, void fraction, the ratio of density to dynamic viscosity, liquid, vapor and equivalent Reynolds numbers, surface tension parameter and liquid Prandtl number are the set of the inputs of closed form, while experimental pressure drop is the output of the closed form in the analyses. Regression analysis has the four-fold cross validation. For that reason, 1177 data points (all data of boiling and condensation in smooth and corrugated tubes) were divided by 4 sets unsystematically, where one of the sets was selected for the test process, and the rest of them (3 sets) were used for the training procedure. These procedures were lasted till there were no untested data sets. It should be considered that despite several architectures were eliminated by tests; just the characteristic one was used in the paper due to limited space.

Four different data sets were tested by the authors [16,27–29] and used for all analyses as the operating conditions of the database. There

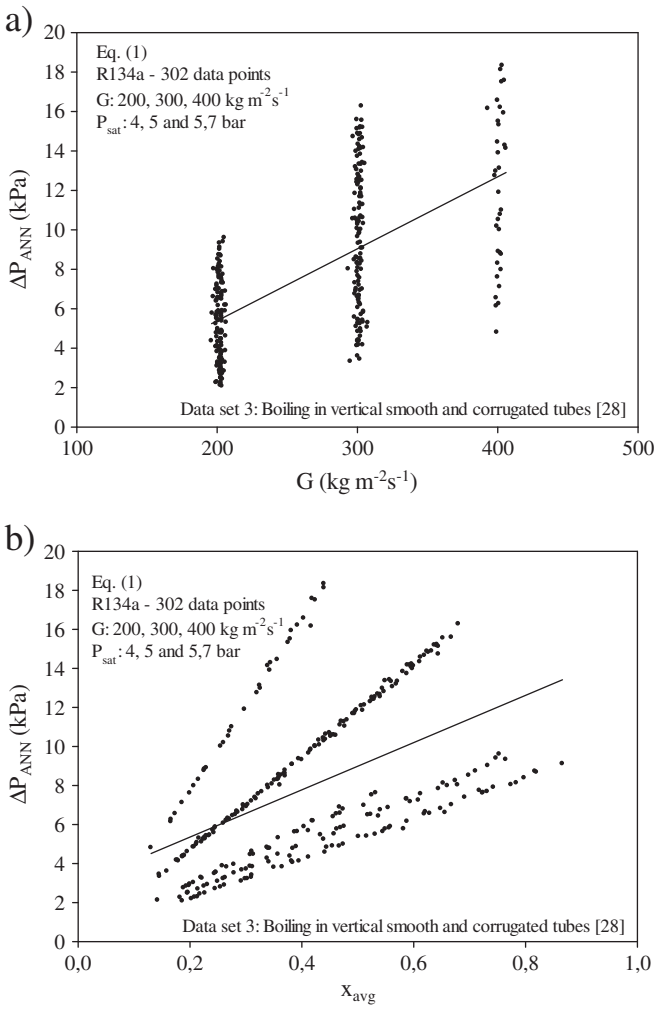

Fig. 6. Alteration of obtained pressure drops with mass flux (a) and average vapor quality (b) for data set 3.

were 1177 data points in the analyses. In-tube flow of condensation of vertical and horizontal orientations has 648 data points whereas in-tube flow of boiling of vertical and horizontal orientations has 529 data points. Five different corrugated tubes and a smooth tube were tested in the experiments. Mass fluxes and vapor qualities had a wide range for the accuracy of the proposed correlations.

Nine different developed empirical correlations for each data set or combination of them were proposed in Table 1 separately. Their success and reliability can be seen from their R^2 values. Eq. (1) in Table 1 has the most importance among the others included in the paper. It can predict all data including condensation/boiling in smooth/corrugated horizontal/vertical tubes at the same time with an acceptable accuracy as shown in all figures. The alteration between the R^2 outputs is by reason of the dificulty of generalization in the two-phase flow.

The dependency of the output parameters from the input ones was shown in Table 2; in other words, this table suggests the most significant dominant dimensionless number on the determination of the total pressure drop. The first 3 most dominant parameters of databases were shown in Table 2 separately. It is possible predict from this table that liquid Prandtl number, Butterworth's void fraction and Lockhart–Martinelli parameter having the biggest effect on the pressure drop, considering condensing and boiling databases with their R^2 values over 0.6. In the analyses, when the input parameter number is only one in all the databases, liquid Prandtl number are the dominant one on the estimation of the pressure drop with the R^2 value of 0.782. For the two known input parameters, liquid Prandtl number and Bond number have the R^2 value of 0.866. For the three known input parameters, liquid Prandtl number, Bond number and equivalent Reynolds number have the R^2 value of 0.88. This result also illustrates the effect of Bond number on the accuracy of the predictability. Data sets 1–3 include the condensation and boiling data sets in vertical smooth and corrugated tubes, data sets 2–4 include the condensation in horizontal tubes and boiling in vertical smooth and corrugated tubes, data sets 1–2 include the condensation in horizontal and vertical plain and corrugated tubes and data sets 3–4 include the boiling in horizontal and vertical smooth and corrugated tubes. Finally, the correctness of determined output value via input values increases along an increasing number of suitable input parameters. Furthermore, they depict less significant input parameters on the estimation of the pressure drop. It is clear that derivation of more results from these tables for each database is possible individually.

This paper focuses intensely on the determination of the pressure drop using all data sets by means of Eq. (1) in Table 1. Its predictability (a) and performance in comparison with other proposed correlations (b) can be seen in Figs. 1, 3, 5 and 7. Majority of data points fall under the ±30% deviation bands for all proposed correlations as it can be seen in these figures. Figs. 2, 4, 6 and 8 show meaningfulness of the proposed correlations' results, considering the trends in the change of the numerical pressure drops and mass fluxes (a) and average vapor qualities (b). As expected, obtained pressure drops from ANN analyses increase with increasing mass fluxes and vapor qualities in all data sets.

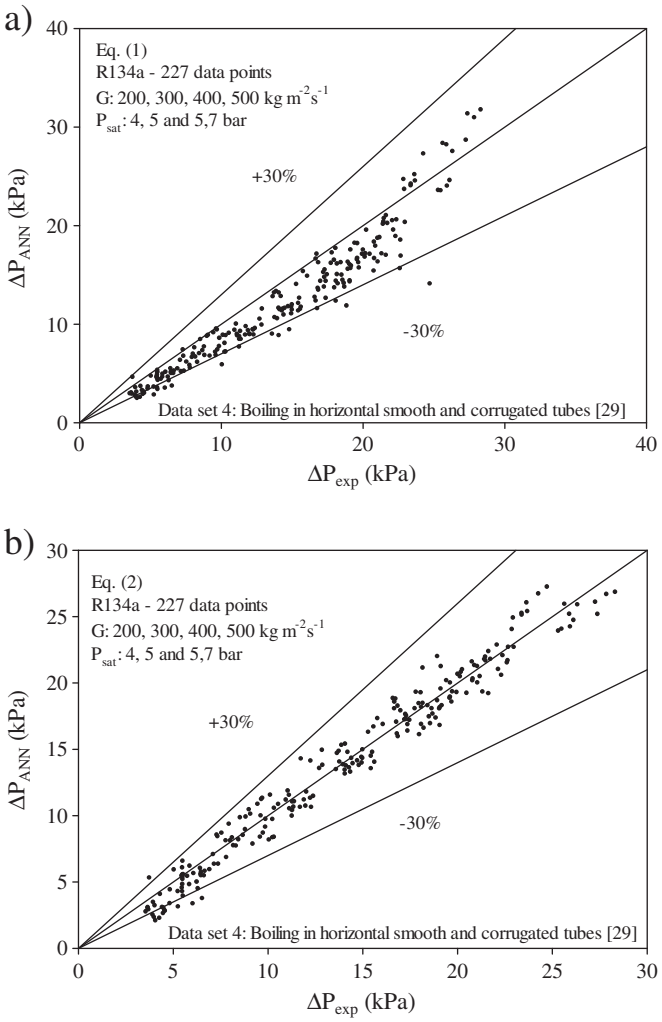

Fig. 7. Performance comparison of Eq. (1) (a) and Eq. (2) (b) for the data set 4.

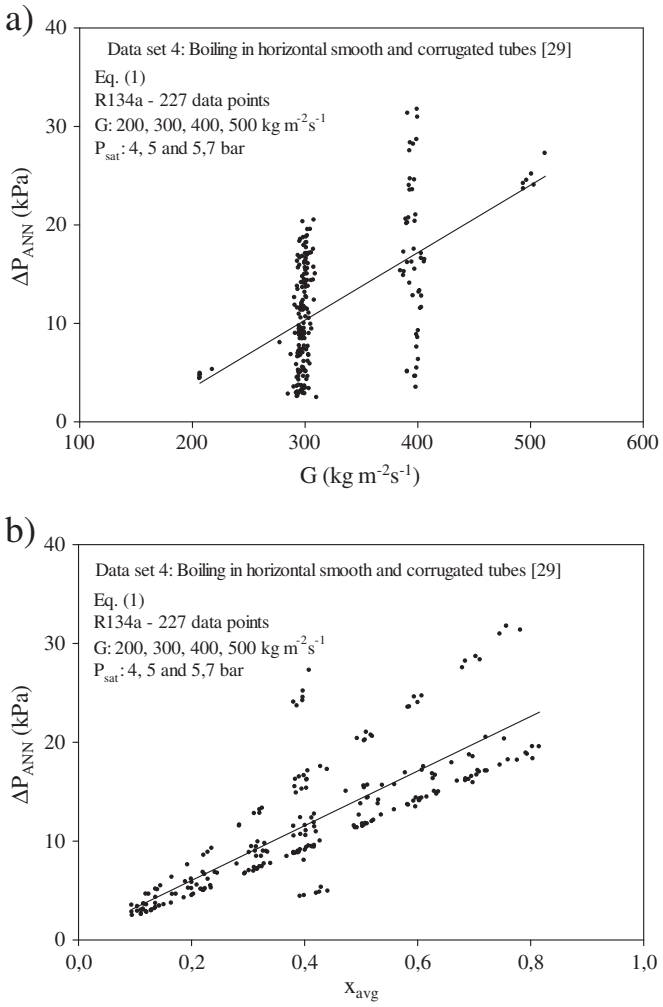

Fig. 8. Alteration of obtained pressure drops with mass flux (a) and average vapor quality (b) for data set 4.

5. Conclusion

Prediction of pressure drop is accomplished and dependable correlations of condensation and boiling in plain and corrugated tubes are developed using computational numerical techniques. The authors' experimental databases in the literature have been benefitted from in the analyses in order to have reliable empirical correlations. This paper reveals that although there are many works on the prediction of two-phase pressure drop in tubes, application of artificial neural networks (ANN) accompanied by non-linear least squares (NLS) to the in-tube boiling and condensation for the aim of correlation development does not appear in the previous papers. Therefore, this investigation's content is supposed to bring new insight to the subject of two-phase flow.

This paper not only proposes some pressure drop empirical correlations for boiling and condensation data sets but also enables researchers to predict both condensation and boiling flows in smooth/corrugated horizontal/vertical tubes by means of a single correlation with a reasonable deviation.

The dependency of output of the ANNs closed form from input values is investigated in the study. Dependency analyses show that liquid Prandtl number, Butterworth's void fraction and Lockhart–Martinelli parameter are the most effective parameters for the tested operating conditions.

Acknowledgements

The third author wishes to thank King Mongkut's University of Technology Thonburi (KMUTT) for providing him with a Post-doctoral fellowship. The fourth author is indebted to the Thailand Research Fund and National Science and Technology Development Agency for its financial support.

References

[1] A.S. Dalkilic, S. Wongwises, Intensive literature review of condensation inside smooth and enhanced tubes, Int. J. Heat Mass Transfer 52 (2009) 3409–3426.
[2] A.S. Dalkilic, S. Wongwises, Book chapter, "Condensation heat transfer in smooth and enhanced geometries - A review of 2010 literature", in the book "Refrigeration Systems, Design Technologies and Developments", Nova Publishers, 2013, ISBN 978-1-62417-230-4.
[3] S. Laohalertdecha, A.S. Dalkilic, S. Wongwises, A review on the heat-transfer performance and pressure-drop characteristics of various enhanced tubes, Int. J. Air Cond. Refrig. 20 (2012) 1–20.
[4] A.S. Dalkilic, S. Wongwises, An investigation of a model of the flow pattern transition mechanism in relation to the identification of annular flow of R134a in a vertical tube using various void fraction models and flow regime maps, Exp. Thermal Fluid Sci. 34 (2010) 692–705.
[5] A.S. Dalkilic, S. Wongwises, Validation of void fraction models and correlations using a flow pattern transition mechanism model in relation to the identification of annular vertical downflow in-tube condensation of R134a, Int. Commun. Heat Mass Transfer 37 (2010) 827–834.
[6] Ahmet Selim Dalkılıç, Theoretical analysis on the prediction of coefficient of performance (COP) of vapour compression refrigeration systems using various alternative refrigerants, J. Therm. Sci. Technol. 32 (2012) 67–79.
[7] A.S. Dalkilic, S. Wongwises, A performance comparison of vapour compression refrigeration system using various alternative refrigerants, Int. Commun. Heat Mass Transfer 37 (2010) 1340–1349.
[8] M. Balcilar, A.S. Dalkilic, S. Wongwises, Artificial neural networks (ANNs) techniques for the determination of condensation heat transfer characteristics during downward annular flow of R134a inside a vertical smooth tube, Int. Commun. Heat Mass Transfer 38 (2011) 75–84.
[9] M. Balcilar, A.S. Dalkilic, B. Bolat, S. Wongwises, Investigation of empirical correlations on the determination of condensation heat transfer characteristics using computational numerical methods during downward annular flow of R134a inside a vertical smooth tube, J. Mech. Sci. Technol. 25 (10) (2011) 1–20.
[10] O. Agra, H. Demir, S. Ozgur Atayilmaz, F. Kantas, A.S. Dalkilic, Numerical investigation of heat transfer and pressure drop in enhanced tubes, Int. Commun. Heat Mass Transfer 38 (2011) 1384–1391.
[11] M. Balcilar, A.S. Dalkilic, O. Agra, S.O. Atayilmaz, S. Wongwises, A correlation development for predicting the pressure drop of various refrigerants during condensation and evaporation in horizontal smooth and micro-fin tubes, Int. Commun. Heat Mass Transfer 39 (2012) 937–944.
[12] A.S. Dalkilic, S. Laohalertdecha, S. Wongwises, Effect of void fraction models on the two-phase friction factor of R134a during condensation in vertical downward flow in a smooth tube, Int. Commun. Heat Mass Transfer 35 (2008) 921–927.
[13] A.S. Dalkilic, S. Laohalertdecha, S. Wongwises, Two-phase friction factor in vertical downward flow in high mass flux region of refrigerant HFC-134a during condensation, Int. Commun. Heat Mass Transfer 35 (2008) 1147–1152.
[14] A.S. Dalkilic, S. Laohalertdecha, S. Wongwises, Effect of void fraction models on the film thickness of R134a during downward condensation in a vertical smooth tube, Int. Commun. Heat Mass Transfer 36 (2009) 172–179.
[15] A.S. Dalkilic, O. Agra, I. Teke, S. Wongwises, Comparison of frictional pressure drop models during annular flow condensation of R600a in a horizontal tube at low mass flux and of R134a in a vertical tube at high mass flux, Int. J. Heat Mass Transf. 53 (2010) 2052–2064.
[16] A.S. Dalkilic, S. Laohalertdecha, S. Wongwises, New experimental approach on the determination of condensation heat transfer coefficient using frictional pressure drop and void fraction models in a vertical tube, Energy Convers. Manag. 51 (2010) 2535–2547.
[17] A.S. Dalkilic, Condensation pressure drop characteristics of various refrigerants in a horizontal smooth tube, Int. Commun. Heat Mass Transfer 38 (2011) 504–512.
[18] A.S. Dalkilic, N.A. Kürekci, S. Wongwises, Effect of void fraction and friction factor models on the prediction of pressure drop of R134a during downward condensation in a vertical tube, Heat Mass Transfer 48 (2012) 123–139.
[19] K. Aroonrat, A.S. Dalkilic, S. Wongwises, Experimental study on evaporative heat transfer and pressure drop of R-134a flowing downward through vertical corrugated tubes with different corrugation pitches, Heat Mass Transfer 26 (2013) 41–63.
[20] A.S. Dalkilic, S. Yildiz, S. Wongwises, Experimental investigation of convective heat transfer coefficient during downward laminar flow condensation of R134a in a vertical smooth tube, Int. J. Heat Mass Transfer 52 (2009) 142–150.
[21] A.S. Dalkilic, S. Laohalertdecha, S. Wongwises, Experimental investigation on heat transfer coefficient of R134a during condensation in vertical downward flow at high mass flux in a smooth tube, Int. Commun. Heat Mass Transfer 36 (2009) 1036–1043.

[22] A.S. Dalkilic, S. Wongwises, Experimental study on the condensation heat transfer coefficients in high mass flux region in annular flow regime of HFC-134a inside the vertical smooth tube, Heat Transfer Eng. 32 (2011) 33–44.
[23] A.S. Dalkilic, I. Teke, S. Wongwises, Experimental analysis for the determination of the convective heat transfer coefficient by measuring pressure drop directly during annular condensation flow of R134a in a vertical smooth tube, Int. J. Heat Mass Transf. 54 (2011) 1008–1014.
[24] S. Saisorn, J. Kaew-On, S. Wongwises, Flow pattern and heat transfer characteristics of R-134a refrigerant during flow boiling in a horizontal circular mini-channel, Int. J. Heat Mass Transf. 53 (2010) 4023–4038.
[25] A.S. Dalkılıç, İ. Teke, S. Wongwises, Heat transfer enhancement during downward laminar flow condensation of R134a in vertical smooth and micro-fin tubes, J. Therm. Sci. Technol. 32 (2012) 19–31.
[26] A.S. Dalkilic, B. Kundu, S. Wongwises, An experimental investigation on the Reynolds analogy applied to annular condensation laminar flow of R134a in a vertical tube, Arab. J. Sci. Eng. 38 (2013) 1493–1507.
[27] S. Laohalertdecha, S. Wongwises, Condensation heat transfer and flow characteristics of R-134a flowing through corrugated tubes, Int. J. Heat Mass Transfer 54 (2011) 2673–2682.
[28] K. Aroonrat, S. Wongwises, Evaporation heat transfer and friction characteristics of R-134a flowing downward in a vertical corrugated tube, Exp. Therm. Fluid Sci. 35 (2011) 20–28.
[29] S. Laohalerdecha, A.S. Dalkilic, S. Wongwises, Correlations for evaporation heat transfer coefficient and two-phase friction factor for R134a flowing through corrugated tubes, Int. Commun. Heat Mass Transfer 38 (2011) 1406–1413.

Journal of Dispersion Science and Technology
Publication details, including instructions for authors and subscription information:
http://www.tandfonline.com/loi/ldis20

Measurement and Correlation of the Viscosity of Water-Based Al_2O_3 and TiO_2 Nanofluids in High Temperatures and Comparisons with Literature Reports

Thaklaew Yiamsawas [a] , Ahmet Selim Dalkilic [b] , Omid Mahian [c] & Somchai Wongwises [a d]
[a] Fluid Mechanics, Thermal Engineering and Multiphase Flow Research Lab. (FUTURE), Department of Mechanical Engineering , Faculty of Engineering, King Mongkut's University of Technology Thonburi , Bangmod , Bangkok , Thailand
[b] Heat and Thermodynamics Division, Department of Mechanical Engineering , Yildiz Technical University, Yildiz , Besiktas , Istanbul , Turkey
[c] Young Researchers and Elite Club, Mashhad Branch, Islamic Azad University , Mashhad , Iran
[d] The Academy of Science, The Royal Institute of Thailand, Sanam Suea Pa , Dusit , Bangkok , Thailand
Accepted author version posted online: 06 Mar 2013.Published online: 14 Nov 2013.

To cite this article: Thaklaew Yiamsawas , Ahmet Selim Dalkilic , Omid Mahian & Somchai Wongwises (2013) Measurement and Correlation of the Viscosity of Water-Based Al_2O_3 and TiO_2 Nanofluids in High Temperatures and Comparisons with Literature Reports, Journal of Dispersion Science and Technology, 34:12, 1697-1703, DOI: 10.1080/01932691.2013.764483

To link to this article: http://dx.doi.org/10.1080/01932691.2013.764483

Journal of Dispersion Science and Technology, 34:1697–1703, 2013

ISSN: 0193-2691 print/1532-2351 online
DOI: 10.1080/01932691.2013.764483

Measurement and Correlation of the Viscosity of Water-Based Al_2O_3 and TiO_2 Nanofluids in High Temperatures and Comparisons with Literature Reports

Thaklaew Yiamsawas,[1] Ahmet Selim Dalkilic,[2] Omid Mahian,[3] and Somchai Wongwises[1,4]

[1]*Fluid Mechanics, Thermal Engineering and Multiphase Flow Research Lab. (FUTURE), Department of Mechanical Engineering, Faculty of Engineering, King Mongkut's University of Technology Thonburi, Bangmod, Bangkok, Thailand*
[2]*Heat and Thermodynamics Division, Department of Mechanical Engineering, Yildiz Technical University, Yildiz, Besiktas, Istanbul, Turkey*
[3]*Young Researchers and Elite Club, Mashhad Branch, Islamic Azad University, Mashhad, Iran*
[4]*The Academy of Science, The Royal Institute of Thailand, Sanam Suea Pa, Dusit, Bangkok, Thailand*

GRAPHICAL ABSTRACT

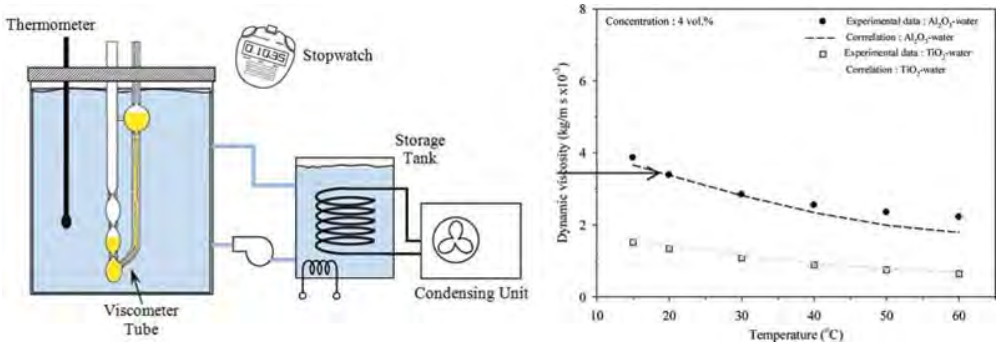

In this article, the viscosity of two common nanofluids including Al_2O_3/water and TiO_2/water is measured at high temperatures, and high concentrations of the nanofluids. The range of temperature is 15–60°C where the volume fraction of nanoparticles varies from 1 to 8%. Next, comparisons have been done with the most well-known theoretical and experimental reports in the literature. Finally, using the experimental data, a helpful correlation is presented.

Keywords Correlation, high temperature, nanofluid, viscosity

Received 13 November 2012; accepted 1 January 2013.

The present study was supported by the Thailand Research Fund (TRF), the National Science and Technology Development Agency, the Office of the Higher Education Commission, and the National Research University Project whose guidance and assistance are gratefully acknowledged. A. S. Dalkilic and O. Mahian thank the Department of Mechanical Engineering, King Mongkut's University of Technology Thonburi and Professor Somchai Wongwises for providing them fellowships for doing their research in Thailand.

Address correspondence to Somchai Wongwises, Fluid Mechanics, Thermal Engineering and Multiphase Flow Research Lab. (FUTURE), Department of Mechanical Engineering, Faculty of Engineering, King Mongkut's University of Technology Thonburi, Bangmod, Bangkok 10140, Thailand. E-mail: somchai.won@kmutt.ac.th

INTRODUCTION

Nanofluids as a new group of working fluids with a small volume fraction of nanometer-sized solid particles in suspension have attracted special attention.[1] Currently, the use of nanofluids to enhance the performance and thermal efficiency of engineering systems is in progress. During the last decades many researches have been done on the preparation, properties, and applications of nanofluids. The readers can refer to some of these studies that have been conducted recently.[2–11]

Up to now, extensive studies have been done on the viscosity of nanofluids. Estimation of the viscosity of nanofluids at different temperatures and concentrations is very important for the design of various thermal engineering systems such as heat exchangers; because the amount of

viscosity determines the pumping power, and consequently the performance costs of thermal systems. Here, the most important studies in the field are reviewed briefly.

Pak and Cho[12] measured the viscosity of Al_2O_3/water and TiO_2/water nanofluids at room temperature using a rotational viscometer. Particle sizes of alumina (Al_2O_3) and titanium dioxide (TiO_2) are 13 nm and 27 nm, respectively. Their results indicated that the viscosity of nanofluids is greater than that of the base fluid. For the volume fraction of 10%, they found that the relative viscosity of TiO_2/water increases by 3 times, whereas the relative viscosity of Al_2O_3/water increases by 200 times. They also showed that the classic model underestimates the viscosity.

Wang et al.[13] examined the viscosity of Al_2O_3 suspended in water and ethylene glycol (EG) solution. They investigated the effects of dispersion methods on the viscosity, which are mechanical blending (method 1), particles coated with polymers (method 2), and filtration (method 3). The authors found that the second and third methods are superior because of providing smaller viscosities than the first method. They also perceived that with increases of concentration, both viscosity quantity and viscosity ratio increase linearly.

He et al.[14] measured the viscosity of the TiO_2/water nanofluid. Particle sizes of TiO_2 are 95, 145, and 210 nm where the concentration range is 1 to 5 wt%. They found that the viscosity ratio increases nonlinearly with the concentration. They found that the increase of particle size leads to increases of the viscosity ratio.

Nguyen et al.[15] studied the effects of temperature, concentration, and particle size on the viscosity of Al_2O_3/water and CuO/water nanofluids. They utilized two dimensions of Al_2O_3 nanoparticles including 36 and 47 nm, and particle size of 36 nm for CuO nanoparticles. The experiments are conducted at a temperature range of 22 to 75°C with a concentration range of 1 to 12 vol%. A piston-type viscometer is used in this research. Results showed that with increasing the temperature, viscosity decreases. On the contrary, the increase of concentration results in an increase of viscosity. It is also found that particle size has no effect on the viscosity of Al_2O_3/water at small concentrations. However, at large concentrations, the increase of particle size increases the viscosity. They also found that CuO–water had greater viscosity than Al_2O_3–water nanofluid. The comparison between the experimental results and theoretical models shows that the theoretical models of Einstein, Brinkman, and Batchelor are not useful to predict the viscosity.

Murshed et al.[16] measured the viscosity of TiO_2 and Al_2O_3 nanofluids, both suspended in deionized water. Particle sizes of TiO_2 and Al_2O_3 are 15 and 80 nm, respectively. The experiments are conducted at a concentration range of 1–5 vol%, and a rotational viscometer is used for measurement.

Duangthongsuk and Wongwises[17] studied the effects of temperature on the viscosity of TiO_2/water nanofluid. A rotational rheometer (Malvern Instrument) is used to measure the viscosity. The particle size of TiO_2 is 21 nm, with a temperature range of 15 to 35°C and concentration range of 0.2 to 2 vol%. They found that with increasing of temperature the viscosity ratio increases, especially at the large volume fraction.

Turgut et al.[18] measured the viscosity of TiO_2 nanofluid mixed in a deionized water base fluid. A vibration viscometer (Vibro A&D) is used to measure the viscosity of nanofluid in a concentration range of 0.2 to 3 vol% and temperature range of 13 to 55°C. They found that the relative viscosity increases nonlinearly with concentration. They showed that classic models of Einstein, Nielsen, and Krieger and Dougherty underestimates the viscosity obtained by the experimental study.

Chandrasekar et al.[19] performed an experimental and theoretical study on the effects of concentration on the viscosity of Al_2O_3/water nanofluid where the particle size is 43 nm. The experiments are conducted at a concentration range of 1 to 5 vol% at room temperature. The Results showed that Al_2O_3/water nanofluid at the volume fractions mentioned is Newtonian.

In a comparative work, Xie et al.[20] compared the viscosity of five different nanofluids including ethylene glycol based MgO, TiO_2, ZnO, Al_2O_3 and SiO_2 nanofluids. They found that for the temperatures range of 10 to 60°C, the viscosity of MgO/EG nanofluid is the smallest. Fedele et al.[21] presented some results for the viscosity of water based TiO_2 nanofluid at a temperature range of 10 to 70°C. Recently, Aladag et al.[22] obtained the viscosity of Al_2O_3/water and CNT/water based nanofluids at low volume fractions and low temperatures (between 2 and 10°C). A review of the latest results on the viscosity of nanofluids is performed by Mahbubul et al.[23]

From the researches mentioned above and with a review of the literature, it is found that the viscosity of nanofluids is greater than that of the base fluid and it increases with concentration, and decreases with temperature. However, there are still many differences and deviations in the research. For instance, the results presented by Duangthongsuk and Wongwises[17] contradict the results reported by Nungyen et al.[15] indicated that the viscosity ratio decreases with temperature, but, Duangthongsuk and Wongwises[17] reached to an opposite result.

In this work, in the first, the viscosities of water based Al_2O_3 and TiO_2 nanofluids are measured at high temperatures (by 60°C) and volume fractions between 1–8%. Next, comparisons with the works reported in the literature are conducted. Finally, a helpful correlation to calculate the viscosity of nanofluids is presented for using in the design of thermal systems. Based on the best knowledge of the authors, the data presented in the present work, have not appeared never in the open literature.

NANOFLUID PREPARTION

In this study, TiO_2 (21 nm) and Al_2O_3 (120 nm) nanoparticles suspended in water, respectively, with weight fractions of 40% and 30% were provided by Degussa Company, Germany. To prepare the desired concentrations of nanofluids, the dilution is mixed with water. Next, using an ultrasonic vibration system the mixture is sonicated for 2 hours to avoid agglomeration.

No sedimentation of nanoparticles is observed after months. In this work, high concentrations of TiO_2/water nanofluid (by 8%) are used, while for Al_2O_3/water nanofluid, only the volume fractions up to 4% are used. It should be noted that Al_2O_3/water nanofluid is non-Newtonian for volume fractions higher than 4%, whereas the suspensions of TiO_2 are Newtonian for concentrations by 8%. This is because of the bigger size of Al_2O_3 nanoparticles (120 nm), which makes it non-Newtonian.

EXPERIMENTAL SETUP

A capillary tube viscometer (Cannon Instrument, USA) is used to measure the viscosity of nanofluids. This type of capillary tube viscometer has very good accuracy so that it is widely used in both industry and laboratory, and has been used by many researchers. The components of the viscometer, is shown in Figure 1. It is composed of a 0.75 mm viscometer tube with a measurement range of 1.6 to 8 cSt. The tube is immersed in a transparent temperature-controlled basin connected to a temperature-controlled water tank. A stopwatch with the accuracy of 0.01 s is used to record the time of passing the fluid from a specified section of the viscometer and a thermometer with the accuracy of 0.1°C is used to measure the temperature.

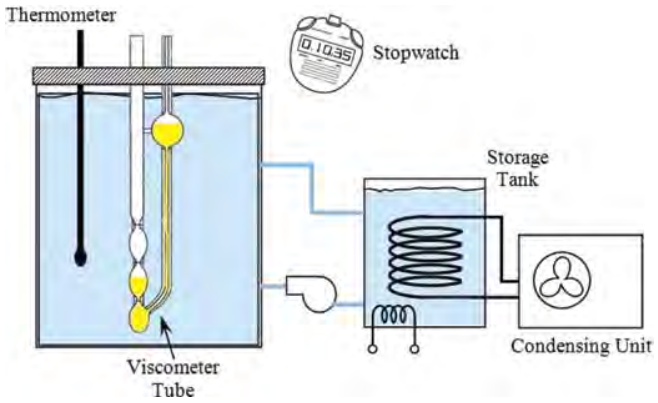

FIG. 1. Schematic diagram of the experimental setup. (Figure available in color online.)

DATA REDUCTION

The viscosity can be obtained by the following relation:

$$\mu = C \cdot \rho t. \quad [1]$$

Where μ is the viscosity (kg/ms), C is a constant fo the viscometer tube obtained from calibration with reference substance supplied by the manufacturer (=0.008 cSt/s), ρ is the density (kg/m^3), and t is the flowing time of the sample substance during each test (s). The density of nanofluid (ρ_{nf}) is obtained by the following well known relation [3]:

$$\rho_{nf} = \phi\rho_p + (1-\phi)\rho_f. \quad [2]$$

In this work, some comparisons have been done by the theoretical models and correlations which the relations are presented here.

Einstein's equation [3]: This model is based on phenomenological hydrodynamic equations and considers suspension containing solute particles in a total volume. This model is as follows:

$$\mu_{nf} = (1+2.5\phi)\mu_f, \quad [3]$$

where μ_{nf} is the viscosity of nanofluid, μ_f is the viscosity of base fluid, and ϕ is the volume fraction (vol%).

Brinkman[3] presented a model to predict the viscosity of mixtures by improving and developing the Einstein's model, which can be derived by considering the effect of the addition of one solute molecule to an existing solution. The model, which can be used in the cases of large concentrations, is as follows:

$$\mu_{nf} = \frac{1}{(1-\phi)^{2.5}}\mu_f \quad [4]$$

Another popular classic model is Batchelor's equation,[3] which is based on the reciprocal theorem in Stokes flow problem. It produces an expression of the bulk stress due to the thermodynamic forces and incorporates both hydrodynamic effects and Brownian motion. The equation is as follows:

$$\mu_{nf} = (1+2.5\phi+6.2\phi^2)\mu_f \quad [5]$$

The above relations are old. Recently, Conrcione[24] presented the following relation:

$$\frac{\mu_{nf}}{\mu_f} = \frac{1}{1-34.87(d_p/d_f)^{-0.3}\phi^{1.03}}, \quad [6]$$

where d_p is nanoparticle size, and d_f is the molecule diameter of base fluid which can be calculated by:

$$d_f = \left[\frac{6M}{N\pi\rho_{f,0}}\right]^{1/3}, \quad [7]$$

where M is the molecular weight of base fluid, N is the Avogadro number, and $\rho_{f,0}$ is the density of base fluid calculated at the temperature of 293 K.

The results of the present work are compared with the above models and the experimental data in the literature.

RESULTS AND DISCUSSIONS

Before performing the experiments with nanofluids, to examine the accuracy of the experimental set up, a comparison of the viscosity of water has been made between the results obtained by the present set up and the results presented in ASHRAE.[25] As it is seen from Figure 2, there is a little difference between the two results (average 7%).

Figure 3 shows the variations of TiO_2/water nanofluid as a function of particle concentration and temperature. The results show that the viscosity increases with increasing of volume fraction and decreasing temperature, as expected. It is seen that with an increase in the temperature, the differences among the values of viscosity at various concentrations are decreased. This means that at high temperatures where the distances among the molecules of base fluid increases, adding nanoparticles is more reasonable for practical applications, because with increasing the temperature, the difference between the viscosity of water and the concentration of 8% is reduced. It is also observed that with an increase in the volume fraction, the viscosity increases.

Figure 4 shows the variations of viscosity of Al_2O_3/water with temperature at different volume fractions. As it is mentioned, for Al_2O_3/water nanofluid, the viscosity only for volume fractions by 4% is measured. A comparison between Al_2O_3/water and TiO_2/water nanofluids at volume fraction of 4% shows that the viscosity of Al_2O_3/water is more than twice the nanofluid of TiO_2/water. This

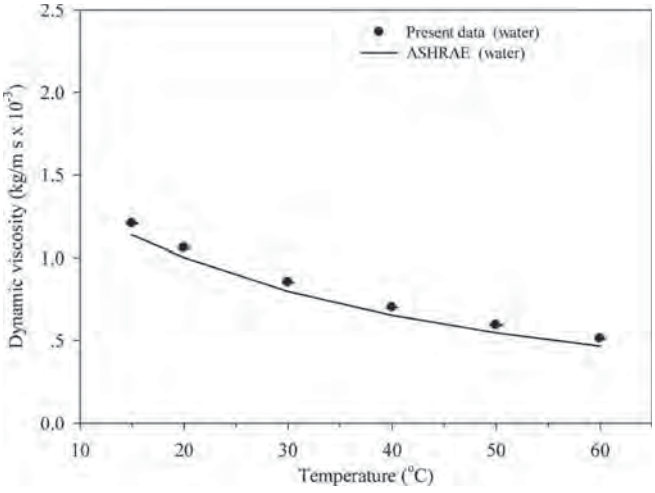

FIG. 2. Comparison of the measured viscosity with reference data.

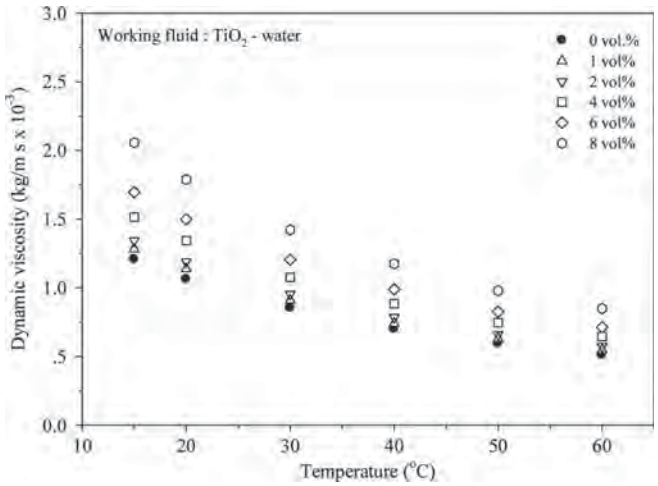

FIG. 3. Viscosity of TiO_2-water nanofluid as a function of temperature and concentration.

difference may be due to larger size of Al_2O_3 nanoparticles. This comparison shows that classic models such as Brinkman, and Batchelor are not suitable models, because the viscosity ratio in these models is only a function of volume fraction and the effect of is not considered.

Figure 5 provides a comparison between the present data and the former workers reported in the literature for TiO_2/water. Figure 5 is plotted to show the trend of variation of viscosity with volume fraction. It is seen that the trend is different for the works. For example, the present data show that the rate of increase in the viscosity ratio with concentration is nearly constant. Masuda et al.[26] and Pak and Cho[12] reached to a similar result. However, Murshed et al.[16] concluded that the rate of increase in the

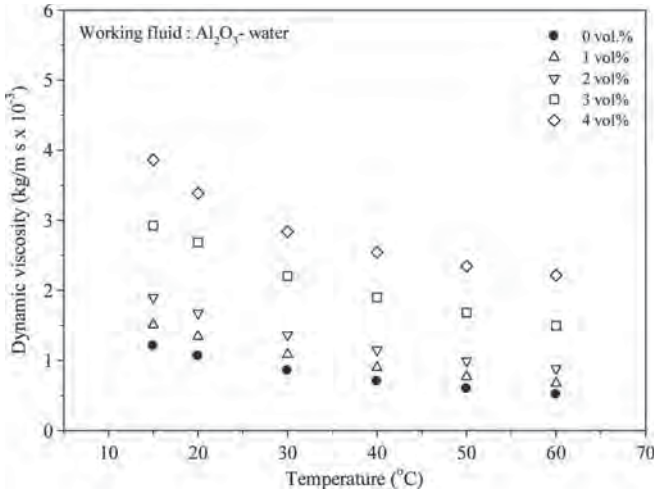

FIG. 4. Viscosity of Al_2O_3-water nanofluid as a function of temperature and concentration.

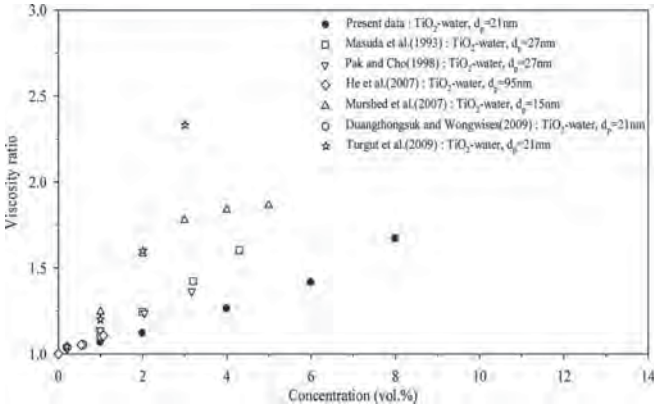

FIG. 5. Effect of concentration on the viscosity ratio of TiO_2/water nanofluid.

viscosity ratio decreases with increasing the concentration. Turgut et al.[18] perceived that the rate of increase in the viscosity ratio increases rapidly with increasing the concentration. As seen, three different trends are presented for TiO_2/water nanofluid.

In Figure 6. the comparisons between the viscosity ratios for Al_2O_3/water nanofluid performed by various researchers are presented. As it is observed, the trend of the present data is in accordance with the works conducted by Kulkalni et al.,[27] Chandrasekar et al.[19] However, other works show nearly a linear variation in the viscosity ratio with increasing the concentration. The differences between the studies for the two nanofluids may be due to various factors such as different shape and size of nanoparticles, different methods of preparation and functionalizing.

Figure 7 provides a comparison between the present data and the theoretical models presented in the literature for the viscosity ratio of TiO_2/water nanofluid. It is observed that the Corcione model overestimates the

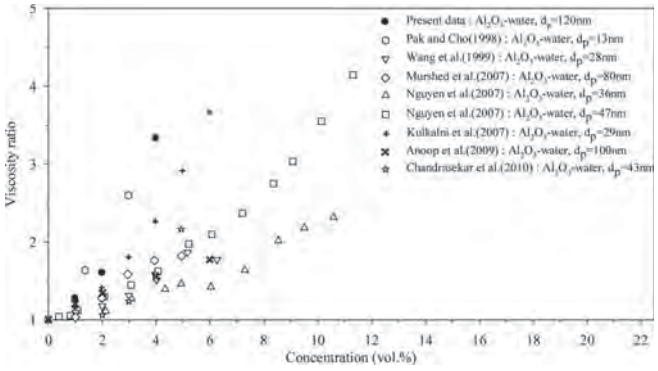

FIG. 6. Effect of concentration on the viscosity ratio of Al_2O_3 nanofluid.

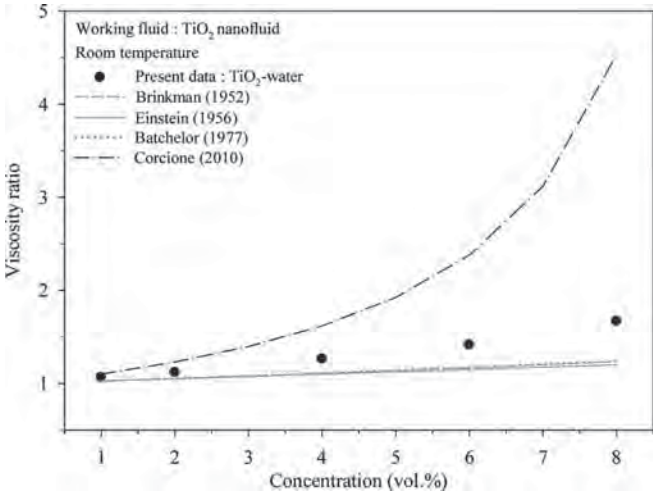

FIG. 7. Comparison of experimental viscosity ratio of TiO_2-water nanofluid with those obtained from various model equations as a function of concentration.

viscosity ratio, while other theoretical models underestimate the viscosity ratio.

Figure 8 gives a comparison between the present data and theoretical models for the viscosity ratio of Al_2O_3/water nanofluid. As shown, the difference between the present data and other models is very large especially at high concentrations

Figure 9 shows that at a given value of concentration (here 4%), the viscosity ratio obtained by the present work is approximately linear and constant with respect to temperature. In comparison with theoretical models, the viscosity ratio provided by this work is about 15% higher than the viscosity ratio calculated by the models.

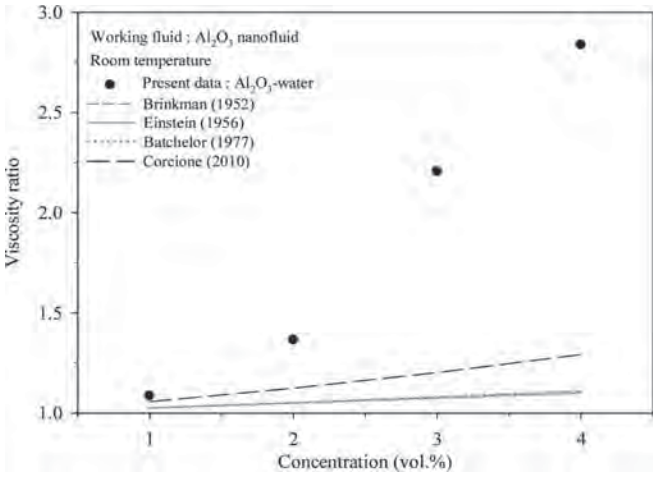

FIG. 8. Comparison of experimental viscosity ratio of Al_2O_3-water nanofluid with those obtained from various model equations as a function of concentration.

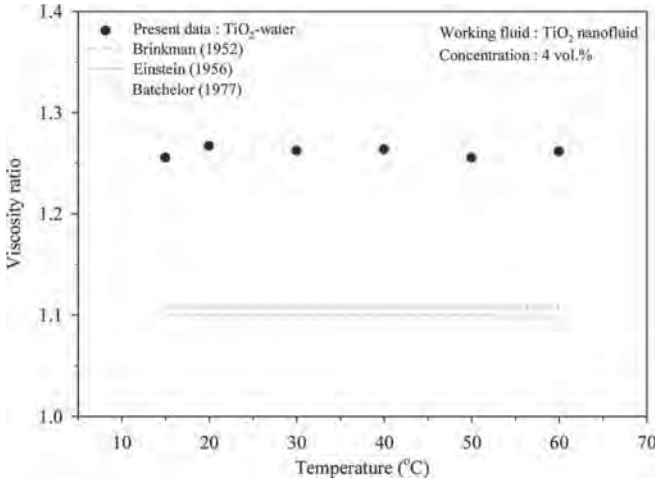

FIG. 9. Comparison of experimental viscosity ratio of TiO_2-water nanofluid with those obtained from various model equations as a function of temperature.

Figure 10 shows the variation of viscosity ratio with temperature for different models.

It is seen that theoretical models fail to predict the viscosity ratio. Also, it is observed that the viscosity ratio predicted by Nguyen et al.[15] is lower than the present data. It may be due to the bigger size of Al_2O_3 nanoparticles tested in this work compared Nguyen et al.[15]

Finally, a correlation is presented for using in the practical applications. In this correlation, the viscosity is a function of temperature, volume fraction and the viscosity of base fluid as:

$$\mu_{nf} = A\phi^B T^C \mu_f^D, \qquad [8]$$

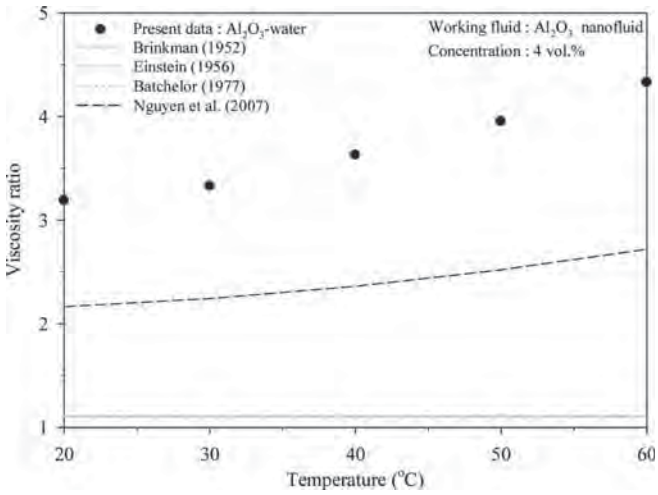

FIG. 10. Comparison of experimental viscosity ratio of Al_2O_3-water nanofluid with those obtained from various model equations as a function of temperature.

TABLE 1
Coefficients for correlations predicting viscosity

	Coefficient			
Nanoparticle	A	B	C	D
Al_2O_3	0.891842	0.739192	0.099205	0.9844
TiO_2	0.837931	0.188264	0.089069	1.100945

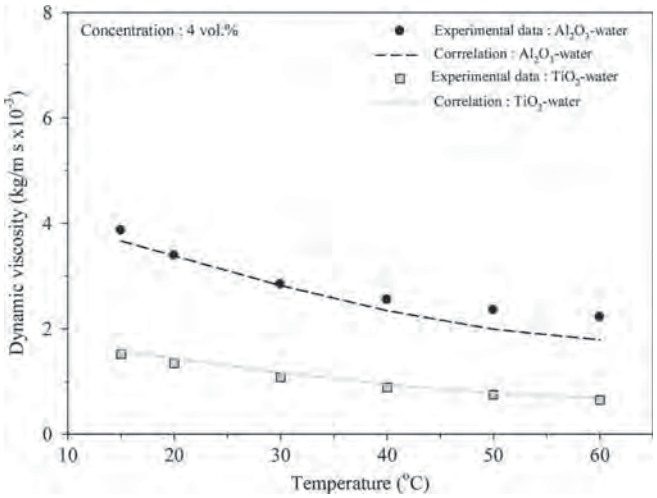

FIG. 11. Comparison of measured viscosity with proposed correlation.

where the coefficients of A, B, C, and D are provided for the two types of nanoparticles in Table 1.

In the above relation, although the coefficient of C (the power of temperature) is positive and one may claim the viscosity of nanofluid increases with increasing the temperature. However, it should be noted that the viscosity of base fluid decreases with increasing the temperature, hence, totally the viscosity of nanofluid decrease. The viscosity of water as the base fluid is obtained by the following relation:

$$\mu_f = 0.0002\,T^2 - 0.0335\,T + 1.6428. \qquad [9]$$

Figure 11 shows the comparison between the correlation and experimental data. The average error in the comparison for TiO2/water nanofluid is about 5%, and for Al_2O_3/water nanofluid is about 9%.

CONCLUSION

The viscosity of TiO_2 and Al_2O_3 nanoparticles suspended in water is measured at high temperatures (by 60°C). The sizes of TiO_2 and Al_2O_3 nanoparticles are respectively 21 and 120 nm where volume fractions 8% and 4% are used for TiO_2 and Al_2O_3 nanoparticles, respectively. Some

comparisons with the reported works in the literature have been done. From the comparison, it is found that the trend of variations of viscosity ratio with concentration is different in various works. In some of them the viscosity ratio increases linearly, and in some of them the viscosity ratio increases rapidly as parabolic. The differences among different studies may be due to various factors such as different shape and size of nanoparticles, different methods of preparation and functionalizing. This study reveals that in the theory models, besides of volume fraction, the size and shape of nanoparticles, and temperature should be considered. Finally, a helpful correlation to use in practical applications is presented in which the viscosity of nanofluid is a function of temperature, volume fraction, and viscosity of base fluid.

REFERENCES

[1] Mahian, O., Mahmud, S., and Heris, S.Z. (2012) *J. Heat Transfer*, 134: 101704.

[2] Saidur, R., Leong, K.Y., and Mohammad, H.A. (2011) *Renewable and Sustainable Energy Reviews*, 15: 1646.

[3] Khanafer, K. and Vafai, K. (2011) *Int. J. Heat Mass Transfer*, 54: 4410.

[4] Mahian, O., Kianifar, A., Kalogirou, S.A., Pop, I., and Wongwises, S. (in press) *International journal of Heat and Mass Transfer*, http://dx.doi.org/10.1016/j.ijheatmasstransfer.2012.10.037

[5] Yu, W., Xie, H., and Wang, X. (2011) *J. Dispersion Science and Technology*, 32: 948.

[6] Chen, L., Xie, H., Yu, W., and Li, Y. (2011) *J. Dispersion Science and Technology*, 32: 550.

[7] Solanki, J.N. and Murthy, Z.V.P. (2011) *J. Dispersion Science and Technology*, 32: 724.

[8] Park, E.J., Lee, J., Jung, D., and Shim, S.E. (2011) *J. Dispersion Science and Technology*, 32: 1485.

[9] Aminfar, H. and Motallebzadeh, R. (2011) *J. Dispersion Science and Technology*, 32: 1311.

[10] Aminfar, H. and Motallebzadeh, R. (2012) *J. Dispersion Science and Technology*, 33: 155.

[11] Hojjat, M., Etemad, S.Gh., Bagheri, R., and Thibault, J. (2012) *J. Dispersion Science and Technology*, 33: 1066.

[12] Pak, B.C. and Cho, Y.I. (1998) *Experimental Heat Transfer*, 11: 151.

[13] Wang, X.Q. and Mujumdar, A.S. (2007) *International Journal of Thermal Science*, 46: 1.

[14] He, Y., Jin, Y., Chen, H., Ding, Y., Cang, D., and Lu, H. (2007) *International Journal of Heat and Mass Transfer*, 50: 2272.

[15] Nguyen, C.T., Desgranges, F., Roy, G., Galanis, N., Mare, T., Boucher, S., and Mintsa, H.A. (2007) *International Journal of Heat and Fluid Flow*, 28: 1492.

[16] Murshed, S.M.S., Leong, K.C., and Yang, C. (2008) *International Journal of Thermal Science*, 47: 560.

[17] Duangthongsuk, W. and Wongwises, S. (2009) *Experimental Thermal and Fluid Science*, 33: 706.

[18] Turgut, A., Tavman, I., Chirtoc, M., Schuchmann H. P., Sauter, C., and Tavman, S. (2009) *Int. J. Thermophys*, 30: 1213.

[19] Chandrasekar, M., Suresh, S., and Bose, A.C. (2010) *Experimental Thermal and Fluid Science*, 34: 210.

[20] Xie, H., Yu, W., and Chen, W. (2010) *Journal of Experimental Nanoscience*, 5: 463–472.

[21] Fedele, L., Colla, L., and Sergio Bobbo. (2012) *International Journal of Refrigeration*, 35: 1359.

[22] Aladag, B., Halelfadl, S., Doner, N., Maré, T., Duret, S., and Estellé, P. (2012) *Applied Energy*, 97: 876.

[23] Mahbubul, I.M., Saidur, R., and Amalina, M.A. (2012) *International Journal of Heat and Mass Transfer*, 55: 874.

[24] Corcione, M. (2011) *Energy Conversion and Management*, 52: 789.

[25] ASHRAE. (2005) American Society of Heating, Refrigerating and Air-Conditioning Engineers Inc., Atlanta, GA.

[26] Masuda, H., Ebata, A., Teramae, K., and Hishinuma, N. (1993) *Netsu Bussei (Japan)*, 7: 227.

[27] Kulkarni, D.P., Das, D.K., and Patil, S.L. (2007) *J. Nanosci. Nanotechno.*, 7: 2318.

Estimation of operational costs due to entropy generation in a vertical annulus

Omid Mahian

Young Researchers and Elite Club,
Mashhad Branch, Islamic Azad University,
Mashhad, Iran
E-mail: omid.mahian@gmail.com

Hakan F. Oztop

Technology Faculty,
Department of Mechanical Engineering,
Fırat University,
Elazig 23119, Turkey
E-mail: hfoztop1@gmail.com

Ahmet Z. Sahin*

Mechanical Engineering Department,
King Fahd University of Petroleum and Minerals,
Dhahran 31261, Saudi Arabia
E-mail: azsahin@kfupm.edu.sa
*Corresponding author

Somchai Wongwises

Fluid Mechanics, Thermal Engineering
and Multiphase Flow Research Lab. (FUTURE),
Department of Mechanical Engineering,
Faculty of Engineering,
King Mongkut's University of Technology Thonburi,
Bangmod, Bangkok 10140, Thailand
E-mail: somchai.won@kmutt.ac.th

Abstract: The study of flow and heat transfer in a vertical annulus is important due to its applications in the cooling of reactors, industrial heat exchangers, microelectronic devices, and so forth. The aim of the present work is to estimate the operational costs due to entropy generation in an annulus with isoflux boundary conditions. For this purpose, the governing equations are simplified and solved analytically to obtain the entropy generation distribution in the annulus. Using the results obtained by the entropy generation analysis, the operational costs due to entropy generation are calculated for various radius

ratios and different quantities of the flow parameters involved in the problem. The results of this study can be helpful in the design of such heat exchangers to reduce the operational costs caused by the irreversibilities.

Keywords: operational cost; isoflux heat exchanger; entropy generation; refrigerant flow; analytical solution.

Reference to this paper should be made as follows: Mahian, O., Oztop, H.F., Sahin, A.Z. and Wongwises, S. (2013) 'Estimation of operational costs due to entropy generation in a vertical annulus', *Int. J. Exergy*, Vol. 13, No. 4, pp.472–486.

Biographical notes: Omid Mahian is a PhD student in Mechanical Engineering (energy conversion) in Ferdowsi University of Mashahd, Iran. He is interested in some topics in heat transfer engineering include entropy generation and exergy analysis, heat and fluid flow of nanofluids, and solar stills. He has more than 13 ISI papers in high quality journals such as *International Journal of Heat and Mass Transfer*, *Journal of Heat Transfer (ASME)*, *Journal of Thermophysics and Heat transfer (AIAA)* and *Energy (Elsevier)*. He is selected as the best researcher student in the department of his university at 2012.

Hakan F. Oztop is an Associate Professor at Mechanical Education Department of Technical Education Faculty of Firat University. He received the BS from Firat University, Department of Mechanical Engineering in 1996, MS and PhD from the same university in 1998 and 2003, respectively. His main research area is numerical heat transfer and fluid flow in forced, mixed and natural convection through porous ducts and cavities and renewable energy sources. He has also experience on second law analysis of thermal and fluid systems. He has published 125 papers in SCI journals and 70 research articles in international or national conferences.

Ahmet Z. Sahin, PhD, is a Professor of Mechanical Engineering at King Fahd University of Petroleum and Minerals (KFUPM), Dhahran, Saudi Arabia. He received his PhD in Mechanical Engineering from the University of Michigan, Ann Arbor, MI, USA, in 1988. He has published over 200 technical journal/conference papers. He received the KFUPM Distinguished Researcher Award three times, in 2000, 2005 and 2010. His research interests include thermodynamic design optimisation, entropy generation minimisation, solar energy and wind energy applications.

Somchai Wongwises is currently a Professor of Mechanical Engineering at King Mongkut's University of Technology Thonburi, Bangmod, Thailand. He received his Doktor-Ingenieur (Dr.-Ing.) in Mechanical Engineering from the University of Hannover, Germany, in 1994. His research interests include two-phase flow, heat transfer enhancement, and thermal system design.

1 Introduction

The analysis of the second law of thermodynamics implies the use of availability to determine irreversibility, or lost work, during a process (Kumar et al., 1989). In the 1980s, Bejan (1982) applied the second law of thermodynamics to find the various effective factors in the loss of available work (exergy) of the thermal systems through entropy generation. During the recent years, many research studies have been carried out

on entropy generation and thermoeconomic analysis in different thermal systems. A number of the recent studies in the field of entropy generation, thermoeconomic analyses of different thermal systems could be found in Ghazi et al. (2012), Anandan and Bhaskaran (2012), Ahmadi et al. (2012), Aydin et al. (2012), Wu et al. (2012), Askar et al. (2012), Matawala and Prabhakaran (2012), Makinde (2012), Aziz and Khan (2012a, 2012b), Ramos-Alvarado et al. (2012) and Sahin (2012).

The entropy generation problems are usually non-linear and it is difficult to solve them. Therefore, a helpful way to determine the entropy generation rate in complex systems is by simplifying the governing equations with reasonable assumptions to obtain analytical expressions for entropy generation distribution in the system. Here, the entropy generation in an annulus has been investigated; hence, a brief review is presented, adapted from the former analytical works related to the entropy generation between two cylinders.

Yilbas (2001) performed an entropy generation analysis for a rotating outer cylinder by neglecting the irreversibility due to fluid friction and assuming a linear velocity profile. Mahmud and Fraser (2002a, 2002b, 2003a) presented an entropy generation analysis within an annulus under the different boundary conditions. They solved the simplified governing equations in cylindrical coordinates to obtain the distributions of entropy generation and Bejan number. Tasnim and Mahmud (2002a, 2002b) investigated that the generation of entropy in vertical annuli by considering the fully developed laminar flow and the mixed convection heat transfer. Mirzazadeh et al. (2008) studied that the entropy generation between the concentric rotating cylinders using a non-linear viscoelastic fluid as the working fluid. Mahian et al. (2012a) investigated that the entropy generation between two rotating cylinders using nanofluids with the different volume fractions and under different isoflux boundary conditions. In another work, Mahian et al. (2012b) examined that the effects of uncertainties in the models presented for thermophysical properties of nanofluids on entropy generation. Mahian et al. (2012c) recently investigated that the effects of MHD flow on the entropy generation between two isothermal rotating cylinders. In addition, Mahian et al. (2013) studied that the effects of nanofluids on entropy generation between two cylinders in the presence of a magnetic field.

A review of the literature shows that there is no work focusing on the estimation of operational costs due to entropy generation (thermoeconomic analysis) in an isoflux annulus with refrigerant, whereas in the former papers the isothermal boundary conditions are applied. Beside this point, in most of the published works, the economic aspects for such heat exchangers are not considered. Of course, for the flow in a pipe, Sahin et al. (2000) estimated that the operational costs due to the entropy generation by considering the fouling effects. Indeed, the main aim of this work is to estimate the operational costs due to irreversibilities for the vertical annulus under different conditions where the working fluid is engine oil.

2 Problem formulation

In the first, the formulation of the velocity and temperature fields is presented. Next, the formulation of entropy generation is given.

2.1 Velocity and temperature fields

Schematic of the problem is shown in Figure 1. Consider a laminar, steady, and incompressible flow of a viscous fluid with inlet velocity U_0 and inlet temperature T_0 entering an isoflux annulus with radii r_i and r_o. The properties of the working fluid are assumed temperature-independent.

Figure 1 Schematic view of the problem (see online version for colours)

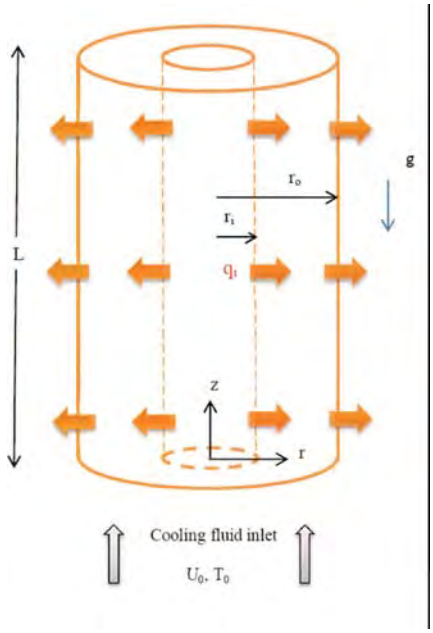

By considering a fully developed flow, the buoyancy effects, and a small variation of temperature in z-direction, the governing equations in dimensionless form can be written as (see Tasnim and Mahmud, 2002a, 2002b; Tasnim et al., 2002; Mahmud and Fraser, 2002c; Sahin et al., 2000):

$$\frac{\partial^2 U}{\partial R^2}+\frac{1}{R}\frac{\partial U}{\partial R}=-\frac{Gr}{\mathrm{Re}}\theta+\frac{\partial P^*}{\partial Z} \tag{1}$$

$$\frac{\partial^2 \theta}{\partial R^2}+\frac{1}{R}\frac{\partial \theta}{\partial R}=0 \tag{2}$$

with the following boundary conditions:

$$\begin{aligned} &U=0 \quad \text{and} \quad \frac{\partial \theta}{\partial R}=-1 \quad \text{at } R=\lambda \\ &U=0 \quad \text{and} \quad \frac{\partial \theta}{\partial R}=F(q_i) \quad \text{at } R=1 \end{aligned} \tag{3}$$

in which the value of $F(q_i)$ is obtained based on the heat flux in the inner cylinder so that the energy equation is satisfied. Of course, because of heat flux boundary conditions, there is no need to obtain the heat flux on outer cylinder. In the above, the dimensionless parameters are defined as follows:

$$U=\frac{V_z}{U_0},\ R=\frac{r}{r_o},\ \mathrm{Re}=\frac{U_0 r_o}{\upsilon},\ P^*=\frac{P}{U_0\mu}r_o,\ Z=\frac{z}{r_o},\ \lambda=\frac{r_i}{r_o}$$
$$\theta=\frac{T-T_0}{q_i r_o/k},\ \mathrm{Gr}=\frac{g\beta\Delta T\quad r_o^3}{\upsilon^2},\ \Delta T=\frac{q_i r_o}{k}. \tag{4}$$

2.2 Entropy generation

The entropy generation rate is obtained by the following relation (see Tasnim and Mahmud (2002a, 2002b) for more details):

$$\dot{S}'''_{\mathrm{gen}}=\frac{k}{T_0^2}\left(\frac{\partial T}{\partial r}\right)^2+\frac{\mu}{T_0}\left(\frac{\partial V_z}{\partial r}\right)^2. \tag{5}$$

The above relation indicates that entropy generation is due to two effects. The first is heat transfer, and the second is fluid friction. The above relation is as follows in dimensionless form:

$$N_S=\frac{\dot{S}'''_{\mathrm{gen}}}{\mu U_0^2/T_0 r_0^2}=\left(\frac{\Omega}{\mathrm{Br}}\right)\left(\frac{\partial\theta}{\partial R}\right)^2+\left(\frac{\partial U}{\partial R}\right)^2=N_H+N_F \tag{6}$$

where N_s is the entropy generation number and N_H, N_F represent the contribution of heat transfer and fluid friction to the entropy generation, respectively. In the above relation, Ω and Br (Brinkman number) are equal to $\Delta T/T_0$ and $U_0^2\mu/k\Delta T$, respectively.

The Bejan number can be defined as:

$$\mathrm{Be}=\frac{N_H}{N_S}. \tag{7}$$

3 Solution to the problem

3.1 Velocity and temperature fields

The governing equations are coupled via the buoyancy term. Therefore, in the first, the energy equation should be solved.

The solution of the energy equation is obtained by twice integrating from the relation with respect to *R*. The solution becomes:

$$\theta(R)=-\lambda\ln(R)+C \tag{8}$$

where *C* is the constant of integration and cannot be obtained in this step, due to isoflux boundary conditions. The velocity field is determined by substituting the temperature distribution in the momentum equation and the solution of the differential equation as follows:

$$U(R) = \Gamma_1 \ln(R) + \Gamma_2 (1 - R^2) + \frac{(-\lambda^3 + \lambda R^2)(\mathrm{Gr}/\mathrm{Re})}{4} \ln(R) \tag{9}$$

where Γ_1 and Γ_2 are constant and are obtained by:

$$\begin{aligned} \Gamma_1 &= \frac{[(C+\lambda)(\mathrm{Gr}/\mathrm{Re}) - (\partial P^*/\partial Z)](\lambda^2 - 1)}{4\ln(\lambda)} \\ \Gamma_2 &= \frac{[(C+\lambda)(\mathrm{Gr}/\mathrm{Re}) - (\partial P^*/\partial Z)]}{4}. \end{aligned} \tag{10}$$

Now, by substituting the velocity distribution in the dimensionless continuity equation, we see that:

$$2\int_{\lambda}^{1} U(R) R \, \mathrm{d}R = (1 - \lambda^2). \tag{11}$$

The constant C is obtained as:

$$C = \frac{1}{4(\mathrm{Gr}/\mathrm{Re})(\lambda^4(\ln(\lambda) - 1) + 2\lambda^2 - \ln(\lambda) - 1)} \left\{ \begin{array}{l} \lambda^5(\mathrm{Gr}/\mathrm{Re})(-7\ln(\lambda) + 4(\ln(\lambda))^2 + 4) \\ +4\lambda^4(\partial P^*/\partial Z)(\ln(\lambda) - 1) \\ +4\lambda^3(\mathrm{Gr}/\mathrm{Re})(\ln(\lambda) - 2) \\ +8\lambda^2(\partial P^*/\partial Z) + \lambda(Gr/\mathrm{Re})(4 + 3\ln(\lambda)) \\ -4(\partial P^*/\partial Z)(1 + \ln(\lambda)) + 32\ln(\lambda)(\lambda^2 - 1) \end{array} \right\}. \tag{12}$$

3.2 Entropy generation number

The entropy generation number distribution is determined based on equation (6) as follows:

$$\begin{aligned} N_S &= \left(\frac{\Omega}{\mathrm{Br}}\right)\left(\frac{-\lambda}{R}\right)^2 + \left(\frac{\Gamma_1}{R} - 2\Gamma_2 R + \frac{-\lambda^3(\mathrm{Gr}/\mathrm{Re})}{4R} + \frac{\lambda(\mathrm{Gr}/\mathrm{Re})(2R\ln(R) + R)}{4}\right)^2 \\ &= N_H + N_F. \end{aligned} \tag{13}$$

4 Estimation of operational costs due to irreversibilities

Total cost due to irreversibility is very important issue in engineering application from energy saving point of view. Sahin et al. (2000) estimated that the total cost due to irreversibility for the flow in a pipe as follows:

$$\dot{C} = C_H T_0 (\dot{S}_{\mathrm{gen}})_H + C_F T_0 (\dot{S}_{\mathrm{gen}})_F \tag{14}$$

where $\dot{C}$ is the total cost of irreversibility (\$/h), C_H is the unit cost of irreversibility due to heat transfer (\$/W h), C_F is the unit cost of irreversibility due to fluid friction (\$/W h), and $\dot{S}_{\mathrm{gen}}$ is the total rate of entropy generation (W/K).

In the current study, the above relation is modified as:

$$\dot{C} = \frac{2\dot{m}^2 \mu L}{\pi \rho^2 r_0^4 (1-\lambda^2)^2} \left[C_H \int_\lambda^1 N_H R \, \mathrm{d}R + C_F \int_\lambda^1 N_F R \, \mathrm{d}R \right]. \tag{15}$$

Another form of equation (15) where the length of the heat exchanger is 1 m is expressed as:

$$\dot{C} = \frac{2\dot{m}^2 \mu C_H}{\pi \rho^2 r_0^4 (1-\lambda^2)^2} \left[\int_\lambda^1 N_H R \, \mathrm{d}R + r_C \int_\lambda^1 N_F R \, \mathrm{d}R \right] \tag{16}$$

where r_c is the cost ratio and in practical situations is more than one (Mahmud and Fraser, 2003b) (a range of 1–20 is considered in this study). The unit cost of irreversibility due to heat transfer C_H may be considered equal to the cost of electricity. The price of electricity shows considerable variation (0.02–0.50 $/kW h) depending on the country (http://en.wikipedia.org/wiki/Electricity_pricing). Therefore a representative value of 0.2 ($/kW h) has been considered for the cost of irreversibility due to heat transfer in the present study, where the electricity price is selected based on the costs in Iran. For the numerical estimations, engine oil is considered as the working fluid in the heat exchanger. The properties of the particular engine oil, its geometry, and its flow characteristics are provided in Table 1.

Table 1 Fluid and flow properties considered for numerical estimations

Parameter	*Numerical value*
C_H ($/kW h)	0.2
$\dot{m}$ (kg/s)	1.0
ρ (kg/ m^3)	876.1
μ (kg/m s)	0.21
r_o (cm)	2.0

5 Results and discussion

Figure 2 shows the velocity distribution in the annulus for $\partial P^*/\partial Z = -0.1$ and two different values of Gr/Re including 5 and 50. The annulus can be divided into two zones based on the variations of velocity with Gr/Re. In the first zone with an increase in Gr/Re, the fluid velocity in the gap increases while in the second zone the velocity decreases. The velocities near the inner cylinder are greater due to higher heat flux in this region.

Figure 3 displays the temperature field for three different values of Gr/Re. It is seen that with an increase in the buoyancy parameter Gr/Re, the temperature decreases in the annulus. The parameter Gr/Re indicates the ratio of natural convection to forced convection. With an increase in Gr/Re, the effects of natural convection increase, and, consequently, the temperature decreases. It is observed from Figure 3 that the profiles of temperature for any value of Gr/Re changes as parallel. This means that the gradients

of temperature remain constant with the changes in the parameter Gr/Re. From the above discussions, one can conclude that, the parameter Gr/Re has considerable effects on the amounts of temperature. However, its effect on gradients of temperature, and, hence entropy generation is not considerable.

The variations of the entropy generation number and Bejan number with respect to radial distance are plotted in Figure 4 for $\partial P^*/\partial Z = -0.1$, $\Omega/\mathrm{Br} = 50$ and two values of Gr/Re, including Gr/Re = 0.1 and Gr/Re = 50. The distribution of the entropy generation number shows an irregular trend in the annulus, such that the annulus is divided into four zones as shown in the figure. In zones 1 and 3, with an increase in Gr/Re, the entropy generation number increases, while with an increase in Gr/Re, the entropy generation number decreases in zones 2 and 4.

Figure 2 Effects of Gr/Re on velocity distribution

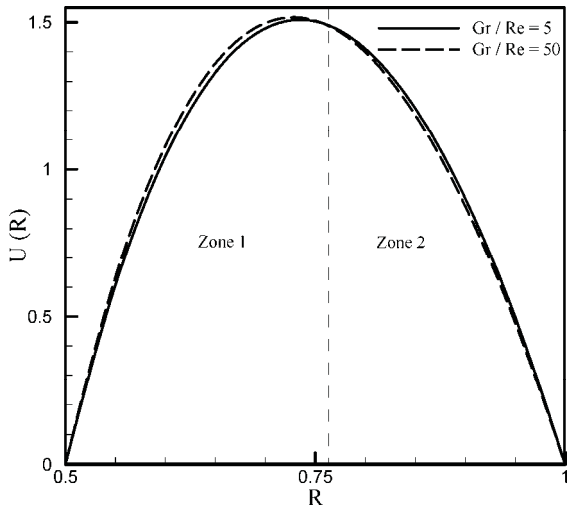

Figure 3 Effects of Gr/Re on temperature distribution

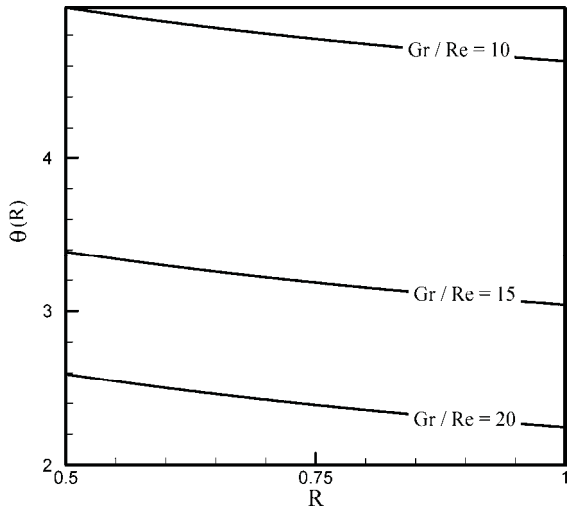

This unpredictable behaviour is due to the interactions of wall effects, heat flux at the inner cylinder, and buoyancy effects in the gap. It should be noted that the total entropy generation demonstrates no considerable change with increases in the flow parameter Gr/Re.

The effect of Gr/Re on the Bejan number is shown in Figure 4(b). It is observed that the Bejan number reaches its maximum near the centreline of the gap ($R = 0.75$), where the effects of the wall on the flow and, hence, the fluid friction effects are minimised. This maximum point moves towards the outer cylinder with decreases in Gr/Re.

Figure 4 Effects of Gr/Re on (a) entropy generation number and (b) Bejan number

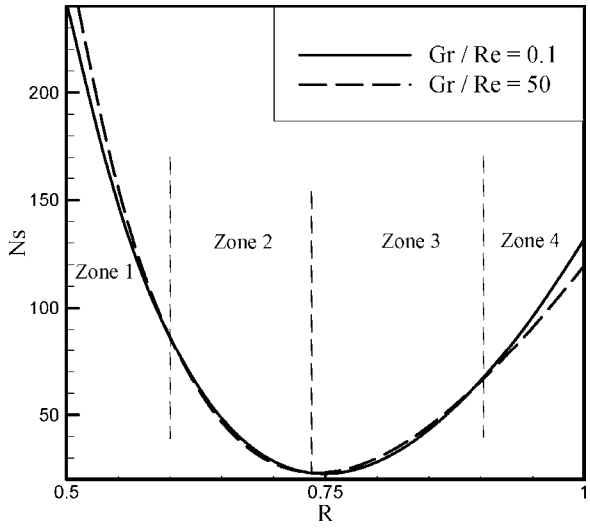

(a)

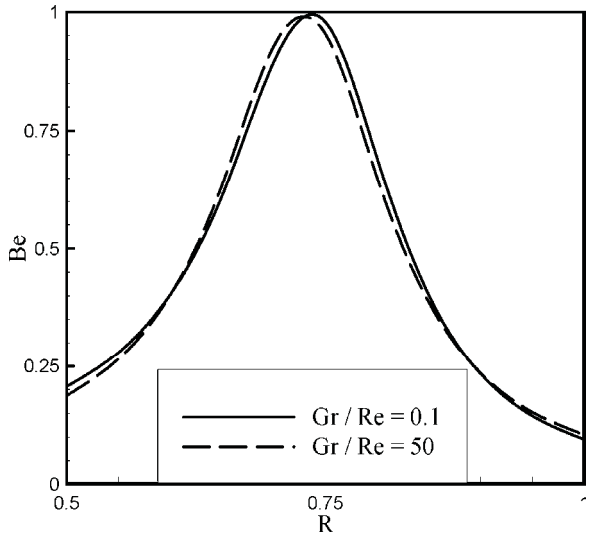

(b)

Figure 5 shows the variations of the entropy generation number and the Bejan number, with radius for $\partial P^*/\partial Z = -0.1$, Gr/Re = 1, and different values of Ω/Br. As expected, entropy generation increases with an increase in Ω/Br. As seen, the entropy generation is the highest on the inner cylinder because of the maximum gradients of velocity and temperature at this point. The profiles of N_s are not symmetric in the annulus due to buoyancy forces.

The effects of Ω/Br on the Bejan number are shown in Figure 5(b). It is seen that an increase in Ω/Br leads to considerable changes in the Bejan number near the walls, while it has no significant effect on the Bejan number in the centreline.

Figure 5 Effects of Ω/Br on the (a) entropy generation number and (b) Bejan number

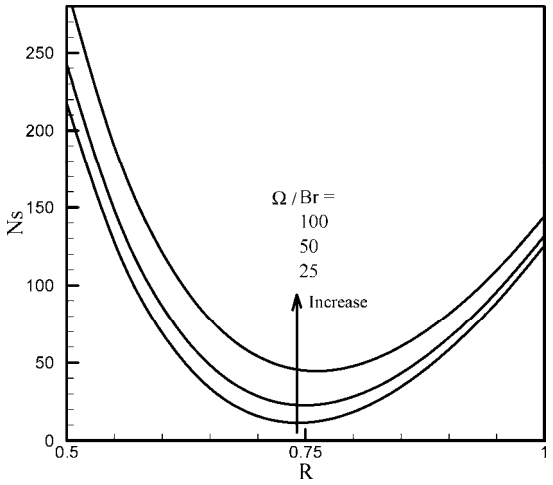

(a)

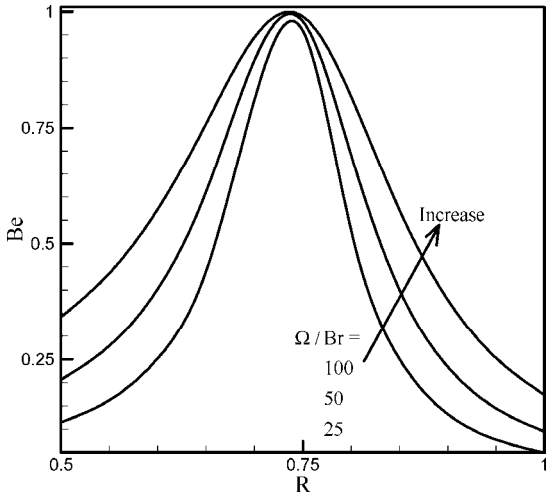

(b)

Figure 6 shows the total cost due to irreversibilities $\dot{C}(\$/\text{day})$, for $r_c = 1$, 10, and 20, $\partial P^*/\partial Z = -0.1$, Gr/Re = 1, and the radius ratio ($\Pi = 1/\lambda$) between 1.5 and 6. It is observed that for $\Pi < 2$, an increase in the parameter r_c results in a considerable change in the total cost. This happens because, in small radius ratios, the irreversibilities increase remarkably in the gap. It is found that for $\Pi = 1.5$ and $r_c = 20$, the total costs in one day exceeds \$10.

Figure 6 Total cost due to irreversibilities for different radius ratios and cost ratios

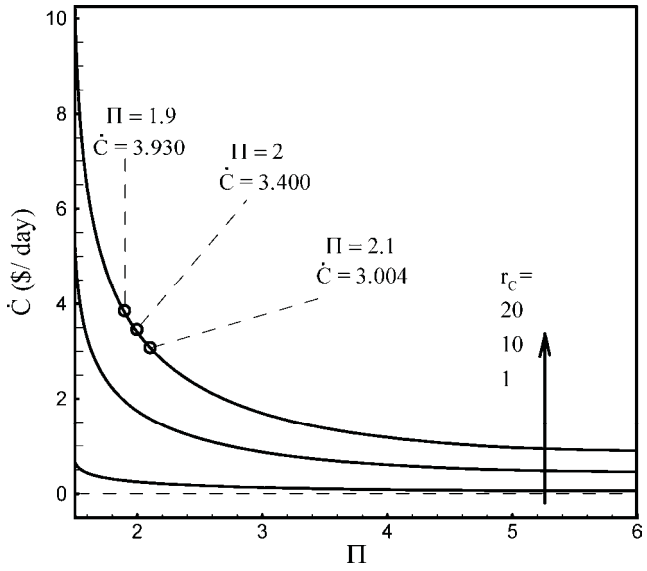

Now, consider a radius ratio of 2 as the base ratio in the design. The aim is to investigate the effect of a small deviation from the base radius ratio on the total costs.

For this purpose, two radius ratios, including $\Pi = 1.9$ and $\Pi = 2.1$, are considered. It is found that if the annulus is manufactured with a radius ratio of 2.1, the total cost drops by nearly 12%, while for $\Pi = 1.9$ the total cost increases by approximately 16%. This shows that the importance of producing an exact design for improving the savings in energy costs.

From another point of view, assume that the radius ratio is reduced from 2 to 1.9 due to fouling in the heat exchanger. By cleaning the heat exchanger and removing the fouling, one can realise a savings of 16% in energy costs.

Figure 7 shows the effects of Ω/Br on the total cost due to entropy generation for $r_c = 10$. The parameter of Ω/Br represents the ratio of the thermal effects to viscosity effects in the annulus. Indeed, by increasing the heat flux at the boundary of the inner cylinder, the parameter of Ω/Br increases. It is observed that when the radius ratio is nearly between 2 and 3, the effects of Ω/Br on the total cost is more visible than the effect of other radius ratios.

Figure 7 Total cost due to irreversibilities for different radius ratios and parameter Ω/Br

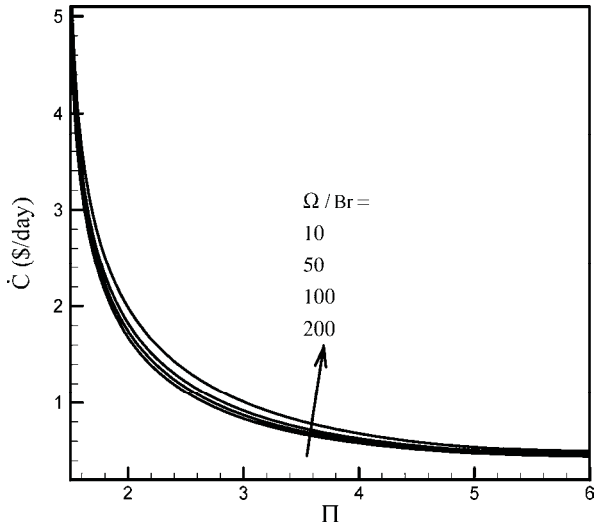

6 Conclusion

In this paper, a thermoeconomic analysis of a heat exchanger was performed to estimate the total costs due to entropy generation for the flow of a refrigerant inside the heat exchanger. The governing equations are simplified and solved analytically to find the distribution of velocity and temperature, and consequently to determine the entropy generation in the heat exchanger, where the walls of the annulus are subjected to a constant heat flux. From the distribution of entropy generation in the annulus, it was found that in the cases investigated the parameter Gr/Re has no considerable effect on entropy generation. Next, using the results of the entropy generation analysis, the total costs due to entropy generation were estimated for different values of the radius ratio. For a base radius ratio of 2, it was concluded that when the radius ratio decreases from 2 to 1.9 (e.g., due to fouling), the total costs increase by 16%. In this work, the aim is only the study of costs due to entropy generation. For the future works, the cost of pipe in different radius ratios can be considered.

Acknowledgements

The first author would like to thank the Thailand Research Fund and the National Research University Project for support. The support provided by the Deanship of Scientific Research at King Fahd University of Petroleum and Minerals (KFUPM) under Research Grant IN090031 is also acknowledged. The fourth author would like to thank the Thailand Research Fund, National Science And Technology Development Agency, and the National Research University Project for support.

References

Ahmadi, P., Enadi, N., Avval, H.B. and Dincer, I. (2012) 'Modelling and exergoeconomic optimisation of a gas turbine with absorption chiller using evolutionary algorithm', *Int. J. Exergy*, Vol. 11, pp.1–18.

Anandan, S.S. and Bhaskaran, A. (2012) 'Thermo-economic analysis of heat pipe heat exchanger for waste heat recovery in thermal systems', *Int. J. Exergy*, Vol. 11, pp.35–51.

Askar, S., Fartaj, A., Dasgupta, E.S. and Quayium, A. (2012) 'Second law analysis of a multiport serpentine micro-channel slab heat exchanger', *Int. J. Exergy*, Vol. 11, pp.379–399.

Aydin, H., Turan, O., Midilli, A. and Karakoc, T.H. (2012) 'Exergetic and exergo-economic analysis of a turboprop engine: a case study for CT7-9C', *Int. J. Exergy*, Vol. 11, pp.69–88.

Aziz, A. and Khan, W.A. (2012a) 'Entropy generation in an asymmetrically cooled hollow sphere with temperature dependent internal heat generation', *Int. J. Exergy*, Vol. 10, pp.110–123.

Aziz, A. and Khan, W.A. (2012b) 'Minimum entropy generation design of a convectively heated pin fin with tip heat loss', *Int. J. Exergy*, Vol. 10, pp.44–60.

Bejan, A. (1982) 'Second-law analysis in heat transfer and thermal design', *Adv. Heat Transfer*, Vol. 15, pp.1–58.

Ghazi, M., Sotoodeh, A.F. and Amidpour, M. (2012) 'Modelling and optimisation of a water-ethanol distillation column based on exergoeconomic analysis', *Int. J. Exergy*, Vol. 11, pp.173–190.

Kumar, S.V., Minkowycz, W.J. and Patel, K.S. (1989) 'Thermodynamic cycle simulation of the diesel cycle: exergy as a second law analysis parameter', *Int. Commun. Heat Mass Transfer*, Vol. 16, pp.335–346.

Mahian, O., Mahmud, S. and Pop, I. (2012c) 'Analysis of first and second laws of thermodynamics between two isothermal cylinders with relative rotation in the presence of MHD flow', *Int. J. Heat Mass Transfer*, Vol. 55, pp.4808–4816.

Mahian, O., Mahmud, S. and Wongwises, S. (2013) 'Entropy generation between two rotating cylinders with magnetohydrodynamic flow using nanofluids', *Journal of Thermophysics and Heat Transfer*, Vol. 27, No. 1, pp.161–169.

Mahian, O., Mahmud, S. and Zeinali Heris, S. (2012a) 'Analysis of entropy generation between co-rotating cylinders using nanofluids', *Energy*, Vol. 44, pp.438–446.

Mahian, O., Mahmud, S. and Zeinali Heris, S. (2012b) 'Effect of uncertainties in physical properties on entropy generation between two rotating cylinders with nanofluids', *ASME-Journal of Heat Transfer*, Vol. 134, p.101704.

Mahmud, S. and Fraser, R.A. (2002a) 'Irreversibility analysis of concentrically rotating annuli', *Int. Commun. Heat Mass Transfer*, Vol. 29, pp.697–706.

Mahmud, S. and Fraser, R.A. (2002b) 'Second law analysis of heat transfer and fluid flow inside a cylindrical annular space', *Int. J. Exergy*, Vol. 2, pp.322–329.

Mahmud, S. and Fraser, R.A. (2002c) 'Analysis of mixed convection – radiation interaction in a vertical channel: entropy generation', *Exergy, An International Journal*, Vol. 2, pp.330–339.

Mahmud, S. and Fraser, R.A. (2003a) 'Analysis of entropy generation inside concentric cylindrical annuli with relative rotation', *Int. J. Thermal Sci.*, Vol. 42, pp.513–521.

Mahmud, S. and Fraser, R.A. (2003b) 'Mixed convection–radiation interaction in a vertical porous channel: Entropy generation', *Energy*, Vol. 28, pp.1557–1577.

Makinde, O.D. (2102) 'Entropy analysis for MHD boundary layer flow and heat transfer over a flat plate with a convective surface boundary condition', *Int. J. Exergy*, Vol. 10, pp.142–154.

Matawala, V.K. and Prabhakaran, P. (2012) 'Exergoeconomic optimisation of steam power plant', *Int. J. Exergy*, Vol. 11, pp.209–227.

Mirzazadeh, M., Shafaei, A. and Rashidi, F. (2008) 'Entropy analysis for non-linear viscoelastic fluid in concentric rotating cylinders', *Int. J. Thermal Sci.*, Vol. 47, pp.1701–1711.

Ramos-Alvarado, B., Hernandez-Guerrero, A. and Rangel-Hernandez, V.H. (2012) 'Irreversibilities reduction of a flow distribution system by means of the EGM methodology', *Int. J. Exergy*, Vol. 10, pp.94–109.

Sahin, A.Z. (2012) 'Critical insulation thickness for maximum entropy generation', *Int. J. Exergy*, Vol. 10, pp.34–43.

Sahin, A.Z., Zubair, S.M., Al-Garni, A.Z. and Kahraman, R. (2000) 'Effect of fouling on operational cost in pipe flow due to entropy generation', *Energy Conversion & Management*, Vo. 41, pp.1485–1496.

Tasnim, S.H. and Mahmud, S. (2002a) 'Entropy generation in a vertical concentric channel with temperature dependent viscosity', *Int. Commun. Heat Mass Transfer*, Vol. 29, pp.907–918.

Tasnim, S.H. and Mahmud, S. (2002b) 'Mixed convection and entropy generation in a vertical annular space', *Int. J. Exergy*, Vol. 2, pp.373–379.

Tasnim, S.H., Mahmud, S. and Mamun, M.A.H. (2002) 'Entropy generation in a porous channel with hydromagnetic effect', *Exergy, An International Journal*, Vo. 2, pp.300–308.

Wu, S.Y., Chen, S.M., Xiao, L. and Li, Y.R. (2012) 'Extended exergo-economic performance evaluation criteria for enhanced heat transfer duct with constant wall heat flux', *Int. J. Exergy*, Vol. 11, pp.89–111.

Yilbas, B.S. (2001) 'Entropy analysis of concentric annuli with rotating outer cylinder', *Int. J. Exergy*, Vol. 1, pp.60–66.

Website

http://en.wikipedia.org/wiki/Electricity_pricing (Accessed 29 September, 2012).

Nomenclature

Be	Bejan number, Be = N_H/N_S
Br	Brinkman number, BR = $U_0^2\mu / k\Delta T$
C	Constant of integration in energy equation
C_H	Unit cost of irreversibility due to heat transfer ($/W h)
C_F	Unit cost of irreversibility due to fluid friction ($/W h)
$\dot{C}$	Total cost of irreversibility ($/hr)
g	gravity (m^2/s)
Gr	Grashof number, Gr = $g\beta\Delta T r_o^3 / \upsilon^2$
K	Thermal conductivity (W/ mK)
L	Axial length of annulus (m)
$\dot{m}$	Mass flow rate (kg/s)
N_F	Entropy generation number, fluid friction
N_H	Entropy generation number, heat transfer
N_S	Entropy generation number, $N_S = \dot{S}'''_{\text{gen}} /(\mu U_0^2 / T_0 r_0^2)$
P	Pressure (Pa)
P^*	Dimensionless Pressure, $P^* = (P/U_0\mu)r_o$
R	Radius (m)

r_c	Cost ratio, $r_c = C_F/C_H$
R	Dimensionless radius, $R = r/r_o$
Re	Reynolds number, $\mathrm{Re} = U_0 r_o/\nu$
$\dot{S}'''_{\mathrm{gen}}$	Volumetric entropy generation rate ($\mathrm{W/m^3K}$)
$\dot{S}_{\mathrm{gen}}$	Total entropy generation rate (W/K)
T	Temperature (K)
T_0	Inlet temperature (K)
U	Dimensionless velocity, $U = V_z/U_0$
U_0	Inlet velocity (m/s)
V_z	Axial velocity (m/s)
Z	Dimensionless axial distance, $Z = z/r_o$
Greek symbols	
Γn	Constants, $n = 1, 2, \ldots$
μ	Dynamic viscosity (kg/m s)
β	Thermal expansion coefficient (1/K)
λ	Radius ratio, $\lambda = r_i/r_o$
Π	Inverse radius ratio, $\Pi = 1/\lambda$
θ	Dimensionless temperature, $\theta = (T - T_0)/(q_i r_o/k)$
ρ	Density ($\mathrm{kg/m^3}$)
Ω	Dimensionless temperature difference, $\Delta T/T_0$
Subscript	
i	Value at the inner cylinder
o	Value at the outer cylinder
H	Heat transfer
F	Fluid friction

Hindawi Publishing Corporation
Advances in Mechanical Engineering
Volume 2013, Article ID 256839, 2 pages
http://dx.doi.org/10.1155/2013/256839

Hindawi

Editorial

Two-Phase Flow and Heat Transfer Enhancement

Somchai Wongwises,[1] Afshin J. Ghajar,[2] Kwok-wing Chau,[3] Octavio García Valladares,[4] Balaram Kundu,[5] Ahmet Selim Dalkılıç,[6] and Godson Asirvatham Lazarus[7]

[1] *Fluid Mechanics, Thermal Engineering and Multiphase Flow Research Lab. (FUTURE), Department of Mechanical Engineering, Faculty of Engineering, King Mongkut's University of Technology Thonburi, Bangmod, Bangkok 10140, Thailand*
[2] *School of Mechanical and Aerospace Engineering, Oklahoma State University, Stillwater, OK 74078, USA*
[3] *Department of Civil & Environmental Engineering, The Hong Kong Polytechnic University Hunghom, Kowloon, Hong Kong*
[4] *Department of Energy Systems, Centro de Investigación en Energía, CIE-UNAM, Privada Xochicalco S/N, 62580 Temixco, MOR, Mexico*
[5] *Department of Mechanical Engineering, Jadavpur University, Kolkata 700032, India*
[6] *Heat and Thermodynamics Division, Department of Mechanical Engineering, Yildiz Technical University, Yildiz, 34349 Istanbul, Turkey*
[7] *Department of Mechanical Engineering, Karunya University, Coimbatore, Tamil Nadu 641 114, India*

Correspondence should be addressed to Somchai Wongwises; somchai.won@kmutt.ac.th

Received 2 December 2013; Accepted 2 December 2013

Gas-liquid two-phase flow and heat transfer processes are commonly encountered in a wide variety of applications, for example, refrigeration and air-conditioning systems, power engineering, and other thermal processing plants. The advantage of high thermal performance in comparison to the single-phase applications leads to various engineering applications including the cooling systems of various types of equipment such as high performance microelectronics, supercomputers, high-powered lasers, medical devices, high heat-flux compact heat exchangers in spacecraft and satellites, and so forth. The aim of this special issue was to collect the original research and review papers on the recent developments in the field of two-phase flow and heat transfer enhancement. Potential topics included advanced heat pipe technologies, boiling and condensation heat transfer, CHF and post-CHF heat transfer, cooling of electronic system, Heat and mass transfer in phase change processes, instabilities of two-phase flow, measurements and modeling of two-phase flow in microchannel, microgravity in two-phase flow, nanofluids science and technology, nuclear reactor applications, passive and active heat transfer enhancement techniques, Refrigeration and air-conditioning technology, two-phase flow with heat and mass transfer, two-phase refrigerant flow, and special topics on the latest advances in two-phase flow and heat transfer. In this special issue, we have invited a few papers that address such issues.

First paper of special issue investigates the effect of convergence angle of microchannel on two-phase flow and heat transfer during steam condensation experimentally. The experimental results show that the condensation heat flux increases with an increase in the convergence angle and/or the steam mass flux at a given coolant flow rate but decreases with an increase in the coolant flow rate at a given steam mass flux. Second paper focuses on simulating mist impingement cooling under typical gas turbine operating conditions of high temperature and pressure in a double chamber model. The results of this paper can provide guidance for corresponding experiments and serve as the qualification reference for future more complicated studies with convex surface cooling. In third paper, economic analysis of rebuilding an aged pulverized coal-fired boiler with a new pulverized coal-fired boiler including flue gas desulfurization unit and a circulating fluidized bed boiler is investigated in existing old thermal power plants. The fourth paper presents the results of a CFD analysis and experimental tests of two identical miniature flat plate heat pipes using sintered and screen

mesh wicks and a comparative analysis and measurement of two solid copper base plates 1 mm and 3 mm thick. In fifth paper, a modeled room was numerically heated from a wall and cooled from the opposite wall in order to create a real-room simulation. The cooled wall simulated heat loss of the room, and the heated wall simulated the heat source of enclosure. The effects of heated and cooled wall temperatures on convective heat transfer coefficient and Nusselt number in the enclosure were investigated numerically for two- and three-dimensional (3D) modeling states.

In summary, this special issue reflects a variety of contemporary research in heat transfer and is expected to promote further research activities and development opportunities.

Acknowledgment

We thank the authors who prepared the paper within the stringent length and time requirements. We thank the reviewers who provided meaningful suggestions on short notice.

Somchai Wongwises
Afshin J. Ghajar
Kwok-wing Chau
Octavio García Valladares
Balaram Kundu
Ahmet Selim Dalkılıç
Godson Asirvatham Lazarus

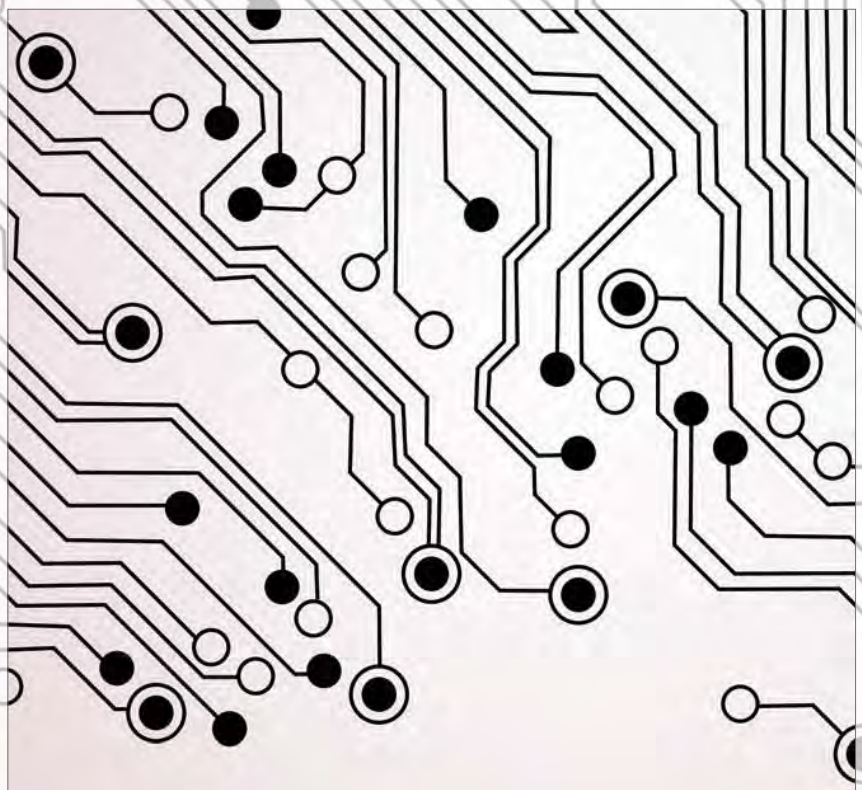

The Scientific World Journal

Hindawi Publishing Corporation
http://www.hindawi.com

Volume 2013

Renewable and Sustainable Energy Reviews 31 (2014) 312–318

Contents lists available at ScienceDirect

Renewable and Sustainable Energy Reviews

journal homepage: www.elsevier.com/locate/rser

Critical review of the current status of wind energy in Thailand

Sakkarin Chingulpitak, Somchai Wongwises *

Fluid Mechanics, Thermal Engineering and Multiphase Flow Research Lab. (FUTURE), Department of Mechanical Engineering, Faculty of Engineering, King Mongkut's University of Technology Thonburi, Bangmod, Bangkok 10140, Thailand

ARTICLE INFO

Article history:
Received 22 August 2012
Received in revised form
22 October 2013
Accepted 18 November 2013

Keywords:
Wind energy
Wind energy potential
Wind farm
Electricity
Renewable energy
Thailand

ABSTRACT

Thailand generates electricity from many sources, including natural gas, coal/lignite, fuel oil, diesel, and renewable energies, such as wind, hydroelectricity, and solar power. In 2012, the main electrical energy sources in Thailand were natural gas (63.8%) and coal/lignite (27.7%). Due to fuel price spikes and global warming, several countries are now more interested in studying and developing sources of renewable energy.

Wind energy – an unlimited and environmentally friendly form of natural energy – has attracted increasing levels of investment, particularly in China, which derives more of its electricity from wind energy generation than any other country in the world. Thailand has also developed and promoted the use of wind turbines to generate electricity. In 2012, Thailand generated about 111.7 MW of electricity from wind energy. By 2021, the Thai government's goals are to increase the use of alternative electric energy to about 25% of fossil fuel use and to achieve 1800 MW of electricity output from wind energy.

This article will present a critical review of the current status of wind energy in Thailand, including future plans for using wind energy in place of fossil fuels – oil, natural gas, and coal – to generate electricity.

Contents

1. Background

For past several decades, energy has been an important, fundamental factor in daily life, business, and industry, including the transportation, manufacturing, and telecommunications sectors. For this reason, a reliable energy supply with sufficient quantity, good quality, and reasonable prices is vital. However, the unstable price of energy in the world market, especially the steadily increasing price of crude oil, has had a serious effect on the economies of several countries, particularly those that must import significant quantities of oil. Furthermore, the use of fossil fuels also contributes to the problem of global warming. As a result, several countries have supported the use of renewable energy to promote energy security and environmental conservation. In 2012, China increased its wind-powered electricity generation and had the highest rate of wind-powered energy generation in the world. Thailand has also developed and promoted wind turbines to generate electricity because it is clean, eco-friendly, and cost-effective.

Abbreviations: AEDP, alternative energy development plan; GWh, gigawatt hour; GRP, glass-reinforced plastic; DEDE, department of alternative energy development and efficiency; EGAT, electricity generating authority of Thailand; EIA, environmental impact assessment; EPPO, energy policy and planning office; ktoe, kilotons of oil equivalent; kWh, kilowatt hour; PDP, Thailand power development plan; PEA, provincial electricity authority; SPPs and VSPPs, small and very small power producers, respectively; US$, US dollar (31.245 baht/US dollar foreign exchange rate, as of 13 August 2013)

* Corresponding author. Tel.: +66 2470 9115; fax: +66 2470 9111.
E-mail address: somchai.won@kmutt.ac.th (S. Wongwises).

1364-0321/$ - see front matter © 2013 Elsevier Ltd. All rights reserved.
http://dx.doi.org/10.1016/j.rser.2013.11.038

This paper presents the current status of electricity generation and the proportion of electricity generated from renewable resources, especially wind energy. Wind energy potential is investigated and compared to other countries in Southeast Asia, including its obstacles to development and promotion, as well as future plans to use wind energy in Thailand.

2. Energy and electricity situations in Thailand

The final energy consumption of Thailand in 2012 was about 73,316 ktoe [1], an increase of 13% [2] from 2007. The total value of the final energy consumption was US$57,545.21 million. As shown in Fig. 1, petroleum products, renewable energy, electricity, coal/lignite, and natural gas represented 48.0%, 18.2%, 18.9%, 7.9%, and 7.0% of the total final energy consumption in 2012, respectively.

Considering the trends in primary energy supply (excluding energy exports) and final energy consumption from 2007 to 2012, as revealed in Fig. 2, it is observed that the primary energy supply

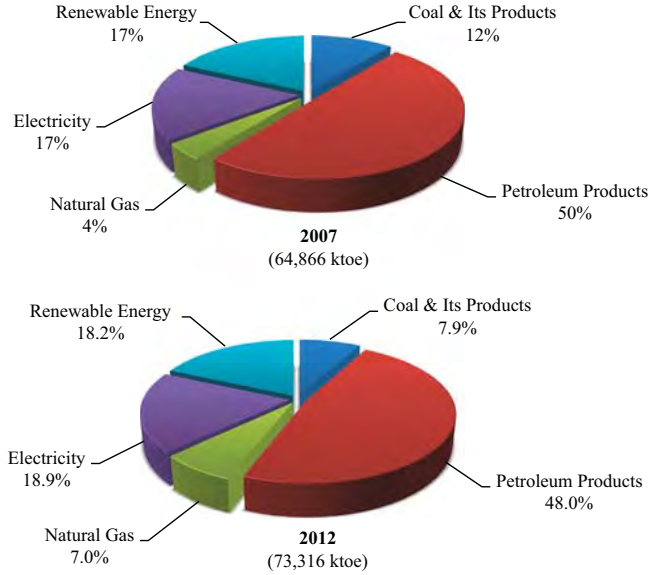

Fig. 1. Final energy consumption by types of Thailand for years 2007 [data from [2]] and 2012 [data from [1]].

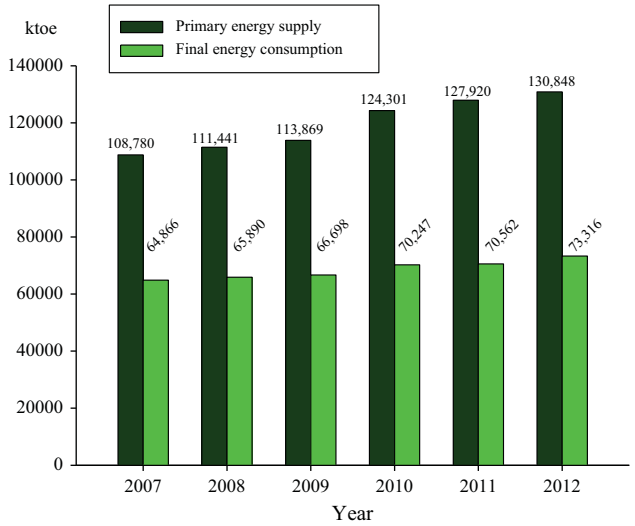

Fig. 2. Primary energy supply and final energy consumption from year 2007 until 2012 [data from [1] and [2]].

increases year-by-year. In 2012, the amount of primary energy supplies was 130,848 ktoe [1]. For primary energy supplies classified by energy type, the highest share, which contributed 82.8% of the total primary energy supply, was from commercial energy (crude oil, lignite, natural gas, and so on), followed by renewable energy, biofuels (ethanol and biodiesel), and other forms of energy (black liquor and residual gas), at 16.2%, 0.8%, and 0.2%, respectively.

Thailand's electricity consumption was 162,668 GWh [1] in 2012. Most of this electrical energy, equal to 82,068 GWh, was consumed by the industrial sector. The commercial sector (including government, non-profit organizations, and street lighting), residential sector, agricultural sector, transportation sector, and other sectors (temporary customers) used 47,210 GWh, 32,097 GWh, 70 GWh, and 930 GWh, respectively.

Table 1 shows electricity generation, installation capacity, consumption, and electricity generation by energy source from 2007 to 2012, according to Thailand Energy Statistics 2012 [1] and 2007 [3]. There is a trend towards increased electricity generation every year. Thailand's electricity consumption in 2010 increased 10.4% from that of 2009, whereas it decreased by 0.4% in 2011, due to severe flooding by that year end. In 2012, Thailand's total electricity generation was 168,471 GWh [1], of which 63.8% was generated by natural gas, followed by coal/lignite (27.7%), and fuel oil and diesel (1.6%), with the balance being renewable energy and other types of energy (6.9%). From Table 1, it is clear that use of natural gas and renewable energy are increasing slightly. On the other hand, use of fuel oil for electricity generation has decreased significantly, due to an unexpected increase in oil prices; thus, promoting alternative energy to replace oil is necessary, especially alternative energy that can be produced in Thailand, such as biomass, biogas, solar energy, hydro energy, wind energy, garbage reclamation, and natural gas.

According to the CIA World Factbook, which lists all countries by electricity consumption, China had the highest electricity consumption, of 4,693,000 GWh [4], followed by the United States, the European Union, Japan, and Russia. Thailand's electricity consumption is rated twenty-fifth in the world and is the highest in Southeast Asia.

3. Wind energy potential in Thailand

Thailand is located near the equator and has low to moderate wind speeds that average about 3–5 m/s. A study of wind energy potential in Thailand began in 1975, when the Department of Energy Affairs of the National Energy Policy Office made a map of wind speed for use in planning, design, and installation of wind turbines. Average wind-speed data were supplied by the Thai Meteorological Department. Field studies then surveyed, measured, collected, and analyzed the wind-speed data. However, since there were several restrictions in making a map of wind-speed potential, the data are only available for low elevations.

In 2001, the map of wind-speed potential in Thailand was improved to include higher-elevation wind data in the analysis. The suitable areas that were selected have average wind speeds of not less than Class 3: 6.4–7.0 m/s or 300–400 kW/m^2 at an elevation of 50 m [5]. The existing data indicate that the coastal area of the Thai Gulf has the best wind energy potential in Thailand, followed by the upper southern region around the western coast of the Thai Gulf, which has an average annual wind speed of 4.4 m/s at an elevation of 50 m, as shown in Table 2 and Fig. 3.

In the same year, the World Bank proposed a wind energy resource atlas report for four countries in Southeast Asia: Cambodia, Laos, Thailand, and Vietnam [6]. As shown in Tables 3 and 4, the report uses simulations based on global winds to demonstrate which areas are best for the development of wind energy. Table 3

Table 1
Electricity generation, installation and consumption, and electricity generation by energy sources [data from [1] and [3]].

	2007	2008	2009	2010	2011	2012
Electric generation (GWh)[a]	143,378	147,427	148,390	159,518	155,986	168,471
Installed capacity (MW)[a]	28,285	30,508	30,607	31,485	31,773	33,177
Electric consumption (GWh)[a]	133,178	135,449	135,209	149,320	148,700	162,668
National grid generation (GWh)[a,b]	128,819	132,781	133,458	144,362	138,247	–
Natural gas	88,166	94,549	97,595	109,454	98,128	–
Coal and lignite	28,716	29,480	28,020	28,207	29,642	–
Hydro	8114	7113	7148	5537	8163	–
Fuel oil	3646	1454	604	997	1986	–
Diesel oil	174	180	79	159	319	–
Other[c]	3	5	12	8	9	–

[a] Excluding private generation for own use.
[b] Excluding generation from small and very small power producers (SPPs and VSPPs) generated from renewable and conventional energy.
[c] Including geothermal, solar cell and wind turbine, etc.

Table 2
Good wind energy sites from a map of wind energy potential [data from [5]].

Area	Province	Wind power classes	Height of 50 m	
			Wind speed (m/s)	Wind power (W/m^2)
1 Tai Rom Yen national park	Nakhon Sri Thammarat	6–7	8.00–11.90	600–2000
2 Khao Luang national park	Nakhon Sri Thammarat	6–7	8.00–11.90	600–2000
3 Khao Pu – Khao Ya national park	Pattalung	6–7	8.00–11.90	600–2000
4 Wang Chao national park	Tak	6	8.00–8.80	600–800
5 Doi Intanon national park	Chiang Mai	4	7.00–7.50	400–500
6 Kaeng Krung national park	Surat Thani	4–5	7.00–7.50	400–600
7 Khao Phanom Bencha	Krabi	6	8.00–8.80	600–800
8 Ranod district	Songkhla	4	7.00–7.50	400–500
9 Songkhla Lake	Songkhla	5–6	7.50–8.00	500–700
10 Laem Tachee	Pattani	4	7.00–7.50	400–500
11 Hua Sai district	Nakhon Sri Thammarat	3	6.40–7.00	300–400

presents the percentages of rural population in the areas of each country where small wind turbines can be used at 30 m. This was estimated by determining the number of villages and towns located within each wind resource class. The data show that more than 30% of the rural population of Vietnam live in areas with good wind resources, whereas only 13%, 9%, and 5% of the rural populations of Laos, Thailand and Cambodia, respectively, live in favorable areas. For large wind turbines, Table 4 shows the land area in each country and total wind energy potential based on each wind speed class at 65 m. It is clear that Vietnam has the opportunity to develop large-scale wind turbines because of its large resource potential, followed by Thailand, due to its moderate resource potential and well-developed energy infrastructure.

In 2008, wind measurement stations were set up in six provinces along the coast of Southern Thailand: Surat thani, Nakhon Si Thammarat, Songkhla, Krabi, Trang, and Satun. Sensors for measuring wind speed and direction were installed at heights of 20, 30, and 40 m [7]. During 2008, the wind statistics that were recorded were used to estimate wind speed at heights of 80, 90, and 100 m. Moreover, the observed wind climate was analyzed for the prediction of 15 km wind resources around the wind station by using WAsP 9.0, the Wind Atlas Analysis and Application Program. The results showed that the average annual wind speeds at heights of 80, 90, and 100 m were between 3.4 and 9.5 m/s. From economic analysis based on very small power producers (VSPP), the study found that wind farm power plants installing wind turbine generators (WTGs) of 1.0, 1.5, and 2.0 MW can generate about 1018, 1038, and 1148 MW of electricity from wind energy, respectively, in the long term.

To measure the potential of wind energy in the upper northern region [8], the wind speed and direction were measured and recorded at heights of 20, 30, and 40 m at Rompothai, Phatung, Norlae, Nonghoi, Monlan, and Killom stations from April 2007 to June 2009. Over the same period, wind speed and direction were recorded at heights of 20, 30, and 80 m at the Maehae station. The wind data recorded were analyzed with WAsP 9.1 to evaluate the potential for electricity generation. In the case of a potential wind farm using a 1 MW wind turbine at a height of 80 m, the total installed capacity of the wind turbines is 68 MW, or around 160 GWh/yr. Moreover, the results of the site survey showed that the suitable areas – Killom, Monlan, and Maehae – were ready to install wind farms with capacities of 1 MW and 3 MW (total capacities of 9 MW and 27 MW), which can produce approximately 18.7 and 44.9 GWh/yr of electricity, respectively.

4. Current status of wind energy in Thailand

Wind-powered electricity generation around the world has increased every year since 1996. In 2012, the global production of wind energy totaled 282,587 MW [9], an increase of 44,799 MW, or 19%, over 2011. Most of the increase occurred in the United States, which accounted for 29.3% of the global increase in wind-powered energy generation. As a result, China had the highest wind-powered energy generation (75,324 MW), followed by the United States (60,007 MW) and Germany (31,308 MW).

Wind-powered energy generation in Thailand began in 1983, when the electricity generating authority of Thailand (EGAT) installed six sets of small turbines for a pilot project at Laem Phromthep in Phuket Province. In 1992, EGAT installed two more turbines with a total capacity of 10 kW. After that, both government and private agencies – particularly educational institutions –

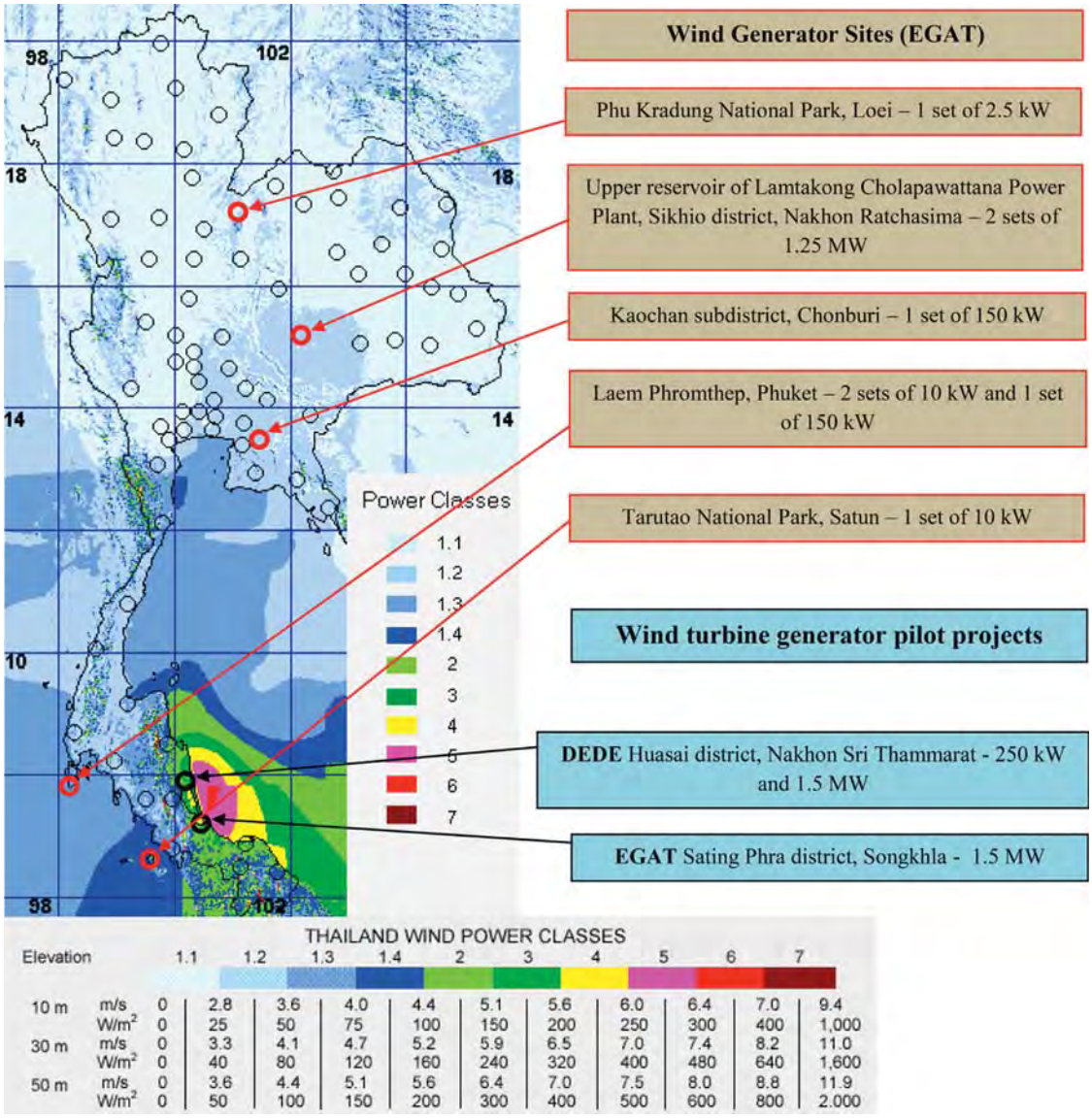

Fig. 3. Map of wind power potential in calm wind conditions – annual average [data and map from [5]].

Table 3
Proportion of rural population in each small wind turbine resource class[a] [data from [6]].

Country	*Poor (%) (< 4 m/s)*	*Fair (%) (4–5 m/s)*	*Good (%) (5–6 m/s)*	*Very good (%) (6–7 m/s)*	*Excellent (%) (> 7 m/s)*
Cambodia	15	79	5	1	0
Laos	55	32	13	0	0
Thailand	26	64	9	0	0
Vietnam	29	31	34	6	1

[a] Wind speeds are for cleared or open land with no obstructions at 30 m height. The proportion of rural population is estimated from the number of towns and villages in each wind resource class from the VMAP database (the US National Imagery and Mapping Agency Vector Map).

paid more attention to the study of wind energy for electricity generation. In 1996, King Mongkut's University of Technology/Thonburi was the first to install 2.5 kW and 10 kW wind turbines at Phu Kradueng National Park, in Loei Province, and Tarutao National Park, in Satun Province, respectively. In the same year, the Recycle Engineering Company Limited installed one 150 kW wind turbine at Koh Chan Sub-district in Chonburi Province to generate electricity for use in buildings. As for government agencies, under the aegis of the Ministry of Energy, the Department of alternative energy development and efficiency (DEDE) installed one 250 kW turbine and one 1.5 MW turbine for electricity generation at Hua Sai District in Nakhon Si Thammarat Province in 2007 and 2009 [10], respectively.

The wind turbines were installed in 2009 by EGAT and connected to the electricity distribution system of the Provincial Electricity Authority (PEA). Two sets of 1.25 MW wind turbines – with a total capacity of 2.5 MW, which became the first large, wind-powered generation plant in Thailand – were installed at the upper reservoir of Lamtakong Cholapawattana Power Plant in Khlongphai Sub-district, Sikhio District, Nakhon Ratchasima [11]. The wind turbines that were used are Chinese-made D6-1250 models, which are three-blade horizontal-axis wind turbines with a pole height of 68 m and a blade diameter of 64 m. The blades are made of glass-reinforced plastic (GRP). The wind turbines turn automatically at wind speeds of 2.8 m/s or greater. The highest wind speed for electricity generation is 12.5 m/s. The turbines stop working when the wind speed reaches 23 m/s and stop generating electricity when the wind speed reaches 50.5 m/s [12].

Later, the provincial electricity authority (PEA) conducted a project to demonstrate the electricity generation from one 1.5 MW

Table 4
Wind energy potential of Southeast Asia at 65 m[a] [data from [6]].

Country	*Characteristic*	*Poor* (< 6 *m/s*)	*Fair* (*6–7 m/s*)	*Good* (*7–8 m/s*)	*Very good* (*8–9 m/s*)	*Excellent* (> 9 *m/s*)
Cambodia	Land area (sq km)	175,468	6155	315	30	0
	% of Total land area	96.4	3.4	0.2	0.0	0.0
	MW potential	NA	24,620	1260	120	0
Laos	Land area (sq km)	184,511	38,787	6070	671	35
	% of Total land area	80.2	16.9	2.6	0.3	0.0
	MW Potential	NA	155,148	24,280	2684	140
Thailand	Land area (sq km)	477,157	37,337	748	13	0
	% of Total land area	92.6	7.2	0.2	0.0	0.0
	MW potential	NA	149,348	2992	52	0
Vietnam	Land area (sq km)	197,342	100,361	25,679	2187	113
	% of Total land area	60.6	30.8	7.9	0.7	0.0
	MW potential	NA	401444	102716	8748	452

[a] Wind speeds are for 65 m height in the predominant land cover with no obstructions. For large wind turbines only. Potential MW estimates an average wind turbine density of 4 MW/km^2 and no exclusions for parks, urban, or inaccessible areas.

turbine at Sating Phra District in Songkhla Province [11]. The wind turbine used was a Chinese-made YFKF01-500/4 model and has the highest productivity in Thailand. The turbine has a horizontal axis driven by an asynchronous generator gear box, with a pole height of 80 m and a blade diameter of 77 m. Its three blades are made of GRP, with a total weight of 160 t. The turbine begins generating electricity at a wind speed of 3 m/s and reaches its maximum productivity at a wind speed of 11.5 m/s. The turbine can resist a maximum wind speed of 21 m/s [13].

The locations of the wind power plants in Thailand described above are shown in Fig. 3. It includes private generation for personal use, educational institutions, and commercial operations. However, in 2013, an updated map for the locations of wind power plants in Thailand was proposed [14], as shown in Fig. 4. It only presents the locations of wind power plants that generate electricity and supply it to the grid system, with a total capacity of 186 MW. The information of wind power plants that are being added are shown below.

The wind power plant “Chang-Hua-Mun” is located in Chang-Hua-Mun Royal Initiative Project, at Khao Krapuk Sub-district, Tha Yang District in Phetchaburi Province. His Majesty the King graciously observed that the landscape of the project area was suitable for the installation of wind turbines [15]. He graciously granted funds for the installation of 205 kW wind turbines (with a total capacity of 100 kW). The electricity used for the project was distributed to residents in the project area. Moreover, it was fed into the grid system of the Provincial Electricity Authority in 2009, with a capacity of 50 kW [15].

Later, the provincial electricity authority (PEA) installed one 250 kW wind turbine at Ko Tao, Ko Pha-ngan District in Surat Thani Province. A data collection and analysis during 2003 that assessed the wind energy potential found average wind speeds of 5.53 m/s. The wind turbine used is a Pioneer Wincon P250/29 model with a total capacity of 250 kW, or 10% of Ko Tao Island's total power consumption. The turbine (three blades) has a horizontal axis with a hub height 50 m and a blade length of 13.4 m. The turbine begins generating electricity at a wind speed of 3 m/s and cuts out at a wind speed of 25 m/s [16].

The “First Korat Wind” and “K.R. Two” projects for wind power generation were established by Wind Energy Holding Co., Ltd. at Huay Bong Sub-district, Dan Khun Tod District, Nakorn Ratchasima province in 2012 and 2013, respectively. The average wind speeds for both projects' areas are 6.2 m/s. In each project, 45 2.3 MW wind turbines (with a total capacity 90 MW) were installed, with a height of 99.5 m and a blade diameter of 101 m. These projects are the first large-scale wind farms in Thailand and have the highest capacity in Southeast Asia. Moreover, they are supported by governmental adder subsidies of about US$0.11/kWh over 10 yr [17].

5. Thailand's wind energy policy

Regarding the promotion and support for the use of renewable energy to generate electricity, the energy policy and planning office (EPPO) specified adder subsidies for several types of renewable energy. Therefore, small and very small power producers (SPPs and VSPPs) can sell their electricity to the electricity generating authority of Thailand (EGAT) or the provincial electricity authority (PEA) at higher-than-normal prices. Wind energy received adder subsidies of about US$0.08–0.11/kWh. The three southern provinces (Yala, Pattani, and Narathiwat) have special adder subsidies of US$0.16/kWh. This adder support lasts 10 yr, starting from the effective date of the contract [18–20].

Regarding the long-term 10-yr alternative energy development plan (AEDP 2012–2021), the Ministry of Energy aims to increase the ratio of alternative energy use to 25% [21] by 2021. Under this policy, renewable energy development projects will be initiated under the Thailand power development plan 2012–2030 (PDP2010: Revision 3) by the Energy Policy and Planning Office (EPPO). Therefore, in 2030, electricity generation from renewable energy will be 20,546.3 MW, or 29% of total electricity generation. Renewable energy sources can be classified into domestic renewable energy and renewable energy from neighboring countries, at 13,688 MW and 6,858 MW [22], respectively. Wind-powered electricity generation will be increased to a productivity of over 1800 MW. In 2012, Thailand had a wind-powered electricity generation of around 111.7 MW [23], as shown in Table 5.

Obstacles to development and promotion of wind energy in Thailand are as follows:

(1) Areas with high wind-energy potential are often located in mountainous or reserved forest areas; thus, private organizations that intend to invest in wind turbines (of more than 1400 MW) often face problems in getting permission to use the area from related governmental agencies. However, this obstacle can be resolved between private organizations and governmental agencies by allowing the installation of wind

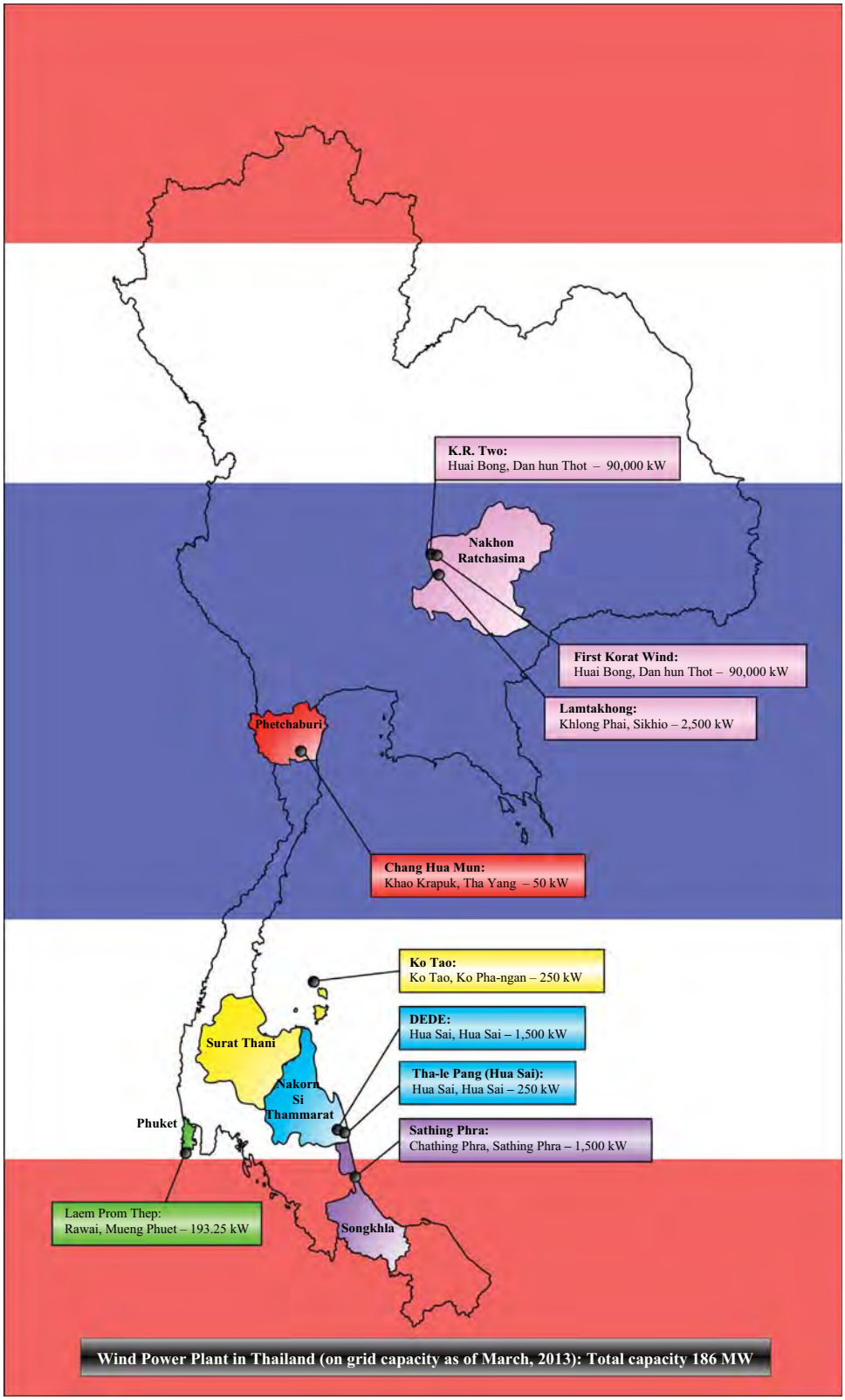

Fig. 4. Map of wind power plant in Thailand [data from [14]]

farms at rental rates of US$0.7/m^2/yr and project durations of no more than 27 yr [20].

(2) Some other problems are the cost of producing and installing wind turbines and the appropriateness of the site. There must be 22, 33, or 115 kV high-current electricity discharge systems within a 10 km radius of the area to connect with the electrical system of the provincial electricity authority (PEA). Because of this, the Thai government plans to improve its power

Table 5
Status and target for use of alternative energy in electricity generation [23].

Type of energy	Output in 2010 (MW)	Output in 2011 (MW)	Output in 2012 (MW)	Target in 2021 (MW)
Wind	*5.6*	*7.3*	*111.7*	*1800*
Solar	48.6	78.7	376.7	3000
Water	58.9	95.7	101.8	324
Biomass	1650.2	1790.2	1959.9	4800
Biogas	103.4	159.2	193.4	3600
Waste	13.1	25.5	42.7	400
New energy	–	–	–	3

infrastructure, including its grid and energy storage systems. In addition, the government has promoted the creation network of wind energy producers and users to facilitate wind energy connections in the future.

(3) There are also environmental problems, such as destruction of scenery, noise pollution, impact on creatures living within the installation area, and so on. To solve these problems, the environmental impact assessment (EIA) should be considered at the potentiality stage of a project.

6. Conclusions

Thailand's best wind-energy potential areas are around the coast of the Thai Gulf and higher-elevation lands, with average annual wind speeds of 6.4 m/s at an elevation of 50 m. Another potentially good area is around the western mountain ridgeline, from the lower northern to the upper southern part. The next-best potential areas, with average annual wind speeds of 4.4 m/s and higher at an elevation of 50 m, are the upper southern portion, the western coast of the Thai Gulf, the northern mountainous areas, the western coast of the south, and the eastern coast of the Thai Gulf.

Wind-powered electricity generation in Thailand has increased continuously in both the governmental and private sectors. In 2012, Thailand generated approximately 111.7 MW of electricity from wind energy. By 2021, Thailand aims to increase the ratio of wind energy use in electricity generation to a total productivity of 1800 MW, or 12.9% of all electricity generated from alternative energy in the country.

Acknowledgments

The authors are indebted to the Thailand Research Fund, the National Science and Technology Development Agency and the National Research University Project for supporting this study.

References

[1] Department of Alternative Energy Development and Efficiency. Ministry of energy, Thailand energy statistics (Preliminary), ⟨http://www.dede.go.th/dede/images/stories/stat_dede/report12/%202555_1.pdf⟩; 2012 [accessed 13.08.13].
[2] Department of Alternative Energy Development and Efficiency. Ministry of energy, Thailand energy statistics, ⟨http://www.dede.go.th/dede/images/stories/stat_dede/file_zip/Report%2011.rar⟩; 2011 [accessed 13.08.13].
[3] Department of Alternative Energy Development and Efficiency. Ministry of energy, electric power in Thailand: annual report, ⟨http://www.dede.go.th/dede/images/stories/stat_dede/electric54_1.pdf⟩; 2011 [accessed 13.08.13].
[4] Central Intelligence Agency (CIA). The World factbook, ⟨https://www.cia.gov/library/publications/the-world-factbook/rankorder/2042rank.html⟩ [accessed 18.04.12].
[5] Department of Energy Affairs. Wind resource assessment of Thailand, final report, central press, Thailand, ⟨http://www2.dede.go.th/dede/renew/Twm/MAIN.htm⟩; 2001 [accessed 19.08.13].
[6] The World Bank Asia Alternative Energy Program. Wind energy resource atlas of Southeast Asia; September 2001.
[7] Waewsak J, Kongruang C, Tirawanichakul Y, Tirawanichakul S, Matan N, Prompat C, et al. The potential of wind power along the coasts of southern Thailand. J Natl Res Counc Thail 2009:51–60 (Special Issue: 50th Anniversary).
[8] Dussadee N, Sasujit K, Suwannasit N, Kangvankij S, Suankamgong A, Kiatsiriroat T. Study on potential of power generation from wind energy in upper northern region. J Natl Res Counc Thail 2009:61–70 (Special Issue: 50th Anniversary).
[9] Global Wind Energy Council. Global wind report: annual market update, ⟨http://www.gwec.net/wp-content/uploads/2012/06/Annual_report_2012_LowRes.pdf⟩; 2012 [accessed 13.08.13].
[10] Ministry of Energy. Thai energy vision, public relations office; 2006. p. 214–31.
[11] Electricity Generating Authority of Thailand. EGAT and wind energy development for electricity generation, ⟨http://www3.egat.co.th/re/egat_wind/egat_wind.htm⟩ [accessed 17.08.13].
[12] Electricity Generating Authority of Thailand. Wind generator at Lamtakhong, Sikhio district, NakhonRatchasima, ⟨http://www3.egat.co.th/re/egat_wind/egat_windlamtakhong/wind_lamtakhong.htm⟩ [accessed 17.08.13].
[13] Sriwelaiwat T. The biggest wind turbine in Thailand, ⟨http://www.oknation.net/blog/nn1234/2010/06/04/entry-1⟩; September 28, 2009 [accessed 17.08.13].
[14] Department of Alternative Energy Development and Efficiency. Ministry of energy, map of wind power plant in Thailand, ⟨http://weben.dede.go.th/webmax/content/map-wind-power-plant-thailand⟩ [accessed 13.08.13].
[15] Provincial Electricity Authority. Electricity production from wind power project of "Chang-Hua-Mun" Royal Initiative Project, ⟨http://peas1.pea.co.th/bangsaphan/images/stories/PDF/wind%20power.pdf⟩ [accessed 23.08.13].
[16] Kitworawut P, Vathananukij H. Wind power: evolution Technology from the past to presence and futurity, ⟨http://gis.eng.ku.ac.th/Research/paper_wind%20energy.pdf⟩ [accessed 26.08.13].
[17] Wind Energy Holding Co., LTD. West Huay Bong 2 and West Huay Bong 3 Wind Farm projects, ⟨http://www.windenergyholding.co.th⟩ [accessed 23.08.13].
[18] Prapakdi S. Wind generator: environmental perspective. J Environ 2009;13:42–8.
[19] Energy Conservation Promotion Fund. Energy conservation plan and guidelines, criteria, conditions and priority of expense, ⟨http://www.eppo.go.th/encon/plan-2551-2554/encon-2551-2554.pdf⟩ [accessed 26.08.13].
[20] Ruangrong P. Thailand's approach to promoting clean energy in the electricity sector. Forum on clean energy, good governance and regulation: Singapore, ⟨http://electricitygovernance.wri.org/files/egi/Thailand.pdf⟩; 16–18 March 2008 [accessed 26.08.13].
[21] Department of Alternative Energy Development and Efficiency. Ministry of energy, the renewable and alternative energy plan for 25 percent in 10 years (AEDP 2012–2021), ⟨http://www.dede.go.th/dede/images/stories/dede_aedp_2012_2021.pdf⟩ [accessed 23.08.13].
[22] Energy Policy and Planning Office. Ministry of energy, summary of Thailand power development plan 2012–2030 (PDP2010: REVISION 3, June 2012), ⟨http://www.egat.co.th/en/images/about-egat/PDP2010-Rev3-Eng.pdf⟩ [accessed 20.08.13].
[23] Department of Alternative Energy Development and Efficiency. Ministry of energy, Thailand alternative energy situation, ⟨http://www.dede.go.th/dede/images/stories/stat_dede/Alternative_1012/thailand%20alternative%20energy%20situation%202012.pdf⟩; 2012 [accessed 20.08.13].

Selection of the most suitable refrigerant for a shell and tube condenser

A. S. Dalkilic, O. Mahian & S. Wongwises

Heat and Mass Transfer
Wärme- und Stoffübertragung

ISSN 0947-7411
Volume 50
Number 2

Heat Mass Transfer (2014) 50:183-197
DOI 10.1007/s00231-013-1235-7

Springer

Heat Mass Transfer (2014) 50:183–197
DOI 10.1007/s00231-013-1235-7

ORIGINAL

Selection of the most suitable refrigerant for a shell and tube condenser

A. S. Dalkilic · O. Mahian · S. Wongwises

Received: 1 March 2012 / Accepted: 17 September 2013 / Published online: 6 October 2013

Abstract A theoretical performance study on a shell and tube condenser with various refrigerant blends was conducted for various ratios proposed by other researchers in the literature. The theoretical results showed that all of the alternative refrigerants investigated in the analysis have a slightly lower convective heat transfer coefficient than their base refrigerants. The refrigerant mixture of R290/R600, R152a/R125/R32 and R32/R134a were found to be the most proper replacement refrigerant among the alternatives.

List of symbols

A	Inside surface area, m^2
CFC	Chlorofluorocarbon
d	Diameter, m
f	Friction factor
F	Correction factor
G	Mass flux, kg $m^{-2}s^{-1}$
GWP	Global warming potential
h	Convective heat transfer coefficient, W $m^{-2}K^{-1}$
HC	Hydrocarbon
HCFC	Hydrochlorofluorocarbon
L	Tube length, m
LMTD	Logarithmic mean temperature difference
m	Flow rate, kg s^{-1}
N	Number of tubes
ODP	Ozone depleting potential
R	Tube radius, m
P	Pitch, m
R	Resistance, $m^2K\ W^{-1}$
Q	Heat rejection duty, kW
U	Overall heat transfer coefficient, W $m^{-2}K^{-1}$
U_∞	Water flow velocity, m s^{-1}
Δh	Enthalpy of phase change, kJ kg^{-1}
ΔP	Pressure drop, Pa
ΔT_m	Mean temperature difference

Greek symbols

ρ	Density, kg m^{-3}
υ	Specific volume, $m^3\ kg^{-1}$
ν	Kinematic viscosity, $m^2\ s^{-1}$
η_p	Pump efficiency

Subscripts

c	Cold
c	Clean
cs	Cold surface
D	Dirty
F	Fouling
g	Gas
h	Hot
i	Inside
l	Liquid
o	Outside
m	Mean
p	Pass

A. S. Dalkilic (✉)
Heat and Thermodynamics Division, Department of Mechanical Engineering, Mechanical Engineering Faculty, Yildiz Technical University, Yildiz, Besiktas, 34349 Istanbul, Turkey
e-mail: dalkilic@yildiz.edu.tr

O. Mahian
Young Researchers and Elite Club, Mashhad Branch, Islamic Azad University, Mashhad, Iran

S. Wongwises
Fluid Mechanics, Thermal Engineering and Multiphase Flow Research Lab. (FUTURE), Department of Mechanical Engineering, Faculty of Engineering, King Mongkut's University of Technology Thonburi, Bangmod, Bangkok 10140, Thailand

r Return
s Shell
sat Saturation
T Total
t Tube
w Water

1 Introduction

Not only has the significance of heat exchangers increased from the perspective of energy recovery, conservation, conversion, and successful implementation of new energy sources in recent decades but its significance is also increasing from the angle of environmental issues such as the contamination of air, water, and waste removal. Heat exchangers are used in the process, power, transportation, air-conditioning and refrigeration, cryogenic, heat recovery, alternate fuels, and manufacturing industries, besides being main aspects of numerous industrial goods that are available in the marketplace. Many publications exist regarding the improvement of heat exchangers in the literature due to their importance in industry and our actual lives. On the contrary, this paper was motivated by the fact that few of the studies available seem to provide detailed analyses with respect to the use of alternative refrigerants in condensers and their selection in terms of cost and economy.

Heat exchangers can be classified according to their transfer processes, number of fluids, heat transfer mechanisms, construction types, flow arrangements, and heat transfer surface area/volume ratio. In this paper, the analyses include a useful sample design procedure for a shell and tube condenser, which is one of the indirect-contact heat exchangers used in the power industry (surface condenser and feed water heater) and the process industry [E, G, H, J, and X shells and total condensation applications (reflux and knockback)].

The latest agreements have reduced and will finally eliminate the production and usage of chlorofluorocarbons (CFCs) and hydrochlorofluorocarbons (HCFCs) in the market. At this stage, the discovery of new refrigerants is needed as a solution to the problems of global warming (GWP) and ozone depletion (ODP). The refrigerant mixtures are used as alternative replacements in the systems. These mixtures may be azeotropic, near-azeotropic, or zeotropic (non-azeotropic). Azeotropic refrigerants act similarly to a single component (pure fluid) under constant pressure and condense and evaporate at a constant temperature, and the composition of the blend will be identical in the vapor and liquid phases. Azeotropic blends have been commonly used in refrigeration, and some of their popular mixtures used in place of R22 are R502, a mixture of R22 and R152a; and R410A, a mixture of R32 and R125. Near-azeotropic blends have slight temperature variations during phase change and a small alteration in the composition in the liquid and vapor phases at equilibrium. The aim of their occurrence is to use a refrigerant alternative beyond pure fluids and azeotropic blends. The mixture of a small amount of R290 to R502 is a sample that was developed to enhance R502's solubility in lubricating oil. Zeotropic blends undergo an important variation in temperature during condensation and evaporation, and the compositions of the vapor and liquid phases are different at the equilibrium state. R407C, a mixture of R32, R125, and R134a, is a common example. Table 1 lists most of the well-known theoretical and experimental refrigerant mixture studies [1–48] in the literature from 1975 to 2011. The development of blends from the past to today and the prediction of new blends to be used in the near future can be evaluated clearly based on this table.

2 Calculations of the design procedure for the investigated shell and tube condenser

In the case studies, refrigerants were evaporated at −10 °C and condensed at various temperatures with the heat of condensation rejected to cooling water taken from a small cooling tower at 25 °C. A shell and tube construction with 1, 2, and 4 pass designs (N_p) on the water side was used in the simulation studies. Copper tubes with inside/outside diameters of 0.012573/0.01588 m (d_i/d_d) were selected due to their compatibility with the refrigerants. The design procedures of a condenser for a 91.92 kW (Q_c) refrigerating system are given in the following section.

2.1 Tube-side calculations

The bulk temperature of water is calculated from Eq. (1) to determine the physical properties:

$$T_{bulk} = \frac{(T_{c1} + T_{c2})}{2} \tag{1}$$

The cold-side flow area is determined as follows:

$$A_{cs} = \frac{\pi d_i^2}{2} \tag{2}$$

The flow velocity of water (U_∞) is varied from 1 to 3 m s^{-1}; thus, the mass flux is determined from Eq. (3):

$$G = \rho_w U_\infty = \frac{U_\infty}{\upsilon_w} \tag{3}$$

The cooling water flow rate per tube is calculated as follows:

Table 1 Literature review on the evaluation of refrigerant mixtures

Researcher	Proposed mixture refrigerant
Lorenz and Meutzner [1]	R22-R11 (50/50 by wt %)
Stoecker [2]	R12/R114 (70/30 by wt %)
Stoecker and Walukas [3]	R12-R114 (50/50 by wt %)
Mishra et al. [4]	R12/R22 (23/77 by wt %)
	R12/R22 (27/73 by wt %)
	R12/R22 (41/59 by wt %)
	R12/R22 (48/52 by wt %)
Singal et al. [5]	R13/R12 (5/95 by wt %)
	R13/R12 (10/90 by wt %)
	R13/R12 (15/80 by wt %)
	R13/R12 (20/85 by wt %)
Kruse and Hesse [6]	R22/R114 (60/40 by wt %)
Kuijpers et al. [7]	R600a/R290 (79/21 by wt %)
Jung et al. [8]	R22/Rl14 (23/71 by wt %)
	R22/R114 (48/52 by wt %)
	R22/R114 (77/23 by wt %)
	Rl2/R152a (21/79 by wt %)
	R12/R152a (88/12 by wt %)
Koyama et al. [9]	R22/R114 (52/48 by wt %)
Kedzierski and Didion [10]	R22/R114 (37.7/62.3 mol %)
Rivis and Bedone [11]	R290/R600a (50/50 and 60/40 by wt %)
Kim et al. [12]	R290/R134a (45/55 by wt %)
	R134a/R600a (80/20 by wt %)
Nozu et al. [13]	R114/R113 (23/36 by wt %)
Richardson and Butterworth [14]	R290/R600 (48/52 by wt %)
	R290/R600a (50/50 by wt %)
Sami and Song [15]	R-32/R-125/R-143a/R-l34a (40/25/25/10 by wt. %)
Doongso et al. [16]	R290/R600a (20/80 by wt %)
	R290/R600a (30/70 by wt %)
	R290/R600a (40/60 by wt %)
	R290/R600a (50/50 by wt %)
	R290/R600a (60/40 by wt %)
Shin et al. [17]	R32/R134a (25/75 by wt %)
	R32/R134a (50/50 by wt %)
	R32/R134a (75/25 by wt %)
	R290/R600a (25/75 by wt %)
	R290/R600a (50/50 by wt %)
	R290/R600a (75/25 by wt %)
	R32/R125 (50/50 by wt %).
Alsaad and Hammad [18]	R290/R600/R600a (24.4/56.4/17.2 by wt. %)
Shao and Granryd [19]	R32/R134a (26.5/73.5 by wt %)
Baskin [20]	R600a/R290 (60/40 by wt %)
	R600a/R290 (70/30 by wt %)

Table 1 continued

Researcher	Proposed mixture refrigerant
Hammad and Alsaad [21]	R290/R600/R600a (50/38.3/11.7 by wt %)
	R290/R600/R600a (75/19.1/5.9 by wt %)
	R290/R600/R600a (25/57/17.5 by wt %)
Jung et al. [22]	R290/R600a (60/40 by wt %)
Miyara et al. [23]	R134a/R123 (50/50 by wt %–R410A)
Chang et al. [24]	R290/R600a (50/50 by wt %)
Choi et al. [25]	R32/R125/R134a (23/25/52 by wt %–R407C)
Tashtoush et al. [26]	R600/R290/R134a (35.71/35.71/28.58 by wt %)
	R600/R290/R134a (31.25/31.25/37.5 by wt %)
	R600/R290/R134a (27.78/27.78/44.44 by wt %)
	R600/R290/R134a (25/25/50 by wt %)
	R600/R290/R134a (22.73/22.73/54.54 by wt %)
Akash and Said [27]	R290/R600/R600a (30/55/15 by wt %–LPG)
Wongwises and Chimres [28]	R290/R600 (60/40 by wt %)
	R290/R600/R600a (70/25/5 by wt %)
	R290/R600/R600a (50/40/10 by wt %)
	R290/R600a (60/40 by wt %)
	R290/R600/R134a (40/30/0/30 by wt %)
	R290/R600a/R134a (40/30/30 by wt %)
Wen and Ho [29]	R290/R600 (55/45 by wt %)
Koyoma et al. [30]	CO_2/RE170 (90/10 by wt %)
Wen et al. [31]	R600/R290 (50/50 by wt %)
Han et al. [32]	R32/R125/R134a (23/25/52 by wt %–R407C)
	R32/R125/R161 (15/34/51 by wt %)
Park et al. [33]	R1270/R290 (20/80 by wt %)
	R1270/R290 (50/50 by wt %)
	R1270/R290 (80/20 by wt %)
	R290/R152a (60/40 by wt %)
	R290/R152a (71/29 by wt %)
	R290/R152a (75/25 by wt %)
Afroz et al. [34]	CO_2/RE170 (39/61 by wt %)
	CO_2/RE170 (21/79 by wt %)
Xue et al. [35]	CO_2/RE170 (95/5 by wt %)
	CO_2/RE170 (90/10 by wt %)
Chen and Yu [36]	R32/R134a (30/70 by wt %)
Lee et al. [37]	R290/R600a (55/45 by wt %)

Table 1 continued

Researcher	Proposed mixture refrigerant
Mani and Selladurai [38]	R290/R600a (68/32 by wt %)
Kim et al. [39]	CO_2/R290 (75/25by wt %)
Wu et al. [40]	R152a/R125/R32 (48/18/34 by wt %)
Onaka et al. [41]	CO_2/RE170 (10/90 by wt %)
	CO_2/RE170 (25/75 by wt %)
Park and Jung [42]	R170/R290 (2/98 by wt %)
	R170/R290 (4/96 by wt %)
	R170/R290 (6/94 by wt %)
	R170/R290 (8/92 by wt %)
	R170/R290 (10/90 by wt %)
Cho et al. [43]	CO_2/R290 (75/25 by wt %)
	CO_2/R290 (50/50 by wt %)
	CO_2/R290 (25/75 by wt %)
Zou et al. [44]	R170/R290 (30/70 by wt %)
Dalkilic and Wongwises [45]	R290/R600 (50/50 by wt %)
	R290/R600 (60/40 by wt %)
	R290/R600 (70/30 by wt %)
	R290/R600 (80/20 by wt %)
	R290/R600a (40/60 by wt %)
Dalkilic and Wongwises [45] (cont.)	R290/R600a (50/50 by wt %)
	R290/R600a (60/40 by wt %)
	R290/R600a (70/30 by wt %)
	R290/R1270 (20/80 by wt %)
	R290/R1270 (50/50 by wt %)
	R290/R1270 (60/40 by wt %)
	R290/R1270 (80/20 by wt %)
	R290/R152a (60/40 by wt %)
	R290/R152a (70/30 by wt %)
	R290/R152a (80/20 by wt %)
	R32/R134a (30/70 by wt %)
Kabul et al. [46]	R125/R134a/R143a (44/4/52)
Yoon et al. [47]	R290/R600 (40/60 by wt %)
Grauso et al. [48]	CO_2/R290 (83.2/16.8 by wt %)
	CO_2/R290 (70/30 by wt %)

$$\dot{m}_t = GA_{cs} \tag{4}$$

The coolant flow rate ($\dot{m}_c$) is obtained from the heat rejection duty (Q_c) as follows:

$$Q_c = \dot{m}_c \, \Delta h_c \tag{5}$$

The number of tubes (N_t) is determined from Eq. (6). It should be noted that the rounding process may be applied to the number of tubes according to its calculated value.

$$\dot{m}_c = \dot{m}_t N_t / N_p \tag{6}$$

The Reynolds number of water inside the tubes is shown in Eq. (7). Its value was over 10,000 for all working conditions, so the flow is determined to be turbulent. Eq. (8) was proposed by Gnielinski's [49] correlation for turbulent flow conditions as the Nusselt number and used in the analyses.

$$Re_l = \frac{Gd_i}{\mu_w}. \tag{7}$$

$$Nu = \frac{(f/2)(Re_l - 1000)\,Pr_l}{1 + 12.7(f/2)^{1/2}(Pr_l^{2/3} - 1)} \tag{8}$$

where the Fanning friction factor is expressed as follows:

$$f = [1.58 \ln(Re_l) - 3.28]^{-2} \tag{9}$$

The heat transfer coefficient of water (h_i) is obtained from the Nusselt number:

$$Nu = \frac{h_i d_i}{k_l} \tag{10}$$

The Nusselt number increases with increasing Reynolds numbers, in other words, the convective heat transfer coefficient of water increases with the increasing in-tube fluid velocity due to the increase in heat transfer. The Fanning friction factor decreases with increasing mass flux. The increase in mass flux will increase the fluid velocity and flow turbulence. This will enable both high heat transfer performance and high pressure drop.

2.2 Shell-side condensing calculations

The bulk temperature of the refrigerant can be assumed to be equal to the refrigerant's condensing temperature to determine the physical properties.

The refrigerant flow rate (m_R) is determined from the heat balance for the coolant and refrigerant:

$$Q_c = Q_R \tag{11}$$

$$m_c \Delta h_c = m_R \Delta h_R \tag{12}$$

The shell-side condensing heat transfer coefficient was proposed by Dhir and Lienhard [50] and modified with the coefficient of N by Incropera and DeWitt [51] and calculated from Eq. (13) as follows:

$$h_o = 0.729 \left[\frac{g(\rho_l - \rho_g)\rho_l \Delta h_g k_l^3}{\mu_l \Delta T N d_o} \right]^{1/4} \tag{13}$$

where the number of tubes in the vertical direction (N) in Eq. (13) is determined by the arrangement as shown in Figs. 1 and 2 for the staggered (square) and line (triangular) pitches. The temperature difference (ΔT) is found from Eq. (14), and it should be noted that the wall temperature (T_{wall}) is assumed and tested during further calculations in this section.

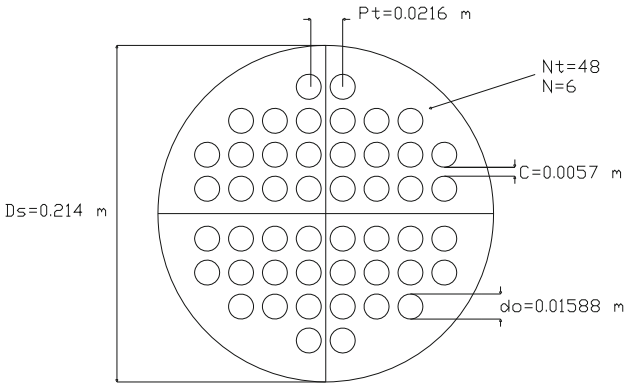

(a) Staggered pitch

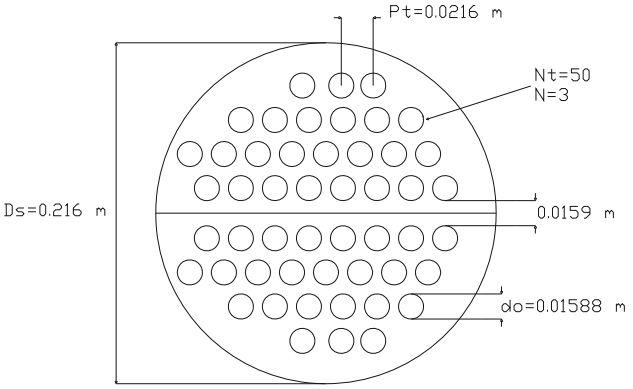

(b) Line pitch

Fig. 1 Tube configuration for two pass shell and tube condenser *plotted* with 1/25 scale in mm

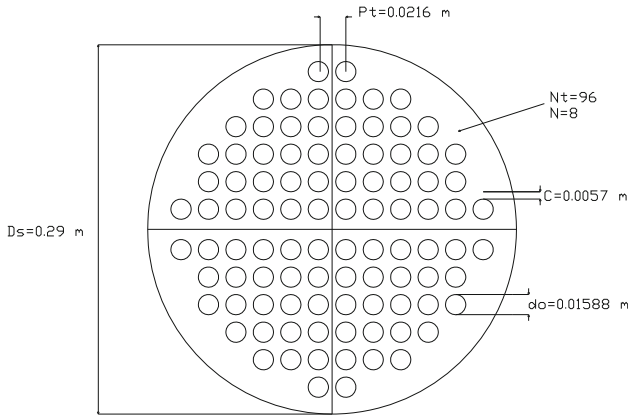

(a) Staggered pitch

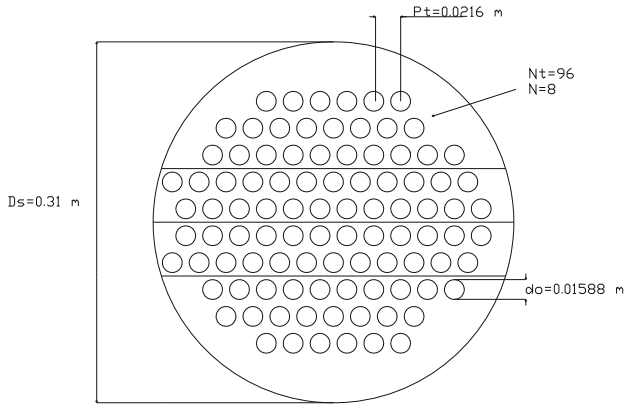

(b) Line pitch

Fig. 2 Tube configurations for four-pass shell and tube condenser *plotted* with 1/25 scale in mm

$$\Delta T = (T_{sat} - T_{wall}) \tag{14}$$

2.3 Dimensions of the condenser

The overall heat transfer coefficient is determined from Eq. (15) for the condition of being either clean or dirty. R_{fi} and R_{fo} should be omitted for clean tubes.

$$U_{oD} = \left[\frac{r_o}{h_i r_i} + \frac{r_o R_{fi}}{r_i} + \frac{r_o \ln(r_o/r_i)}{k_t} + R_{fo} + \frac{1}{h_o}\right]^{-1} \tag{15}$$

The logarithmic mean temperature difference (LMTD) and the mean temperature difference (ΔT_m) are calculated as follows:

$$LMTD = \frac{\Delta T_1 - \Delta T_2}{\ln \frac{\Delta T_1}{\Delta T_2}} = \frac{(T_h - T_{c1}) - (T_h - T_{c2})}{\ln \frac{(T_h - T_{c1})}{(T_h - T_{c2})}} \tag{16}$$

$$\Delta T_m = LMTDxF \tag{17}$$

where the correction factor (F) is 1 for a condenser.

The heat transfer surface area of the condenser (A_o) is calculated from the heat transfer rate in Eq. (18) as:

$$Q_c = U_o A_o \Delta T_m \tag{18}$$

where the tube length is obtained from Eq. (19). It should be calculated separately for either clean or dirty tubes or staggered or line pitches.

$$A_o = N_t \pi d_o L \tag{19}$$

The shell diameter (d_s) is estimated assuming $C_a = 1.1$, $C_L = 1$, and $PR = P_t/d_t$ in Eq. (20). It should be also checked by the tube arrangement figures as shown in Figs. 1 and 2.

$$d_s = C_a \sqrt{(C_L/2.5)(A/L)(PR)^2 d_t} \tag{20}$$

The temperature difference (ΔT) in Eq. (14) is also recalculated from Eq. (21). The same value of ΔT should be obtained for staggered or line pitches separately, including clean and dirty tubes, by means of a trial and error method using a computer program.

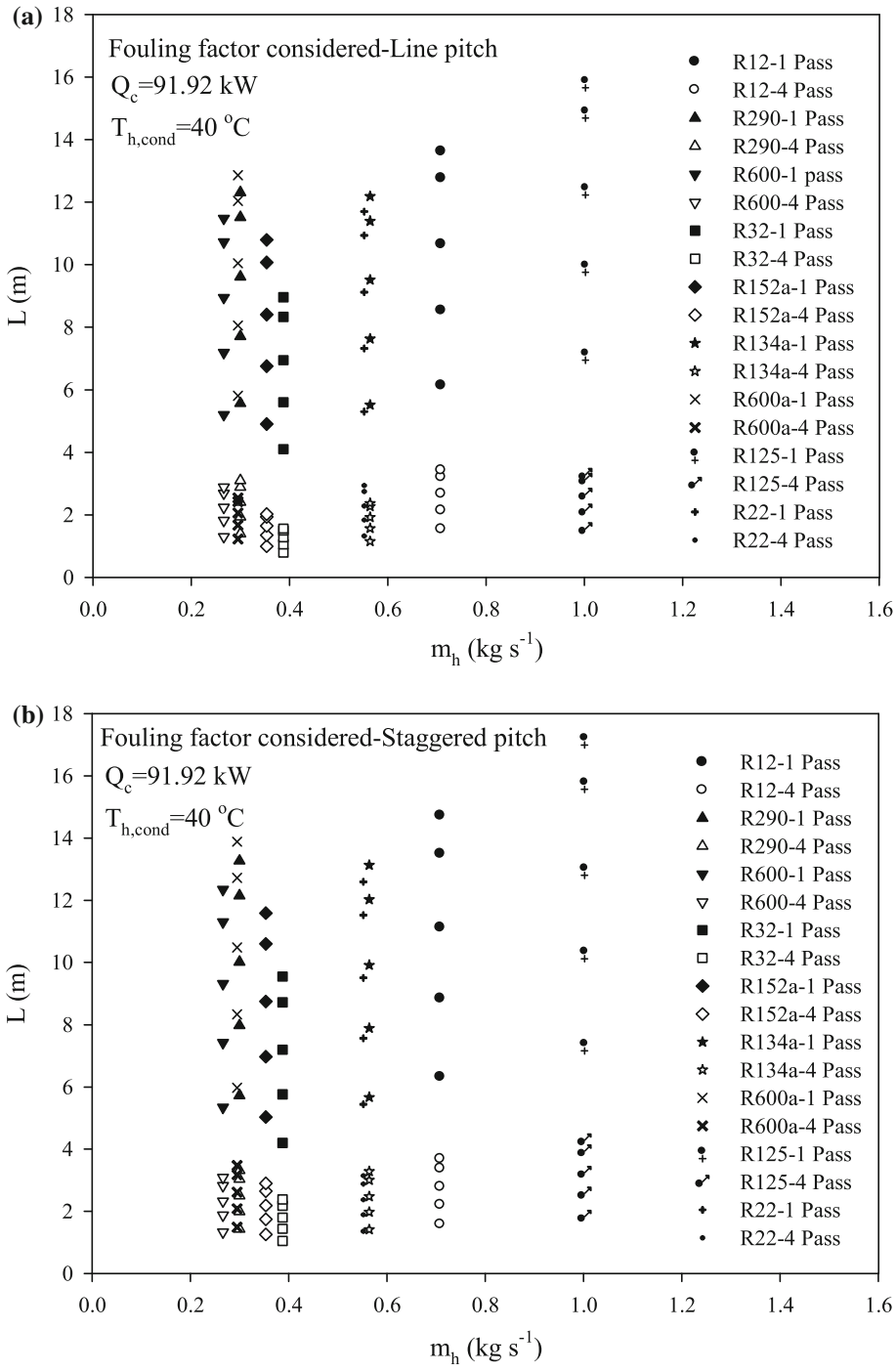

Fig. 3 Tube lengths versus refrigerant flow rates

$$q = \frac{Q_c}{A_o} = h_o(T_s - T_{w2}) = h_o \Delta T \tag{21}$$

2.4 Water-side pressure drop

The water-side pressure drop for all the tubes is determined from Eq. (22) as follows:

$$\Delta P_t = \frac{4fLN_pG^2 v_l}{2d_i} \tag{22}$$

where the friction factor is defined in Eq. (9) for the turbulent flow conditions in the tubes.

The fluid has an extra loss because of sudden expansions and contractions during a return [52].

Table 2 A case study for the conditions of $d_i = 12.57$ mm, $N_p = 2$, $T_{evap} = -10$ °C, $Q_c = 91.92$ kW (Line pitch with fouling factor)

Tube side						Shell side						
Refrigerant	$T_{c,i}$ (°C)	$T_{c,o}$ (°C)	u_c (m s^{-1})	N_t	h_i (W $m^{-2}K^{-1}$)	Refrigerant	$T_{h,cond}$ (°C)	m (kg s^{-1})	L (m)	h_o (W $m^{-2}K^{-1}$)	u_o (W $m^{-2}K^{-1}$)	W_p (kW)
Water	25	30	1	72	5,110.8	R290	40	0.299	2.78	1,156.71	744.29	49.16
Water	25	30	1.5	48	7,305.02	R290	40	0.299	3.86	1,196.4	806.03	126.92
Water	25	30	2	36	9,379.99	R290	40	0.299	4.81	1,259.47	861.67	249.94
Water	25	30	2.5	28	11,374.14	R290	40	0.299	5.77	1,352.21	923.81	429.55
Water	25	30	3	24	13,307.92	R290	40	0.299	6.19	1,499.53	1,006.35	638.56
Water	25	30	1	72	5,110.8	R600	40	0.266	2.6	1,286.87	967.29	47.29
Water	25	30	1.5	48	7,305.02	R600	40	0.266	3.6	1,330.02	1,070.24	121.4
Water	25	30	2	36	9,379.99	R600	40	0.266	4.48	1,399.5	1,164.42	238.3
Water	25	30	2.5	28	11,374.14	R600	40	0.266	5.384	1,502.51	1,271.93	408.58
Water	25	30	3	24	13,307.92	R600	40	0.266	5.77	1,666.31	1,419.16	607.19
Water	25	30	1	72	5,110.8	R600a	40	0.295	2.91	1,083.44	713.26	50.42
Water	25	30	1.5	48	7,305.02	R600a	40	0.295	4.03	1,121.23	771.2	130.6
Water	25	30	2	36	9,379.99	R600a	40	0.295	5.04	1,180.44	823.93	257.73
Water	25	30	2.5	28	11,374.14	R600a	40	0.295	6.04	1,267.38	883.41	443.59
Water	25	30	3	24	13,307.92	R600a	40	0.295	6.46	1,405.4	963.06	659.56
Water	25	30	1	72	5,110.8	R125	40	1.001	3.55	810.94	584.06	57.08
Water	25	30	1.5	48	7,305.02	R125	40	1.001	4.96	841.13	627.48	150.12
Water	25	30	2	36	9,379.99	R125	40	1.001	6.06	913.4	684.29	294.02
Water	25	30	2.5	28	11,374.14	R125	40	1.001	7.44	951.9	717.63	517.73
Water	25	30	3	24	13,307.92	R125	40	1.001	7.941	1,054.84	784.43	770.7

$$\Delta P_r = \frac{4N_p \rho U_{m^2}}{2} \tag{23}$$

The total pressure drop is the sum of the pressure in the tube (Eq. 22) and due to returns (Eq. 23).

$$\Delta P_T = \Delta P_t + \Delta P_r \tag{24}$$

The fluid pumping power (P) is proportional to the pressure drop in the fluid across a heat exchanger and shown in Eq. (26) as:

$$W_p = \frac{m\Delta P}{\rho \eta_p} \tag{25}$$

where η_p is the pump efficiency, assumed to be 0.85.

It should be noted that details of this procedure can be found in Kakac [53].

2.5 Cost analysis

According to Shah and Sekulic [54], the lifetime costs of a heat exchanger—in other words, the overall total cost—may be grouped as the capital, installation, operating, and disposal costs. The costs related to design, materials, manufacturing (machinery, labor, and overhead), testing, shipping, installation, and depreciation are included in the capital (total installed) cost. The installation cost of some shell-and-tube and plate heat exchangers may be considerable in comparison to the capital cost. The other costs of heat exchangers associated with fluid pumping power, a warranty, insurance, maintenance, repair, cleaning, lost production/downtime caused by failure, energy costs related with utilities (steam, fuel, and water) are included in the operating cost. The cost estimation sometimes may be hard to determine, so the best estimates are made at the design stage [54]. This information shows the importance of the design process for heat exchangers. The unit cost value of C_{UA} in Eq. (26) was obtained from Shah and Sekulic [54] according to the calculated UA values of the operating conditions in the case studies.

$$\text{Cost} = C_{UA}\left(\frac{q}{\Delta T_m}\right) \tag{26}$$

3 Results and discussion

The costs of evaporators, condensers, and other heat exchangers comprise approximately 30 % of the total cost of a thermal power plant. These costs are significant in applications where heat exchangers should have very large surface areas due to their low logarithmic mean temperature differences. Many techniques have been investigated in recent years to improve heat transfer to reduce the sizes

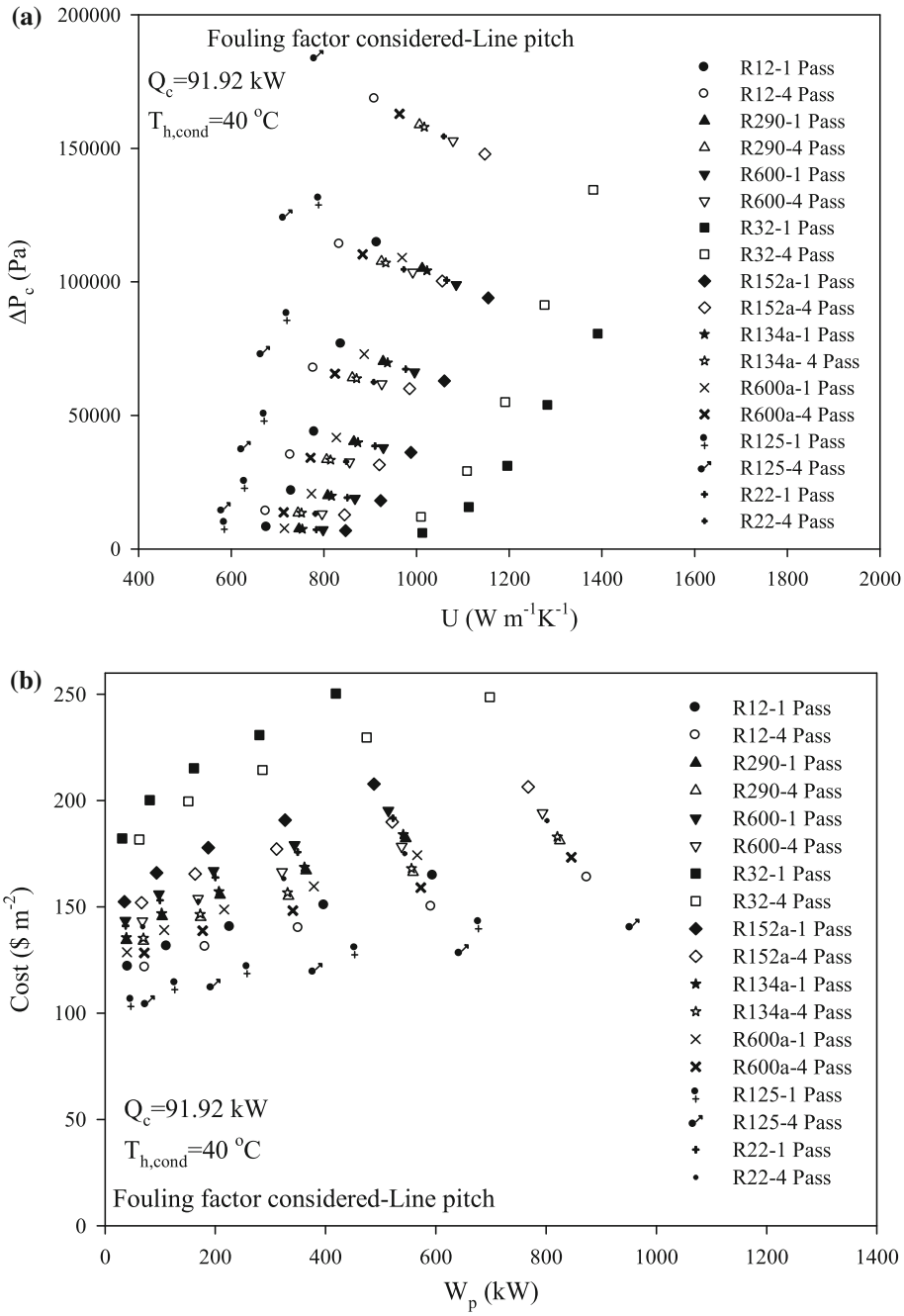

Fig. 4 **a** Pressure drop versus overall heat transfer coefficient **b** Cost versus pumping power

and costs of these heat exchangers as a solution to the cost problem. In this paper, a simple parametric analysis is given in terms of the use of alternative refrigerants. The thermodynamics and transport properties of the blend refrigerants were evaluated with the REFPROP computer program, version 6.01 [55]. It should be noted that this analysis is applied when condensate does not flood any tubes. In general, refrigerant is first determined based on system's operating conditions. And then, optimal design of each component is made. In this work, however, the order is reversed. A condenser design is made and then refrigerant is selected which can best fit to this condenser.

R12, R290, R600, R32, R152a, R134a, R600a, R125, and R22, and their mixtures of R290/R600 (40/60 by wt %); R125/R134a/R143a (44/4/52); R290/R600a (40/60 by wt %); R290/R1270 (20/80 by wt %); R170/R290 (30/70 by wt %); CO_2/R290 (50/50 by wt %); R152a/R125/R32 (48/18/34 by wt %); R32/R134a (30/70 by wt %); and R290/R152a (75/25 by wt %) are used as shell-side condensing hot refrigerants, while cooling water is used as the in-tube cold-side fluid in the investigated condenser. The evaporation temperature of the refrigerants was taken as constant at −10 °C, the condensing temperatures were varied from 35 to 55 °C, and the water-side conditions

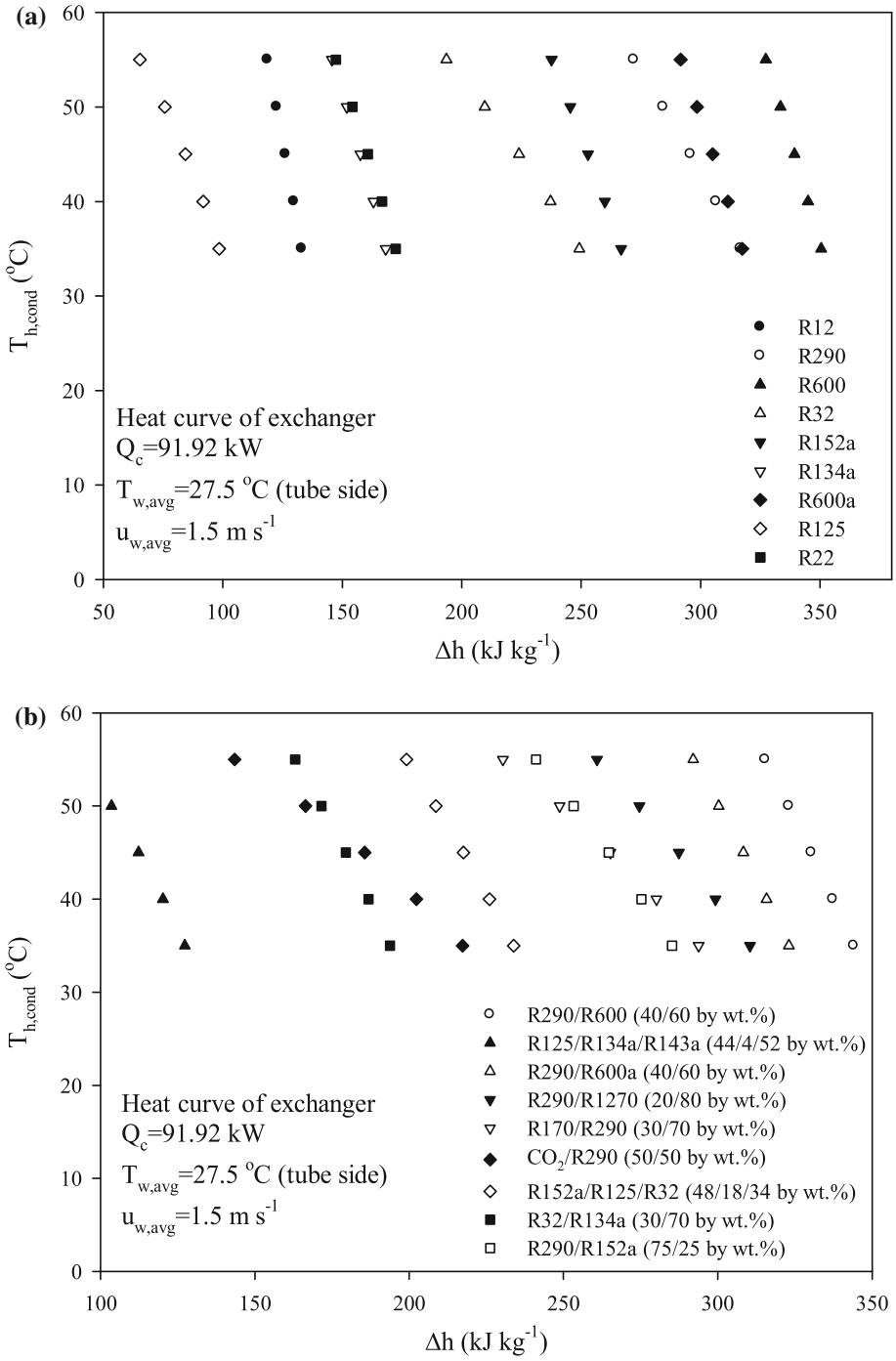

Fig. 5 Enthalpy change versus condensing temperatures for **a** pure refrigerants **b** refrigerant mixtures

were the same for all investigated conditions. Specifically, from Figs. 3 to 5, the operating conditions include in-tube water velocities ranging from 1 to 3 m s^{-1} with various tube numbers changing according to tube pass numbers for a constant condensing temperature of 40 °C in shell side, and from Figs. 6 to 9, it has a constant in-tube water velocity of 1.5 m s^{-1} with a constant tube numbers 24 for 1 pass design, 48 for 2 pass design and 96 for 4 pass design for different condensing temperatures varying from 35 to 55 °C. It should be noted that all calculations were performed for a constant cooling load of 91.92 kW.

The process of developing a new refrigerant started with the use of chlorofluorocarbons (CFCs) such as R12 (GWP = 8,500, ODP = 1) and R22 (GWP = 1,700, ODP = 0.05) in the 1980s, as shown in Table 1. In the 1990s, the mixtures were obtained using hydrochlorofluorocarbons (HCFCs) and hydrocarbons (HCs) such as R134a (GWP = 1,300, ODP = 0), R290 (GWP = 20,

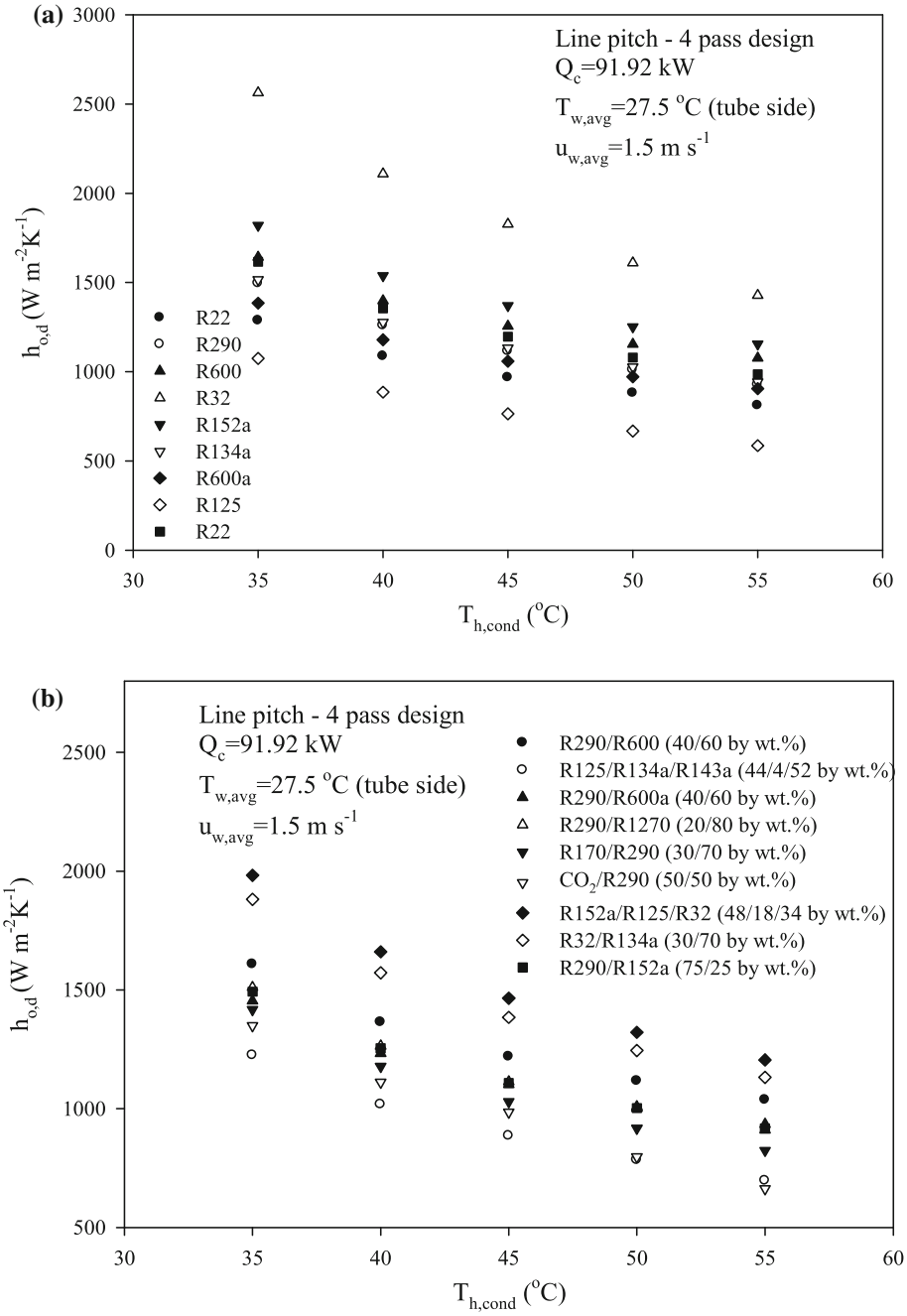

Fig. 6 Convective heat transfer coefficients versus condensing temperatures for **a** pure refrigerants **b** refrigerant mixtures

ODP = 0), and R600a (GWP = 20, ODP = 0). Since the 2000s, refrigerant blend studies have addressed mostly pairs of hydrocarbons (HCs) such as R290, R600 (GWP = 0.1, ODP = 0), R600a, R32 (GWP = 0.11, ODP = 0), and R1270 (GWP = 3, ODP = 0) due to their low global warming potential (GWPs) and ozone depleting potential (ODPs). In the near future, CO_2 (GWP = 1, ODP = 0) is expected to be employed in mixture studies. Ammonia (NH_3) (GWP = 0, ODP = 0) is also a refrigerant considered for enhancement by new compositions. It has far better heat transfer and pressure drop characteristics compared to HFCs. In this study, the selected refrigerant mixtures, listed Table 1, have been associated with the latest trends in the literature since 2007.

Table 2 describes a case study of pure refrigerants to determine the shell-side flow rates, tube lengths, shell-side convective heat transfer coefficients, overall heat transfer coefficients, and pumping powers for various in-tube fluid velocities ranging from 1 to 3 m s^{-1}, a constant cooling load of 91.92 kW, and 1 shell-2 tube pass design. R290,

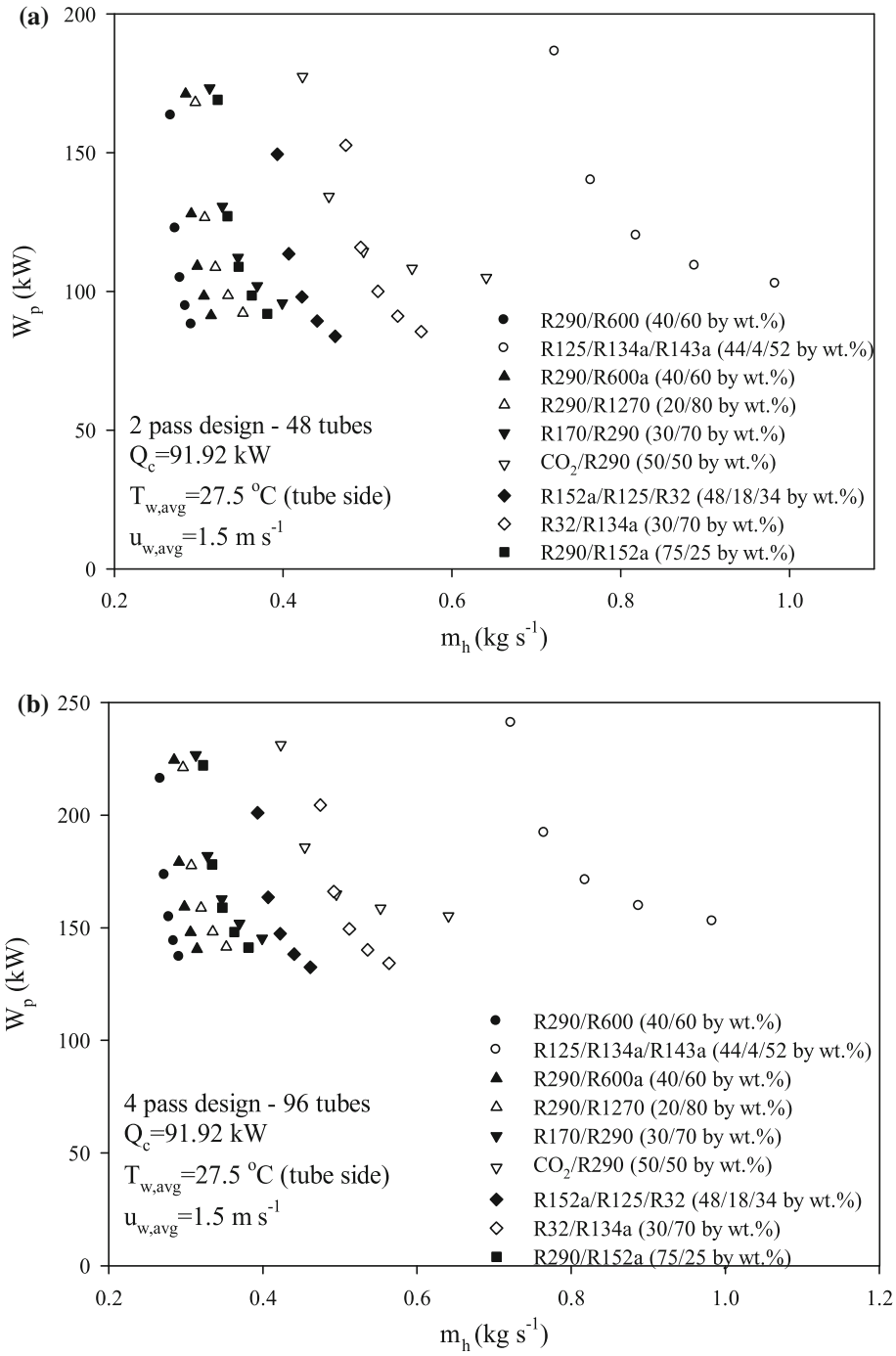

Fig. 7 Comparison of pumping powers of water in tube side according to various condensing temperatures of various refrigerant mixtures for **a** 2 pass and **b** 4 pass designs

R600, and R600a seem to have the shortest tube lengths and pumping powers, according to the table. These results prove their high efficiency and wide usage as optimum refrigerants.

Figure 3 shows the alteration of tube length and pure refrigerant flow rate in the shell side of the condenser according to the staggered or line tube arrangements and tube pass numbers 1 and 4. The desirable specification for the refrigerant is to have a short tube length and low flow rate in these figures. R32, R600, R600a, and R152a seem to fulfill this requirement, according to Fig. 3. A high tube pass number reduces the tube length as expected. This figure also shows the importance of the use of errors in the calculations. It should be also noted that the visual differences in the arrangements with tube pass numbers can be seen clearly in Figs. 1 and 2.

Figure 4 shows some of the important parameters of the condenser with respect to the selection of the optimum refrigerant. The differences in the physical properties of the investigated refrigerants affect the pressure drop of cooling

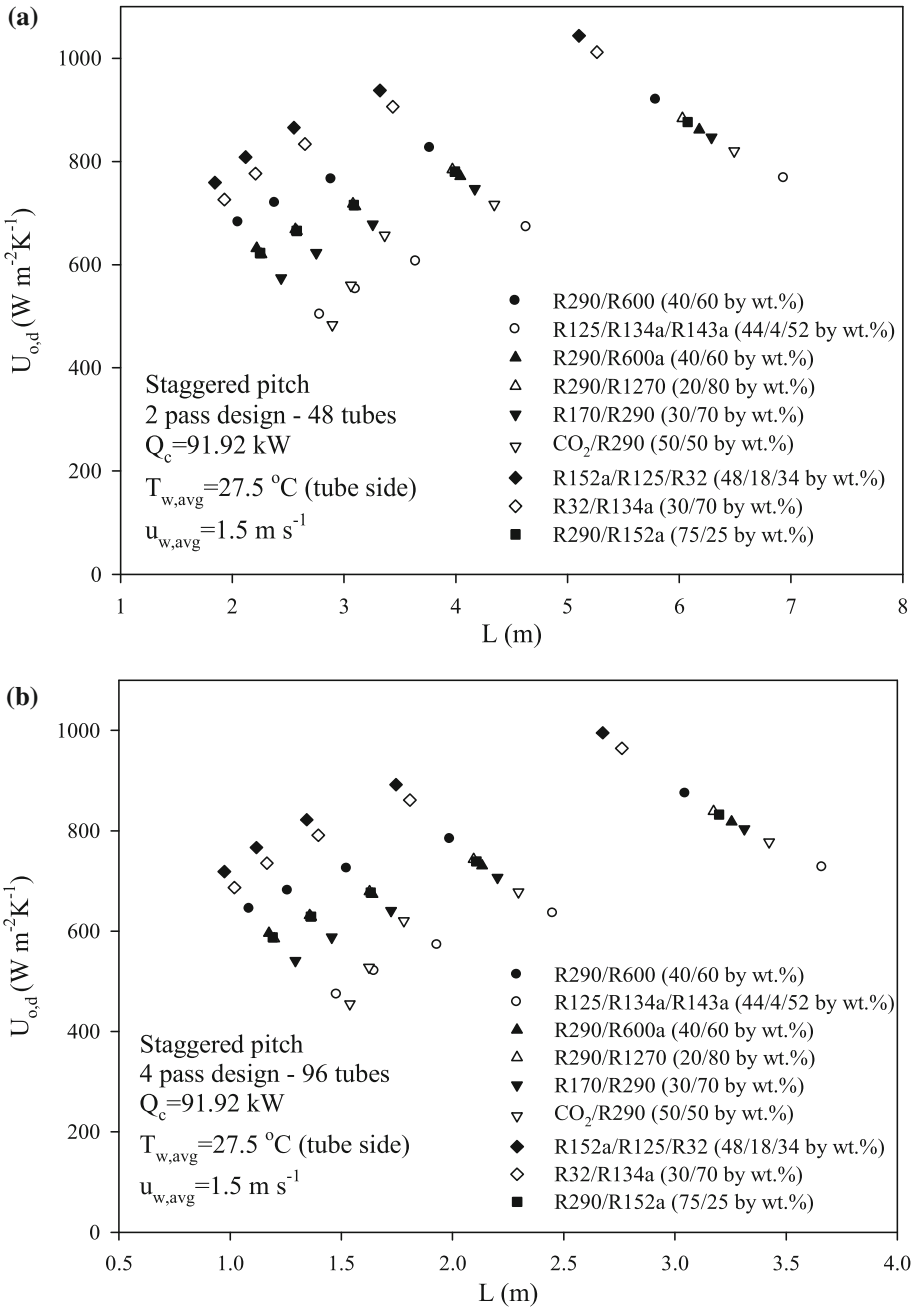

Fig. 8 Overall heat transfer coefficient versus tube length for **a** 2 pass and **b** 4 pass designs

water in-tube, and all of them have different total pressure drop values as a result, as shown in Fig. 4a. R32, R600, R600a, and R152a seem to have lower pressure drop values in comparison to the others for a constant cooling load. It is also seen that increasing tube pass numbers increase the pressure drop, as anticipated and shown in Fig. 4a. It can also be seen that total pressure drop of water increases with increasing overall heat transfer coefficient, in other words, decreasing condensing temperatures in shell side for constant in-tube water side conditions. The cost of the condenser increases with increasing pumping power, as shown in Fig. 4b. Hydrocarbon refrigerants (HCs) showed similar results.

Phase transitions are accompanied by changes in enthalpy and entropy. Because phase changes generally occur at constant pressure, the heat can be described by a change in enthalpy. Figure 5 shows the phase change enthalpies of the pure and blended refrigerants according to various condensing temperatures ranging from 35 to 55 °C. It can be seen from this figure that most of the refrigerant mixtures show improvement in the value of the phase change enthalpy compared to their base refrigerants. For instance, the mixture of R290/R600 (40/60 by wt.) has higher phase change enthalpy than R290 and slightly lower phase change enthalpy than R600 according to this figure.

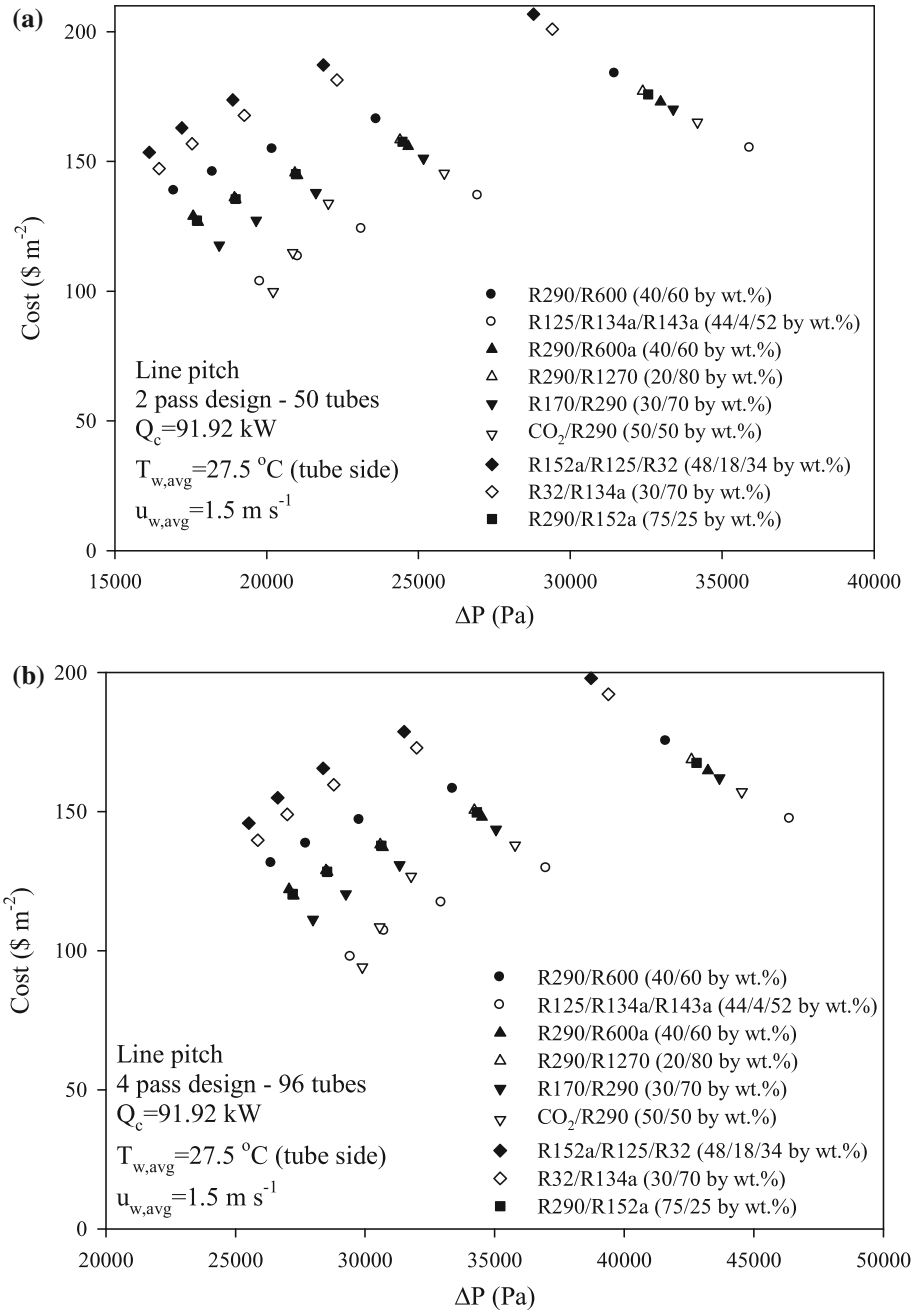

Fig. 9 Cost versus pressure drop for **a** 2 pass and **b** 4 pass designs

Figure 6 shows the alteration of the convective heat transfer coefficients of pure (a) and blended (b) refrigerants in the shell side of the condenser for a constant evaporation temperature of −10 °C and various condensing temperatures ranging from 35 to 55 °C. The figure shows that blended refrigerants did not have higher convective heat transfer coefficients than the pure refrigerants.

Figure 7 illustrates the difference in the pumping power results in terms of the tube arrangement (two or four pass design) and number or tubes (48 and 96) according to the flow rates of the blended refrigerants flowing in the shell side of the condenser. As expected, a four pass condenser has more tubes and requires more pumping power than a two pass condenser for a constant cooling load.

Figure 8 depicts the alterations of the overall heat transfer coefficients and the calculated tube lengths for different tube arrangements in the condenser. In spite of the fact that a four pass condenser has slightly lower overall heat transfer coefficients, they have a significant reduction in the tube length.

Figure 9 reveals the cost of the condensers designed as two and four pass systems according to the calculated total pressure drops in-tube. The two pass condenser has higher cost values than the four pass designed condenser and

lower pressure drops. The R125/R134a/R143a (44/4/52 by wt %) mixture has the minimum cost values regarding with the manufacturing of its condenser in spite of its high pressure drop values. Besides, the same refrigerant hasn't got the lowest required tube length and highest overall heat transfer coefficient in Fig. 8. These kinds of results can be obtained from previous figures, and this situation shows the necessity of finding the optimum refrigerant for efficient and effective condenser designs. Moreover, R290/R600 (40/60 by wt %) proposed by Yoon et al. [47], R152a/R125/R32 (48/18/34 by wt %) proposed by Wu et al. [40] and R32/R134a (30/70 by wt %) proposed by Dalkilic and Wongwises [45] can be considered as the optimum blend refrigerants with their high convective heat transfer coefficients in Fig. 6b, moderate pumping powers in Fig. 7 and low pressure drops in Fig. 9. It should be noted that the determination of the most proper refrigerant depends on the needing and aims of the systems.

4 Conclusion

The analyses include the important parameters of the condenser such as its basic geometry, flow rate, pressure drop, and pumping power to increase heat transfer, reduce pumping power, and reduce condenser size using alternative refrigerants in comparison to those required for their pure base refrigerants for a constant heat duty.

Hydrocarbon refrigerants and blended refrigerants are found to be reasonable alternatives to the older ones and optimum refrigerants, according to the analyses. Blends have the advantage of modifying the composition to meet various temperature demands. Their negative attributes, such as toxicity, flammability, and oil miscibility, can be reduced by influencing the composition. Therefore, they have greater use nowadays and investigation of them will not stop in the future due to the problems of global warming and ozone depletion. In particular, the use of zeotropic mixtures requires greater attention due to the change in their physical properties in case of leakage.

Acknowledgments The present study was supported financially by the Thailand Research Fund, the National Research University Project and National Science and Technology Development Agency, whose guidance and assistance are gratefully acknowledged. The first and second authors would like to thank Professor Somchai Wongwises for providing him fellowships during his research in the Department of Mechanical Engineering, King Mongkut's University of Technology Thonburi.

References

1. Lorenz A, Meutzner K (1975) On application of non-azeotropic two component refrigerants in domestic refrigerators and home freezers. XIV International Congress of Refrigeration, Moscow
2. Stoecker WF (1982) Energy Characteristics of a two-evaporater refrigerator using a refrigerant mixture, U.S. Department of Energy Office of Buildings and Community Systems, Phase II–Project X01 7762
3. Stoecker WF, Walukas DJ (1981) Conserving energy in domestic refrigerators through the use of refrigerant mixtures. ASHRAE Transactions 87:279–281
4. Mishra MP, Varma HK, Sharma CP (1981) Heat transfer coefficients in forced convection evaporation of refrigerants mixtures. Int J Heat Mass Transf 8:127–136
5. Singal LC, Sharma CP, Varma HK (1983) Experimental heat transfer coefficient for binary refrigerant mixtures of R13 and R12. ASHRAE Transact 2747:175–188
6. Kruse H, Hesse U (1988) Possible substitutes for fully halogenated clorofluorocarbons using fluids already marketed. Int J Refrig 11:276–283
7. Kuijpers LJM, de Wit JA, Janssen MJP (1988) Possibilities for the replacement of CFC12 in domestic equipment. Int J Refrig 11:284–291
8. Jung DS, McLinden M, Radermachert R, Didion D (1989) A study of flow boiling heat transfer with refrigerant mixtures. Int J Heat Mass Transf 32:1751–1764
9. Koyama S, Miyara A, Takamatsu H, Fujii T (1990) Condensation heat transfer of binary refrigerant mixtures of R22 and R114 inside a horizontal tube with internal spiral grooves. Int J Refrig 13:256–263
10. Kedzierski MA, Didion DA (1990) Visualization of nucleate flow boiling for an R22/R114 mixture and its components. Exp Heat Trans 3:447–463
11. Rivis E, Bidone A (1994) Isobutane/propane mixtures: comparison with traditional refrigerants. The Day After Conference. Padua, Italy
12. Kim MS, Mulroy WJ, Didion DA (1994) Performance evaluation of two azeotropic refrigerant mixtures of HFC-134a with R-290 (Propane) and R-600a (Isobutane). Trans ASME 148:148–154
13. Nozu S, Honda H, Nishida S (1995) Condensation of a zeotropic CFC114-CFC113 refrigerant mixture in the annulus of a double-tube coil with an enhanced inner tube. Exp Thermal Fluid Sci 11:364–371
14. Richardson R, Butterworth J (1995) The performance of propane/isobutane mixtures in vapor compression systems. Int J Refrig 18:58–62
15. Sami SM, Song B (1996) Heat transfer and pressure drop characteristics of hfc quaternary refrigerant mixtures inside horizontal enhanced surface tubing. Appl Therm Eng 16:461–473
16. Dongsoo J, Chong KB, Byoung LH, Hong LW (1996) Testing of a hydrocarbon mixture in domestic refrigerators, Symposia AT-96-19-3, ASHRAE Trans 1077–1084
17. Shin JY, Kim MS, Ro ST (1997) Experimental study on forced convective boiling heat transfer of pure refrigerants and refrigerant mixtures in a horizontal tube. Int J Refrig 20:267–275
18. Alsaad MA, Hammad MA (1998) The application of propane/butane mixture for domestic refrigerators. Appl Therm Eng 18:911–918
19. Shao DW, Granryd E (1998) Experimental and theoretical study on flow condensation with non-azeotropic refrigerant mixtures of R32/R134a. Int J Refrig 21:230–246
20. Baskin E (1998) Synopsis of residential refrigerator/freezer alternative refrigerants evaluation, ASHRAE Trans 266–273
21. Hammad MA, Alsaad MA (1999) The use of hydrocarbon mixtures as refrigerants in domestic refrigerators. Appl Therm Eng 19:1181–1189
22. Jung D, Kim CB, Song K, Park B (2000) Testing of propane/isobutane mixture in domestic refrigerators. Int J Refrig 23:517–527

23. Miyara A, Nonaka K, Taniguchi M (2000) Condensation heat transfer and flow pattern inside a herringbone-type micro-fin tube. Int J Refrig 23:141–152
24. Chang YS, Kim MS, Ro ST (2000) Performance and heat transfer characteristics of hydrocarbon refrigerants in a heat pump system. Int J Refrig 23:232–242
25. Choi TY, Kim YJ, Kim MS, Ro ST (2000) Evaporation heat transfer of R-32, R-134a, R-32/134a, and R-32/125/134a inside a horizontal smooth tube. Int J Heat Mass Transf 43:3651–3660
26. Tashtoush B, Tahat M, Shudeifat MA (2002) Experimental study of new refrigerant mixtures to replace R12 in domestic refrigerators. Appl Therm Eng 22:495–506
27. Akash BA, Said SA (2003) Assessment of LPG as a possible alternative to R-12 in domestic refrigerator. Energy Convers Manage 44:381–388
28. Wongwises S, Chimres N (2005) Experimental study of hydrocarbon mixtures to replace HFC-134a in a domestic refrigerator. Energy Convers Manage 46:85–100
29. Wen MY, Ho CY (2005) Evaporation heat transfer and pressure drop characteristics of R-290 (propane), R-600 (butane), and a mixture of R-290/R-600 in the three-lines serpentine small-tube bank. Appl Therm Eng 25:2921–2936
30. Koyama S, Takato N, Kuwahara K, Jin D, Xue J, Miyara A (2006) Experimental study on the performance of a refrigerant mixture CO2/DME system. Proceedings of JSRAE Annual Conference, JASRAE, pp 133–136
31. Wen MY, Ho CY, Hsieh JM (2006) Condensation heat transfer and pressure drop characteristics of R-290 (propane), R-600 (butane), and a mixture of R-290/R-600 in the serpentine small-tube bank. Appl Therm Eng 26:2045–2053
32. Han XH, Wang Q, Zhu ZW, Chen GM (2007) Cycle performance study on R32/R125/R161 as an alternative refrigerant to R407C. Appl Therm Eng 27:2559–2565
33. Park KJ, Seo T, Jung D (2007) Performance of alternative refrigerants for residential air-conditioning applications. Appl Energy 84:985–991
34. Afroz HMM, Miyara A, Tsubaki K (2008) Heat transfer coefficients and pressure drops during in-tube condensation of CO_2/DME mixture refrigerant. Int J Refrig 31:1458–1466
35. Xue J, Takata N, Ochiai A, Kuwahara K, Koyama S, Miyara A (2008) Experiments on performance evaluation of a heat pump system using CO2/DME mixture, Proceedings of JSRAE Annual Conference, JASRAE, E234-1–4
36. Chen J, Yu J (2008) Performance of a new refrigeration cycle using refrigerant mixture R32/R134a for residential air-conditioner applications. Energy Build 40:2022–2027
37. Lee MY, Lee DY, Kim Y (2008) Performance characteristics of a small-capacity directly cooled refrigerator using R290/R600a (55/45). Int J Refrig 31:734–741
38. Mani K, Selladurai V (2008) Experimental analysis of a new refrigerant mixture as drop-in replacement for CFC12 and HFC134a. Int J Therm Sci 47:1490–1495
39. Kim JH, Cho JM, Kim MS (2008) Cooling performance of several CO2/propane mixtures and glide matching with secondary heat transfer fluid. Int J Refrig 31:800–806
40. Wu J, Chu Y, Hu J, Liu Z (2009) Performance of mixture refrigerants R152a/125/R32 in domestic air-conditioner. Int J Refrig 32:1049–1057
41. Onaka Y, Miyara A, Tsubaki K (2010) Experimental study on evaporation heat transfer of CO_2/DME mixture refrigerant in a horizontal smooth tube. Int J Refrig 33:1277–1291
42. Park KJ, Jung D (2009) Performance of heat pumps charged with R170/R290 mixture. Appl Energy 86:2598–2603
43. Cho JM, Kim YJ, Kim MS (2010) Experimental studies on the characteristics of evaporative heat transfer and pressure drop of CO2/propane mixtures in horizontal and vertical smooth and micro-fin tubes. Int J Refrig 33:170–179
44. Zou X, Gong MQ, Chen GF, Sun ZH, Zhang Y, Wu JF (2010) Experimental study on saturated flow boiling heat transfer of R170/R290 mixtures in a horizontal tube. Int J Refrig 33:371–380
45. Dalkilic AS, Wongwises S (2010) A performance comparison of vapour compression refrigeration system using various alternative refrigerants. Int Commun Heat Mass Trans 37:1340–1349
46. Kabul A, Kızılkan Ö, Yakut AK (2010) Energy and exergy analysis of a refrigeration system with shell and tube heat exchanger using R404A Isı Bilimi ve Tekniği Dergisi. JThermal Sci Technol 30:85–93
47. Yoon WJ, HJ Chung KS, Lee EJ, Kim Y (2012) Performance optimization of a Lorenz-Meutzner cycle charged with hydrocarbon mixtures for a domestic refrigerator-freezer, International Journal of Refrigeration 35 36–46
48. Grauso S, Mastrullo R, Mauro AW, Vanoli GP (2011) CO_2 and propane blends Experiments and assessment of predictive methods for flow boiling in horizontal tubes. Intern J Refrig 34:1028–1039
49. Gnielinski V (1976) New equations for heat and mass transfer in turbulent pipe and channel flow. Intern Chem Eng 16:359–368
50. Dhir VK, Lienhard J (1971) Laminar film condensation on plan and axisymmetric bodies in non-uniform gravity. J Heat Transfer 93:97–100
51. Incropera FP, DeWitt DP (2002). Fundamentals of heat and mass transfer, John Wiley and Sons, 2002
52. Kern DQ (1950) Process heat transfer, McGraw-Hill
53. Kakac S (1996) Fundamentals and applications. Technical University of Istanbul, Heat exchanger design course
54. Shah RK (2003) D.P. Sekulic. Fundamentals of heat exchanger design, John Wiley & Sons
55. McLinden MO, Klein SA, Lemmon EW (1998) REFPROP, Thermodynamic and transport properties of refrigerants and refrigerant mixtures. NIST Standard Reference Database-version 6.01

Neural Network Based Analyses for the Determination of Evaporation Heat Transfer Characteristics During Downward Flow of R134a Inside a Vertical Smooth and Corrugated Tube

M. Balcilar, A. S. Dalkilic, K. Aroonrat & S. Wongwises

Arabian Journal for Science and Engineering

ISSN 1319-8025
Volume 39
Number 2

Arab J Sci Eng (2014) 39:1271-1290
DOI 10.1007/s13369-013-0659-1

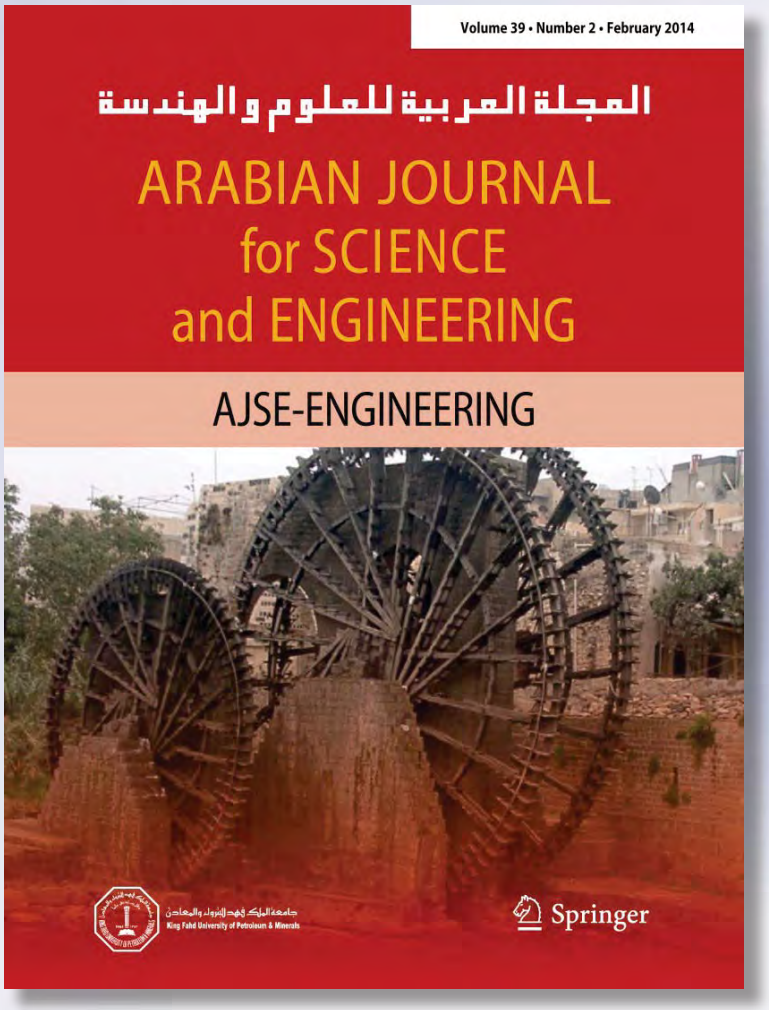

Springer

Arab J Sci Eng (2014) 39:1271–1290
DOI 10.1007/s13369-013-0659-1

RESEARCH ARTICLE - MECHANICAL ENGINEERING

Neural Network Based Analyses for the Determination of Evaporation Heat Transfer Characteristics During Downward Flow of R134a Inside a Vertical Smooth and Corrugated Tube

M. Balcilar · A. S. Dalkilic · K. Aroonrat · S. Wongwises

Received: 24 April 2011 / Accepted: 4 July 2013 / Published online: 5 September 2013

Abstract The heat transfer characteristics of the refrigerant HFC–134a are investigated, such as convective heat transfer coefficient and pressure drop during evaporation inside a vertical smooth and five pieces of corrugated tube, using experimental data with the aim of numerically determining the best artificial intelligence method. The double tube test sections are 0.5 m long with refrigerant flowing in the inner tube and heating water flowing in the annulus. Input of the ANNs are the 14 numbers of dimensional and dimensionless values of test section, such as mass flux, heat flux, temperature difference between the tube wall and saturation temperature, average vapour quality, evaporating temperature, two-phase friction factor, two-phase multiplier, liquid and vapour Reynolds numbers, Bond number, Froude number, Weber number, depth of corrugation and helix angle for the tested corrugated tubes, whereas the outputs of the ANNs are the experimental condensation heat transfer coefficient and measured pressure drop from the analysis. The evaporation heat transfer characteristics of R134a are modelled to decide the best approach, using several ANN methods such as multi layer perceptron (MLP) and radial basis networks (RBFN). The performance of the method of MLP with 10-5-1 architecture and RBFNs with the spread coefficient of 100,000 and a hidden layer neuron number of 200 were found to be in good agreement, predicting the evaporation heat transfer coefficient and pressure drop. Dependency of outputs of the ANNs from input values is investigated and new ANN-based heat transfer coefficient correlations are developed as a result of the analyses.

Keywords Evaporation · Boiling · Heat transfer coefficient · Pressure drop · Modeling · Neural network

M. Balcilar
Computer Engineering Department,
Yildiz Technical University, 34220 Davutpasa,
Esenler, Istanbul, Turkey

A. S. Dalkilic (✉)
Heat and Thermodynamics Division,
Department of Mechanical Engineering,
Yildiz Technical University, Yildiz,
Besiktas, Istanbul 34349, Turkey
e-mail: dalkilic@yildiz.edu.tr

K. Aroonrat · S. Wongwises (✉)
Fluid Mechanics, Thermal Engineering
and Multi phase Flow Research Lab. (FUTURE),
Department of Mechanical Engineering,
Faculty of Engineering, King Mongkut's
University of Technology Thonburi, Bangmod,
Bangkok 10140, Thailand
e-mail: somchai.won@kmutt.ac.th

الخلاصة

تم التحقيق في خصائص نقل الحرارة لمبرد HFC-134a، مثل معامل انتقال الحمل الحراري وانخفاض الضغط في أثناء التبخر داخل تمليس عمودي وخمس قطع من أنبوب مموج، وذلك باستخدام البيانات التجريبية بهدف تحديد ـ عدديا ـ أفضل طريقة ذكاء اصطناعي ، وكان طول أقسام أنبوب الاختبار المزدوج 0.5 م مع تدفق المبردات في الأنبوب الداخلي وتسخين المياه المتدفقة في الحلقة ، ومدخلات الشبكات العصبية الصناعية هي 14 رقما من قيم بعدية وغير بعدية لمقطع الاختبار للأنابيب المموجة التي تم اختبارها، مثل التدفق الشامل، والتدفق الحراري، والفرق في درجة الحرارة بين جدار الأنبوب ودرجة الحرارة التشبع، ومتوسط جودة البخار، ودرجة حرارة التبخير، ومعامل الاحتكاك ذي مرحلتين، والمضاعف ذي مرحلتين ، وأرقام رينولدز للسائل والبخار، وعدد بوند، وعدد فرويد، وعدد

وبير، وعمق التمويج وزاوية اللولب، في حين أن مخرجات الشبكات العصبية الصناعية هي معامل اننقال حرارة التكثيف التجريبي وهبوط الضغط المقاس من التحليل. وقد تمت نمذجة خصائص نقل حرارة التبخر ل R134a لتحديد أفضل نهج، وذلك باستخدام عدة أساليب ANN مثل مستقبلات الطبقة المتعددة (MLP) وشبكات القاعدة الشعاعية (RBFN)، ووجد أن أداء طريقة MLP مع هندسة معمارية 1-5-10 وRBFNs مع معامل انتشار خلايا عصبيه بمقدار 100،000 وعدد خلايا عصبية لطبقة مخفية مقداره 200 هو في اتفاق جيد، ويتوقع معامل انتقال حرارة التبخر وانخفاض الضغط ، وتم التحقيق في اعتمادية مخرجات الشبكات العصبية الصناعية على قيم الإدخال، وطورت معاملات ارتباط نقل حرارة جديدة على أساس ANN كنتيجة للتحليلات.

Abbreviations

A	Surface area, m^2
ANFIS	Adaptive neuro–fuzzy inference system
ANN	Artificial neural network
Bo	Bond number
CHF	Critical heat flux
c_p	Specific heat, J kg^{-1} K^{-1}
d	Internal tube diameter, m
E	Error
EHD	Electro hydrodynamic
f	Friction factor
Fr	Froude number
G	Mass flux, kg m^{-2} s^{-1}
GA	Genetic algorithm
GRNN	Generalized regression neural network
h	Heat transfer coefficient, W m^{-2} K^{-1}
HFC	Hydro fluorocarbons
I	Input
i	Enthalpy, J kg^{-1}
i_{fg}	Latent heat of condensation, J kg^{-1}
k	Thermal conductivity, W m^{-1} K^{-1}
L	Length of test tube, m
m	Mass flow rate, kg s^{-1}
MLP	Multi-layer perception
N	Element number
N_i^j	ith Neuron of jth hidden layer
O	Output
P	Pressure, N m^{-2}
ΔP	Pressure drop, N m^{-2}
R	Refrigerant
Re	Reynolds number
RBFN	Radial basis networks
S	Slip ratio
sp	Spread coefficient
Q	Heat transfer rate, W
q	Heat flux, kW m^{-2}
T	Temperature, °C
ΔT	Temperature difference, K
x	Average vapor quality
X_{tt}	Lockhart–Martinelli parameter
We	Weber number

Greek Symbols

φ_l^2	Two-phase multiplier
α	Void fraction
ρ	Density, kg m^{-3}
μ	Dynamic viscosity, kg m^{-1} s^{-1}
σ	Surface tension, N m^{-1}

Subscripts

avg	Average
calc	Calculated
eq	Equivalent
exp	Experimental
F	Frictional term
g	Gas/vapor
G	Gravitational term
i	Number of test data
in	Inlet
l	Liquid
M	Momentum term
ph	Preheater
o	Outlet
ref	Refrigerant
sat	Saturation
TS	Test section
tp	Two-phase
w	Water
wi	Wall inside

1 Introduction

The thermal performance of heat transfer equipment can be improved using heat transfer enhancement techniques. The rough surface technique is one of them that usually involves surface modification to promote turbulent flow and increases the heat transfer surface area. Normally, smooth tubes are replaced by corrugated tubes in many heat exchangers to increase the heat transfer rate by mixing and also limiting the fluid boundary layers close to the heat transfer surfaces. Moreover, they can promote two-phase heat transfer enhancement. Some of works regarding the heat transfer and flow characteristics of corrugated tubes are summarised below.

Nozu et al. [1,2] investigated local heat transfer and pressure gradients in pure R-114, R-113 and a zeotropic refrigerant mixture during condensation in a tube-in-tube heat exchanger. The results showed that the frictional pressure gradient data and measured heat transfer data were approximately 11 and 13 %, respectively. Dong et al. [3] investigated turbulent friction and heat transfer characteristics of four spirally corrugated tubes with various geometrical parameters. Water and oil were used as the working fluid. Their results

showed that the heat transfer coefficient enhancement varied from 30 to 120 %, while the friction factor increased from 60 to 160 % when compared with a smooth tube. One of most productive studies has been performed by Zimparov [4]. The heat transfer enhancement of a combination of three-start spirally corrugated tubes with a twisted tape was investigated. Two three-start spirally corrugated tubes combined with five twisted tape inserts with different relative pitches were employed as the test section. The results showed that the friction factor and heat transfer coefficients of three-start spirally corrugated tubes with a twisted tape were significantly higher than those of a smooth tube under the same operating conditions. Zimparov [5] presented the heat transfer enhancement using a combination of single-start spirally corrugated tubes with a twisted tape. The friction factors and inside heat transfer coefficients obtained from these tubes were higher than those obtained from the smooth tube under the same conditions. In addition, Zimparov [6,7] applied a simple mathematical model to predict the friction factors and heat transfer coefficients in a spirally corrugated configuration combined with twisted tape inserts flowing in the turbulent flow regime. The calculated friction factors and heat transfer coefficients were compared with the experimental data. The results showed that the agreement between the predicted and experimental data was fairly good.

Existing numerical studies on the subject of in-tube evaporation and boiling in the literature are summarised briefly in the following paragraphs.

Nafey [8] proposed a new method using artificial neural networks (ANN) to predict the critical heat flux (CHF) for a steam–water mixture flowing in pipes. The testing processes is performed by means of a large volume of experimental data. The algorithm of Levenberg–Marquardt was used in the analysis of ANN. Accuracy of the validation was good and a new correlation was proposed to determine the CHF. Wang et al. [9] developed a generalised neural network correlation for boiling heat transfer coefficient of R22 and its alternative refrigerants R134a, R407C and R410A, inside horizontal smooth tubes. The input of the neural network analysis was selected from four kinds of dimensionless parameter groups while the Nusselt number was used as the output. As a result of the analysis, the input parameter group based on the Gungor–Winterton correlation was found to be better than the other three groups. Scalabrin et al. [10] investigated the flow boiling inside horizontal smooth tubes for mixtures and proposed a new modelling method based on ANN for heat transfer. They extended their former study [11], which was about the same topic using pure fluids in smooth tubes, to mixtures. Their new numerical method was stated to be better than the conventional methods with regard to its accuracy. Wongwises and Disawas [12] experimentally investigated the two-phase heat transfer coefficient characteristics of HFC-134a evaporating under forced flow conditions inside a smooth horizontal tube. Different from most previous studies, the present experiments have been performed with lubricating oil in the refrigerant loop at high flow rate and high heat flux conditions. The effects of heat flux, mass flux, evaporation pressure and lubricating oil on the convection heat transfer coefficients were discussed. Sripattrapan and Wongwises [13] presented the results of simulations using a two-phase separated flow model to study the heat transfer and flow characteristics of refrigerants during evaporation in a horizontal tube. A one-dimensional annular flow model of the evaporation of refrigerants under constant heat flux was developed. Their proposed model is used to predict the variation of the temperature, heat transfer coefficient and pressure drop of various pure refrigerants flowing along a horizontal tube. Wongwises and Polsongkram [14] investigated the two-phase heat transfer coefficient and pressure drop of HFC-134a during evaporation inside a smooth, helically coiled concentric tube-in-tube heat exchanger. New correlations for the convection heat transfer coefficient and pressure drop were proposed for practical applications. Kaew-On and Wongwises [15] investigated the evaporation heat transfer coefficient and pressure drop of R-410A flowing through a horizontal aluminium rectangular multiport mini-channel of 3.48 mm hydraulic diameter. Their analysis showed that the average heat transfer coefficient of R-410A during evaporation tended to increase with increasing average quality, mass flux and heat flux, but tended to decrease with increasing saturation temperature. The pressure drop increased with increasing the mass flux, but decreased with increasing the saturation temperature, and the heat flux has no significant effect on the pressure drop. Posew et al. [16] investigated the heat transfer enhancement using the electrohydrodynamic (EHD) technique during evaporation inside horizontal smooth and micro-fin tubes. The test section was a counter-flow concentric tube-in-tube heat exchanger with R-134a flowing inside the inner tube and heating water flowing in the annulus. The maximum heat transfer enhancement ratios were 1.25 and 1.15 for smooth tube and micro-fin tube, respectively. Laohalertdecha and Wongwises [17] investigated the effects of corrugation pitch on the evaporation of R-134a flowing inside horizontal corrugated tubes. The effects of average vapour quality, equivalent Reynolds number and corrugation pitch were discussed. Differently from most previous studies, Aroonrat and Wongwises [18] studied the heat transfer and friction characteristics of the pure refrigerant HFC-134a during evaporation inside a vertical corrugated tube. The effects of heat flux, mass flux and evaporation temperature on the heat transfer coefficient and two-phase friction factor were also discussed. It is found that the percentage increases of the heat transfer coefficient and the two-phase friction factor of the corrugated tubes compared with those of the smooth tube were approximately 0–10 and 70–140 %, respectively. Balcilar et al. [19] investigated the best artificial intelligence method

to estimate the measured convective heat transfer coefficient and pressure drop of R134a flowing downward inside a vertical smooth copper tube using several ANN methods, such as multi layer perceptron (MLP), radial basis networks (RBFN), generalised regression neural network (GRNN) and adaptive neuro-fuzzy inference system (ANFIS). Colorado et al. [20] developed a physical–empirical model to investigate heat transfer of helical coil in oil and glycerol/water solution. They benefited from an artificial neural network (ANN) model working with equations of continuity, momentum and energy in each flow to have a reliable the natural convection heat transfer correlations. As a result of their analyses, it was found that saving time and improving general system performance were achieved using ANN.

Despite worthwhile experimental studies in the literature, relatively little information is currently available on numerical work such as ANN analysis on the evaporation heat transfer and flow characteristics in smooth and corrugated tubes. As mentioned previously, it is evident that the corrugated tubes have greater heat transfer potential than smooth tubes. As a consequence, in the present study the main concern is to fill this gap in the literature. The results for the solution of neural network analysis on the evaporation two-phase heat transfer coefficient and pressure drop, which have never before appeared in open literature, are presented. The large amount of measured data obtained from the experimental study regarding the convective heat transfer coefficient and pressure drop are compared with the results from ANN methods such as MLP and RBFN. In addition to this, the effect of input parameters (mass flux, heat flux, the temperature difference between the tube wall and saturation temperature, average vapour quality, evaporating temperature, two-phase friction factor, two-phase multiplier, liquid and vapour Reynolds numbers, Bond number, Froude number, Weber number, depth of corrugation and helix angle for the tested corrugated tubes) on the output parameters (convective heat transfer coefficient (h), pressure drop (ΔP)) is shown and discussed as a primary study on this subject in the literature. Moreover, correlation development study is performed to calculate the evaporation heat transfer coefficient using the most effective input parameters and the measured pressure drop values.

2 Experimental Apparatus and Method

A schematic diagram of the test apparatus is shown in Fig. 1. The refrigerant loop consists of a pre-heating loop, test sec-

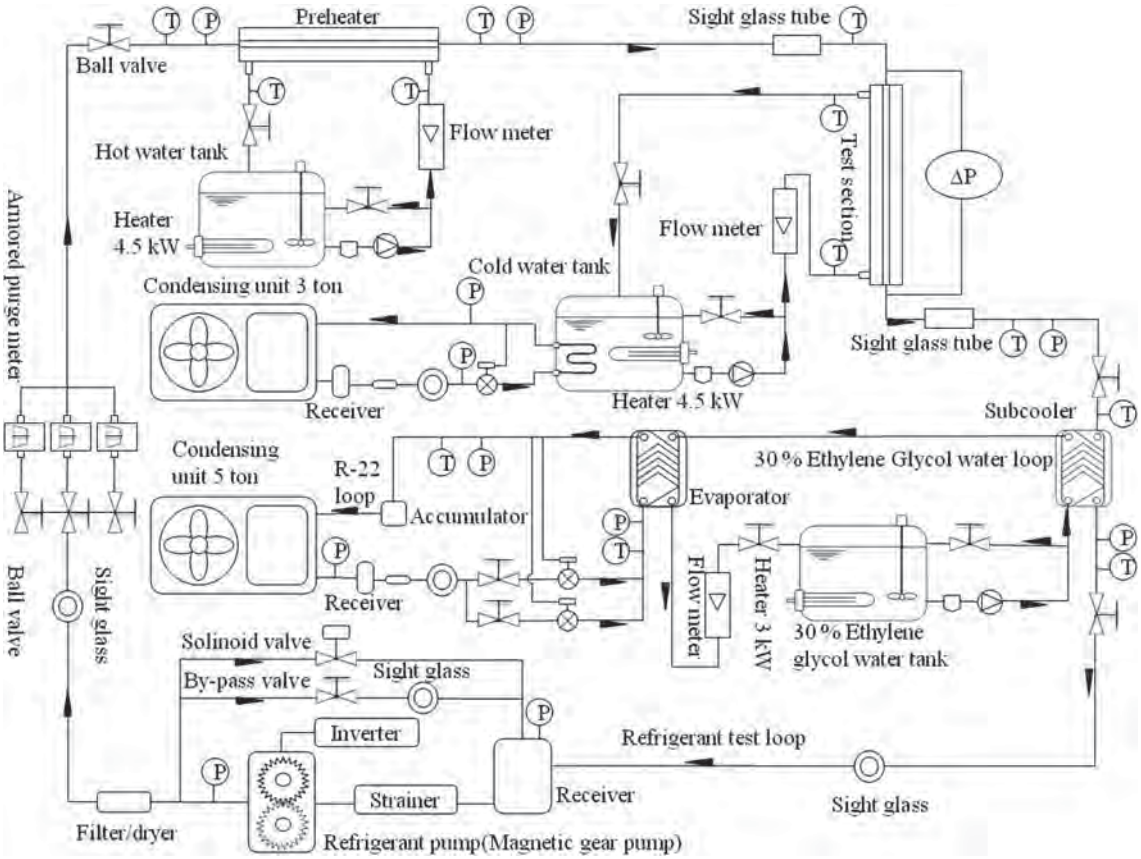

Fig. 1 Schematic diagram of experimental apparatus (from Aroonrat and Wongwises [18], with permission from Elsevier)

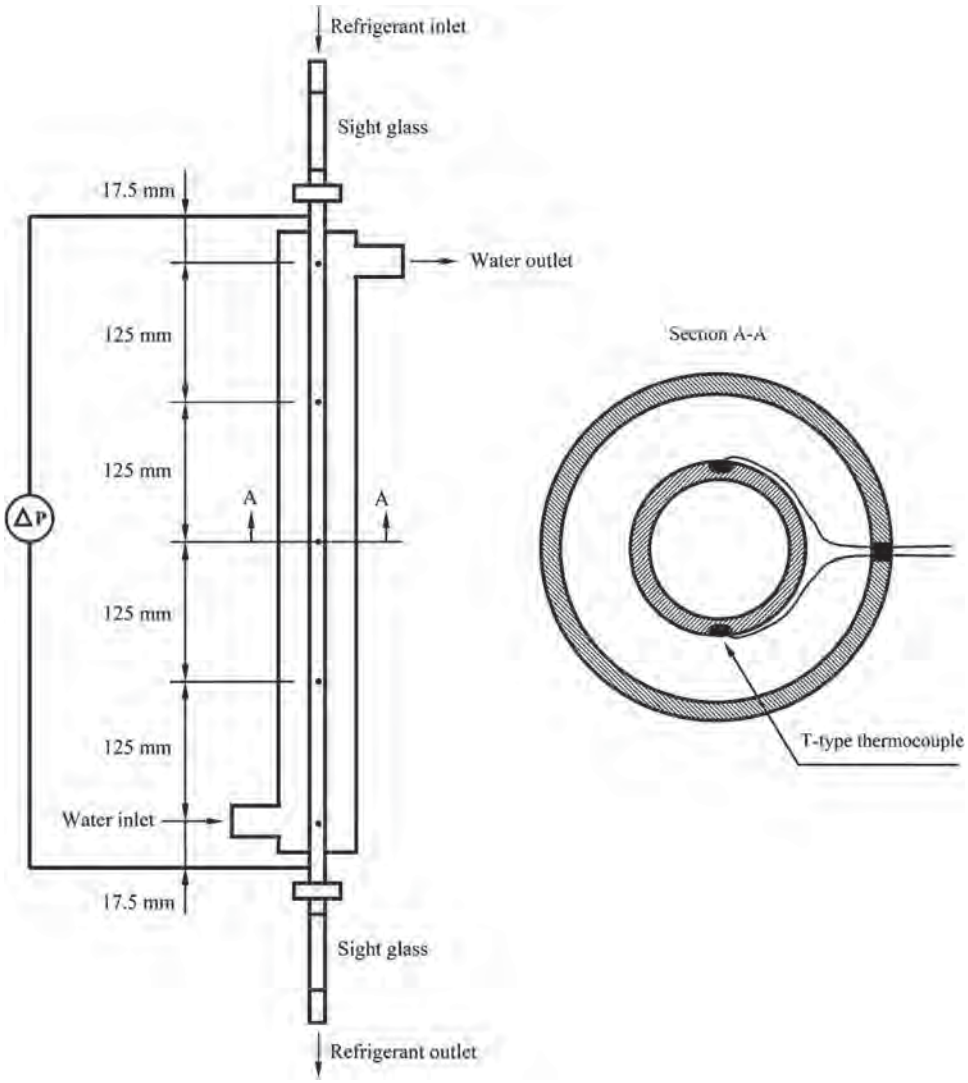

Fig. 2 Schematic diagram of the test section (from Aroonrat and Wongwises [18], with permission from Elsevier)

tion, heating loop and chilling loop. For the refrigerant circulating loop, liquid refrigerant is forced by a gear pump which can be adjusted to the flow rate using an inverter. The refrigerant then passes in series through a filter/dryer, a refrigerant flow meter, a pre-heater, and a sight glass and enters the test section. The pre-heater controls the inlet quality before entering the test section. It consists of a spiral counter-flow tube-in-tube heat exchanger which is designed to supply heat to prepare an inlet quality for the vaporization of the refrigerant. Leaving the test section, the refrigerant vapour then condenses inside a sub-cooler and is collected in a receiver. After leaving the chilling loop, the refrigerant returns from a two-phase refrigerant to a sub-cooled state. Eventually, the refrigerant returns to the refrigerant pump to complete the cycle.

Details of the test section are shown schematically in Fig. 2. The test section is a vertical counter-flow double tube heat exchanger with refrigerant flowing downward in the inner tube and heating water flowing upward in the annulus. The test sections are one smooth tube and five corrugated tubes, which are made from copper. The inner diameter and outer diameter of the inner tube are 8.7 and 9.52 mm, respectively. The length of the test section is 500 mm. Figure 3 shows a sketch and a photograph of a corrugated tube. The dimensions of the test section and the range of experimental conditions tested are listed in Tables 1 and 2, respectively. T-type thermocouples are installed at the inlet and outlet of the test section to measure the saturation temperature of the refrigerant. Similarly, the differential pressure transducer is installed to measure the pressure drop across the test section. The length between the pressure taps is 850 mm. There are 10 thermocouples located at five positions along the test section. All of the wall thermocouples are fixed with special glue having low thermal conductivity. The test section is insulated with rubber foam with a thermal conductivity of 0.04 W/mK. All of the thermocouples are well calibrated by standard thermometers with a precision of 0.1 °C. The refrigerant flow meter is a variable area type

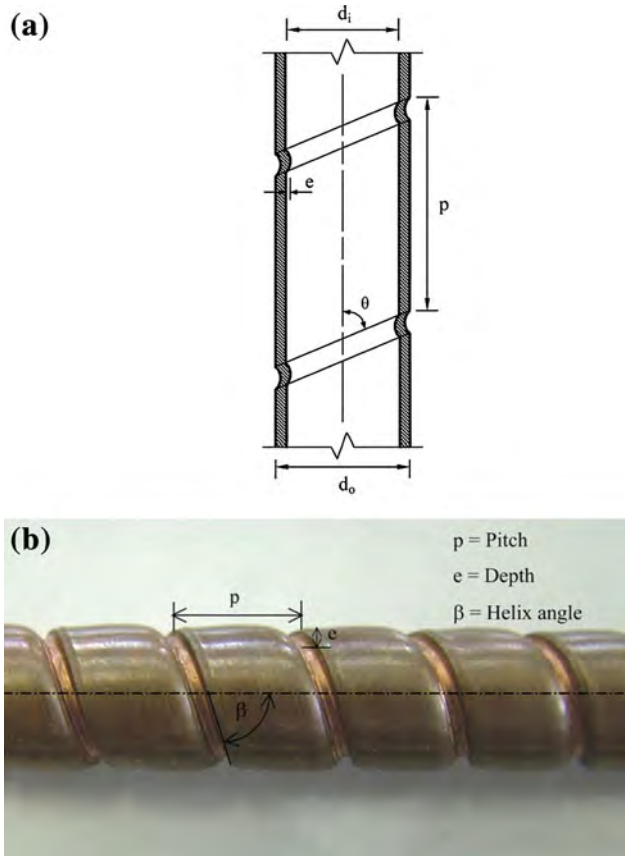

Fig. 3 Sketch (**a**) and photograph (**b**) of helically corrugated tube (from Aroonrat and Wongwises [18], with permission from Elsevier)

and is specially calibrated in the range of 0.2–3.4 LPM for R-134a by the manufacturer, as is the differential pressure transducer.

In the experiments, the inlet quality of the test section is varied by small increments. The imposed heat flux, mass flux and saturation temperature are kept constantly at the desired values. The system is allowed to approach a steady state before any data are recorded. During experiments, the temperature and pressure are continuously recorded along the test section by the data acquisition system. The uncertainties of measured quantities and calculated parameters, which are calculated from the root mean sum square method, are shown in Table 3.

3 Data Reduction and Experimental Uncertainty

The data reduction of the measured results can be analysed as follows:

3.1 The Inlet Vapour Quality of the Test Section ($X_{TS,in}$)

$$X_{TS,in} = \frac{i_{TS,in} - i_{l@T_{TS,in}}}{i_{fg@T_{TS,in}}}, \tag{1}$$

where $i_{l@T_{TS,in}}$ is the enthalpy of the saturated liquid based on the temperature of the test section inlet, $i_{fg@T_{TS,in}}$ is the enthalpy of vaporisation based on the temperature of the test section inlet, $i_{TS,in}$ is the refrigerant enthalpy at the test section inlet and is given by

$$i_{TS,in} = i_{ph,in} + \frac{Q_{ph}}{m_{ref}}, \tag{2}$$

where $i_{ph,in}$ is the inlet enthalpy of the liquid refrigerant before entering the pre-heater, m_{ref} is the mass flow rate of the refrigerant and Q_{ph} is the heat transfer rate in the pre-heater:

$$Q_{ph} = m_{w,ph} c_{p,w} (T_{w,in} - T_{w,o})_{ph}, \tag{3}$$

where $m_{w,ph}$ is the mass flow rate of the water entering the preheater, $c_{p,w}$ is the specific heat of water and $(T_{w,in} - T_{w,o})_{ph}$ is the temperature difference between inlet and outlet positions of the preheater.

3.2 The Outlet Vapour Quality of the Test Section ($X_{TS,o}$)

$$X_{TS,o} = \frac{i_{TS,o} - i_{l@T_{TS,o}}}{i_{fg@T_{TS,o}}}, \tag{4}$$

where $i_{TS,o}$ is the refrigerant enthalpy at the test section outlet, $i_{l@T_{TS,o}}$ is the enthalpy of the saturated liquid based on

Table 1 The dimensions of the test sections

Parameters	Smooth tube	Corrugated tube (A)	Corrugated tube (B)	Corrugated tube (C)	Corrugated tube (D)	Corrugated tube (E)
Outer diameter (mm)	9.52	9.52	9.52	9.52	9.52	9.52
Inner diameter (mm)	8.7	8.7	8.7	8.7	8.7	8.7
Length of test section (mm)	500	500	500	500	500	500
Inside tube area (mm^2)	13,665.9	14,514	14,938.1	15,362.1	15,951.4	16,582.8
Pitch of corrugation (mm)	–	12.7	12.7	12.7	8.46	6.35
Depth of corrugation (mm)	–	0.5	0.75	1	1	1
Helix angle (°)	–	53.875	53.875	53.875	64.07	69.95

Table 2 Experimental conditions

Controlled variable	Range
Refrigerant	R134a
Test tube material	Copper
Evaporating pressure, P_{sat}(bar)	4.14, 4.88, 5.71
Evaporating temperature, T_{sat} (°C)	10, 15, 20
Mass flux, G (kg m^{-2} s^{-1})	200, 300, 400
Heat flux, q (kW m^{-2})	19.91–30.64
Temperature difference, $\Delta T = T_{wi} - T_{sat}$, K	4.27–8.01
Average vapor quality, x	0.14–0.86

Table 3 Uncertainties of measured quantities and calculated parameters

Parameter	Uncertainty
Temperature, (T °C)	±0.1
Pressure drop, ΔP (kPa)	±0.37
Mass flow rate of refrigerant, m_{ref} (%)	±2 Full scale
Heat transfer rate of test section, Q_{TS} (%)	±15.01
Heat transfer rate of pre-heater, Q_{ph} (%)	±10.04
Average heat transfer coefficient, h_{exp} (%)	±15.01
Two-phase friction factor, f_{tp} (%)	±13.52
Average quality, x (%)	±7.63
Equivalent Reynolds number, Re_{eq} (%)	±6.03

the temperature of the test section outlet, and $i_{fg@T_{TS,o}}$ is the enthalpy of vaporisation. The outlet enthalpy of the refrigerant flow is calculated as follows:

$$i_{TS,o} = i_{TS,in} + \frac{Q_{TS}}{m_{ref}}, \tag{5}$$

where the heat transfer rate, Q_{TS}, in the test section is obtained from

$$Q_{TS} = m_{w,TS} c_{p,w} (T_{w,in} - T_{w,o})_{TS}, \tag{6}$$

where $m_{w,TS}$ is the mass flow rate of the water entering the test section, and $(T_{w,in} - T_{w,o})_{TS}$ is temperature difference between the outlet and inlet position of the test section.

3.3 The Average Heat Transfer Coefficient

$$h_{exp} = \frac{Q_{TS}}{A_{wi}(T_{wi} - T_{ref,sat})} \tag{7}$$

where h_{exp} is the experimental average heat transfer coefficient, Q_{TS} is the heat transfer rate in the test section, T_{wi} is the average temperature of the inner wall, $T_{ref,sat}$ is the average temperature of the refrigerant at the test section inlet and outlet, and A_{wi} is the inside surface area of the test section:

$$A_{wi} = \pi \mathrm{dL} \tag{8}$$

where d is the inside diameter of the test tube, and L is the length of the test tube.

3.4 Calculation Procedure for the Generalised Artificial Neural Networks (ANNs) Model

An ANN is an information-processing system that has certain performance characteristics in common with biological neural networks. ANNs have been developed as generalisations of mathematical models of human cognition or neural biology, based on the assumptions that (1) information processing occurs at many simple elements called neurons, (2) signals are passed between neurons over connection links, (3) each connection link has an associated weight, which, in a typical neural net multiplies the signal transmitted, and (4) each neuron applies an activation function (usually non-linear) to its net input (sum of weighted input signals) to determine its output signal [21].

ANNs are such factors that can utilize machine learning for the duty of considered necessary mapping of the inputs to the outputs. A dataset is divided into three parts such as training, testing and validation. ANNs determine a function between the inputs and outputs generalizing the training group. The success of this group is calculated using the test group. The training duration of ANNs is determined by the validation group. When the training group has over fitting as a result of long time training, ANNs memorize the training group and its success on the test group reduces. The optimum point for the stop of training is determined using validation group.

As the ANNs are one of the most commonly used and developed models to investigate the relationship between linear or non-linear input–output patterns, they try to generalise the training group and then estimate the test group. Performance of ANNs is measured by the success of the prediction. There are many described ANN types and their architectures (different size of layers, neuron numbers and spread coefficients) related to function approximation in the literature. The most known methods are multi layer perceptron (MLP), radial basis functions networks (RBFN), generalised regression neural networks (GRNN) and artificial neural fuzzy inference system (ANFIS) which is the combination of fuzzy logic decision systems and ANNs. Schematic diagrams of artificial intelligence models used in the analysis, obtained by Matlab software [22], are shown in Fig. 4.

3.4.1 Multi Layer Perceptron (MLP)

An artificial neuron performs the duty of taking weighted total of the inputs and evaluates it by an activation function. The single-layer perceptron is used for the linear problems and cannot be applied for the non-linear in nature. All perceptrons of MLP are arranged in an orderly manner of layers.

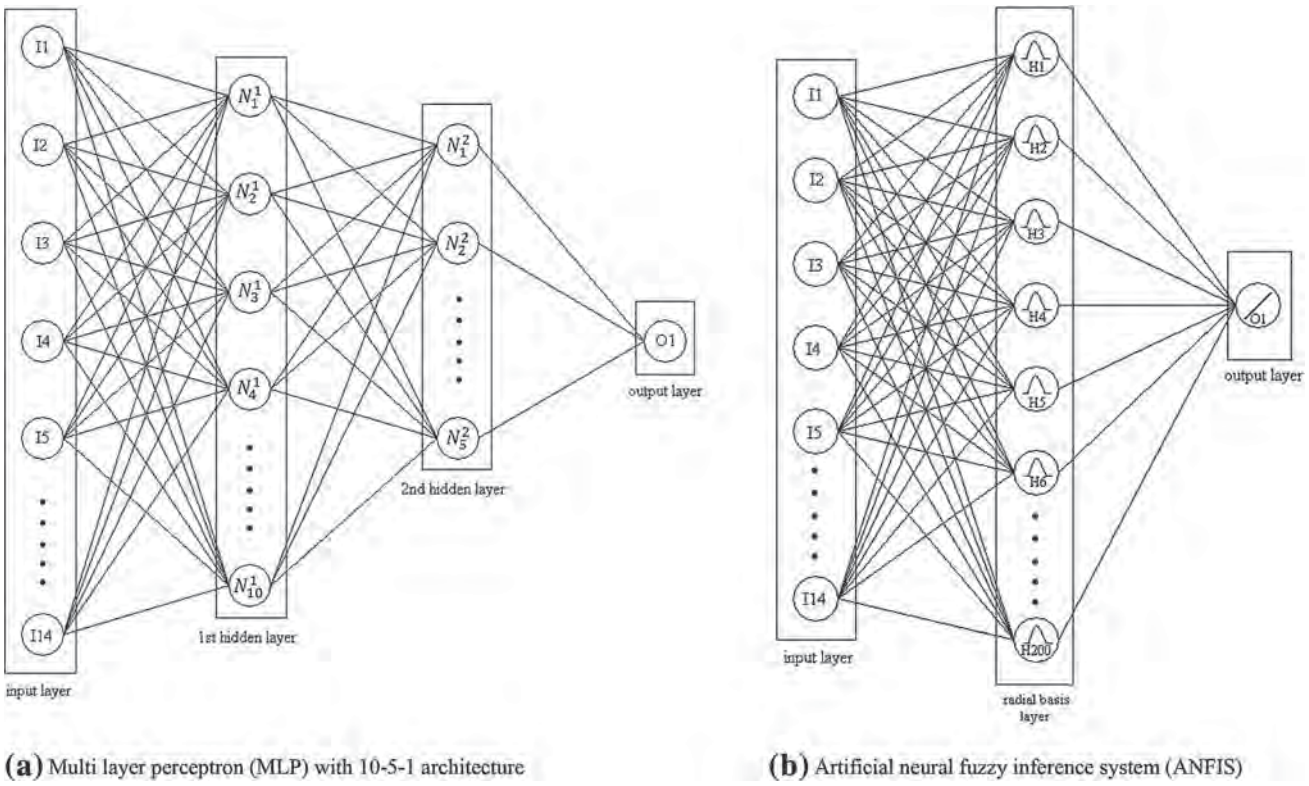

Fig. 4 Schematic diagrams of artificial intelligence models used in the analysis

The initial layer is the input layer and is called as passive layer. It should be noted that the inputs are passed to the next layer for processing after the first one. The output layer forms the last layer and is called as the active layer. These neurons take the inputs in the structure of neural connections among the neurons. Each connection has a weight connected with it. The computation of the weighted average of the input and its application to the activation function are performed by each neuron.

MLP is the member of the feed-forward network family. According to this method, the number of input and output neurons is equal to the number of input and output parameters, and there are some layers including neurons between them. Specification of non-linearity and calculation process increases with increasing numbers of hidden layers and neurons. Different architectures of MLP were used for the calculation of heat transfer coefficient and pressure drop. All neurons of MLP are connected with another neurons in the next layer making massive number of connections between the various connections and the direction of these connections are forward which means that the way of the connection among neurons is not recurrent. A Levenberg–Marquardt algorithm, based on the method of back propagation, was used for the training process to model the outputs using inputs of the problem.

3.4.2 Radial Basis Function Networks (RBFN)

This model has a simple 3-layer ANN architecture: input layer, hidden layer and output layer.

RBFN architecture has a single hidden layer and some similarities with the MLP method. On the other hand, it has a different calculation process for the determination of the neuron number, different activation function including Gaussian or exponential manner and difference in neuron number in the hidden layer. RBFN's single-layer architecture has equal neuron numbers with the element numbers in the training group. Bias numbers are the control parameters of RBFN architecture and should be determined by the user as trial and error method during calculations in Matlab Software [22]. Training of this architecture, in other words, values of neuron connections, are calculated using training group by means of least square method [22] as its training algorithm.

3.5 Correlation Development

Determination of heat transfer characteristics of compact systems such as heat transfer coefficient, frictional pressure drop, flow type between the fluids and heat transfer surface area in heat exchangers should be determined accurately for the optimum design. The two-phase heat trans-

fer systems have a higher thermal heat transfer performance than single-phase heat transfer systems in limited apparatus volumes. The advantage of high thermal performance in comparison with the single-phase applications includes smaller, more compact systems regarding tube length, tube diameter and internal tube geometry shape in a wide variety of applications, e.g. refrigeration and air conditioning systems, power engineering and other thermal processing plants. Before doing any numerical work on this subject, the validation process of the experimental setup and data is very significant with regard to the reliability of the study. The correctness of experimental data should be evaluated by either graphics regarding the characteristics of trend lines such as alteration of heat transfer coefficient versus quality, heat flux versus temperature difference between the vapour and inlet wall temperature, pressure drop versus vapour quality etc., or by widely accepted correlations in the literature, and desired working conditions should be agreeable with the heat balance correlations and flow type observations by means of sight glasses at the different points of the experimental apparatus.

There have been a number of studies on the in-tube evaporation heat transfer coefficient and pressure drop. The frictional, acceleration and gravitational components determine the two-phase total pressure drop in tubes. Determination of the void fraction is required to compute the acceleration and gravitational components, and in a similar way the determination of either the two-phase friction factor or the two-phase frictional multiplier is required to compute the frictional component of the pressure drop. Generally, empirical methods have been used to compute the evaporation heat transfer coefficients and pressure drops in tubes.

The correlation for the laminar and turbulent flow inside the test tube was developed as a form of Dittus and Boelter's [23] correlation in Eq. (9) by means of several dimensionless numbers which were defined in the following section. As a result, Eq. (9) is formed to predict the convective condensation heat transfer coefficient in terms of the above explanations as follows:

$$h = A\left(\frac{k_l}{d}\right)(\mathrm{Re}_g)^B(f_{\mathrm{tp}})^C(\mathrm{Fr})^D(x)^E(\mathrm{Bo})^F(\Delta \mathrm{T}_{\mathrm{sat}})^G(\phi_l^2)^H \times(\mathrm{We})^I\left(\Delta P\frac{L}{P}\right)^J(\mathrm{Re}_l)^K \quad (9)$$

3.6 Definition of Input Parameters of the Artificial Neural Network (ANN) Analysis

The total pressure gradient is the sum of three contributions: the gravitational pressure gradient, the momentum pressure gradient and the frictional pressure gradient as follows:

Table 4 Elimination of ANN methods belonging to all the tested tubes according to the error rates for pressure drop (a) and convective heat transfer coefficients (b) for the mass fluxes of 200, 300, 400 kg m^{-2} s^{-1} and T_{sat} = 10, 15 and 20 °C.

ΔP L^{-1} (kPa m^{-1})	Error analysis /ANN methods		Square law
	R square	Proportional (%)	
(a)			
MLP 10-5-1	0.999993	0.001677	0.043752
MLP 10-1	0.999988	0.012214	0.754229
MLP 5-1	0.999991	0.006793	0.22766
MLP 2-1	0.998872	0.054519	10.9036
RBF 1,000	0.029942	5.06416	66761.6
RBF 10,000	0.723309	3.712494	35227.66
RBF 100,000	0.980169	0.370425	502.1212
RBF 1,000,000	0.976075	0.462784	647.2979
RBF 1,000,000	0.905844	2.537781	14,664
(b)			
MLP 10-5-1	0.9999996	0.358	0.000198
MLP 10-1	0.999993	0.438	0.000316
MLP 5-1	0.999998	0.561	0.000259
MLP 2-1	0.999905	5.685	0.030739
RBF 1,000	0.447754	682.017	1,927.148
RBF 10,000	0.731676	59.682	8.71043
RBF 100,000	0.995606	18.519	0.538876
RBF 1,000,000	0.994327	22.937	0.649612
RBF 1,000,000	0.871393	98.393	2.556523

$$\frac{d\mathrm{P}}{dz} = \left(\frac{d\mathrm{P}}{dz}\right)_G + \left(\frac{d\mathrm{P}}{dz}\right)_M + \left(\frac{d\mathrm{P}}{dz}\right)_F \quad (10)$$

Pressure drop due to gravity can be determined from

$$(\Delta P)_G = -g\left(\alpha\rho_g + (1-\alpha)\rho_l\right)L \quad (11)$$

where the void fraction, a, can be determined from the Zivi correlation [24] stated below:

$$\alpha = \frac{1}{1+\left(\frac{1-x}{x}\right)\left(\frac{\rho_g}{\rho_l}\right)S} \quad (12)$$

$$S = \left(1 - x + x\frac{\rho_l}{\rho_g}\right)^{1/2} \quad (13)$$

The momentum pressure gradient can be defined as follows:

$$\left(\frac{d\mathrm{P}}{dz}\right)_M = -G^2\frac{d}{dz}\left[\frac{x^2}{\rho_g\alpha} + \frac{(1-x)^2}{\rho_l(1-\alpha)}\right] \quad (14)$$

The two-phase frictional pressure gradient can be obtained by subtracting the gravitational and momentum terms from the total measured pressure drop as follows:

Table 5 The most predictive input parameters according to the error rates for all tested tubes

Inputs														Input number	Outputs	
I	II	III	IV	V	VI	VII	VIII	IX	X	XI	XII	XIII	XIV		R^2–ΔP (%)	R^2–h (%)
0	0	0	0	0	0	0	0	0	0	0	0	1	0	1	0.614656	0.619369
0	0	0	0	0	0	0	0	0	1	0	0	0	0	1	0.606841	0.643204
0	0	0	0	0	0	0	0	0	0	0	1	0	0	1	0.561001	0.556516
1	0	0	0	0	0	0	0	0	0	0	0	0	0	1	0.271441	0.289444
0	0	0	0	1	0	0	0	0	0	0	0	0	0	1	0.219961	0.128164
0	0	0	0	0	1	0	0	0	0	0	0	0	0	1	0.215296	0.134689
0	1	0	0	0	0	0	0	0	0	0	0	0	0	1	0.178929	0.209764
0	0	0	0	0	0	0	0	0	0	1	0	0	0	1	0.124609	0.145161
0	0	1	0	0	0	0	0	0	0	0	0	0	0	1	0.080089	0.191844
0	0	0	1	0	0	0	0	0	0	0	0	0	0	1	0.038416	0.148225
0	0	0	0	0	0	1	0	0	0	0	0	0	0	1	0.000289	0.008649
0	0	0	0	0	0	0	0	1	0	0	0	0	0	1	0.0036	0.000961
0	0	0	0	0	0	0	0	0	0	0	0	0	1	1	0.088209	0.020736
0	0	0	0	0	0	0	1	0	0	0	0	0	0	1	0.093636	0.053824

Table 6 The most predictive combinations of input parameters according to the error rates for the two known input parameters

Inputs														Input number	Outputs	
I	II	III	IV	V	VI	VII	VIII	IX	X	XI	XII	XIII	XIV		R^2–ΔP (%)	R^2–h (%)
0	0	0	0	0	0	1	0	0	1	0	0	0	0	2	0.970225	0.863041
0	0	0	0	0	0	1	0	0	0	0	1	0	1	2	0.929296	0.748225
0	0	0	0	0	1	0	0	0	0	0	0	1	0	2	0.915849	0.8836
0	0	0	0	1	0	0	0	0	0	0	0	1	0	2	0.913936	0.799236
0	0	0	0	0	1	0	0	0	1	0	0	0	0	2	0.893025	0.876096
0	0	0	0	1	0	0	0	0	1	0	0	0	0	2	0.891136	0.776161
0	0	0	1	0	0	0	0	0	0	0	0	0	1	2	0.874225	0.9999
0	0	0	0	0	1	0	0	0	0	0	1	0	0	2	0.872356	0.801025
0	0	0	0	0	0	1	0	0	0	0	0	1	0	2	0.870489	0.802816
0	0	0	0	0	0	0	1	0	0	0	0	0	1	2	0.848241	0.986049
0	0	0	0	1	0	0	0	0	0	0	1	0	0	2	0.8464	0.710649
0	0	0	0	0	0	0	0	0	1	0	0	0	1	2	0.817216	0.933156
0	0	0	0	0	0	0	0	0	0	0	0	1	1	2	0.762129	0.948676
0	0	0	0	0	0	0	0	0	0	0	1	0	1	2	0.677329	0.877969
1	0	0	0	0	0	0	0	0	0	0	0	0	1	2	0.6724	0.7744
0	0	0	0	0	0	0	0	0	0	1	0	0	1	2	0.627264	0.727609
0	0	0	0	0	0	0	0	1	0	0	0	1	0	2	0.616225	0.664225
0	0	0	0	0	1	1	0	0	0	0	0	0	0	2	0.611524	0.64

$$\left(\frac{d\mathrm{P}}{dz}\right)_F = \left(\frac{d\mathrm{P}}{dz}\right)_{\mathrm{Exp}} - \left(\frac{d\mathrm{P}}{dz}\right)_G - \left(\frac{d\mathrm{P}}{dz}\right)_M \tag{15}$$

The two-phase friction factor is calculated by the following equation based on the equivalent Reynolds number:

$$f_{\mathrm{tp}} = \left(\frac{d\mathrm{P}}{dz}\right)\frac{\rho_l d^3}{2\mathrm{Re}_{\mathrm{eq}}^2 \mu_l^2}, \tag{16}$$

where the all liquid equivalent Re number is determined from

$$\mathrm{Re}_{\mathrm{eq}} = \frac{G_{\mathrm{eq}} d}{\mu_l} \tag{17}$$

and the equivalent liquid mass flux is defined as

$$G_{\mathrm{eq}} = G\left((1-x) + x\left(\frac{\rho_l}{\rho_g}\right)^{0,5}\right) \tag{18}$$

Table 7 The most predictive combinations of input parameters according to the error rates for the three known input parameters

Inputs														Input number	Outputs	
I	II	III	IV	V	VI	VII	VIII	IX	X	XI	XII	XIII	XIV		R^2–ΔP (%)	R^2–h (%)
0	0	0	0	0	0	1	0	1	0	0	0	1	0	3	0.998001	0.933156
0	1	0	0	0	0	1	0	0	0	0	0	1	0	3	0.998001	0.923521
0	0	0	0	0	0	1	0	0	1	0	0	1	0	3	0.998001	0.906304
1	0	0	0	0	0	1	0	0	0	0	0	1	0	3	0.998001	0.942841
0	0	0	0	0	0	1	0	0	0	0	1	1	0	3	0.998001	0.893025
0	0	0	0	0	0	1	0	0	0	1	0	1	0	3	0.996004	0.925444
0	0	0	0	0	0	1	0	1	0	0	1	0	0	3	0.994009	0.933156
1	0	0	0	0	0	1	0	1	0	0	0	0	0	3	0.994009	0.900601
1	0	0	0	0	0	1	0	0	1	0	0	0	0	3	0.994009	0.948676
0	0	0	0	0	0	1	0	1	1	0	0	0	0	3	0.992016	0.944784
0	0	0	0	0	0	1	0	0	0	1	1	0	0	3	0.992016	0.819025
0	0	0	0	0	0	1	0	1	0	1	0	0	0	3	0.990025	0.946729
0	1	0	0	0	0	1	0	1	0	0	0	0	0	3	0.990025	0.9409
0	1	0	0	0	0	1	0	0	1	0	0	0	0	3	0.990025	0.925444
0	0	0	0	0	0	1	1	0	1	0	0	0	0	3	0.988036	0.8836
1	1	0	0	0	0	1	0	0	0	0	0	0	0	3	0.986049	0.929296
1	0	0	0	0	0	1	0	0	0	0	1	0	0	3	0.984064	0.829921
0	0	0	0	0	0	1	0	0	1	1	0	0	0	3	0.984064	0.887364
0	0	0	0	0	0	1	0	0	1	0	1	0	0	3	0.984064	0.887364
0	0	0	0	0	0	1	1	0	0	0	1	0	0	3	0.982081	0.904401
0	0	1	0	0	0	1	0	0	0	0	1	0	0	3	0.976144	0.887364
0	1	0	0	0	0	1	0	0	0	1	0	0	0	3	0.972196	0.946729
0	0	0	0	1	0	1	0	0	1	0	0	0	0	3	0.972196	0.891136
0	0	1	0	0	0	1	0	0	1	0	0	0	0	3	0.972196	0.877969
0	0	0	0	0	1	1	0	0	1	0	0	0	0	3	0.972196	0.906304
1	0	0	0	1	0	0	0	0	0	0	0	1	0	3	0.970225	0.885481
0	0	0	0	1	0	0	0	0	0	0	1	1	0	3	0.970225	0.8836
0	0	0	0	1	0	0	0	0	1	0	0	1	0	3	0.964324	0.885481
0	1	0	0	0	1	0	0	0	0	0	1	0	0	3	0.964324	0.948676
0	0	0	0	0	0	1	0	0	1	0	0	0	1	3	0.964324	0.9801
0	1	0	0	0	0	1	0	0	0	0	0	0	1	3	0.964324	0.908209
0	0	0	0	1	0	0	0	1	1	0	0	0	0	3	0.962361	0.908209
0	0	0	0	0	1	0	0	0	0	0	1	1	0	3	0.962361	0.952576
0	0	0	0	1	0	0	0	0	0	0	0	1	0	3	0.962361	0.6724
0	1	0	0	0	1	0	0	0	0	0	0	1	0	3	0.962361	0.962361
0	0	0	0	0	1	0	0	1	0	0	0	1	0	3	0.962361	0.950625
1	0	0	0	1	0	0	0	0	1	0	0	0	0	3	0.962361	0.906304
0	0	0	0	0	1	0	0	1	1	0	0	0	0	3	0.9604	0.9409
0	1	0	0	0	1	0	0	1	0	0	0	0	0	3	0.9604	0.956484
1	1	0	0	1	0	0	0	0	0	0	0	0	0	3	0.9604	0.923521
0	0	0	0	0	1	0	0	1	0	0	1	0	0	3	0.9604	0.956484
0	0	0	0	1	0	0	1	0	0	0	0	1	0	3	0.9604	0.906304
1	0	0	0	0	1	0	0	0	0	0	1	0	0	3	0.958441	0.861184
1	0	0	0	0	1	0	0	1	0	0	0	0	0	3	0.956484	0.935089
0	1	0	0	0	1	0	0	0	1	0	0	0	0	3	0.956484	0.844561
0	0	0	0	0	1	0	0	0	1	0	0	1	0	3	0.956484	0.950625

Table 7 continued

Inputs														Input number	Outputs	
I	II	III	IV	V	VI	VII	VIII	IX	X	XI	XII	XIII	XIV		R^2–ΔP (%)	R^2–h (%)
1	0	0	0	0	1	0	0	0	1	0	0	0	0	3	0.956484	0.948676
0	1	0	0	1	0	0	0	0	0	1	0	0	0	3	0.954529	0.912025
0	1	0	0	1	0	0	0	0	0	0	0	1	0	3	0.954529	0.906304
0	0	0	0	0	0	1	1	0	0	0	0	1	0	3	0.954529	0.887364
0	0	0	0	1	0	0	0	0	1	1	0	0	0	3	0.954529	0.896809
0	0	0	0	1	0	0	0	1	0	0	0	1	0	3	0.952576	0.906304
0	0	0	0	0	0	1	0	0	0	0	0	1	1	3	0.952576	0.982081

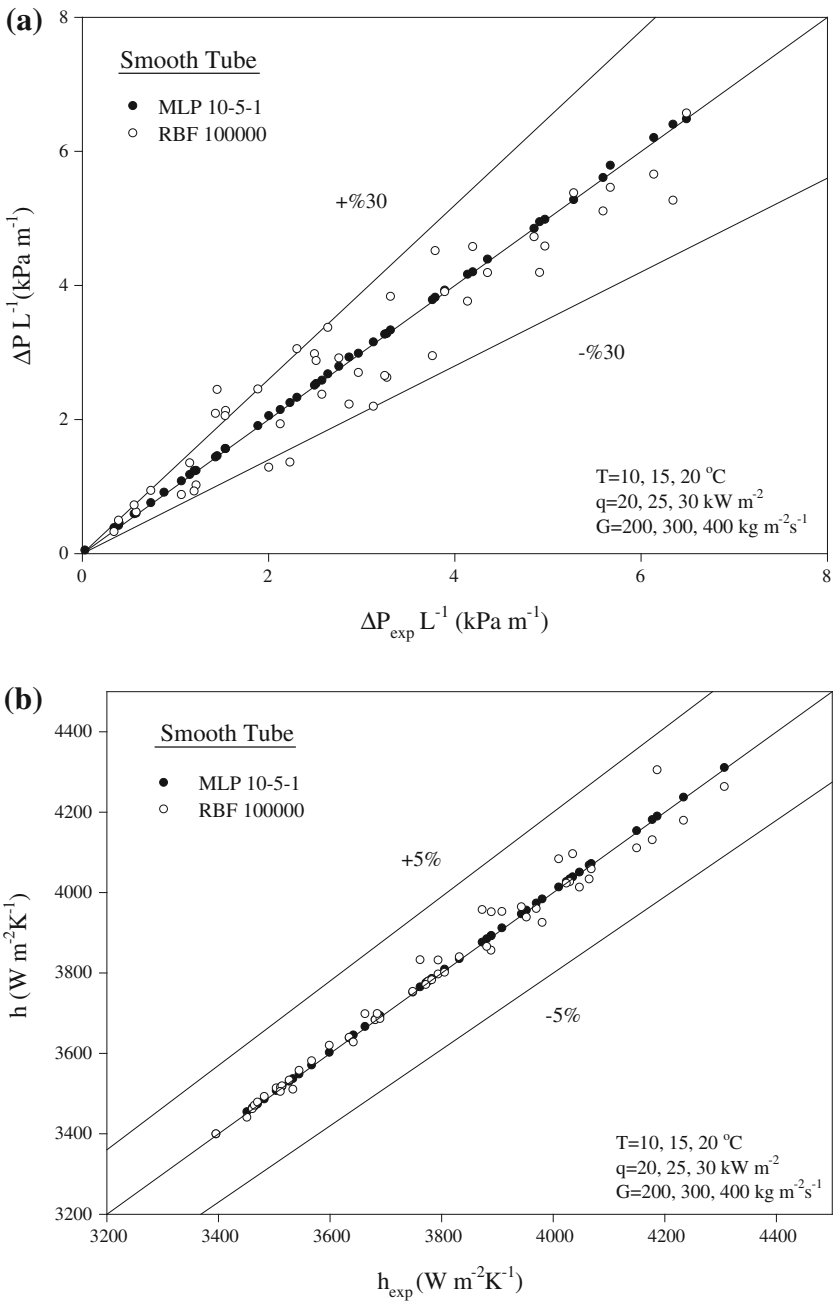

Fig. 5 Comparisons of experimental pressure drop (**a**) and convective heat transfer coefficients (**b**) with the artificial neural network methods for the smooth tube

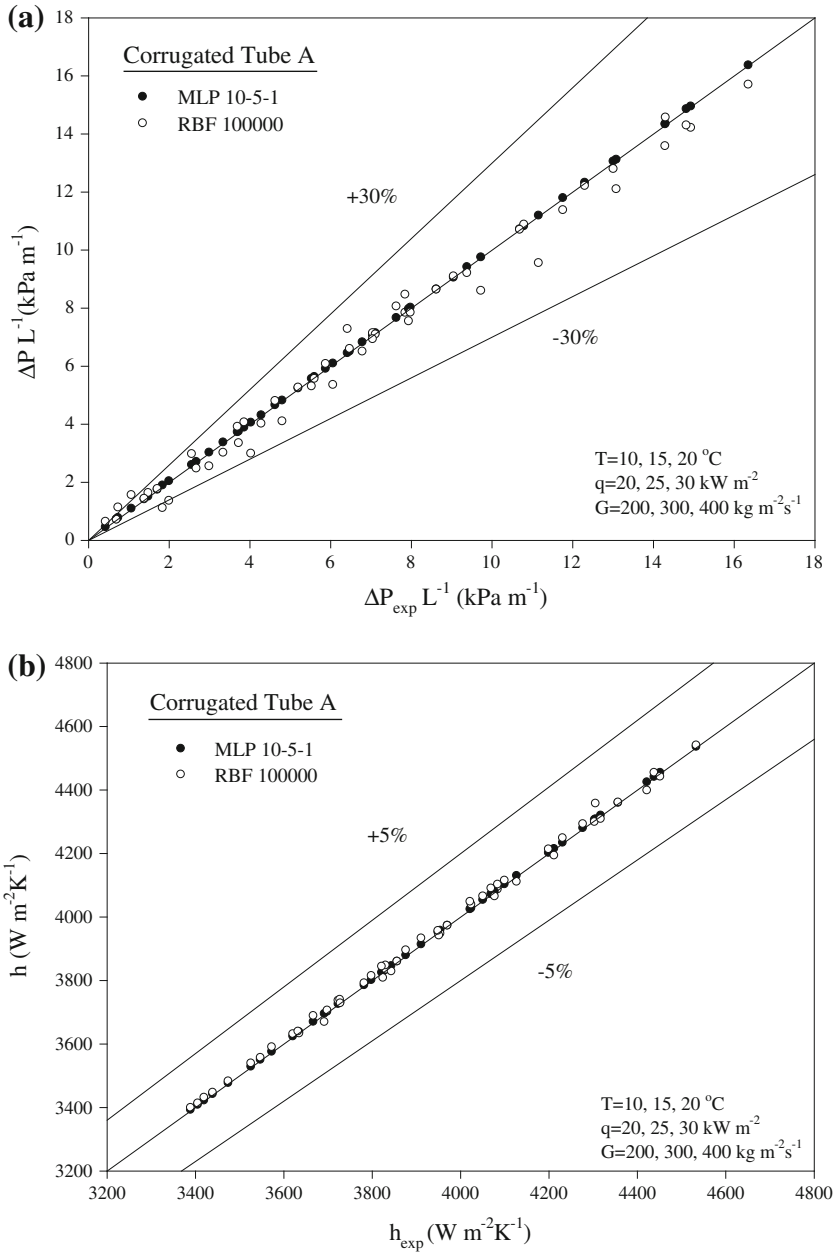

Fig. 6 Comparisons of experimental pressure drop (**a**) and convective heat transfer coefficients (**b**) with the artificial neural network methods for the corrugated tube A

Bond number (Bo), liquid and vapour Reynolds numbers ($\mathrm{Re_l}$, $\mathrm{Re_g}$), two-phase multiplier (ϕ_l^2), Froude number (Fr) and Weber number (We) are defined, respectively, as follows:

$$\mathrm{Bo} = \frac{q}{i_{\mathrm{fg}} G} \tag{19}$$

$$\mathrm{Re}_l = \frac{\mathrm{Gd}(1-x)}{\mu_l} \tag{20}$$

$$\mathrm{Re}_g = \frac{\mathrm{Gdx}}{\mu_g} \tag{21}$$

$$\phi_l^2 = 1 + \frac{C}{X} + \frac{1}{X^2} \tag{22}$$

where Martinelli parameter is defined as

$$X_{\mathrm{tt}} = \left(\frac{1-x}{x}\right)^{0.9} \left(\frac{\rho_g}{\rho_l}\right)^{0.5} \left(\frac{\mu_l}{\mu_g}\right)^{0.1} \tag{23}$$

The constant C in Eq. (22) is the parameter which indicates the two-phase flow condition. The value of this parameter, proposed by Chisholm [25] and varying from 5 to 20, depends on the flow condition of the vapour and liquid. For instance, the constant $C = 20$ when the vapour and liquid flow is in the turbulent region, and $C = 5$ if the two-phase flow is in the laminar region.

$$\mathrm{Fr} = \frac{G^2}{\mathrm{gd}\rho_{\mathrm{TP}}^2}, \tag{24}$$

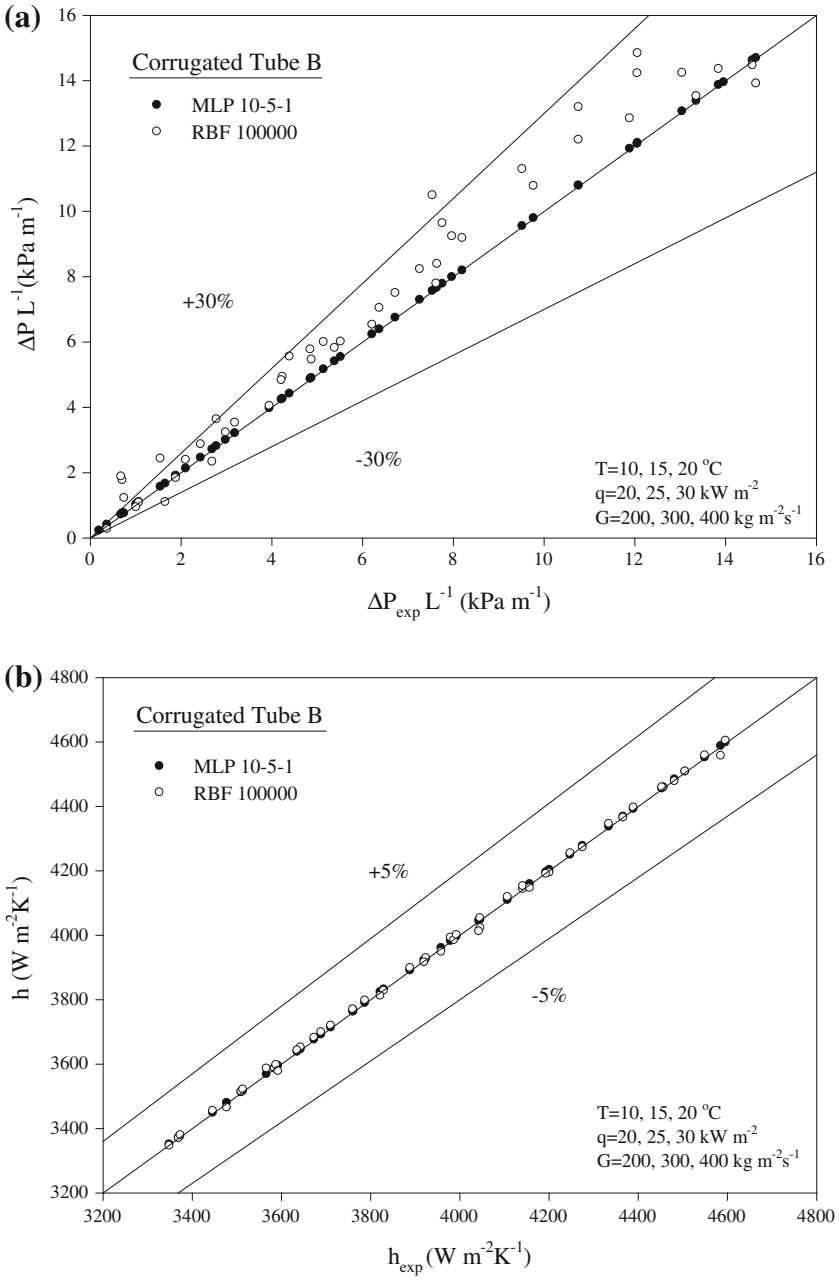

Fig. 7 Comparisons of experimental pressure drop (**a**) and convective heat transfer coefficients (**b**) with the artificial neural network methods for the corrugated tube B

where the two-phase density is determined from

$$\rho_{\mathrm{TP}} = \left(\frac{x}{\rho_g} + \frac{1-x}{\rho_l}\right)^{-1} \tag{25}$$

$$\mathrm{We} = \frac{G^{2\mathrm{d}}}{\rho_{\mathrm{TP}}\sigma} \tag{26}$$

Reynolds equivalent number, Lockhart and Martinelli parameter, Weber number, Bond and Froude numbers were used as the most significant variables in the proposed correlation. Reynolds number gives a measure of the ratio of inertial forces to viscous forces characterising different flow regimes such as laminar and turbulent flow. Lockhart and Martinelli parameter is used in internal two-phase flow calculations expressing the liquid fraction of a flowing fluid. Weber number is used for fluid flows where there is an interface between two different fluids, and it can be considered as a measure of the relative significance of the fluid's inertia compared with its surface tension. Bond number expresses the ratio of body forces to surface tension forces, low Bond numbers indicate the surface tension domination on the system and Froude number is used to compare inertial and gravitational forces. The effect of other important parameters belonging to the fluid properties such as liquid and vapour phases of

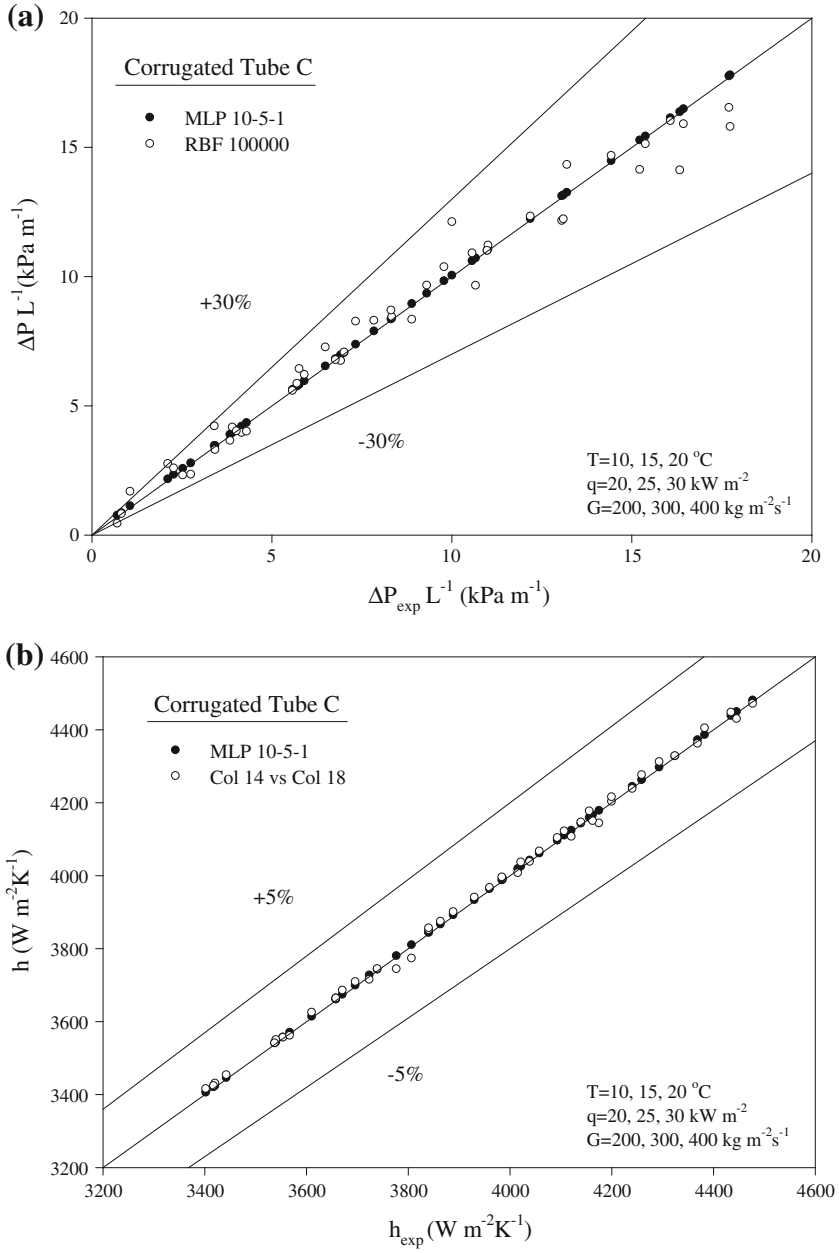

Fig. 8 Comparisons of experimental pressure drop (**a**) and convective heat transfer coefficients (**b**) with the artificial neural network methods for the corrugated tube C

density, dynamic viscosity, kinematic viscosity and thermal diffusivity exist in the Prandtl number and other dimensionless numbers.

3.7 Error Analysis

Error analysis of the study is performed by means of Eqs. (27), (28) and (29) and the results are given in Tables 4, 5, 6 and 7. In these equations, N is the element number of the test group, h^i_{exp} and h^i_{calc} are the experimental and calculated results of the heat transfer coefficient obtained from "i" number of test data, and $\overline{h}_{\text{exp}}$ and $\overline{h}_{\text{calc}}$ are the average values of experimental and calculated results of heat transfer coefficient obtained from the numerical analysis. It should be noted that error analysis of pressure drop was carried out similarly.

The R-square error is determined as follows:

$$E_{\text{Rsquare}} = \frac{\left(\sum_{i=1}^{N}(h^i_{\text{exp}} - \overline{h}_{\text{exp}})(h^i_{\text{calc}} - \overline{h}_{\text{calc}})\right)^2}{\left(\sum_{i=1}^{N}(h^i_{\text{exp}} - \overline{h}_{\text{exp}})^2\right)\left(\sum_{i=1}^{N}(h^i_{\text{calc}} - \overline{h}_{\text{calc}})^2\right)} \tag{27}$$

Proportional error is calculated as follows:

$$E_{\text{ratio}} = \frac{100}{N}\sum_{i=1}^{N}\frac{\left|h^i_{\text{exp}} - h^i_{\text{calc}}\right|}{h^i_{\text{exp}}} \tag{28}$$

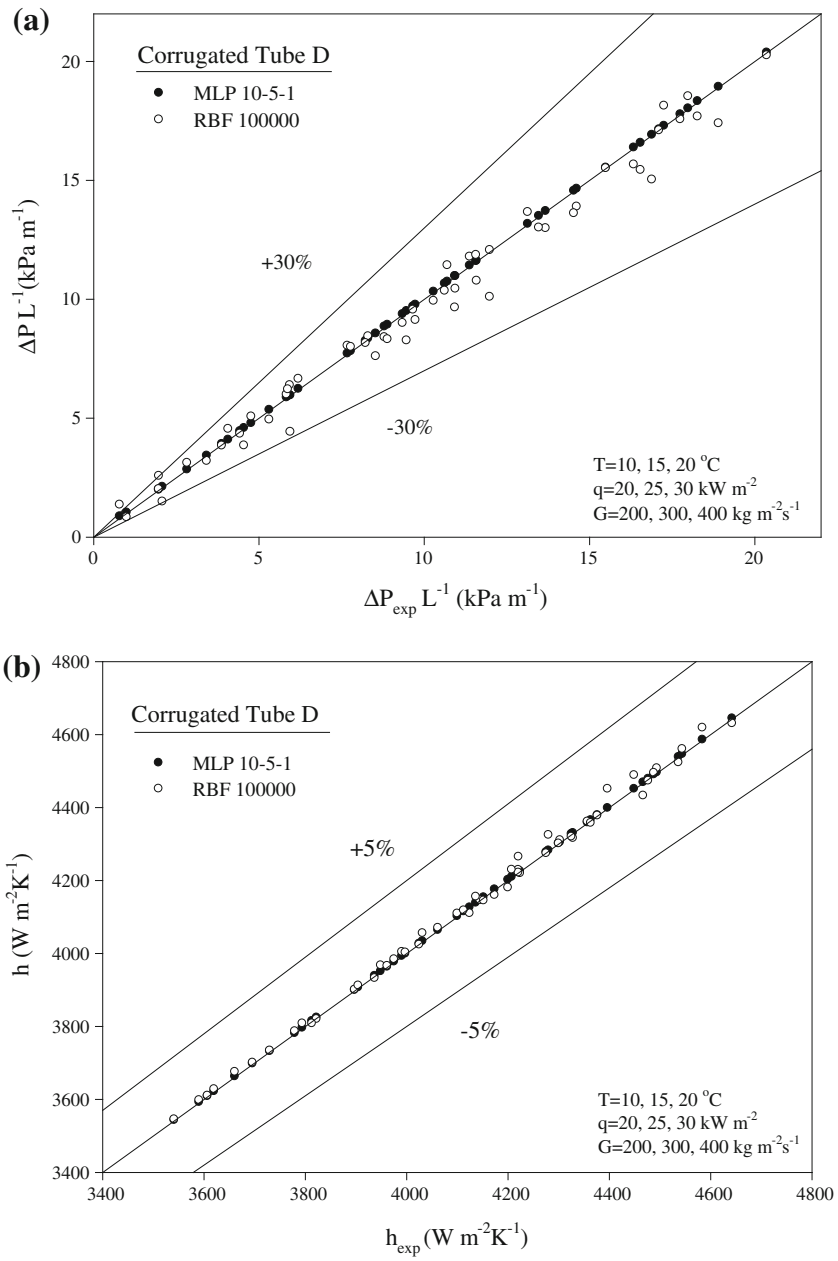

Fig. 9 Comparisons of experimental pressure drop (**a**) and convective heat transfer coefficients (**b**) with the artificial neural network methods for the corrugated tube D

Square law error is estimated as follows:

$$E_{\text{square}} = \sqrt{\frac{1}{N}.\sum_{i=1}^{N}(h^i_{\text{exp}} - h^i_{\text{calc}})^2} \tag{29}$$

4 Results and Discussion

The experiments of the present study were performed at the Fluid Mechanics, Thermal Engineering and Multiphase Flow Research Lab. (FUTURE) in KMUTT. Pure HFC-134a was used in the experiments. Special attention was paid to the accuracy of the measurements during the experiments as can be seen from authors' previous publications on in-tube evaporation processes.

Numerical analysis of artificial intelligence includes six-dimensional input parameters, such as mass flux (G, kg m^{-2} s^{-1}), heat flux (q, kW m^{-2}), saturation temperature (T_{sat}, °C), temperature difference between the tube wall and saturation temperature ($\Delta T_{\text{sat}} = T_{\text{wi}} - T_{\text{sat}}$), depth of corrugation (e, mm) and helix angle (β,°) for the tested corrugated tubes and eight-dimensionless input parameters, such as average vapour quality (x), two-phase friction factor (f_{tp}), two-phase multiplier (ϕ_l^2), liquid and vapour Reynolds numbers (Re_l, Re_g), Bond number (Bo), Froude number (Fr), Weber

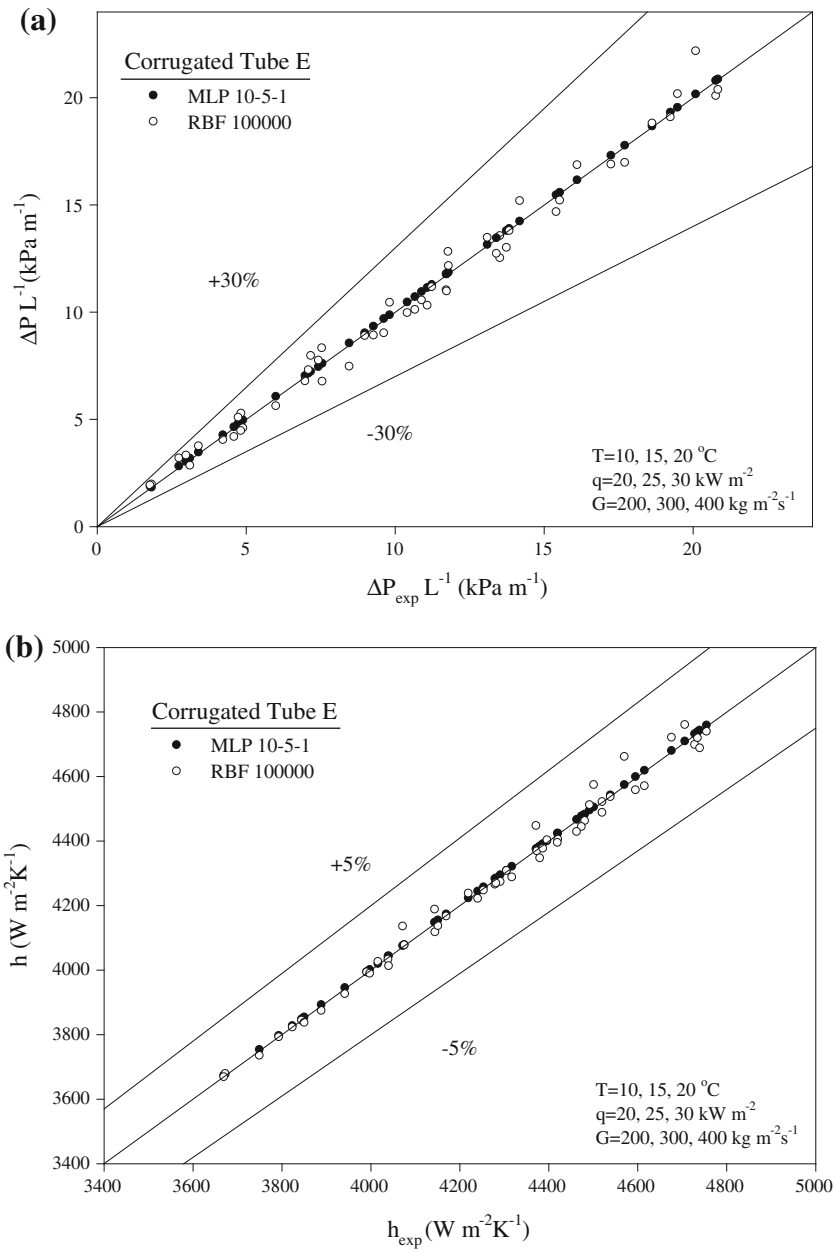

Fig. 10 Comparisons of experimental pressure drop (**a**) and convective heat transfer coefficients (**b**) with the artificial neural network methods for the corrugated tube E

number (We), two-dimensional output parameters such as convective heat transfer (h, W m^{-2} K^{-1}) and pressure drop (ΔP, Pa).

The K-fold cross validation algorithm is one of the best ways to measure the modelling success of the experimental data [26]. The coefficient of this algorithm (K) was chosen as 5. First, all data (300 data points) were divided into 5 equal sets according to this algorithm. Then, one of the 5 sets was assigned as test one, the other 4 sets became training one and the system was started to train. After that, the success rate was checked for the separated test set. At this stage, the systems' success had been measured for 1/5 data. This process was continued by changing the data sets which were used for test and training, and the success of the system was measured using the altered test set. As a result, the modelling performance of all data was measured at the end. There are several architectures tried in the analysis such as 10-5-1, 10-1 and 2-1. The random set for 20 % of the training sets was separated to prevent excess learning of the artificial intelligence during the application of the MLP algorithm. In this case, the sets of training, validation and test were determined with 192, 48 and 60 data points, respectively, during the training process of the MLP algorithm in a loop. The best architecture was investigated by changing the radial basis layer neuron number and spread coefficient as a parameter of Radial basis function (RBF). The tests were performed using the a

Table 8 Coefficients of the main proposed correlation (Eq. 9) obtained by ANN analyses

Eq. (9): $h = A(\frac{k_l}{d})(\mathrm{Re}_g)^B(f_{\mathrm{tp}})^C(\mathrm{Fr})^D(x)^E(\mathrm{Bo})^F(\Delta T_{\mathrm{sat}})^G(f_l^2)^H(\mathrm{We})^I(\Delta P\frac{L}{P})^J(\mathrm{Re}_l)^K$

Equations/ coefficients	Eq. (30)	Eq. (31)	Eq. (32)	Eq. (33)	Eq. (34)	Eq. (35)	Eq. (36)	Eq. (37)	Eq. (38)	Eq. (39)
A	60.19365	0.100143	−0.06397	3.327234	3.550174	6.20412	5.867284	21.73028	21.77796	21.70193
B	0.171773	0.516859	0.096179	−0.06397	−0.13991	−1.01466	−1.01955	−0.92148	8.05E-05	8.04E-05
C	0	−0.16681	0.511016	0.096179	0.095697	−0.00078	−0.00017	−0.00024	−0.92141	−0.92182
D	0	0	−0.13459	0.511016	0.090395	1.005651	1.001148	1.003015	−0.00036	−0.00036
E	0	0	0	−0.13459	0.55255	1.165526	1.164891	1.008696	1.003108	1.003111
F	0	0	0	0	−0.11753	−0.081	0.004695	0.002929	1.008488	−0.00047
G	0	0	0	0	0	−1.00624	−0.08187	−0.09576	0.002944	1.009437
H	0	0	0	0	0	0	−1.00106	0.092417	−0.09589	0.002547
I	0	0	0	0	0	0	0	−1.00344	0.092563	−0.09586
J	0	0	0	0	0	0	0	0	−1.00354	0.092303
K	0	0	0	0	0	0	0	0	0	−1.00353

spread coefficient of 100, 1,000, 10,000, 100,000, 1000,000, 10,000,000 and for the radial basis layer 50, 100, 150, 200, 250, 300, 350, 400, 450, 500.

The experimental data include the mass fluxes of 200, 300 and 400 kg m^{-2} s^{-1} belonging to the saturation temperatures of 10, 15 and 20 °C as shown in Table 3 and also in Figs. 5, 6, 7, 8, 9, 10, 11. Table 4 shows the best predictive method for the convective heat transfer coefficient (a) and pressure drop (b) regarding with the several error analysis such as R-square, proportional error and means square error (MSE). The performance of the method of multi-layer perception (MLP) with 10-5-1 architecture and radial basis function networks (RBFN) with the spread coefficient (sp) of 100,000 and hidden layer neuron number of 200, shown in Table 4, were found to be superior to other methods and architectures by means of satisfactory results with their deviations within the range of ±0.001677 % for the estimated pressure drop (Table 4a), and ±0.358 % for the estimated evaporation heat transfer coefficient (Table 4b). In addition to this, according to the evaporation temperatures of 10, 15 and 20 °C, comparison of the experimental heat transfer coefficients and pressure drops with those from various artificial neural network methods of test groups of all the tested tubes are shown in Figs. 5, 6, 7, 8, 9, 10 in a 30 % deviation line for the pressure drop and 5 % deviation line for the evaporation heat transfer coefficient. It can be clearly seen from these figures and tables that the radial basis function networks (RBFN) have poorer predictability of experimental data than the method of multi-layer perceptron (MLP).

In terms of the use of high data numbers for the accuracy and validation process of the experiments, numerical calculations are done by means of 300 experimental data points in all tables and figures. Tables 5, 6, 7 show the dependency of the input parameters on the outputs of the study according

Table 9 Evaluation of proposed correlations of convective heat transfer coefficient obtained from ANN analysis that belong to the all tested tubes according to the error rates for the mass fluxes of 200, 300, 400 kg m^{-2} s^{-1} and T_{sat} = 10, 15 and 20 °C

h (W m^{-2} K^{-1})	Error analysis/ANN methods		
	R square	Proportional (%)	Square law
Eq. (30)	0.536928	4.821048	53,059.02
Eq. (31)	0.766083	3.348161	26,881.77
Eq. (32)	0.852823	2.692073	16,573.89
Eq. (33)	0.8784	2.418055	13,687.29
Eq. (34)	0.901808	2.195584	11,052.15
Eq. (35)	0.999891	0.068428	12.22074
Eq. (36)	0.999952	0.040852	5.360154
Eq. (37)	0.99997	0.034258	3.372134
Eq. (38)	0.99997	0.034129	3.364506
Eq. (39)	0.99997	0.034181	3.361205

to the error rates of the test group of ANN, as a result of the most predictive ANN method of the MLP 10-5-1 architecture for the mass fluxes of 200, 300, 400 kg m^{-2} s^{-1} and evaporation temperatures of 10, 15 and 20 °C. They also show the most predictive combinations of input parameters, whose deviations are over 0.5 %, according to the error rates for the determination of evaporation heat transfer coefficient (h) and pressure drop (ΔP). The input parameters are shown with numbers in these tables as follows: average vapour quality (I), mass flux (II), evaporating temperature (III), heat flux (IV), depth of corrugation (V), helix angle of corrugation (VI), two-phase friction factor (VII), Bond number (VIII), liquid Reynolds number (IX), vapour Reynolds number (X), two–phase multiplier (XI), Froude number (XII),Weber number (XIII) and temperature difference between the tube wall and

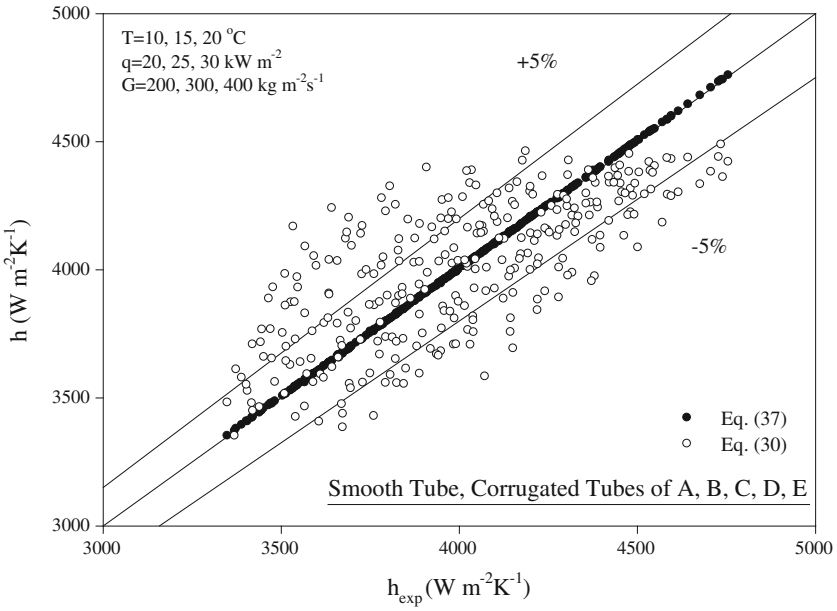

Fig. 11 Comparisons of experimental convective heat transfer coefficients (**b**) with the proposed empirical correlations by artificial neural network methods for all tubes

saturation temperature (XIV). Table 5 shows each input parameter's predictability of the outputs of experimental pressure drop and evaporating heat transfer coefficient separately. They are ordered from the best predictive to the worst predictive one in all tables considering the experimental pressure drop. For instance, artificial intelligence was able to determine the experimental pressure drop and evaporation heat transfer coefficient with an accuracy of over 74 % by means of the separate use of inputs of vapour Reynolds number (X), Froude number (XII) and Weber number (XIII) in Table 5. In Tables 6 and 7, neural network analyses tried to determine the outputs by means of two and three known input combinations. Prediction rates on these tables increase with increasing added input numbers due to the result of the learning process of the artificial intelligence. For example, when the helix angle of corrugation (VI) and two-phase friction factor (VII) are selected as known inputs in Table 6, their predictabilities are found as 78.2 and 80 % for the outputs of pressure drop and heat transfer coefficient, respectively. In Table 7, when the vapour Reynolds number (X) is added to the selected inputs of the helix angle of corrugation (VI) and two-phase friction factor (VII), the prediction rate increases to 98.6 % for the pressure drop and 95.2 % for the evaporating heat transfer coefficient in comparison with the former situation. As a result, it is possible to derive many results from these figures on the input combination performance. For another example, it should be noted that in spite of the rather low self-prediction rate of two-phase friction factor (IV) in Table 5, it produced a good combination with others and increased the predictability in these tables.

The correlation development study results are shown in Tables 8 and 9, and also in Fig. 11. The main frame of the proposed correlation is shown in Eq. (9) which has 12 possible dominant parameters on the evaporation heat transfer coefficient. Artificial intelligence decided the coefficients of these significant parameters step by step in Table 8 and their error rates can be seen in Table 9. It is possible to see the success of each term in Eq. (9) in this table. It also shows that the accuracy of the estimated output values by means of added input values increases with increasing added proper input parameters into Eq. (9). Equation (30) is found to have the lowest predictability, while Eq. (37) has the optimum predictability in Table 9 and their performance comparison is shown in Fig. 11. The majority of the data obtained from the ANN analysis of Eq. (30) fall between the deviations of ±5 % in this figure. It can be seen that Eq. (37) showed a great success with its accuracy in Fig. 11.

A large number of graphics could be generated from the output of the calculations; however, due to space limitation only the typical results are shown from the experimental database of the authors. It should also be noted that detailed information on the evaporation heat transfer characteristics of the study with some additional figures and different experimental parameters can be seen in the authors' previous publications.

5 Conclusion

Comparison of the numerical evaporation heat transfer coefficient and pressure drop values with the measured values by means of artificial intelligence methods was performed in this paper. There is no research on the content of this paper considering its parameters in current literature. The results of this study are expected to fill this gap in the literature.

Except for the different architectures of the artificial neural network (ANN) methods of multi-layer perceptron (MLP)

and radial basis networks (RBFN), the performance of the method of MLP with 10-5-1 architecture and RBFN with the spread coefficient of 100,000 are found to be capable of predicting the evaporation heat transfer coefficient and pressure drop of R134a in a vertical tube within the range of ±30 % and also within very small error rates.

Convective heat transfer coefficient and pressure drop of R134a in the paper are found to be dependent on mass flux, heat flux, the temperature difference between the tube wall and saturation temperature, average vapour quality, evaporating temperature, two-phase friction factor, two-phase multiplier, liquid and vapour Reynolds numbers, Bond number, Froude number, Weber number, depth of corrugation and helix angle for the tested corrugated tubes according to the results of the analysis.

The new empirical correlations, based on this simple architecture which have never appeared in the literature, for predicting the convective heat transfer coefficient valid for the evaporation process in a smooth tube and five different corrugated tubes, are proposed for practical applications.

Acknowledgments The first author wishes to thank King Mongkut's University of Technology Thonburi (KMUTT) for providing him with a Post-doctoral fellowship. The third and fourth authors wish to thank the Thailand Research Fund, the Office of the Higher Education Commission and the National Research University Project for financial support for this study.

References

1. Nozu, S.; Honda, H.; Nakata, H.: Condensation of refrigerants CFC11 and CFC113 in the annulus of a double-tube coil with an enhanced inner tube. Exp. Therm. Fluid Sci. **11**, 40–51 (1995)
2. Nozu, S.; Honda, H.; Nishida, S.: Condensation of a zeotropic CFC 114-CFC 113 refrigerant mixture in the annulus of a double-tube coil with an enhanced inner tube. Exp. Therm. Fluid Sci. **11**, 364–371 (1995)
3. Dong, Y.; Huixiong, L.; Tingkuan, C.: Pressure drop, heat transfer and performance of single-phase turbulent flow in spirally corrugated tubes. Exp. Therm. Fluid Sci. **24**, 131–138 (2001)
4. Zimparov, V.: Enhancement of heat transfer by a combination of three-start spirally corrugated tubes with a twisted tape. Intern. J. Heat Mass Transf. **44**, 551–574 (2001)
5. Zimparov, V.: Enhancement of heat transfer by a combination of a single-start spirally corrugated tubes with a twisted tape. Exp. Therm. Fluid Sci. **25**, 535–546 (2002)
6. Zimparov, V.: Prediction of friction factors and heat transfer coefficients for turbulent flow in corrugated tubes combined with twisted tape inserts. Part 1: friction factors. Intern. J. Heat Mass Transf. **47**, 589–599 (2004)
7. Zimparov, V.: Prediction of friction factors and heat transfer coefficients for turbulent flow in corrugated tubes combined with twisted tape inserts. Part 2: heat transfer coefficients. Intern. J. Heat Mass Transf. **47**, 385–393 (2004)
8. Nafey, A.S.: Neural network based correlation for critical heat flux in steam-water flows in pipes. Intern. J. Therm. Sci. **48**, 2264–2270 (2009)
9. Wang, W.J.; Zhao, L.X.; Chun-Lu, Z.: Generalized neural network correlation for flow boiling heat transfer of R22 and its alternative refrigerants inside horizontal smooth tubes. Intern. J. Heat Mass Transf. **49**, 2458–2465 (2006)
10. Scalabrin, G.; Condosta, M.; Marchi, P.: Mixtures flow boiling: modeling heat transfer through artificial neural networks. Intern. J. Therm. Sci. **45**, 664–680 (2006)
11. Scalabrin, G.; Condosta, M.; Marchi, P.: Modeling flow boiling heat transfer of pure fluids through artificial neural networks. Intern. J. Therm. Sci. **45**, 643–663 (2006)
12. Wongwises, S.; Disawas, S.: Two-phase evaporative heat transfer coefficients of refrigerant HFC-134a under forced flow conditions in a small horizontal smooth tube. Intern. Commun. Heat Mass Transf. **27**, 35–48 (2000)
13. Sripattrapan, W.; Wongwises, S.: Two-phase flow of refrigerants during evaporation under constant heat flux in a horizontal tube. Intern. Commun. Heat Mass Transf. **32**, 386–402 (2005)
14. Wongwises, S.; Polsongkram, M.: Evaporation heat transfer and pressure drop of HFC-134a in a helically coiled concentric tube-in-tube heat exchanger. Intern. J. Heat Mass Transf. **49**, 658–670 (2006)
15. Kaew–On, J.; Wongwises, S.: Experimental investigation of evaporation heat transfer coefficient and pressure drop of R-410A in a multiport mini-channel. Intern. J. Ref. **32**, 124–137 (2009)
16. Posew, K.; Laohalertdecha, S.; Wongwises, S.: Evaporation heat transfer enhancement of R-134a flowing inside smooth and microfin tubes using the electrohydrodynamic technique. Energy Conv. Manag. **50**, 1851–1861 (2009)
17. Laohalertdecha, S.; Wongwises, S.: An experimental study into the evaporation heat transfer and flow characteristics of R-134a refrigerant flowing through corrugated tubes. Intern. J. Ref. **34**, 280–291 (2011)
18. Aroonrat, K.; Wongwises, S.: Evaporation heat transfer and friction characteristics of R-134a flowing downward in a vertical corrugated tube. Exp. Therm. Fluid Sci. **35**, 20–28 (2011)
19. Balcilar, M.; Dalkilic, A.S.; Wongwises, S.: Artificial neural network techniques for the determination of condensation heat transfer characteristics during downward annular flow of R134a inside a vertical smooth tube. Intern. Commun. Heat Mass Transf. **38**, 75–84 (2011)
20. Colorado, D.; Ali, M.E.; Garcia-Valladares, O.; Hernandez, J.A.: Heat transfer using a correlation by neural network for natural convection from vertical helical coil in oil and glycerol/water solution. Energy **36**, 854–863 (2011)
21. Fausett, L.: Fundamentals of neural networks, architectures, algorithms, and applications, Prentice-Hall, Inc. Press, Prentice–Hall (1994)
22. Matlab, R2010a, 2010, http://mathworks.com/
23. Dittus, F.W.; Boelter, L.M.E.: Engineering publication, vol. 2, p. 443, University of California, California (1930)
24. Zivi, S.M.: Estimation of steady-state steam void-fraction by means of the principle of minimum entropy production. Trans. ASME J. Heat Transf. Ser. C **86**, 247–252 (1975)
25. Chisholm, D.: Pressure gradients due to friction during the flow of evaporating two-phase mixtures in smooth tubes and channels. Intern. J. Heat Mass Transf. **16**, 347–358 (1973)
26. Duda, R.O.; Hard, P.E.; Stork, D.G.: Pattern classification (2nd Edn). Wiley, New York (2002)

Heat Mass Transfer (2014) 50:469–482
DOI 10.1007/s00231-013-1252-6

ORIGINAL

Prediction of heat transfer coefficients and friction factors for evaporation of R-134a flowing inside corrugated tubes

S. Laohalertdecha · K. Aroonrat · A. S. Dalkilic · O. Mahian · S. Kaewnai · S. Wongwises

Received: 12 May 2012 / Accepted: 17 September 2013 / Published online: 27 October 2013

Abstract In this study, experimental and simulation studies of the evaporation heat transfer coefficient and pressure drop of R-134a flowing through corrugated tubes are conducted. The test section is a horizontal counter-flow concentric tube-in-tube heat exchanger 2.0 m in length. A smooth tube and corrugated tubes with inner diameters of 8.7 mm are used as the inner tube. The outer tube is made from a smooth copper tube with an inner diameter of 21.2 mm. The corrugation pitches used in this study are 5.08, 6.35, and 8.46 mm. Similarly, the corrugation depths are 1, 1.25, and 1.5 mm, respectively. The results show that the maximum heat transfer coefficient and pressure drop obtained from the corrugated tube are up to 22 and 19 % higher than those obtained from the smooth tube, respectively. In addition, the average difference of the heat transfer coefficient and pressure drop between the simulation model and experimental data are about 10 and 15 %, respectively.

S. Laohalertdecha · K. Aroonrat · S. Kaewnai · S. Wongwises (✉)
Fluid Mechanics, Thermal Engineering and Multiphase Flow Research Lab. (FUTURE), Department of Mechanical Engineering, Faculty of Engineering, King Mongkut's University of Technology Thonburi, Bangmod, Bangkok 10140, Thailand
e-mail: somchai.won@kmutt.ac.th

A. S. Dalkilic
Heat and Thermodynamics Division, Department of Mechanical Engineering, Yildiz Technical University, Yildiz, Besiktas, 34349 Istanbul, Turkey

O. Mahian
Young Researchers and Elite Club, Mashhad Branch, Islamic Azad University, Mashhad, Iran

List of symbols

A	Surface area of the test section (m^2)
c_p	Specific heat at constant pressure (J/kg °C)
d	Inner diameter (m)
D	Outer diameter (m)
e	Corrugation depth (mm)
f	Friction factor
G	Mass flux (kg/m^2 s)
h	Heat transfer coefficient (W/m^2 °C)
i	Enthalpy (J/kg)
i_f	Enthalpy of the saturated liquid (J/kg)
i_{fg}	Enthalpy of vaporization (J/kg)
k	Thermal conductivity (W/m °C)
L	Length of the test tube (m)
LMTD	Logarithmic mean temperature difference
m	Mass flow rate (kg/s)
Nu	Nusselt number
p	Corrugation pitch (mm)
Pr	Prandtl number
Q	Heat transfer rate (W)
Re	Reynolds number
q''	Heat flux (W/m^2)
T	Temperature (°C)
U	Overall heat transfer coefficient (W/m^2 K)
x	Vapour quality
X	Martinelli parameter

Greek letters

α	Void fraction
β	Helix angle (degree)
ε	Relative roughness (m)
ρ	Density (kg/m^3)
ϕ_l^2	Two-phase multiplier
μ	Dynamic viscosity (Pa s)
ΔP	Pressure drop (Pa/m)

Subscripts

a	Acceleration
avg	Average
eq	Equivalent
f	Friction
g	Gravitation
i	Inside
in	Inlet
l	Liquid
o	Outside
out	Outlet
ph	Pre-heater
ref	Refrigerant
sat	Saturation
tp	Two-phase
$T_{TS,in}$	Based on temperature of the test section inlet
$T_{TS,out}$	Based on temperature of the test section outlet
TS	Test section
v	Vapor
w	Water

1 Introduction

Heat transfer enhancement techniques can be used to reduce the thermal resistance in a conventional heat exchanger by promoting a higher convection heat transfer coefficient and to minimize the size of the heat exchanger for a given heat duty. One of them is using a corrugated tube to replace the smooth tube. Typically, for the corrugated tube, the increase in heat transfer coefficient is higher than that in pressure drop. The corrugated tube can improve the performance of the heat exchanger by increasing fluid mixing, unsteadiness, turbulence flow, or limiting the growth of the fluid boundary layers close to the heat transfer surfaces. Corrugated tubes are sometimes chosen in the design of industrial shell-and-tube heat exchangers for heat transfer enhancement purpose. As a result, many researchers have investigated the heat transfer performance and flow characteristics of corrugated tubes. Several subsequently published articles involving the use of corrugated tubes are described in the following sections.

Nozu et al. [1, 2] investigated local heat transfer and pressure gradients in pure R-114, R-113, and a zeotropic refrigerant mixture during condensation in a tube-in-tube heat exchanger. A corrugated copper tube with an O.D. of 19.1 mm was used as the test section. Mass flows were tested in the range from 80 to 240 kg/m^{2}s. The results showed that the frictional pressure gradient and heat transfer data were correlated by the prediction method presented in this study with a mean absolute deviation of 11 and 13 %, respectively.

Dong et al. [3] investigated the turbulent friction and heat transfer characteristics of four spirally corrugated tubes with various geometrical parameters. Water and oil were used as the working fluids. The experimental conditions gave Reynolds numbers ranging from 6,000 to 93,000 for water and from 3,200 to 19,000 for oil. Their results showed that the heat transfer enhancement varied from 30 to 120 %, while the friction factor increased from 60 to 160 % when compared with a smooth tube.

Barba et al. [4] experimentally studied the heat transfer and pressure drop of single phase flows in a corrugated tube that could be used in the chemical and food industries. The Reynolds number ranged from 100 to 800. Ethylene glycol was used as the working fluid. The results gave a heat transfer enhancement of around 100 %, while the friction factor increased between 83 and 145 % compared to the smooth tube. Based on the experimental data, Nusselt number and friction factor correlations were proposed for the fully developed region.

Rainieri and Pagliarini [5] studied experimentally the thermal performance of corrugated tubes in an attempt to increase the convection heat transfer. Helical and transverse corrugated tubes with different pitch values were used as the test section. Ethylene glycol was employed as the working fluid. The test conditions were conducted at Reynolds numbers ranging from 90 to 800. A comparison of helical and transverse corrugated tubes to a smooth tube demonstrated that the transverse corrugated tubes give higher heat transfer enhancement than the helical corrugated tubes.

Among these previous studies, the most productive studies have been performed by Zimparov [6]. The heat transfer enhancement of a combination of three-start spirally corrugated tubes with a twisted tape was investigated. Two three-start spirally corrugated tubes combined with five twisted tape inserts with different relative pitches were employed as the test section. The experimental conditions were conducted at Reynolds numbers ranging from 3,000 to 60,000. There were two corrugated tubes with the height-to-diameter ratio (e/Di) of 0.0407 and 0.0569. Five twisted tapes with different relative pitch (H/Di) of 15.3, 12.2, 7.7, 5.8, and 4.7 were used in this study. The results showed that the friction factor and heat transfer coefficients of three-start spirally corrugated tubes with a twisted tape insert were significantly higher than those of a smooth tube under the same operating conditions.

Zimparov [7] presented the heat transfer enhancement using a combination of single-start spirally corrugated tubes with a twisted tape. The friction factors and inside heat transfer coefficients obtained from these tubes were higher than those obtained from the smooth tube under a given condition. In addition, Zimparov [8, 9] applied a simple mathematical model to predict the friction factors

and heat transfer coefficients in a spirally corrugated configuration combined with twisted tape inserts under the turbulent flow regime. The calculated friction factors and heat transfer coefficients were compared with the experimental data. The results showed that the agreement between the predicted and experimental data was fairly good.

Rousseau et al. [10] presented a mathematical formulation and numerical method to investigate the heat transfer and pressure drop characteristics of a fluted tube refrigerant-to-water condenser. In this model, the surface area was divided into three regions as follows: superheated, two-phase, and sub-cooled regions in which all properties of the refrigerant and water can be calculated. The proposed model was formulated based on the effectiveness-NTU method. For the water side, the existing empirical correlations for the friction factor and heat transfer coefficient were used. Unfortunately, for the refrigerant side, it was reported that there were no available correlations for calculating the friction factor and heat transfer coefficient of the fluted tube-in-tube condenser. Thus, the existing correlations for a smooth tube combined with an enhancement ratio based on the available correlations for helical coils as well as an enhancement factor based on empirical data for a fluted tube condenser were employed. Data for two commercial fluted tube heat exchangers were used to validate the proposed model. The average difference between the measured and the predicted pressure drop was 7.27 %. Similarly, the log mean temperature difference was 4.41 %.

Vicente et al. [11, 12] presented measurements of the mixed convection heat transfer and isothermal pressure drop in corrugated tubes for laminar, transition, and turbulent flow regions. Water and ethylene glycol were used as the working fluids. The results indicated that corrugated tubes gave a higher pressure drop and heat transfer coefficient than the smooth tube. The pressure drop obtained from the laminar to transition flow and turbulent flow increased by up to 25 and 300 %, respectively. Similarly, the Nusselt number obtained from laminar to transition flow and turbulent flow increased by up to 30 and 250 %, respectively.

Targanski and Cieslinski [13] experimentally studied the heat transfer coefficient and pressure drop of pure R407C and R407C/oil mixtures during evaporation inside a smooth stainless steel tube, smooth copper tubes, and two enhanced tubes. The inlet and outlet vapor quality were set at 0 and 0.7, respectively. The mass flow was varied from 250 to 500 kg/m^{2}s. The average saturation temperature was 0 °C. It was found that the heat transfer coefficient and pressure drop for the enhanced tubes were distinctly higher than those of the smooth tube. The maximum heat transfer enhancement factor and pressure drop penalty factor for the corrugated tube were 1.25 and 1.8, respectively.

Laohalertdecha and Wongwises [14–16] experimentally investigated the effect of pitch on the heat transfer coefficient and pressure drop of R134a flowing in corrugated tubes under condensation and evaporation conditions. The results indicated that the heat transfer coefficient and pressure drop obtained from the corrugated tube were higher than those of the smooth tube for all of the experimental conditions. Moreover, the results also showed that the corrugation surface promotes turbulent flow significantly. However, the effect of pitch on the heat transfer coefficient had absolute significance of high average quality. On the other hand, the effect of pitch on pressure drop was insignificant.

In addition, Laohalertdecha and Wongwises [17] formed heat transfer coefficient and two-phase friction factor correlations using approximately 200 data points for five different corrugated tube geometries and then proposed, in terms of Nusselt numbers, equivalent Reynolds numbers, Prandtl numbers, corrugation pitch and depth, and inside diameters. The results showed that 81 % of the Nusselt number data and 79 % of the two-phase friction factor data fell within a deviation of ±20 %.

As mentioned above, a number of researchers have studied mainly the effect of corrugated tubes on heat transfer and flow characteristics in a single phase. The results show that corrugated tubes have greater heat transfer potential than smooth tubes. However, very few studies have been conducted on the heat transfer and flow characteristics of the two-phase flow of the refrigerants through a corrugated copper tube. The effects of corrugation pitch and depth on the evaporation heat transfer coefficient and pressure drop of the refrigerant flowing inside horizontal corrugated tubes remain unstudied. Similarly, there is still no simulation model to determine the heat transfer and flow behaviour of a refrigerant flowing inside a corrugated tube. As a consequence, this study mainly presents the effect of pitch and depth on the evaporation heat transfer coefficient and pressure drop of R-134a flowing through corrugated copper tubes. In addition, a simulation model of the heat transfer coefficient and pressure drop during the evaporation of R-134a flowing through corrugated tubes is also investigated.

2 Experimental apparatus and procedure

A schematic diagram of the test apparatus is shown in Fig. 1. The experimental apparatus was designed to determine the heat transfer coefficient and pressure drop of pure R-134a over the length of the test tube. The test loop consists of a test section, refrigeration loop, cooling water flow loops, sub-cooling loop and relevant instrumentation. The objective of the water loop before the test section is to

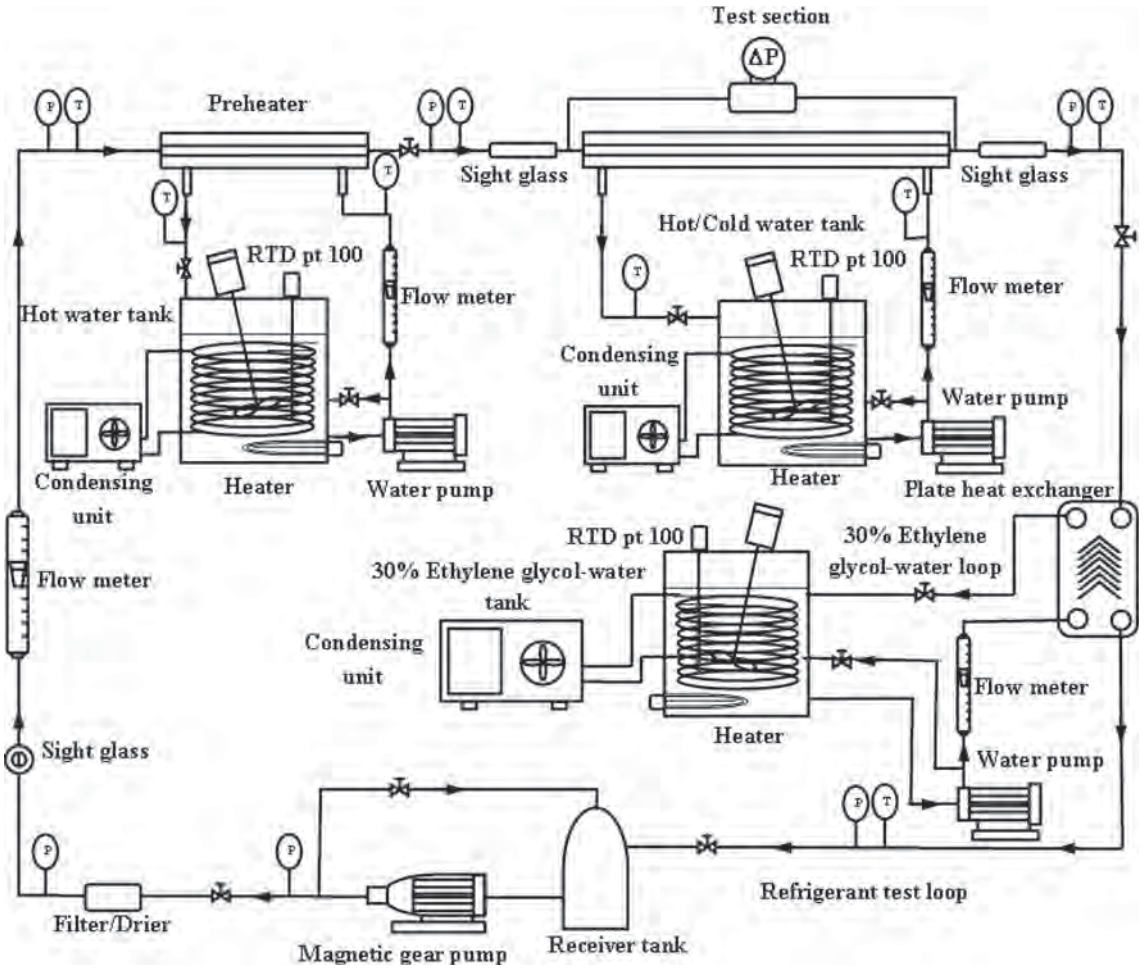

Fig. 1 Schematic diagram of the experimental apparatus (Laohalertdecha and Wongwises [14], with permission from Elsevier)

provide a controlled inlet vapour quality. The second water loop located in the test section provides a controlled heat output from the test section. The sub-cooling loop is used to prevent any two-phase flow condition of the refrigerant occurring before it enters the refrigerant pump.

For the refrigeration circulating loop, liquid refrigerant is discharged by a gear pump regulated by an inverter. The refrigerant passes in series through a filter/dryer, a sight glass tube, flow meter, pre-heater and enters the test section. The inlet vapour quality before entering the test section is controlled by the pre-heater. The pre-heater is a spiral counter flow heat exchanger that supplies energy to provide a controlled inlet vapour quality for vaporization of the refrigerant. On leaving the test section, the refrigerant is then condensed and sub-cooled by a chilling loop that removes the heat input from the pre-heater and test section and then it returns from the two-phase refrigerant to a sub-cooled state, which later collects in a receiver and eventually returns to the refrigerant pump to complete the cycle.

The test section is a horizontal counter-flow double tube heat exchanger. The length of the heat exchanger is 2,000 mm. The detailed dimensions of the heat exchanger and the location of the thermocouples are shown in Fig. 2. A photograph of a corrugated tube and nomenclature to describe the geometry is shown in Fig. 3. The dimensions of the test section are shown in Table 1.

The inlet temperature of the water is controlled by a thermostat. A differential pressure transducer and thermocouples are installed in the test section to measure the pressure drop and temperature across the test section. The length between pressure taps is 2,500 mm. In the present study, the pressure of the refrigerant is mainly controlled by a high-pressure limit switch. High-pressure limit switches (Danfoss Type KP 5) are devices for regulating the pressure of a system so that the pressure is maintained near a desired set point pressure in order to prevent the damage to the apparatus.

The refrigerant temperature and tube wall temperature in the test section are measured by T-Type thermocouples. A total of 15 thermocouples are soldered to the top, bottom and at five points along side of the tube as shown in Fig. 2. All the temperature measuring devices are well calibrated in

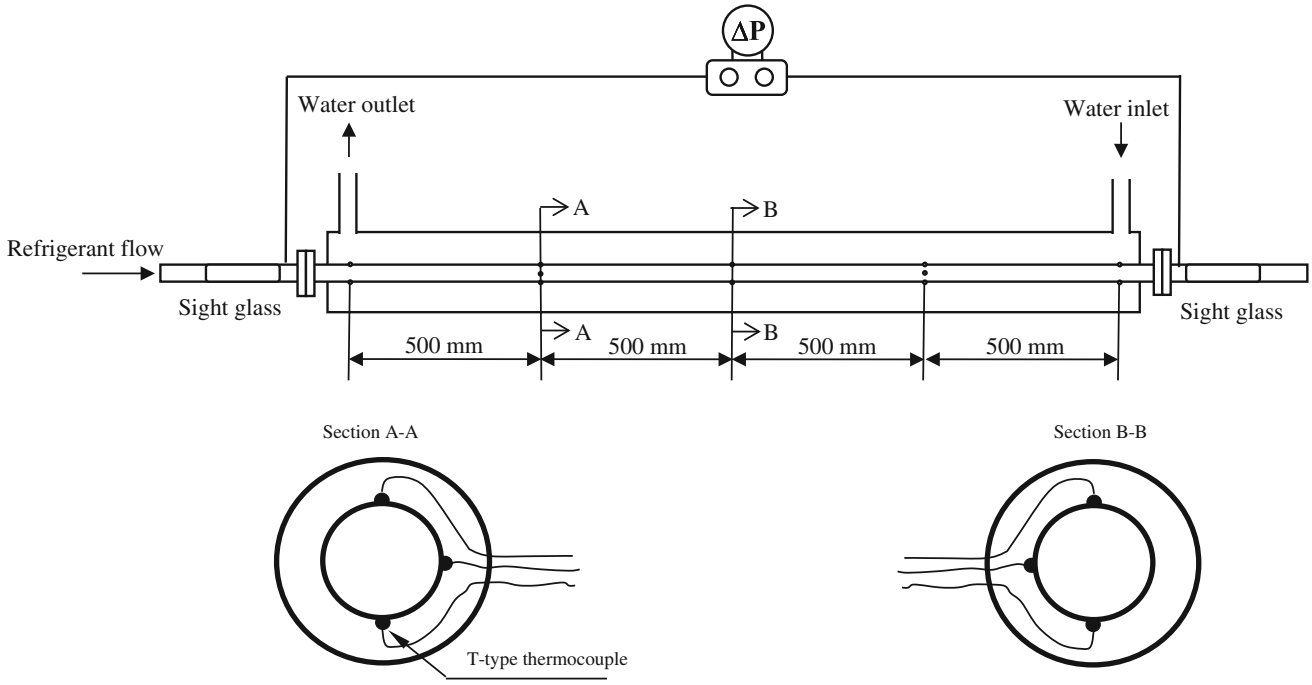

Fig. 2 Schematic diagram of the test section (Laohalertdecha and Wongwises [14], with permission from Elsevier)

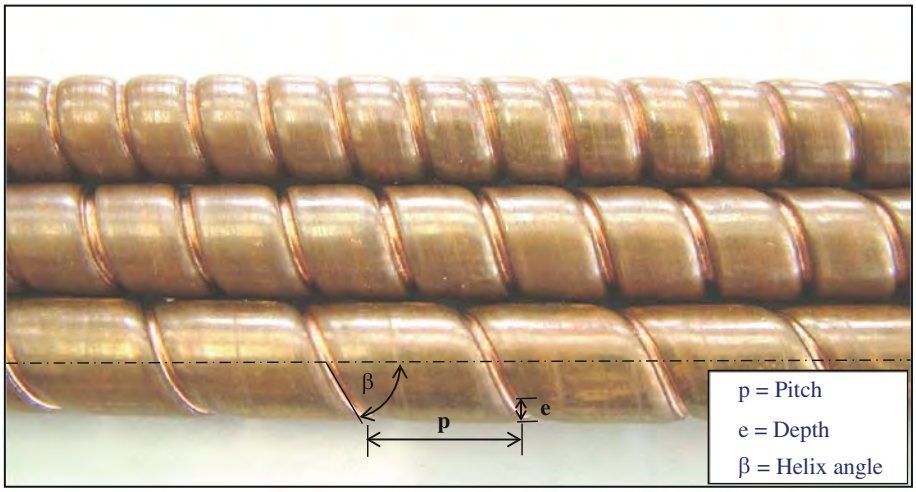

Fig. 3 Photograph of the corrugated tube (Laohalertdecha and Wongwises [16], with permission from Elsevier)

a controlled temperature bath using standard precision mercury glass thermometers. The uncertainty of the temperature measurements as recorded by the data acquisition system is ±0.1 °C. All static pressure taps are mounted on the tube wall. The refrigerant flow meter is a variable area type and specially calibrated in the range of 0.2–3.4 LPM for R-134a by the manufacturer. Also, the differential pressure transducer is calibrated by the manufacturer.

Experiments were conducted with various flow rates, average vapour qualities, heat fluxes and saturation temperatures. In the experiments, the refrigerant flow rate in the test section was controlled by adjusting the speed of the magnetic gear pump. To vary the vapour quality at the inlet of the test section, the heating water flow and the cooling water flow rates were varied by small increments while the refrigerant flow rate was kept constant. The hot water in the test section was re-circulated by a centrifugal pump to supply heat to the refrigerant. During each experiment, the heat transferred from the test section was kept at a desired value. This might be obtained by simultaneously adjusting and controlling the temperature and flow rate of the hot water entering the test section. The system was allowed to approach a steady state before any data was recorded. After stabilisation, the temperature on the tube wall, the

Table 1 The dimensions of the test section

Number	p (mm)	e (mm)	w (mm)	β (degree)	d_i (mm)	L (mm)
1	5.08	1	1	79.47	8.7	2,000
2	5.08	1.25	1	79.47	8.7	2,000
3	5.08	1.5	1	79.47	8.7	2,000
4	8.46	1.5	1	74.20	8.7	2,000
5	6.35	1.5	1	76.56	8.7	2,000
6	Smooth tube				8.7	2,000

Table 2 Uncertainties of measured quantities and calculated parameters

Parameter	Uncertainty
Temperature, T (°C)	±0.1
Pressure drop, ΔP (kPa)	±0.37
Mass flow rate of refrigerant, m_{ref}	±2 %
Mass flow rate of water, m_w	±2 %
Heat transfer rate at test section, Q_{TS}	±10 %
Heat transfer rate at pre-heater, Q_{ph}	±5 %
Evaporation heat transfer coefficient, h	±10 %
Average vapour quality, x	±5 %

temperature of the refrigerant at the locations mentioned above, the inlet and outlet temperatures of the heating water and flow rates of heating water and refrigerant were all recorded. The pressure drop was measured by a differential pressure transducer installed between the inlet and outlet of the test section. The experiments could be carried out by increasing the refrigerant flow rate while the saturation temperature in the test section was kept constant. The accuracy of the direct measurements and the uncertainties in the derived experimental values are shown in Table 2.

3 Data reduction

The data reduction for calculating the two-phase heat transfer coefficient and pressure drop of R-134a flowing in horizontal smooth and corrugated tubes under evaporation conditions can be summarized as follows:

3.1 The inlet vapour quality of the test section ($x_{TS,in}$)

The inlet vapour quality entering the test section can be calculated as follows:

$$x_{TS,in} = \frac{i_{TS,in} - i_{f,T_{TS,in}}}{i_{fg,T_{TS,in}}} \tag{1}$$

The refrigerant enthalpy at the test section inlet ($i_{TS,in}$) is given by:

$$i_{TS,in} = i_{ph,in} + \frac{Q_{ph}}{m_{ref}} \tag{2}$$

The heat transfer rate in the pre-heater (Q_{ph}) is calculated as follows:

$$Q_{ph} = m_{w,ph} c_{p,w} (T_{w,in} - T_{w,out})_{ph} \tag{3}$$

3.2 The outlet vapour quality of the test section ($x_{TS,out}$)

Similarly, Eq. (4) can be used to calculate the exit vapour quality of the test section:

$$x_{TS,out} = \frac{i_{TS,out} - i_{f,T_{TS,out}}}{i_{fg,T_{TS,out}}} \tag{4}$$

The outlet enthalpy of the refrigerant flow is calculated as:

$$i_{TS,out} = i_{TS,in} + \frac{Q_{TS}}{m_{ref}} \tag{5}$$

The heat transfer rate in the test section is obtained from:

$$Q_{TS} = m_{w,TS} c_{p,w} (T_{w,in} - T_{w,out})_{TS} \tag{6}$$

3.3 The inside heat transfer coefficient (h_i)

The inside heat transfer coefficient is calculated as follows:

$$h_i = \frac{1}{\left(\frac{1}{U_i}\right) - \left(\frac{1}{2k}\right) d_i \ln\left(\frac{d_o}{d_i}\right) - \left(\frac{d_i}{d_o}\right)\left(\frac{1}{h_o}\right)} \tag{7}$$

The overall heat transfer coefficient based on the inside surface area (U_i) can be determined by:

$$U_i = \frac{Q_{TS}}{A_i (LMTD)} \tag{8}$$

The logarithmic mean temperature difference is defined as follows:

$$LMTD = \frac{\Delta T_1 - \Delta T_2}{\ln\left(\frac{\Delta T_1}{\Delta T_2}\right)} \tag{9}$$

$$\Delta T_1 = T_{w,out} - T_{ref,in} \tag{10}$$

$$\Delta T_2 = T_{w,in} - T_{ref,out} \tag{11}$$

The outside heat transfer coefficient (h_o) is obtained from:

$$h_o A_o = \frac{Q_{TS}}{T_{w,avg} - T_{wall,avg}} \tag{12}$$

The Nusselt number is determined as:

$$Nu = \frac{hd}{k_l} \tag{13}$$

3.4 The frictional pressure drop (ΔP_f)

The total pressure drop, ΔP_{total}, is expressed as the sum of the three different components, as follows:

$$\Delta P_{total} = \Delta P_f + \Delta P_a + \Delta P_g \tag{14}$$

The gravitational pressure drop (ΔP_g) is zero in a horizontal tube. The acceleration pressure drop, ΔP_a, was proposed by Tran [18]:

$$\Delta P_a = G^2\left(\left(\frac{x_{out}^2}{\rho_v \alpha_{out}} + \frac{(1-x_{out})^2}{\rho_l(1-\alpha_{out})}\right) - \left(\frac{x_{in}^2}{\rho_v \alpha_{in}} + \frac{(1-x_{in})^2}{\rho_l(1-\alpha_{in})}\right)\right) \tag{15}$$

The void fraction, α, can be determined from Zivi's correlation [19] as follows:

$$\alpha = \left(1 + \frac{(1-x)}{x}\left(\frac{\rho_v}{\rho_l}\right)^{\frac{2}{3}}\right)^{-1} \tag{16}$$

The frictional pressure drop, ΔP_f, can be obtained by subtracting the acceleration pressure drop from the total measured pressure drop. The two-phase friction factor is defined in terms of the equivalent mass flux (G_{eq}) proposed by Akers et al. [20], as shown in Eq. (17).

$$f_{tp} = \frac{d_i \Delta P_f \rho_l}{2G_{eq}^2} \tag{17}$$

$$G_{eq} = G\left[(1-x) + x\left(\frac{\rho_l}{\rho_g}\right)^{0.5}\right] \tag{18}$$

3.5 Equivalent Reynolds number (Re_{eq})

The equivalent Reynolds number is defined as:

$$\text{Re}_{eq} = \text{Re}_l + \text{Re}_v\left(\frac{\mu_v}{\mu_l}\right)\left(\frac{\rho_l}{\rho_v}\right)^{0.5} \tag{19}$$

The liquid Reynolds number (Re_l) and vapour Reynolds number (Re_v) can be obtained from Eqs. (20) and (21) as follows:

$$\text{Re}_l = \frac{Gd_i(1-x)}{\mu_l} \tag{20}$$

$$\text{Re}_v = \frac{Gd_i x}{\mu_v} \tag{21}$$

4 Mathematical modeling

In this present simulation model, the test section is a horizontal counter-flow concentric double-tube heat exchanger with refrigerant flows in the inner tube, whereas hot water flows in the annulus. In addition, the outer tube surface is well-insulated. The following assumptions are employed.

1. Steady, one-dimensional flow of the refrigerant is analysed.
2. Heat loss along the test section is negligible.

4.1 Heat transfer coefficient

The concept of the overall heat transfer coefficient based on the inside surface is applied in the heat exchanger as shown below:

$$\frac{1}{U_i A_i} = \frac{1}{h_i A_i} + \frac{\ln(d_o/d_i)}{2\pi kL} + \frac{1}{h_o A_o} \tag{22}$$

The overall heat transfer coefficient (U_i) is determined from Eq. (8). The outside heat transfer coefficient (h_o) was proposed by Laohalertdecha and Wongwises' [17] correlation as follows:

$$Nu_o = 0.006\text{Re}_{eq}^{0.8}\,\text{Pr}_l^{\frac{1}{3}}\left(\frac{ep}{D_{eq}^2}\right)^{-0.1} \tag{23}$$

where Nu_o is determined by:

$$Nu_o = \frac{h_o D_{eq}}{k_w} \tag{24}$$

where D_{eq} is defined as follows:

$$D_{eq} = \frac{D_i^2 - d_o^2}{d_o} \tag{25}$$

Therefore, the inside heat transfer coefficient can be calculated as Eq. (7). The average heat transfer coefficient can be calculated by:

$$h_{avg} = \frac{1}{L}\int_0^z h_z dz \tag{26}$$

4.2 Pressure drop

The total pressure drop (ΔP_{total}) is expressed as the sum of the three different components, as shown in Eq. (14). The frictional pressure drop of the refrigerant flowing inside the corrugated tube is calculated as follows:

$$\Delta P_f = \frac{2f_{tp}G_{eq}^2 L}{d_i \rho_l} \tag{27}$$

Equivalent mass flux (G_{eq}) is determined from Eq. (18). The two-phase friction factor (f_{tp}) is determined by using the correlation proposed by Laohalertdecha and Wongwises [17] as follows:

$$f_{tp} = 33.368\text{Re}_{eq}^{-0.68}\left(\frac{ep}{d_i^2}\right)^{0.1} \tag{28}$$

The equivalent Reynolds number (Re_{eq}) is defined as Eq. (19). From Eq. (18), the average quality can be

determined by:

$$x = \frac{x_{ref,in} + x_{ref,out}}{2} \tag{29}$$

The accelerational pressure drop, ΔP_a, is defined by Eq. (15). For the horizontal tube, the gravitational pressure drop (ΔP_g) is zero.

5 Solution methodology

Figure 4 shows the details of the solution method in the types of flow diagrams. The selected input parameters used in the present simulation model are the corrugated tube geometries, inlet and outlet water temperatures, inlet temperature of the refrigerant, the water and refrigerant mass flow rates, and the inlet quality of the refrigerant.

The first step in the simulation model is intended to find the limited scope of calculation by guessing the values of the outlet refrigerant temperature ($T_{ref,out}$), as shown in Fig. 4. The outlet refrigerant temperature can be converted into the outlet pressure. The calculation is terminated when the error between the total pressure drop found using calculation Eq. (14) and that shown in the saturation table is smaller than 10^{-3}.

$$\text{if } \frac{(\Delta P_{total})_{cal} - (\Delta P_{total})_{sat.table}}{(\Delta P_{total})_{sat.table}} > 10^{-3}$$

then change value of T_{guess}

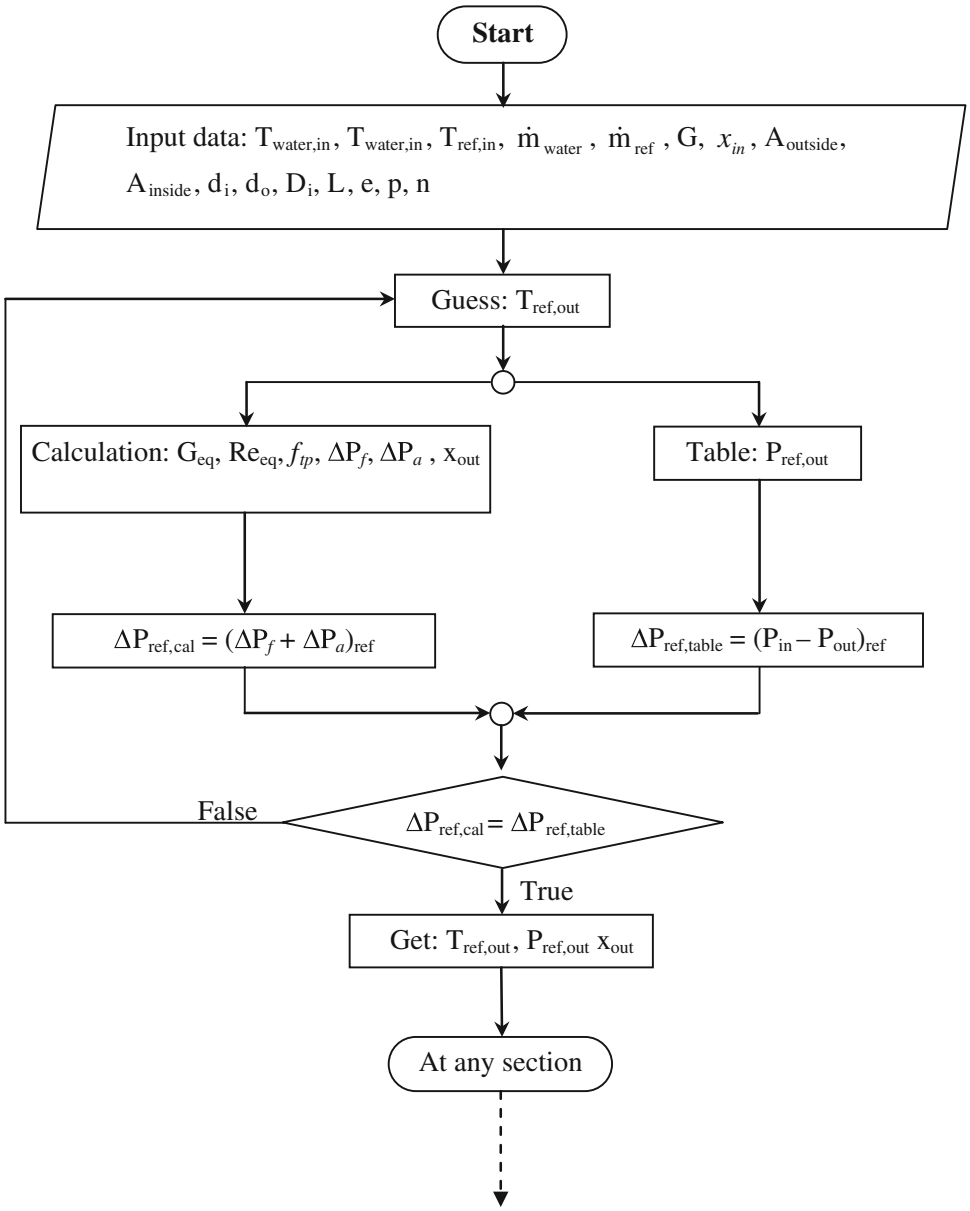

Fig. 4 Flow diagram of simulation method

Fig. 4 continued

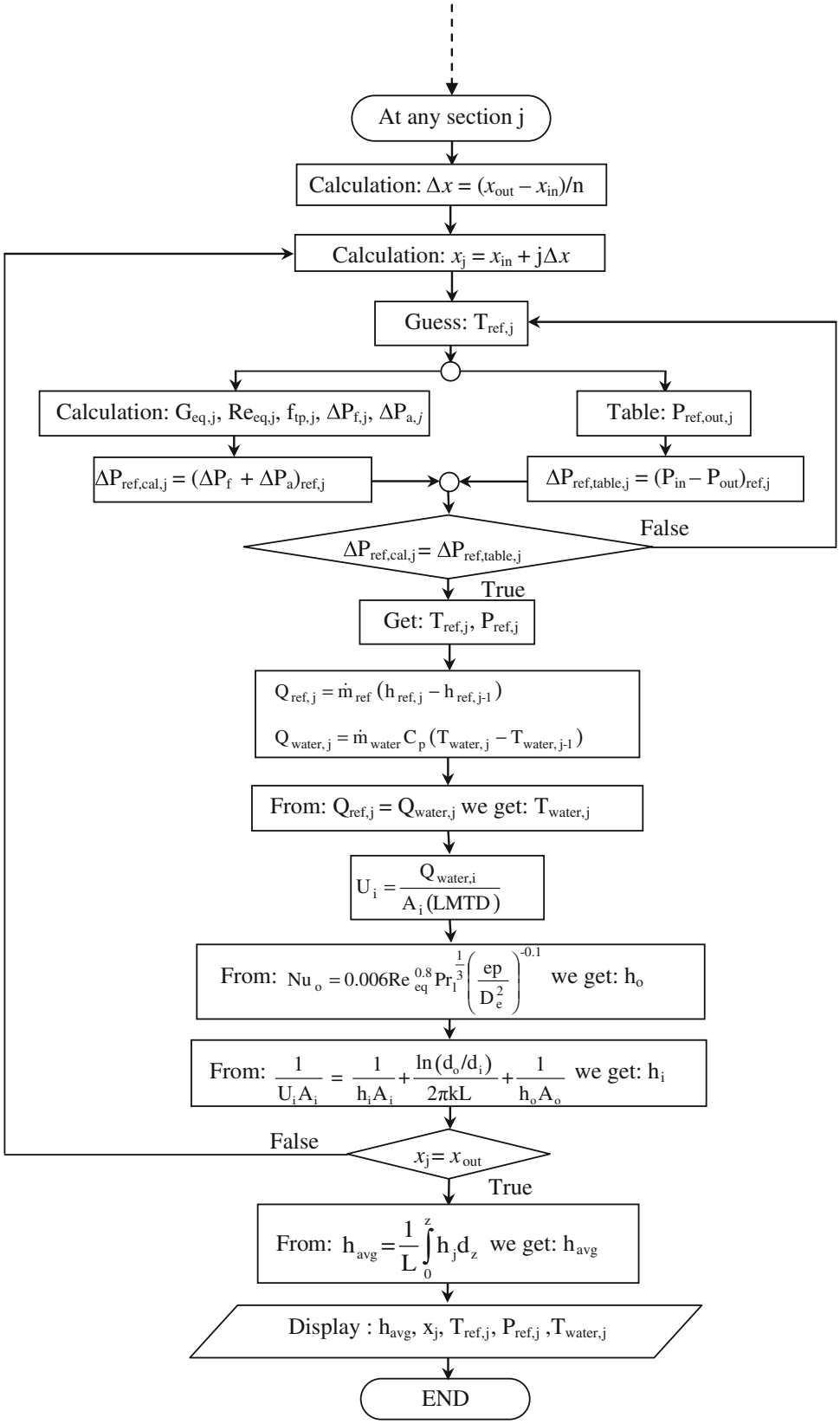

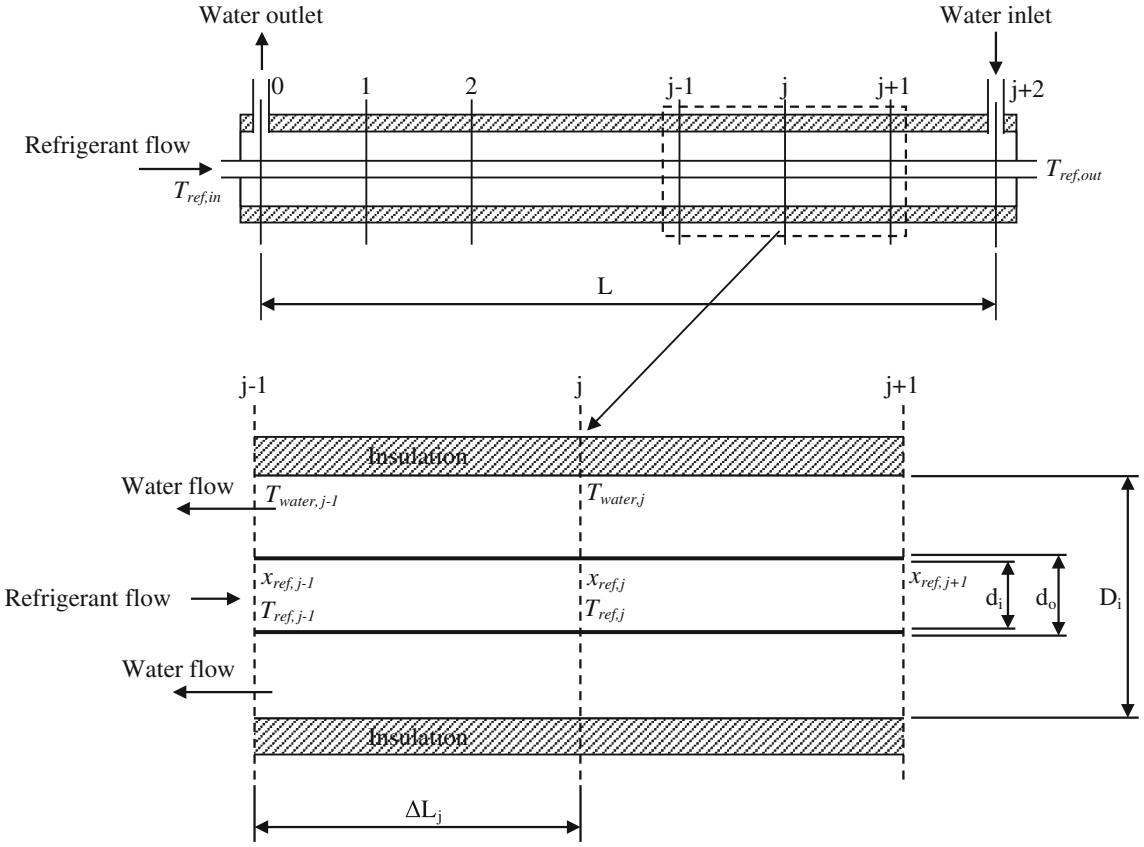

Fig. 5 Schematic diagram of simulation approach for a corrugated tube

if $\dfrac{(\Delta P_{total})_{cal}-(\Delta P_{total})_{sat.table}}{(\Delta P_{total})_{sat.table}} \leq 10^{-3}$

then $T_{guess} \cong T_{ref,out}$

The total pressure drop obtained from the saturation table is the pressure difference between the inlet pressure and outlet pressure of the test section. The REFPROP program, version 6.01 [21] is used to calculate the thermophysical properties of the refrigerant. Once the $T_{ref,out}$ is known, the outlet quality is obtained.

As shown in Fig. 5, the corrugated tube can be divided into 16 sections by constant quality increments. The quality of each section j is calculated by:

$$\Delta x = \frac{\left(x_{ref,out} - x_{ref,in}\right)}{n} \tag{30}$$

$$x_{ref,j} = x_{ref,in} + j\Delta x \tag{31}$$

where n is the number of sections.

$j = 1, 2 \ldots, 16$

The corrugated tube length of each section can be calculated by:

$$\Delta L_j = \frac{L}{n} \tag{32}$$

Thereafter, the temperature and pressure of the refrigerant at the outlet of each section can be calculated by a process similar to the one shown in Fig. 4. The outlet water temperature is determined by energy balance between the refrigerant side and the water side.

$$Q_{ref,j} = Q_{water,j} \tag{33}$$

$$\dot{m}_{ref}\left(h_{ref,j} - h_{ref,j-1}\right) = \dot{m}_{water} C_p \left(T_{water,j} - T_{water,j-1}\right) \tag{34}$$

Rearranging Eq. (34) yields:

$$T_{water,j} = \frac{\dot{m}_{ref}}{\dot{m}_{water} C_p}\left(h_{ref,j} - h_{ref,j-1}\right) + T_{water,j-1} \tag{35}$$

The inside and outside heat transfer coefficients are calculated by Eqs. (7) and (23), respectively. The whole process of section-by-section analysis is then repeated until $x_{ref,j} = x_{ref,out}$. Finally, the average heat transfer coefficient can be calculated by:

$$h_{avg} = \frac{1}{L}\int_0^z h_j dz \tag{36}$$

6 Results and discussion

The effects of the corrugation pitch and depth on the evaporation heat transfer coefficient and frictional pressure drop of R-134a flowing through horizontal corrugated tubes are studied experimentally. Moreover, this work presents the results of a simulation model used to describe the heat transfer coefficient and pressure drop of R-134a flowing through a corrugated tube. Before measuring the evaporation heat transfer coefficient and pressure drop, a single-phase liquid flowing through a smooth tube is first conducted to check the energy balance. The results indicate that the energy balance between the cold water and the refrigerant is within 10 % for all runs [14]. Moreover, the experimental Nusselt number and the frictional pressure drop are compared with well-known correlations. The results show that almost all correlations are in agreement with the present data [15].

6.1 Effects of depth and pitch on the heat transfer coefficient

Figure 6 displays the effect of depth on the evaporation heat transfer coefficient at $G = 300$ kg/m^2 s, $q'' = 10$ kW/m^2, and $T_{sat} = 20$ °C. The results show that the average heat transfer coefficient increases with increasing average vapor quality. This is because at higher vapor quality, the higher vapor velocity led to higher interfacial shear stress between the vapor core and liquid film. The increasing interfacial shear stress causes the liquid film thinner, resulting in lower thermal resistance. Therefore, the average heat transfer coefficient tends to increase as the average vapor quality increases. The average heat transfer coefficients at the same average quality obtained from the corrugated tubes are clearly higher than those obtained from the smooth tube across the range of the average quality because the corrugated surface has a simultaneous effect on the axial flow, secondary fluid motion, and swirl mixing. Moreover, the corrugation depth has a significant effect on the heat transfer coefficient because the tube with higher corrugation depth yields higher turbulence. The maximum heat transfer enhancement is obtained up to 22, 19 and 13 % for a depth of 1.5, 1.25, and 1 mm, respectively, in comparison with the smooth tube.

Figure 7 shows the effect of corrugation pitch on the average heat transfer coefficient at $G = 300$ kg/m^{2}s, $q'' = 5$ kW/m^2, and $T_{sat} = 15$ °C. The average heat transfer coefficient increases with decreasing corrugation pitch. The reason for this is similar to the explanation above. In other words, the tube with lower corrugation pitch promotes more turbulence by increasing the amount of the swirl flow induced by higher number of corrugation. As a consequence, the highest heat transfer coefficient can be obtained by the tube with the lowest corrugation pitch. The maximum value of heat transfer coefficient obtained from a pitch of 5.08 mm is 21 % in comparison with the smooth tube.

6.2 Effects of depth and pitch on frictional pressure drop

As shown in Figs. 8 and 9, the effects of depth and pitch on frictional pressure drop are plotted against the average vapor quality. In the smooth tube and corrugated tubes, the increasing pressure drop depends on increased average vapor quality. This is because the vapor velocity is increased at higher vapor quality, resulting in more shear

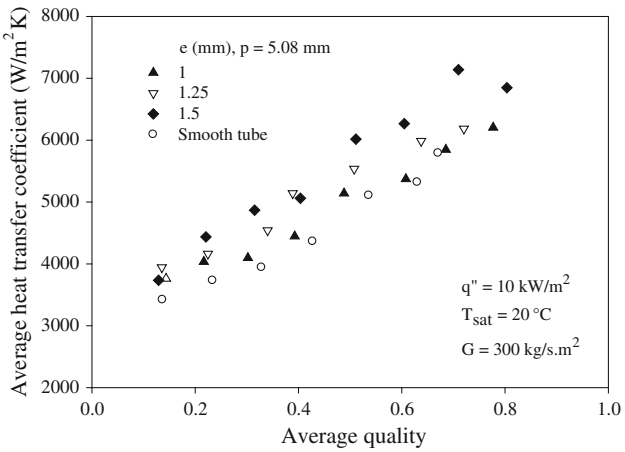

Fig. 6 Average heat transfer coefficient versus average quality at $T_{sat} = 20$ °C, $G = 300$ kg/m^{2}s and $q'' = 10$ kW/m^2 for different depths

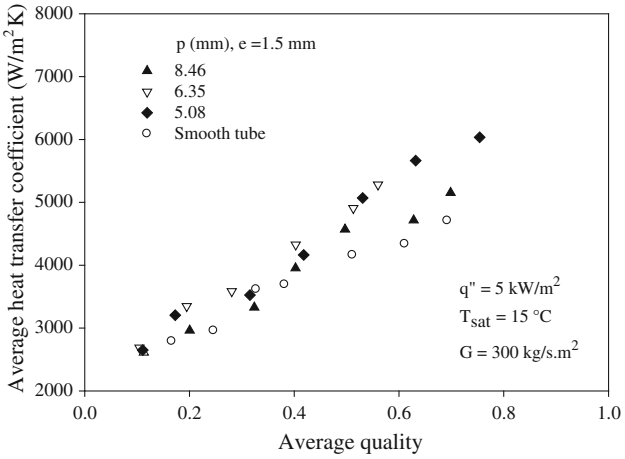

Fig. 7 Average heat transfer coefficient versus average quality at $T_{sat} = 15$ °C, $G = 300$ kg/m^{2}s and $q'' = 5$ kW/m^2 for different pitches

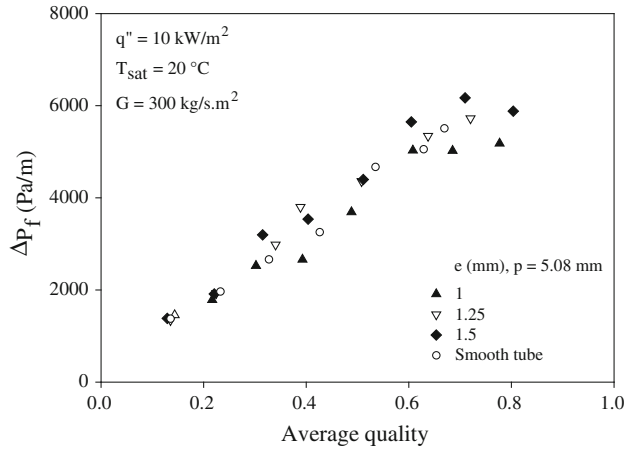

Fig. 8 Frictional pressure drop versus average quality at $T_{sat} = 20$ °C, $G = 300$ kg/m^{2}s and $q'' = 10$ kW/m^2 for different depths

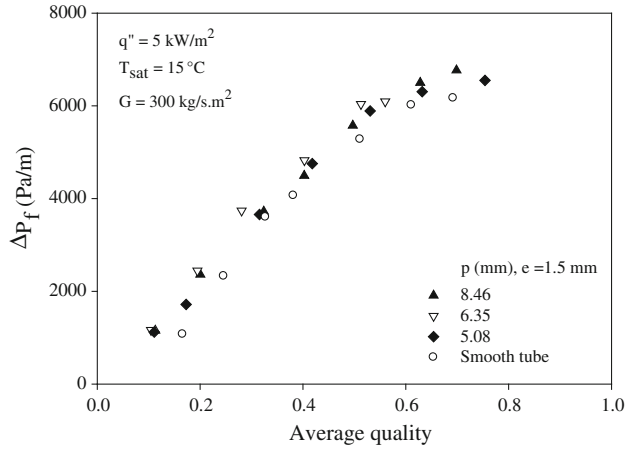

Fig. 9 Frictional pressure drop versus average quality at $T_{sat} = 15$ °C, $G = 300$ kg/m^{2}s and $q'' = 5$ kW/m^2 for different pitches

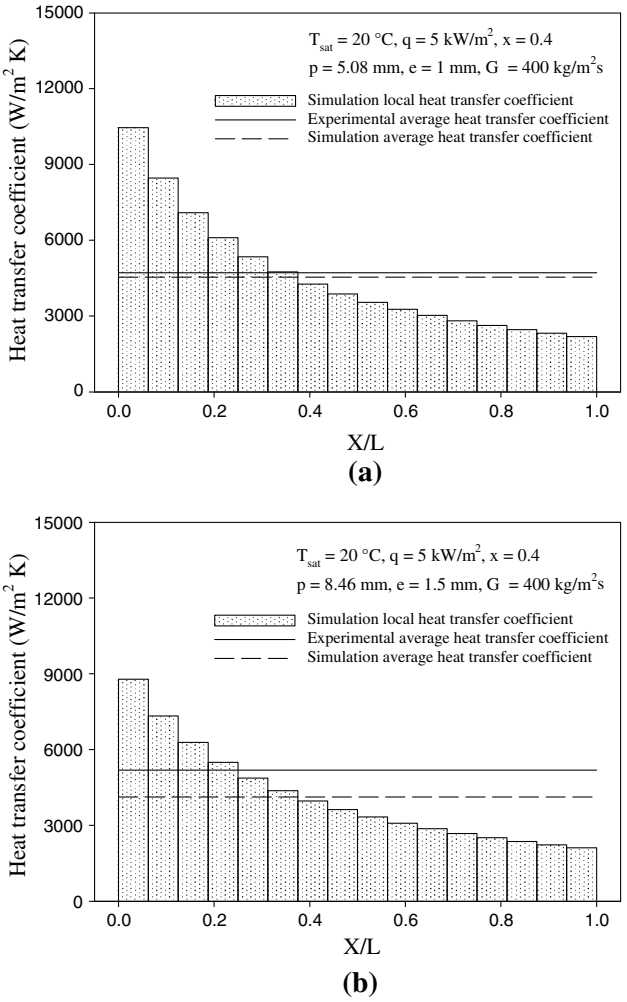

Fig. 10 Comparison of the heat transfer coefficient with those obtained from measured data and calculated values from the present model

stress at the interface of the vapor and liquid film, causing the increase of flow turbulence. At the same quality, the pressure drop obtained from the corrugated tube is higher than that from a smooth tube because the corrugation surface has an effect on the turbulent flow. In other words, the corrugation surface produces rotational flow, which led to more effect on turbulence of the fluid flow. However, the effects of the corrugation pitch and depth on the frictional pressure drop are not significant. This may be due to very small difference in variation of corrugation pitch and depth. The maximum value of frictional pressure drop obtained from a pitch of 5.08 mm and a depth of 1.5 mm is about 19 % in comparison with the smooth tube at the mass flux of 300 kg/m^{2}s, heat flux of 10 kW/m^2, and saturation temperature of 20 °C.

6.3 Simulation results

Figure 10 shows the distributions of the simulation local heat transfer coefficient, simulation average heat transfer coefficient, and experimental average heat transfer coefficient along the test section (X/L). The bar chart represents the predicted local heat transfer coefficient obtained from the proposed simulation. The solid line and the dashed line represent the average values for the heat transfer coefficient obtained from the measured data and the predicted value from the simulation, respectively. These figures show that the simulation local heat transfer coefficient decreases with increasing tube length. Compared with the experimental data, the results show that the simulation average heat transfer coefficient has good agreement with the measured data. In addition, the average difference of the heat transfer coefficient between the simulation and experimental data is about 10 %.

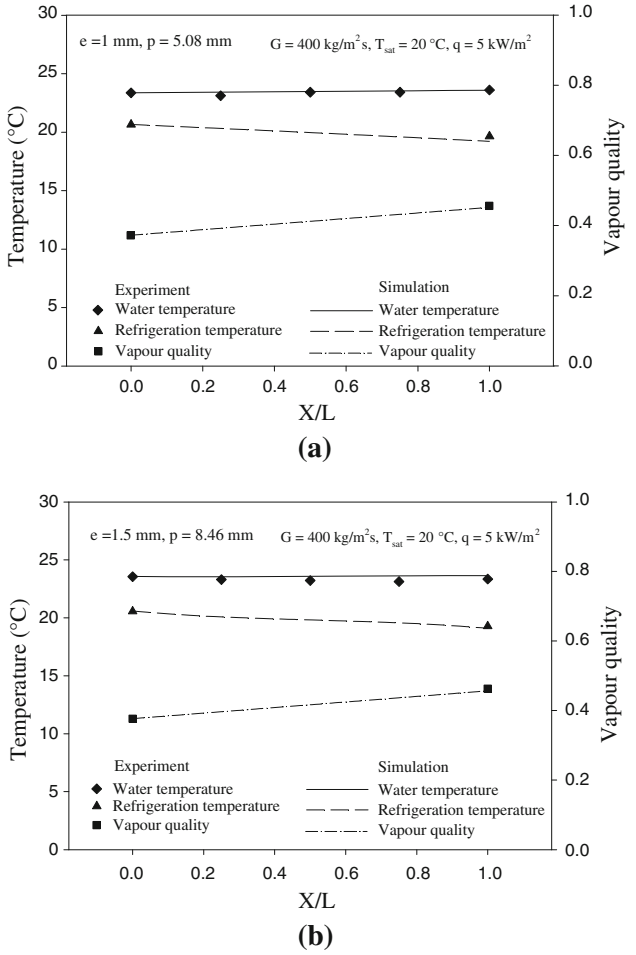

Fig. 11 Comparison of the water temperature, refrigerant temperature and vapor quality with those obtained from measured data and calculated values from the present model

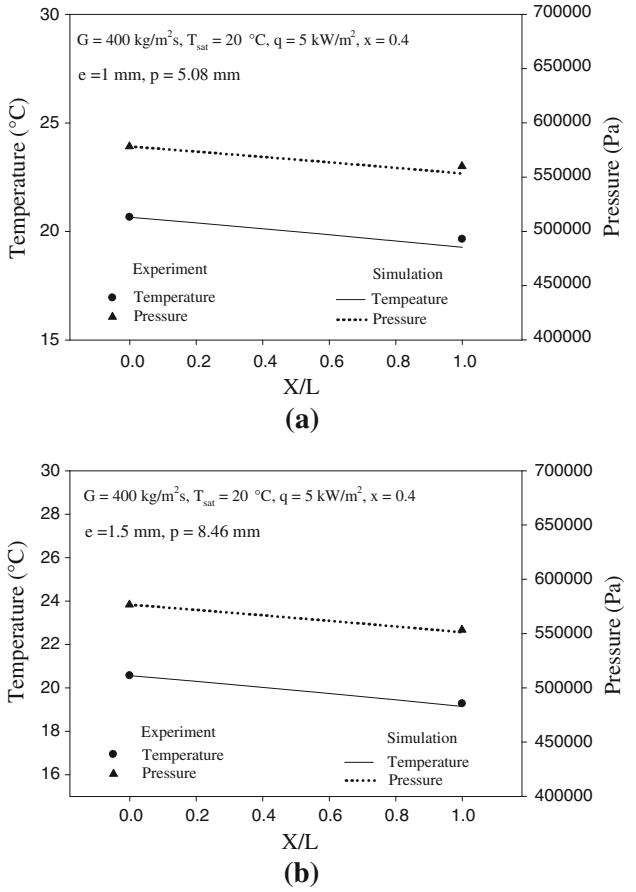

Fig. 12 Comparison of the refrigerant temperature and pressure with those obtained from measured data and calculated values from the present model

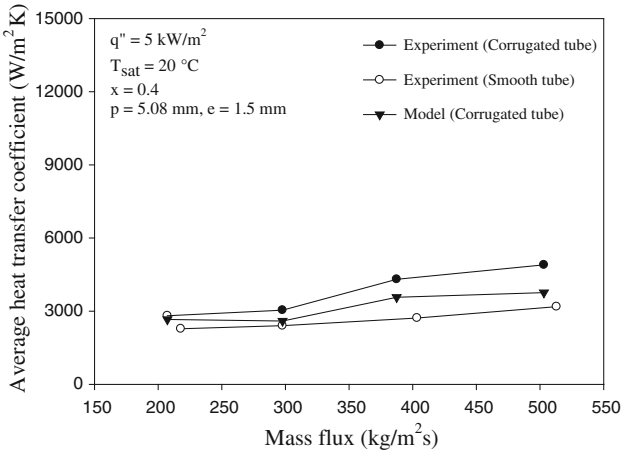

Fig. 13 Calculated values from the present model versus experimental data

Figure 11 displays the temperature and vapour quality distribution along the test tube obtained from the measured data and then compared with the simulation value. The lines and the symbols represent the simulation results and the experimental data, respectively. The results show that the refrigerant temperature decreases with the axial length of the tube, which corresponds with the saturation pressure. The vapour quality increases gradually along the tube because the energy from the water is supplied to the refrigerant. Moreover, the results also indicate that the inlet water temperatures are higher than the outlet water temperatures due to the evaporation condition. However, the simulation results have good agreement with the experimental data.

Figure 12 shows the saturation temperature and pressure distribution along the test tube obtained from the measured data and compared with the simulation values. The results show that the saturation temperature and pressure decrease along the tube due to friction. In addition, the average difference of the pressure drop between the simulation and experimental data are about 15 %.

Figure 13 illustrates the comparison between the average heat transfer coefficients obtained from the simulation

data and those obtained from experimental data. The results show that all of the simulation data are lower than the experimental data obtained from the corrugated tube within 2–10 %. However, all the simulation data are higher than the measured data obtained from the smooth tube.

7 Conclusion

Experimental and simulation studies of the evaporation heat transfer coefficient and pressure drop of R-134a flowing through corrugated tubes were conducted. A new simulation model was presented for predicting the heat transfer behavior of the refrigerant flowing through corrugated tubes. The 2.0 m test section is a tube-in-tube heat exchanger placed in the horizontal direction in which a refrigerant flows in the inner tube and hot water flows in the annulus. The corrugation pitches used in this study were 5.08, 6.35, and 8.46 mm. Similarly, the corrugation depths were 1, 1.25, and 1.5 mm, respectively. The measured heat transfer coefficient and pressure drop were presented. It was found that the heat transfer coefficient and pressure drop increased with increasing average vapour quality as well as mass flux. The heat transfer coefficient and pressure drop obtained from the corrugated tubes were higher than those of a conventional smooth tube under all test conditions. The corrugation pitches and depths had a significant effect on the heat transfer coefficient for all tested conditions. However, based on our test section, the effects of the corrugation pitch and depth on the frictional pressure drop were not significant. The maximum heat transfer coefficient and pressure drop obtained from the corrugated tube were up to 22 and 19 % higher than those obtained from the smooth tube, respectively. Moreover, the average difference of the heat transfer coefficient and pressure drop between the simulation model and the experimental data were about 10 and 15 %, respectively.

Acknowledgments The present study was supported financially by the Thailand Research Fund, the National Research University Project and National Science and Technology Development Agency, whose guidance and assistance are gratefully acknowledged. The third and fourth authors would like to thank Professor Somchai Wongwises for providing him fellowships during his research in the Department of Mechanical Engineering, King Mongkut's University of Technology Thonburi.

References

1. Nozu S, Honda H, Nakata H (1995) Condensation of refrigerants CFC11 and CFC113 in the annulus of a double-tube coil with an enhanced inner tube. Exp Therm FluidSci 11:40–51
2. Nozu S, Honda H, Nishida S (1995) Condensation of a zeotropic CFC 114-CFC 113 refrigerant mixture in the annulus of a double-tube coil with an enhanced inner tube. Exp Therm FluidSci 11:364–371
3. Dong Y, Huixiong L, Tingkuan C (2001) Pressure drop, heat transfer and performance of single-phase turbulent flow in spirally corrugated tubes. Exp Therm FluidSci 24:131–138
4. Barba A, Rainieri S, Spiga M (2002) Heat transfer enhancement in a corrugated tube. Int Commun Heat Mass Transfer 29:313–322
5. Rainieri S, Pagliarini G (2002) Convective heat transfer to temperature dependent property fluids in the entry region of corrugated tubes. Int J Heat Mass Transf 45:4525–4536
6. Zimparov V (2001) Enhancement of heat transfer by a combination of three-start spirally corrugated tubes with a twisted tape. Int J Heat Mass Transf 44:551–574
7. Zimparov V (2002) Enhancement of heat transfer by a combination of a single-start spirally corrugated tubes with a twisted tape. Exp Therm FluidSci 25:535–546
8. Zimparov V (2004) Prediction of friction factors and heat transfer coefficients for turbulent flow in corrugated tubes combined with twisted tape inserts. Part 1: friction factors. Int J Heat Mass Transf 47:589–599
9. Zimparov V (2004) Prediction of friction factors and heat transfer coefficients for turbulent flow in corrugated tubes combined with twisted tape inserts. Part 2: heat transfer coefficients. Int J Heat Mass Transf 47:385–393
10. Rousseau PG, Eldik MV, Greyvenstein GP (2003) Detailed simulation of fluted tube water heating condenser. Int J Refrig 26:232–239
11. Vicente PG, Garcia A, Viedma A (2004) Experimental investigation on heat transfer and friction factor characteristics of spirally corrugated tubes in turbulent flow at different Prandtl number. Int J Heat Mass Transf 47:671–681
12. Vicente PG, Garcia A, Viedma A (2004) Mixed convection heat transfer and isothermal pressure drop in corrugated tubes for laminar and transition flow. Int Commun Heat Mass Transf 31:651–662
13. Targanski T, Cieslinski JT (2007) Evaporation of R407C/oil mixtures inside corrugated and micro-fin tubes. Appl Therm Eng 27:2226–2232
14. Laohalertdecha S, Wongwises S (2010) The effects of corrugation pitch on the condensation heat transfer coefficient and pressure drop of R-134a inside horizontal corrugated tube. Int J Heat Mass Transf 53:2924–2931
15. Laohalertdecha S, Wongwises S (2011) An experimental study into the evaporation heat transfer and flow characteristics of R-134a refrigerant flowing through corrugated tubes. Int J Refrig 34:280–291
16. Laohalertdecha S, Wongwises S (2011) Condensation heat transfer and flow characteristics of R-134a flowing through corrugated tubes. Int J Heat Mass Transf 54:2673–2682
17. Laohalertdecha S, Wongwises S (2011) Correlations for evaporation heat transfer coefficient and two-phase friction factor for R-134a flowing through corrugated tubes. Int Commun Heat Mass Transf 38:1406–1413
18. Tran TN (1998) Pressure drop and heat transfer study of two-phase flow in small channels. Ph.D. Dissertation, Texas Tech University, Lubbock, Texas
19. Zivi SM (1964) Estimation of steady-state steam void-fraction by mean of the principle of minimum entropy production. Trans ASME J Heat Transf 86:247–252
20. Akers WW, Deans HA, Crasser OK (1959) Condensing heat transfer within horizontal tubes. Chem Eng Prog Symp 55:171–176
21. REFPROP (1998) Refrigerant properties database version 6.01. NIST, Gaithersburg

International Journal of Heat and Mass Transfer 73 (2014) 186–194

Contents lists available at ScienceDirect

International Journal of Heat and Mass Transfer

journal homepage: www.elsevier.com/locate/ijhmt

Heat transfer characteristics and pressure drop of COOH-functionalized DWCNTs/water nanofluid in turbulent flow at low concentrations

Mohammad Hemmat Esfe [a,*], Seyfolah Saedodin [a], Omid Mahian [b,c,*], Somchai Wongwises [c]

[a] Faculty of Mechanical Engineering, Semnan University, P.O. Box 3513119111, Semnan, Iran
[b] Young Researchers and Elite Club, Mashhad Branch, Islamic Azad University, Mashhad, Iran
[c] Fluid Mechanics, Thermal Engineering and Multiphase Flow Research Lab. (FUTURE), Department of Mechanical Engineering, Faculty of Engineering, King Mongkut's University of Technology Thonburi, Bangmod, Bangkok 10140, Thailand

ARTICLE INFO

Article history:
Received 28 September 2013
Received in revised form 31 January 2014
Accepted 31 January 2014

Keywords:
Heat transfer
Pressure drop
Functionalized carbon nanotube
Turbulent flow

ABSTRACT

In this paper, an experimental study is performed to assess the heat transfer characteristics and pressure drop of low concentrations of a new class of nanotubes, i.e. COOH-functionalized double-walled carbon nanotubes (DWCNTs) suspended in water under turbulent flow in a double tube heat exchanger. First, the thermal conductivity and viscosity of nanofluids at volume fractions of 0.01%, 0.02%, 0.05%, 0.1%, 0.2%, and 0.4% are measured and corresponding correlations are presented. Next, the heat transfer and pressure drop of the nanofluids through the double tube heat exchanger are evaluated. The results indicate that even the use of low concentration of the nanofluid, i.e. 0.4%, leads to a remarkable increase in heat transfer coefficient (by 32%) in comparison with the distilled water. On the other hand, the pressure drop due to using the volume fraction of 0.4% raised by 20%. Finally, analysis of the heat transfer and pressure drop data via thermal performance factor reveals that in spite of the pressure drop penalty, the COOH-functionalized DWCNTs/water nanofluid with volume fraction of 0.4% is a good option to use in the double tube heat exchanger.

1. Introduction

In recent years, there has been an increasing interest in nanofluids and their applications in various thermal engineering devices. Application of nanofluids is established in many fields such as cooling of electronic devices, nuclear reactors, engine cooling, solar energy, cooling and heating of buildings, and so on [1,2].

The physical and chemical specifications of the nanoparticles and the base fluid will determine the thermal characteristics of nanofluids. Therefore, the use of a suitable type of nanoparticles is very important to have a nanofluid with a high efficiency. Some types of nanoparticles such as aluminium oxide, titanium dioxide, copper oxide, copper, zinc oxide, silicon dioxide, silver and carbon nanotubes are the most common particles used in the literature. In the present work, a new type of carbon nanotubes i.e. COOH-functionalized double-walled carbon nanotubes (DWCNTs) has been used. The heat transfer and pressure drop due to the suspension of very low volume fractions of this new type of nanoparticles in water are estimated under turbulent flow in a double tube heat exchanger.

Here, a brief review of the experimental studies on the nanofluid flow in the double tube heat exchangers under the turbulent regime is performed.

Yu et al. [3] performed the experiments on the silicon carbide/water nanofluid flow in a circular tube and a range of Reynolds number between 3000 and 13,000. They concluded that using nanofluid with volume fraction of 3.7% leads to heat transfer enhancement by 60%. Sundar et al. [4] investigated the turbulent flow and pressure drop of Al_2O_3/water nanofluid in a circular tube where the tube is equipped with twisted tapes. Their results showed that in the range of H/D tested, the heat transfer coefficient is enhanced by 23% for the case of the tube having tape insert compared to the plain tube.

Farajollahi et al. [5] studied the turbulent flow of γ-Al_2O_3/water and TiO_2/water nanofluids in a double tube heat exchanger for the Peclet numbers between 20,000 and 60,000. They found the optimum nanofluid concentration in which the heat transfer is maximized. Duangthongsuk and Wongwises [6–8] investigated the TiO_2/water nanofluid flow in a double tube heat exchanger under the turbulent regime. They investigated the effects of nanofluid

* Corresponding authors. Tel.: +98 9131680130.
E-mail addresses: M.hemmatesfe@gmail.com (M. Hemmat Esfe), omid.mahian@gmail.com (O. Mahian).

http://dx.doi.org/10.1016/j.ijheatmasstransfer.2014.01.069
0017-9310/

concentration, using different thermophysical models on the heat transfer characteristics and pressure drop of the nanofluid flow. Duangthongsuk and Wongwises [8] conducted the tests for volume fractions between 0.2% and 2% and found that the optimum particle loading is 1% in which the heat transfer is maximized. Sundar and Sharma [9] accomplished the experiments for Al_2O_3/water nanofluid flow through a plain tube where the Reynolds number changes in the range of 10,000 to 22,000. They studied the effects of inserting the tapes with different twist ratios inside the tube on the nanofluid flow and heat transfer. Based on the experimental results, they suggested suitable correlations to estimate the Nusselt number and friction factor. Zhang et al. [10] examined the effects of nanoparticle size (three different sizes i.e. 23, 51, 76 nm) on the heat transfer of CuO/water nanofluids in the turbulent flow. They perceived that using nanoparticles with a bigger size leads to higher heat transfer rate. Amrollahi et al. [11] measured the heat transfer rate of functionalized multi walled carbon nanotubes suspended in water as the base fluid under laminar and turbulent regimes. In their work, the nanofluid flows through a horizontal circular tube in entrance region. They reported the increases of 33–40% in heat transfer coefficient where the working fluid changes from pure water to the nanofluid with weight fraction of 0.25%.

Hojjat et al. [12,13] performed the tests on the turbulent flow of three types of nanoparticles including Al_2O_3, CuO, and TiO_2 suspended in an aqueous solution of carboxymethyl cellulose in a circular tube so that the nanofluids have a non-Newtonian behaviour.

Suresh et al. [14] studied the heat transfer and friction factor of CuO/water nanofluid in the Reynolds number range of 2500 to 6000 with the simple and helically dimpled tubes under constant heat flux boundary conditions. They revealed that using the nanofluid with concentration of 0.3% through the dimpled tube leads to 39% heat transfer enhancement in comparison with the case in which the pure water flows in the simple tube. Tumuluri et al. [15] investigated experimentally the turbulent flow of the nanofluids which are combined with multi-walled carbon nanotubes (MWCNT) and microencapsulated phase change materials (MPCMs) through a circular tube under constant heat flux. Suresh et al. [16] inserted spiral rods inside a circular tube and investigated the heat transfer and friction factor of Al_2O_3/water nanofluid with the maximum volume fraction of 0.5%. They reported a maximum heat transfer enhancement by 48%. Godson et al. [17] studied the heat transfer and pressure drop due to silver/water nanofluid in a counter flow heat exchanger under laminar and turbulent regimes. Their results indicated that using the nanofluid with the concentration of 0.9%, increases the heat transfer coefficient about 70%. Arani and Amani [18] performed their tests on the TiO_2/water nanofluid in a horizontal double tube counter flow heat exchanger where the Reynolds number changes between 8000–51,000. They concluded that using nanofluid at the Reynolds numbers lower than 30,000 is more advantageous by considering the heat transfer rate and pumping power. Darzi et al. [19] tested the heat transfer and pressure drop due to SiO_2/water nanofluid in corrugated tubes. Azmi et al. [20] investigated the turbulent flow of SiO_2/water nanofluid in a circular tube under constant heat flux where the nanofluid concentration does not exceed 4% and the Reynolds number is between 5000 and 27,000. They found the optimum volume fraction of nanoparticles in which the heat transfer rate is maximized. Recently, Esfe et al. [21] investigated the flow of MgO nanofluids with volume fractions less than 1% in a circular tube. The range of Reynolds number was between 3000 and 18,000. They reported remarkable heat transfer enhancement due to using nanofluids. To save the space, other papers in this field are not reviewed, but the readers can refer to the literature [22–26].

The aim of the present work is to investigate the turbulent flow of a new type of nanofluids i.e. COOH-functionalized double-walled carbon nanotubes suspended in water through a double tube heat exchanger. First, the thermal conductivity and viscosity of nanofluids are measured, then the tests are carried out in the range of Reynolds numbers between 4000–31,000 and low concentrations of the nanofluids (up to 0.4%). The results of heat transfer and pressure drop are reported for different volume fractions of nanoparticles.

2. Nanofluid preparation

In the most of studies on the flow and heat transfer of nanofluids, common nanoparticles such as Al_2O_3, TiO_2, and Cu are used as the additives to the base fluids. In this study, COOH-functionalized double-walled carbon nanotubes with purity of more than 60% (supplied by US research nanomaterials, Inc) are dispersed in water to prepare low volume fractions of nanofluids i.e. 0.01%, 0.02%, 0.05%, 0.1%, 0.2%, and 0.4%. A TEM image of COOH-functionalized DWCNTs is shown in Fig. 1 to display an approximation of the size and shape of the particles. It should be noted that by functionalizing the carbon nanotubes with COOH, the dispersion of nanotubes will be better in the base fluid. Therefore; there is no need to use a surfactant to have a stable suspension. In this way, the negative effects of surfactant on the thermophysical properties will not be observed. Properties of the nanotubes have been presented in Table 1.

For a given volume fraction of the nanofluid, a specific amount of COOH-functionalized DWCNTs is added to the distilled water and then a magnetic stirrer is used to mix the particles and water for 2 h. After mixing, the suspension is inserted inside an ultrasonic processor (Hielscher company, Germany) with the power of 400 W and frequency of 24 kHz for 5 h. This breaks down the agglomeration between the particles and avoids the sedimentation issue. The prepared samples are stable for a long time (at least 1 week) and no sedimentation is observed with naked eyes.

3. Thermophysical properties of nanofluids

Determination of thermophysical properties of nanofluids is important to estimate the heat transfer rate, pumping power, and efficiency of the thermal engineering systems. In this work, thermal conductivity and viscosity of COOH-functionalized DWCNTs/water nanofluids are measured and related correlations

Fig. 1. TEM image of the COOH-functionalized DWCNTs.

Table 1
Properties of COOH-functionalized DWCNT.

Outer diameter	2–4 nm
Inner diameter	1–3 nm
Length	50 um
SSA	>350 m^2/g
True density	2.1 g/cm^3
Electric conductivity	>100 S/cm
Color	black
Manufacturing method	CVD

are obtained by using regression analysis. The presented correlations are helpful to use in other studies in which the working fluid is the same.

3.1. Thermal conductivity

A transient hot-wire (THW) technique is used to measure the thermal conductivity which is a fast and reliable method. For this purpose, a KD2 Pro thermal properties Analyzer (Decagon devices, Inc., USA) is used where the maximum error of measurement is ±5%. Before measuring the thermal conductivity of nanofluids, the device is calibrated with distilled water. The tests for any volume fraction are repeated three times. The experimental data of thermal conductivity are compared with the following models:

Hamilton–Crosser (H–C) model [27] is a classic relation to estimate the effective thermal conductivity of solid–liquid mixtures. This model is applicable when the ratio of solid phase thermal conductivity to that of the liquid phase is bigger than 100. The H–C equation is:

$$K_{nf} = \frac{k_p + (n-1)k_f + (n-1)\phi(k_p - k_f)}{k_p + (n-1)k_f - \phi(k_p - k_f)} k_f \quad (1)$$

in which k_f, k_p, *and* k_{nf} are the thermal conductivities of the base fluid, nanoparticles, and nanofluid, respectively. Also, ϕ is the volume fraction of nanoparticles and n is the empirical shape factor, given by $n = \frac{3}{\psi}$ so that ψ is the particle sphericity. The sphericity for the spherical and cylindrical particles is 1 and 0.5, respectively.

Yu and Choi [28] considered the effect of the liquid nanolayer thickness on the surface of the nanoparticles, as:

$$k_{nf} = \frac{k_p + 2k_f + 2(k_p - k_f)(1+\gamma)^3\phi}{k_p + 2k_f - 2(k_p - k_f)(1+\gamma)^3\phi} k_p \quad (2)$$

The thermal conductivity of the samples is measured in the range of 300–340 °C.

3.2. Viscosity

The viscosity of nanofluids is measured using a Brookfield viscometer supplied by Brookfield engineering laboratories of USA. The accuracy of this device is ±5%. Before doing the tests, it is calibrated with distilled water at room temperature. For each concentration, the tests are repeated three times, and the average is recorded. It is found during the tests that for volume fractions less than 0.45% the nanofluids behave as a Newtonian fluid. The experimental data are compared with the following models for viscosity:

Einstein [29] presented a relation to calculate the viscosity of solid–liquid mixtures as a function of volume fraction (concentrations lower than 2%) as follows:

$$\mu_{nf} = \mu_f(1 + 2.5\phi) \quad (3)$$

Wang et al. [30,31] proposed the following equation for nanofluids:

$$\mu_{nf} = \mu_f(1 + 7.3\phi + 123\phi^2) \quad (4)$$

Although, it is known that CNTs are cylindrical (not spherical), but Eqs. (3), (4) only used for comparison purposes, and more studies are needed to present some relations to calculate the viscosity of nanofluids containing cylindrical particles.

4. Experimental set-up and procedure

The schematic of the experimental set-up is shown in Fig. 2. The set-up mainly consists of a test section, a pump, collection tanks for water and nanofluid, and a plate heat exchanger to cool down the working fluid. The test section consists of two concentric tubes made of copper. Hot water flows inside the annular with inner and outer diameters of 3.79 cm, and 3.82 cm, respectively. Nanofluid flows inside the inner tube with outer diameter of 8.1 mm and the inner diameter of 7.05 mm. Nanofluid absorbs the heat of the hot water that flows in the annulus. The annulus is insulated with glass wool with a thickness of 7 cm.

To avoid the axial heat conduction, two plastic fittings at the inlet and outlet of the test section are mounted.

In turbulent flow, the hydrodynamic and thermal entry can be obtained as ($L_e/D \approx 4.4 \times Re^{1/6}$) [32]. In the present work, the entrance length is about 17 cm, therefore all measurements are conducted after the length.

The length of the test section is about 1.1 m to have fully developed turbulent flow. To measure the bulk temperatures at the inlet and outlet of inner tube two calibrated RTD-PT100 thermometers with digital indicator and the accuracy of 0.1 °C are used. To determine the wall temperature of inner tube, eight K-type thermocouples (Chromel–Alumel) with a distance about 13 cm from each other and the accuracy of 0.5 °C are utilized. The inlet temperature of hot water is controlled with a PT100 sensor. Pressure drop due to nanofluid flow is measured using a differential pressure transmitter Rosemount 3051 cd (Rosemount, Inc., USA) with the accuracy of 0.1%. Also, two K-type thermocouples are used to measure the bulk temperature at the inlet and outlet of the annulus. A simple thermometer is used to record the ambient temperature. All the temperature measurement devices are calibrated before each test.

Nanofluid is pumped via a magnetic pump towards the test section. Before entering the test section, the flow rate of nanofluid is measured and controlled. At the same time, hot water is pumped to the annulus to heat up the nanofluid. The nanofluid after heating and exiting of the test section flows towards a plate heat exchanger to cool down. The tests for each concentration and flow rate are repeated several times (3 times) to be sure that the experiments are repeatable.

5. Data reduction and uncertainty analysis

Heat transfer coefficient (h) and Nusselt number (Nu) can be obtained by using the first law of thermodynamics (the conversation of energy) for the inner tube as follows:

$$\frac{dT_b}{dx} = \frac{S}{\dot{m}C_{nf}} h(T_s - T_b) \quad (5)$$

In which T_b is the bulk temperature, S is the periphery of the tube, $\dot{m}$ is mass flow rate, C_{nf} is the specific heat of nanofluid, and T_s is the surface (wall) temperature.

C_{nf} is calculated as [33]:

$$C_{nf} = \frac{\rho_f C_f(1-\phi) + \rho_p C_p \phi}{\rho_{nf}} \quad (6)$$

where ρ is the density and the density of nanofluid (ρ_{nf}) can be obtained according to [33]:

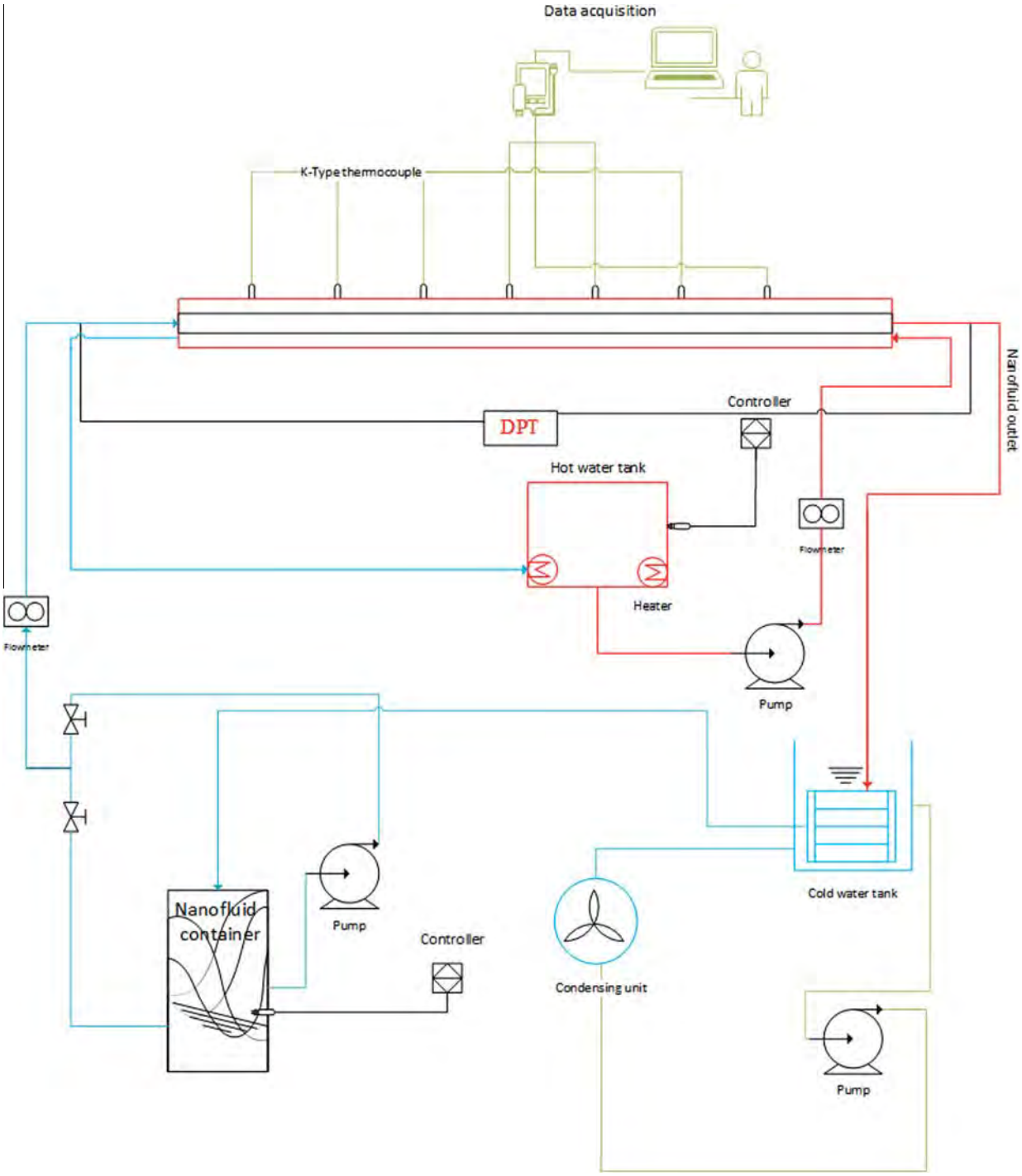

Fig. 2. A schematic view of the experimental set up.

$$\rho_{nf} = \rho_f(1-\phi) + \rho_p\phi \tag{7}$$

By integrating along the tube length (L), heat transfer coefficient can be determined as:

$$\bar{h} = \frac{\dot{m}C_{nf}}{SL} Ln\left(\frac{T_s - T_{b,i}}{T_s - T_{b,o}}\right) \tag{8}$$

where subscripts of i and o indicate the conditions are at the inlet and outlet, respectively.

Also, the Reynolds number and Nusselt number are defined as:

$$\mathrm{Re} = \frac{\rho_{nf}\overline{V}d}{\mu_{nf}}, \quad Nu = \frac{\bar{h}d}{k_{nf}} \tag{9}$$

where d is the diameter of the inner tube and $\overline{V}$ is the average velocity which can be calculated by dividing the flow rate to cross section area of the tube.

To estimate the costs of pumping, it is important to know the pressure drop (ΔP) and friction factor (f). Friction factor is determined as follows:

$$f = \frac{2\Delta P}{\rho_{nf}\overline{V}^2}\frac{d}{L} \tag{10}$$

The uncertainty in the reported data including heat transfer coefficient, Nusselt number, Reynolds number and friction factor

are computed based on the method of Kline and Mcclintock [34]. In general, to calculate the uncertainty of parameter R, the following relation is used:

$$U_R = \left[\sum_{i=1}^{n}\left(\frac{\partial R}{\partial V_i}U_{V_i}\right)^2\right]^{\frac{1}{2}} \tag{11}$$

in which U_R and U_{Vi} are the uncertainties associated with the parameter R and independent variable (V_i), respectively. In addition, n is the number of the independent variables. Using the above equation for the equations of heat transfer coefficient, Nusselt number, Reynolds number and friction factor, the uncertainty related to each parameter can be determined easily. The values of uncertainty for heat transfer coefficient, Nusselt number, Reynolds number and friction factor are ±4.3%, ±5.4%, ±3.2%, and ±6.1%, respectively.

6. Results and discussion

In the first, the results related to thermophysical properties are presented and then the data related to the tests on the double tube heat exchanger are exhibited. Fig. 3 shows the variations of dimensionless effective thermal conductivity with volume fraction in the experimental data and the results obtained based on the models. The comparison reveals that the models fail to estimate the experimental data so that at the maximum concentration of the nanofluid i.e. 0.4%, there is a remarkable difference, about 40%, between the experimental data and Yu-Choi model.

Fig. 4 displays the variations of dimensionless effective thermal conductivity with solid volume fraction for the temperature range of 300–340 K. It is observed that at low concentration of nanofluid, temperature has no significant effect on the dimensionless effective thermal conductivity, whereas with increasing the volume fraction of particles, the effects of temperature are more considerable. This phenomenon can be described as follows. At a given volume of the nanofluid (e.g. 1 lit), when the solid volume fraction increases, it means that the number of particles and consequently the number of collisions due to Brownian motion of particles increases. On the other hand, with an increase in the temperature, the kinetic energy of particles increases and hence the number of collisions among the particles increases. Therefore, increasing the temperature boosts the effects of volume fraction raising.

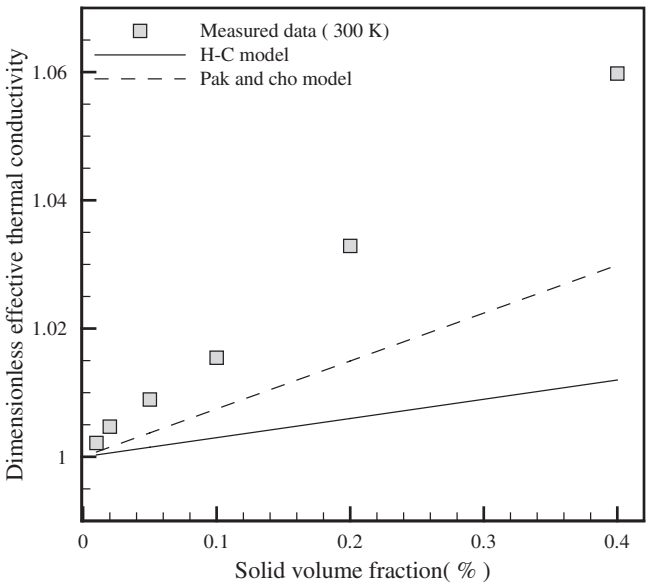

Fig. 3. Comparison between the experimental data and theoretical models for effective thermal conductivity.

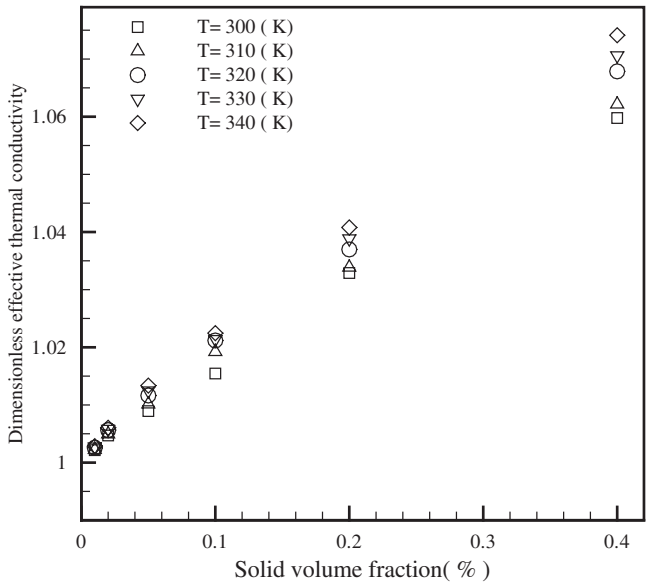

Fig. 4. Effective thermal conductivity at different temperatures.

Fig. 5 is plotted to show the fact that temperature has no significant effect on the effective thermal conductivity at low concentrations as mentioned in discussions of Fig. 4. As can be seen from Fig. 5, at volume fraction of 0.4%, the effective thermal conductivity increases up to 15% when increasing the temperature from 300 to 340 K.

Based on the experimental data a correlation can be presented using the regression analysis. This correlation is a function of the temperature and volume fraction of nanotubes as follows:

$$\frac{k_{nf}}{k_f} = \frac{\phi}{0.17981 - 0.000369T} + 1.0026 \tag{12}$$

Fig. 6 presents a comparison between the results obtained from experimental data and the two models of Einstein and Wang at T = 300 K and different quantities of solid volume fraction. As it is

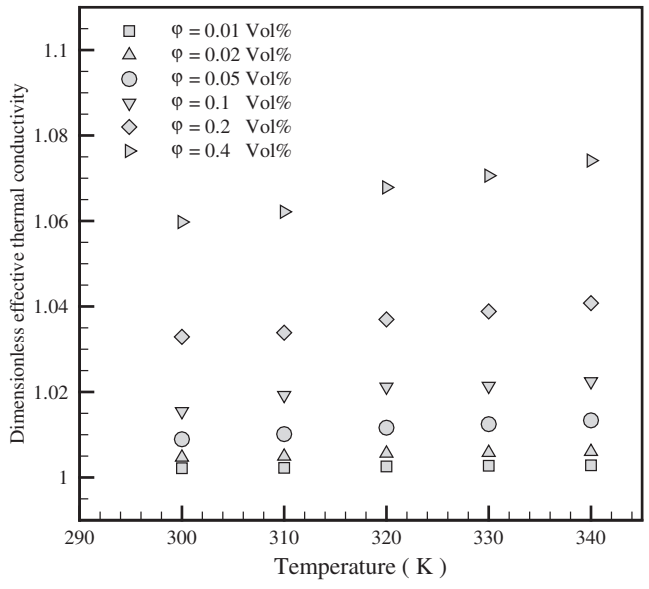

Fig. 5. Effective thermal conductivity at different volume fractions.

observed, the results predicted by Wang equation is close to the experimental data while Einstein model underestimates the viscosity of nanofluids.

Based on the experimental data, a correlation is presented to estimate the viscosity ratio as a function of volume fraction as follows:

$$\frac{\mu_{nf}}{\mu_f} = 1 + 3.575\phi + 6032.93\phi^2 - 1153669\phi^3 \quad (13)$$

Fig. 7 is plotted to verify the accuracy of the presented correlation.

Now, the results on the nanofluid flow in the heat exchanger are presented. First, to be sure about the accuracy of experiments, some tests have been done to evaluate the Nusselt number and friction factor where the working fluid is distilled water and the obtained results are compared with the most well-known correlations. The approximate range of Reynolds number is between 4000 and 31,000. The correlations used to estimate the Nusselt number are as follows:

Grielinski equation [35]:

$$Nu = \frac{f/8(\mathrm{Re}-1000)\mathrm{Pr}}{1+12.7\sqrt{\frac{f}{8}}\left(\mathrm{Pr}^{\frac{2}{3}}-1\right)}\left(\frac{\mathrm{Pr}}{\mathrm{Pr}_f}\right)^{0.11}\left[1+\left(\frac{d}{L}\right)^{\frac{2}{3}}\right] \quad (14)$$

This relation is valid for $0.5 < \mathrm{Pr} < 10^6$ and $2300 < \mathrm{Re} < 5 \times 10^6$. In this formulation, the Darcy coefficient is proposed as follows:

$$f = \frac{1}{(1.82log_{10}\mathrm{Re} - 1.64)^2} \quad (15)$$

where Re is the Reynolds number, Pr and $\mathrm{Pr_f}$ are the Prandtl numbers calculated at the water bulk temperature and at the inner wall temperature respectively; L is the tube length and d is the tube diameter. The bulk temperature is an average between the inlet and outlet fluid temperatures.

Dittues Bulter relation [36]:

$$Nu = 0.023\mathrm{Re}^{0.8}\mathrm{Pr}^{0.4} \quad (16)$$

Xuan and Li equation [37]:

$$Nu = 0.0059(1 + 7.62\varphi^{0.6886}Pe_d^{0.001})\mathrm{Re}^{0.9238}\mathrm{Pr}^{0.4} \quad (17)$$

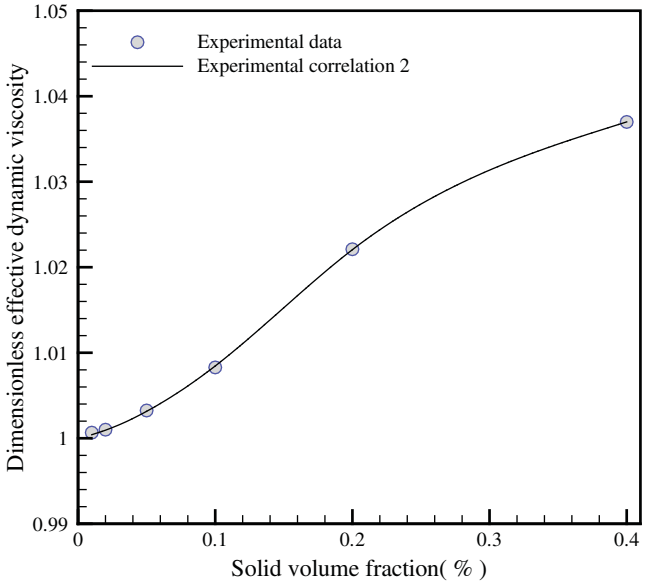

Fig. 7. Correlation for effective viscosity.

Petukhov correlation [38]:

$$Nu = \frac{(f/8)\mathrm{RePr}}{1.07 + 12.7(f/8)^{0.5}\left(\mathrm{Pr}^{\frac{2}{3}}-1\right)} \quad (18)$$

Which is applied in the range of $0.5 < \mathrm{Pr} < 200$ and $104 < \mathrm{Re} < 5 \times 10^6$.

Fig. 8 shows the comparison among different correlations and that one obtained from the tests on pure water. It is seen that the data are in good agreement with Xuan and Li correlation.

Fig. 9 gives a comparison between the friction factor obtained from the experiments and the values of friction factor obtained from Blasius equation($f = 0.25\mathrm{Re}^{-0.25}$).

As can be seen, the experimental data are very close to the results obtained from the equation.

After validating the results obtained by the set up, the experiments on the nanofluids at different volume fractions of

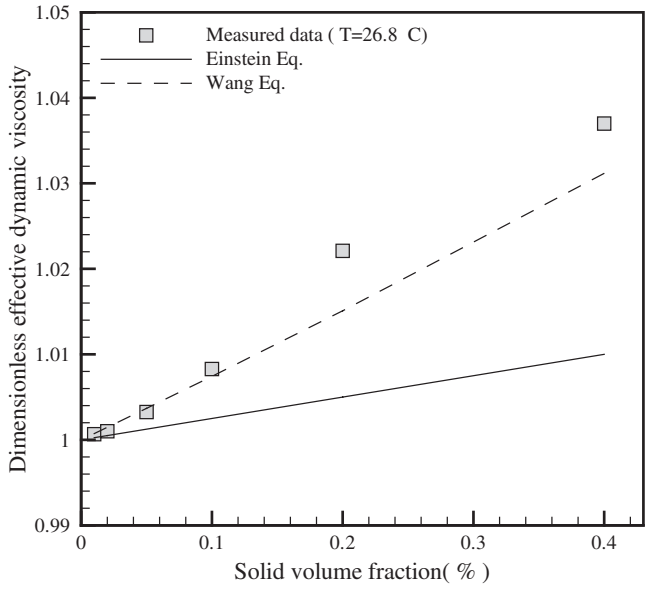

Fig. 6. Effective viscosity based on experimental data and the models.

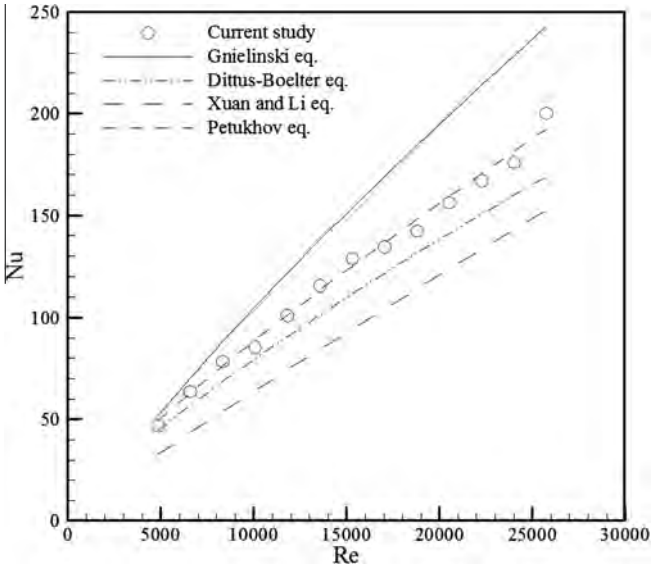

Fig. 8. Experimental Nusselt number and predictions correlations for pure water versus Reynolds number.

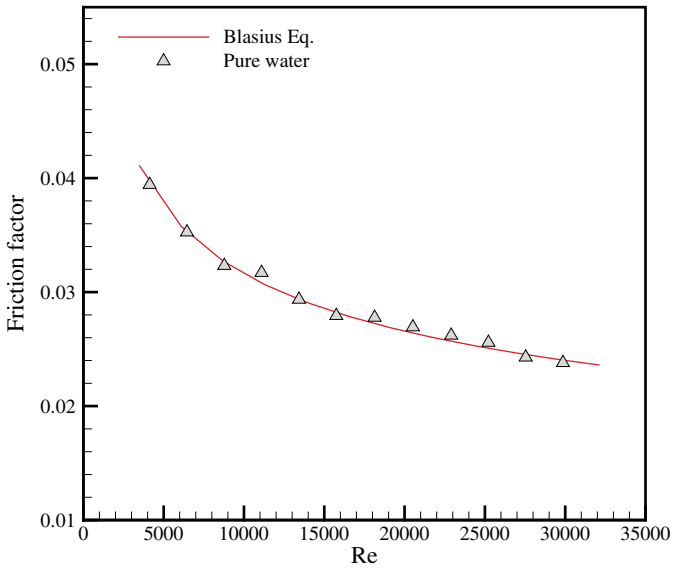

Fig. 9. Comparison of measured friction factor of water with Blasius theory.

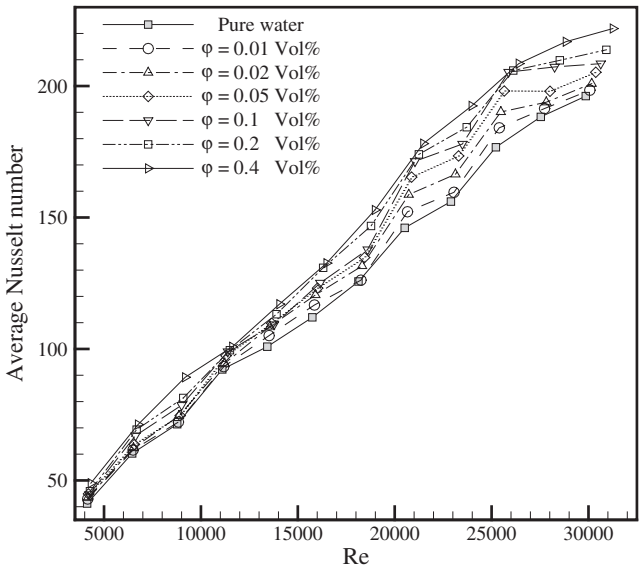

Fig. 11. Variations of average Nusselt number with the Reynolds number.

nanoparticles have been done. Fig. 10 shows the variation of heat transfer coefficient with the Reynolds number in different concentrations of nanofluids. As it is seen, with increasing the Reynolds number the effects of adding the nanoparticles to the pure water on the heat transfer enhancement is more visible. By increasing the Reynolds number, the turbulency of flow increases, on the other hand, with an increase in the particle loading the number of collisions among the particles increase, hence the effects of turbulency will be intensified. A higher number of collisions imply a greater thermal conductance, and hence heat transfer rate inside the tube. The data in the figure reveal that in the range of Reynolds numbers investigated on average the heat transfer coefficient is increased by 25% when the volume fraction of DWCNTs increases from 0 (pure water case) to 0.4%. This amount of enhancement (25%) which is obtained by adding a very low amount of particles to the pure water is so noticeable. The most likely reasons for this enhancement could be presented as follows. The first reason is the high thermal conductivity of DWCNTs that is about 3000 W/m K and enhances the effective thermal conductivity by 6% at 0.4% of

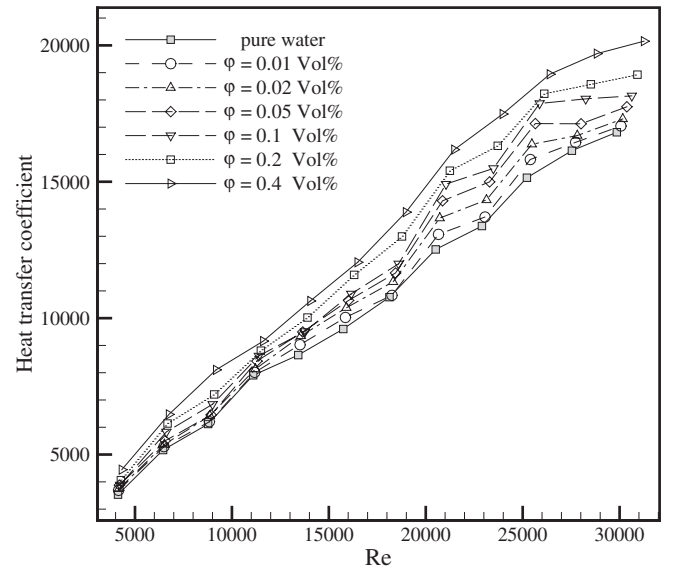

Fig. 10. Variations of heat transfer coefficient with the Reynolds number.

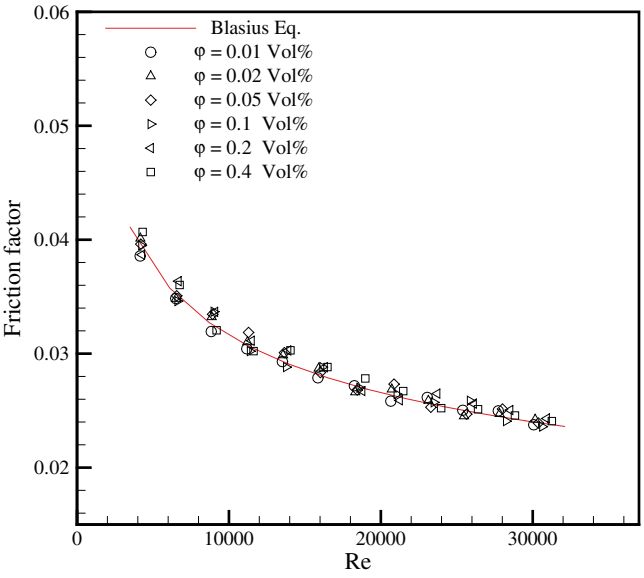

Fig. 12. Variations of friction factor with the Reynolds number.

particle loading (as shown in Fig. 3). Another reason is the cylindrical shape of nanotubes. The cylindrical shape of the particles causes greater contact area among the particles and hence a higher rate of heat transfer. Also, using the functionalized nanotubes due to better surface activity may be another reason for the heat transfer rate. It should be noted that the thermal conductivity of nanotubes is measured in stationary conditions, then the above mentioned reasons are more considerable when the nanofluid flows in turbulent conditions.

Using the data for heat transfer coefficient the average Nusselt number is demonstrated in Fig. 11, for the different concentrations of nanofluids. On average, the Nusselt number for 0.4% of the volume fraction of nanoparticles in comparison with the pure water increases by 18% .

The variations of friction factor with the Reynolds number is presented in Fig. 12 and the results are compared with Blasius equation. The effects of particle loading on the friction factor is more visible for low Reynolds numbers. At low Reynolds numbers,

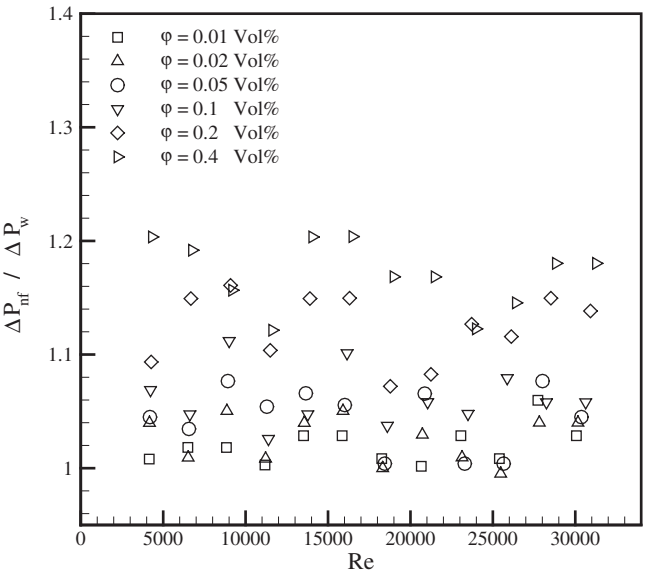

Fig. 13. Variations of pressure drop ratio with the Reynolds number.

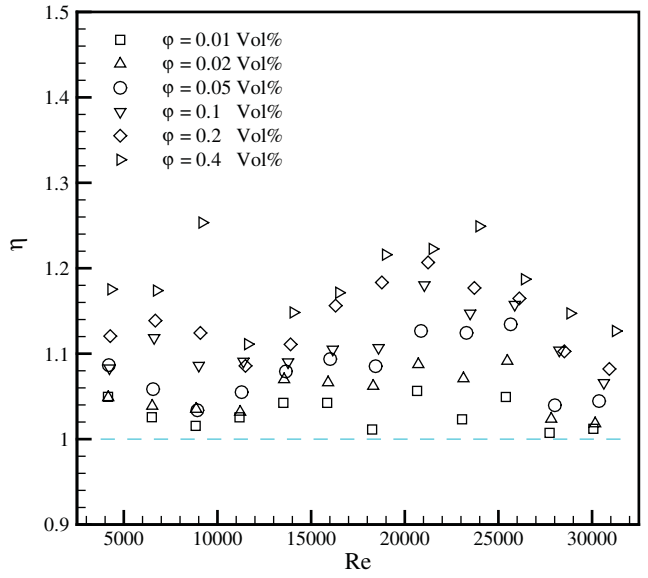

Fig. 14. Variations of thermal performance factor with the Reynolds number.

the friction factor increases with an increase in the volume fraction of nanoparticles. This happens because at low velocities of the flow, the ratio of the viscous forces to the inertia forces is greater, therefore; adding the cylindrical nanoparticles to pure water leads to more increase of shear stress among the fluid layers and hence the friction factor increases more considerable.

Fig. 13 is drawn to show the ratio of pressure drop due to the nanofluid flow to water flow. The findings indicate that for 0.4% of nanofluid concentration the pressure drop ratio is about 20%.

Now, using the thermal performance factor which is defined as:

$$\eta = (Nu_{nf}/Nu_f)/(f_{nf}/f_f)^{1/3} \quad (19)$$

one can evaluate the usefulness of nanofluids to apply in thermal systems. A higher thermal performance factor implies the greater usefulness. The thermal performance factor is shown in Fig. 14 for different Reynolds numbers and volume fractions. The results suggest that using the lowest quantities of volume fractions of nanotubes(i.e. 0.01%) is not so advantageous because the heat transfer enhancement effects are spoiled with the undesirable effects of pressure drop augmentation.

7. Conclusion

An experimental study is performed to evaluate the effects of adding low concentrations of a new class of nantubes i.e. COOH-functionalized double-walled carbon nanotubes (DWCNTs) to pure water on the heat transfer characteristics and pressure drop of nanofluid flow in a double tube heat exchanger. First, the thermal conductivity and viscosity of nanofluids are measured and it is found that the theoretical models for the two properties fail to predict the experimental data. After that, the tests are conducted under turbulent flow and the concentrations 0.01% to 0.4% of the nanofluid. The results indicate that even using a very low quantity of COOH-functionalized DWCNTs (0.4 vol.%) leads to remarkable enhancement in the heat transfer coefficient (on average 25%). Also, the average Nusselt number has increased on average by 18% while the pressure drop increases up to 20%. Finally, utilizing the definition of thermal performance factor, it was perceived that using 0.01% of nanotubes is not so advantageous due to the unfavourable effects of raising in pressure drop.

Acknowledgments

The authors sincerely would like to thank the Science and Technology Park of Semnan University for extending nano-reological laboratory facilities for this research work. The fourth author would like to thank the Thailand Research Fund, The National Science and Technology Development Agency, and the National Research University Project for the support.

References

[1] R. Saidur, K.Y. Leong, H.A. Mohammad, A review on applications and challenges of nanofluids, Renewable and Sustainable Energy Rev. 15 (3) (2011) 1646–1668.
[2] O. Mahian, A. Kianifar, S.A. Kalogirou, I. Pop, S. Wongwises, A review of the applications of nanofluids in solar energy, Int. J. Heat Mass Transfer 57 (2) (2013) 582–594.
[3] W. Yu, D.M. France, D.S. Smith, D. Singh, E.V. Timofeeva, J.L. Routbort, Heat transfer to a silicon carbide/water nanofluid, Int. J. Heat Mass Transfer 52 (2009) 3606–3612.
[4] L.S. Sundar, K.V. Sharma, Y.R. Sekhar, D.V. Rao, T. Subramanyam, J.V. Ramana Rao, Turbulent forced convection of Al_2O_3 nanofluid in a circular tube with tape inserts at low volume concentration, Int. J. Nano Biomater. 2 (1–5) (2009) 60–69.
[5] B. Farajollahi, S.Gh. Etemad, M. Hojjat, Heat transfer of nanofluids in a shell and tube heat exchanger, Int. J. Heat Mass Transfer 53 (1–3) (2010) 12–17.
[6] W. Duangthongsuk, S. Wongwises, Effect of thermophysical properties models on the prediction of the convective heat transfer coefficient for low concentration nanofluid, Int. Commun. Heat Mass Transfer 35 (2008) 1320–1326.
[7] W. Duangthongsuk, S. Wongwises, Heat transfer enhancement and pressure drop characteristics of TiO_2–water nanofluid in a double-tube counter flow heat exchanger, Int. J. Heat Mass Transfer 52 (2009) 2059–2067.
[8] W. Duangthongsuk, S. Wongwises, An experimental study on the heat transfer performance and pressure drop of TiO_2–water nanofluids flowing under a turbulent flow regime, Int. J. Heat Mass Transfer 53 (15) (2010) 334–344.
[9] L.S. Sundar, K.V. Sharma, Turbulent heat transfer and friction factor of Al_2O_3 nanofluid in circular tube with twisted tape inserts, Int. J. Heat Mass Transfer 53 (7–8) (2010) 1409–1416.
[10] S. Zhang, Z. Luo, T. Wang, C. Shou, M. Ni, K. Cen, Experimental study on the convective heat transfer of CuO–water nanofluid in a turbulent flow, J. Enhanced Heat Transfer 17 (2) (2010) 183–196.
[11] A. Amrollahi, A.M. Rashidi, R. Lotfi, Emami, M. Meibodi, K. Kashefi, Convection heat transfer of functionalized MWNT in aqueous fluids in laminar and turbulent flow at the entrance region, Int. Commun. Heat Mass Transfer 37 (6) (2010) 717–723.
[12] M. Hojjat, S.G. Etemad, R. Bagheri, J. Thibault, Convective heat transfer of non-Newtonian nanofluids through a uniformly heated circular tube, Int. J. Therm. Sci. 50 (4) (2011) 525–531.

[13] M. Hojjat, S.G. Etemad, R. Bagheri, J. Thibault, Turbulent forced convection heat transfer of non-Newtonian nanofluids, Exp. Therm. Fluid Sci. 35 (7) (2011) 1351–1356.
[14] S. Suresh, M. Chandrasekar, S. Chandra Sekhar, Experimental studies on heat transfer and friction factor characteristics of CuO/water nanofluid under turbulent flow in a helically dimpled tube, Exp. Therm. Fluid Sci. 35 (2011) 542–549.
[15] K. Tumuluri, J.L. Alvarado, H. Taherian, C. Marsh, Thermal performance of a novel heat transfer fluid containing multiwalled carbon nanotubes and microencapsulated phase change materials, Int. J. Heat Mass Transfer 54 (2011) 5554–5567.
[16] S. Suresh, P. Selvakumar, M. Chandrasekar, V.S. Raman, Experimental studies on heat transfer and friction factor characteristics of Al_2O_3/water nanofluid under turbulent flow with spiraled rod inserts, Chem. Eng. Process. 53 (2012) 24–30.
[17] L. Godson, B. Raja, D. Mohan Lal, S. Wongwises, Convective heat transfer characteristics of silver–water nanofluid under laminar and turbulent flow conditions, J. Therm. Sci. Eng. Appl. 4 (3) (2012) (art. no. 031001).
[18] A.A. Abbasian Arani, J. Amani, Experimental study on the effect of TiO2/water nanofluid on heat transfer and pressure drop, Exp. Therm. Fluid Sci. 42 (2012) 107–115.
[19] A.A.R. Darzi, M. Farhadi, K. Sedighi, R. Shafaghat, K. Zabihi, Experimental investigation of turbulent heat transfer and flow characteristics of SiO_2/water nanofluid within helically corrugated tubes, Int. Commun. Heat Mass Transfer 39 (9) (2012) 1425–1434.
[20] W.H. Azmi, K.V. Sharma, P.K. Sarma, R. Mamat, S. Anuar, V. D.Rao, Experimental determination of turbulent forced convection heat transfer and friction factor with SiO2 nanofluid, Exp. Therm. Fluid Sci., 2013, article in press.
[21] M. Hemmat Esfe, S. Saedodin, M. Mahmoodi, Experimental studies on the convective heat transfer performance and thermophysical properties of MgO–water nanofluid under turbulent flow, Exp. Therm. Fluid Sci., 2013, article in press.
[22] A.A.R. Darzi, M. Farhadi, K. Sedighi, Heat transfer and flow characteristics of AL_2O_3–water nanofluid in a double tube heat exchanger, Int. Commun. Heat Mass Transfer 47 (2013) 105–112.
[23] A.M. Hussein, K.V. Sharma, R.A. Bakar, K. Kadirgama, The effect of nanofluid volume concentration on heat transfer and friction factor inside a horizontal tube, J. Nanomater. (2013) (art. no. 859563).
[24] G.P. Celata, F. D'Annibale, A. Mariani, L. Saraceno, R. D'Amato, R. Bubbico, Heat transfer in water-based SiC and TiO_2 nanofluids, Heat Transfer Eng. 34 (13) (2013) 1060–1072.
[25] W. Yu, D.M. France, E.V. Timofeeva, D. Singh, J.L. Routbort, Comparative review of turbulent heat transfer of nanofluids, Int. J. Heat Mass Transfer 55 (2012) 5380–5396.
[26] R. Hamilton, O. Crosser, Thermal conductivity of heterogeneous two component systems, Ind. Eng. Chem. Fund. 1 (3) (1962) 187–191.
[27] W. Yu, S.U.S. Choi, The role of interfacial layers in the enhanced thermal conductivity of nanofluids: a renovated Maxwell model, J. Nanopart. Res. 5 (2003) 167–171.
[28] A. Einstein, Eine neue bestimmung der molekuldimensionen, Ann. Phys. Leipzig 19 (1906) 289–306.
[29] X. Wang, X. Xu, S.U.S. Choi, Thermal conductivity of nanoparticle–fluid mixture, J. Thermophys. Heat Transfer 13 (4) (1999) 474–480.
[30] I.M. Mahbubul, R. Saidur, M.A. Amalina, Latest developments on the viscosity of nanofluids, Int. J. Heat Mass Transfer 55 (2012) 874–885.
[31] F.M. White, Viscous Fluid Flow, second ed., McGraw Hill, New York, 2006.
[32] O. Mahian, A. Kianifar, C. Kleinstreuer, M.A. Nimr, I. Pop, A.Z. Sahin, S. Wongwises, A review of entropy generation in nanofluid flow, Int. J. Heat Mass Transfer 65 (2013) 514–532.
[33] S.J. Kline, F.A. Mcclintock, Describing uncertainties in single-sample experiments, Mech. Eng. 75 (1953) 3–8.
[34] V. Gnielinski, Int. Chem. Eng. 16 (1976) 359.
[35] F.P. Incropera, D.P. De Witt, Fundamentals of Heat and Mass Transfer, fourth ed., John Wiley, New York, 1996.
[36] Yimin. Xuan, Qiang. Li, Investigation on convective heat transfer and flow features of nanofluids, J. Heat Transfer 125 (2003) 151–155.
[37] B.S. Petukhov, Heat transfer and friction in turbulent pipe flow with variable physical properties, in: T.F. Irvine Jr., J.P. Hartnett (Eds.), Advances in Heat Transfer, vol. 6, Academic Press Inc., New York, 1970, pp. 504–564.

International Journal of Heat and Mass Transfer 73 (2014) 231–238

Contents lists available at ScienceDirect

International Journal of Heat and Mass Transfer

journal homepage: www.elsevier.com/locate/ijhmt

A comparative experimental study on the natural convection heat transfer of different metal oxide nanopowders suspended in turbine oil inside an inclined cavity

Saeed Zeinali Heris [a,*], Masoumeh Borhani Pour [a], Omid Mahian [b,c,*], Somchai Wongwises [c]

[a] Department of Chemical Engineering, Ferdowsi University of Mashhad, Mashhad, Iran
[b] Young Researchers and Elite Club, Mashhad Branch, Islamic Azad University, Mashhad, Iran
[c] Fluid Mechanics, Thermal Engineering and Multiphase Flow Research Lab. (FUTURE), Department of Mechanical Engineering, Faculty of Engineering, King Mongkut's University of Technology Thonburi, Bangmod, Bangkok 10140, Thailand

ARTICLE INFO

Article history:
Received 25 October 2013
Received in revised form 30 January 2014
Accepted 30 January 2014

Keywords:
Natural convection
Inclination angle
Nanofluids
Experimental study

ABSTRACT

An experimental study is conducted to investigate the effects of inclination angle on the natural convection of nanofluids inside a cubic cavity with the side size of 10 cm. One of the surfaces of the cavity is kept in cold temperature and another one (opposite side) in hot temperature while the other four surfaces are insulated. The mixtures of three different types of nanoparticles including Al_2O_3, TiO_2, and CuO within turbine oil (TO) are used as the heat transfer fluid. The heat transfer in the cavity is investigated in three inclination angles with respect to the horizontal position including 0°, 45° and 90° where the weight fractions of nanoparticles are 0.2%, 0.5%, and 0.8%. The Nusselt number results are presented for the three types of nanofluids, and different angles of inclination, Rayleigh number, and weight fraction of nanoparticles. The results reveal that the turbine oil has the highest Nusselt number in any inclination angle of the cavity compared to the nanofluids. Also, it is found that at the inclination angle of 90°, and the weight fraction 0.2%, the application of TiO_2 particles results in the maximum Nusselt number while for weight fraction of 0.8%, the maximum Nusselt number is associated with the CuO nanopowders.

1. Introduction

Natural convection flow in enclosures is one of the classic problems that is important due to its application in many thermal engineering devices such as solar collectors, energy storage systems, electronic devices, and so on. Recent developments in the field of nanofluids as an advanced type of liquids with surprising properties have led to a renewed interest in the study of natural convection in enclosures where a nanofluid is the working fluid. The satisfactory effects of using nanofluids on the heat transfer enhancement are proven in many applications such as solar cells, solar collectors, nuclear reactors, automobiles, microchannels, electronic devices, phase change materials, and so on [1,2].

Here, some studies on the natural convection in cavities using nanofluids are reviewed briefly. First, the numerical works are reviewed. Ho et al. [3] in a numerical work investigated the effects of using different models to calculate the viscosity and thermal conductivity on the natural convection heat transfer inside a square cavity. The bottom and top walls were insulated while one of the side walls was assumed cold and another one hot. They used alumina/water nanofluids as the working fluid where the volume concentrations do not exceed 4%. They concluded that using different thermophysical models may lead to the estimations in an opposite trend for the Nusselt number especially in high solid volume fractions. Abu-Nada and Oztop [4] examined numerically the effects of inclination angle (between 0° and 120°) of a square cavity filled with Cu/water nanofluid (volume fractions upto 10%) on the heat transfer. The boundary conditions in this work were similar to the boundary conditions considered by Ho et al. [3]. Öğüt [5] simulated the natural convection of five different water based nanofluids (volume fractions upto 20%) containing Cu, Ag, CuO, Al_2O_3, and TiO_2 nanoparticles in a cavity where one of the side walls was heated using a heater mounted on the wall. The cavity angle was varied between 0° and 90°. They indicated that with increasing the concentration, the heat transfer rate increases. This increase was more considerable for the particles with higher thermal conductivity (i.e. Ag and Cu). In a similar work to the study of

* Corresponding authors. Tel./fax: +98 511 8816840.
E-mail addresses: zeinali@ferdowsi.um.ac.ir (S.Z. Heris), omid.mahian@gmail.com (O. Mahian).

http://dx.doi.org/10.1016/j.ijheatmasstransfer.2014.01.071
0017-9310/

Nomenclature

A	heat transfer area
c_p	specific heat (kJ/kg K)
d_p	diameter of the alumina particles (nm)
g	gravitational acceleration (m/s^2)
h	surface-averaged heat transfer coefficient (W/m^2 K)
k	thermal conductivity (W/m K)
l	length of cavity (m)
Nu_{nf}	average Nusselt number
q''	surface-averaged heat flux from the hot wall (W/m^2)
Pr_{nf}	Prandtl number
Ra_{nf}	Rayleigh number
T	temperature (C)

Greek symbols

α	thermal diffusivity (m^2/s)
β	volumetric thermal expansion coefficient (1/K)
μ	dynamic viscosity (kg/m s)
ρ	density (g/cm^3)

Subscripts

bf	base fluid
c	cold wall
h	hot wall
m	mean value
nf	nanofluid
p	nanoparticles

Ho et al. [3], Abu-Nada et al. [6] investigated the effects of uncertainties in thermophysical properties on the heat transfer of Al_2O_3–water and CuO–water nanofluids (volume fractions upto 9%) in the cavity. They concluded that the average Nusselt number has a higher sensitivity to viscosity compared to thermal conductivity at high Rayleigh numbers, hence, a suitable viscosity model should be selected for such conditions.

Ghasemi and Aminossadati [7] analysed numerically the flow of Cu, Al_2O_3 and TiO_2 nanoparticles suspended in water in a cavity where the top and bottom walls are insulated, right wall is kept cold and the left wall is subjected to a periodic heat flux. They found that using Cu and TiO_2 (volume fractions upto 20%) leads to the maximum and minimum heat removal from the heat source, respectively. Shahi et al. [8] considered the flow of Cu/water nanofluid (volume fractions upto 5%) in a square cavity where the bottom wall is subjected a constant heat flux, while the cooling of the cavity is conducted by entering a nanofluid flow from the left wall and exiting from the right wall. They concluded that an increase in the volume fraction increases the average Nusselt number in the cavity. Lin and Violi [9] simulated the effects of particle size on the natural convection flow of Al_2O_3/water nanofluid (volume fraction upto 5%) in a cavity. Their results indicated that by decreasing the nanoparticle size from 250 nm to 5 nm, the heat transfer rate increases.

Kahveci [10] conducted a work similar to Ref. [5], with this difference that the cavity can rotate from 0° to 90°. The author revealed that with the increase of the Rayleigh number, the inclination angle in which the maximum heat transfer rate occurs, changes from 45° to 30°. He also found that using Ag nanopartilces results in the maximum heat transfer rate, while the heat transfer rate is minimum for TiO_2 nanoparticles. Corcione [11] obtained the optimum particle loading for the nanofluid flow in a cavity with different aspect ratios. The author concluded that with the decrease of nanoparticle size, the level of optimal volume fraction increases. Mahmoudi et al. [12] studied the mixed convection flow of Cu/water nanofluid in a cavity where four different configurations were considered based on the inlet and outlet flow. In another work, Mahmoudi et al. [13] solved the natural convection problem where the thickness of the left wall is considered.

The interested readers can refer to other numerical works are as follows. The effects of temperature dependent models on the natural convection were considered by Abu-Nada [14], the natural convection of nanofluids in a cavity using the lattice Boltzmann method was studied by Lee and Yang [15], investigation of thermophoresis and Brownian motion effects on natural convection by Haddad et al. [16], double-diffusive natural convection of nanofluid was studied by Parvin et al. [17], heatline analysis of nanofluid flow in natural convection has been conducted by Basak and Chamkhah [18], the effect of nanoparticle shape was investigated by Ooi and Popov [19], free convection in a complicated cavity was studied by Nasrin and Alim [20], and finally the free convection in a cavity filled with nanofluids was considered by Garoosi et al. [21] where several pairs of coolers and heaters were installed inside the cavity. A comprehensive review on the natural convection of nanofluids in cavities with different structures is performed by Haddad et al. [22].

However, also some experimental works on the natural convection of nanofluids in cavities are observed in the literature.

Wen and Ding [23] during an experimental work on the natural convection of TiO_2/water nanofluid between two parallel disks, concluded that using nanofluids leads to the decrease of the heat transfer rate in the enclosure. They used the nanofluids at low volume concentrations (not more than 0.57%). Nnanna [24] tested Al_2O_3–water nanofluids with volume fractions upto 8% in a partially heated cavity. It was found that using nanofluids with concentrations upto 2% results in the increase in the heat transfer rate while for volume fractions greater than 2%, due the unfavorable effects of viscosity the heat transfer rate decreases. Li and Peterson [25] sought for the possible reasons behind the heat transfer detraction due to using Al_2O_3/water nanofluids (volume fractions upto 6%) in a vertical cylindrical cavity. In separate experiments, they could find that the Brownian motion and thermophoresis phenomena affect the heat transfer rate. In a nice work, Ho et al. [26] examined the natural convection of Al_2O_3/water nanofluid (volume fractions upto 4%) in the vertical cavities with three different aspect ratios. They concluded that increasing the particle loading (more than about 1%) leads to the decrease of the average Nusselt number especially at lower Rayleigh numbers.

As it is seen, although extensive numerical studies have been performed on the natural convection in a cavity using nanofluids, but there has been little experimental works in this field. This is due to the difficulties in the experimental study of such flows. Also, in most of the studies the base fluids were water or ethylene glycol.

The present work aims to provide a comprehensive investigation on the effects of using three different turbine oil (TO) based nanofluids including Al_2O_3, TiO_2, and CuO nanoparticles in a cubic cavity. After preparing the suspensions of nanofluids, the effects of the inclination angle, Rayleigh number, and volume fraction of nanoparticles on the Nusselt number are investigated. Utilizing three different types of nanoparticles let to find out the effects of thermal conductivity, heat capacity, density and thermal expansion of nanoparticles on the heat transfer rate.

Table 1
Properties of nanoparticles and turbine oil in room temperature.

Nanoparticle type	Mean diameter (nm)	Thermal expansion coefficient (1/K)	Density (kg/m^3)	Heat capacity (J/kg K)	Thermal conductivity (W/m K)
TiO_2	20	0.9×10^{-5}	4250	686.2	8.95
CuO	60	1.8×10^{-5}	6400	535.6	76.5
Al_2O_3	20	0.85×10^{-5}	3970	765	40
Turbine oil	–	64×10^{-5}	875	2000	0.133

2. Nanofluid preparation

Nanoparticles of Al_2O_3 (20 nm), TiO_2 (20 nm), and CuO (60 nm) have been purchased from the NIPPON AEROSIL company, Japan while the turbine oil is provided by Behran Oil company, Iran. The thermophysical properties of nanoparticles and turbine oil are presented in Table 1. To prepare a given concentration of the nanofluids, a specified quantity of the nanoparticles is weighed, then it is added to the turbine oil little by little. Simultaneously, by using a magnetic stirrer the suspension is mixed well for 30–45 min. After mixing, the samples are inserted inside an ultrasonic vibrator (Misonix Inc. XL2020) for about 1 h to have a homogenous mixture and breaking down the agglomeration between the nanoparticles.

The samples are provided in three different concentrations including 0.2 wt.%, 0.5 wt.%, and 0.8 wt.%. By converting the concentrations in terms of volume fraction, one can find that the concentrations do not exceed 0.5 vol.%. This reveals that low concentrations of nanofluids used in the present work. Fig. 1 shows the photographs of the prepared samples and the pure turbine oil. It should be noted that the samples were stable during the tests and no sedimentation is observed with naked eyes, but; in general, CuO/TO nanofluids were stable for a shorter time in comparison with TiO_2/TO and Al_2O_3/TO nanofluids. The lower level of stability

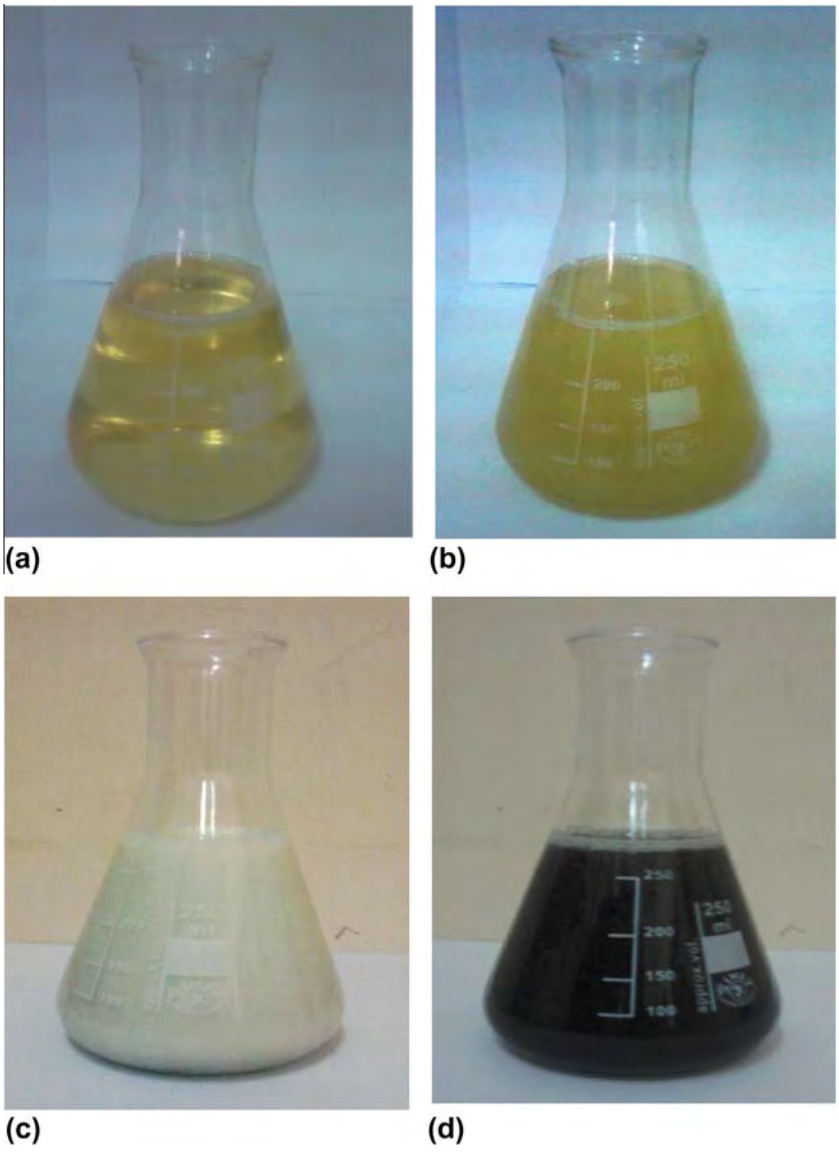

Fig. 1. Photographs of the samples: (a) turbine oil, (b) Al_2O_3/ TO, (c) TiO_2/ TO, and (d) CuO/TO.

of CuO/TO nanofluids may be due to the higher density and bigger size of its particles compared to other ones.

3. Experimental set up and procedure

The schematic view and photograph of the experimental set up is shown in Fig. 2.

The experimental set up is composed of a test cell, insulator materials, nanofluid tank, DC power supply, and electrical panel. The test cell is a cubic cavity with the side size of 10 cm. One of the walls is cooled down by cooling water while another wall at the opposite side is heated by a heating element with the maximum power of 1000 W. The power of heating element is regulated by varying the voltage of DC power supply. The cold and hot walls are made of copper with a thickness of 2 mm, and other walls are made of steel and the thickness of 2 mm. All walls are insulated with a ceramic fiber insulating blanket with a thickness of 50 mm. PT 100 thermocouples with an accuracy of 0.1 °C are used to measure the surface temperature of the hot and cold walls. The thermocouples are calibrated in a constant temperature bath equipped with a digital thermometer with an accuracy of 0.1 °C. After about 3 h the system reaches the steady state conditions so that no change is observed in the temperatures. The temperatures are recorded in the steady state conditions. After each test, the enclosure is cleaned well. The tests are repeated 3–4 times to be sure about the repeatability of the data.

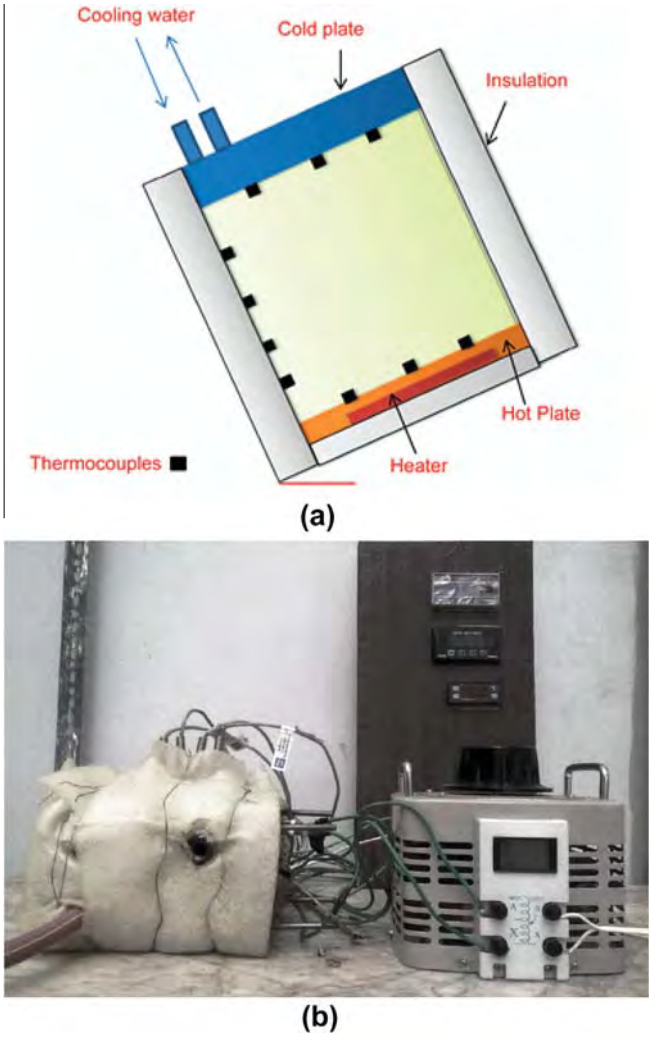

Fig. 2. (a) Schematic view of the inclined cavity, and (b) photograph of the experimental set up.

4. Data reduction

The steady state heat flux applied on the hot wall is obtained by multiplying the voltage (V) and current (I) as follows:

$$q'' = VI \tag{1}$$

Therefore the heat transfer coefficient (h) and the Nusselt number (Nu) can be determined as:

$$\bar{h} = \frac{q''}{A(T_h - T_c)} \tag{2}$$

$$Nu = \frac{\bar{h}l}{k_{nf}} \tag{3}$$

In which T_h and T_c are the temperatures of hot and cold walls, respectively. Also, l is the size of cavity, and k_{nf} is the thermal conductivity of nanofluid.

Also, the Rayleigh number is computed by:

$$Ra = \frac{g\rho_{nf}^2 c_P \beta_{nf}(T_h - T_c)l^3}{k_{nf}\mu_{nf}} \tag{4}$$

The thermophysical properties of the nanofluid are calculated at the mean temperature of the hot and cold walls ($T_h + T_c/2$) as follows. Thermal conductivity is obtained by Hamilton–Crosser equations [27]:

$$K_{nf} = \frac{k_p + (n-1)k_f + (n-1)\phi(k_p - k_f)}{k_p + (n-1)k_f - \phi(k_p - k_f)}k_f \tag{5}$$

Density (ρ_{nf}), heat capacity (C_{nf}) and thermal expansion coefficient (β_{nf}) are calculated by Khanafer and Vafai [28]:

$$\rho_{nf} = \rho_f(1-\phi) + \rho_p\phi \tag{6}$$

$$C_{nf} = \frac{\rho_f C_f(1-\phi) + \rho_p C_p \phi}{\rho_{nf}} \tag{7}$$

$$\beta_{nf} = \frac{(1-\phi)(\rho\beta)_f + \phi(\rho\beta)_p}{\rho_{nf}} \tag{8}$$

The viscosity is determined by the Brinkman relation [29]:

$$\mu_{nf} = \frac{\mu_f}{(1-\phi)^{2.5}} \tag{9}$$

As mentioned the volume concentrations used in the present work do not exceed 0.5%, therefore, as it is confirmed by Ho et al. [3] and Abu-Nada et al. [6] the uncertainties in thermophysical models have no effect on the reported results in low concentrations.

5. Results and discussion

In this section, the effects of concentration, inclination angle, and nanoparticle type in different Rayleigh numbers on the Nusselt number are investigated.

5.1. Effects of concentration

Fig. 3 shows the variations of the Nusselt number with the Rayleigh number for different concentrations of TiO_2/TO, Al_2O_3/TO, and CuO/TO nanofluids and inclination angles of 0, 45, and 90. As it is observed, at all inclination angles for TiO_2/TO nanofluid, the Nusselt number decreases with an increase in the weight fraction of nanoparticles. However, for the two other nanofluids there is

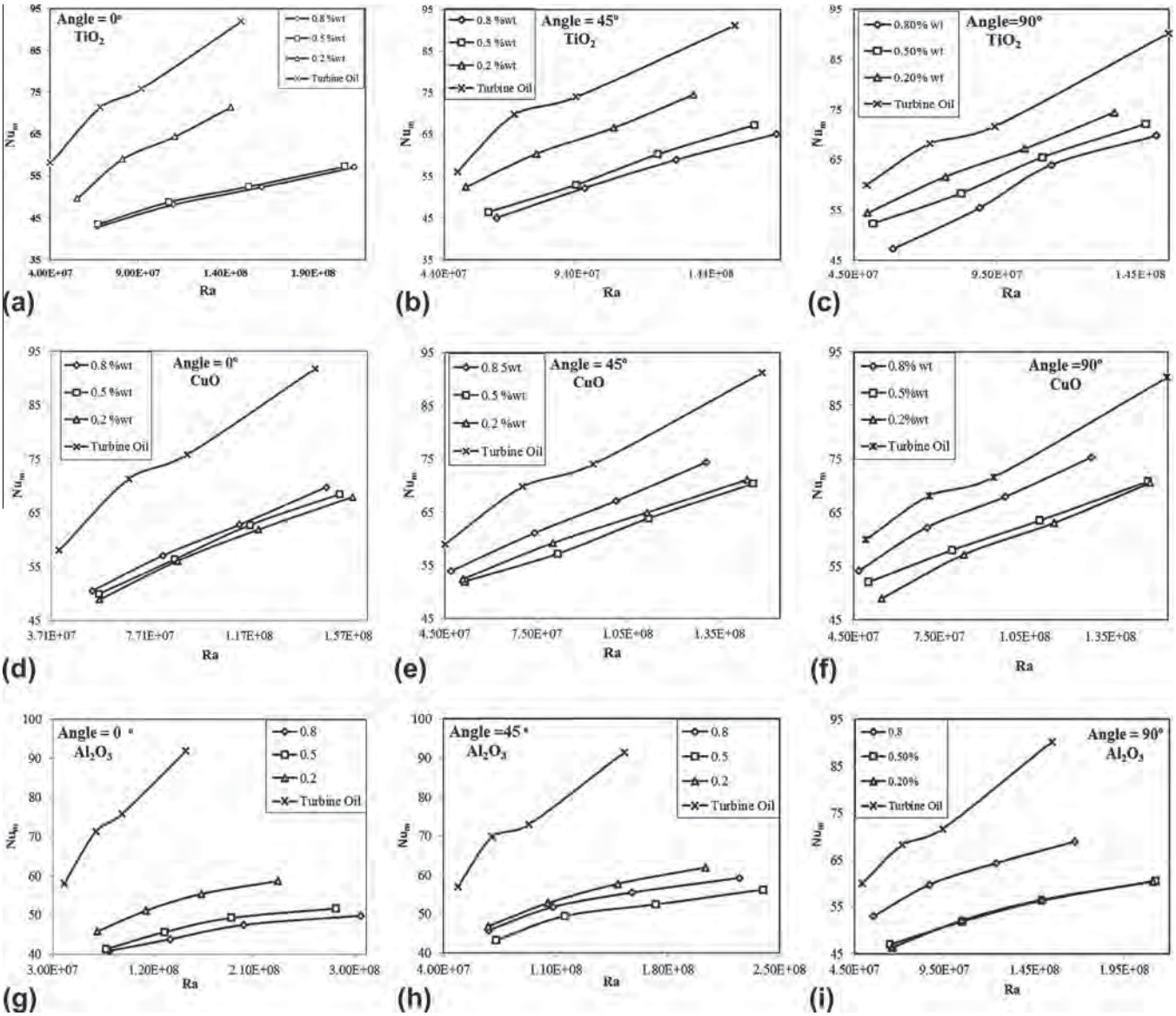

Fig. 3. Effects of concentration on the Nusselt number for different nanoparticles.

no a specified trend for the changes in the Nusselt number. The following relation can help to describe the reasons behind the changes in the Nusselt number [26]:

$$\frac{h_{nf}}{h_f} \approx \left(\frac{\beta_{nf}}{\beta_f}\right)^{n} \left(\frac{\rho_{nf}}{\rho_f}\right)^{2n} \left(\frac{C_{p,nf}}{C_{p,f}}\right)^{n} \left(\frac{k_{nf}}{k_f}\right)^{1-n} \left(\frac{\mu_{nf}}{\mu_f}\right)^{-n} \tag{10}$$

The above relation can be developed in terms of the Nusselt number as follows:

$$\frac{Nu_{nf}}{Nu_f} \approx \left(\frac{\beta_{nf}}{\beta_f}\right)^{n} \left(\frac{\rho_{nf}}{\rho_f}\right)^{2n} \left(\frac{C_{p,nf}}{C_{p,f}}\right)^{n} \left(\frac{k_{nf}}{k_f}\right)^{-n} \left(\frac{\mu_{nf}}{\mu_f}\right)^{-n} \tag{11}$$

or:

$$\frac{Nu_{nf}}{Nu_f} \approx (\beta_r)^{n} (\rho_r)^{2n} (C_{p,r})^{n} (k_r)^{-n} (\mu_r)^{-n} \tag{12}$$

where n is considered equal to 1/3, and the subscript r indicates the ratio of the properties. With an increase in the concentration of nanofluids, the density, thermal conductivity and viscosity ratios increase while the heat capacity and thermal expansion coefficient ratios decrease. However, it should be considered that the power of n for the thermal conductivity and viscosity ratios in the relation is negative. Therefore, the Nusselt number increases with particle loading due to the increase of density ratio. On the other hand, the Nusselt number decreases with particle loading due to the decrease of thermal conductivity, viscosity, heat capacity and thermal expansion coefficient ratios. The outcome of these changes is the decrease of the Nusselt number for the TiO_2/TO nanofluid. For Al_2O_3/TO and CuO/TO nanofluids it is not predictable that which concentration yields the minimum Nusselt number, as shown in figure. More experiments are needed to know the reasons behind these unusual changes. However, the physical and chemical specifications of nanoparticles such as the shape, size, heat absorption and the level of surface activity should be considered as possible reasons. Moreover, CuO and Al_2O_3 particles have higher thermal conductivity compared to TiO_2 particles. This may affect the thermophoresis phenomenon which is occurring in the cavity. Thermophoresis is sensitive to the changes in the temperature gradient and hence the variations of the thermal conductivity. In all cases, the

Nusselt number increases with an increase in the Rayleigh number due to the increases in the buoyancy force. The rate of increase in the Nusselt number for nanofluids is lower than the pure turbine oil. This may happen because of the agglomeration and probable sedimentation of nanoparticles on the hot plate which deteriorates the heat transfer.

5.2. Effects of inclination angle

Now, the aim is to focus on the effects of inclination angle on the Nusselt number for the three types of nanofluids. As it is shown in Fig. 4, for all types of nanofluids and any concentration, the Nusselt number is minimized at the inclination angle of 0° where the hot plate is placed on the ground. This happens because in this case the heat transfer is deteriorated due to the lower velocity of particles that is due to the gravitational effects.

For TiO_2 particles, the maximum heat transfer occurs at the angle of 90°. For Al_2O_3 and CuO the heat transfer is highest at 90° in the weight fractions of 0.8% and 0.5%. However, for 0.2% particle loading, the maximum heat transfer happens at 45° due to the higher migration velocity of particles in this angle compared to 90°.

5.3. Effects of nanoparticle type

Finally, the effects of using different nanoparticles in the cavity on the Nusselt number are investigated. Fig. 5 shows the variation of the Nusselt number with the Rayleigh number at the inclination angle of 90°. As it is seen, for the weight fraction of 0.2%, the use of TiO_2 particles leads to the maximum Nusselt number in the cavity, although its thermal conductivity is the smallest. By increasing the weight fraction of nanoparticles from 0.2% to 0.8%, Cuo/To nanofluid shows a higher Nusselt number compared to TiO_2/TO nanofluid. Also, it is perceived that for the weight fraction of 0.8%, the magnitude of the Nusselt number for Al_2O_3/TO nanofluid is higher than TiO_2/TO nanofluid at lower Rayleigh numbers.

Referring to Eq. (11) and with the development of it for two particles, one can write:

$$\frac{Nu_{nf})_{p_2}}{Nu_{nf})_{P_1}} \approx \left(\frac{\beta_{nf,p_2}}{\beta_{nf,p_1}}\right)^n \left(\frac{\rho_{nf,p_2}}{\rho_{nf},p_1}\right)^{2n} \left(\frac{C_{p,nf,p_2}}{C_{p,nf},p_1}\right)^n \left(\frac{k_{nf},p_1}{k_{nf},p_2}\right)^n \left(\frac{\mu_{nf},p_1}{\mu_{nf},p_2}\right)^n \tag{13}$$

where the subscripts $p_1$and p_2 indicates the particle type #1 and particle type #2. To explain the reasons behind the changes of the

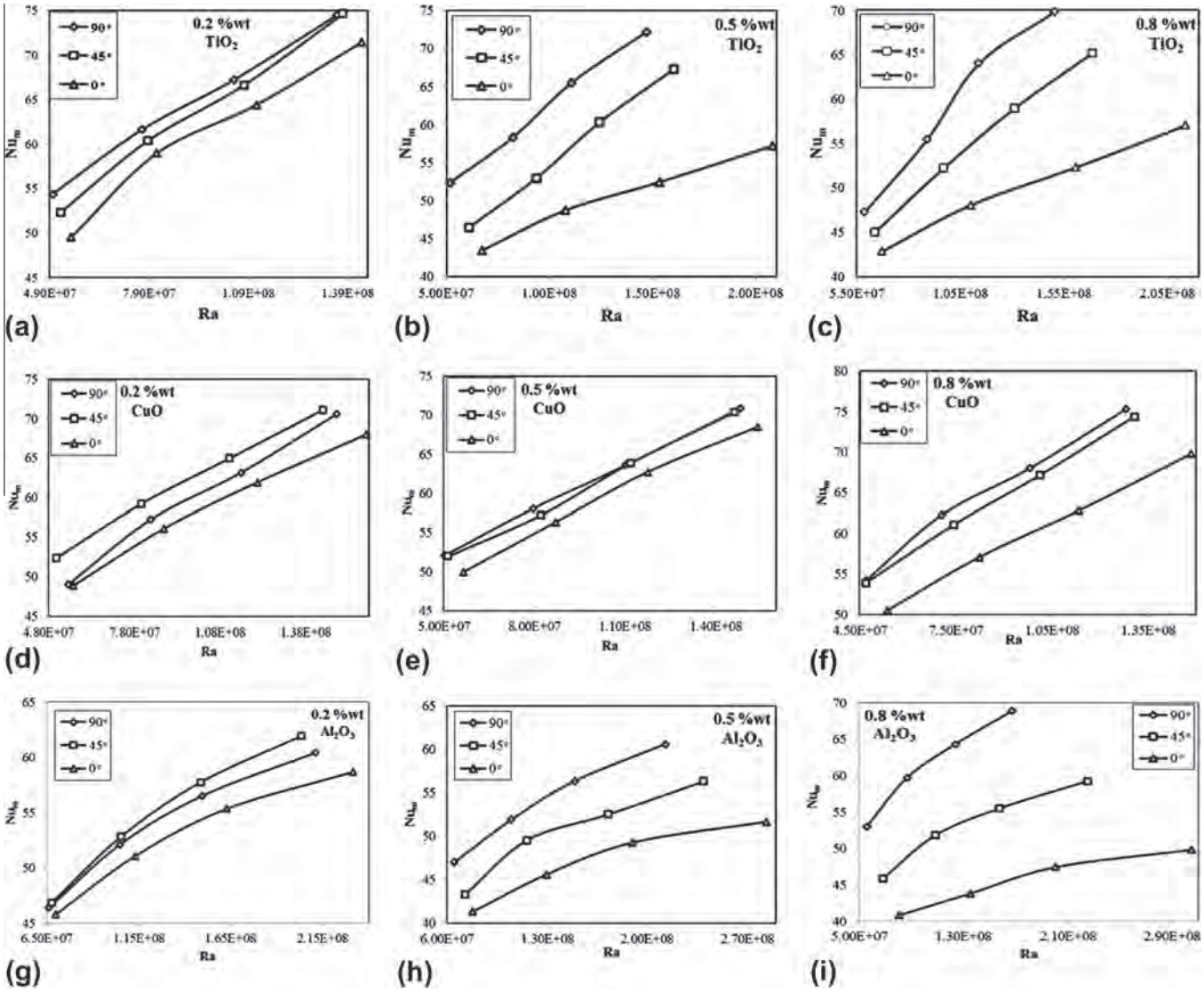

Fig. 4. Effects of inclination angle on the Nusselt number for different nanoparticles.

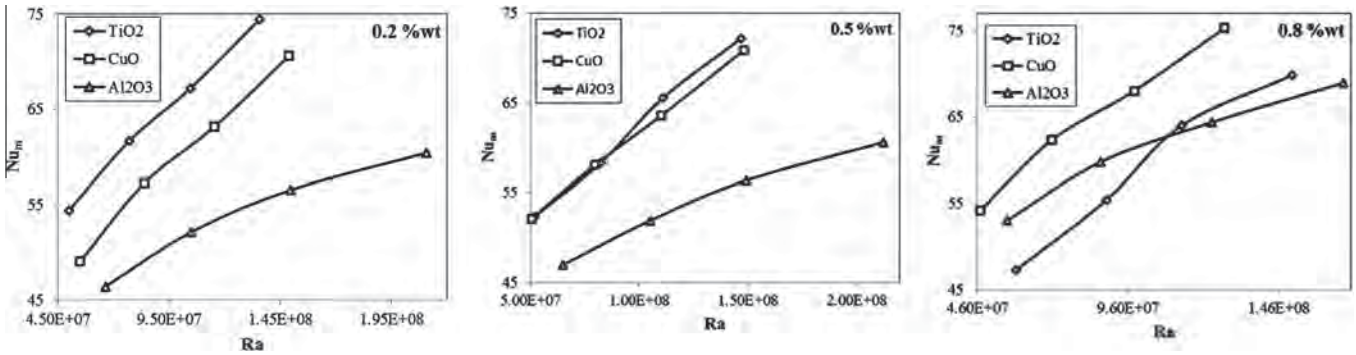

Fig. 5. Effects of different nanoparticles on the Nusselt number for the inclination angle of 90°.

Nusselt number, besides the above relation, the effects of size,-shape, heat absorption, and Brownian motion of nanoparticles should be considered. Also, the van der Waals' forces between the nanoparticles are another important factor. As the van der Waals' forces increase, the agglomeration of nanoparticles increases which it can reduce the effect of buoyancy force and consequently the Nusselt number decreases. Therefore, more experiments in microscopic and macroscopic scales should be done to find out the reasons behind the changes in the Nusselt number for different nano materials.

6. Uncertainty analysis

Uncertainty analysis is performed to determine the percentages of error in each experiment. In the following, the uncertainty analysis for important parameters such as the heat transfer coefficient, Nusselt number, and Rayleigh number is conducted in details.

The maximum possible error (E_{Mi}) in the measurement of parameter M is determined by:

$$E_{Mi} = \frac{X_i}{M}\frac{\partial M}{\partial X_i}E_{x_i} \tag{14}$$

in which X_i is an independent parameter that can be determined directly through the measurements. M is the d that is calculated through X. E_{Xi} is obtained by dividing the measurement accuracy of the device that is used for measuring a parameter to the minimum value of the measured quantity during the tests.

Another form of the above equation is as follows:

$$MaxE_M = \left[\left(\frac{X_1}{M}\frac{\partial M}{\partial X_1}E_{x_1}\right)^2 + \left(\frac{X_2}{M}\frac{\partial M}{\partial X_2}E_{x_2}\right)^2 + \cdots + \left(\frac{X_n}{M}\frac{\partial M}{\partial Xn}E_{x_n}\right)^2\right]^{1/2}$$

6.1. Calculation of errors

In this section, E_{Xi} for all measured parameters are calculated.

The mass of nanoparticle : $E_m = \pm\frac{0.001}{1.752} = \pm 5.71 \times 10^{-4}$

The temperature : $E_{(T_h - T_c)} = \pm\frac{0.1}{22.8} = \pm 4.93 \times 10^{-3}$

The length of cavity : $E_l = \pm\frac{0.001}{0.1} = \pm 0.01$

The surface area of the cavity : $E_A = \pm\left[E_l^2 + E_l^2\right]^{1/2} = \pm 0.014$

Voltage : $E_V = \pm\frac{1}{25} = \pm 0.04$

Current : $E_I = \pm\frac{0.001}{0.648} = \pm 1.54 \times 10^{-3}$

6.2. Maximum error in the estimation of heat transfer parameters

First, the maximum error in the estimation of heat transfer coefficient is determined as follows:

$$MaxE_{\bar{h}} = \pm\left[E_V^2 + E_I^2 + (-E_A)^2 + (-E_{(T_h - T_c)})^2\right]^{1/2} = \pm 0.0426$$

Therefore, the maximum error in the measurement of heat transfer coefficient is 4.26%. In a similar way, the uncertainties in the estimation of the Nusselt number and the Rayleigh number are 7.43% and 9.45%, respectively.

7. Conclusions

A comparative experimental study is conducted to examine the effects of metal oxide nanopowders including TiO_2, CuO, and Al_2O_3 suspended in turbine oil on the natural convection flow inside a titled cube cavity. Three inclination angles of 0, 45, and 90° and three weight fractions of 0.2%, 0.5%, and 0.8% are investigated in the work. The results show that for any inclination angle and the Rayleigh number, the Nusselt number is higher for turbine oil compared to the nanofluids. For TiO_2/TO nanofluids, with increasing the inclination angle from 0 to 90, the Nusselt number increases. In other words, the optimum inclination angle for TiO_2/TO nanofluids is 90°. However, the tests on the two other nanofluids indicate that at the low concentration (i.e. 0.2 wt%), the maximum heat transfer occurs at the inclination angle of 45°. Also, it is found that for the angle of 90°, in the weight fraction of 0.2%, using TiO_2/TO nanofluid results in the maximum Nusselt number while for 0.8% wt.% the maximum Nusselt number is caused by the CuO/TO nanofluid flow. It was concluded that besides some factors such as shape, size, heat absorption, Brownian motion, and physical and chemical properties of the nanoparticles, future experimental studies are needed to know the possible reasons behind the changes in the Nusselt number for different nano materials.

Acknowledgments

The authors acknowledge Iranian Nano Technology Initiative for the financial support of this study. The third author wishes to thank Prof. Somchai Wongwises for the supports during his research at FUTURE, King Mongkut's University of Technology Thonburi, Thailand. The fourth author wishes to thank the National Science and Technology Development Agency, the Thailand Research Fund and the National Research University Project for the support.

References

[1] R. Saidur, K.Y. Leong, H.A. Mohammad, A review on applications and challenges of nanofluids, Renewable Sustainable Energy Rev. 15 (3) (2011) 1646–1668.

[2] O. Mahian, A. Kianifar, S.A. Kalogirou, I. Pop, S. Wongwises, A review of the applications of nanofluids in solar energy, Int. J. Heat Mass Transfer 57 (2013) 582–594.

[3] C.J. Ho, M.W. Chen, Z.W. Li, Numerical simulation of natural convection of nanofluid in a square enclosure: Effects due to uncertainties of viscosity and thermal conductivity, Int. J. Heat Mass Transfer 51 (17–18) (2008) 4506–4516.

[4] E. Abu-Nada, H.F. Oztop, Effects of inclination angle on natural convection in enclosures filled with Cu–water nanofluid, Int. J. Heat Fluid Flow 30 (4) (2009) 669–678.

[5] E. Büyük Öğüt, Natural convection of water-based nanofluids in an inclined enclosure with a heat source, Int. J. Therm. Sci. 48 (11) (2009) 2063–2073.

[6] E. Abu-Nada, Z. Masoud, H.F. Oztop, A. Campo, Effect of nanofluid variable properties on natural convection in enclosures, Int. J. Therm. Sci. 49 (3) (2010) 479–491.

[7] B. Ghasemi, S.M. Aminossadati, Periodic natural convection in a nanofluid-filled enclosure with oscillating heat flux, Int. J. Therm. Sci. 49 (1) (2010) 1–9.

[8] M. Shahi, A.H. Mahmoudi, F. Talebi, Numerical study of mixed convective cooling in a square cavity ventilated and partially heated from the below utilizing nanofluid, Int. Commun. Heat Mass Transfer 37 (2) (2010) 201–213.

[9] K.C. Lin, A. Violi, Natural convection heat transfer of nanofluids in a vertical cavity: effects of non-uniform particle diameter and temperature on thermal conductivity, Int. J. Heat Fluid Flow 31 (2) (2010) 236–245.

[10] K. Kahveci, Buoyancy driven heat transfer of nanofluids in a tilted enclosure, J. Heat Transfer 132 (6) (2010) 1–12.

[11] M. Corcione, Heat transfer features of buoyancy-driven nanofluids inside rectangular enclosures differentially heated at the sidewalls, Int. J. Therm. Sci. 49 (9) (2010) 1536–1546.

[12] A.H. Mahmoudi, M. Shahi, F. Talebi, Effect of inlet and outlet location on the mixed convective cooling inside the ventilated cavity subjected to an external nanofluid, Int. Commun. Heat Mass Transfer 37 (8) (2010) 1158–1173.

[13] A.H. Mahmoudi, M. Shahi, A.H. Raouf, Modeling of conjugated heat transfer in a thick walled enclosure filled with nanofluid, Int. Commun. Heat Mass Transfer 38 (1) (2011) 119–127.

[14] E. Abu-Nada, Rayleigh–Bénard convection in nanofluids: effect of temperature dependent properties, Int. J. Therm. Sci. 50 (9) (2011) 1720–1730.

[15] F.-H. Lai, Y.-T. Yang, Lattice Boltzmann simulation of natural convection heat transfer of Al_2O_3/water nanofluids in a square enclosure, Int. J. Therm. Sci. 50 (10) (2011) 1930–1941.

[16] Z. Haddad, E. Abu-Nada, H.F. Oztop, A. Mataoui, Natural convection in nanofluids: are the thermophoresis and Brownian motion effects significant in nanofluid heat transfer enhancement?, Int J. Therm. Sci. 57 (2012) 152–162.

[17] S. Parvin, R. Nasrin, M. Alim, N. Hossain, Double-diffusive natural convection in a partially heated enclosure using a nanofluid, Heat Transfer – Asian Res. 41 (6) (2012) 484–497.

[18] T. Basak, A.J. Chamkha, Heatline analysis on natural convection for nanofluids confined within square cavities with various thermal boundary conditions, Int. J. Heat Mass Transfer 55 (21–22) (2012) 5526–5543.

[19] E.H. Ooi, V. Popov, Numerical study of influence of nanoparticle shape on the natural convection in Cu–water nanofluid, Int. J. Therm. Sci. 65 (2013) 178–188.

[20] R. Nasrin, M.A. Alim, Free convective flow of nanofluid having two nanoparticles inside a complicated cavity, Int. J. Heat Mass Transfer 63 (2013) 191–198.

[21] F. Garoosi, G. Bagheri, F. Talebi, Numerical simulation of natural convection of nanofluids in a square cavity with several pairs of heaters and coolers (HACs) inside, Int. J. Heat Mass Transfer 67 (2013) 362–376.

[22] Z. Haddada, H.F. Oztop, E. Abu-Nada, A. Mataoui, A review on natural convective heat transfer of nanofluids, Renewable Sustainable Energy Rev. 16 (7) (2012) 5363–5378.

[23] D. Wen, Y. Ding, Formulation of nanofluids for natural convective heat transfer applications, Int. J. Heat Fluid Flow 26 (2005) 855–864.

[24] A.G.A. Nnanna, Experimental model of temperature-driven nanofluid, J. Heat Transfer 129 (2007) 697–704.

[25] C.H. Li, G.P. Peterson, Experimental studies of natural convection heat transfer of Al_2O_3/DI water nanoparticle suspensions (nanofluids), Adv. Mech. Eng. (2010) (Article ID 742739).

[26] C.J. Ho, W.K. Liu, Y.S. Chang, C.C. Lin, Natural convection heat transfer of alumina-water nanofluid in vertical square enclosures: an experimental study, Int. J. Therm. Sci. 49 (8) (2010) 1345–1353.

[27] R.L. Hamilton, O.K. Crosser, Thermal conductivity of heterogeneous two component systems, I&EC Fundam. 1 (1962) 182–191.

[28] K. Khanafer, K. Vafai, A critical synthesis of thermophysical characteristics of nanofluids, Int. J. Heat Mass Transfer 54 (2011) 4410–4428.

[29] H.C. Brinkman, The viscosity of concentrated suspensions and solutions, J. Chem. Phys. 20 (1952) 571.

International Communications in Heat and Mass Transfer 53 (2014) 98–108

Contents lists available at ScienceDirect

International Communications in Heat and Mass Transfer

journal homepage: www.elsevier.com/locate/ichmt

Numerical investigation for the calculation of TiO_2–water nanofluids' pressure drop in plain and enhanced pipes ☆

Ali Celen [a], Nurullah Kayaci [a], Alican Çebi [a], Hakan Demir [a], Ahmet Selim Dalkılıç [a,*], Somchai Wongwises [b]

[a] Heat and Thermodynamics Division, Department of Mechanical Engineering, Yildiz Technical University (YTU), Yildiz, Besiktas, Istanbul 34349, Turkey
[b] Fluid Mechanics, Thermal Engineering and Multiphase Flow Research Lab. (FUTURE), Department of Mechanical Engineering, Faculty of Engineering, King Mongkut's University of Technology Thonburi (KMUTT), Bangmod, Bangkok 10140, Thailand

ARTICLE INFO

Available online 1 March 2014

Keywords:
Pressure drop
Nanofluid
Single-phase flow
CFD
ANN

ABSTRACT

In this investigation, a numerical model having two-dimensional equations was obtained by a CFD program and authors' experimental data were evaluated for the verification procedure of the numerical outputs. The experimental case study includes the single-phase flow of pure water in plain and micro-fin pipes whereas the numerical one has the simulated results of TiO_2 particles suspended in single phase water flow in equivalent pipes at a constant heat flux. Hydrodynamics and thermal behaviors of the water–TiO_2 flow were calculated by constant heat flux and temperature-dependent settings. Physical specifications of nanofluids were calculated by means of the results of authors' previous ANN analyses. This study illustrates local and average values of temperature, pressure, and velocity distributions in the tested pipes; furthermore, comparisons of pressure drop characteristics are given in terms of nanoparticle concentrations and tube types.

1. Introduction

The productivity of a fluid regarding heat transfer applications depends on thermal conductivity significantly. Applications in the electronic, automotive, and aerospace industries are affected from traditional heat transfer fluids' (e.g. water, oil, ethylene glycol mixtures) low thermal conductivity values resulting as the restriction for the improvement of productivity and smallness in heat exchangers. Having suspended tiny particles in the base liquid improves the thermal conductivity and thus the increase in heat transfer performance is expected. In case there may be abrasion and clogging problems, the millimeter size suspended particles have not been used for a long time. The particle sizes from 10 to 100 nm are preferred to have uniform and stable suspensions. Some of recent experimental and numerical works on the single-phase flow of nanofluids are given as shown below:

Anoop et al. [1] have done an experimental investigation to determine the effect of particle size in the flow regarding laminar developing region. They had constant heat flux regarding nanofluid flow including 45 nm and 150 nm sized alumina particles suspended in base fluid in the investigated pipe. According to the results, nanofluids have the heat transfer enhancement in comparison to its base fluid; besides smaller sized particles with water mixture has greater heat transfer coefficients than those of larger one. They also obtained higher heat transfer coefficients in the developing region than those in the developed region. Finally, they correlated an equation for heat transfer in the developing region.

Heidary and Kermani [2] prepared a numerical work using nanofluid on the heat transfer and flow field in a wavy channel. They used copper particles in pure water for their simulation study. They studied on the influences of Reynolds number, nano-fluid volume fraction, and wave amplitude on the local and average Nusselt numbers and the skin friction coefficient. Authors validated their results with those in the literature and showed heat transfer increase regarding with the use of nanofluid flow in channels having wavy horizontal walls.

Heidary and Kermani [3] investigated nanofluid's heat transfer in a channel having some specified blocks. Their numerical study was subjected to the parameters of Reynolds number, nanofluid volume fraction and the block number. They studied those parameters' effects on the local and average Nusselt numbers and determined some enhancement on heat transfer using nanofluids flowing in a channel having attached blocks.

Wang and Chen [4] studied the heat transfer rate for flow through a specially designed channel benefitting from the techniques of simple coordinate transformation and the spline alternating-direction implicit numerically. Authors showed the influences on the wavy geometry, Reynolds number and Prandtl number on the skin-friction and Nusselt number. According to their results, the rise in the Reynolds number and the amplitude–wavelength ratio increase the values of the Nusselt number and the skin-friction coefficient.

☆ Communicated by W.J. Minkowycz.

* Corresponding author.
E-mail address: dalkilic@yildiz.edu.tr (A.S. Dalkılıç).

http://dx.doi.org/10.1016/j.icheatmasstransfer.2014.02.022
0735-1933/

Nomenclature

Cp	specific heat [J kg^{-1} K^{-1}]
D	tube diameter [m]
e	height of fin [m]
f	friction factor
k	thermal conductivity [W m^{-1} K^{-1}]
L	length of test tube [m]
m	mass flow rate [kg s^{-1}]
n	number of fins
p	distance between microfins [m]
Re	Reynolds number
t	thickness [m]
V	velocity [m s^{-1}]
μ	dynamic viscosity [Pa·s]
ρ	density [kg m^{-3}]
ϕ	volume fraction [%]
ΔP	pressure drop [Pa]
α	helix angle [°]

Subscripts

exp	experimental
f	fluid
i	inside
m	mean
nf	nanofluid
num	numerical
o	outside
p	particle
w	water

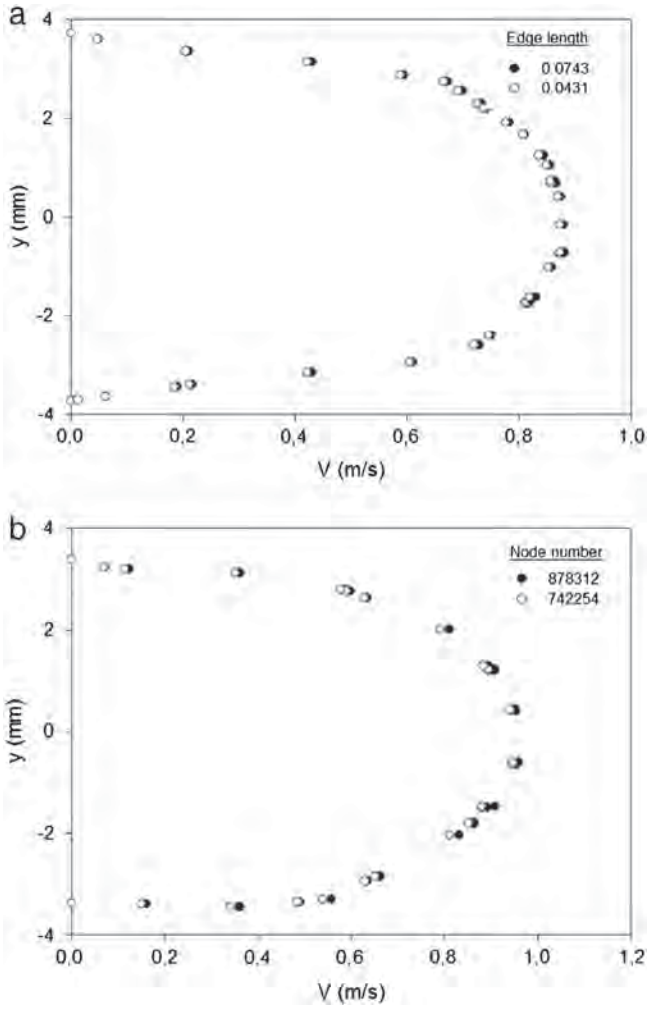

Fig. 1. Achieving the grid independency for velocity profiles of smooth tube 3 (a) and microfin tube (b) for mass flow rate of 0.0312 kg/s.

Yang et al. [5] calculated the heat transfer coefficients during laminar flow of various nanofluids in a horizontal heat exchanger. They used the graphitic particles in nature and reported some enhancement in thermal conductivity values because of used particles. Authors concluded that the experimental heat transfer coefficients have lesser increases than calculated ones.

Khanafer et al. [6] defined a numerical model regarding with the heat transfer enhancement in a two-dimensional enclosure considering solid particle dispersion of nanofluids. They validated and compared their findings with those in their previous work. Their analysis includes the influence of suspended tiny metallic particles on the fluid flow and heat transfer applications within the enclosure on thermal conductivity improvement. Their proposed Nusselt correlation has the parameters of Grashof number and volume fraction.

Xuan and Li [7] presented a theoretical model regarding with the nanofluid flow in a tube considering dispersion of solid particles. Their method includes the preparation of sample nanofluids. They obtained TEM images to show the stability and evenness of suspension. Thermal conductivity values were determined by means of both the hot-wire technique experimentally and their theoretical model. The volume fraction, dimensions, shapes and specifications of the nanoparticles are considered as important parameters in their study.

Shokouhmand et al. [8] performed a numerical simulation study related with Darcy–Brinkman–Forchheimer flow model and convective flow model in an enhanced round micro/nano channel. They considered velocity slip and temperature jump in their model and investigated the influence of Knudsen number and Darcy coefficient on velocity and temperature spreading.

Table 1
Geometrical parameters of the investigated tubes.

Parameter	Unit	Smooth tube 1	Smooth tube 2	Smooth tube 3 (simulated)	Micro-fin tube
Length (L)	mm	1100	1100	1100	1100
Outside diameter (D_o)	mm	8	10	8.48	8
Inside diameter (D_i)	mm	6	8	7.48	7.48
Thickness (t)	mm	1	1	1	0.26
Fin Height (e)	mm	–	–	–	0.22
Fin pitch (p)	mm	–	–	–	0.34
Helix angle (α)	°	–	–	–	35
Number of fins (n)	–	–	–	–	65
e/D	–	–	–	–	0.027

Mohammed et al. [9] concentrated on the influences of the use of louvered strip inserts installed in a round double tube heat exchanger on the thermal and flow fields. They used several kinds of nanoparticles having various sizes and concentrations dispersed in water in their numerical study based on finite volume technique. According to their analyses, the highest Nusselt number was obtained by using SiO_2 nanofluid comparing with Al_2O_3, ZnO, and CuO. Nusselt number decreases with increasing nanoparticle diameter size and the increase in volume fraction of nanoparticles enhances the Nusselt numbers. They also studied the significant parameters' effects on the skin friction coefficient factor.

Moraveji et al. [10] studied the convective nanofluid flow in the developing region of a pipe with constant heat flux numerically. They used numerical (CFD) analyses for the nanoparticles of Al_2O_3 having various sizes and concentrations with its base fluid of water. Their analyses included the influence of particle size on single phase heat transfer

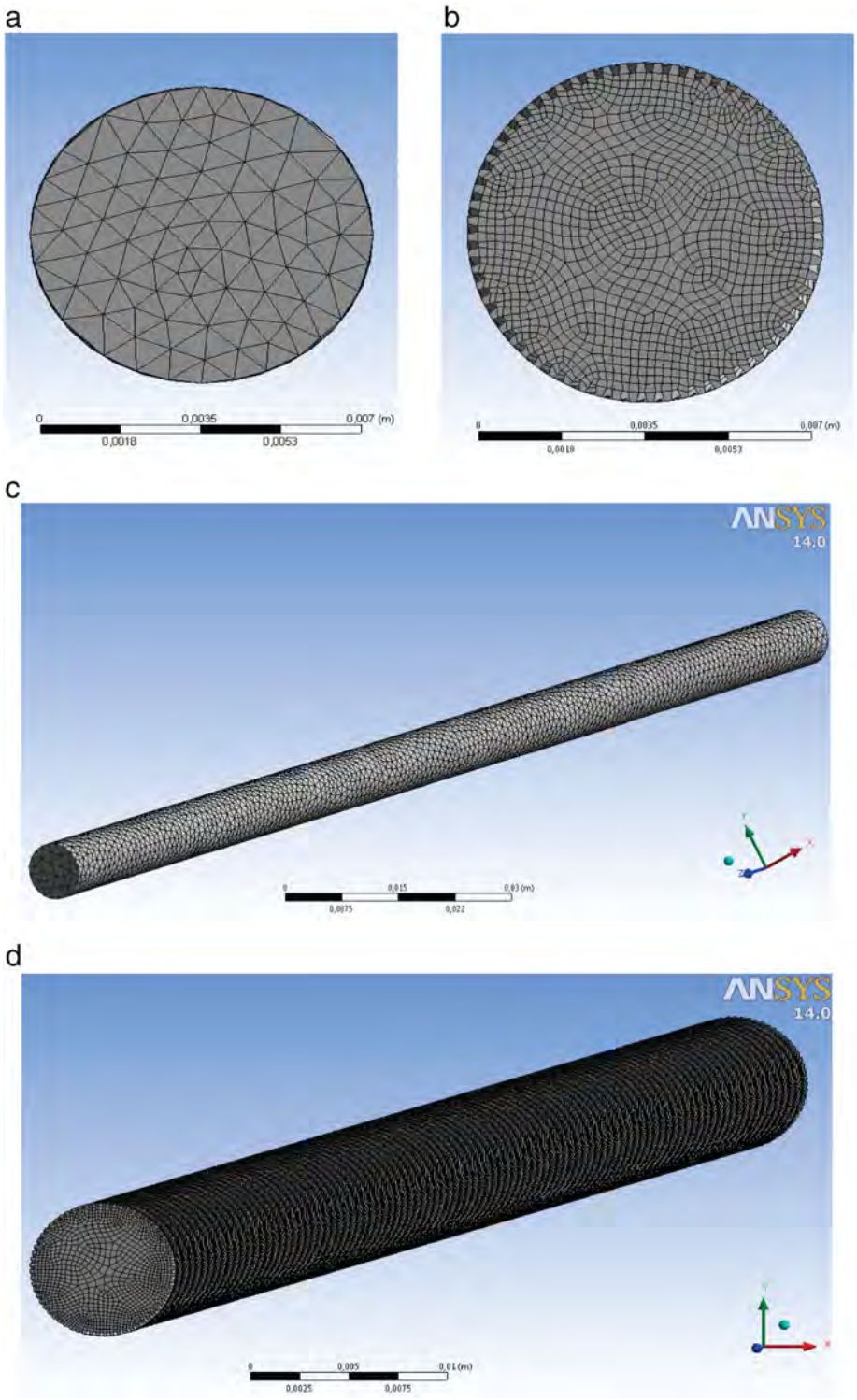

Fig. 2. Grid structures of investigated tubes. (a) Front view of smooth tube 3. (b) Front view of microfin tube. (c) Isometric view of smooth tube 3. (d) Isometric view of microfin tube.

coefficient for a limited range of Reynolds numbers. They proposed a correlation having dimensionless numbers to determine Nusselt numbers as according to their outputs.

A lot of investigations have been prepared to determine the heat transfer augmentation of nanofluids in the literature so far. It should be considered that there have insufficient numbers of studies; including artificial neural network based physical properties [17], on the nanofluid flows in enhanced tubes. Solid Works software [24] was used for the draw of plain and micro-fin pipes and then they were imported into ANSYS Fluent software [25] for CFD analysis. Before the simulation of the smooth and micro-fin tubes in the CFD program, the validation process of experimental data was accomplished for the convective single phase flow of pure water in authors' previous study [23]. The measured data and simulated one for nanofluid flow having TiO_2 particles with its base fluid of water were analyzed by the CFD program to determine the pressure drops, temperature, pressure and velocity distributions in plain and enhanced pipes. Moreover, the measured and numerical outputs were evaluated as a comparison and also their variations with Reynolds number and flow rate were also shown for the investigated tubes in the study. It can be said that this paper is a continuation of authors' previous works on nanofluids [10–23].

2. Experimental apparatus

Additional knowledge on the experimental setup for investigating single phase heat transfer flow of pure water inside plain and microfin horizontal pipes exists in Celen et al. [23]. Specifications of the tested pipes are shown in Table 1. For the comparison of smooth and microfin tubes having the same equivalent diameter, smooth tube 3 is simulated by using smooth tube 1 and 2' experimental data.

3. Data reduction

3.1. Calculation of pressure drop in pipes

In practice, pressure drop is calculated by means of an equation given below. This equation can be used for smooth or rough surfaces, laminar or turbulent flows, smooth or rough surfaces [26].

$$\Delta P = f \cdot \frac{L}{D} \cdot \frac{\rho V_m{}^2}{2}. \tag{1}$$

In Eq. (1) f is friction factor and it can be changed according to the type of flow (laminar or turbulent). The friction factor for fully developed turbulent flow in a smooth tube expressed respectively as follows

$$\begin{aligned} f &= 0.316/Re^{0.25} \text{ for } 2300 < Re < 20000 \text{ and} \\ f &= 0.184/Re^{0.2} \text{ for } 20000 < Re < 400000 \end{aligned} \tag{2}$$

where Reynolds number is determined as follows:

$$Re = \frac{\rho \cdot V_m \cdot D}{\mu}. \tag{3}$$

Detailed list of turbulent friction factor equations for plain and microfin pipes can be seen in Celen et al. [23].

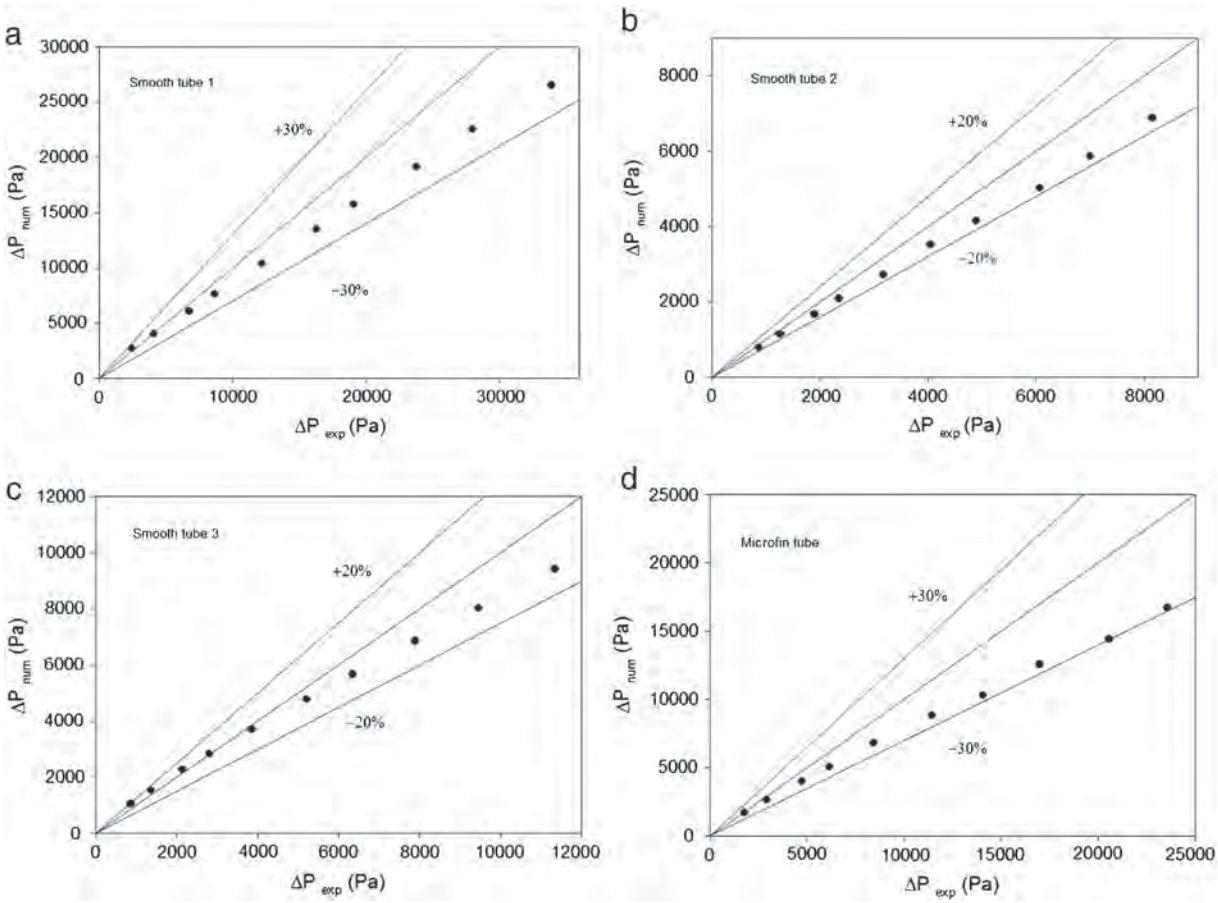

Fig. 3. The comparison of experimental and numerical pressure drop results for smooth tubes 1 (a), 2 (b), 3 (c) and (d) microfin tube.

3.2. Specifications of nanofluids

The greatest confirmed equations were taken from Kayaci et al. [17] and used for the determination of the physical properties of TiO_2–water nanofluids. In their work, they summarized the literature on almost all empirical correlations for nanofluid dynamic viscosity, thermal conductivity and specific heat capacity at constant pressure. They also developed two different ANN models in order to conclude the proper grouping of specifications for the TiO_2 nanofluid. The ANN model 1 inputs were the empirical equations of specifications, the nanoparticle concentration, the velocity of water and the average temperature in the test tube. The outputs of the ANN model 1 were pressure drop, friction factor, shear stress, and convective heat transfer coefficient and heat flux. The ANN model 2 inputs were the empirical equations of physical properties and the inlet and outlet temperatures and velocity of the water in the investigated pipe. The ANN model 2 outputs were the pressure drop and the convective heat transfer coefficient. According to their study, the best agreeable equations were obtained from the ANN 1 model for the specifications (k, μ, Cp) of nanofluids and they are given as follows:

The thermal conductivity of the nanofluid was calculated from Bhattacharya et al. [27] correlation, as:

$$k_{nf} = k_p\phi + (1-\phi)k_f. \tag{4}$$

The dynamic viscosity of the nanofluid was calculated from Wang et al. [28] correlation as:

$$\mu_{nf} = \mu_f\left(306\phi^2 - 0.19\phi + 1\right). \tag{5}$$

The heat capacity of nanofluid was calculated from Maxwell [29] as:

$$Cp_{nf} = (1-\phi)Cp_f\left(1 + 2.5\phi_p\right)\mu_f. \tag{6}$$

The density of the nanofluid was calculated from Pak and Cho's [30] equation, as follows:

$$\rho_{nf} = \rho_p\phi + (1-\phi)\rho_f. \tag{7}$$

3.3. Numerical method — CFD approach

In CFD analysis one of the most used software is the ANSYS Fluent program [25]. The detailed information about the program and its algebraic models exists in the Fluent User's Guide. In order to transform governing equations into algebraic definitions, the control volume theory is used by the program and their numerical solution is possible with giving an important investigation clarification. The control volume method operates with the integration of the governing definitions for each control volume, and at that point by discretizing the formulas that conserve each quantity based on the control volume.

Because leading equations could be given numerical analyses afterward their transformation into a set of algebraic formulas, classic single-phase conservation formulas were presented with a solution in the control volume method. Whole scalar values and velocity components are determined at the center of control volume interfaces, where grid schemes are done widely. The Semi-Implicit Method for Pressure Linked Equations (SIMPLE) was evaluated to match pressure and velocity. A point-implicit (Gauss–Seidel) linear equation solver, in conjunction with an algebraic multigrid method, was applied in the Fluent CFD program to evaluate the linear systems resulting from

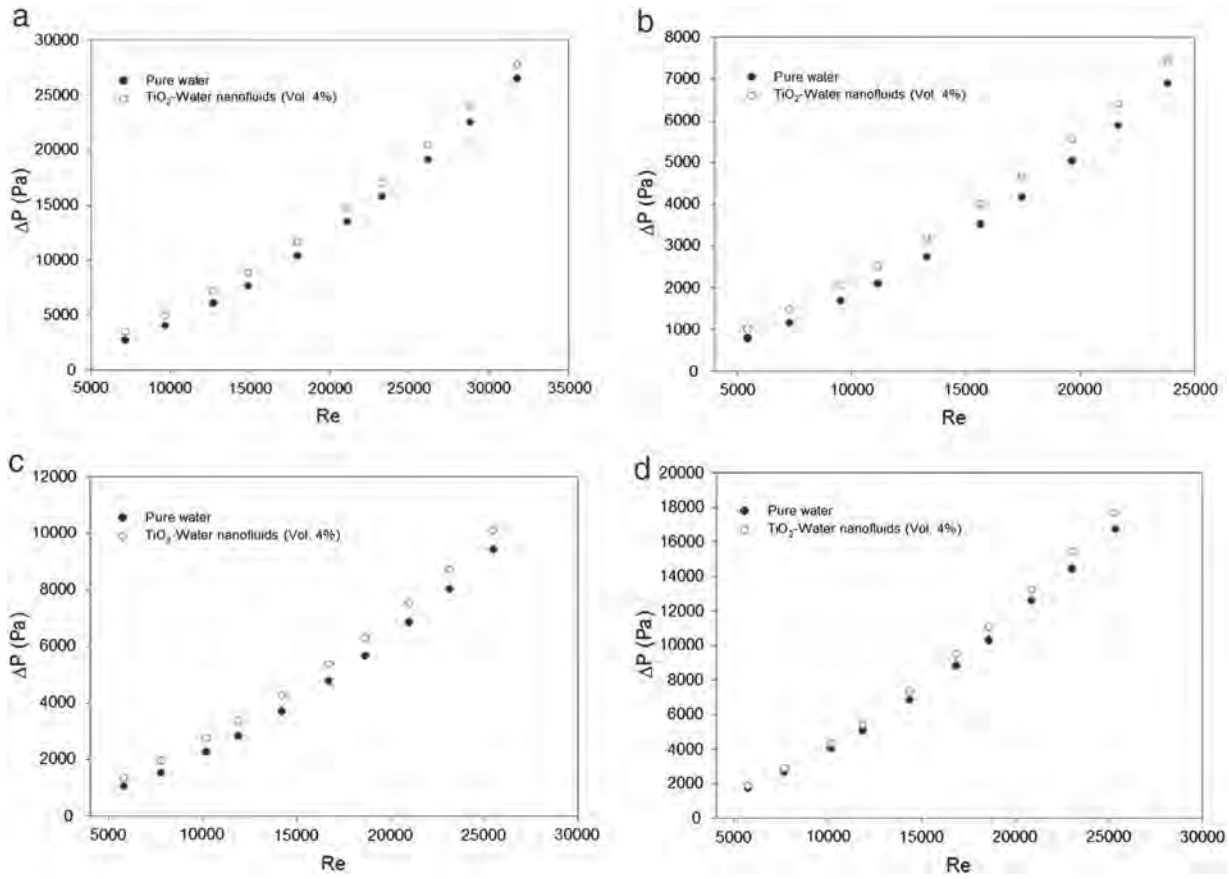

Fig. 4. Numerical pressure drop comparison of water and TiO_2–water nanofluids flowing in smooth tubes 1 (a), 2 (b), 3 (c) and (d) microfin tube.

discretization schemes. k-ε turbulence models were selected as viscous model. In the course of the iterative procedure, residuals were thoroughly observed and all outputs were thought to have converged when the residuals for each governing equation drop below 10^{-6}. Boundary conditions were recognized for the velocity inlet at the tube inlet and for the pressure outlet at the tube exit; turbulence intensity and equivalent diameter were identified for the turbulence parameters. Constant heat flux was determined to the tube surface.

According to Fig. 1(a), in order to display grid-independent solutions in smooth tube 3, two different edge lengths were considered in the tetrahedron grid type for mass flow rate of 0.0312 kg/s. Fig. 1(b) shows grid-independent solutions in micro-fin tubes by using two different node numbers for mass flow rate of 0.0312 kg/s. Fig. 1(a) and (b) shows the velocity profile distributions at the different mesh sizes, which are nearly identical in each other.

4. Results and discussion

In order to confirm the numerical results, some experimental data points was obtained for the single-phase flow of pure water in horizontal smooth and micro-fin tubes with inner diameters of 6, 7.48 and 8 mm at a Mechanical Engineering Lab in YTU. The experiments have been performed by pure water. Evaluation of the outputs is illustrated in sequence in below paragraphs:

In the numerical study, the commercial software package ANSYS Fluent [25] was used for the investigation of pressure drop of plain and microfin pipes. Investigated tubes were created by means of Solid Works program [24] and they were imported to ANSYS Geometry. After this process, meshing process was applied to the tubes by using ANSYS Meshing program. The mesh affects the accuracy, convergence, and speed of the solution. Moreover, the meshing time to develop a model frequently takes an important percentage of the necessary time to obtain outcomes from the analyses; this explanation reveals that the better and extra computerized the meshing tools, the better the solution. Grid structures of investigated tubes are illustrated in Fig. 2.

Fig. 3 depicts the comparison of experimental and numerical pressure drop outputs for plain and microfin pipes. According to Fig. 1, numerical and experimental pressure drop results of smooth tube 1, smooth tube 2, smooth tube 3 and microfin tube were observed in the deviation bands of ±21.8%, ±17.2%, ±20.3% and ±29.8%, respectively.

Fig. 4 shows numerical pressure drop comparison pure water and nanofluids with TiO_2 volume concentrations of 0.4% flowing in smooth and microfin tubes. It is clear that the pressure drop of nanofluid is greater than the pure water for all tested tubes. The maximum augmentation of pressure drop outputs for plain pipe 1, plain pipe 2, plain pipe 3 and microfin pipe were 28.1%, 28.9%, 29.1% and 8%, respectively. The result can be explained with relation between dynamic viscosity and pressure drop of the fluid. Because nanoparticle addition in a base fluid generally increases dynamic viscosity of the fluid, it is obvious that the usage of nanoparticles in water raises pressure drop results.

Fig. 5 shows comparison of numerical pressure drop results of pure water and TiO_2–water nanofluids with 4% volumetric particle concentrations flowing inside plain and micro-fin pipes. As shown in the figure, the pressure drop enlarged regularly as mass flow rate increased for both plain and microfin pipes. It was also observed that the smooth tube 1 had higher pressure drop when it was matched with plain pipes 2 and 3. Compared with plain tube, microfin pipe has higher pressure drop.

Figs. 6(a) and 7(a) represent velocity profiles of pure water and TiO_2–water nanofluids having volume concentration of 4% flowing in smooth tube 3. Figs. 8(a) and 9(a) represent velocity profiles of pure water and TiO_2–water nanofluids having volume concentration of 4% flowing in microfin tube. The velocity of the fluid at the place where fluid and pipe wall contact with each other is zero because of no slip condition. It increases with increasing distance from the pipe wall. The velocity profile of the fluid is related to the surface properties of the pipe wall. The smooth tubes have more uniform velocity profile than the microfin tubes.

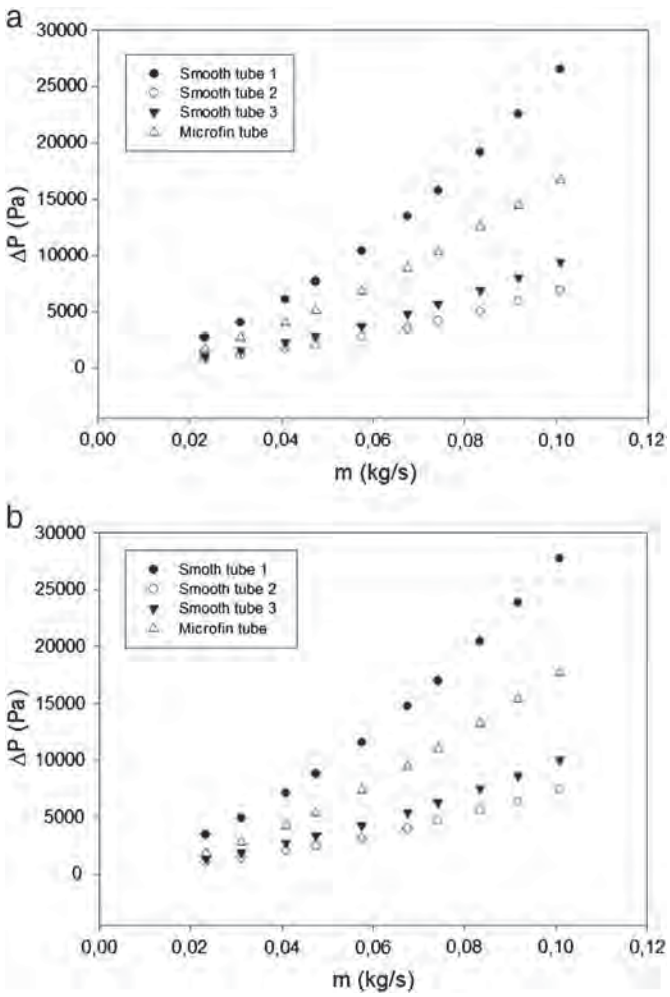

Fig. 5. Comparison of numerical pressure drop results of tubes used in the study. a) Pure water and b) TiO_2–water nanofluids (vol. 4%).

Figs. 6(b) and 7(b) represent temperature profiles of pure water and TiO_2–water nanofluids having volume concentration of 4% flowing in smooth tube 3. Figs. 8(b) and 9(b) represent temperature profiles of pure water and TiO_2–water nanofluids having volume concentration of 4% flowing in microfin tube. The temperature of the fluid has its minimum rate on the wall and maximum rate at the entrance of the tube. Because cold water flows outside of the pipe (annulus side of double pipe heat exchanger), the temperature of the fluid also decreases with increasing distance from the entrance.

Figs. 6(c) and 7(c) represent temperature profiles of pure water and TiO_2–water nanofluids having volume concentration of 4% flowing in smooth tube 3. Figs. 8(c) and 9(c) represent temperature profiles of pure water and TiO_2–water nanofluids having volume concentration of 4% flowing in microfin tube. The fluid pressure has its highest rate at inlet of the tube and it decreases with increasing distance from inlet of the pipe.

It is should be noted that the velocity, temperature and pressure profiles represented in Figs. 6–9 were obtained for mass flow rate of 0.0312 kg/s.

Many figures and tables might be produced from the results of the analyses, but, caused by the space restriction, just characteristic conclusions are illustrated. Moreover, the additional knowledge about the information above and some extra graphics with various experimental factors regarding with the work exists in the authors' published publications previously in open sources.

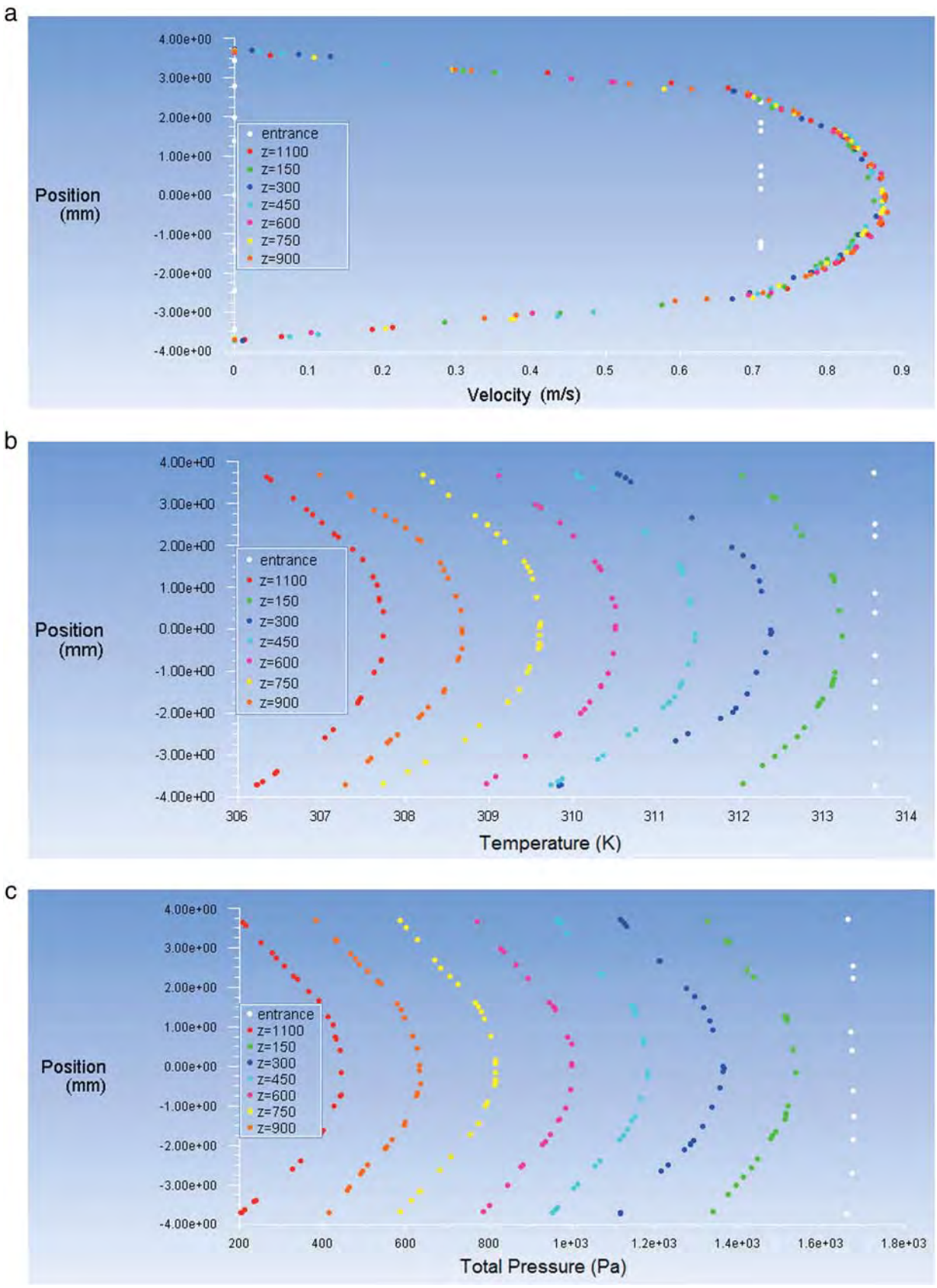

Fig. 6. Velocity (a), temperature (b) and pressure (c) profiles at various locations in smooth tube 3 for pure water.

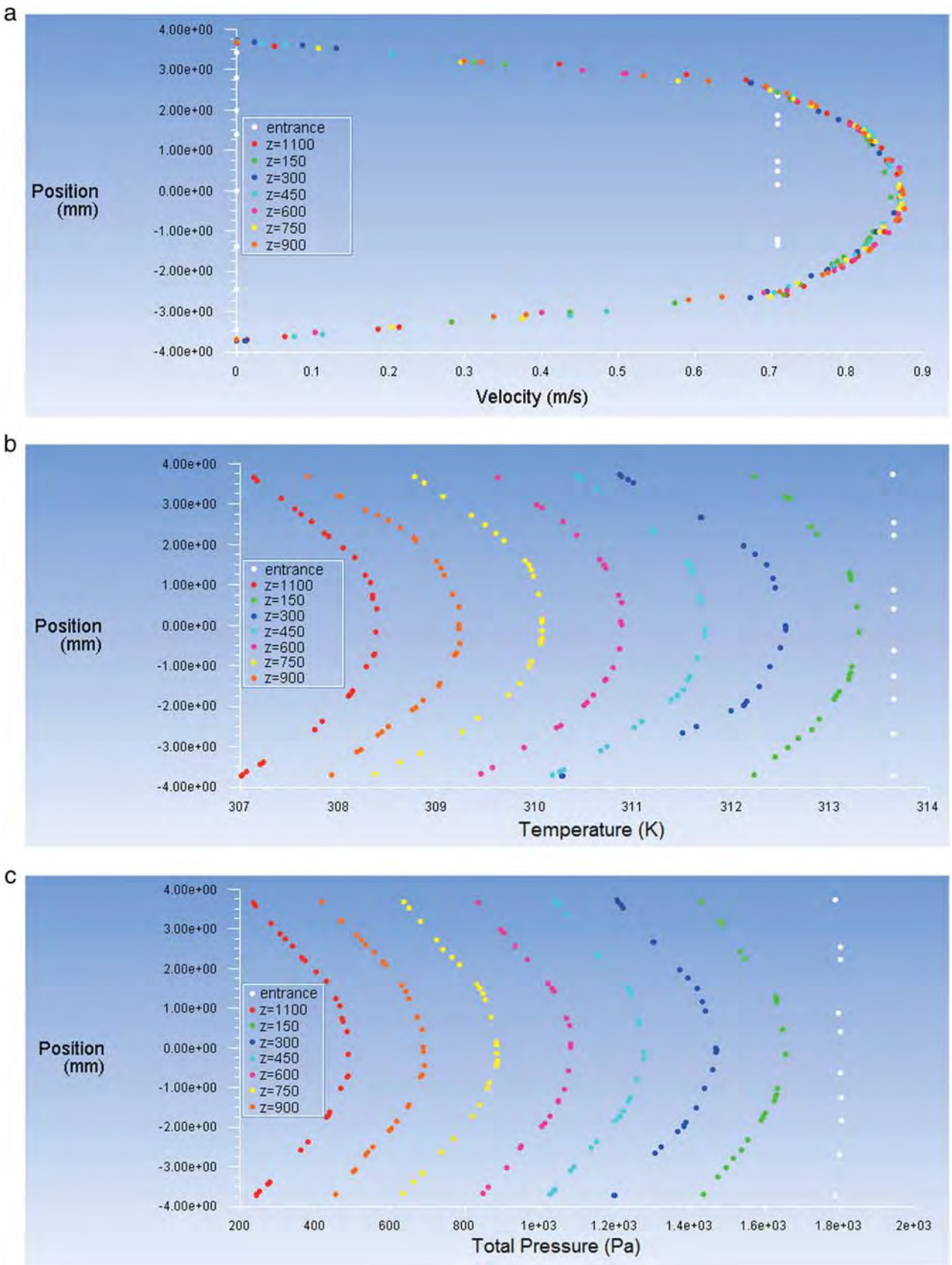

Fig. 7. Velocity (a), temperature (b) and pressure (c) profiles at various locations in smooth tube 3 for TiO_2–water nanofluids (vol. 4%).

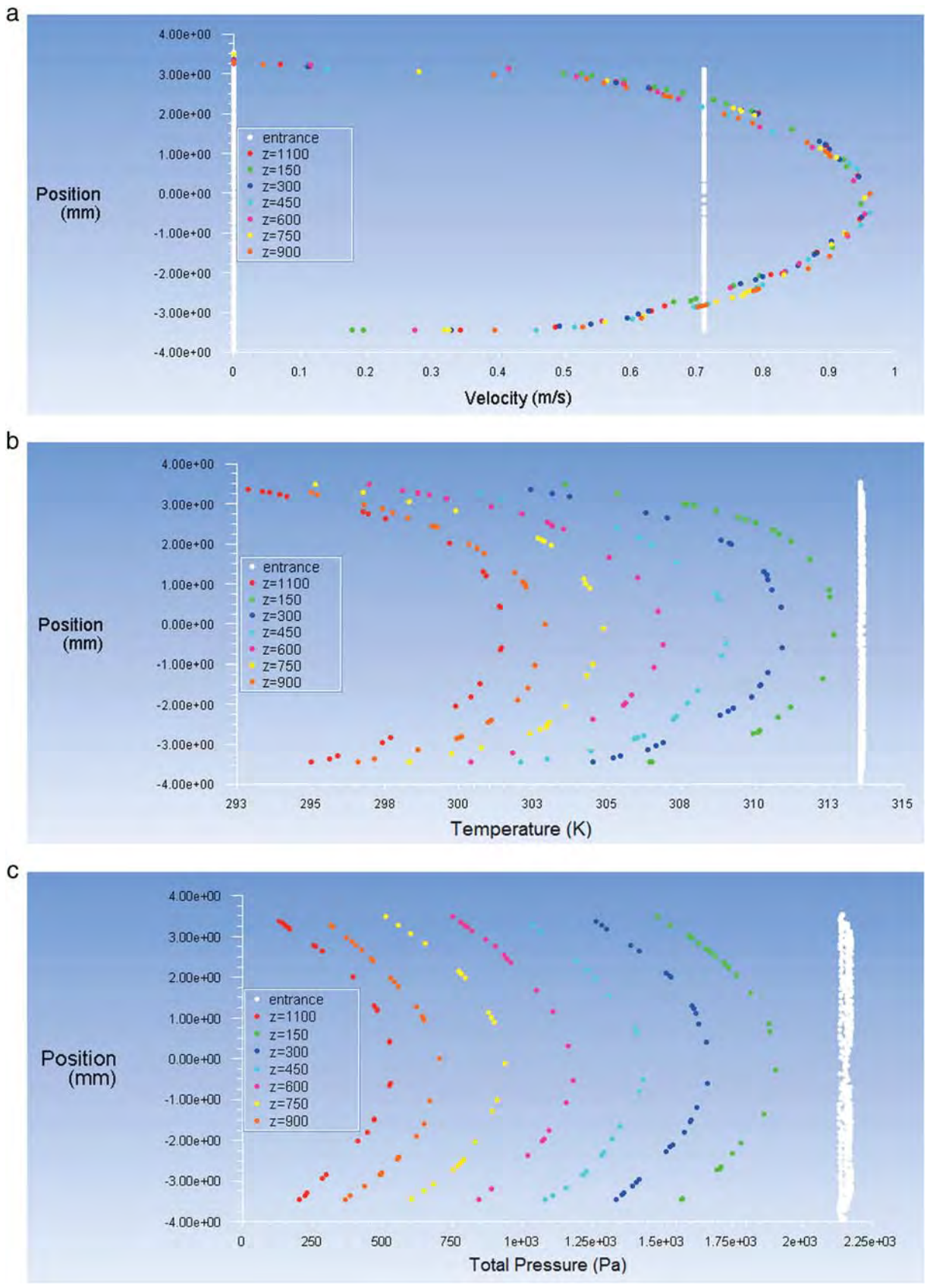

Fig. 8. Velocity (a), temperature (b) and pressure (c) profiles at various locations in microfin tube for pure water.

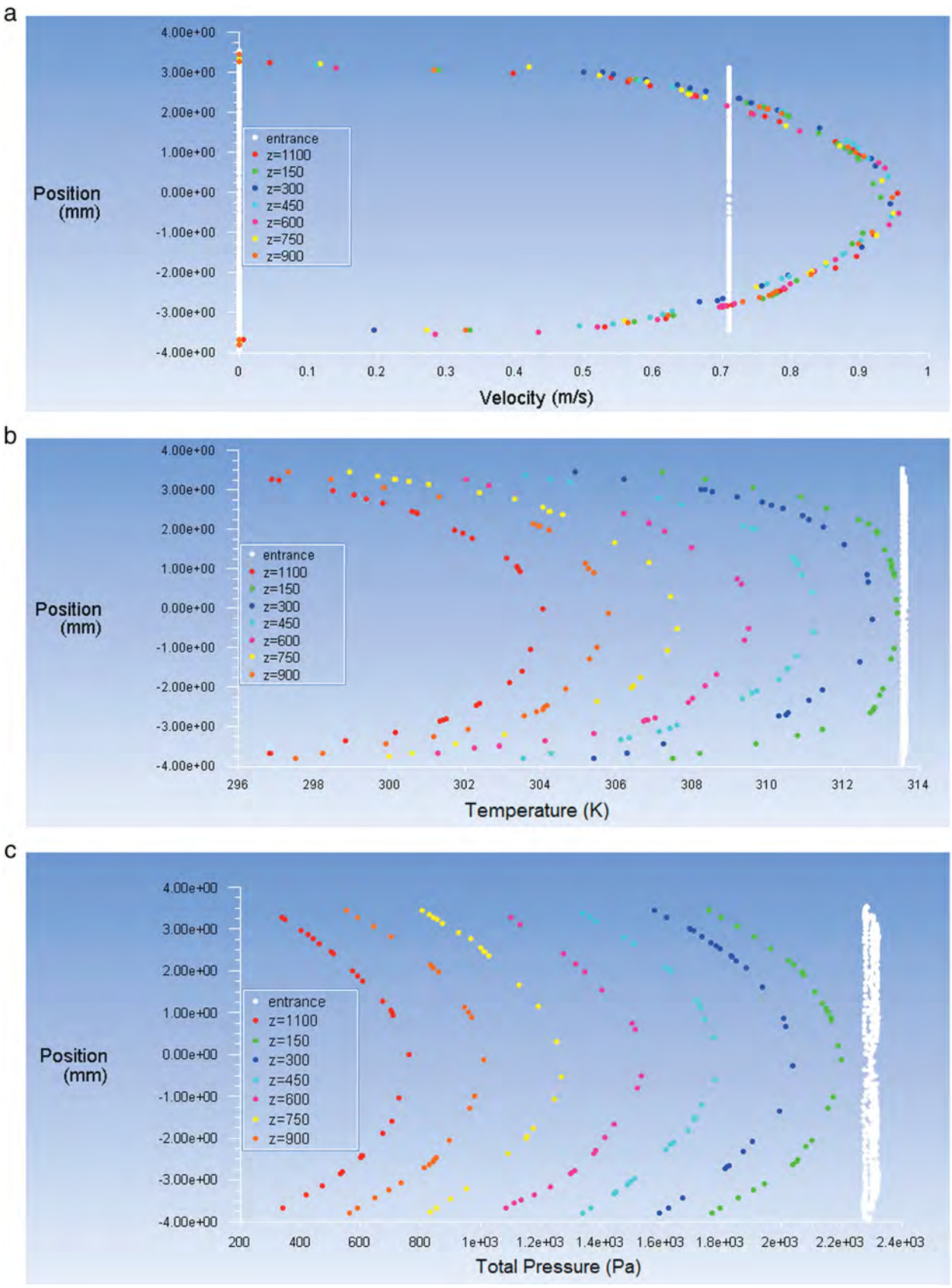

Fig. 9. Velocity (a), temperature (b) and pressure (c) profiles at various locations in microfin tube for TiO_2–water nanofluids (vol. 4%).

5. Conclusion

This investigation studied the pressure drop of pure water and TiO_2–water nanofluid flowing inside plain and micro-fin pipes by means of CFD analysis using authors' accurate and repeatable single-phase flow data. The results of current work are summarized herein below:

a. Experimental and numerical pressure drop results for pure water and TiO_2–water nanofluids were compared and determined in the tolerable range of $\pm 30\%$ for investigated tubes.
b. The numerical pressure drop results of TiO_2–water nanofluids were higher compared to pure water for both plain and microfin pipes.
c. The numerical outcomes showed that the pressure drop in plain pipe having smaller inside diameter was greater than in the plain pipe having larger inside diameter.
d. The numerical pressure drop of pure water flowing in microfin tube was greater than those in the plain one having the same inside diameter.
e. The numerical pressure drop of TiO_2–water nanofluids flowing in microfin tube was greater than plain one having the same inside diameter.
f. The temperature, pressure, and velocity distributions in the smooth and microfin tubes were illustrated by using CFD analysis.

This study indicates that a computational fluid dynamics (CFD) program can be evaluated for the pure water and TiO_2 particles suspended in water mixture flowing in plain and microfin tubes.

Acknowledgments

The fifth author wishes to thank KMUTT for providing him with a Post-doctoral fellowship. The sixth author is indebted to the Thailand Research Fund, the National Research University Project and the National Science and Technology Development Agency for their financial support. This research has been supported by Yildiz Technical University Scientific Research Projects Coordination Department. Project number: 2013-06-01-KAP01.

References

[1] K.B. Anoop, T. Sundararajan, Sarit K. Das, Effect of particle size on the convective heat transfer in nanofluid in the developing region, Int. J. Heat Mass Transfer 52 (2009) 2189–2195.
[2] H. Heidary, M.J. Kermani, Effect of nano-particles on forced convection in sinusoidal-wall channel, Int. Commun. Heat Mass Transfer 37 (2010) 1520–1527.
[3] H. Heidary, M.J. Kermani, Heat transfer enhancement in a channel with block(s) effect and utilizing nano-fluid, Int. J. Therm. Sci. 57 (2012) 163–171.
[4] C.-C. Wang, C.-K. Chen, Forced convection in a wavy-wall channel, Int. J. Heat Mass Transfer 45 (2002) 2587–2595.
[5] Y. Yang, Z.G. Zhang, E.A. Grulke, W.B. Anderson, G. Wu, Heat transfer properties of nanoparticle-in-fluid dispersions (nanofluids) in laminar flow, Int. J. Heat Mass Transfer 48 (2005) 1107–1116.
[6] K. Khanafer, K. Vafai, M. Lightstone, Buoyancy-driven heat transfer enhancement in a two-dimensional enclosure utilizing nanofluids, Int. J. Heat Mass Transfer 46 (2003) 3639–3653.
[7] Y. Xuan, Q. Li, Heat transfer enhancement of nanofluids, Int. J. Heat Fluid Flow 21 (2000) 58–64.
[8] H. Shokouhmand, A.H. Meghdadi Isfahani, E. Shirani, Friction and heat transfer coefficient in micro and nano channels filled with porous media for wide range of Knudsen number, Int. Commun. Heat Mass Transfer 37 (2010) 890–894.
[9] H.A. Mohammed, Husam A. Hasan, M.A. Wahid, Heat transfer enhancement of nanofluids in a double pipe heat exchanger with louvered strip inserts, Int. Commun. Heat Mass Transfer 40 (2013) 36–46.
[10] M.K. Moraveji, M. Darabi, S.M.H. Haddad, R. Davarneja, Modeling of convective heat transfer of a nanofluid in the developing region of tube flow with computational fluid dynamics, Int. Commun. Heat Mass Transfer 38 (2011) 1291–1295.
[11] H. Demir, A.S. Dalkilic, N.A. Kurekci, W. Duangthongsuk, S. Wongwises, Numerical investigation on the single phase forced convection heat transfer characteristics of TiO_2 nanofluids in a double-tube counter flow heat exchanger, Int. Commun. Heat Mass Transfer 38 (2011) 218–228.
[12] M. Balcilar, A.S. Dalkilic, A. Suriyawong, T. Yiamsawas, S. Wongwises, Investigation of pool boiling of nanofluids using artificial neural networks and correlation development techniques, Int. Commun. Heat Mass Transfer 39 (2012) 424–431.
[13] W. Duangthongsuk, A.S. Dalkilic, S. Wongwises, Convective heat transfer of Al_2O_3–water nanofluids in a microchannel heat sink, Curr. Nanosci. 8 (2012) 317–322.
[14] T. Yiamsawas, A.S. Dalkilic, S. Wongwises, Measurement of the thermal conductivity of titania and alumina nanofluids, Thermochim. Acta 545 (2012) 48–56.
[15] A.S. Dalkilic, N. Kayacı, M. Tabatabaei, O. Yıldız, A. Celen, W. Daungthongsuk, S. Wongwises, Forced convective heat transfer of nanofluids — a review of the recent literature, Curr. Nanosci. 8 (2012) 949–969.
[16] T. Yiamsawas, A.S. Dalkilic, S. Wongwises, Measurement of specific heat of nanofluids, Curr. Nanosci. 8 (2012) 939–944.
[17] N. Kayaci, M. Balcilar, M. Tabatabaei, A. Celen, O. Yıldız, A.S. Dalkilic, S. Wongwises, Determination of the single-phase forced convection heat transfer characteristics of TiO2 nanofluids flowing in smooth and micro-fin tubes by means of CFD and ANN analyses, Curr. Nanosci. 9 (2013) 61–80.
[18] W. Duangthongsuk, T. Yiamsawas, A.S. Dalkilic, S. Wongwises, Pool boiling heat transfer characteristics of Al_2O_3–water nanofluids on a horizontal cylindrical heating surface, Curr. Nanosci. 9 (2013) 56–60.
[19] T. Yiamsawas, O. Mahian, A.S. Dalkilic, S. Kaewnai, S. Wongwises, Experimental studies on the viscosity of TiO_2 and Al_2O_3 nanoparticles suspended in a mixture of ethylene glycol and water for high temperature applications, Appl. Energy 111 (2013) 40–45.
[20] P. Nitiapiruk, O. Mahian, A.S. Dalkilic, S. Wongwises, Performance characteristics of a microchannel heat sink using TiO2/water nanofluid and different thermophysical model, Int. Commun. Heat Mass Transfer 47 (2013) 98–104.
[21] T. Yiamsawas, A.S. Dalkilic, O. Mahian, S. Wongwises, Measurement and correlation of the viscosity of water based Al_2O_3 and TiO_2 nanofluids in high temperatures and comparisons with literature reports, J. Dispers. Sci. Technol. 34 (2013) 1697–1703.
[22] A. Suriyawong, A.S. Dalkilic, S. Wongwises, Nucleate pool boiling heat transfer correlation for TiO_2–water nanofluids, J. ASTM Int. 9 (2012) 1–12.
[23] A. Celen, A.S. Dalkilic, S. Wongwises, Experimental analysis of the single phase pressure drop characteristics of smooth and microfin tubes, Int. Commun. Heat Mass Transfer 46 (2013) 58–66.
[24] SolidWorks, SolidWorks Corporation, 300 Baker Avenue, Concord, MA 01742. Available from: http://www.solidworks.com/ .
[25] ANSYS Fluent, ANSYS Inc., 10 Cavendish Court Lebanon, NH 03766 Available from: http://www.ansys.com/ .
[26] Y.A. Çengel, Heat Transfer: A Practical Approach, 3rd ed. McGraw Hill, 2006.
[27] P. Bhattacharya, S.K. Saha, A. Yadav, P.E. Phelan, R.S. Prasher, Brownian dynamics simulation to determine the effective thermal conductivity of nanofluids, J. Appl. Phys. 95 (2004) 6492–6494.
[28] X. Wang, X. Xu, S.U.S. Choi, Thermal conductivity of nanoparticle–fluid mixture, J. Thermophys. Heat Transfer 13 (1999) 474–480.
[29] J.C. Maxwell, Electricity and Magnetism, Clarendon Press, Oxford UK, 1873.
[30] B.C. Pak, Y.I. Cho, Hydrodynamic and heat transfer study of dispersed fluids with submicron metallic oxide particles, Exp. Heat Transfer 11 (1998) 151.

International Communications in Heat and Mass Transfer 53 (2014) 185–194

Contents lists available at ScienceDirect

International Communications in Heat and Mass Transfer

journal homepage: www.elsevier.com/locate/ichmt

Classification of in-tube boiling R134a data belonging to the smooth and corrugated tubes ☆

M. Balcilar [a,*], A.S. Dalkilic [b], A.C. Sonmez [c], S. Wongwises [d]

[a] Computer Engineering Department, Yildiz Technical University,Davutpasa, Esenler, Istanbul 34349, Turkey
[b] Heat and Thermodynamics Division, Department of Mechanical Engineering, Yildiz Technical University (YTU), Yildiz, Besiktas, Istanbul 34349, Turkey
[c] Faculty of Computer and Informatics, Istanbul Technical University, Maslak, 34469, Istanbul, Turkey
[d] Fluid Mechanics, Thermal Engineering and Multiphase Flow Research Lab. (FUTURE), Department of Mechanical Engineering, Faculty of Engineering, King Mongkut's University of Technology Thonburi (KMUTT), Bangmod, Bangkok 10140, Thailand

ARTICLE INFO

Available online 1 March 2014

Keywords:
Artificial intelligence
Machine learning
Pattern classification
Naive Bayes Classifier (NBC)
Quadratic Discriminant Classifier (QDC)
Linear Discriminant Analysis (LDA)
Mahalanobis distance
Principle component
Boiling

ABSTRACT

Different types of tubes have been used to improve cooling systems regarding the performance, cost and compactness. Corrugated tubes are tubes with their inner surface enhanced in these systems. One of the applications of machine learning, named as pattern classification, is often used to separate the human faces, voices, finger prints etc. In this study, it is used to separate the R134a data taken in-tube boiling process in smooth and enhanced tubes automatically. In other words, the developed numerical algorithms enabled artificial intelligence to predict the type of tubes having equivalent diameters used in the experiments. Systematical experiments, including saturation temperatures of 10, 15 and 20 °C, mass fluxes of 200, 300 and 400 kg m^{-2} s^{-1} and heat fluxes of 20, 25 and 30 W m^{-2}, are carried out for the comparisons using smooth and 5 different types of corrugated tubes having various corrugation depths and helix angles. The boiling process in the test tubes has been measured with 300 data points, having 30 individual parameters (inputs) for varying tube types for the reduction process by the Linear Discriminant Analysis (LDA) and Principle Component Analysis (PCA). The classification success rates of the methods of Linear Discriminant Classifier (LDC), Quadratic Discriminant Classifier (QDC), Naive Bayes Classifier (NBC) and Minimum Mahalanobis Distance Classifier (MMDC) by each dimensional reduction and the total area occupying under receiver operating characteristic (ROC) curves are determined according to 3-fold cross validation method. NBC method has the highest classification success with the accuracy of 98.33% as a result of the reduction to 3 dimensions by LDA method. In addition to this, QDC method has the highest area under curve (AUC) with the value of 0.9994 according to the reduction to 3 dimensions by LDA method. Dependency analyses showed that the use of 8 dimensional experimental parameters as the most important input is enough to determine the type of test tubes with a high accuracy.

1. Introduction

Machine Learning is a kind of programming concept to optimize a performance criterion using example data or past experience [1]. The act of taking in raw data and making an action, based on the category of pattern, is called as pattern classification [2]. Pattern classification is the most important field of Machine Learning. Humans are able to classify the patterns which they come across in their daily lives very easily. Amongst common examples of pattern classification is the human ability to identify the caller on the phone, to recognize individual persons in a photograph or to read and guess the author of an unfamiliar text without being given any information about the author. The pattern classification problem arises due to the human desire to have the machines do all these tasks which are easily done by human beings. There are a lot of classification methods described in the literature developed utilizing computer science research on how these methods can be applied to different problems.

In pattern classification problems, the methods in use are probability-based methods such as Maximum-likelihood Estimation, Bayesian Estimation, Naïve Bayes Classification, Expectation–Maximization, and Hidden Markov Model, non-parametric models such as Parzen Windows and K-nearest Neighbor [2], linear models such as Linear Discriminant Functions, Probabilistic Discriminant Functions, and Logistic Regression [3], neural network models such as Multi-Layer Perceptron, Radial Basis Function, and Probabilistic Neural Network, non-metric models such as Decision Trees and Decision Forests [2], kernel-based methods such as Support Vector Machines and Quadratic Discriminant Functions [3], minimum distance classifier methods defined accordingly

☆ Communicated by Dr. W.J. Minkowycz.

* Corresponding author: Tel.: +90212835758; fax: +902123835732.
E-mail addresses: muhammet@ce.yildiz.edu.tr (M. Balcilar), dalkilic@yildiz.edu.tr (A.S. Dalkilic).

http://dx.doi.org/10.1016/j.icheatmasstransfer.2014.02.020
0735-1933/

with several distance metrics [4], and fuzzy logic-based methods such as Fuzzy Classification and Adaptive Neuro Fuzzy Inference System [5].

However, in heat transfer literature, the pattern classification methods have started being utilized very recently. The first example is the study which aimed to detect the faults occurring in the cooling systems by using Bayesian Classification Methods [6]. In the study, the signals obtained from the machine were classified based either on their fault pattern or non-fault pattern characteristics. Another study aimed to classify the heat resistance of steel structure. In this study, the aim was to classify the properties detecting them from images of steel structures [7]. A different study showed that, there is an important difference between fire retardant treated and untreated wood products in terms of heat release and therefore these products can be classified only with measurements and observations. However, a specific classification algorithm was not applied [8]. Another study investigated the classification of different types of milk obtained from different places based on the values measured by electronic nose device. Support vector machine was used in this study [9].

There has been no study in the literature yet to date; investigating the automatic classification of different types of tubes used refrigeration systems during two-phase flows. For this reason, this study is expected to be a model for future studies and fill the gap in the literature.

2. Experimental setup

A schematic diagram of the test apparatus can be seen from author's publications in the literature. The refrigerant loop consists of a preheating loop, test section, heating loop, and chilling loop. For the refrigerant circulating loop, liquid refrigerant is forced by a gear pump which can be adjusted to the flow rate using an inverter. The refrigerant then passes in series through a filter/dryer, a refrigerant flow meter, a preheater, and a sight glass and enters the test section. The pre-heater controls the inlet quality before entering the test section. It consists of a spiral counter-flow tube-in-tube heat exchanger which is designed to supply heat in order to prepare an inlet quality for the vaporization of the refrigerant. Leaving the test section, the refrigerant vapor then condenses inside a sub-cooler and is collected in a receiver. After leaving the chilling loop, the refrigerant returns from a two phase refrigerant to a sub-cooled state. Eventually, the refrigerant returns to the refrigerant pump to complete the cycle.

Details of the test section are shown schematically in Fig. 1a. The test section is a vertical counter-flow double tube heat exchanger with refrigerant flowing downward in the inner tube and heating water flowing upward in the annulus. The test sections are one smooth tube and two corrugated tubes, which are made from copper. The inner diameter and outer diameter of the inner tube are 8.7 and 9.52 mm, respectively. The length of the test section is 500 mm. Fig. 1b shows a sketch of a corrugated tube. T-type thermocouples are installed at the inlet and outlet of the test section to measure the saturation temperature of the refrigerant. Similarly, the differential pressure transducer is installed in order to measure the pressure drop across the test section. The length between the pressure taps is 850 mm. There are 10 thermocouples located at five positions along the test section. All of the wall thermocouples are fixed with special glue having low thermal conductivity. The test section is insulated with rubber foam with a thermal conductivity of 0.04 W/mK. All of the thermocouples are well calibrated by standard thermometers with a precision of 0.1 °C. The refrigerant flow meter is a variable area type and is specially calibrated in the range of 0.2–3.4 LPM for R-134a by the manufacturer, as is the differential pressure transducer. In the experiments, the inlet quality of the test section is varied by small increments. The imposed heat flux, mass flux, and saturation temperature are kept constantly at the desired values. The system is allowed to approach a steady state before any data are recorded. During experiments, the temperature and pressure are continuously recorded along the test section by the data acquisition system.

It should be noted that the detailed information on the experimental setup belonging to the subject tubes in this study can be seen from authors' previous publications [10,11].

3. Methodology

One of the application fields of Machine Learning is pattern classification problem. Definition of this problem is shown mathematically as follows [3].If each value measured by the experiments is represented by x scalar and each vector consisting of the values measured at each point of the experiment is represented by X, m dimensional vector belonging to n number test point can be shown as follows:

$$X_i = \left\{x_{i,1}, x_{i,2}, \ldots\ldots\ldots, x_{i,m}\right\} \quad i = 1 \ldots n \tag{1}$$

X_i vector in Eq. (1) is called as pattern. If the discrete class to which each pattern belongs is named as s_i and if s_i is an element of a set (which consists of C number elements) which has a finite number of elements, this is expressed as follows:

$$s_i \in \{1, 2, 3, \ldots C\} \tag{2}$$

When X_i is known, finding what s_i value corresponding to this vector is called classification problem.

Generally classification problem can be considered as the investigation of a function that takes X_i input to s_i output like the equation below.

$$f(X_i) = s_i \tag{3}$$

In this case, the only difference between the classification problem and regression problem is that function outputs are not continuous but they are members of a discrete set [2].

3.1. Dimensionality reduction

Pattern classification algorithms can directly use the value (which can be named as feature) obtained from the test environment and classify them. Similarly, the success of classification can be increased by reducing some features obtained by dimensionality reduction algorithms to a fewer number of features. This dimension reduction process can be done in two ways, namely feature selection and feature extraction. While feature selection process is done using some of the measured values (features) and not the others, feature extraction process is realized by using some of the combinations of all measured values. The method that will be used to select the linear combinations determines the name of dimensionality reduction algorithm. The number of the combinations to be used indicates the number of dimensions the new features will have. In this study, the main focus is to increase the success of classification methods by using the dimensional reduction through Principal Component Analysis and Linear Discriminant Analysis [12].

3.1.1. Principal Component Analysis (PCA)

Some dimensions (features) of p-dimensional X_i measurements obtained from the experiment environment can have high correlations with each other. In this case, it is quite redundant for the classification algorithm to take each feature with high correlation into consideration, bearing in mind that it may lead to wrong classification results [13]. Under these circumstances, the characteristic vector should have a linear transformation such that new characteristic vector features generated by this transformation could have the lowest correlation possible. New features having minimum correlation are called Principle Components. Principle Component Analysis (PCA) is an orthogonal transformation which changes the p-dimensional X_i feature vector into k-dimensional Y_i vector whose correlation is minimal between these dimensions. Principle Components obtained by PCA are determined as transformation elements through a process which orders

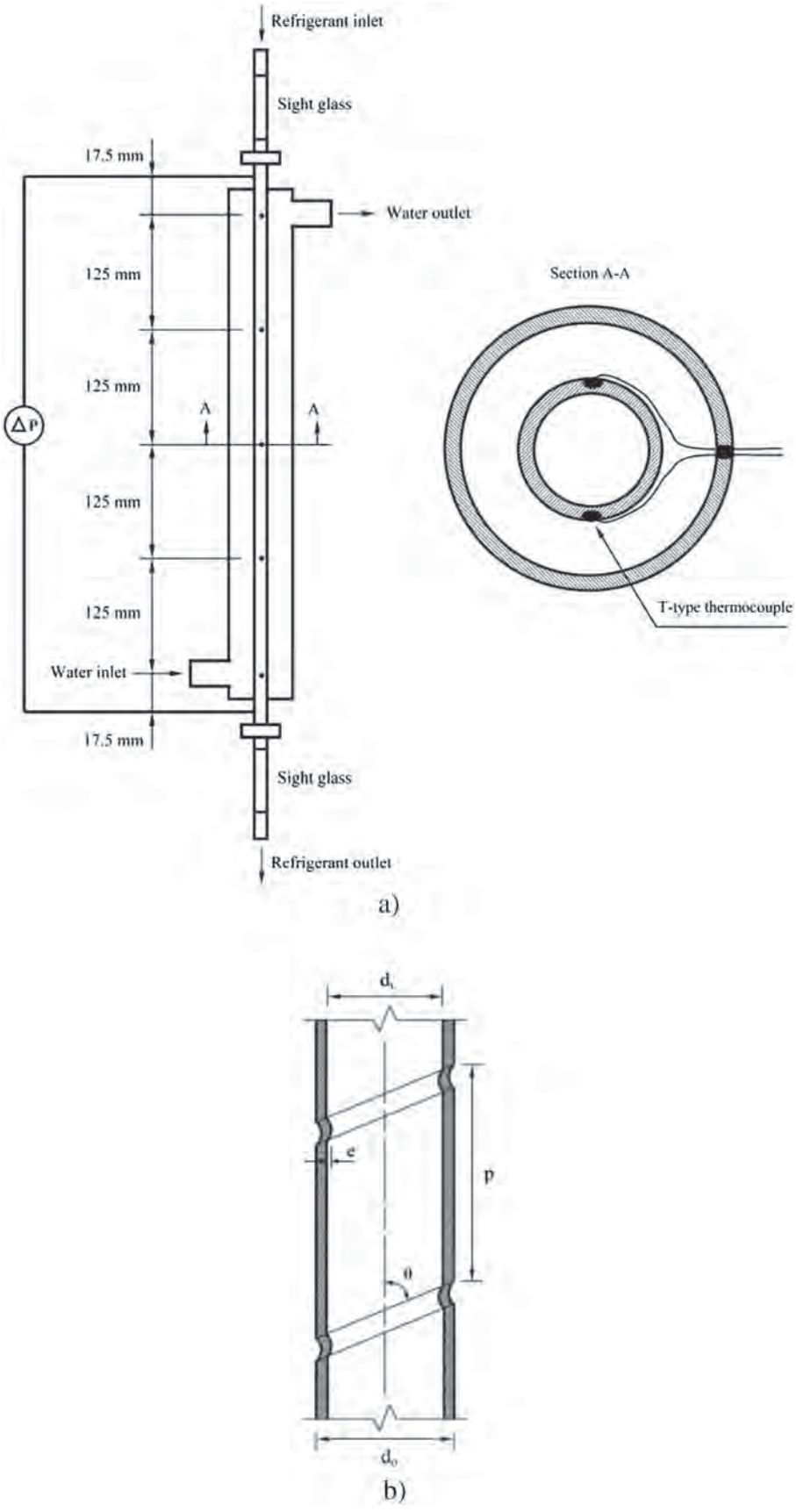

Fig. 1. Schematic diagram of the test section (a) and sketch of a grooved tube (b).
From Aroonrat and Wongwises [10], with permission from Elsevier.

them according to their variance values and gets k number with the highest variance. For the method to become a dimensionality reduction, evidently the relation between k and p must be $k < p$ [2]. Details of method are explained as follows. n number and p dimensional measurements obtained from the test environment are presented in Eq. (4) as:

$$\begin{aligned} X_1 &= \left\{x_{1,1}, x_{1,2}, \ldots, x_{1,p}\right\} \\ X_2 &= \left\{x_{2,1}, x_{2,2}, \ldots, x_{2,p}\right\} \\ X_n &= \left\{x_{n,1}, x_{n,2}, \ldots, x_{n,p}\right\} \end{aligned} \tag{4}$$

If the mean vector of this measurement values is presented by $\bar{X}$, the equation will take its form in Eq. (5) as:

$$\bar{X} = \frac{1}{n}\sum_{i=1}^{n} X_i \tag{5}$$

With subtraction of the measured vector and mean vector of n number vectors, mean zero (0) vectors are obtained as follows:

$$\vec{x}_i = X_i - \bar{X} \tag{6}$$

A matrix, which consists of mean zero feature vectors, n rows and p column, is defined as:

$$A = \begin{bmatrix} \vec{x}_1 \\ \vec{x}_2 \\ \vec{x}_n \end{bmatrix} \tag{7}$$

C matrix is obtained by multiplying the transpose of A matrix and itself.

$$C = A^T A \tag{8}$$

The values of $\vec{x}_i$ and λ_1, corresponding Eq. (9), are found in order to be represented with eigenvalue λ and eigenvector $\vec{x}$.

$$C\vec{x}_i = \lambda_i \vec{x}_i \tag{9}$$

The eigenvectors corresponding to k number of all the resulting eigenvectors, which have the highest value, become the principal components to be found. T matrix consisting of principle components is called as a transformation matrix.

$$T_{PCA} = [\vec{x}_1 \quad \vec{x}_2 \quad \vec{x}_k] \tag{10}$$

PCA dimensions can be obtained by using the obtained T matrix with p row and k column.

$$Y_i = \vec{x}_i \cdot T_{PCA} \tag{11}$$

3.1.2. Linear Discriminant Analysis (LDA)

The PCA method mentioned in the previous section does not use the data class information. However, the LDA method suggests a linear transformation by using the class information from a group in which all data belonging to the same class have the minimum variance, while data coming from different classes have the maximum variance in comparison to each other. This is an example of where within-class variances are minimum while between-class variances are maximum. In this way, the classes can be separated from each other more clearly in the new dimension [13].

The details of the method are summarized in this paragraph [2]. If the feature vector is obtained from the test environment taken as in Eq. (4), then the discrete class to which each of these vectors belong can be represented as in Eq. (2) and the mean of the features vector can be represented as in Eq. (5), and the average of cth class can be represented by $\overline{X}_c$. Similarly, if the number of elements in cth class is taken as n_c and the total experiment points as n, the average of each class can be found as follows:

$$\overline{X}_c = \frac{1}{n_c}\sum_{i=1}^{n} \delta_{ic} X_i \quad c = 1..C. \tag{12}$$

In this equation δ_{ic} is a coefficient which defines whether ith experiment point belongs to c^{th} class and it is expressed as follows:

$$\delta_{ic} = \begin{Bmatrix} 1, & s_i = c \\ 0, & s_i \neq c \end{Bmatrix} \tag{13}$$

When each element is subtracted from the class average it belongs to, experimental points that come from the same class can have 0 averages amongst themselves.

$$\vec{x}_i = X_i - \sum_{c=1}^{c} \delta_{ic} \cdot \overline{X}_c \quad i = 1..n \tag{14}$$

S scatter matrix defining variance belonging to each class is calculated as:

$$S_c = \sum_{i=1}^{n} \delta_{ic} \vec{x}_i^{\,T} \vec{x}_i \quad c = 1..C \tag{15}$$

Within-class scatter matrix defining total variance with-in class is determined as:

$$S_w = \sum_{c=1}^{c} S_c \tag{16}$$

Between-class scatter matrix defining between-class variance is obtained as:

$$S_B = \sum_{c=1}^{c} 2.\left(\overline{X}_c - \overline{X}\right)^T.\left(\overline{X}_c - \overline{X}\right) \tag{17}$$

When within-class variance is minimum and between-class variance is maximum, fitness function reaches its maximum and the fitness function can be expressed as follows:

$$J(W) = \frac{\left|w^T \cdot S_B \cdot w\right|}{\left|w^T \cdot S_W \cdot w\right|} \tag{18}$$

LDA seeks the transformation which is the maximum of the W transformation matrix making function. W vector making J function maximum is the solution of Generalized Rayleigh quotient problem, also very well known in mathematical physics [14]. Analytical solution of this problem is a combination of W_i and λ_i values proving the equation below.

$$S_B W_i = \lambda_i S_w W_i \tag{19}$$

W_i values are eigenvectors of $S_w^{-1} \cdot S_B$ matrix and λ_i values are eigenvalues of $S_w^{-1} \cdot S_B$ matrix. T matrix, which is composed of the eigenvectors corresponding to k number of all eigenvectors having the highest values, is called as LDA transformation matrix.

$$T_{LDA} = [W_1 \quad W_2 \quad W_k] \tag{20}$$

LDA dimensions can be determined by using the subject T matrix with row p and column k in Eq. (21) as:

$$Y_i = (X_i - \bar{X}) T_{LDA} \tag{21}$$

S_w matrix must not be singular in order to define eigenvectors of Eq. (19). However, in some cases S_w matrix can be singular. In this case, first of all, p dimensional number is reduced to d by applying PCA to all the data in the form of determinant of S_w matrix not being equal to 0, and then d dimensional number is reduced to k by applying LDA. Evidently, the relation between dimensional numbers must be $k < d < p$.

3.2. Classification methods

Vectors with new features, which are obtained from dimensional reduction process, are classified by using Linear Discriminant Classifier, Quadratic Discriminant Classifier, Naive Bayes Classifier, and Minimum Mahanolobis Distance Classifier methods, and this section aims to give detailed information on each of these methods.

3.2.1. Linear Discriminant Classifier (LDC)

Discriminant functions are functions which can separate feature vectors and the resulting data point belonging to 2 different classes in the space they are located. They can also separate the space into 2 regions. Linear Discriminant Function is also used in cases where the function in question is linear with regard to the feature comprising the data. In this case, Linear Discriminant Function can be written as below [2].

$$\begin{aligned} g(X) &= w_0 + \sum_{j=1}^{k} w_j x_j \\ g(X) &= w^T \cdot X + w_0 \end{aligned} \tag{22}$$

where X is a vector having k features in the form of $\{x_1, x_2, \ldots\ldots\ldots, x_k\}$, W is the weight vector having k number of weights in the form of $\{w_1, w_2, \ldots\ldots\ldots, w_k\}$, w_0 is the threshold value, and g is the Linear discriminant function. When an element in the form of $x_0 = 1$ is added to the vector X, X becomes $\{1, x_1, x_2, \ldots\ldots\ldots, x_k\}$, and if w_0 value is added to the vector W, it becomes $\{w_0, w_1, w_2, \ldots\ldots\ldots, w_k\}$. In this case, discriminant function can be written as below.

$$g(X) = w^T X \tag{23}$$

If $g(X) > 0$, it means that X feature belongs to vector class 1 and if $g(X) < 0$, it means that X feature belongs to vector class 2. In order to find the values comprising W weight vector in Eq. (23), J error function needs to be defined and try to be minimized. If the cluster of misclassified feature vectors is represented by Y, error function is written as follows.

$$J(W) = \sum_{i \in Y} -w^T X_i \tag{24}$$

Minimization problem can be solved by optimization methods such as Gradient Descent and Newton optimization.

According to Gradient Descent method, the algorithm started from a random W value update w vector in each j step like the update step below.

$$W^{j+1} = W^j - \eta^j \nabla J(W) \tag{25}$$

where ∇J is the gradient vector of error function, and η^j is the amount of step.

According to Newton optimization method, a random W value is taken as a starting point, but in the update step the inverse of Hessian (H) matrix, which is comprised of second order partial derivation of J error function, is used.

$$W^{j+1} = W^j - H^{-1} \nabla J(W) \tag{26}$$

Both methods update W weight vector until the defined stopping criteria are proven. When stopping criteria are proven, the resulting vector W defines boundary separating class 1 from class 2.

In this study, instead of using Gradient Descent and Newton optimization methods, an LDA based method is used. The preferred LDA based method can find the smallest error analytically without using iteration but instead an eigenvector, having taken the mean square errors of the expected class and the actual class is taken as the error function.

In this method, experimental points aiming to separate 2 classes are reduced to one dimension with LDA as mentioned in Section 3.1.2. If resulting value is higher than 0, it belongs to class 1, otherwise, it belongs to class 2. If discriminant function equation, separating 2 classes from each other, is represented by Eq. (22), then equivalent W vector and w_0 can be represented as below.

$$\begin{aligned} W &= n S_w^{-1} (\bar{X}_1 - \bar{X}_2) \\ w_0 &= -\bar{\bar{X}} W \end{aligned} \tag{27}$$

where n is the total element number, S_w is within-class scatter matrix calculated by Eq. (16), $\bar{X}_i$ is the mean of data points belonging to ith class given in Eq. (12), and $\bar{X}$ is the mean of all data points in the Eq. (5).

Above mentioned methods are for determining the boundary lines separating 2 classes from each other. For multi class case, multiple separators of 2 classes need to be taken, 2 different methods in the literature, one of them being one-to-one strategy and the other being one-to-all strategy. In one-to-one strategy, C number discriminant function is used for C number class. Each discriminant function determines whether a vector belongs to that class or one of the all other classes.

$$g_i(X) = w_i^T X + w_{i,0} \qquad i = 1 \ldots C \tag{28}$$

In this case, $\hat{s}$ is the prediction class of X feature vector and found in Eq. (29).

$$\hat{s} = i, \quad if \;\; g_i(X) > g_j(X) \qquad for\ all\ j \neq i \tag{29}$$

In one to one strategy a different discriminant function is written for each pair. $C(C\text{-}1)/2$ number discriminant functions are written for C number class. These functions are expressed in Eq. (30).

$$g_{ij}(X) = W_{ij}^T X + w_{ij,0} \qquad i = 1 \ldots C-1, \quad j = i+1 \ldots C \tag{30}$$

In this case, $\hat{s}$ is the prediction class of X feature vector and found in Eq. (31).

$$\hat{s} = i, \quad if \;\; g_{ij}(X) > 0 \quad for\ all\ j \neq i \tag{31}$$

In this study one-to-all strategy is preferred.

3.2.2. Quadratic Discriminant Classifier (QDC)

The only difference between QDC and LDC method is that in QDC, the discriminant function is not linear with the feature vector while it comprises a second order function. If feature vector X is like $\{x_1, x_2, \ldots\ldots\ldots, x_k\}$, then the discriminant function for QDC is written as follows [2].

$$g(X) = w_0^s + \sum_{j=1}^{k} w_j^l x_j + \sum_{i=1}^{k} \sum_{j=i}^{k} w_{ij}^q x_i x_j \tag{32}$$

where w^s defines a scalar number representing threshold value, w^l defines a vector representing linear coefficients, and w^q defines a matrix representing quadratic coefficients. In order to reduce Eqs. (32) to (22), $w_0 = w_0^s$ substitution is made. Descriptions of X feature vector and W weight vector are changed as below.

$$\begin{aligned} X &= \left\{ x_1, \ldots, x_k, x_1^2, x_1 x_2, \ldots, x_1 x_k, x_2^2, \ldots, x_2 x_k, \ldots x_k^2 \right\} \\ W &= \left\{ w_1^l, \ldots, w_k^l, w_{1,1}^q, w_{1,2}^q, \ldots, w_{1,k}^q, w_{2,2}^q, \ldots, w_{2,k}^q, \ldots, w_{k,k}^q \right\} \end{aligned} \tag{33}$$

In this case, discriminant function of QDC method can be expressed with Eq. (22).

$$g(X) = w^T X + w_0 \tag{34}$$

Further calculations use the same procedure as LDC method.

3.2.3. Minimum Mahalanobis Distance Classifier (MMDC)

MMDC is a distance based method. In addition, it is called the parametric method since the elements of the classes use primary thesis suggesting that they are distributed in space with a normal distribution depending on the mean and covariance of the class. According to this algorithm, first of all, the mean and the covariance of each class need to be predicted. Since the mean and the covariance of the subject training set used are the best predictions of the average and covariance of all classes, these parameters are calculated as a starting point [4].

$\bar{X}_c$ value, which is the mean value of cth class, is calculated with Eq. (12). If the number of the elements in cth class is represented by n_c, the covariance of cth class is calculated by Eq. (35) as:

$$\sum_c = \frac{1}{n_c}\sum_{s_i=c}(X_i-\bar{X}_c)^T(X_i-\bar{X}_c) \qquad c = 1...C \tag{35}$$

Mahalanobis distance between X_i feature vector and cth class (d_{ic}) is calculated as below:

$$d_{ic} = (X_i-\bar{X}_c)\sum_c^{-1}(X_i-\bar{X}_c)^T \quad c = 1...C \tag{36}$$

In this case, $\hat{s}$ is the prediction class of X feature vector, and can be calculated in Eq. (37) as:

$$\hat{s}_i = argmin_c(d_{ic}) \tag{37}$$

3.2.4. Naive Bayes Classifier (NBC)

NBC method is a probability based simple classifier. This method which is based on Bayes theorem has been widely used because of both its simplicity, and better performance compared to more complicated classifiers.

NBC method makes classification with the assumption that all features comprising data are independent from each other. Therefore, the data obtained from the test environment give bad results if applied without dimension reduction. The advantage of this method is that it is highly accurate in small training sets requiring only a few class parameters to be predicted, since all features are taken into account independent from each other, only the mean and the variance of these features need to be predicted. There is no need to predict the variance of the features with respect to one another.

The details of the method are summarized below [15].

If there are data belonging to C number different classes in the training set which have n number of elements, prior probability belonging to each class is defined as

$$p(s_c) = \frac{\sum_{i=1}^{n}\delta_{ic}}{n} c = 1...C \tag{38}$$

The feature vector belonging the test set is represented as $X = \{x_1, x_2,.....,x_k\}$ and its probability to belong to s_c class.

$$p(s_c|X) = p(s_c|x_1, x_2, ..., x_k) \tag{39}$$

Conditional probability can be written by using Bayes theorem as follows.

$$p(s_c|X) = \frac{p(s_c)p(x_1, x_2, ..., x_k|s_c)}{p(x_1, x_2, ..., x_k)} \tag{40}$$

Because measured values cannot be known, all values have an equal probability to be measured; the denominator of Eq. (40) will be the same for all X values. Therefore, probability can be written as below.

$$p(s_c|X) = p(s_c)p(x_1, x_2, ..., x_k|s_c) \tag{41}$$

This method makes conditional independence assumptions. Therefore, if the features comprising joint probability are considered as independent and written in the form of a multiplication, the probability can be expressed as follows:

$$p(s_c|X) = p(s_c)\prod_{j=1}^{k}p(x_j|s_c) \tag{42}$$

where $p(x_j|s_c)$ is the possibility of jth feature of X vector to be in class c. While calculating this value, s_c class can be considered to have a normal distribution according to the mean and variance of j^{th} feature.

In this case, $p(x_j|s_c)$ can be calculated as below:

$$p(x_j|s_c) = \frac{1}{\sqrt{2\pi\sigma_{c,j}^2}}e^{-\frac{(x_j-\mu_{c,j})^2}{2\pi\sigma_{c,j}^2}} \tag{43}$$

where $\mu_{c,j}$ defines the mean of j^{th} feature of cth class, and $\sigma_{c,j}^2$ defines the variance of jth feature of c^{th} class.

With all this definition, the probability of the X vector given in Eq. (42) existing in cth class $p(s_c|X)$ can be calculated. C value making Eq. (42) maximum determines which class X vector will belong to.

If $\hat{s}$ is defined as the predicted class of the X vector being an element of the test set, then it is calculated as:

$$\hat{s} = argmax_c(p(s_c|X)) \tag{44}$$

3.3. Validation and performance criteria

Validation process must be carried out to measure how successful the classification has been. Validation is made by using algorithms that have been utilized in supervised learning method, acquiring data points from the experiment. The most well-known validation methods are Hold-out validation, K-fold cross validation, and Leave-one-out cross validation methods.

In addition, correct classifying ratio (success rate) is used as criteria showing the success of this classification. Similarly, the area under curve (AUC), which is the total area under receiver operating characteristic (ROC) curve showing to what degree the classes can be separated from each other, is used.

3.3.1. K-fold cross validation

According to this method, n number of data obtained from the experiments is divided randomly by k number set in the form of each cluster having equal element and each set being numbered from 1 to k.

$$v_i \in \{1, 2, ..., k\} \qquad i = 1...n \tag{45}$$

First of all, data, whose v_i values are equal to 1, are taken as a test set and data whose values are different from 1 are taken as a training set.

Suggested method is to train with training set and to examine with test set. Then data whose v_i values are 2 are sent to test set, and data whose v_i values are different from 2 are sent to training set. The method is retrained with a new training set and examined with the test set. This process continues until all layers are tested [1].

3.3.2. Success rate

One of the performance criteria used is success rate ratio. This ratio is obtained by the ratio of correctly classified data to total data number.

If the real class of vector represented by feature vector X_i is s_i and predicted class through classification method is $\hat{s}_i$, success rate is calculated as follows.

$$Success\ Rate = \frac{1}{n}\sum_{i=1}^{n}D(s_i, \hat{s}_i) \tag{46}$$

Definition of D function is shown as follows.

$$D = \begin{Bmatrix} 1, & s_i = \widehat{s}_i \\ 0, & s_i \neq \widehat{s}_i \end{Bmatrix} \tag{47}$$

3.3.3. Area under receiver operating characteristic (ROC) curve

If measuring the performance of classification is considered inadequate, then ROC curve could be utilized. ROC curve is a metric curve which measures to what degree the classifier separates the classes from each other and how far the boundaries of classes are away from each other [16].

This curve is the measure of performance for the classifier separating two classes.

Outputs of classifiers classifying data sets consisting of two classes one of which is positive and the other is negative are normalized between [0 1]. In this case, if the classifier generates 0 for X vector, it will be negative and if it generates 1, it will be positive. The probability density function of the values generated in the output by the elements of positive and negative sets can be represented by $L_1(x)$ and $L_0(x)$ respectively. In this case, any threshold value between [0 1] is called a hit rate, connected to $H(t)$, in other words, the rate of the elements which are both in the positive class and classified as positive,

$$H(t) = \int_t^1 L_1(x)dx \tag{48}$$

False alarm rate, $F(t)$, is the rate of the elements which are classified as positive although they are negative,

$$F(t) = \int_t^1 L_0(x)dx \tag{49}$$

The ROC curve is a tool realized by the $\{F(t), H(t)\}$ points in the two dimensional space. Therefore, the area below [0 1] in ROC can be defined as the Area Under Receiver (AUC).

$$AUC = \int_0^1 H(t)dF(t) \tag{50}$$

The AUC value is between 0 and 1. When the value is close to 1, it means that the classes are well separated from each other. When the value is 0.5, this shows that the classifier is of no use at all because the value obtained in random classification is 0.5. Any resulting value under 0.5, shows that the data have been ordered in a reverse manner.

The statement in Eq. (50) is only for the classifier which separates the data set consisting of two classes. In the C-class problem, C-number of classes needs to be defined according to one-to-all strategy in order to apply it to multiclass problems. For each classifier, the class in question is labeled as positive while others are labeled as negative. The AUC value is calculated for each pair of classifiers. This value is defined as the average of calculated AUCs for all classes.

4. Results and discussion

In the data set used in the application, there are 300 data points belonging to six different types of tubes. All test conditions have been kept constant except for the pipes. Names of the pipes used, numbers of the measurements done, depth of corrugation and helix angles are shown in Table 1.

Totally 30 values have been collected for each test point. The values used in the experiment are represented as follows.

Table 1
Tube properties used in the experiment and number of the test points.

Tube name	Number of test points	Depth of corrugation	Helix angle
ST	50	–	–
CT1	51	0.5	53.875
CT2	48	0.75	53.875
CT3	46	1	53.875
CT4	54	1	64.07
CT5	51	1	69.95

Total pressure drop ΔP_{total}; inlet, outlet and average vapor qualities x_{in}, x_{out}, x_{avg} liquid and vapor densities $\rho 1$, ρ_v, liquid and vapor dynamic viscosities μ_1, μ_v; mass flux G, inlet, outlet and average refrigerant temperatures $T_{ref,in}$, $T_{ref,out}$, $T_{ref,avg}$; inlet, outlet and average water temperatures $T_{w,in}$, $T_{w,out}$, $T_{w,avg}$; average wall temperatures $T_{wall,avg}$; enthalpies of liquid, vapor and phase changes i_l, i_v, i_{lv}; thermal conductivity k; specific heat at constant pressure c_p; inlet, outlet and average Zivi's void fractions α_{in}, α_{out}, α_{avg}; equivalent mass flux G_{eq}; equivalent Reynolds number Re_{eq} gravitational pressure drop ΔP_g; the acceleration pressure drop ΔP_a; frictional pressure drop ΔP_f; and friction factor of tube f_{tp}.

In this case, the feature vector to be used is defined as:

$$X = \Big\{\Delta P_{total}, x_{in}, x_{out}, x_{avg}, \rho_l, \rho_v, \mu_l, \mu_v, G, T_{ref,in}, T_{ref,out}, T_{ref,avg}, T_{w,in}, T_{w,out}, T_{w,avg}, T_{wall,avg}, i_l, i_v, i_{lv}, k, c_p, \alpha_{in}, \alpha_{out}, \alpha_{avg}, G_{eq}, Re_{eq}, \Delta P_g, \Delta P_a, \Delta P_f, f_{tp}\Big\} \tag{51}$$

The identified X feature has been subjected to dimension reduction through both PCA and LDA, and via 3-fold validation, the performance of each classifier has been measured according to success rate. Fig. 2 shows the success rate graphics based on the numbers of PCA and LDA's number of dimensions changing with each classifier.

Dimension numbers with the highest success numbers, which are obtained through a PCA and an LDA dimension reduction, and the success rates and AUC values of these models, are given in Table 2a.

According to the table, in all classifier methods, LDA dimension reduction precedes PCA. In addition, the highest classification success has been obtained through the reduction of the values to three dimensions that all the classifiers have. With the reduction of the classifier methods to 3 dimensions through LDA, the details of the resulting AUC values are given in Table 2b.

According to this table, corrugated tube 1 and corrugated tube 5 have been defined with the highest accuracy with regard to all methods. The error of the classification is due to other tubes. With regard to the success rate criteria, NBC has given the worst result when used with PCA, but the best result with LDA. This finding is a result of the fact that the Naïve Bayes method evaluates the features independently. Without doubt, one cannot argue that the features obtained from the test environment are not related. Since the LDA method can separate the classes in the best way possible and find new features that are unrelated to each other, the NBC method is successful with LDA.

Although NBC is the highest in the success rate, QDC is the most successful one according to the AUC metric. The AUC metric tests the ability of the classifier to separate between the classes. In this case, it can be argued that the QDC is the best method to separate between the classes. The reason why it cannot outperform NBC in success rate can be explained by the fact that after the classes are separated, this method can no longer measure the boundary between the classes in an efficient way.

For the investigation of the most effective methods in classification, 3-fold validation success of the data, which was reduced to 3 dimensions through LDA, in LDC method, is used. Through Forward-Sequential feature selection method, the most effective parameters were investigated. According to this method, the feature, which makes the classification

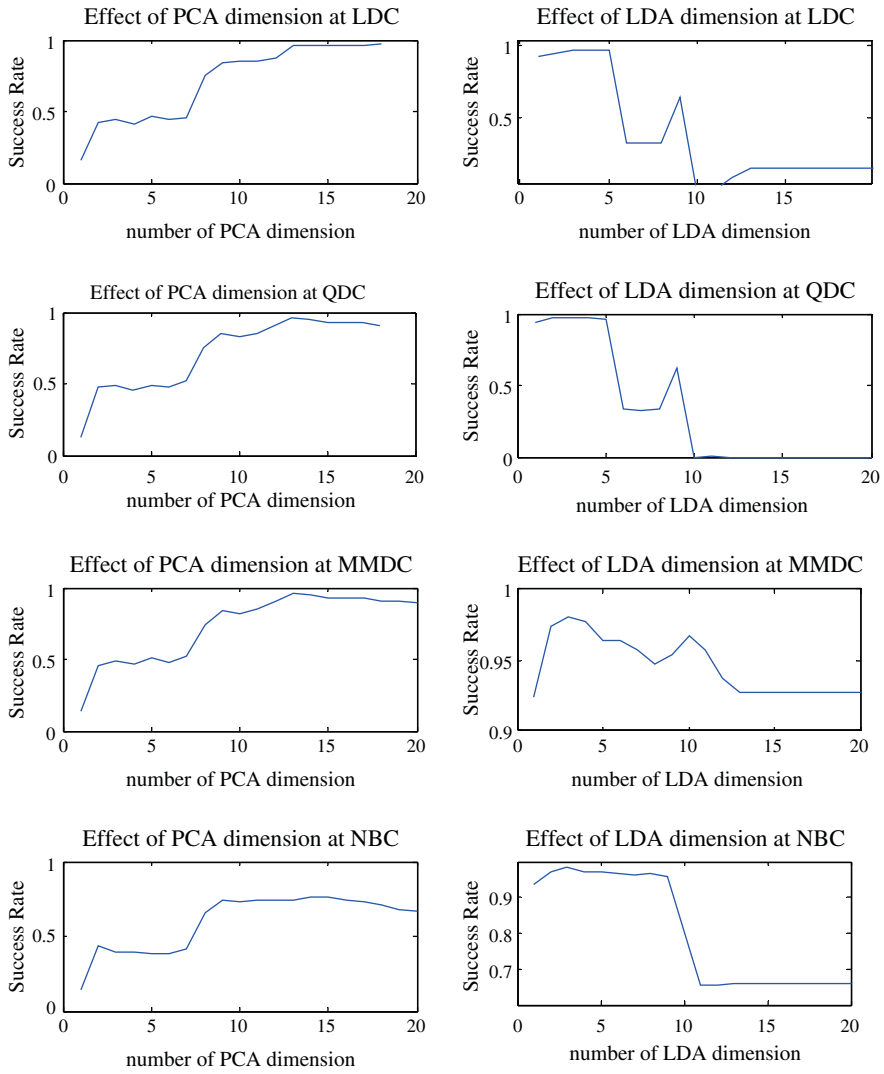

Fig. 2. Success rate graphics according to number of PCA and LDA dimensions changing for each classifier.

Table 2
Success of classification methods (a) and detailed success table of classification methods according to AUC metric (b).

a)

Classification method	Dimensionality reduction	Best dimension	Success rate	Mean AUC
LDC	PCA	18	0.97	0.9985
	LDA	3	0.97	0.9988
QDC	PCA	13	0.96	0.9893
	LDA	3	0.9767	0.9994
NBC	PCA	14	0.7633	0.9272
	LDA	3	0.9833	0.9993
MMDC	PCA	13	0.9567	0.9825
	LDA	3	0.98	0.9959

b)

Classification method	LDC	QDC	NBC	MMDC
ST to other	1.0000	1.0000	1.0000	0.9964
CT1 to other	1.0000	1.0000	1.0000	0.9999
CT2 to other	0.9991	0.9988	0.9999	0.9846
CT3 to other	0.9944	0.9977	0.9958	0.9968
CT4 to other	0.9994	1.0000	0.9998	0.9994
CT5 to other	1.0000	1.0000	1.0000	0.9981
Mean AUC	0.9988	0.9994	0.9993	0.9959

success maximum, is added to the specification subset one by one. When the increase in success stops or does not surpass the threshold value, the choice of specification is finished [17]. The specifications and success obtained from the research are as given in Table 3. Classification success reaches 97% with LDC method by selecting 8 properties from this table.

The pattern how the classifiers divide the 2-d space into regions and how LDA groups the test points in the space are shown in Fig. 3. While this shape was being formed, all data points were put into the training set and reduced to two features through LDA, after which classifiers were applied.

5. Conclusion

The tubes used in refrigeration systems are classified in quite a successful when the suggested features are reduced to three dimensions through the LDA method. In addition, it has been shown in this paper that property cluster can give significantly successful results even with a subset consisting of 8 elements. This study is the first one using classification algorithms to differentiate the type of enhanced tubes from each other during two-phase boiling flow. For that reason, it is expected to fill the gap in the literature presenting the new finding using this technique.

Table 3
8 properties affecting the success of classification most and classification success of these properties when selected cumulatively.

Number of feature	1	2	3	4	5	6	7	8
Adding feature	f_{tp}	ΔP_{total}	x_{out}	$T_{ref,in}$	$T_{w,out}$	$T_{w,in}$	$T_{wall,avg}$	ΔP_a
Success rate (%)	0.45	0.5533	0.5967	0.6367	0.6867	0.9233	0.9567	0.97
AUC	0.8001	0.8837	0.9061	0.9129	0.9327	0.989	0.9961	0.9978

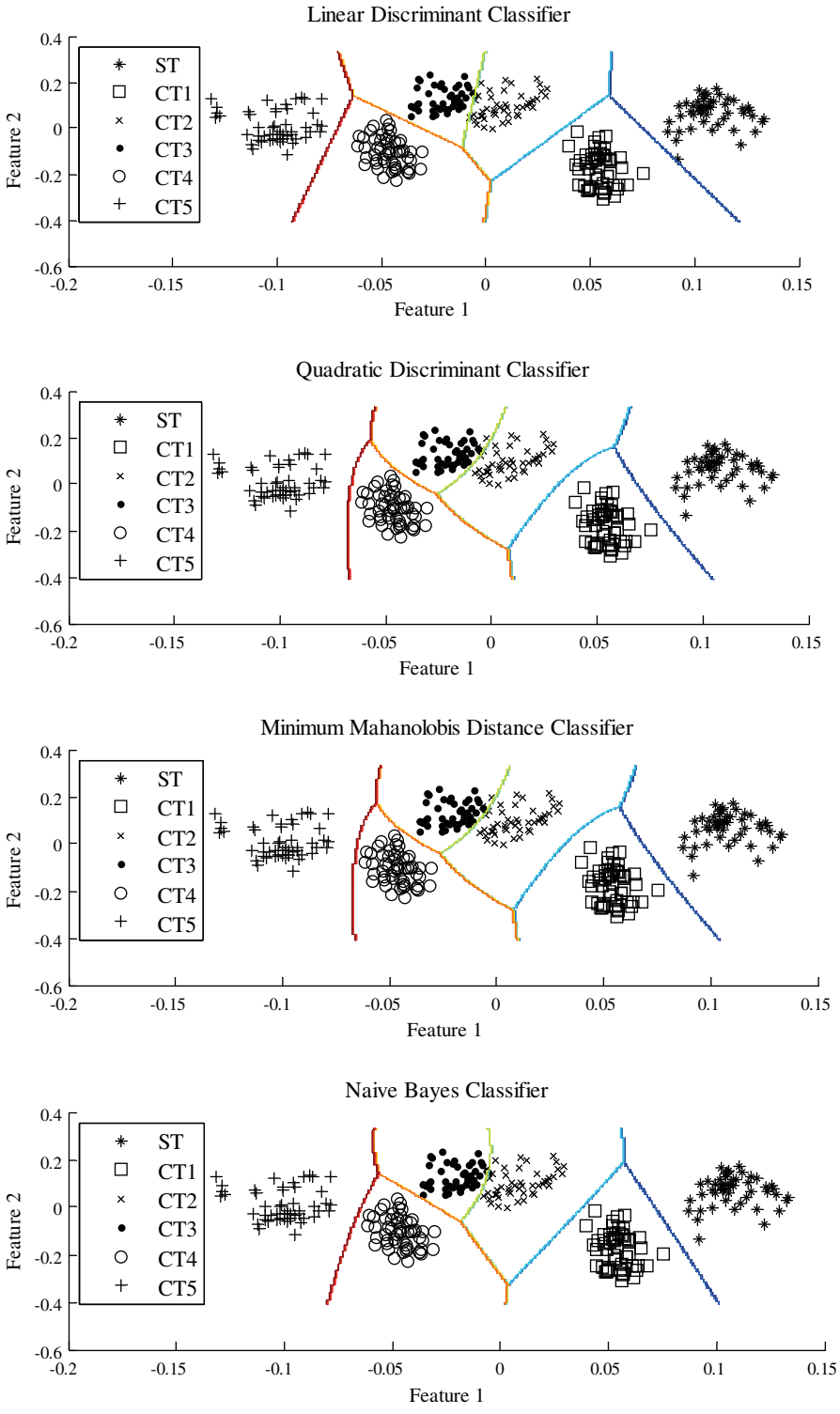

Fig. 3. Locations of experiment points with LDA in 2-d space and boundary lines of classifiers.

Acknowledgment

The second author wishes to thank King Mongkut's University of Technology Thonburi (KMUTT) for providing him with a Post-doctoral fellowship. The fourth author wishes to thank the Thailand Research Fund, the National Research University Project and the National Science and Technology Development Agency.

References

[1] E. Alpaydin, Introduction to Machine Learning, vol. 56, no. 2The MIT Press, 2004. 387–399.
[2] R.O. Duda, P.E. Hart, D.G. Stork, Pattern Classification, vol. 2, no. 6Wiley, 2001. 654.
[3] C.M. Bishop, Pattern Recognition and Machine Learning, vol. 4, no. 4Springer, 2006. 738.
[4] T.M. Mitchell, Machine Learning, vol. 1, no. 3McGraw-Hill, 1997. 414.
[5] J.S.R. Jang, C.T. Sun, E. Mizutani, Neuro-fuzzy and Soft Computing, Prentice Hall, 1997.
[6] Y. Guo, J. Wall, J. Li, S. West, A machine learning approach for fault detection in multi-variable systems, ATES Second International Workshop on Agent technology for Energy Systems, 2011, pp. 23–¯30.
[7] I. Topalova, A. Mihailov, A. Tzokev, Automated classification of heat resistant steel structures based on neural networks, IEEE Convention of Electrical and Electronics Engineers in Israel Proceedings, 2008, pp. 437–440.
[8] T. Yamashita, L.D. Tsantaridis, Heat release and classification of fire retardant wood products, Fire Mater. 19 (1994) (1995) 253–258.
[9] K. Brudzewski, S. Osowski, T. Markiewicz, Classification of milk by means of an electronic nose and SVM neural network, Sensors Actuators B Chem. 98 (2–3) (2004) 291–298.
[10] K. Aroonrat, S. Wongwises, Evaporation heat transfer and friction characteristics of R-134a flowing downward in a vertical corrugated tube, Exp. Thermal Fluid Sci. 35 (1) (2011) 20–28.
[11] S. Laohalertdecha, S. Wongwises, An experimental study into the evaporation heat transfer and flow characteristics of R-134a refrigerant flowing through corrugated tubes, Int. J. Refrig. 34 (1) (2011) 280–291.
[12] I. Guyon, A. Elisseeff, An introduction to variable and feature selection, J. Mach. Learn. Res. 3 (7–8) (2003) 1157–1182.
[13] J. Li, B. Zhao, H. Zhang, J. Jiao, Face recognition system using SVM classifier and feature extraction by PCA and LDA combination, 2009 International Conference on Computational Intelligence and Software, Engineering, 2009, pp. 1–4.
[14] M.A. Golberg, A generalized Rayleigh quotient for eigenvalue problems nonlinear in the parameter, J. Optim. Theory Appl. 11 (2) (1973) 146–158.
[15] H. Zhang, The optimality of naive Bayes, Mach. Learn. 1 (2) (2004) 3.
[16] T. Fawcett, An introduction to ROC analysis, Pattern Recogn. Lett. 27 (8) (2006) 861–874.
[17] A. Marcano-Cedeno, J. Quintanilla-Dominguez, M.G. Corthina-Januchs, D. Andina, Feature selection using sequential forward selection and classification applying artificial metaplasticity neural network, Cell (2010) 2845–2850.

Experimental Thermal and Fluid Science 55 (2014) 54–61

Contents lists available at ScienceDirect

Experimental Thermal and Fluid Science

journal homepage: www.elsevier.com/locate/etfs

Heat transfer characteristics of gas–liquid flow in horizontal rectangular micro-channels

Sira Saisorn [a,c], Piyawat Kuaseng [b], Somchai Wongwises [c,*]

[a] Department of Mechanical Engineering, King Mongkut's Institute of Technology Ladkrabang, Prince of Chumphon Campus, Chumphon 86160, Thailand
[b] Department of Mechanical Engineering, King Mongkut's Institute of Technology Ladkrabang, Bangkok 10520, Thailand
[c] Fluid Mechanics, Thermal Engineering and Multiphase Flow Research Lab. (FUTURE), Department of Mechanical Engineering, Faculty of Engineering, King Mongkut's University of Technology Thonburi, Bangmod, Bangkok 10140, Thailand

ARTICLE INFO

Article history:
Received 17 October 2013
Received in revised form 28 January 2014
Accepted 3 February 2014
Available online 11 February 2014

Keywords:
Flow pattern
Micro-channel
Heat transfer

ABSTRACT

An experimental study of heat transfer characteristics of air–water flow in horizontal micro-channels was carried out in this work. The gas–liquid mixture from a y-shaped mixing chamber was forced to pass through a plenum inlet and entered 21 parallel rectangular micro-channels 40 mm long in the direction of flow. Each channel had a width and a depth of 0.45 and 0.41 mm, respectively. The test runs were done at a heat load of 80 W, with superficial Reynolds numbers of gas and liquid ranging between 54–142 and 131–373, respectively. A Stereozoom microscope and camera system were employed to conduct flow visualization. To explore the dependence of a Nusselt number on the flow characteristics, two inlet sections with different designs were used in this work. The experiments revealed that the formation of small gas slugs instead of gas core flow involves an increase in Nusselt numbers. In this work, the gas–liquid flow gave heat transfer enhancement up to 80% over the liquid flow.

1. Introduction

Two-phase flow studies have been carried out extensively over the years. However, there have been a relatively small amount of publications dealing with micro-channels when compared with those for ordinarily sized channels. Capillary force is likely to play an important role for two-phase flow characteristics in micro-channels, resulting in flow phenomena significantly different from those observed in ordinarily sized channels. Serizawa et al. [1], for instance, investigated the visualization of the two-phase flow pattern in circular micro-channels. The flowing mixture of air and water in channels of 20, 25 and 100 μm in diameter and that of steam and water in a channel of 50 μm in diameter were conducted experimentally. The study confirmed that the surface wettability had a significant effect on the two-phase flow patterns in very small channels. The discrepancies between micro-scale and macro-scale flows have been reported in the literature [2–7].

Two-phase flow in micro-channels has gained significant attention in engineering due to wide application, extending to such fields as bioengineering, fuel cells, compact heat exchangers, heat sinks, and so on. For cooling purposes, various applications of micro-channels are discussed in detail by Mudawar [8]. Due to the rapid development of modern miniature devices generating large amounts of heat, the single-phase micro-channel flow seems no longer a highly effective cooling method.

Two-phase flow in small channels has become another effective means for dissipating heat. Flow boiling, for instance, involves very high heat transfer rate but backflow and instabilities, which are considered as drawbacks [9], have to be carefully controlled. According to the open literature, two-phase heat transfer in micro-channels have been mainly reported for flow boiling studies. The effects of such parameters as mass flux and heat flux on flow boiling phenomena have been reported in several publications [10–12]. Moreover, the up-to-date comprehensive discussions on flow boiling in micro-scale channels were given by Ribatski [13] and Tibirica and Ribatski [14]. In contrast, the data corresponding to heat transfer characteristics during non-boiling two-phase flow in micro-channels is still limited.

Bao et al. [15] carried out experiments to explore the heat transfer performance of air–water flow in a channel having a diameter of 1.95 mm. They reported that at a fixed liquid flow rate, the heat transfer coefficient increased with the increase in air flow rate caused by the flow pattern transition. Hetsroni et al. [16] performed experiments to study two-phase flow regimes and bubble behavior in triangular parallel micro-channels made from $15 \times 15 \times 0.53$ mm^3 square-shape silicon substrate. In this study, air–water and steam-water were chosen as working fluids and

* Corresponding author. Tel.: +66 24709115; fax: +66 24709111.
E-mail address: somchai.won@kmutt.ac.th (S. Wongwises).

http://dx.doi.org/10.1016/j.expthermflusci.2014.02.006
0894-1777/

Nomenclature

A	area (m^2)
H	height (m)
h	heat transfer coefficient (W/m^2 K)
k	thermal conductivity (W/m K)
m	$(hP/kA_c)^{1/2}$
Nu	Nusselt number
P	perimeter (m)
Q	heat transfer rate (W)
q	heat flux (W/m^2)
Re_{GS}	superficial Reynolds number of gas
Re_{LS}	superficial Reynolds number of liquid
T_f	fluid temperature (K)
T_w	wall temperature (K)
W	width (m)

Greek symbols

η	fin efficiency

Subscripts

b	base
c	cross-section
ch	channel
f	fin
L	liquid phase
TP	two-phase

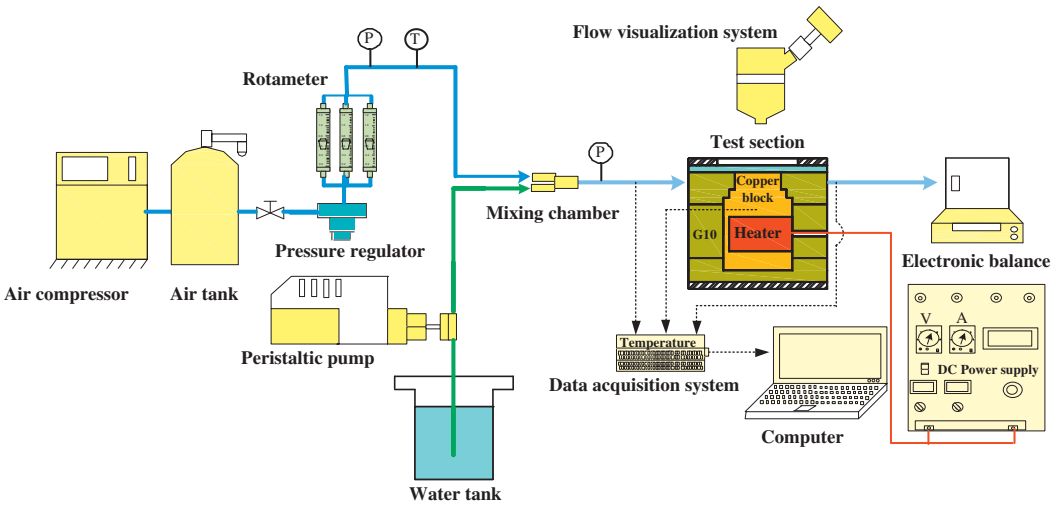

Fig. 1. Schematic diagram of experimental apparatus.

the differences between flow patterns of the two cases were addressed. It is noted from Triplett et al. [17,18] that based on different channel cross-sectional shapes, the adiabatic two-phase air–water flow characteristics in semi-triangular micro-channels were similar to those obtained from circular channels. The heat transfer of an air–water flow in parallel micro-channels of 0.1 mm in hydraulic diameter was experimentally investigated by Hetsroni et al. [19]. Their results showed a decrease in the Nusselt number with an increasing gas flow rate, which was opposite to the results obtained by Bao et al. [15]. Betz and Attinger [20] showed segmented flow, an intermittent pattern of gas bubbles and liquid slugs, resulting in the heat transfer enhancement up to 140% in a micro-channel heat sink when compared with single-phase liquid flow.

Heat transfer characteristics of a non-boiling two-phase flow in micro-channels with different diameters were studied by Choo and Kim [21]. Air and water were used as working fluids to examine the dependence of Nusselt number on the channel diameter. They found that with channel diameters of 0.506 and 0.334 mm, the Nusselt number increased with the increment of gas flow rate, but decreased with increasing gas flow rate when the channel diameters of 0.222 and 0.140 were employed.

Marchitto et al. [22] studied two-phase flow distribution in parallel upward channels. They reported that the phase distribution

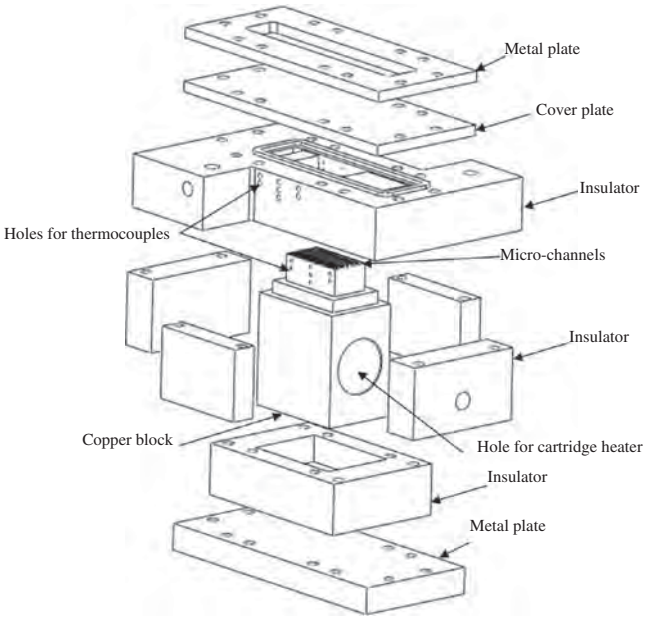

Fig. 2. Schematic diagram of test section assembly.

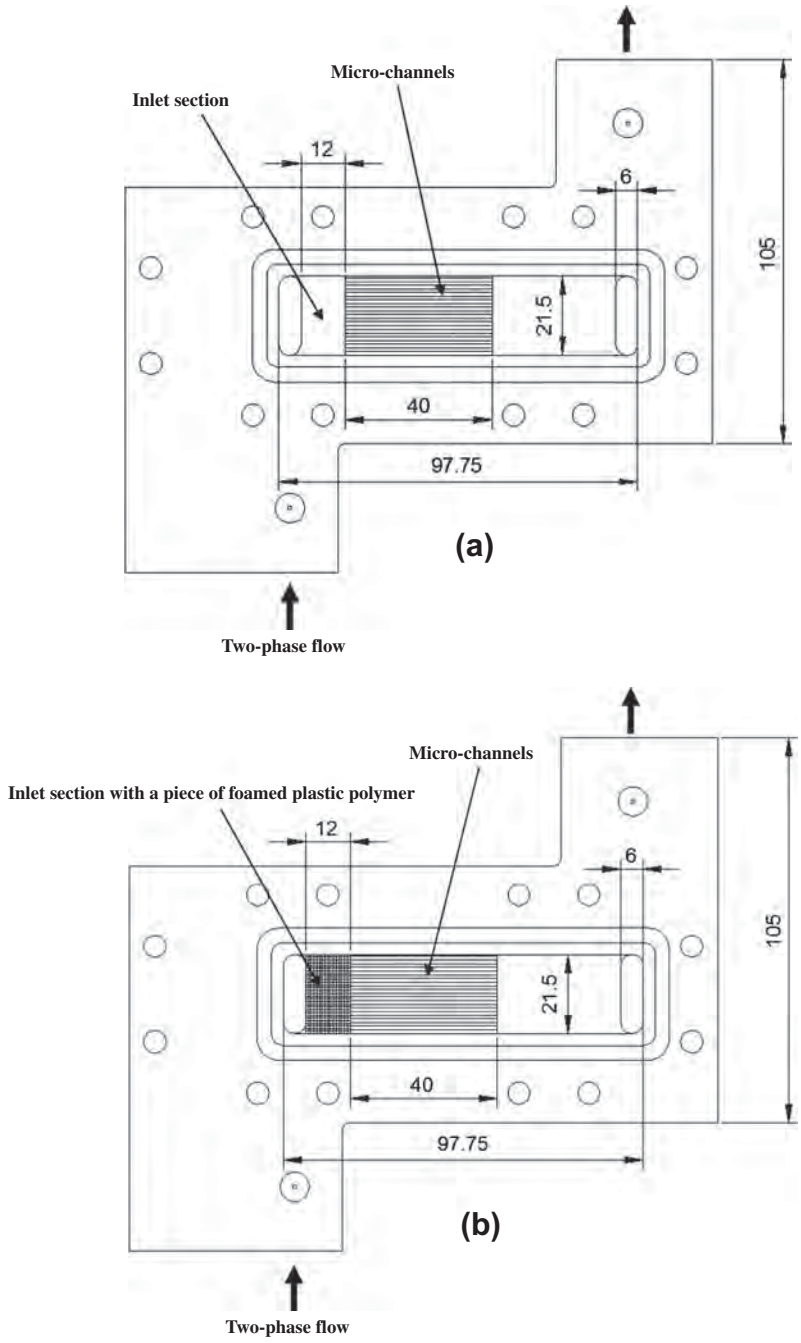

Fig. 3. Schematic diagram of test sections with different inlet sections. (a) Inlet section without a piece of foamed plastic polymer, and (b) inlet section with a piece of foamed plastic polymer.

was improved by using a special fitting, acting as distributor, which was installed inside the header.

Thus, the available results for non-boiling gas–liquid flow in micro-channels are not conclusive. Furthermore, important information associated with flow pattern and heat transfer data is still lacking. Consequently, the aim of this work is to explore heat transfer results for different gas–liquid flow patterns in horizontal micro-channels, an area needed to be clarified. In this paper, the flow pattern behaviors obtained from flow visualization and the heat transfer results are discussed.

Table 1
Experimental uncertainty.

Parameter	Uncertainty
Channel dimensions	±0.01 (mm)
Liquid superficial velocity	±3.3%
Gas superficial velocity	±5.2–10.5%
Heat transfer coefficient	±3.0–6.9%

2. Experimental apparatus and procedure

A schematic diagram of the experimental apparatus is shown in Fig. 1. A peristaltic pump with adjustable flow rate was used to supply liquid flow through the test section. The liquid mass flow rates were determined by using an electronic balance

(320 ± 0.001 g) to measure weight of the liquid flowing from the test section outlet over a sufficient time, whereas the flow rates of gases were measured by three sets of rotameters within the range of 5–50, 50–500, and 200–2500 cm^3/min, respectively. An air–water y-shaped mixer served to introduce fluids smoothly along the test section. Thermocouples and pressure transducers were installed at various positions to monitor the flow condition of the working fluids.

Fig. 2 illustrates an exploded view of the test section. The 21 parallel rectangular micro-channels of 0.45×0.41 mm (width $\times$ depth) with a 0.54 mm wall thickness between each channel were fabricated on the copper block in which a cartridge heater with adjustable input power was installed. The length of the micro-channels was 40 mm. On the top of the test section, the cover plate made of polycarbonate was placed to allow optical access for flow visualization. The copper block was well insulated by G10 epoxy. Metal plates and the insulators were bolted together with the copper block and the cover plate to firm up the assembly.

The cover plate, which is transparent, served as a viewing window for flow visualization. The detailed formation of flow pattern was registered by precise Stereozoom microscope mounted together with a camera having shutter speeds of 1/15–1/10,000 s. An adjustable LED light source was placed perpendicular to the viewing section.

A set of 14 K-type thermocouples was embedded in the copper block. For each side of the test section presented in Fig. 2, there were seven thermocouples inserted at equal distances of 16 mm along the channel length and 4.3 mm along the direction perpendicular to the channel length. These temperature measurements were done to determine surface temperatures at six positions using linear extrapolation. The arithmetic mean of these surface temperatures was used to calculate the average heat transfer coefficient. In addition, T-type thermocouples were installed at the inlet and outlet of the test section to measure the fluid temperature. All thermocouples and relevant instruments installed in the experimental apparatus were well calibrated.

To explore different flow phenomena in micro-channels, different inlet sections were used in the experiments, as shown in Fig. 3. The inlet section, presented in Fig. 3a, led the gas–liquid mixture directly to the micro-channels. For the other, as illustrated in Fig. 3b, the mixture was led to flow through a piece of foamed plastic polymer, a porous material, and subsequently entered the micro-channels.

In this work, the experiments for each inlet section were conducted so the air flow rate increased by small increments while the water flow rate was constant at the desired value. To keep the flow from boiling conditions, the heat load of 80 W was provided by a DC power supply during the experiments. The system was allowed to approach a steady state before the flow pattern and relevant data are recorded. The uncertainties associated with different parameters are given in Table 1.

3. Data reduction

Due to the cover plate, which was made of polycarbonate, an adiabatic fin tip was assumed to obtain the wall heat flux, q_w, calculated based on the effective area, given by

$$q_w = \frac{q_b(W_{ch} + W_f)}{(W_{ch} + 2\eta H_f)} \quad (1)$$

where W_{ch}, W_f, H_f and η represent, respectively, channel width, fin thickness, channel depth and fin efficiency. q_b, which is the heat flux from the heater to the working fluid, was obtained from a steady-flow thermal energy equation with no changes in latent energy.

The average heat transfer coefficient is given by

$$h = \frac{q_w}{T_w - T_f} \quad (2)$$

where T_f is fluid temperature and T_w denotes the average wall surface temperature (at prime surface).

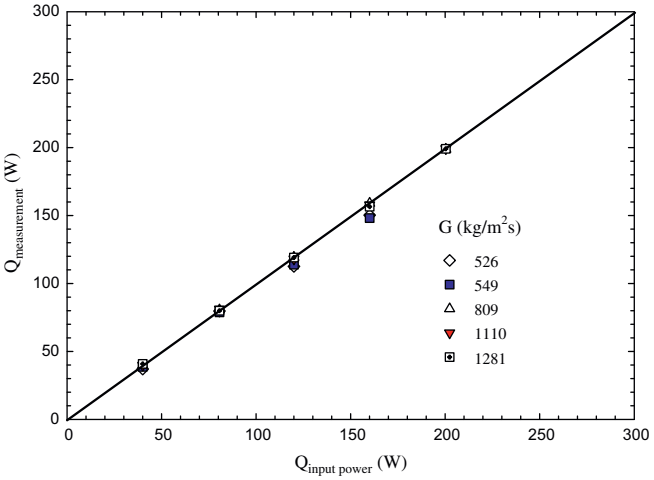

Fig. 4. Energy balance applied on the test section.

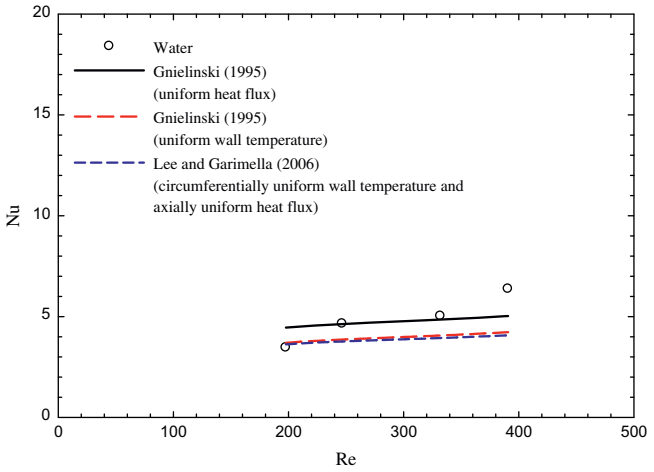

Fig. 5. Theoretical and measured values of Nusselt numbers for single-phase flow versus Reynolds numbers.

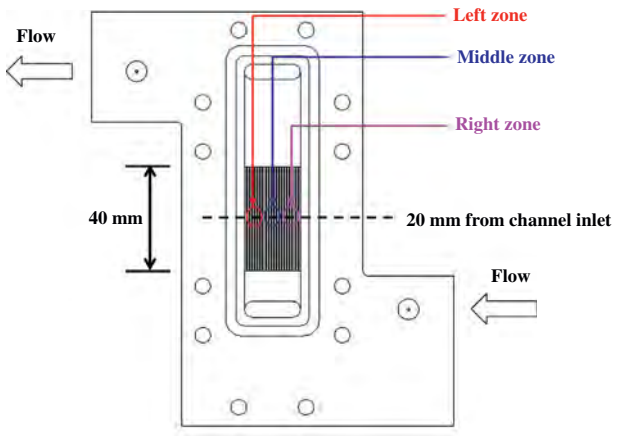

Fig. 6. Locations for flow visualization.

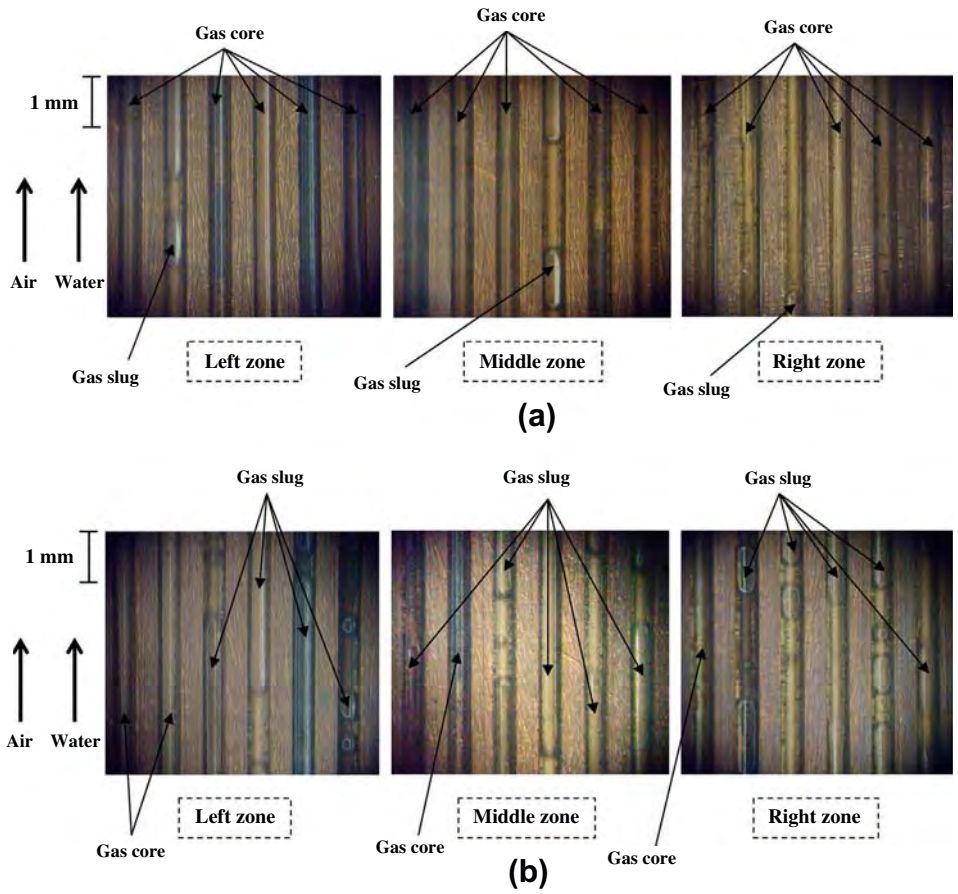

Fig. 7. Flow patterns for different inlet sections (Re_{GS} = 50, Re_{LS} = 132). (a) Inlet section without a piece of foamed plastic polymer, and (b) inlet section with a piece of foamed plastic polymer.

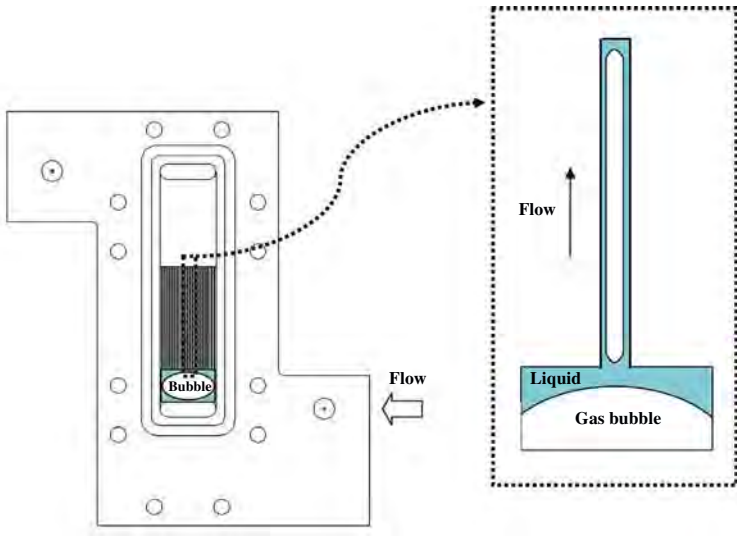

Fig. 8. Schematic diagram of gas core flow formation in micro-channels.

For one dimensional heat conduction with adiabatic fin tip, the fin efficiency is expressed by

$$\eta = \frac{\tanh(mH_f)}{mH_f} \tag{3}$$

where m is defined as

$$m^2 = \frac{hP}{kA_c} \tag{4}$$

In Eq. (4), P stands for fin perimeter, k for thermal conductivity and A_c for fin cross-sectional area.

As suggested by Park and Thome [23], an iteration process for Eqs. (1)–(4) was needed to determine the wall heat flux and heat

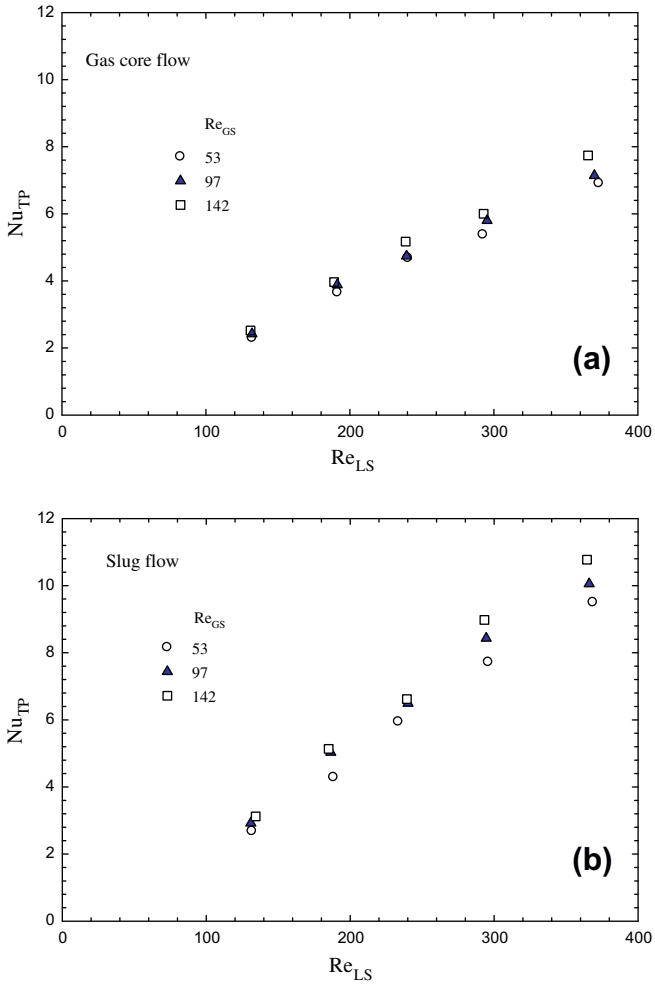

Fig. 9. Heat transfer data for different superficial Reynolds numbers.

transfer coefficient. The process was carried out until the fin efficiency converged to a fixed value.

4. Results and discussion

These single-phase flow experiments were the first to be conducted to check the validity of the experimental system. The energy balance of the test section is illustrated in Fig. 4, indicating the test section, which was well insulated. The single-phase Nusselt numbers were also compared with the prediction methods of Gnielinski [24] and Lee and Garimella [25], which were applied for laminar developing flow. The comparisons presented in Fig. 5 indicate that the experimental results tended to agree fairly with the predictions, corresponding to a uniform heat flux boundary condition.

The following sections present the two-phase flow results, including flow pattern and heat transfer.

4.1. Flow pattern results

A Stereozoom microscope and camera system were employed to conduct flow visualization, carried out at a distance of 20 mm from the channel inlet. Based on this distance, the images were recorded at three different zones: left zone, middle zone, and right zone. Fig. 6 illustrates the locations at which the images were captured.

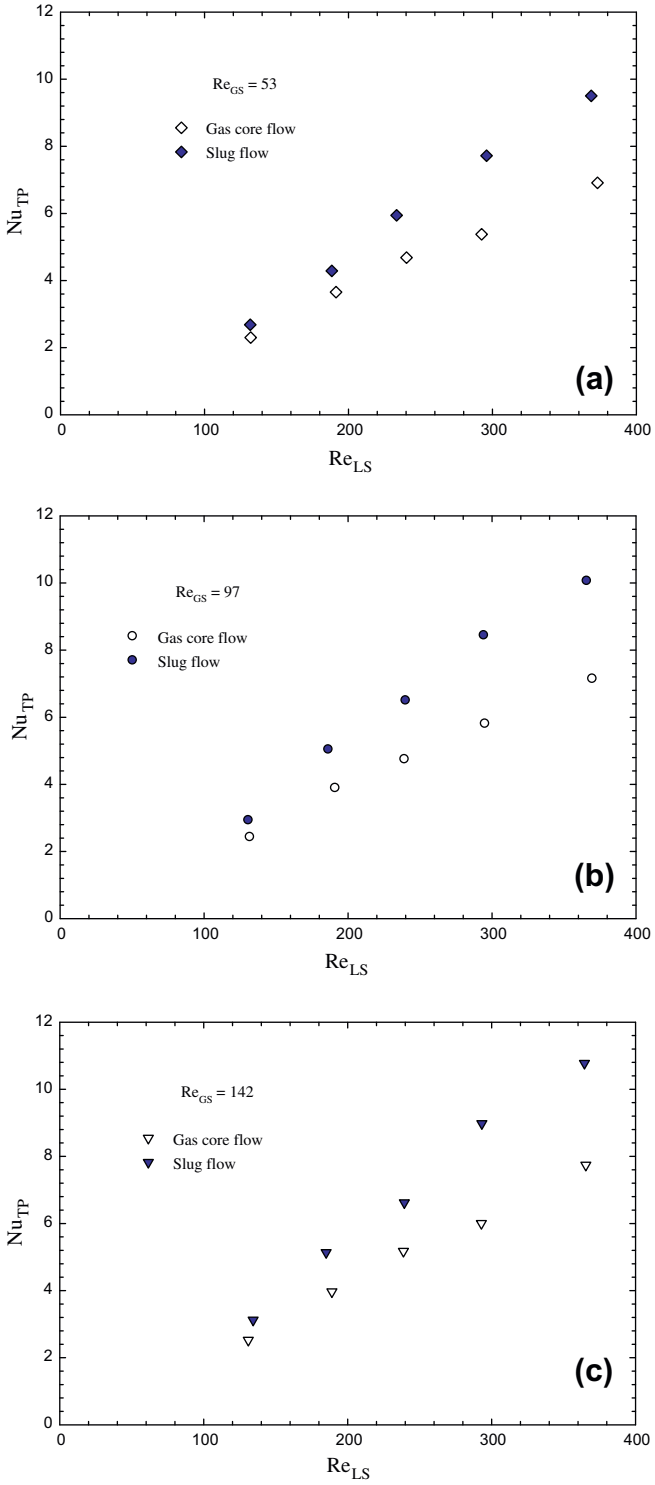

Fig. 10. Effect of flow pattern on gas–liquid heat transfer.

For two-phase flow, Reynolds numbers for gas and liquid phases can be defined respectively by gas superficial Reynolds number, Re_{GS}, and liquid superficial Reynolds number, Re_{LS}, which are expressed by the following equations.

$$Re_{LS} = \frac{\rho_L j_{LS} D_h}{\mu_L} \tag{5}$$

$$Re_{GS} = \frac{\rho_G j_{GS} D_h}{\mu_G} \tag{6}$$

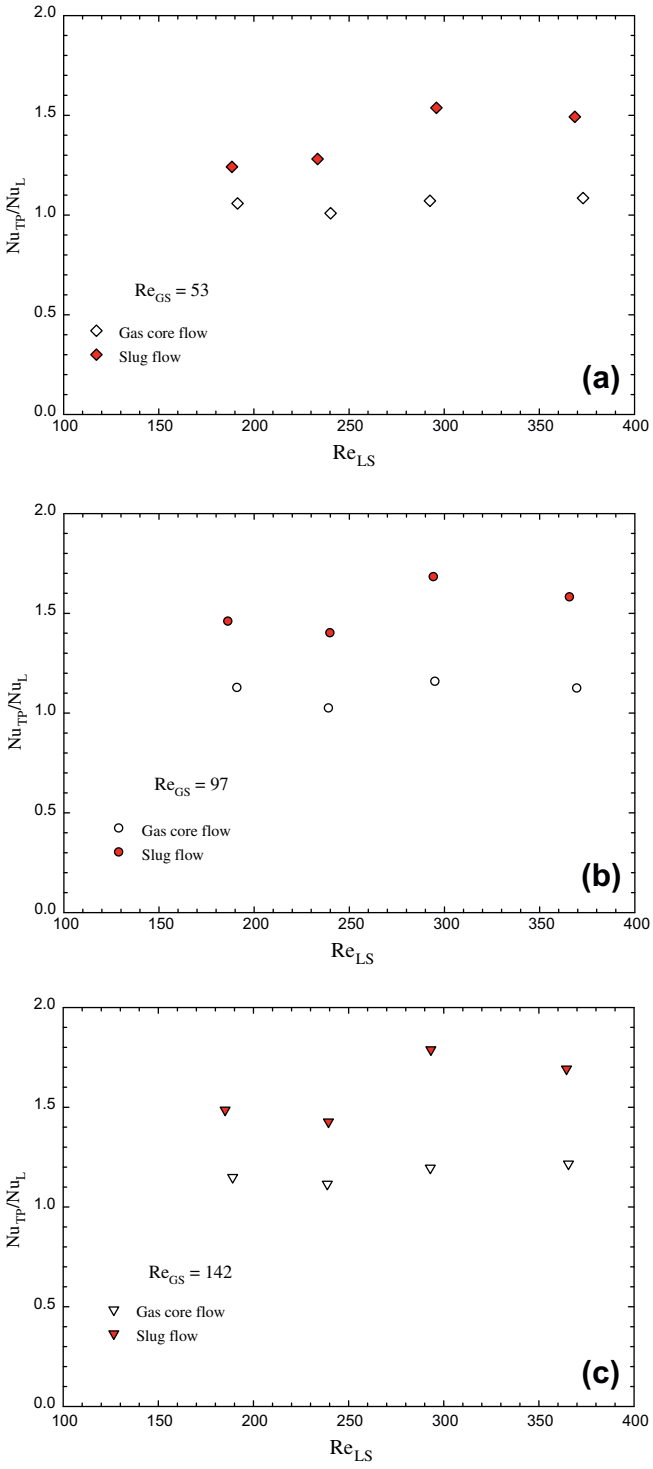

Fig. 11. Heat transfer enhancement ratio for different flow patterns.

From Eqs. (5) and (6), D_h is channel hydraulic diameter, j_{LS} and j_{GS} are liquid and gas superficial velocities, respectively, ρ_L and ρ_G are liquid and gas densities, respectively, and μ_L and μ_G are liquid and gas viscosities, respectively.

The flow visualization indicated that flow behaviors under the present conditions (superficial Reynolds numbers of gas and liquid ranging between 54–142 and 131–373, respectively) can be significantly affected by the change in inlet section. The flow pattern identification was mostly observed under a given flow condition. Fig. 7 shows flow patterns at different locations.

Slug flow, characterized by elongated bubbles flowing in the axial direction, and gas core flow, which is defined as long gas slug occupied over a length of channel, were observed. As shown in Fig. 7a, for the inlet section which led the gas–liquid mixture directly to the micro-channels, large gas bubbles in the chamber could expand along the channel length, leading to gas core flow in most channels. The formation of gas core flow is schematically depicted in Fig. 8. Comparatively, almost all the channels could be occupied by slug flow, as seen in Fig. 7b, when a piece of foamed plastic polymer inserted in the inlet section was used to induce the discrete bubbles before entering the channels.

In this work, the flow pattern results were taken simultaneously with the heat transfer data. Flow patterns were expected to affect the heat transfer phenomena. Different flow patterns may give differences in heat transfer mechanisms during gas–liquid flow. The effect of flow pattern on heat transfer characteristics is discussed next.

4.2. Heat transfer results

The average Nusselt numbers were plotted against superficial Reynolds numbers, as presented in Figs. 9 and 10. As seen in Fig. 9, the results, as expected, showed monotonous increases of the Nusselt numbers with the liquid superficial Reynolds numbers. As also shown in the figure, the Nusselt number increases with increasing the gas superficial Reynolds number. Hetsroni et al. [19] studied heat transfer characteristics in the channels of 0.1 mm in size and reported that an increase in gas superficial Reynolds number involved a decrease in heat transfer, which was opposite to the present results corresponding to micro-channels of 0.4 mm in size. The behavior observed by Hetsroni et al. [19] may be mainly due to, as suggested by Chung and Kawaji [2], significant effects of surface tension as well as liquid viscosity, which prohibit agitation of the gas–liquid interface in very small channels. Such different observations were also reported by Choo and Kim [21]. Based on their work, the heat transfer results for the channels with diameters of 0.14 mm and 0.22 mm revealed the trend similar to that of Hetsroni et al. [19]. On the other hand, for the 0.33 mm and 0.5 mm channels, Choo and Kim [21] reported the Nusselt number increasing with increasing the air flow rate.

The effect of flow pattern on gas–liquid heat transfer is shown in Fig. 10. The Nusselt number was higher for slug flow (Fig. 7b) than for gas core flow (Fig. 7a). This result indicates that the installation of a piece of foamed plastic polymer can improve the distribution of phases in micro-channels. As shown in Fig. 10, the Nusselt number can be enhanced up to 40% at high flow rates. The improvement of heat transfer may be mainly attributed to the small gas slugs contributing to agitation in the liquid film on the wall.

There have been several factors influencing the two-phase flow maldistribution in parallel channels. The relevant factors were recently given in details by Dario et al. [26].

Interestingly, the results based on micro-scale flow boiling involving complex mechanisms, reported by Ong and Thome [27] and Saisorn et al. [6], indicated that slug flow appeared with low heat transfer coefficient in comparison to the vapor core flow.

Fig. 11 illustrates heat transfer enhancement ratio for the present flow conditions. For slug flow, a heat transfer enhancement up to 80% was obtained over the single-phase flow.

5. Conclusions

Heat transfer and fluid flow characteristics of non-boiling gas–liquid flow in horizontal micro-channels were carried out in this work. For a constant heat load with a range of superficial

Reynolds numbers (Re_{GS} = 54–142 and Re_{LS} = 131–373), the experiments were performed in parallel rectangular micro-channels to obtain flow pattern and heat transfer data. The conclusions from this study can be drawn as follows.

1. Slug flow can result in higher heat transfer enhancement in comparison to gas core flow.
2. The Nusselt number increases with the increase in superficial Reynolds numbers.
3. Two-phase gas–liquid flow yields heat transfer enhancement up to 80% when compared with the single-phase liquid flow.

Acknowledgements

The authors would like to express their appreciation to the Thailand Research Fund, the National Science and Technology Development Agency, the National Research University Project and KMITL Research Fund for providing financial support for this study.

References

[1] A. Serizawa, Z. Feng, Z. Kawara, Two-phase flow in micro-channels, Exp. Therm. Fluid Sci. 26 (2002) 703–714.
[2] P.M.-Y. Chung, M. Kawaji, The effect of channel diameter on adiabatic two-phase flow characteristics in microchannels, Int. J. Multiphase Flow 30 (2004) 735–761.
[3] S.G. Kandlikar, Scale effects on flow boiling heat transfer in microchannels: a fundamental perspective, Int. J. Therm. Sci. 49 (2010) 1073–1085.
[4] C.L. Ong, J.R. Thome, Macro-to-microchannel transition in two-phase flow: part 1-two-phase flow patterns and film thickness measurements, Exp. Therm. Fluid Sci. 35 (2011) 37–47.
[5] J.-T. Oh, A.S. Pamitran, K.-I. Choi, P. Hrnjak, Experimental investigation on two-phase flow boiling heat transfer of five refrigerants in horizontal small tubes of 0.5, 1.5 and 3.0 mm inner diameters, Int. J. Heat Mass Transfer 54 (2011) 2080–2088.
[6] S. Saisorn, J. Kaew-On, S. Wongwises, An experimental investigation of flow boiling heat transfer of R-134a in horizontal and vertical mini-channels, Exp. Therm. Fluid Sci. 46 (2013) 232–244.
[7] H. Ide, M. Kawaji, Effect of tube diameters on the flow phenomena of gas-liquid two-phase flow in microchannels, in: ASME 2013 11th International Conference on Nanochannels, Microchannels, and Minichannels (ICNMM2013), Sapporo, Japan, June 16–19, 2013.
[8] I. Mudawar, Two-phase microchannel heat sinks: theory, applications and limitations, J. Electron. Packag. 133 (2011) 1–31.
[9] L. Tadrist, Review on two-phase flow instabilities in narrow spaces, Int. J. Heat Fluid Flow 28 (2007) 54–62.
[10] A.A. Arcanjo, C.B. Tibirica, G. Ribatski, Evaluation of flow patterns and elongated bubble characteristics during the flow boiling of halocarbon refrigerants in a micro-scale channel, Exp. Therm. Fluid Sci. 34 (2010) 766–775.
[11] C.B. Tibirica, G. Ribatski, Flow boiling heat transfer of R134a and R245fa in a 2.3 mm tube, Int. J. Heat Mass Transfer 53 (2010) 2459–2468.
[12] C.L. Ong, J.R. Thome, Macro-to-microchannel transition in two-phase flow: part 2 – flow boiling heat transfer and critical heat flux, Exp. Therm. Fluid Sci. 35 (2011) 873–886.
[13] G. Ribatski, A critical overview on the recent literature concerning flow boiling and two-phase flows inside micro-scale channels, Exp. Heat Transfer 26 (2013) 198–246.
[14] C.B. Tibirica, G. Ribatski, Flow boiling in micro-scale channels – synthesized literature review, Int. J. Refrigeration 36 (2013) 301–324.
[15] Z.Y. Bao, D.F. Fletcher, B.S. Haynes, An experimental study of gas–liquid flow in a narrow conduit, Int. J. Heat Mass Transfer 43 (2000) 2313–2324.
[16] G. Hetsroni, A. Mosyak, Z. Segal, E. Pogrebnyak, Two-phase flow patterns in parallel micro-channels, Int. J. Multiphase Flow 29 (2003) 341–360.
[17] K.A. Triplett, S.M. Ghiaasiaan, S.I. Abdel-Khalik, D.L. Sadowski, Gas–liquid two-phase flow in microchannels part I: two-phase flow patterns, Int. J. Multiphase Flow 25 (1999) 377–394.
[18] K.A. Triplett, S.M. Ghiaasiaan, S.I. Abdel-Khalik, A. LeMouel, B.N. McCord, Gas–liquid two-phase flow in microchannels part II: void fraction and pressure drop, Int. J. Multiphase Flow 25 (1999) 395–410.
[19] G. Hetsroni, A. Mosyak, E. Pogrebnyak, Z. Segal, Heat transfer of gas–liquid mixture in micro-channel heat sink, Int. J. Heat Mass Transfer 52 (2009) 3963–3971.
[20] A.R. Betz, D. Attinger, Can segmented flow enhance heat transfer in microchannel heat sinks?, Int J. Heat Mass Transfer 53 (2010) 3683–3691.
[21] K. Choo, S.J. Kim, Heat transfer and fluid flow characteristics of nonboiling two-phase flow in microchannels, J. Heat Transfer 133 (2011) 1–7.
[22] A. Marchitto, M. Fossa, G. Guglielmini, The effect of the flow direction inside the header on two-phase flow distribution in parallel vertical channels, Appl. Therm. Eng. 36 (2012) 245–251.
[23] J.E. Park, J.R. Thome, Critical heat flux in multi-microchannel copper elements with low pressure refrigerants, Int. J. Heat Mass Transfer 53 (2010) 110–122.
[24] V. Gnielinski, Ein neues berechnungsverfahren fur die warmeubertragung im ubergangsbereich zwischen laminaren und turbulenter rohstromung, Forsch. Ingenieurwesen – Eng. Res. 61 (1995) 240–248.
[25] P.-S. Lee, S.V. Garimella, Thermally developing flow and heat transfer in rectangular microchannels of different aspect ratios, Int. J. Heat Mass Transfer 49 (2006) 3060–3067.
[26] E.R. Dario, L. Tadrist, J.C. Passos, Review on two-phase flow distribution in parallel channels with macro and micro hydraulic diameters: main results, analyses, trends, Appl. Therm. Eng. 59 (2013) 316–335.
[27] C.L. Ong, J.R. Thome, Flow boiling heat transfer of R134a, R236fa and R245fa in a horizontal 1.030 mm circular channel, Exp. Therm. Fluid Sci. 33 (2009) 651–663.

Springer

Dear Author,

Here are the proofs of your article.

- You can submit your corrections **online**, via **e-mail** or by **fax**.
- For **online** submission please insert your corrections in the online correction form. Always indicate the line number to which the correction refers.
- You can also insert your corrections in the proof PDF and **email** the annotated PDF.
- For fax submission, please ensure that your corrections are clearly legible. Use a fine black pen and write the correction in the margin, not too close to the edge of the page.
- Remember to note the **journal title**, **article number**, and **your name** when sending your response via e-mail or fax.
- **Check** the metadata sheet to make sure that the header information, especially author names and the corresponding affiliations are correctly shown.
- **Check** the questions that may have arisen during copy editing and insert your answers/ corrections.
- **Check** that the text is complete and that all figures, tables and their legends are included. Also check the accuracy of special characters, equations, and electronic supplementary material if applicable. If necessary refer to the *Edited manuscript*.
- The publication of inaccurate data such as dosages and units can have serious consequences. Please take particular care that all such details are correct.
- Please **do not** make changes that involve only matters of style. We have generally introduced forms that follow the journal's style.
  Substantial changes in content, e.g., new results, corrected values, title and authorship are not allowed without the approval of the responsible editor. In such a case, please contact the Editorial Office and return his/her consent together with the proof.
- If we do not receive your corrections **within 48 hours**, we will send you a reminder.
- Your article will be published **Online First** approximately one week after receipt of your corrected proofs. This is the **official first publication** citable with the DOI. **Further changes are, therefore, not possible.**
- The **printed version** will follow in a forthcoming issue.

Please note

After online publication, subscribers (personal/institutional) to this journal will have access to the complete article via the DOI using the URL: http://dx.doi.org/[DOI].
If you would like to know when your article has been published online, take advantage of our free alert service. For registration and further information go to: http://www.link.springer.com.

Due to the electronic nature of the procedure, the manuscript and the original figures will only be returned to you on special request. When you return your corrections, please inform us if you would like to have these documents returned.

Metadata of the article that will be visualized in OnlineFirst

Please note: Images will appear in color online but will be printed in black and white.

ArticleTitle	Thermal conductivity of Al_2O_3/water nanofluids: measurement, correlation, sensitivity analysis, and comparisons with literature reports	
Article Sub-Title		
Article CopyRight	Akadémiai Kiadó, Budapest, Hungary (This will be the copyright line in the final PDF)	
Journal Name	Journal of Thermal Analysis and Calorimetry	
Corresponding Author	Family Name	**Esfe**
	Particle	
	Given Name	**Mohammad Hemmat**
	Suffix	
	Division	Faculty of Mechanical Engineering
	Organization	Semnan University
	Address	Semnan, Iran
	Email	m.hemmatesfe@gmail.com
Corresponding Author	Family Name	**Mahian**
	Particle	
	Given Name	**Omid**
	Suffix	
	Division	Young Researchers and Elite Club, Mashhad Branch
	Organization	Islamic Azad University
	Address	Mashhad, Iran
	Email	omid.mahian@gmail.com
Author	Family Name	**Saedodin**
	Particle	
	Given Name	**Seyfolah**
	Suffix	
	Division	Faculty of Mechanical Engineering
	Organization	Semnan University
	Address	Semnan, Iran
	Email	
Author	Family Name	**Wongwises**
	Particle	
	Given Name	**Somchai**
	Suffix	
	Division	Fluid Mechanics, Thermal Engineering and Multiphase Flow Research Lab. (FUTURE), Department of Mechanical Engineering, Faculty of Engineering
	Organization	King Mongkut's University of Technology Thonburi
	Address	Bangmod, 10140, Bangkok, Thailand
	Email	

Schedule	Received	22 October 2013

Revised

Accepted 15 March 2014

Abstract

A considerable number of studies can be found on the thermal conductivity of nanofluids in which Al_2O_3 nanoparticles are used as additives. In the present study, the aim is to measure the thermal conductivity of very narrow Al_2O_3 nanoparticles with the size of 5 nm suspended in water. The thermal conductivity of nanofluids with concentrations up to 5 % is measured in a temperature range between 26 and 55 °C. Using the experimental data, a correlation is presented as a function of the temperature and volume fraction of nanoparticles. Finally, a sensitivity analysis is performed to assess the sensitivity of thermal conductivity of nanofluids to increase the particle loading at different temperatures. The sensitivity analysis reveals that at a given concentration, the sensitivity of thermal conductivity to particle loading increases when the temperature increases.

Keywords (separated by '-') Thermal conductivity - Nanofluid - Correlation - Sensitivity analysis

Footnote Information

J Therm Anal Calorim
DOI 10.1007/s10973-014-3771-x

Thermal conductivity of Al_2O_3/water nanofluids: measurement, correlation, sensitivity analysis, and comparisons with literature reports

Mohammad Hemmat Esfe · Seyfolah Saedodin · Omid Mahian · Somchai Wongwises

Received: 22 October 2013 / Accepted: 15 March 2014

Abstract A considerable number of studies can be found on the thermal conductivity of nanofluids in which Al_2O_3 nanoparticles are used as additives. In the present study, the aim is to measure the thermal conductivity of very narrow Al_2O_3 nanoparticles with the size of 5 nm suspended in water. The thermal conductivity of nanofluids with concentrations up to 5 % is measured in a temperature range between 26 and 55 °C. Using the experimental data, a correlation is presented as a function of the temperature and volume fraction of nanoparticles. Finally, a sensitivity analysis is performed to assess the sensitivity of thermal conductivity of nanofluids to increase the particle loading at different temperatures. The sensitivity analysis reveals that at a given concentration, the sensitivity of thermal conductivity to particle loading increases when the temperature increases.

Keywords Thermal conductivity · Nanofluid · Correlation · Sensitivity analysis

M. H. Esfe (✉) · S. Saedodin
Faculty of Mechanical Engineering, Semnan University, Semnan, Iran
e-mail: m.hemmatesfe@gmail.com

O. Mahian (✉)
Young Researchers and Elite Club, Mashhad Branch, Islamic Azad University, Mashhad, Iran
e-mail: omid.mahian@gmail.com

S. Wongwises
Fluid Mechanics, Thermal Engineering and Multiphase Flow Research Lab. (FUTURE), Department of Mechanical Engineering, Faculty of Engineering, King Mongkut's University of Technology Thonburi, Bangmod, Bangkok 10140, Thailand

Introduction

In 1995, Choi [1] called the mixture of very fine particles suspended in common liquids a "Nanofluid." From that time until now, many researchers worldwide have paid attention to this new field of thermal and fluid sciences. The applications of nanofluids have been established in many branches of thermal engineering, such as solar energy, nuclear reactors, medical applications, automobiles, electronic equipment, and so on [2, 3]. The replacement of common heat transfer fluids with nanofluids is reasonable because the thermal conductivity of nanofluids containing solid nanoparticles is higher than that of the usual fluids. As a result, using a fluid with a higher thermal conductivity enhances the heat transfer rate and, consequently, results in a more compact system. Therefore, the measurement of the thermal conductivity of nanofluids and knowing the factors (e.g., temperature, size of particles, etc.) that affect its magnitude are important issues. Based on the literature, aluminum oxide (Al_2O_3) nanoparticles are one of the most common particles that are used to prepare the nanofluids.

In the following, a literature review of the studies on the thermal conductivity of nanofluids containing Al_2O_3 nanoparticles has been conducted. Wang et al. [4] provided Al_2O_3/water and Al_2O_3/ethylene glycol nanofluids in which the particle size was 28 nm. Using the steady-state parallel plates method, the thermal conductivity of nanofluid samples was measured. The thermal conductivity enhancements were approximately 16 % and 24 % for 5.5 % of particle loading in water and 5 % of particle loading in ethylene glycol, respectively.

Das et al. [5] measured the thermal conductivity of Al_2O_3/water nanofluids using the temperature oscillation method at a temperature range between 21 and 51 °C,

Journal : Large 10973 | Dispatch : 26-3-2014 | Pages : 7
Article No. : 3771 | ☐ LE | ☐ TYPESET
MS Code : JTAC-D-13-01090 | ✔ CP | ✔ DISK

where the volume fractions of particles do not exceed 4 %. The nanoparticle's size in the study was about 38 nm. Their results indicated that with the increase of the temperature and concentration of nanofluids, the effective thermal conductivity increases. For the 4 % volume fraction of nanoparticles and the temperature of 51 °C, the thermal conductivity enhancement was about 24.3 %, as compared to pure water. Putra et al. [6] studied the thermal conductivity of Al_2O_3 nanoparticles with an average size of 131 nm dispersed in water. The steady-state parallel plates approach was utilized to measure the thermal conductivity. The thermal conductivity enhancement was equal to 24 %, for the concentration of 4 %. Masuda et al. [7] investigated the thermal conductivity of Al_2O_3 nanoparticles with the diameter of 13 nm suspended in pure water using the transient hot wire technique. They perceived that the particle loading up to 4.4 % leads to increasing the effective thermal conductivity by 33 %. Lee et al. [8] provided two types of nanofluids containing Al_2O_3 nanoparticles with a diameter of 38.4 nm. These two types are Al_2O_3/water and Al_2O_3/ethylene glycol nanofluids and their thermal conductivities were measured by the transient hot wire procedure. They found that the thermal conductivity of water-based nanofluids increases by 11 % for the 4.3 % volume fraction, while for ethylene glycol-based nanofluids the maximum enhancement of thermal conductivity was 19 % at the concentration of 5 %. Chon et al. [9] examined the thermal conductivity of Al_2O_3/water nanofluids by the transient hot wire method where the temperature changes from 21 to 71 °C and the particle sizes of 11 nm, 47 nm, and 150 nm. They concluded that increasing the particle size results in the decrease of the thermal conductivity enhancement. Also, for the 4 % concentration, a temperature of 71 °C, and a particle size of 47 nm, the enhancement magnitude was 28 %. Li and Peterson [10] studied the effect of the particle size of Al_2O_3 nanoparticles dispersed in water on the thermal conductivity enhancement by the steady-state parallel plates method. They pointed out that for the 6 % volume fraction of nanoparticles, when the size of particles increases from 36 nm to 47 nm, the thermal conductivity enhancement decreases by about 2 % (changes from 28 % to 26 %). Zhang et al. [11] reported an increase of 15 % in the thermal conductivity of the Al_2O_3/water nanofluid with a concentration of 5 % and particle size of 20 nm. The transient hot wire approach was applied for the measurement. Timofeeva et al. [12] evaluated the thermal conductivity enhancement of Al_2O_3/water nanofluids with the maximum particle volume fraction of 5 % by utilizing the transient hot wire method. They found that the enhancements in the thermal conductivity for particle sizes of 11 nm, 20 nm, and 40 nm were 8, 7, and 10 %, respectively. Wong and Kurma [13] showed that the thermal conductivity of the Al_2O_3/water nanofluid at 46.6 °C, compared to water at room temperature, increases by 22 % where the concentration is 8.47 Vol%. The particle size in this study was 36 nm. More research on the thermal conductivity of Al_2O_3/water nanofluids has been done by Ju et al. [14]. The maximum concentration was considered 10 Vol%, where the tests were performed with three different sizes of nanoparticles including 20, 30, and 45 nm. Oh et al. [15] applied the 3ω method to measure the thermal conductivity of Al_2O_3/water and Al_2O_3/ethylene glycol nanofluids. Sommers and Yerkes [16] prepared suspensions of propanol and Al_2O_3 nanoparticles with the size of 10 nm. They indicated that the thermal conductivity changes linearly against the particle loading. Sundar and Sharma [17] measured the thermal conductivity of aqueous suspensions of Al_2O_3 nanoparticles with the size of 47 nm and volume fractions of 0.2, 0.4, and 0.8 %. Longo and Zilio [18] conducted the experiments to determine the thermal conductivity of sonicated and stirred Al_2O_3/water nanofluids with concentrations between 1 and 4 Vol% for the temperature range from 1 to 40 °C. Their results showed that the thermal conductivity enhancement is negative for temperatures close to 1 °C. Yiamsawasd et al. [19] measured the thermal conductivity of Al_2O_3 nanoparticles suspended in a mixture of water and ethylene glycol (80:20 weight ratio) for volume fractions by 8 % and temperatures between 15 and 65 °C. They reported an increase by 30 % for the thermal conductivity in the range of measurements. The size of particles in this work was 120 nm. Recently in a nice work, Barbes et al. [20] measured thermal conductivity of Al_2O_3 nanoparticles suspended in water and ethylene glycol using steady-state coaxial cylinders method.

The aim of the present work is to study of the thermal conductivity of Al_2O_3/water nanofluids at a particle volume fraction range from 0.25 to 5 % and the temperature range between 26 and 55 °C. Based on the best knowledge of the authors, the particle size used in this work is the smallest one used in the literature (i.e., 5 nm). After measuring the thermal conductivity, a model is presented for the thermal conductivity as a function of the temperature and volume fraction. Finally, a sensitivity analysis is conducted on the experimental data.

Nanofluid preparation

The first step for studying the nanofluids and their properties is the preparation of the fluid. Due to the sedimentation and agglomeration of nanoparticles in the base fluid, special methods should be utilized to create a suspension with an acceptable stability. In this work, the nanofluids at volume concentrations of 0.25, 0.5, 1.0, 2.0, 3.0, 4.0, and 5.0 % were prepared by dispersing Al_2O_3 nanoparticles in DI Water as the base fluid.

Journal : Large 10973 | Dispatch : 26-3-2014 | Pages : 7
Article No. : 3771 | ☐ LE | ☐ TYPESET
MS Code : JTAC-D-13-01090 | ✔ CP | ✔ DISK

Table 1 Characteristics of Al_2O_3 nanoparticles

Nanoparticles (Al_2O_3) purity	99.99 %
Nanoparticles (Al_2O_3) APS	5 nm—very narrow particle size range
Nanoparticles (Al_2O_3) SSA/m^2 g^{-1}	>150
Nanoparticles (Al_2O_3) Morphology	Nearly spherical
Nanoparticles (Al_2O_3) color	White
Specific heat capacity/ J Kg^{-1} K^{-1}	880
Density/Kg m^{-3}	3,890
Bulk Density/g ml^{-1}	0.18

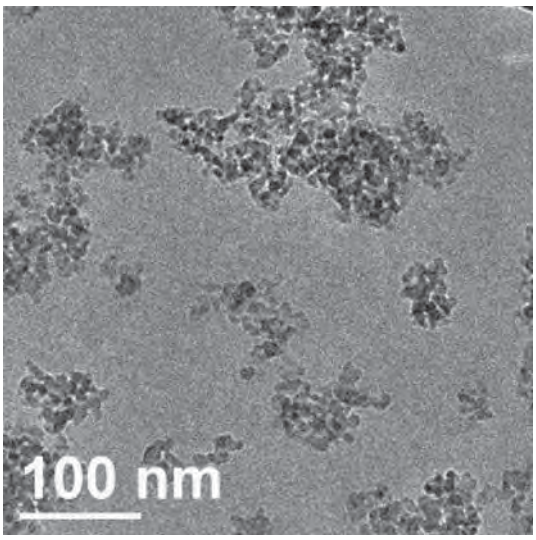

Fig. 1 Transmission electron microscopy (TEM) image of Al_2O_3 nanoparticles

A two-step method was utilized to prepare the nanofluids. The nanoparticles with a diameter of 5 nm were purchased from US Research Nanomaterial, Inc. The properties of the nanoparticles are presented in Table 1. Also, a TEM image of the particles taken from the company is displayed in Fig. 1. As shown in the TEM image, the particles are almost spherical in shape. Nanoparticles are weighed carefully for any volume concentration and then are added to the water little by little. The mixture is stirred for 30 to 45 min, and after that the suspension is inserted inside an ultrasonic vibrator (Hielschercompany, Germany) for 3 h to break down the agglomeration of particles. Using the stirrer and ultrasonic vibrator results in a more stable and uniform nanofluid. No sedimentation in the samples is observed with the naked eyes for a long time (at least 1 week).

Measurement of thermal conductivity

Thermal conductivity of Al_2O_3-water nanofluids with various concentrations and the temperature range between 26 and 55 °C was measured by a KD2 Pro instrument manufactured by Decagon Devices Inc. This instrument acts based on the transient hot wire approach; the KD2 Pro takes measurements at 1 s intervals during a 90 s measurement cycle. The accuracy of the device is ± 5 %. The experiments are repeated three times for each case and the average value is reported. A hot water bath is used to stabilize the temperature and a thermometer with accuracy of 0.1^C is used to measure the temperature.

Results and discussions

The experimental data are compared with the most well-known theoretical models including Hamilton−Crosser and Yu–Choi. One of the basic models to calculate the thermal conductivity of solid–liquid mixtures, k_{eff}, is the Hamilton–Crosser (H–C) model [21]. This model is able to predict the thermal conductivity of solid–liquid mixtures in which the thermal conductivity ratio of the solid phase to the liquid phase is larger than 100; this model is described as follows:

$$\frac{k_{eff}}{k_f} = \frac{k_p + (n-1)k_f + (n-1)\,\varphi\,(k_p - k_f)}{k_p + (n-1)k_f - \varphi(k_p - k_f)}, \quad (1)$$

where k_p, k_f, are the thermal conductivity of particles and fluid, respectively. φ is the volume fraction of nanoparticles and n is the empirical shape factor defined as

$$n = \frac{3}{\psi} \quad (2)$$

in which ψ indicates the sphericity of particles. The sphericity for cylindrical and spherical particles is 0.5 and 1, respectively. Therefore, in the present work, n is considered equal to 3 because of the spherical shape of Al_2O_3 nanoparticles.

Yu and Choi [22] is another model that is considered for the comparative purposes. The relation reads as

$$k_{eff} = \frac{k_p + 2k_f + 2(k_p - k_f)(1+\beta)^3\varphi}{k_p + 2k_f - 2(k_p - k_f)(1+\beta)^3\varphi}\,k_f, \quad (3)$$

where β is the ratio of the nanolayer thickness to the original particle radius; normally it is assumed to be 0.1.

Figure 2 presents a comparison between the experimental data for the dimensionless thermal conductivity (k_{eff}/k_f) and the results obtained by the H–C and Yu–Choi models. The comparison is conducted at different temperatures. As it can be observed from Fig. 2a, at a low temperature (i.e., 26 °C), the Yu–Choi model is able to predict

Journal : Large 10973 Dispatch : 26-3-2014 Pages : 7
Article No. : 3771 LE TYPESET
MS Code : JTAC-D-13-01090 CP DISK

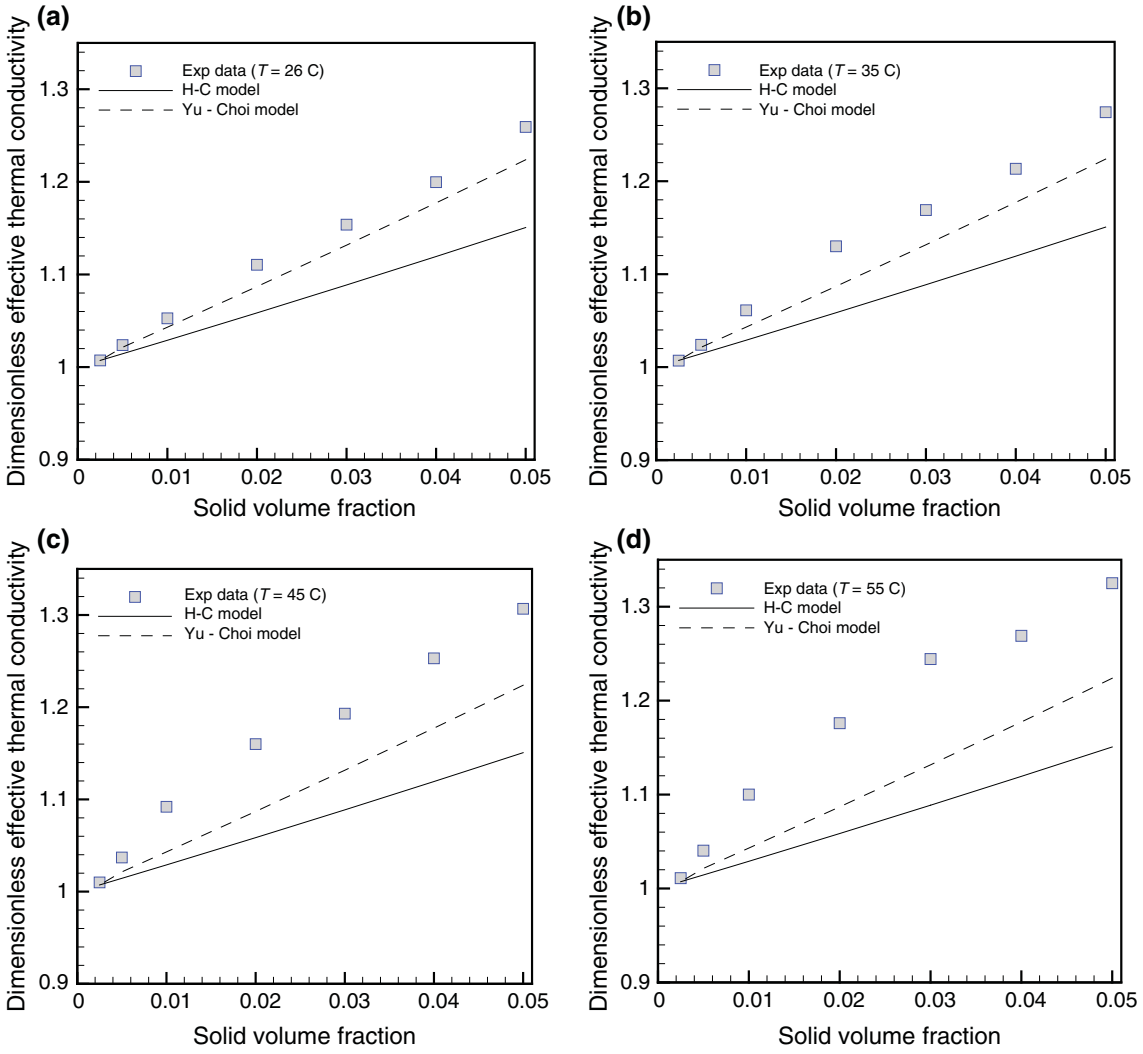

Fig. 2 Comparison between the measured data and the theoretical models

the experimental data. By increasing the temperature, the difference between the measured data and the results of Yu–Choi model increases considerably. Looking at Fig. 2d reveals that the Yu–Choi model underestimates the measured data by about 10 %. Therefore, it is found that the temperature is a significant factor that should be involved in the models that are presented to predict the thermal conductivity.

Figure 3 shows the thermal conductivity enhancement against the solid volume fraction at different temperatures. It is found that the thermal conductivity of nanofluid with the volume concentration of 5 % is enhanced compared to the base fluid (pure water) from 25 % to 32 %, depending on the temperature. A higher temperature results in a bigger enhancement.

Figure 4 is plotted to show the variations of dimensionless thermal conductivity with temperature at different volume fractions. It is seen that for low concentrations of nanofluids (less than 1 %), there is no visible change in the dimensionless thermal conductivity with temperature. Collision between the solid particles is a main factor which determines the thermal conductivity of a nanofluid. By increasing the number of collisions, the internal energy of particles, and hence the effective thermal conductivity of the nanofluid increases. At low concentrations, the number of particles in a given volume of nanofluid is less than at higher concentrations. Consequently, the space between the solid molecules is bigger at low concentrations; this reduces the probability and number of collisions between the particles due to heating. Table 2 provides the values of dimensionless thermal conductivity at different temperatures and concentrations.

Now, the present data are compared with the results of some experimental works on the Al_2O_3/water nanofluids [7, 8, 23–26] at room temperature, as shown in Fig. 5. The data are extracted from the review paper by Khanafer and

Journal : Large 10973 Dispatch : 26-3-2014 Pages : 7
Article No. : 3771 LE TYPESET
MS Code : JTAC-D-13-01090 CP DISK

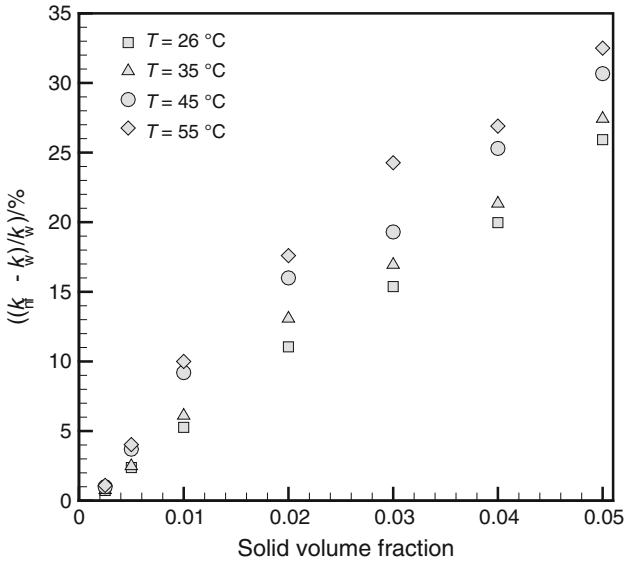

Fig. 3 Thermal conductivity enhancement against the solid volume fraction at different temperatures

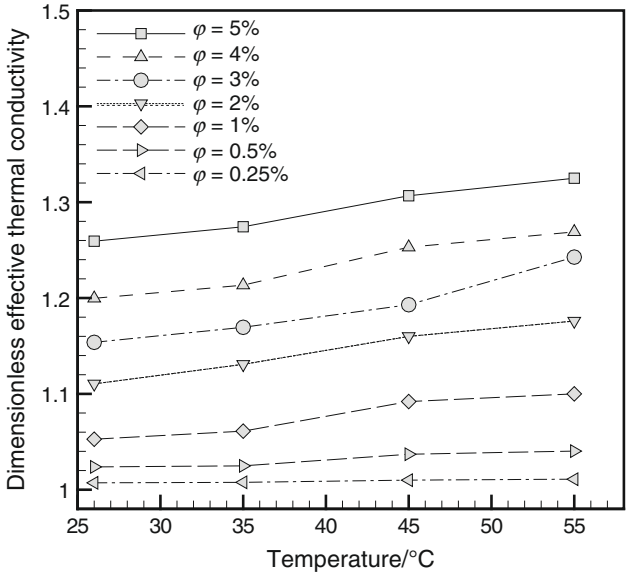

Fig. 4 Variations of dimensionless thermal conductivity with temperature at different volume fractions

Vafai [27] on the thermophysical properties of nanofluids. It is observed from the figure that the present results are very close to the results of Murshed et al. [26], although the nanoparticle size used in the present work is 5 nm and in the study of Murshed et al. [26] it is 80 nm. Also, it is seen that the difference between the present data and the data by Minsta et al. [25] is very high. Besides the difference in size, the differences in preparation method, measurement approaches, and experimental conditions should be considered in the comparisons of various works.

Table 2 Effective thermal conductivity of Al_2O_3/water nanofluids in various temperatures

Volume fraction	T = 26 °C	T = 35 °C	T = 45 °C	T = 55 °C
0.05	1.259	1.274	1.307	1.325
0.04	1.199	1.213	1.253	1.269
0.03	1.153	1.169	1.193	1.243
0.02	1.110	1.130	1.160	1.176
0.01	1.053	1.061	1.092	1.101
0.005	1.023	1.025	1.037	1.040
0.0025	1.007	1.008	1.010	1.011

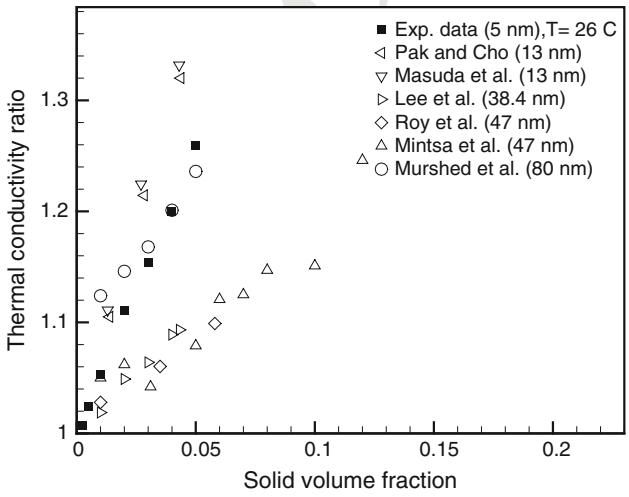

Fig. 5 Comparison between the measured data and other experimental works

Based on the experimental data, a model as a function of temperature and solid volume fraction is proposed. The model is valid for Al_2O_3/water nanofluids, $26 \leq T(^{\circ}C) \leq 55$, and $0.0025 \leq \phi \leq 0.05$. The model is presented as follows:

$$\frac{k_{nf}}{k_f} = 0.911 \times T^{\left(-0.0415-\frac{0.404}{\ln(\varphi)}\right)}. \quad (4)$$

To examine the accuracy of the presented model, the margin of deviation can be defined as follows:

$$\text{Margin of deviation } (\%) = \frac{k_c - k_m}{k_m} \times 100, \quad (5)$$

where k_c is the thermal conductivity calculated through the correlation, and k_m is the thermal conductivity measured during the tests. Figure 6 illustrates the margin of deviation at different temperatures. The margin of deviation does not exceed 2 %, which indicates the acceptable accuracy of the presented model to predict the thermal conductivity.

Journal : Large 10973 Dispatch : 26-3-2014 Pages : 7
Article No. : 3771 LE TYPESET
MS Code : JTAC-D-13-01090 CP DISK

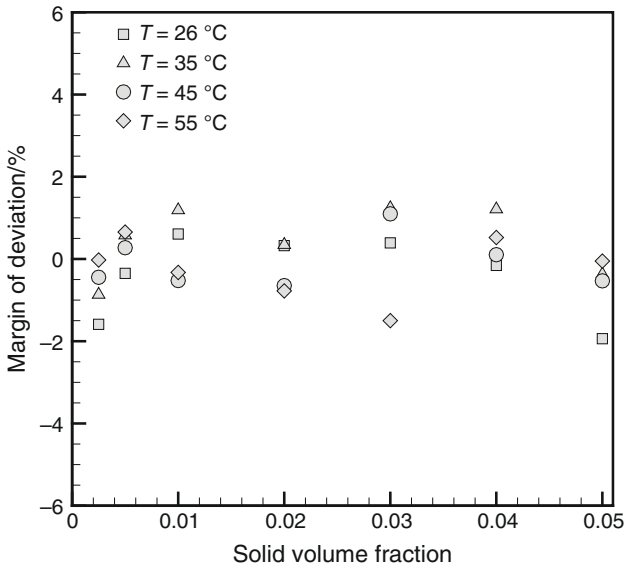

Fig. 6 Margin of deviation of the presented correlation

Finally, a sensitivity analysis is conducted based on Ref.

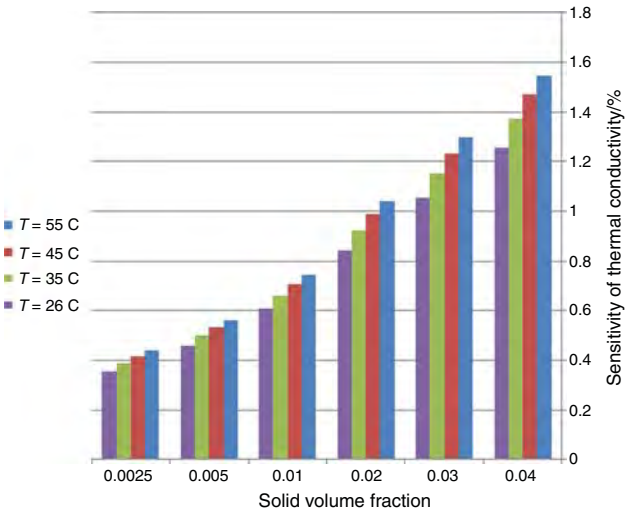

Fig. 7 Sensitivity analysis of thermal conductivity at different temperatures and concentrations

[28]. The sensitivity analysis shows how much the thermal conductivity is sensitive to the changes in particle loading at a given temperature. In the present work, the sensitivity analysis is performed by considering 10 % change in particle loading. For example, consider the volume fraction of 2 % and a temperature of 26 °C. The sensitivity in this temperature can be calculated as follows:

$$\text{Sensitivity } (\%) = \frac{k(\phi = 2.2\%) - k(\phi = 2\%)}{k(\phi = 2\%)} \times 100. \qquad (6)$$

Figure 7 provides the results of the sensitivity analysis. As it can be seen, with an increase in the temperature, the sensitivity of thermal conductivity increases. This means that at a moderate volume fraction, adding a specified amount of nanoparticles to the nanofluid at a high temperature is more effective than at low temperatures.

Conclusions

An experimental study was performed to measure the thermal conductivity of aqueous suspensions of Al_2O_3 nanoparticles with the diameter of 5 nm using the transient hot wire approach. In the work, the temperature changed from 26 to 55 °C, while the solid volume fraction range was between 0.0025 and 0.05. The measured data were compared with the results of theoretical models, including the Hamilton–Crosser and Yu–Choi relations. The comparisons showed that the Yu–Choi model gives acceptable estimations at low temperature, but with increased temperatures, it fails to predict the measured data with an acceptable accuracy. The present data were also compared with the results of other experimental works available in the literature. It was indicated that many factors, such as the particle size, environmental conditions, and methods of preparation and measurement of the thermal conductivity, affect the measured results. Based on the data, a model was proposed as a function of the temperature and solid volume fraction. Finally, the sensitivity analysis of data showed that the thermal conductivity is more sensitive to particle loading at higher temperatures.

Acknowledgements The authors would like to acknowledge the assistance provided by the Nanofluid Laboratory of Semnan University Science and Technology Park for providing necessary instruments to carry out the sample preparation and help in the analysis of samples to complete the article in time. The third and fourth authors wish to thank the National Science and Technology Development Agency and the National Research University Project for the support. Also, Omid Mahian wishes to thank Prof. Somchai Wongwises for his supports during his research at King Mongkut's University of Technology Thonburi, Thailand.

References

1. Choi SUS. Enhancing thermal conductivity of fluids with nanoparticles. Dev Appl Non Newton Flows. 1995;231:99–105.
2. Saidur R, Leong KY, Mohammad HA. A review on applications and challenges of nanofluids. Renew Sust Energ Rev. 2011;15:1646–68.
3. Mahian O, Kianifar A, Kalogirou SA, Pop I, Wongwises S. A review of the applications of nanofluids in solar energy. Int J Heat Mass Transf. 2013;57:582–94.
4. Wang X, Xu X, Choi SUS. Thermal conductivity of nanoparticle-fluid mixture. J Thermophys Heat Transf. 1999;13:474–80.
5. Das SK, Putra N, Thiesen P, Roetzel W. Temperature dependence of thermal conductivity enhancement for nanofluids. J Heat Transf. 2003;125:567–74.
6. Putra N, Roetzel W, Das SK. Natural convection of nano-fluids. Heat Mass Transf. 2003;39:775–84.

Journal : Large 10973 | Dispatch : 26-3-2014 | Pages : 7
Article No. : 3771 | LE | TYPESET
MS Code : JTAC-D-13-01090 | CP | DISK

7. Masuda H, Ebata A, Teramae K, Hishinuma N. lteration of thermal conductivity and viscosity of liquid by dispersing ultra-fine particles(dispersion of Al2O3, SiO2 and TiO2 ultra-fine particles). Netsu Bussei. 1993;4:227–33.
8. Lee S, Choi SUS, Li S, Eastman JA. Measuring thermal conductivity of fluids containing oxide nanoparticles. J Heat Transf. 1999;121:280–9.
9. Chon CH, Kihm KD, Lee SP, Choi SUS. Empirical correlation finding the role of temperature and particle size for nanofluid (Al2O3) thermal conductivity enhancement. Appl Phys Lett. 2005;87:153107.
10. Li CH, Peterson GP. The effect of particle size on the effective thermal conductivity of Al2O3-water nanofluids. J Appl Phys. 2007;101:044312.
11. Zhang X, Gu H, Fujii M. Effective thermal conductivity and thermal diffusivity of nanofluids containing spherical and cylindrical nanoparticles. J Appl Phys. 2006;100:1–5.
12. Timofeeva EV, Gavrilov AN, McCloskey JM, Tolmachev YV. Thermal conductivity and particle agglomeration in alumina nanofluids: experiment and theory. Phys Rev E. 2007;76:061203.
13. Wong KFV, Kurma T. Transport properties of alumina nanofluids. Nanotechnology. 2008;19:345702.
14. Ju YS, Kim J, Hung MT. Experimental study of heat conduction in aqueous suspensions of aluminum oxide nanoparticles. J. Heat Transf. 2008;130:092403.
15. Oh DW, Jain A, Eaton JK, Goodson KE, Lee JS. Thermal conductivity measurement and sedimentation detection of aluminum oxide nanofluids by using the 3ω method. Int J Heat Fluid Flow. 2008;29:1456–61.
16. Sommers AD, Yerkes KL. Experimental investigation into the convective heat transfer and system-level effects of Al2O3-propanol nanofluid. J. Nanoparticle Res. 2010;12:1003–14.
17. Sundar LS, Sharma KV. Turbulent heat transfer and friction factor of Al2O3 nanofluid in circular tube with twisted tape inserts. Int J Heat Mass Transf. 2010;53:1409–16.
18. Longo GA, Zilio C. Experimental measurement of thermophysical properties of oxide-water nano-fluids down to ice-point. Exp Therm Fluid Sci. 2011;35:1313–24.
19. Yiamsawasd T, Dalkilic AS, Wongwises S. Measurement of the thermal conductivity of titania and alumina nanofluids. Thermochim Acta. 2012;545:48–56.
20. Barbés B, Páramo R, Blanco E, Pastoriza-Gallego MJ, Piñeiro MM, Legido JL, Casanova C. Thermal conductivity and specific heat capacity measurements of Al2O3 nanofluids. J. Thermal Anal Calorim. 2013;11:1615–25.
21. Hamilton RL, Crosser OK. Thermal conductivity of heterogeneous two-component systems. I&EC Fundam. 1962;1:182–91.
22. Yu W, Choi SUS. The Role of Interfacial Layers in the Enhanced Thermal Conductivity of Nanofluids: A Renovated Maxwell Model. J Nanopart Res. 2003;5:167–71.
23. Pak BC, Cho YI. Hydrodynamic and Heat Transfer Study of Dispersed Fluids with Submicron Metallic Oxide Particles. Exp Heat Transfer. 1998;11:151–70.
24. Roy G, Nguyen CT, Lajoie PR. Numerical investigation of laminar flow and heat transfer in a radial flow cooling system with the use of nanofluids. Superlatt Microstruct. 2004;35:497–511.
25. Minsta HA, Roy G, Nguyen CT, Doucet D. New temperature dependent thermal conductivity data for water-based nanofluids. Int J Therm Sci. 2009;48:363–71.
26. Murshed SMS, Leong KC, Yang C. Investigations of thermal conductivity and viscosity of nanofluids. Int J Therm Sci. 2008;47:560–8.
27. Khanafer K, Vafai K. A critical synthesis of thermophysical characteristics of nanofluids. Int J Heat Mass Transf. 2011;54:4410–28.
28. Mahian O, Kianifar A, Wongwises S. Dispersion of ZnO nanoparticles in a mixture of ethylene glycol–water, exploration of temperature-dependent density, and sensitivity analysis. J Clust Sci. 2013;24:1103–14.

Journal : Large 10973 | Dispatch : 26-3-2014 | Pages : 7
Article No. : 3771 | ☐ LE | ☐ TYPESET
MS Code : JTAC-D-13-01090 | ✔ CP | ✔ DISK

AUTHOR QUERY FORM

ELSEVIER	**Journal: HMT** **Article Number: 10728**	**Please e-mail or fax your responses and any corrections to:** **E-mail: corrections.eseo@elsevier.sps.co.in** **Fax: +31 2048 52799**

Dear Author,

Please check your proof carefully and mark all corrections at the appropriate place in the proof (e.g., by using on-screen annotation in the PDF file) or compile them in a separate list. Note: if you opt to annotate the file with software other than Adobe Reader then please also highlight the appropriate place in the PDF file. To ensure fast publication of your paper please return your corrections within 48 hours.

For correction or revision of any artwork, please consult http://www.elsevier.com/artworkinstructions.

Any queries or remarks that have arisen during the processing of your manuscript are listed below and highlighted by flags in the proof. Click on the 'Q' link to go to the location in the proof.

Location in article	Query / Remark: click on the Q link to go Please insert your reply or correction at the corresponding line in the proof
Q1	Please confirm that given name(s) and surname(s) have been identified correctly.
Q2	Please update the following Ref. [12].

Please check this box if you have no corrections to make to the PDF file ☐

Thank you for your assistance.

International Journal of Heat and Mass Transfer xxx (2014) xxx–xxx

Contents lists available at ScienceDirect

International Journal of Heat and Mass Transfer

journal homepage: www.elsevier.com/locate/ijhmt

Pressure drop during condensation of R134a flowing inside a multiport minichannel

Kittipong Sakamatapan, Somchai Wongwises*

Fluid Mechanics, Thermal Engineering and Multiphase Flow Research Lab. (FUTURE), Department of Mechanical Engineering, Faculty of Engineering, King Mongkut's University of Technology Thonburi, Bangmod, Bangkok 10140, Thailand

ARTICLE INFO

Article history:
Received 1 October 2013
Received in revised form 27 February 2014
Accepted 27 February 2014
Available online xxxx

Keywords:
Condensation
Frictional pressure gradient
R-134a
Multiport minichannel
Correlation

ABSTRACT

This paper is a continuation of the authors' previous work on the condensation of R134a flowing inside a multiport minichannel (Sakamatapan et al., 2013) [22]. The pressure drop's characteristics during condensation were investigated in an experiment for R134a flowing inside a multiport minichannel. The pressure drop characteristics were observed under mass flux range of 345–685 kg/m^2, heat flux of 15–25 kW/m^2, and saturation temperature of 35–45 °C. Two types of multiport minichannels having 14 channels, one with a 1.1 mm hydraulic diameter and another with 8 channels with a 1.2 mm hydraulic diameter, were designed as a counter flow tube in a tube heat exchanger. The results showed that the total pressure drop is dominated by the frictional pressure drop. The frictional pressure gradient increased with the augmentation of mass flux and vapor quality, but the increase of the saturation temperature and channel size play an important role in the decrease of frictional pressure gradient. On the other hand, the heat flux had an insignificant effect on the frictional pressure gradient. Moreover, the miniscale correlations were conducted to predict the frictional pressure gradient, and it was found that only the multiport minichannel correlations gave a reasonable result. A new two-phase friction factor correlation was proposed using the equivalent Reynolds number concept to predict the frictional pressure gradient during condensation.

1. Introduction

The multiport minichannel is commonly used in automotive air conditioning systems as a condenser. There are many advantages of using the minichannel, such as that it has a high heat transfer area per unit volume, compact size, low refrigerant charge, supported high pressure operation, reduced air-side, and pressure drop; however, sound understanding about heat transfer and pressure drop characteristics during condensation of a refrigerant in a multiport minichannel is still important and requires more attention from researchers. A few studies on pressure drop characteristics in multiport minichannels have been conducted by the following researchers.

Yang and Webb [1] measured adiabatic single and two phase pressure drop of R-12 flowing through 1.56 and 2.64 mm hydraulic diameters, which were made from an extruded aluminum tube with and without microfin, respectively. The tested conditions were conducted within the range of Reynolds number 2500–23,000 for single-phase liquid flow, mass flux 400–1400 kg/m^2 s, and vapor qualities 0.1–0.9 for two-phase flow. For two-phase flow, the pressure drop increased with the augmentation of the mass flux and vapor quality. The pressure drop of the microfin tube was higher than that of the plain tube. They developed the pressure drop correlation by using the equivalent mass velocity concept proposed by Akers et al. [2]. In addition, they concluded that surface tension force had an insignificant effect on frictional pressure drop in the microfin tube.

Single-phase and two-phase pressure drop for R134a, R22, and R404A flow in a multiport extruded aluminum tube with a hydraulic of 2.13 mm, and two circular copper tubes with an inside diameter of 3.25 and 6.25 mm, respectively, were measured by Zhang and Webb [3]. The Blasius correlation [4] was used to predict the single-phase friction factor within a ±10% error rate. The correlation of Friedel [5] was modified by including the employment of reduced pressure for their new two-phase friction factor correlation.

Koyama et al. [6] investigated the condensation of R134a in two multiport extruded tubes. One had 8 channels with a 1.11 hydraulic diameter, and the other had 19 channels with a 0.8 hydraulic diameter. They used pressure-measuring ports to measure the

* Corresponding author. Tel.: +66 2 470 9115; fax: +66 2 470 9111.
E-mail address: somchai.won@kmutt.ac.th (S. Wongwises).

http://dx.doi.org/10.1016/j.ijheatmasstransfer.2014.02.071
0017-9310/

Nomenclature

c	specific heat at constant pressure (kJ kg^{-1} K^{-1})
d_h	hydraulic diameter (m)
G	mass flux (kg m^{-2} s^{-1})
I	current (A)
i	enthalpy (kJ kg^{-1})
k	thermal conductivity (W m^{-1} K^{-1})
$\dot{m}$	mass flow rate (kg s^{-1})
L	length of multiport minichannel (m)
N	number of channels
P	pressure (kPa)
$\dot{Q}$	heat transfer rate (kW)
q''	heat flux (kW m^{-2})
Re	Reynolds number, $Re = \frac{Gd}{\mu}$
T	temperature (°C)
v	specific volume (m^3 kg^{-1})
V	voltage (V)
x	vapor quality
Greek lettersΔP	
	pressure drop (kPa)
μ	dynamic viscosity (Pa-s)
α	void fraction
ρ	density (kg m^{-3})
σ	surface tension (N m^{-1})
Subscripts$a$	
	acceleration
avg	average
$cont$	contraction
eq	*equivalent*
exp	expansion
f	friction
in	inlet
l	liquid
v	vapor
out	outlet
ref	refrigerant
sat	saturation
tot	total
tp	two phase
TS	test section
w	water

pressure drop at a distance of 191 mm. The positive agreement of the frictional pressure drop was found between the correlation of Mishima and Hibiki [7]. Therefore, the heat transfers' correlation of Haraguchi et al. [8] was modified by calculating the two-phase multiplier from the Mishima and Hibiki correlation [7].

Cavallini et al. [9] discussed the adiabatic two phases of the frictional pressure gradient of R236ea, R134a, and R410A, which were available in a wide range of reduced pressure for the multiport minichannel with a hydraulic diameter of 1.4 mm. The frictional pressure gradient was observed by the saturation temperature drop measurement of the frictional pressure gradient of R410A, which was lower than those of R134a and R236ea, respectively. Moreover, the experimental data were compared with several frictional pressure drop correlations available in the literature. The results showed that the frictional pressure gradient of R134a was in strong agreement but was not accurate for R236ea and R410A.

Garimella et al. [10] developed the multiple flow regime model for predicting pressure drop during all processes of condensation by a combined and modified intermittent and annular regime model, which were developed earlier. When comparing the predicted values with the measured data that was taken from mass flux between 150 and 750 kg/m^2 s in five circular microchannels, 82% of the data were within ±20% error rate.

The pressure drop of CO_2 during condensation was investigated by Park and Hrnjak [11]. This study was conducted at the saturation temperature of −15 and −25 °C by, mass fluxes of 200–800 kg/m^2 s, and wall sub-cooling temperature from 2 to 4 °C for a 0.89 mm microchannel. It was found that the two-phase pressure drop in the adiabatic condition increased with the augmentation of mass flux and vapor quality, but it decreased when saturation temperature increased. The comparison between the values predicted by conventional tubes and small tubes correlations, and the experimental data was also reported. It was shown that several correlations predicted the experimental data well.

Heo et al. [12] investigated the pressure drop of CO_2 during condensation in the multiport microchannel with a hydraulic diameter of 1.5 mm. The experiment was tested under mass flux from 400 to 1000 kg/m^2 s and saturation temperature from −5 to 5 °C. The pressure drop increased with the augmentation of mass flux and vapor quality, but it decreased with the increasing saturation temperature. It was also found that the correlation of Misima and Hibiski [7] could be predicted the data with a mean deviation of 29.1%.

Due to the difficulties in constructing the test section, which is a type of heat exchanger for condensation experiment, the information on heat transfer and pressure drop characteristics during the condensation of working fluids in a multiport minichannel is still limited, compared to the evaporation experiment. As described above, there have been only works carried out by [1,3,6,9–12] dealing with this issue. However, it can be noted that the experimental investigations found in the literature described above focused on the effect of the specific parameter, and the particular detailed investigation is still lacking. To the best of our knowledge, among these works, only one work, which was carried out by Park and Hrnjak [11], reported the effect of all parameters.

Although some information is currently available, there still remains room for further research. In the present study, the working fluid and the test section used are different from those used by the previous study. The effects of all involved parameters are presented for condensing flow, including mass flux, heat flux, saturation temperature, and vapor quality on the pressure drop characteristics, which have never before appeared in the available literature.

2. Apparatus and method

The schematic diagram of the experimental setting, which is also used in the flow boiling heat transfer and pressure drop in the multiport minichannel study [13,14], is presented in Fig. 1. The main system components consisted of the refrigerant loop, cooling water loop, subcooling loop, data acquisition system, and test section.

For the refrigerant circulating loop, as shown in Fig. 1, the liquid refrigerant is pumped by a gear pump through a filter and dryer, refrigerant flow meter, preheater, inlet sight glass tube, test section, again to the outlet sight glass tube, and plate heat exchanger. Then, it is collected in a receiver tank and returned to the refrigerant gear pump to complete the cycle. The refrigerant flow rate is controlled by a gear pump that can be regulated by an inverter. The desired inlet quality of the test section is controlled by the

Please cite this article in press as: K. Sakamatapan, S. Wongwises, Pressure drop during condensation of R134a flowing inside a multiport minichannel, Int. J. Heat Mass Transfer (2014), http://dx.doi.org/10.1016/j.ijheatmasstransfer.2014.02.071

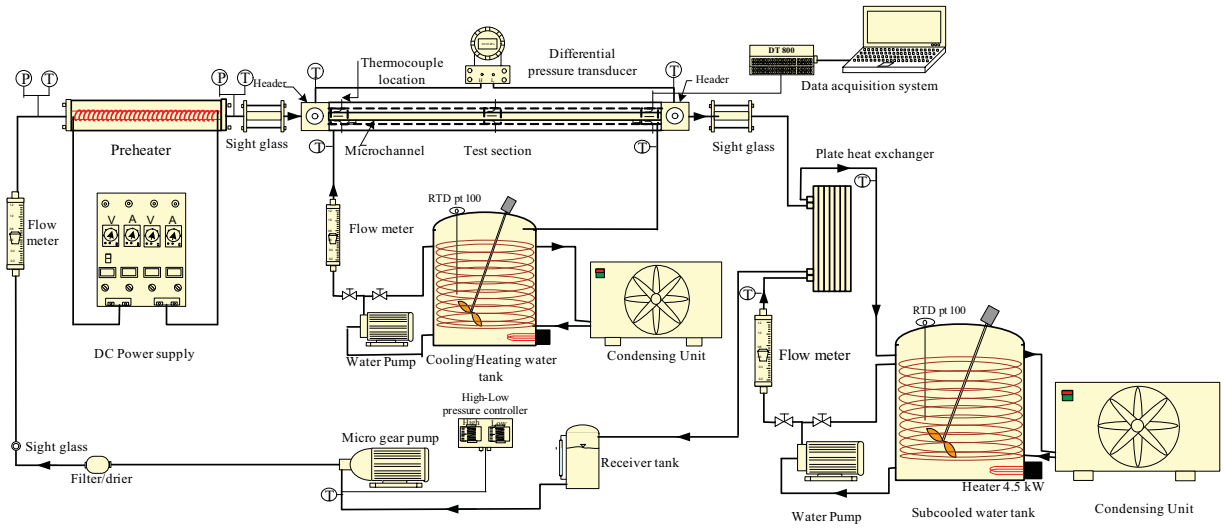

Fig. 1. Schematic diagram of the experimental apparatus. [Sakamatapan et al. [22], with permission from Elsevier]

preheater. A DC power supply is used to supply power to the preheater, which can be controlled by adjusting the supply voltage and current. After leaving the test section, the two-phase refrigerant condenses to a liquid phase in the plate heat exchanger by transferring its heat to the subcooling water loop. To monitor the state of the refrigerant, all of the signals from the thermocouples and differential pressure transducer are collected by a data acquisition. All instruments are installed at various positions, which is clearly seen in Fig. 1.

Fig. 2 shows a schematic diagram of the test section for this study, and the test section is designed as a counter flow tube in the tube heat exchanger with refrigerant flowing in the multiport minichannel and cooling water flowing in the annular gap. The multiport minichannel is aluminum that has 14 channels with a 1.1 mm hydraulic diameter (Type 1) and 8 channels with a 1.2 mm hydraulic diameter (Type 2). The outer tube is made from 12 mm thick clear acrylic and is designed as a rectangular annulus, which is used to absorb heat flux from the tested tubes. The photographs of these multiport minichannels are presented in Fig. 3. In addition, the inlet and outlet saturation temperatures are measured by T-type thermocouples installed at the inlet and outlet points of the test section headers. For measuring the pressure drop, which goes 250 mm across the test section, a differential pressure transducer, which has an accuracy of the differential pressure drop, is ±0.25% of the full scale, or ±0.125 kPa is installed on the other side of the header. The thermocouples are also installed at the inlet and outlet of the water channel to measure the inlet and outlet cooling water temperatures. Moreover, the test section is composed of rubber foam with 0.04 W/m K of thermal conductivity, which provides thermal insulation for this section. The refrigerant flow meter is a variable-area type. The flow meter is specially calibrated in the range of 0.2–1.8 LPM for R134a by the manufacturer. The tested conditions are presented in Table 1. The details of the test section are presented in Table 2. The accuracies of the direct measurements and the uncertainties in the derived experimental values determined by standard method are shown in Table 3.

3. Data reduction

The data reduction is provided for determining the average vapor quality as well as the pressure gradient components of the measured data.

The average vapor quality between the inlet and the outlet vapor quality of the test section can be calculated from the relation

$$x_{ave} = \frac{x_{TS,in} + x_{TS,out}}{2} \quad (1)$$

where $i_{TS,in}$ is the refrigerant enthalpy at the test section inlet, and $i_{TS,out}$ is the refrigerant enthalpy at the test section outlet.

The inlet vapor quality of the test section is determined as follows:

$$x_{TS,in} = \frac{i_{TS,in} - i_{l@TS,in}}{i_{lv@TS,in}} \quad (2)$$

where $i_{l@TS,in}$ is the enthalpy of saturated liquid refrigerant based on the temperature at the test section inlet, and $i_{lv@TS,in}$ is the enthalpy of vaporization based on the temperature at the test section inlet, which is given by

$$i_{TS,in} = i_{l@ph} + \frac{\dot{Q}_{lat}}{\dot{m}_{ref}} \quad (3)$$

where $i_{l@ph}$ is the enthalpy of the saturated liquid refrigerant based on saturation temperature at the preheater, $\dot{m}_{ref}$ is the mass flow rate of the refrigerant, and $\dot{Q}_{lat}$ is the latent heat transfer rate in the preheater, which is calculated as follows:

$$\dot{Q}_{ph} = \dot{Q}_{lat} + \dot{Q}_{sen} \quad (4)$$

where $\dot{Q}_{ph}$ is the electrical power from a heater to the refrigerant flowing through the pre-heater, and $\dot{Q}_{sen}$ is the sensible heat transfer rate in the pre-heater, which is defined as

$$\dot{Q}_{ph} = (VI)_{@ph} \quad (5)$$

$$\dot{Q}_{sen} = \dot{m}_{ref} c_{ref} \left(T_{ph,out} - T_{ph,in}\right) \quad (6)$$

The outlet vapor quality of the test section is also determined from

$$x_{TS,out} = \frac{i_{TS,out} - i_{l@TS,out}}{i_{lv@TS,out}} \quad (7)$$

where $i_{TS,out}$ is the refrigerant enthalpy at the test section outlet, $i_{l@TS,out}$ is the enthalpy of saturated liquid refrigerant based on the temperature of the test section outlet, and $i_{lv@TS,out}$ is the enthalpy of vaporization. As a consequence, the enthalpy of the refrigerant flow at the test section outlet can be determined from

$$i_{TS,out} = i_{TS,in} - \frac{\dot{Q}_{TS}}{\dot{m}_{ref}} \quad (8)$$

Please cite this article in press as: K. Sakamatapan, S. Wongwises, Pressure drop during condensation of R134a flowing inside a multiport minichannel, Int. J. Heat Mass Transfer (2014), http://dx.doi.org/10.1016/j.ijheatmasstransfer.2014.02.071

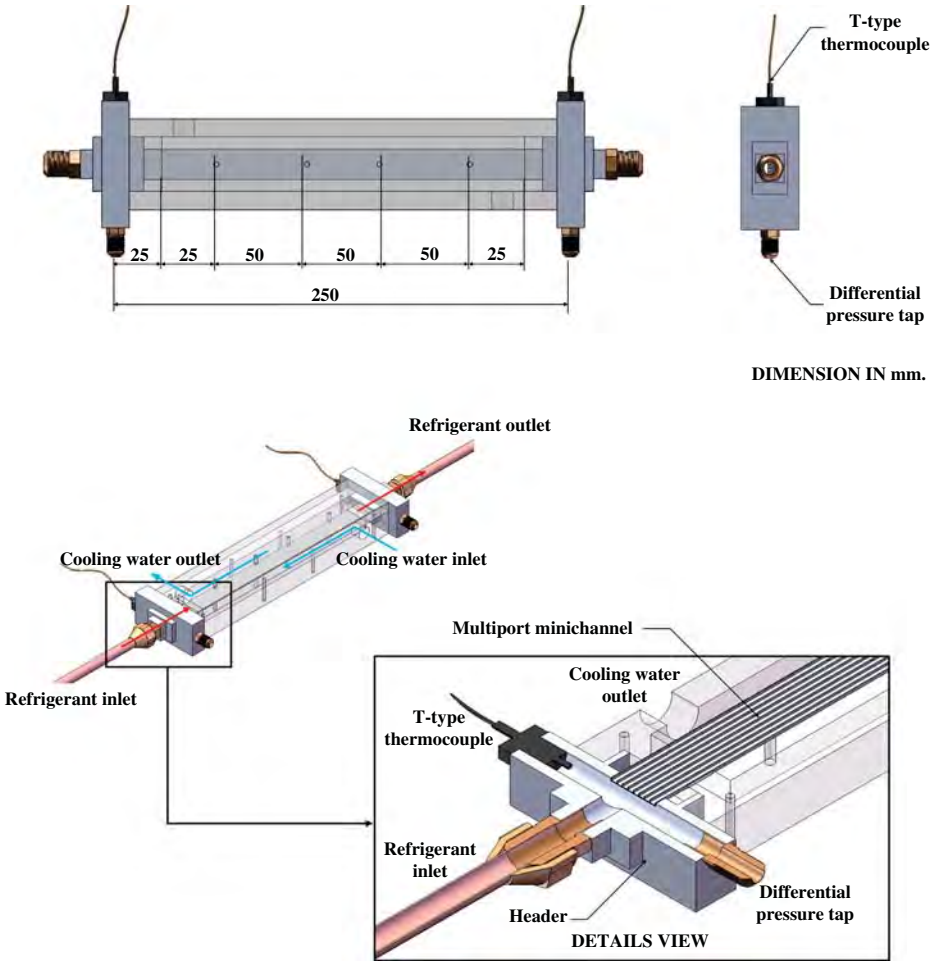

Fig. 2. Schematic diagram of the test section. [Sakamatapan et al. [22], with permission from Elsevier]

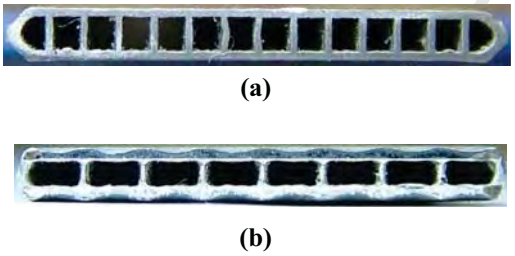

Fig. 3. Photographs of cross section of the multiport minichannels: (a) Type 1 (d_h = 1.1 mm, n = 14), (b) Type 2 (d_h = 1.2 mm, n = 8). [Sakamatapan et al. [22], with permission from Elsevier]

Table 1
The experimental conditions.

Refrigerant	R134a
Hydraulic diameter (mm)	1.1 and 1.2
Number of channels, (N)	8 and 14
Mass flux (kg/m^2 s)	340–680
Heat flux (kW/m^2)	15–25
Saturation temperature (°C)	35–45
Average vapor quality	0.1–0.8
• Inlet vapor quality	0.15–0.85
• Outlet vapor quality	0.05–0.75

where $\dot{Q}_{TS}$ is obtained from the heat and absorbed from the refrigerant to the cooling water, which can be calculated from

$$\dot{Q}_{TS} = \dot{m}_w c_w (T_{w,out} - T_{w,in}) \quad (9)$$

The total pressure drop is the summation of the frictional pressure drop, the sudden contraction and sudden expansion pressure drop due to the headers at the inlet and outlet of the test section, and the momentum or acceleration pressure drop, which can be expressed as follows:

$$\Delta P_{tot} = \Delta P_f + \Delta P_{exp} + \Delta P_{cont} + \Delta P_a \quad (10)$$

The sudden expansion pressure drop at outlet of multiport minichannel is calculated using Eq. (11) [15].

$$\Delta P_{exp} = G^2 \sigma (1-\sigma) v_l \left[\frac{(1-x)^2}{(1-\alpha)^2} + \left(\frac{v_v}{v_l}\right) \frac{x^2}{\alpha} \right] \quad (11)$$

Please note that void fraction is assumed as a constant in Eq. (11).

For the homogeneous model, the sudden contraction pressure drop at inlet of multiport minichannel is calculated from Eq. (12) [15].

$$\Delta P_{cont} = \frac{G^2 v_l}{2} \left[\left(\frac{1}{C_c} - 1 \right)^2 + \left(1 - \frac{1}{\sigma^2} \right) \right] \left[1 + \left(\frac{v_{lv}}{v_l} \right) x \right] \quad (12)$$

where σ is area ratio, and C_c is the coefficient of contraction which is a function of σ.

Please cite this article in press as: K. Sakamatapan, S. Wongwises, Pressure drop during condensation of R134a flowing inside a multiport minichannel, Int. J. Heat Mass Transfer (2014), http://dx.doi.org/10.1016/j.ijheatmasstransfer.2014.02.071

Table 2
The details of multiport minichannel.

Type	Hydraulic diameter (mm)	Number of channels	Channel width (mm)	Channel height (mm)	Aspect ratio	Outer surface (mm^2)	Surface roughness (μm)
1	1.1	14	1	1.25	1.25	5797.5	0.20
2	1.2	8	1.8	1.8	0.5	6171	0.18

Table 3
The accuracies of the direct measurements and the uncertainties in the derived experimental values.

Parameter	Uncertainty
Temperature (°C)	±0.1
Mass flow rate of refrigerant (kg/s)	±2.4%
Differential pressure transducer (kPa)	±125
Heat transfer rate of test section (kW)	±14%
Average quality (–)	±8.6%
Frictional pressure gradient (kPa/m)	±6.4%

Finally, the momentum or acceleration pressure drop is the loss due to the change in quality across the test section, the following equation recommended by Carey [16] is used.

$$\Delta P_a = G^2 \left\{ \left[\frac{(1-x)^2}{\rho_l(1-\alpha)} + \frac{x^2}{\rho_v \alpha} \right]_{out} - \left[\frac{(1-x)^2}{\rho_l(1-\alpha)} + \frac{x^2}{\rho_v \alpha} \right]_{in} \right\} \quad (13)$$

where the void fraction α can be determined by the Zivi [17] correlation, which is expressed as follows:

$$\alpha = \frac{1}{1 + \frac{(1-x)}{x}\left(\frac{\rho_v}{\rho_l}\right)^{2/3}} \quad (14)$$

The frictional pressure gradient can be determined by subtracting the sudden expansion, sudden contraction, and momentum pressure drop into the terms of the total measured pressure drop and dividing the length of multiport minichannel.

4. Results and discussion

The pressure gradient during condensation of R134a flowing inside multiport minichannel from this study under the condition: mass flux 340–680 kg/m^2 s, heat flux 15–25 kW/m^2, and saturation temperature 35–45 °C is presented and discussed in this topic.

It should be noted that the flow pattern of this study was an annular flow, which was predicted by a flow pattern map of Soliman [18], Coleman and Garimella [19,20], and Garimella [21], as presented in the study of condensation heat transfer characteristic inside multiport minichannel [22].

4.1. The pressure gradient components

The total pressure gradient can be expressed as the sum of the four terms of the frictional pressure drop, the sudden contraction pressure drop, the sudden expansion pressure drop, and the momentum or acceleration pressure drop.

The components of the pressure drop with the variation of heat fluxes at the mass flux of 350 kg/m^2 s and saturation temperature of 40 °C are presented in Fig. 4. The results showed that the total pressure drop was dominated by the frictional pressure drop, which was approximately 79.42% of total pressure gradient. It was also found that the sudden contraction pressure drop, the sudden expansion pressure drop, and the momentum pressure drop amount was 22.35%, 4.21%, and 5.98% of total pressure drop, respectively.

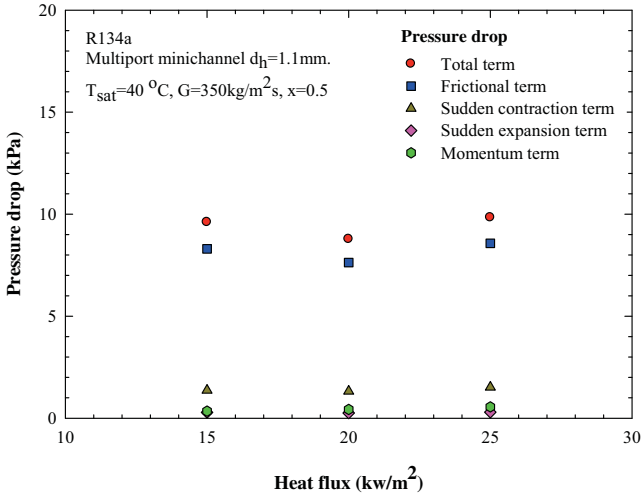

Fig. 4. Heat flux vs. total pressure gradient for various mass fluxes.

4.2. The frictional pressure gradient

Fig. 5 shows the frictional pressure gradient as a function of vapor quality with variation of mass fluxes. It was found that the increasing mass flux had a significant effect on the increase of frictional pressure gradient. Moreover, it was also demonstrated that the frictional pressure gradient increased with the augmentation of vapor quality. The increase of the frictional pressure gradient was due to the effects of higher shear stress. The increasing mass flux and the increasing vapor quality have a direct effect on higher flow velocity and flow velocity differences between liquid and vapor phase. Consequently, it leads to an increase in wall shear stress and interfacial shear, which results in frictional pressure gradient increase.

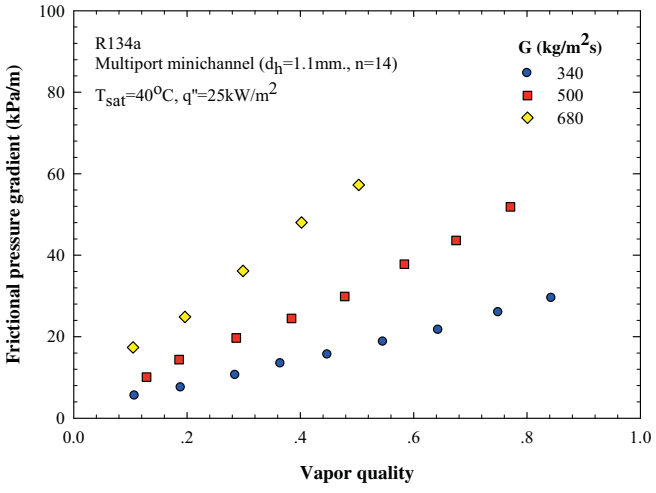

Fig. 5. Average vapor quality vs. frictional pressure gradient for various mass fluxes.

Please cite this article in press as: K. Sakamatapan, S. Wongwises, Pressure drop during condensation of R134a flowing inside a multiport minichannel, Int. J. Heat Mass Transfer (2014), http://dx.doi.org/10.1016/j.ijheatmasstransfer.2014.02.071

The present study, as shown in Fig. 6, shows the variation of frictional pressure gradient in vapor quality for different heat fluxes. It can be clearly seen that the heat flux had an insignificant effect on the frictional pressure gradient. These phenomena may occur from the increase of heat flux, presenting a minimal effect on the viscosity and velocity of the flowing refrigerant.

The influence of saturation temperature on the frictional pressure gradient is presented in Fig. 7. The results showed that the frictional pressure gradient increased with the decreasing saturation temperature. Consider that the property of refrigerant under saturation temperature decreased from 45 to 35 °C. The viscosity ratio (μ_l/μ_v) increased from 11.93 to 14.18, and the density ratio (ρ_l/ρ_v) decreased from 19.51 to 26.88, which makes the quantity of shear stress higher. Therefore, this occurrence causes a frictional pressure gradient increase.

The measured frictional pressure gradient between the two different tubes in all of the similar tested conditions was also compared, as shown in Fig. 8. The frictional pressure gradient of the multiport minichannel of Type 1 was higher than those of Type 2 about 16.4%. The refrigerant velocities in the multiport minichannel of Type 1 are equal to those in Type 2; however, due to the smaller hydraulic diameter, a higher frictional pressure gradient in multiport minichannel Type 1 is obtained.

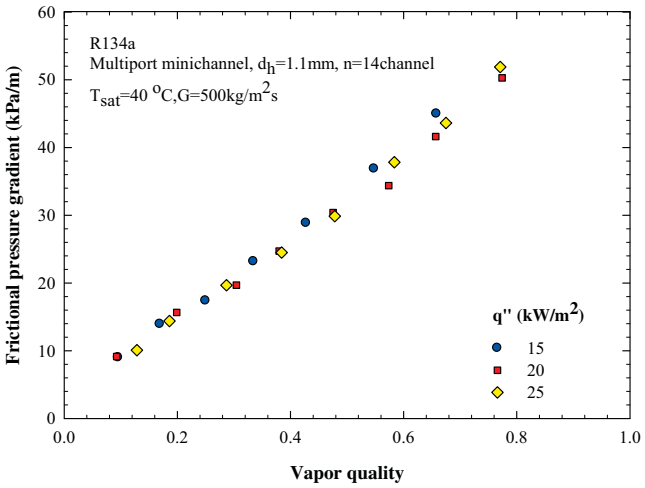

Fig. 6. Average vapor quality vs. frictional pressure gradient for various heat fluxes.

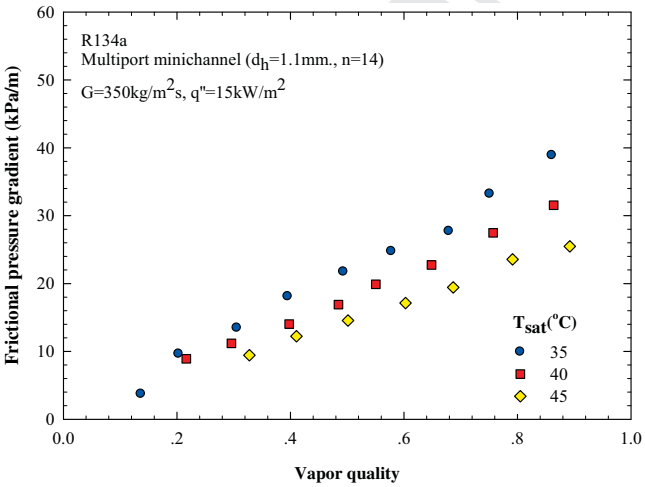

Fig. 7. Average vapor quality vs. frictional pressure gradient for various saturation temperature.

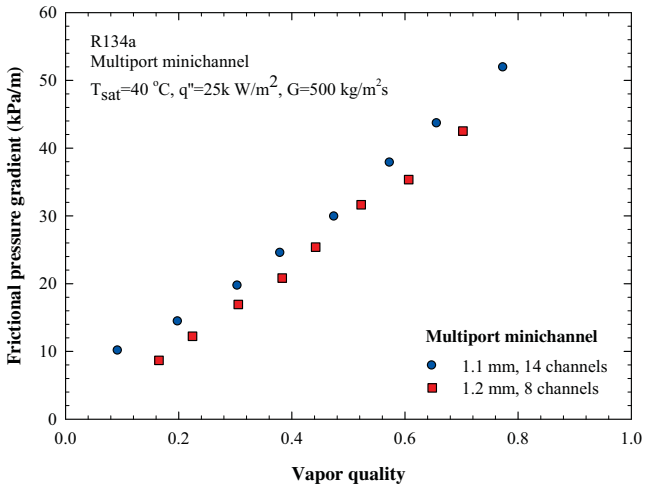

Fig. 8. Comparison of frictional pressure gradient between multiport minichannel Type 1 and multiport minichannel Type 2.

4.3. The comparison with the existing correlations

Experimental data were compared against the five well-known correlations that were particularly developed for predicting frictional pressure gradient in minichannels in both single and multiport, which were proposed by Chen et al. [23], Zhang and Webb [24], Garimella et al. [25], Cavallini et al. [26], Cavallini et al. [30], and Bodal et al. [31]. The available experimental information of the correlations is reviewed in Table 4.

Chen et al. [23] informed the effects of surface tension and gravity by conducting the Bond number and the Webber number of the Friedel correlation [5], when this was used for their single minichannel correlation. The comparison with the Chen et al. correlation [23] is presented in Fig. 9. The Chen et al. [23] correlation underestimated the experimental data as 94% of data had 50% of the errors. The frictional pressure drop in multiport minichannel correlation of Zhang and Webb [24] was also done by including the reduced pressure into the Friedel correlation [5]. In Fig. 10, the Zhang and Webb correlation [24] could predict 72% of the data with ±30% error. Garimella et al. [25] developed the correlation for pressure drops during condensation by combining the correlation of the intermittent flow model and annular flow in both circular and non-circular microchannel, and 87% of the predicted data falling within the ±20% error band as presented in Fig. 11. The correlation was developed by Cavallini et al. [26], which was interpolated from Cavallini et al. [27], Coleman [28], and Zhang [29] regarding the frictional pressure gradient in minichannel correlations. The results of this work found that 82% of the data calculated by the Cavallini et al. [26] correlation was within a ±20% error rate, as shown in Fig. 12. Fig. 13 shows an experimental frictional pressure gradient plotted against predicted frictional pressure gradient obtained from Cavallini et al. [30]. The correlation was improved from the previous one (Cavallini et al. [26]) by including the effect of surface roughness. The plot shows that 71% of the data fall within ±20% of the correlation. Over 75.5% of the calculated data was within 50% of the error rate by comparing with the Bohdal et al. [31] correlation, which was based on the refrigerant R134a and R404A condensing flow in singleport minichannel, as reported in Fig. 14.

4.4. New proposed correlation

To predict the frictional pressure gradient of R134a flowing inside the multiport minichannel, the correlation of the two-phase fiction factor is proposed in this topic. The correlation is one of

Please cite this article in press as: K. Sakamatapan, S. Wongwises, Pressure drop during condensation of R134a flowing inside a multiport minichannel, Int. J. Heat Mass Transfer (2014), http://dx.doi.org/10.1016/j.ijheatmasstransfer.2014.02.071

Table 4
The available experimental information of the correlations.

Author(s)	Working fluid	Hydraulic diameter (mm)	Channel/orientation/conditions	Rang/ applicability
Chen et al. [23]	Air–water	1.02, 3.17, 5.05, 7.02	Single minichannal/horizontal/adiabatic	Room temperature G = 50–3000 kg/ m^2 s x = 0.001–0.9
	R410A	3.17, 5.05, 7.02, 9		T_{sat} = 5, 15 °C G = 50–600 kg/ m^2 s x = 0.1–0.9
Zhang and Webb [24]	R22, R134a and R404A	2.13	Multiport minichannel/horizontal/adiabatic	T_{sat} = 20–65 °C G = 200–1000 kg/ m^2 s
Garimella et al. [25]	R134a	0.5–4.91	Multiport minichannel/horizontal/condensation	T = 52 °C x = 0–1 G = 150–750 kg/ m^2 s
Cavallini et al. [26] and [30]	R236ea, R134a and R410A		Smooth multiport minichannel and rough singleport minichannel horizontal/adiabatic	T_{sat} = 40 °C G = 200–1400 kg/ m^2 s x = 0.25, 0.5, 0.75
Bohdal et al. [31]	R134a and R404A	0.31–3.3	Single minichannal/horizontal/condensation	T_{sat} = 20–40 °C G = 100–1300 kg/ m^2 s x = 0–1

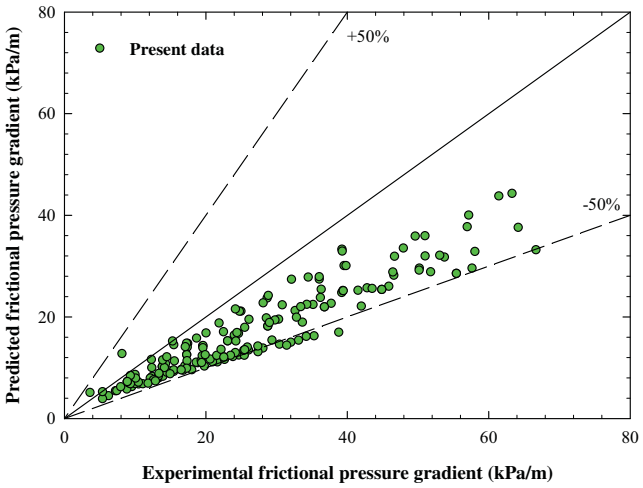

Fig. 9. Comparison of the experimental data with the correlation of Chen et al. [23].

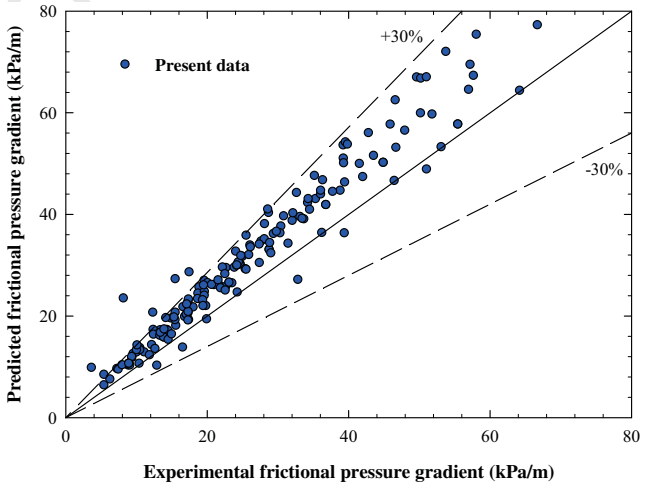

Fig. 10. Comparison of the experimental data with the correlation of Zhang and Webb [24].

the important equipment in order to design the condenser for automobile industrial usage.

Based on the dimensional analysis, the two-phase friction factor correlation was developed by using the equivalent Reynolds number concept of Akers et al. [2] to include the effect of the involved parameter.

The two-phase pressure gradient is calculated by the following equation based on the equivalent Reynolds number.

$$\left(\frac{\Delta P}{L}\right)_f = \frac{2f_{tp}Re_{eq}^2\mu_l^2}{\rho_l d_h^3} \tag{15}$$

where the equivalent Reynolds number is determined by

$$Re_{eq} = \frac{G_{eq}d_h}{\mu_l} \tag{16}$$

and equivalent mass flux is defined as

$$G_{eq} = G\left[(1-x) + x\sqrt{\frac{\rho_l}{\rho_v}}\right] \tag{17}$$

Finally, the two-phase friction factor as a function of the equivalent Reynolds number was fitted to the following correlation:

$$f_{tp} = 6977\mathrm{Re}_{eq}^{-0.337}x^{-0.031}\left[\frac{\rho_l}{\rho_v}\right]^{6.510}\left[\frac{\mu_l}{\mu_v}\right]^{-11.883} \tag{18}$$

Fig. 15 shows the experimental two phase friction factor plotted against the predicted two-phase friction factor calculated from the proposed correlation. It was found that 90% of data fell within a deviation of 20%.

5. Conclusion

The flow characteristics of R134a during the condensing flow inside the multiport minichannel are some of the essential factors

Please cite this article in press as: K. Sakamatapan, S. Wongwises, Pressure drop during condensation of R134a flowing inside a multiport minichannel, Int. J. Heat Mass Transfer (2014), http://dx.doi.org/10.1016/j.ijheatmasstransfer.2014.02.071

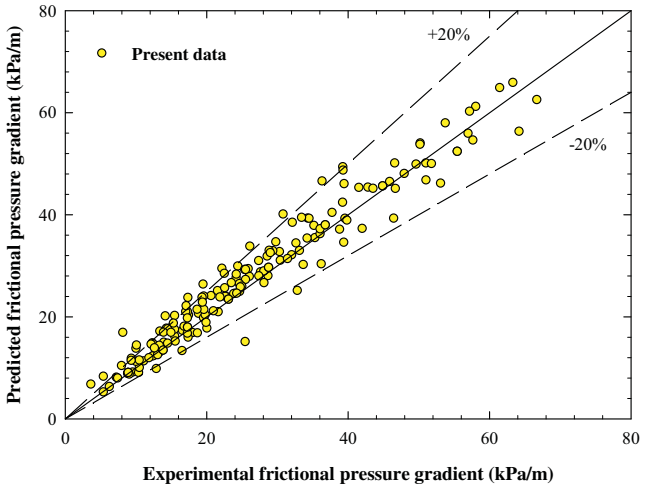

Fig. 11. Comparison of the experimental data with the correlation of Garimella et al. [25].

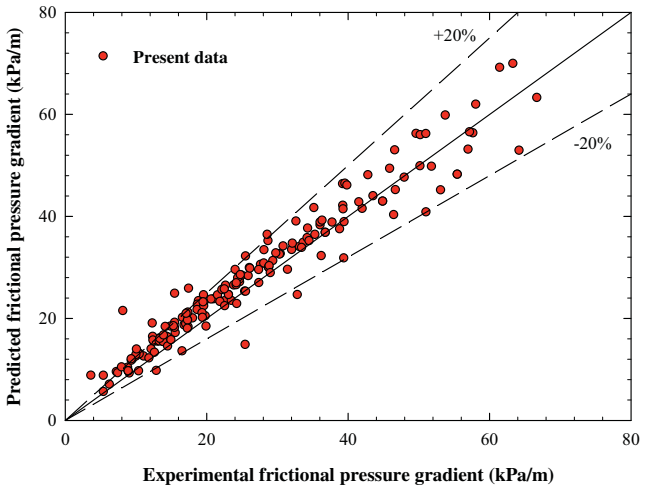

Fig. 12. Comparison of the experimental data with the correlation of Cavallini et al. [26].

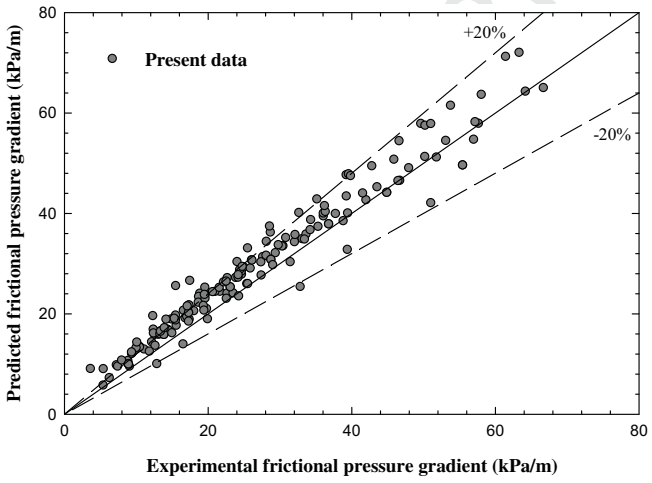

Fig. 13. Comparison of the experimental data with the correlation of Cavallini et al. [30].

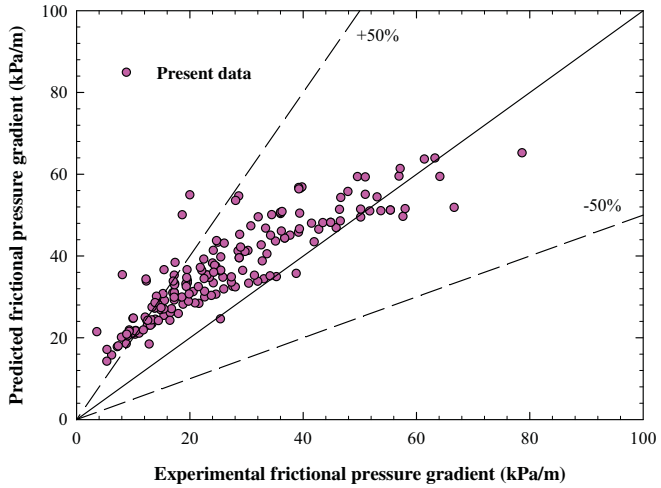

Fig. 14. Comparison of the experimental data with the correlation of Bohdal et al. [31].

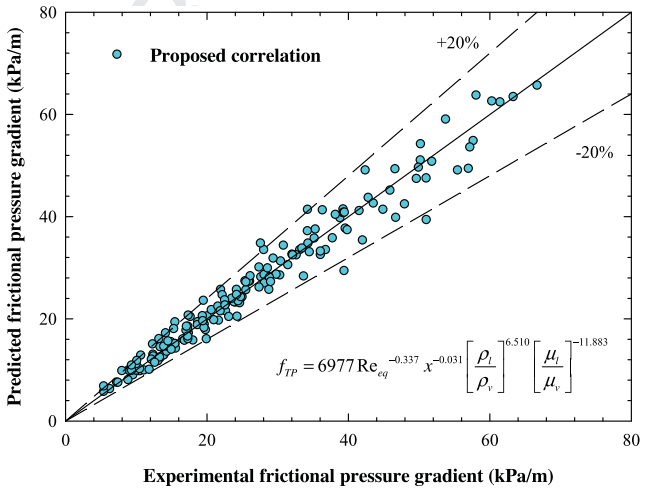

Fig. 15. Comparison of measured with predicted frictional pressure gradient using proposed correlation of two phase friction factor.

of designing the condenser in the automotive air conditioning system. The friction is the main cause of the total pressure drop as the frictional pressure drop, which is 79.42% of the total pressure drop. There are four flow parameters that have an influence on the increase of the frictional pressure gradient, which are increasing the mass flux and vapor quality and decreasing the saturation temperature and size of the channel.

The measured frictional pressure gradient is compared with two types of correlations that were developed for single minichannel and three correlations, specially developed for the multiport minichannel. There are only multiport minichannel correlations that give an accurate prediction, which was not to exceed 20% of the error rate when compared with the measured data. Correlations for the single minichannel give an imprecise prediction with the measured data.

The correlation of the two-phase friction factor for the multiport minichannel under dimension analysis is proposed by using the equivalent Reynolds number to correlate the effects of involved parameters.

Acknowledgement

The authors would like to express their appreciation to the National Science and Technology Development Agency, the Thailand

Please cite this article in press as: K. Sakamatapan, S. Wongwises, Pressure drop during condensation of R134a flowing inside a multiport minichannel, Int. J. Heat Mass Transfer (2014), http://dx.doi.org/10.1016/j.ijheatmasstransfer.2014.02.071

Research Fund and the National Research University Project for providing financial support for this study.

References

[1] C.Y. Yang, R.L. Webb, Friction pressure drop of R-12 in small hydraulic diameter extruded aluminum tubes with and without micro-fins, Int. J. Heat Mass Transfer 39 (1996) 801–809.
[2] W.W. Akers, H.A. Deans, O.K. Crosser, Condensation heat transfer within horizontal tubes, Chem. Eng. Prog. Symp. Ser. 55 (1959) 171–176.
[3] M. Zhang, R.L. Webb, Correlation of two-phase friction for refrigerant in small-diameter tubes, Exp. Therm. Fluid Sci. 25 (2001) 131–139.
[4] P.R.H. Blassius, Das Aehnlichkeitsgesetz bei Reibungvorgangen in Flussigkeiten, Forschungsheft 131 (1913) 1–41.
[5] L. Friedel, Improved friction pressure drop correlations for horizontal and vertical two-phase pipe flow, in: Proceedings of the European Two Phase-Flow Group Meeting, Ispra, Itary, 1979.
[6] S. Koyama, K. Kuwahara, K. Nakashita, K. Yamamoto, An experiment study on condensation of refrigerant R134a in a multi-port extruded tube, Int. J. Refrig. 24 (2003) 425–432.
[7] K. Mishima, T. Hibiki, Effect of inner diameter on some characteristics of air–water two-phase flows in capillary tubes, Trans. JSME 61 (1995) 99–106.
[8] H. Haraguchi, S. Koyama, T. Fujii, Condensation of refrigerants HCFC22, HFC134a and HCFC123 in horizontal smooth tube, Trans. JSME 60 (1994) 245–252.
[9] A. Cavallini, D. Del Col, L. Doretti, M. Matkovic, C. Zilio, Two-phase friction pressure gradient of R236ea, R134a and R410A inside multi-port mini-channels, Exp. Therm. Fluid Sci. 29 (2005) 861–870.
[10] S. Garimella, A. Agarwal, J.D. Killion, Condensation pressure drop in circular minichannels, Heat Transfer Eng. 26 (2005) 1–8.
[11] C.Y. Park, P. Hrnjak, CO_2 flow condensation heat transfer and pressure drop in multi-port microchannels at low temperatures, Int. J. Refrig. 32 (2009) 1129–1139.
[12] J. Heo, H. Park, R. Yun, Condensation heat transfer and pressure drop characteristic of CO_2 in microchannel, *Int. J. Refrig.* (in press).
[13] J. Kaew-On, K. Sakamatapan, S. Wongwises, Flow boiling heat transfer of R134a in the multiport minichannel heat exchangers, Exp. Therm. Fluid Sci. 35 (2011) 364–374.
[14] J. Kaew-On, K. Sakamatapan, S. Wongwises, Flow boiling pressure drop of R134a in the counter flow multiport minichannel heat exchangers, Exp. Therm. Fluid Sci. 36 (2012) 107–117.
[15] J.G. Colliier, J.R. Thome, Convective Boiling and Condensation, third ed., Oxford University Press, Oxford, UK., 1994.
[16] V.P. Carey, Liquid–Vapor Phase-change Phenomena, second ed., Taylor and Francis, New York, USA, 2007.
[17] S.M. Zivi, Estimation of steady-state steam void-fraction by mean of the principle of minimal entropy production, Trans. ASME J. Heat Transfer 86 (1964) 247–252.
[18] H.M. Soliman, Mist-annular transition during condensation and its influence on the heat transfer mechanism, Int. J. Multiphase Flow 12 (1986) 277–288.
[19] J.W. Coleman, S. Garimella, Characterization of two-phase flow patterns in small diameter round and rectangular tubes, Int. J. Heat Mass Transfer 42 (1999) 2869–2881.
[20] J.W. Coleman, S. Garimella, Two-phase flow regime transition in microchannel tubes: the effect of hydraulic diameter, ASME HTD 366 (2000) 71–83.
[21] S. Garimella, Condensation flow mechanisms in microchannels: basis for pressure for pressure drop and heat transfer models, Heat Transfer Eng. 25 (2004) 104–116.
[22] K. Sakamatapan, J. Kaew-On, A.S. Dalkilic, O. Mahian, S. Wongwises, Condensation heat transfer characteristics of R-134a flowing inside the multiport minichannels, Int. J. Heat Mass Transfer 64 (2013) 976–985.
[23] I.Y. Chen, K.S. Yang, Y.J. Chang, C.C. Wang, Two-phase pressure drop of air–water and R-410A in small horizontal tubes, Int. J. Multiphase Flow 27 (2001) 1293–1299.
[24] M. Zhang, R.L. Webb, Correlation of two-phase friction for refrigerants in small-diameter tubes, Exp. Therm. Fluid Sci. 25 (2001) 131–139.
[25] S. Garimella, A. Agarwal, J.D. Killion, Condensation pressure drop in circular microchannels, Heat Transfer Eng. 26 (2005) 1–8.
[26] A. Cavallini, L. Doretti, M. Matkovic, L. Rossetto, Update on condensation heat transfer and pressure drop inside minichannels, Heat Transfer Eng. 27 (2006) 74–87.
[27] A. Cavallini, D. Del Col, L. Doretti, M. Matkovic, L. Rossetto, C. Zilio, Measurement of Pressure Gradient during two-phase flow inside multi-port mini-channel, in: Third International Symposium on Two-phase Flow Modeling and Experimentation, Pisa, 2004, pp. 22–24.
[28] J.W. Coleman, Flow visualization and pressure drop for refrigerant phase change and air–water flow in small hydraulic diameter geometries (Ph.D. thesis), Iowa State University, Ames, Iowa, 2009.
[29] M. Zhang, A new equivalent Reynolds number model for vapor shear-controlled condensation inside smooth and micro-fin tubes (Ph.D. thesis), The Pennsylvania State University, 1998.
[30] A. Cavallini, D. Del Col, M. Matkovic, L. Rossetto, Frictional pressure drop during vapour–liquid–liquid flow in minichannels: modelling and experimental evaluation, Int. Heat Fluid Flow 30 (2009) 131–139.
[31] T. Bohdal, H. Charun, M. Sikora, Comparative investigations of the condensation of R134a and R404A refrigerants in pipe minichannels, Int. J. Heat Mass Transfer 54 (2011) 1963–1974.

ELSEVIER SCIENCE

INTERNATIONAL JOURNAL OF HEAT AND MASS TRANSFER
INTERNATIONAL COMMUNICATIONS IN HEAT AND MASS TRANSFER

Professor W.J. Minkowycz
Editor-in-Chief
University of Illinois at Chicago
Mechanical Engineering (M/C 251)
842 West Taylor Street, 2049 ERF
Chicago, Illinois 60607-7022
Tel: (312) 996-3467
Fax: (312) 413-0447
E-mail: wjm@uic.edu

March 16, 2014

Dr. Somchai Wongwises
Fluid Mechanics, Thermal Engineering and Multiphase Flow Research Lab
King Mongkut's University of Technology
Thonburi, Bangmod, Bangkok 10140 Thailand
somchai.won@kmutt.ac.th

Subj: CJ14/5834 — "Measurement of Void Fraction of R-134a Flowing Through Horizontal Tube" by R. Srisomba, S. Wongwises

Dear Dr. Wongwises:

Thank you for the above-referenced manuscript which you have submitted for possible publication in the ***International Communications in Heat and Mass Transfer***. I am pleased to advise you that the reviews and recommendations to me from two members of the Board of Editors are favorable. I have also reviewed the paper carefully and find it to be of good quality. Indeed, the quality standard of the paper merits its acceptance for publication without further review and, therefore, I intend to accept your work for the journal.

Please note that the final revision cannot exceed 24 pages, using 1½ space typing, with each individual figure page (which can have separate figures such as Fig. 1, Fig. 2, Fig. 3, ..., properly positioned and cut-and-pasted on the page) being counted as one page of text. Papers using a font size smaller than 11 point will not be accepted. The entire manuscript must be typed in the *same* font face and the *same* font size. Also, please note that color illustrations cannot normally be hard-copy printed in a journal, unless paid by the author. The charge will be determined by the publisher.

Please proofread and revise your paper to make certain that all possible errors have been eliminated. **A Word, Word Perfect or a TeX copy of the manuscript must be included as an attachment by email. The enclosed Manuscript Acceptance Form must also be filled out and returned in a pdf format to this office.** Upon receipt of the above material, the publisher will then advise you of the publication schedule of your paper.

Please note the new revision submission instructions. Hard copy submissions are no longer accepted. Thank you for your cooperation and interest in the ***Communications*** journal.

Sincerely yours,

W.J. Minkowycz
Editor-in-Chief and
James P. Hartnett Professor of Mechanical Engineering

WJM:rms
enclosure

ELSEVIER
MANUSCRIPT ACCEPTANCE FORM

Name of Journal: ***INTERNATIONAL COMMUNICATIONS IN HEAT AND MASS TRANSFER***

Author *(Fill out and return)*

Corresponding author's name: S. Wongwises *Mandatory for Final Acceptance*

Please ensure that the following information is supplied for the corresponding author:

☐ E-mail address: _____

☐ Full postal address: _____

_____

_____

☐ Telephone: _____ ☐ Fax: _____

Checklist:

☐ Are the attachments and the final revised version of the manuscript identical?
☐ Are all text pages supplied?
☐ Are the keywords supplied? *(if appropriate for journal)*
☐ Are all original figures supplied, especially photographs?
☐ Are all figure captions supplied?
☐ Are all tables supplied?
☐ Are all tables captions supplied?
☐ Are copyright permission letters enclosed for any artwork/tables previously published, including those published on the world-wide-web?

If any of the illustrations are to be printed in colour please indicate this below:

Attachments

☐ Yes

Media format:
☐ PC
☐ Mac
☐ Other _____

Electronic text format:
☐ WordPerfect
☐ MS Word
☐ TeX
☐ Other _____

Editor-in-Chief

Name: *Professor W.J. Minkowycz*

Editorial manuscript ref. no: CJ 14/5834
(please ensure this reference is also indicated on the manuscript)

Manuscript date details:
Date ms. received: 1/29/14
Date revised: _____
Date accepted: _____

Section of journal in which manuscript is to appear:
(If applicable)

Editor's Notes *(please indicate any special instructions or requirements)*

Manuscript type:
(please tick one box)
☐ Book review
☐ Correspondence
☐ Discussion
☐ Erratum
☒ Full length article
☐ Review article
☐ Short communication
☐ Other _____

Editor's signature _____ Date _____